UNIVERSITY OF ADELAIDE
19·8·92
LIBRARY

Barotropic depth-averaged and three-dimensional tidal programs for shallow seas

by

Peter John Bills, B.Sc (Hons) (Math.Sc)

Thesis submitted for degree of
Doctor of Philosophy at the
The University of Adelaide

Department of Applied Mathematics



September, 1991

Signed statement

I hereby declare that this thesis contains no material which has been accepted for the award of any other degree or diploma in any University and that, to the best of my knowledge and belief, the thesis contains no material previously published or written by any other person, except where due reference is made in the text of the thesis.

If accepted for the award of the degree, I give my consent that this thesis be made available for photocopying and loan.

Peter John Bills

Acknowledgements

I wish to thank my supervisor, Assoc. Prof. John Noye, for his indefatigable support, encouragement and enthusiasm throughout the development of this work and its reporting. I also thank him for his accessibility at all hours in considering aspects of the work, and the many hours spent in discussion and proof-reading.

Many thanks are also due to David Beard for extraordinary support and assistance with computing over the years, from VAX's to SPARC's, VMS to UNIX ... for the use of his plotting programs, the tidal versions of which he and Bill Mitchell put together ... for fixing things at nights, weekends and public holidays, and from home via modem.

Special thanks to Dr. Paul Blythe and Libby Blythe for consistent support and encouragement through the period of this work. Paul was instrumental in encouraging me to commence this PhD and offered helpful perspectives on the "PhD process" throughout.

Thank you to John Nixon for expert, prompt and thorough proof-reading beyond any expectation.

Thank you to Prof. G. W. Lennon for several useful critical discussions concerning aspects of the work. Thank you also for the provision of tidal constants and ellipse characteristics through the National Tidal Facility. These have been essential to the work.

Thanks to Bill Mitchell for proof-reading Chapter 5 and many helpful discussions over the years concerning tidal dynamics and physical oceanography.

Thanks also to Dr. Alan Easton for some useful suggestions concerning time-centring the Coriolis terms, and possible consequences to Ward Spit in the event of mean sea level rises. Thanks also for the use of the tidal analysis programs! Thanks to Dr. David Provis for suggesting I align the model with the axis of the Gulf. Thanks to Dr. Doug Sweet and Dr. Sylvan Elhay for discussions concerning filtering of grid-scale waves. Thanks also to Dr. Hugh Possingham for some polished proof-reading.

Thanks to Dr. K. T. Jung for practical discussions on tidal modelling, Dr. R. J. Arnold for his general encouragement and Peter Steinle for the use of his von Neumann stability analysis programs used in Chapter 6.

Thanks to Dr. Malcolm Stevens for numerous discussions and practical assistance with the "writing-up" process, and the inset map used in Figure 8.1.

Special thanks to my sister, Margaret-Anne Cowley, for typing drafts for Chapters 4, 6 and 7, and thanks to my parents who were always there, offering firm support.

I also wish to acknowledge the friendship of several special friends especially in the last stages of this work: Cecily Orenstein, Stewart Clarke and Nerida Russell. Many others are not named but they know who they are!

Thanks to the lecturing, tutoring and professional support and secretarial staff of the Department of Applied Mathematics, The University of Adelaide, for providing the space, work environment and facilities so necessary, especially during the last couple of months.

I wish to also acknowledge the financial assistance of the South Australian Department of Transport in the early years of this work and their provision of a postgraduate scholarship: thanks to David Bray, Margaret Starrs and Mike Phillipson who took a keen interest in my progress.

Contents

Glossary of Symbols iv

List of Figures xiv

List of Tables xxi

Summary xxiii

1 Introduction 1

2 Mathematical Formulation 7
- 2.1 Introduction . . . 7
- 2.2 The three-dimensional equations . . . 7
- 2.3 The depth-averaged equations . . . 15
- 2.4 Summary . . . 16

3 Finite Difference Formulation 17
- 3.1 Introduction . . . 17
- 3.2 The finite difference grid . . . 18
- 3.3 The computational scheme . . . 22
- 3.4 The finite difference expressions . . . 24
- 3.5 The element classification scheme . . . 33
- 3.6 Subordinate approximation for advective and diffusive terms near boundaries 54
- 3.7 Summary . . . 69

4 Analytical and numerical verification of program code 71
- 4.1 Introduction . . . 71
- 4.2 Lynch and Gray 1D linear solutions . . . 72
  - 4.2.1 Case 1: Estuary with constant depth . . . 72
  - 4.2.2 Case 1: Numerical tests . . . 74
  - 4.2.3 Case 1: Wave propagation characteristics . . . 78
  - 4.2.4 Case 2: Estuary with parabolic depth profile . . . 83
  - 4.2.5 Case 2: Numerical tests . . . 85
- 4.3 Knight 1D approximate non-linear solution . . . 87
  - 4.3.1 Numerical tests . . . 90
- 4.4 Rienecker and Teubner 2D horizontal linear solution . . . 95
  - 4.4.1 Numerical tests . . . 97
  - 4.4.2 Wave propagation characteristics . . . 99

4.4.3 Wave propagation characteristics for a finite difference scheme used near an open boundary . . . 102
4.5 Johns' vertical and horizontal linear solution . . . 113
4.5.1 Numerical tests using Johns' vertical eddy viscosity . . . 119
4.5.2 The surface velocity approximation . . . 121
4.5.3 Numerical tests using a symmetric parabolic vertical eddy viscosity coefficient . . . 126
4.5.4 Wave propagation characteristics . . . 130
4.6 Summary . . . 136

5 A depth-averaged model of Spencer Gulf 140
5.1 Introduction . . . 140
5.2 Review of the literature . . . 142
5.3 Depth-averaged model of Spencer Gulf . . . 151
5.4 Calibrating the depth-averaged Spencer Gulf model . . . 156
5.5 Presentation of results and discussion . . . 170
5.6 Summary . . . 202

6 An investigation of open boundary conditions for tidal models of shallow seas 204
6.1 Introduction . . . 204
6.2 Benchmark solution . . . 207
6.3 Sommerfeld condition . . . 208
6.4 Orlanski-Sommerfeld condition . . . 211
6.5 Forcing strategies for the O-S condition . . . 216
6.6 Blumberg and Kantha condition . . . 217
6.7 Modified B&K condition . . . 221
6.8 Time varying the influence of the terms of the B&K condition . . . 223
6.9 Open boundary conditions and forcing . . . 226
6.10 Modified B&K conditions, revisited . . . 229
6.11 Second order accurate schemes for the O-S condition . . . 230
6.12 Discussion . . . 234
6.13 Summary . . . 236

7 A three-dimensional model of Spencer Gulf 237
7.1 Introduction . . . 237
7.2 Review of the literature . . . 237
7.3 Calibration of the model . . . 240
7.4 Presentation of results and discussion . . . 247
7.5 Summary . . . 288

8 A depth-averaged fine-grid model of Northern Spencer Gulf with tidal flats 292
8.1 Introduction . . . 292
8.2 Review of the literature . . . 293
8.3 The model of Northern Spencer Gulf . . . 295
8.4 Mathematical formulation of the tidal flat scheme . . . 295
8.5 Grid-scale waves . . . 301

8.6 Calibrating the model of Northern Spencer Gulf 304
8.7 Presentation of results and discussion 321
8.8 An application of the tidal flat model 335
8.9 Summary 343

9 Conclusions **346**

Bibliography **363**

Glossary of Symbols

Symbol	Meaning	Pg[1]
a	reduced eddy coefficient	26
$\widehat{a}$	magnitude of the complex amplitude of either the numerical or true wave	80
a_i^n	analytical elevation solution at position i, time level n	75
a_k, b_k, c_k, d_k	known coefficients and constants at gridpoint u_i, depth level k, time level $(n+1)$, in the implicit equation for solution of u^{n+1} field	27
a_m	amplitude of constituent m	13
a_m	coefficient of mth term in Fourier expansion	210
a^-	length of clockwise component of current vector	178
a^+	length of anticlockwise component of current vector	178
c	phase speed	14
c	$= \sqrt{gh_0}$, wave celerity for the Knight (1973) model	88
c	symbol for constituent	161
c_{10}	dimensionless drag coefficient depending on wind speed	13
d	Darcy coefficient (English)	87
e	exponential	72
e	symbol for a phase error	227
f	$= 2\Omega \sin \Phi$, formula for the Coriolis parameter	8
f_i	value of Coriolis parameter at the ζ_i gridpoint	26
f_m	amplitude correction factor for constituent m	13
g	acceleration due to gravity; assumed constant at 9.81 m/sec^2	9
h	distance of sea bed below mean sea level	8
hU	x-directed stream velocity (m^2/sec)	34
hV	y-directed stream velocity (m^2/sec)	34
h_a	average depth of the parabolic depth Lynch and Gray (1978) estuary over the interval $[x_1, x_2]$	85
h_b	mean sea level depth at element b on the open boundary	14
h_i	mean sea level depth at the ζ_i gridpoint	25
h_p	constant depth parameter for a Lynch and Gray (1978) model	72
h_0	constant depth value	72
h_2	parameter with dimension m^{-1} associated with the parabolic depth profile solution of Lynch and Gray (1978)	85

[1] Page on which symbol is explained, or first appears

i	index of the central computational Type 1 element	18
i–1	index of element to the "left" of the ith element	20
i+1	index of element to the "right" of the ith element	20
i+2	index of element to the "right" of the (i+1)th element	36
i_1	index of element "above" the ith element	20
i_1–1	index of element "above" and to the "left" of the ith element	20
i_1+1	index of element "above" and to the "right" of the ith element	20
i_{11}	index of element "above" the i_1th element	20
i_2	index of element "below" the ith element	20
i_2–1	index of element "below" and to the "left" of the ith element	20
i_2+1	index of element "below" and to the "right" of the ith element	20
i_{22}	index of element "below" the i_2th element	20
k	depth level index	20
k	constant linear friction coefficient with units m/sec ($=\tau h_0$, implicitly)	72
k	coefficient of linear friction	167
k	a dimensionless calibration constant (c.f. β calibration coefficient)	239
k_b	roughness height	169
k_m	wavenumber of mth Fourier mode	210
k_p	wavenumber (in direction θ) of the pth Fourier component	99
k_t	complex frequency of the numerical wave	78
$\widehat{k}_t$	complex frequency of the true wave	79
$\widehat{k}_t^{[p]}$	pth iterate for $\widehat{k}_t$	133
k_x	x-component of (real) wavenumber	78
k_y	y-component of (real) wavenumber	99
m	complex wavenumber of the Johns (1966) solution	115
m^*	dimensionless m	123
n	co-ordinate of outward normal direction $\underline{n}$	14
n	counter on the (present) time level of the tidal simulation	22
n	Manning roughness coefficient	170
n_1,n_2	complex exponents defined for the Johns (1966) solution	117
$\underline{n}$	vector normal to model coastline	12
$o_{c,s}$	observed amplitude or phase of constituent c at station s	161
p	pressure resulting from both the head of the fluid and atmospheric pressure	8
p	exponent specifying the depth profile of the Lynch and Gray (1978) analytical models	72
p_{a_i}	value of atmospheric pressure at the ζ_i gridpoint	26
$p_{c,s}$	predicted amplitude or phase of constituent c at station s	161
q	speed of the numerical wave	81
q	number of grid spacings in a wavelength	302
$\widehat{q}$	speed of the true wave	80
$q\|_{z=z^*}$	notation meaning that q is evaluated at (depth level) $z = z^*$	9
r	$= \Delta t/(2\Delta x)$, the maximum numerical speed of propagation	78
r	number of time steps in one period	303
r_k	$= \Delta\eta_{k-1}/\Delta\eta_k$, ratio of successive depth level spacings	26
r_1	coefficient relating the hydraulic radius to the mean depth	87
r_2	breadth/(mean depth) ratio of the Knight (1973) model	87

s	station	161
s	Wolf's (1983) σ-variable	239
s_1,s_2	complex exponents defined for the Lynch and Gray (1978) parabolic depth profile solution	83
t	time, measured relative to the start of the epoch, 00:00 hr on 1/1/1900 (G.M.T.)	8
t^*	dimensionless t	74
u, v, w	depth-dependent velocity components corresponding to the positive x, y, z directions	8
$\widehat{u}$	u velocity solution for the true wave	131
u^n, v^n, w^n	respective fields of values of u, v, w at time level n	23
u^*	dimensionless u	119
u_i	u velocity value at u gridpoint of element i	18
$u^n_{i,k}$	u-component of depth-dependent velocity at u_i gridpoint, depth level k, time level n	26
u_{10}, v_{10}	x, y horizontal components, respectively, of wind velocity recorded 10 m above MSL	13
$u_{10}\|^n_i$	u-component of wind velocity 10 m above sea surface at gridpoint ζ_i, time level n	28
$v_{10}\|^n_i$	v-component of wind velocity 10 m above sea surface at gridpoint ζ_i, time level n	28
v_i	v velocity value at v gridpoint of element i	18
$v^n_{i,k}$	v-component of depth-dependent velocity at v_i gridpoint, depth level k, time level n	26
x, y, z	rectangular cartesian coordinates with the x and y axes in the plane of mean sea level and the z-axis directed vertically upwards from MSL	8
x^*	dimensionless x	74
x_i	$= i(2\Delta x)$, position of a gridpoint	165
x_1, x_2	x-wise location of the head and open boundary, respectively, of a Lynch and Gray (1978) model estuary	72
w^*	dimensionless w	119
w_0	characteristic value of w	119
A, B	complex constants used in the Lynch and Gray (1978) analytical solution for a channel with parabolic depth profile	83
Adjust	inclination in degrees, anticlockwise, of model's x-axis to East	178
B	breadth of the Knight's (1973) model	87
C	constant in definition of de Chèzy quadratic friction coefficient	170
C.S.T.	(abbrev.) Central Standard Time (Australian), −9.5 hr G.M.T.	143
C_b	dimensionless coefficient of quadratic bottom friction	15
C_b	dimensionless coefficient of quadratic bottom friction for one-dimensional flow	87
C_r	Courant number (dimensionless) — ratio of speed of the true wave to the maximum speed with which the wave can propagate across the numerical grid	98
C_x	Courant number in the x-direction	74
C_{x_a}	Courant number based on the average depth h_a defined for the Lynch	85

	and Gray (1978) channel with parabolic depth profile	
C_1, C_2	complex constants defined for the Johns (1966) solution	117
D	mean sea level depth	166
F	a dimensionless constituent Coriolis number	98
$F(s)$	Wolf's (1983) vertical eddy viscosity form	239
F_k	numerical value of $F(\eta)$, the vertical variation of horizontal velocity in the Johns (1966) model, at depth level k	121
F_z	z-component of external forces, attributed to gravitational acceleration g	9
$F(\eta)$	prescribed η-variation of vertical eddy viscosity coefficient	10
$F(\eta)$	a factor carrying the η-dependence of horizontal velocity in the case of the Johns (1966) solution	115
$F(\eta_k)$	vertical eddy viscosity coefficient evaluated at depth level k	27
G.M.T.	(abbrev.) Greenwich Mean Time	8
G_m	gain, time variation of the error term	210
H	$= \zeta + h$, the total depth	9
H_b	$= \zeta_b + h_b$, total depth at element b of the open boundary	14
H_{dry}	value of total depth at or below which the associated gridpoint is regarded as dry	299
H_i^n	total depth at the ζ_i gridpoint at time level n	24
H_0	a parameter used to limit the growth of frictional dissipation	299
H^n	total depth field at time level n	23
$H_{u_i}^{n+1}$	estimate for total depth at the u_i gridpoint at time level $(n+1)$	28
ISLW	(abbrev.) Indian Spring Low Water	157
K	dimensionless constituent friction number	74
K_1	lunisolar diurnal constituent, period 23.93 hr	14
L	length of model estuary	74
M_2	principal lunar constituent, period 12.42 hr	14
M_3	a shallow water constituent	200
M_4	a shallow water constituent	200
M_6	a shallow water constituent	200
MK_3	a shallow water constituent	200
MN_4	a shallow water constituent	200
MO_3	a shallow water constituent	200
MSf	a shallow water constituent	200
MSL	(abbrev.) Mean Sea Level	13
MSN_6	a shallow water constituent	200
MS_4	a shallow water constituent	200
N	total number of stations	161
N	set of Natural numbers (1,2,3, ...)	165
NC1	code of neighbour element (i_1-1)	37
NC2	code of neighbour element i_1	37
NC3	code of neighbour element (i_1+1)	37
NC4	code of neighbour element $(i+1)$	37
NC5	code of neighbour element (i_2+1)	37
NC6	code of neighbour element i_2	37
NC7	code of neighbour element (i_2-1)	37

NC8	code of neighbour element (i–1)	37
NC15	code of neighbour element (i+2)	36
NC19	code of neighbour element i_{22}	36
NK	number of depth intervals; there are (NK+1) depth levels, including surface and bed levels	21
$NL1$	number of Type 1 elements used in the model, or the number of spatial sampling positions along a model estuary's length	74
N_b	bed viscosity value	127
N_f	$= T_f/\Delta t$	218
$N^n_{i,k}$	value of N_η evaluated at the $u^n_{i,k}$ gridpoint, i.e. at gridpoint u_i, depth level k, time level n	27
N_k	numerical value of N_η at depth level k	118
$N_{\max}$	characteristic value of vertical eddy viscosity, taken as the maximum prescribed value in the water column	119
N_s	surface viscosity value	127
N_s	Wolf's (1983) vertical eddy viscosity coefficient	239
N_x, N_y, N_z	eddy viscosity coefficients in the indicated directions	9
N_L	dimensionless number of grid spacings in the length of the model basin	74
N_S	number of grid spacings in the side S	98
N_T	number of time steps in a period	75
N_λ	dimensionless number of grid spacings in a wavelength	74
N_η	transformed vertical eddy viscosity coefficient	113
N^*_η	dimensionless N_η	119
NSG	(abbrev.) Northern Spencer Gulf	292
O_1	principal lunar diurnal constituent, period 25.82 hr	14
$Q(t)$	current strength at time t	178
$Q^-(t)$	clockwise component of current vector at time t	178
$Q^+(t)$	anticlockwise component of current vector at time t	178
R	hydraulic radius	87
R	tidal type, a ratio of diurnal to semidiurnal amplitudes	142
R	set of real numbers	302
S	linear dimension of the square Rienecker and Teubner (1980) model	98
S_x, S_y	x and y components, respectively, of surface wind stress	13
$S^{n+1}_{u_i}$	estimate of surface stress at the u_i gridpoint at time level (n+1)	28
S_2	principal solar constituent, period 12.00 hr	14
SG	(abbrev.) Spencer Gulf	75
T	$= 2\pi/\sigma$, period of the oscillation	74
T_{exp}	time scale related to an exponential weighting of the O-S and height specified conditions	225
T_f	time scale over which the Blumberg and Kantha (1985) condition approaches behaviour as a the height specified condition	217
T_{f*}	$= L/c$, theoretical time for a wave to traverse a region of length L at speed c	223
T_{hyp}	time scale related to an hyperbolic weighting of the O-S and height specified conditions	226
T_B	simulation time value	224

T_S	a specified time scale	224
U, V	x, y components, respectively, of depth-averaged velocity	10
U^*	dimensionless U	74
$\widehat{U}$	U velocity solution for the true wave	79
U_a	complex amplitude of U velocity of a given Fourier mode	78
U_a	amplitude of the U-component of tidal velocity	178
$\overline{U}_i$	three-point filter on U	301
U_i^n	depth-averaged velocity component U at the u_i gridpoint at time level n	24
U_p	phase of the U-component of tidal velocity	178
U^n, V^n	respective fields of values of U, V at time level n	23
$U(\eta), V(\eta)$	integrals of u, v, respectively, over the interval $\eta' \in [0, \eta]$	12
$U(\eta_k)_i^n$	numerical value of $U(\eta)$ at gridpoint u_i, depth level k, time level n	29
U_0	characteristic value of U	74
$\widehat{V}$	V velocity solution for the true wave	102
V_a	complex amplitude of V velocity of a given Fourier mode	99
V_a	amplitude of the V-component of tidal velocity	178
V_i^n	depth-averaged velocity component V at the v_i gridpoint at time level n	24
V_p	phase of the V-component of tidal velocity	178
$\overline{V}_{U_i}$	four-point spatial filter on V	303
$V(\eta_k)_i^n$	numerical value of $V(\eta)$ at gridpoint v_i, depth level k, time level n	29
V_0	phase, relative to Greenwich, for a given constituent at the start of the epoch (00:00 hr, 1/1/1900)	13
V_0	characteristic value of V	97
X, Y	dimensionless numbers whose values are used to quantify the stability of the Knight (1973) solution	89
Z	elevation of a given Fourier mode; associated with the second form of the elevation calculation	78
Zone	time difference (hr) of local time relative to G.M.T.	181
Z_a	complex amplitude of elevation of a given Fourier mode; associated with the second form of the elevation calculation	78
$2MN_6$	a shallow water constituent	200
$2MS_6$	a shallow water constituent	200
$2SM_2$	a shallow water constituent	200
$2SM_6$	a shallow water constituent	200
α	minimum (or background) absolute value for N_η (m^2/sec)	10
α	increase in amplitude of the numerical wave after one wave period of duration $t = 2\pi/\nu$	81
α	wavenumber	301
$\widehat{\alpha}$	increase in amplitude of the true wave after one wave period of duration $t = 2\pi/\widehat{\nu}$	81
α_0	dimensionless number expressing the ratio of constituent wavelength to estuary length	74
α_2	$= T\sqrt{gh_2}$, dimensionless number expressing the ratio of constituent wavelength to estuary length in the case of the Lynch and Gray (1978) solution for a channel with parabolic depth profile	85

β	dimensionless calibration constant associated with vertical eddy viscosity coefficient	10
β	complex wavenumber (m^{-1})	72
β	real wavenumber (m^{-1})	165
β_0	dimensionless number expressing the ratio of constituent wavelength to breadth of bay	98
γ	dimensionless vertical eddy viscosity number	119
$\gamma(t)$	time dependent weighting of the O-S and height specified boundary conditions over a simulation	223
γ_m	phase of constituent m	13
γ_1	reference viscosity at the fluid bed	113
γ_2	arbitrary parameter defining the surface viscosity value	113
ϵ	$= \zeta_0/h_0$, a measure of the degree of non-linearity of the Knight (1973) solution	91
ϵ	parameter specifying minimum gradient of an advancing wave	299
$\widehat{\epsilon}$	argument of the complex amplitude of either the numerical or true wave	80
ε	dimensionless amplitude and phase error, combined by means of expressing the tide-height constants as a complex polar vector for all constituents at all calibration stations	162
ε_a	dimensionless amplitude error, an average over all constituents at all calibration stations	162
ε_c	dimensionless amplitude or phase constituent error, expressed as a percentage	161
ε_p	dimensionless phase error, average over all constituents at all calibration stations	162
ε_F^*	dimensionless error in calculation of $F(\eta)$, the vertical variation of horizontal velocity of the Johns (1966) model	125
ε_ζ^*	dimensionless elevation error, expressed as a percentage	75
ε^-	phase of clockwise component of current vector at time $t = 0$	178
ε^+	phase of anticlockwise component of current vector at time $t = 0$	178
ζ	free surface elevation measured in the direction of increasing z from mean sea level	8
ζ^*	dimensionless ζ	74
$\widehat{\zeta}$	elevation of the true wave	79
ζ_a	complex amplitude of oscillation of a Fourier mode representing elevation	78
ζ_b	tidal elevation at position b on the open boundary	13
ζ_i	elevation value at ζ gridpoint of element i	18
ζ_i^n	elevation at ζ_i gridpoint at time level n	24
ζ_k	equilibrium (meteorological and tidal) solution for elevation	217
ζ_s	specified elevation	208
ζ^n	field of elevation values at time level n	22
ζ_0	amplitude of tidal forcing at open boundary	72
η	$= (\zeta - z)/(\zeta + h)$, a "sigma" transformation mapping sea surface and sea bed to flat surfaces for ease of numerical computation in the vertical	9

η	$= \Im m\{k_t\}$, the imaginary part of the complex frequency of the right going numerical wave solution	81
η	$= -z/h_0$, the linearized form of η used for the Johns (1966) model	114
$\widehat{\eta}$	$= \Im m\{\widehat{k}_t\}$, the imaginary part of the complex frequency of the right going true wave solution	80
η_k	depth at level k, in terms of the η coordinate	20
θ	angle, measured anti-clockwise to the positive x-direction (defined as θ=0°)	99
κ	parameter that controls the concentration of depth levels in the Kappa method	20
λ	wavelength	74
μ	relative wave speed of finite difference method, i.e. ratio of computed to true wave speeds	81
μ_m	phase correction for tidal constituent m	13
μ_o, μ_p	observed and predicted amplitude of constituent c at station s	162
ν	$= -\Re e\{k_t\}$, the real part of the complex frequency of the right going numerical wave solution	81
$\widehat{\nu}$	$= -\Re e\{\widehat{k}_t\}$, the real part of the complex frequency of the right going true wave solution	80
ξ	$= \exp\{\imath k_t \Delta t\}$, an expression involving the complex frequency k_t of the numerical wave	78
ξ	an error due to round-off	210
π	$\simeq 3.141592654...$	74
ρ	density of sea water, assumed constant at 1027 kg/m^3	8
ρ_a	density of air, assumed constant at 1.225 kg/m^3)	13
σ	angular frequency of forcing	72
τ	constant linear friction coefficient, with units sec^{-1}	72
$\underline{\tau}_b$	bottom stress vector (m^2/sec)	167
ϕ_o, ϕ_p	observed and predicted phase of constituent c at station s	162
χ	amplitude response of finite difference equation, i.e. ratio of amplitudes of computed and true waves	81
ω	velocity in the η-direction in the transformed frame	9
ω^*	dimensionless ω	119
$\omega^n_{i,k}$	value of ω component of depth-dependent velocity at ζ_i gridpoint, depth level k, time level n	26
ω_m	angular frequency of tidal constituent m	13
ω^n	field of ω values at time level n	23
ω_0	characteristic value for ω	119
Δs	spacing between gridpoints in x or y directions in the case of the Rienecker and Teubner (1980) model with square elements	98
Δt	computational time step	22
$\Delta x, \Delta y$	spacing between gridpoints in the x and y directions, respectively; the dimensions of a grid element are therefore $2\Delta x \times 2\Delta y$	18
$\Delta\eta$	constant depth level spacing	121
$\Delta\eta_k$	distance between the η_k and η_{k+1} depth levels	20
Φ	latitude north (Φ is negative in the southern hemisphere)	8
Ω	$= 2\pi/(3600 * 23.9333)$ sec^{-1}, Earth's angular velocity of rotation	8

$\imath$	$=\sqrt{-1}$	72
$\Re e\{\}$	notation used to specify the real part of a complex expression	72
$\{\}^n_{\zeta_i}$	notation used to denote centring about time level n and gridpoint ζ_i	24
$O(\Delta x)$	truncation error of the corresponding discretisation is a multiple of the factor (Δx)	59
$O(\Delta x)^2$	truncation error of the corresponding discretisation is a multiple of the factor $(\Delta x)^2$	52
$O(\Delta y)$	truncation error of the corresponding discretisation is a multiple of the factor (Δy)	57
$O(\Delta y)^2$	truncation error of the corresponding discretisation is a multiple of the factor $(\Delta y)^2$	57
$O(\Delta y)^3$	truncation error of the corresponding discretisation is a multiple of the factor $(\Delta y)^3$	57
0	"Type 0" element — one whose elevation gridpoint lies on land	36
1	"Type 1" element — one whose elevation gridpoint lies on water within the model	36
2	"Type 2" element — one whose elevation gridpoint lies on an open sea boundary	36
4	"Type 4" element — one whose elevation gridpoint lies on water outside the model	36
"1's"	computational neighbourhood configuration of Type 1 elements	42
"0–1's"	computational neighbourhood configuration of Type 0 and Type 1 elements	42
"0–1–2's"	computational neighbourhood configuration of Type 0, Type 1 and Type 2 elements	42
DuDx	program variable name of $\partial u/\partial x$	51
DuDy	program variable name of $\partial u/\partial y$	61
DTR4DX	program variable name of $\Delta t/(4\Delta x)$	46
DTR4DY	program variable name of $\Delta t/(4\Delta y)$	46
D2uDx2	program variable name of $\partial^2 u/\partial x^2$	62
D2uDy2	program variable name of $\partial^2 u/\partial y^2$	62
H	program variable name of the total depth field H for Type 1 elements	46
H2	program variable name of the total depth field H for Type 2 elements	48
I	program variable name of i	41
Index_Value_I1M1	program variable name of list of index values for neighbour elements $(i_1{-}1)$ of Type 1 elements i	43
IIM1	program variable name of index $i-1$ of a Type 2 element	48
IIP1	program variable name of index $i+1$ of a Type 2 element	48
II1	program variable name of index $i-1$ of a Type 2 element	48
II1M1	program variable name of index $(i_1{-}1)$ of a Type 2 element	44
II2	program variable name of index i_2 of a Type 2 element	48
IM1	program variable name of index $i-1$ of a Type 1 element	46
IPOS	program variable name of position of ith Type 1 element in L list	41
IP1	program variable name of index $i+1$ of a Type 1 element	46
I1	program variable name of index i_1 of a Type 1 element	46
I1M1	program variable name of index $(i_1{-}1)$ of a Type 1 element	43
I2	program variable name of index i_2 of a Type 1 element	46

K	program variable name of depth level k	51
L	list form of the neighbourhood code array	39
LR	list of Type 1 and Type 2 elements ranked according to the order of their appearance in list L; Type 0 and Type 4 elements are assigned rank 0	40
L1	cross-reference list of Type 1 elements using their rank to find their position in the L list	40
L2	cross-reference list of Type 2 elements using their rank to find their position in the L list	40
Neigh_Code_1	program variable name of list of NC1 values for neighbour element (i_1–1) of Type 1 elements	41
NC	program variable name of number of columns in neighbourhood code array	41
NCN_U	program variable name of list of neighbourhood code numbers for Type 1 u elements	43
NCN_V	program variable name of list of neighbourhood code numbers for Type 1 v elements	43
NCN_Z	program variable name of list of neighbourhood code numbers for Type 1 ζ, ω, w elements	42
NC23_both_0	program variable name of (1–((1+NC2)/2))*(1–((1+NC3)/2))	61
NC23_both_2	program variable name of (NC2/2)*(NC3/2)	61
NC4TWO	program variable name of (1–(NC4/2))	61
NC65_both_0	program variable name of (1–((1+NC6)/2))*(1–((1+NC5)/2))	61
NC65_both_2	program variable name of (NC6/2)*(NC5/2)	61
R4DX	program variable name of $(1/(4\Delta x))$	51
R4DXS	program variable name of $1/(4(\Delta x)^2)$	62
R4DY	program variable name of $(1/(4\Delta y))$	61
R4DYS	program variable name of $1/(4(\Delta y)^2)$	62
U	program variable name of the array storing the u depth-dependent velocity field for Type 1 elements	43
UA	program variable name of the list storing the U depth-averaged velocity field for Type 1 elements	46
UA2	program variable name of the list storing the U depth-averaged velocity field for Type 2 elements	48
U2	program variable name of the array storing the u depth-dependent velocity field for Type 2 elements	43
VA	program variable name of the list storing the V depth-averaged velocity field for Type 1 elements	46
VA2	program variable name of the list storing the V depth-averaged velocity field for Type 2 elements	48
Z	program variable name of the list storing the ζ field for Type 1 elements	46

List of Figures

1.1 Major coastal towns and important features of Spencer Gulf. 2
1.2 Location maps, bathymetry and coastal detail in Northern Spencer Gulf. . . 2

2.1 Diagram illustrating the general effect of the η transformation. 11

3.1 Plan view of the ith grid element showing the ζ_i, u_i and v_i gridpoints, and the horizontal grid step sizes. 18
3.2 Plan view of the ith element and index labels used for its 8 immediate neighbours. 20
3.3 An η cross-section of the transformed vertical region indicating the unequally plced depth levels and spacings. 21
3.4 Diagrammatic view of the overall finite difference scheme. 22
3.5 Computational molecule corresponding to the first finite difference form of the continuity equation. 25
3.6 Computational molecule corresponding to the second finite difference form of the continuity equation. 30
3.7 The computational stencils for the ζ, u, v, ω, w finite difference approximations. 32
3.8 Labelling convention for the immediate eight neighbour codes of a central Type 1 element. 37
3.9 The ζ, u, v, ω, w computational stencils drawn on a network of possible coastal line segments. 37
3.10 A simple model region bounded by coastal and open sea boundaries. 38
3.11 Neighbourhood code array corresponding to model region of the previous figure. 40
3.12 Plan view of the u_i computational stencil with central element of Type 2. . 45
3.13 Plan view of the ζ_i computational stencil near a coastal boundary. 46
3.14 Plan view of the ζ_i computational stencil at a coastal boundary. 47
3.15 Plan view of the ζ_i computational stencil near the junction of a coastal and open sea boundary. 49
3.16 Plan view of the u_i computational stencil in the vicinity of an open sea boundary. 53
3.17 Example of a 9-element block not catered for in the present program. . . . 54
3.18 Example of element strips not catered for in the present program. 54
3.19 Plan view of the ζ_i computational stencil at the junction of a coastal and open sea boundary. 55
3.20 Plan view of the u_i computational stencil near a coastal/open boundary junction. 56

3.21 Plan view of the v_i computational stencil at the junction of a coastal and open sea boundary. 59
3.22 Plan view of the ith computational element in the vicinity of a corner in the coastal boundary. 60
3.23 Residual velocity vectors generated by three strategies of treatment of advective and diffusive terms near coastal and open sea boundaries. 64
3.24 Residual stream vectors generated by three strategies of treatment of advective and diffusive terms near coastal and open sea boundaries. 65

4.1 The Lynch and Gray (1978) idealized estuary with constant depth profile. . 73
4.2 Error plot for numerical tests using Lynch and Gray's (1978) constant depth estuary with Spencer Gulf parameters. 77
4.3 Wave propagation characteristics for the numerical scheme applied to the Lynch and Gray (1978) linear system using parameters representative of the Spencer Gulf model. 82
4.4 The Lynch and Gray (1978) idealized estuary with parabolic depth profile. 84
4.5 Error plot for numerical tests using Lynch and Gray's (1978) parabolic depth estuary model with Spencer Gulf parameters. 86
4.6 Diagram illustrating Knight's (1973) constant depth idealized estuary. . . . 87
4.7 Plots of numerical errors in conducting Knight (1973) Tests 2 and 3. 93
4.8 Diagram illustrating the rectangular bay and boundary conditions used in the Rienecker and Teubner (1980) study. 96
4.9 Error plots for numerical experiments carried out using the Rienecker and Teubner (1980) rectangular bay. 100
4.10 (a) Amplitude response and (b) relative wave speed of the numerical scheme for three waves propagating along the x-axis ($\theta = 0°$) in the Rienecker and Teubner (1980) rectangular bay. 103
4.11 (a) Amplitude response and (b) relative wave speed of the numerical scheme for three waves propagating obliquely to the x-axis ($\theta = 30°$) in the Rienecker and Teubner (1980) rectangular bay. 104
4.12 (a) Amplitude response and (b) relative wave speed of the numerical scheme for three waves propagating diagonally to the x-axis ($\theta = 45°$) in the Rienecker and Teubner (1980) rectangular bay. 105
4.13 Computational schemes for Coriolis terms of elements adjacent to open boundaries facing toward the north, south, east or west. 107
4.14 Computational schemes for Coriolis terms of elements adjacent to open boundaries facing toward the north-east, north-west, south-east or south-west. 108
4.15 (a) Amplitude response and (b) relative wave speed of the open boundary scheme for waves propagating obliquely to the x-axis ($\theta = 30°$) in the Rienecker and Teubner (1980) rectangular bay. 110
4.16 (a) Amplitude response and (b) relative wave speed of the open boundary scheme for waves propagating diagonally to the x-axis ($\theta = 45°$) in the Rienecker and Teubner (1980) rectangular bay. 111
4.17 The shape of the vertical eddy viscosity coefficient used by Johns (1966). . 114
4.18 Diagram illustrating the notation used to describe the transformed Johns (1966) estuary. 116

η	$= -z/h_0$, the linearized form of η used for the Johns (1966) model	114
$\widehat{\eta}$	$= \Im m\{\widehat{k}_t\}$, the imaginary part of the complex frequency of the right going true wave solution	80
η_k	depth at level k, in terms of the η coordinate	20
θ	angle, measured anti-clockwise to the positive x-direction (defined as θ=0°)	99
κ	parameter that controls the concentration of depth levels in the Kappa method	20
λ	wavelength	74
μ	relative wave speed of finite difference method, i.e. ratio of computed to true wave speeds	81
μ_m	phase correction for tidal constituent m	13
μ_o, μ_p	observed and predicted amplitude of constituent c at station s	162
ν	$= -\Re e\{k_t\}$, the real part of the complex frequency of the right going numerical wave solution	81
$\widehat{\nu}$	$= -\Re e\{\widehat{k}_t\}$, the real part of the complex frequency of the right going true wave solution	80
ξ	$= \exp\{\imath k_t \Delta t\}$, an expression involving the complex frequency k_t of the numerical wave	78
ξ	an error due to round-off	210
π	$\simeq 3.141592654...$	74
ρ	density of sea water, assumed constant at 1027 kg/m^3	8
ρ_a	density of air, assumed constant at 1.225 kg/m^3)	13
σ	angular frequency of forcing	72
τ	constant linear friction coefficient, with units sec^{-1}	72
$\underline{\tau}_b$	bottom stress vector (m^2/sec)	167
ϕ_o, ϕ_p	observed and predicted phase of constituent c at station s	162
χ	amplitude response of finite difference equation, i.e. ratio of amplitudes of computed and true waves	81
ω	velocity in the η-direction in the transformed frame	9
ω^*	dimensionless ω	119
$\omega^n_{i,k}$	value of ω component of depth-dependent velocity at ζ_i gridpoint, depth level k, time level n	26
ω_m	angular frequency of tidal constituent m	13
ω^n	field of ω values at time level n	23
ω_0	characteristic value for ω	119
Δs	spacing between gridpoints in x or y directions in the case of the Rienecker and Teubner (1980) model with square elements	98
Δt	computational time step	22
$\Delta x, \Delta y$	spacing between gridpoints in the x and y directions, respectively; the dimensions of a grid element are therefore $2\Delta x \times 2\Delta y$	18
$\Delta\eta$	constant depth level spacing	121
$\Delta\eta_k$	distance between the η_k and η_{k+1} depth levels	20
Φ	latitude north (Φ is negative in the southern hemisphere)	8
Ω	$= 2\pi/(3600 * 23.9333)\,\text{sec}^{-1}$, Earth's angular velocity of rotation	8
$\imath$	$= \sqrt{-1}$	72
$\Re e\{\}$	notation used to specify the real part of a complex expression	72

5.23 Contour charts for the diurnal constituent K_1 of tide-height taken from the depth-averaged model. 174
5.24 Contour charts for the semi-diurnal constituent M_2 of tide-height taken from the depth-averaged model. 175
5.25 Contour charts for the semi-diurnal constituent S_2 of tide-height taken from the depth-averaged model. 175
5.26 Ellipses for the O_1 constituent of depth-averaged current taken from the depth-averaged model. 179
5.27 Ellipses for the K_1 constituent of depth-averaged current taken from the depth-averaged model. 179
5.28 Ellipses for the M_2 constituent of depth-averaged current taken from the depth-averaged model. 180
5.29 Ellipses for the S_2 constituent of depth-averaged current taken from the depth-averaged model. 180
5.30 Major constituent tidal ellipses for the elements on the model rows containing stations Mike and Lima. 183
5.31 The tide-height signal at Wallaroo station. 189
5.32 Snapshots of predicted flow during a neap period. 190
5.33 Snapshots of predicted flow during a spring period. 191
5.34 Snapshots of depth-averaged K_1 current taken from the K_1 ellipses. 192
5.35 Snapshots of depth-averaged M_2 current taken from the M_2 ellipses. 193
5.36 Residuals taken from the depth-averaged model for depth-averaged velocity over a 29 day period. 196
5.37 Residuals taken from the depth-averaged model for elevation over a 29 day period. 197
5.38 Depth-averaged velocity residuals with residual gyres marked. 199

6.1 Predicted and observed tidal elevation at Wedge Island station obtained using the height specified condition. 206
6.2 Open boundary of the Spencer Gulf model with corner element removed. . 208
6.3 Gridpoints used in the Orlanski differencing of the Sommerfeld equation. . . 209
6.4 Gridpoints used in the Orlanski-Sommerfeld differencing of the Sommerfeld equation. 212
6.5 Values of phase velocity at a neap and a spring period obtained using the Orlanski (1976) criteria. 214
6.6 Regions of stable operation for the Blumberg and Kantha (1985) condition. 219
6.7 Examining the performance of the Blumberg and Kantha (1985) condition for various values of parameter T_f. 220
6.8 Stability regions for the modified Blumberg and Kantha condition. 221
6.9 Stability diagrams for modified Blumberg and Kantha conditions with forcing supplied only through the time derivative. 222
6.10 Exponential and hyperbolic weight functions. 225
6.11 Normalized counts of the occurrence of the zero value for c. 228
6.12 Computational stencil for a spatially second order accurate Orlanski-Sommerfeld scheme. 231
6.13 Normalized counts of the occurrence of $c > 0.5$. 233
6.14 Stencil for an alternative second order spatial differencing. 234

7.1 Plots of calibration error ε (cm) against κ for three-dimensional models using $\alpha = 0.0005\,\mathrm{m}^2/\mathrm{sec}$. 243
7.2 The structures of different kappa grids for 11 depth levels. 244
7.3 Plots of calibration error ε (cm) against κ for three-dimensional models using $\gamma_1 = 0\,\mathrm{m}^2/\mathrm{sec}$. 246
7.4 Contour charts for the diurnal constituent O_1 of tide-height taken from the three-dimensional model. 249
7.5 Contour charts for the diurnal constituent K_1 of tide-height taken from the three-dimensional model. 249
7.6 Contour charts for the semi-diurnal constituent M_2 of tide-height taken from the three-dimensional model. 250
7.7 Contour charts for the semi-diurnal constituent S_2 of tide-height taken from the three-dimensional model. 250
7.8 Ellipses for the O_1 constituent of depth-averaged current taken from the three-dimensional model. 251
7.9 Ellipses for the K_1 constituent of depth-averaged current taken from the three-dimensional model. 251
7.10 Ellipses for the M_2 constituent of depth-averaged current taken from the three-dimensional model. 252
7.11 Ellipses for the S_2 constituent of depth-averaged current taken from the three-dimensional model. 252
7.12 Depth-averaged velocity residuals taken from the three-dimensional model based on 29 days of predicted data. 253
7.13 Elevation residuals taken from the three-dimensional model from 29 days of predicted data. 253
7.14 Amplitude and phase for the U and V-components of depth-averaged O_1 tidal velocity taken from the three-dimensional model. 255
7.15 Amplitude and phase for the U and V-components of depth-averaged K_1 tidal velocity taken from the three-dimensional model. 256
7.16 Amplitude and phase for the U and V-components of depth-averaged M_2 tidal velocity taken from the three-dimensional model. 257
7.17 Amplitude and phase for the U and V-components of depth-averaged S_2 tidal velocity taken from the three-dimensional model. 258
7.18 Ellipses for the O_1 constituent of depth-dependent tidal current at the surface level. 260
7.19 Ellipses for the K_1 constituent of depth-dependent tidal current at the surface level. 260
7.20 Ellipses for the M_2 constituent of depth-dependent tidal current at the surface level. 261
7.21 Ellipses for the S_2 constituent of depth-dependent tidal current at the surface level. 261
7.22 Ellipses for the O_1 constituent of depth-dependent tidal current at the mid-depth level. 262
7.23 Ellipses for the K_1 constituent of depth-dependent tidal current at the mid-depth level. 262
7.24 Ellipses for the M_2 constituent of depth-dependent tidal current at the mid-depth level. 263

7.25 Ellipses for the S_2 constituent of depth-dependent tidal current at the mid-depth level. . . . 263
7.26 Ellipses for the O_1 constituent of depth-dependent tidal current at level $k = 9$ (near the bed). . . . 264
7.27 Ellipses for the K_1 constituent of depth-dependent tidal current at level $k = 9$ (near the bed). . . . 264
7.28 Ellipses for the M_2 constituent of depth-dependent tidal current at level $k = 9$ (near the bed). . . . 265
7.29 Ellipses for the S_2 constituent of depth-dependent tidal current at level $k = 9$ (near the bed). . . . 265
7.30 Snapshots at 15 min intervals of depth-dependent current at the surface level during a neap period. . . . 267
7.31 Snapshots at 15 min intervals of depth-dependent current at the mid-depth level during the same neap period. . . . 268
7.32 Snapshots at 15 min intervals of depth-dependent current at the surface level during a spring period. . . . 269
7.33 Snapshots at 15 min intervals of depth-dependent current at the mid-depth level during the same spring period. . . . 270
7.34 Residuals for depth-dependent current at the surface level taken over a 29 day period. . . . 271
7.35 Residuals for depth-dependent current at the mid-depth level taken over a 29 day period. . . . 271
7.36 Residuals for depth-dependent current at the $k = 9$ (near bed) level taken over a 29 day period. . . . 272
7.37 Depth-dependent ellipse characteristics at station Mike. . . . 274
7.38 Depth-dependent ellipse characteristics at station Lima. . . . 275
7.39 Depth-dependent ellipse characteristics at station Yarraville Shoals. . . . 276
7.40 Depth-dependent ellipse characteristics at station Red. . . . 277
7.41 Depth-dependent ellipse characteristics at station Yellow. . . . 278
7.42 Depth-dependent ellipse characteristics at station Blue. . . . 279
7.43 Depth-dependent ellipse characteristics at station White. . . . 280
7.44 Snapshots of velocity component profiles at Mike and Lima during a neap event. . . . 289
7.45 Snapshots of velocity component profiles at Mike and Lima during a spring event. . . . 290

8.1 Location map for the Northern Spencer Gulf model. . . . 293
8.2 Element code array for the Northern Spencer Gulf model. . . . 296
8.3 Indian Spring Low Water depth field for the Northern Spencer Gulf model. 297
8.4 Mean Sea Level depth field for the Northern Spencer Gulf model. . . . 298
8.5 Numerical tests with parameters ϵ and C_b. . . . 310
8.6 Numerical tests with parameters H_0 and C_b. . . . 311
8.7 Numerical tests with parameters H_{dry} and C_b. . . . 312
8.8 Tidal flat elements of Ward Spit and Cockle Spit. . . . 313
8.9 Final four days of predicted elevation signals at the elements of Ward Spit and Cockle Spit obtained using various values of the constant quadratic friction coefficient. . . . 314

8.10 Numerical tests with parameters ϵ and n. 315
8.11 Numerical tests with parameters H_0 and n. 316
8.12 Numerical tests with parameter H_{dry}. 317
8.13 Transition counts at Ward Spit and Cockle Spit. 319
8.14 Predicted elevation signals at the elements of Ward Spit and Cockle Spit generated using the de Chèzy quadratic friction coefficient with $n = 0.018$. . 320
8.15 Histogram of transition counts for a 29 day period using the control parameter set and n=0.018. 321
8.16 Tidal flat elements and associated transition counts of the south east coastal region of the Northern Spencer Gulf model. 322
8.17 Average transition count across each row of the model, north to south. . . . 323
8.18 Contours for amplitude and phase of the O_1 tidal constituent. 324
8.19 Contours for amplitude and phase of the K_1 tidal constituent. 324
8.20 Contours for amplitude and phase of the M_2 tidal constituent. 325
8.21 Contours for amplitude and phase of the S_2 tidal constituent. 325
8.22 Ellipses for the O_1 constituent of depth-averaged current. 329
8.23 Ellipses for the K_1 constituent of depth-averaged current. 329
8.24 Ellipses for the M_2 constituent of depth-averaged current. 329
8.25 Ellipses for the S_2 constituent of depth-averaged current. 329
8.26 Depth-averaged current residuals predicted by the Northern Spencer Gulf model. 331
8.27 Two-hourly wetting/drying sequence for a neap period. 336
8.28 Two-hourly wetting/drying sequence for a spring period. 337
8.29 Two-hourly wetting/drying sequence for a spring period, assuming a fall in MSL of 0.5 m. 338
8.30 Two-hourly wetting/drying sequence for a spring period, assuming a rise in MSL of 0.5 m. 339
8.31 Two-hourly wetting/drying sequence for a spring period, assuming a rise in MSL of 1.0 m. 340
8.32 Residuals in depth-averaged current predictions for the Ward Spit region assuming various changes in MSL. 342

List of Tables

4.1 Dimensionless error values arising from Test 1 of the Knight tests: using pseudo-laboratory values. 92
4.2 Dimensionless error values arising from Test 2 of the Knight tests: a diurnal wave of amplitude $\zeta_0 = 0.4\,\mathrm{m}$ in an estuary 90 km long. 93
4.3 Dimensionless error values arising from Test 3 of the Knight tests: a diurnal wave of amplitude $\zeta_0 = 0.8\,\mathrm{m}$ in an estuary 45 km long. 94
4.4 Table of (real) values of the vertical variation of horizontal velocity and dimensionless wavenumber calculated analytically and numerically (using second and third order accurate approximations for surface velocity). 124

5.1 Tide-height constants for the four major tidal constituents at 18 stations within Spencer Gulf. 143
5.2 The "tidal type" at each station. 144
5.3 Map position and model representation error of each station. 152
5.4 Tide-height constants for the four major constituents at the four stations sited at the entrance to the Gulf. 155
5.5 Tidal constants used for the four major constituents at each of the open boundary elements. 156
5.6 Tide-height calibration table for the depth-averaged model. 172
5.7 Summary of calibration summary when stations more than $0.71(2\Delta x)$ distant from their representative gridpoint are excluded. 173
5.8 Table of calibration errors for each constituent taken from the linear Spencer Gulf model. 177
5.9 Comparison of predicted and observed depth-averaged ellipse characteristics at stations Mike and Lima. 184
5.10 Comparison of predicted and observed depth-averaged ellipse characteristics at stations Yarraville Shoals, Red and Yellow. 185
5.11 Comparison of predicted and observed depth-averaged ellipse characteristics at stations Blue and White. 186
5.12 Predicted and observed amplitudes for the seven largest shallow water constituents in Spencer Gulf separable by the analysis program. 201

7.1 Tide-height calibration table for the three-dimensional model. 248
7.2 Comparison of predicted depth-averaged ellipse characteristics from the three-dimensional and depth-averaged models at stations Mike, Lima and Yarraville Shoals. 282

7.3 Comparison of predicted ellipse characteristics from the depth-averaged results of the three-dimensional and depth-averaged models for stations Red, Yellow, Blue and White. 283
7.4 Comparison of predicted and observed ellipse characteristics for the four major tidal current constituents at stations Mike, Yarraville Shoals and Red at the indicated depths. 284
7.5 Comparison of predicted and observed ellipse characteristics for the four major tidal current constituents at stations Lima and Yellow at the indicated depths. 285
7.6 Comparison of predicted and observed ellipse characteristics for the four major tidal current constituents at stations Blue and White at the indicated depths. 286

8.1 Table of calibration perspectives for the SG model. 305
8.2 List of tidal constants of the four major constituents for possible use as forcing information at the open boundary elements of the NSG model. . . . 307
8.3 Observed and predicted tide-height constants for the depth-averaged Northern Spencer Gulf model. 326
8.4 Observed and predicted ellipse characteristics for station Mike. 328
8.5 Comparison of predicted (coarse-grid and fine-grid) and observed amplitudes for the seven shallow water constituents considered in Chapter 5. . . 334
8.6 Predicted and observed phases for the seven shallow water constituents considered in Chapter 5. 335
8.7 Comparison of approximate error measure values corresponding to various adjustments to MSL. 341

Summary

Barotropic depth-averaged and three-dimensional
tidal programs for shallow seas.

This thesis reports the development and testing of three programs for computing tides in shallow seas and their particular application to Spencer Gulf, South Australia.

The first program solves the three-dimensional barotropic non-linear long-wave equations discretised using finite differences. The σ-transformation is used in the vertical with non-uniform depth-level spacing. The overall difference scheme is three-level in time and of leap-frog type for the computation of tidal elevations, and two-level in time for velocity calculations. It uses explicit differencing in the horizontal direction and implicit differencing in the vertical. The second program solves the depth-averaged analogue of these equations. The third program is an adaptation of the depth-averaged program to include the modelling of the covering and uncovering of tidal flats.

All three programs are designed to handle general boundary configurations while using only four distinct element types. Appropriate forms of the discretised equations for a particular element configuration are automatically selected using the element type numbers in algebraic switches.

The coding and accuracy of the differencing used is checked by comparing predicted results with analytical solutions for idealized basins. Wave propagation analyses of the difference formulations for linearized forms of the equations are also carried out.

Depth-averaged and three-dimensional models of Spencer Gulf are developed with the open boundary at the entrance to the Gulf. Height-specified and combined radiation/height-specified open boundary conditions are compared in the case of the depth-averaged model. Three formulations for bottom stress (depth-averaged model) and two forms for vertical eddy viscosity coefficient (three-dimensional model) are examined. The role of the horizontal eddy viscosity terms in introducing artificial friction is discussed. Both models are driven simultaneously by the four major tidal constituents O_1, K_1, M_2 and S_2. Comparisons of results using linear and non-linear equations are made in the depth-averaged case. Results clarify and extend the work from earlier numerical models of Spencer Gulf and predict new features of tidal flow near Wallaroo.

A modification of the method for incorporating the wetting and drying of tidal flats due to Flather and Heaps (1975) is presented and applied in a depth-averaged fine-grid model of Northern Spencer Gulf. It gives stable predictions over a 32 day simulation. Stability and accuracy are enhanced if a de Chèzy coefficient of quadratic friction is used. This suggests that a locally depth-dependent coefficient of quadratic friction is more suited to very shallow tidal modelling than a constant coefficient. An appraisal of the built-in filtering behaviour of some common finite difference formulations and their role in suppressing grid-scale oscillations is presented.

The Northern Spencer Gulf tidal flat model numerically confirms the observation of a residual gyre south of Lowly Point. A complementary gyre is predicted to the north of Lowly Point. The model predicts that Ward Spit, a large sand bar to the east of Port Bonython, is uncovered only at low springs. This prediction is supported by annotation on an old map of the region. A mechanism for the creation and maintenance of Ward Spit is suggested based on a plot of residual vectors for depth-averaged velocity.

UNIVERSITY OF ADELAIDE LIBRARY

Chapter 1

Introduction

During the early 1970's, much controversy arose over a proposal to establish a petrochemical works near Redcliff Point on the far north-east coast of Spencer Gulf, South Australia (see Figure 1.1).

Key points made during the environmental debate that ensued were that the water off Redcliff Point is very shallow and lined with coastal mangroves, and is part of the northern region of the Gulf where important prawn and fish nurseries are located. In the event of spillage of hydrocarbon raw materials or by-products, it seemed unlikely that natural tidal flushing could adequately disperse the hydrocarbons quickly enough to avoid a significant impact on marine life. Green (1984) was of the view that the waters of the Gulf in this region are arranged in cells, formed according to the local coastal topography, and generally insulated from the main flushing effect of the tides.

On the other hand, development of South Australia's gas reserves was proceeding and it seemed sensible to process the hydrocarbons accompanying gas production locally, rather than burn them off or export them elsewhere for processing.

In due course plans for a smaller scale hydrocarbon processing plant further south at what is now known as Port Bonython were unveiled in the late 1970's. Included in the new initiative was a proposal to build a 2 km long jetty at the end of which would be placed a loading berth aligned in the direction of the prevailing tidal stream. This project has gone ahead.

While satisfying industrial needs and meeting environmental safeguards, the facility at Port Bonython also provides a new site for a tide gauge and the development has rekindled interest in the tidal dynamics of the region.

For example, "north of Lowly Point residual currents superposed on the oscillatory tidal currents, and reported by fishermen, were ... found to be of the order of $0.25\,\mathrm{m\,s^{-1}}$. They were directed southerly in the eastern channels and northerly in western channels. However, buoys lost from their moorings were recovered in almost the same place some days later. These apparently contradictory lines of evidence are explained by Green (1984) as residual currents organized in cells of circulation, driven by the tides and separated by nodes where the residual current is a minimum" (Noye, 1984c, p.206). Green (1984) and Noye (1984c) also refer to a gyre formed during the ebb flow just south of Lowly Point. The Environmental Impact Study says: "The eddy is located between Stony Point and Lowly Point at 1 km to 2 km offshore and appears to maintain its stability for most of the tidal cycle, perhaps breaking down for a few hours at the slack water between flood and ebb tides" (SANTOS Limited, 1981). Direct observations of this feature have been made.

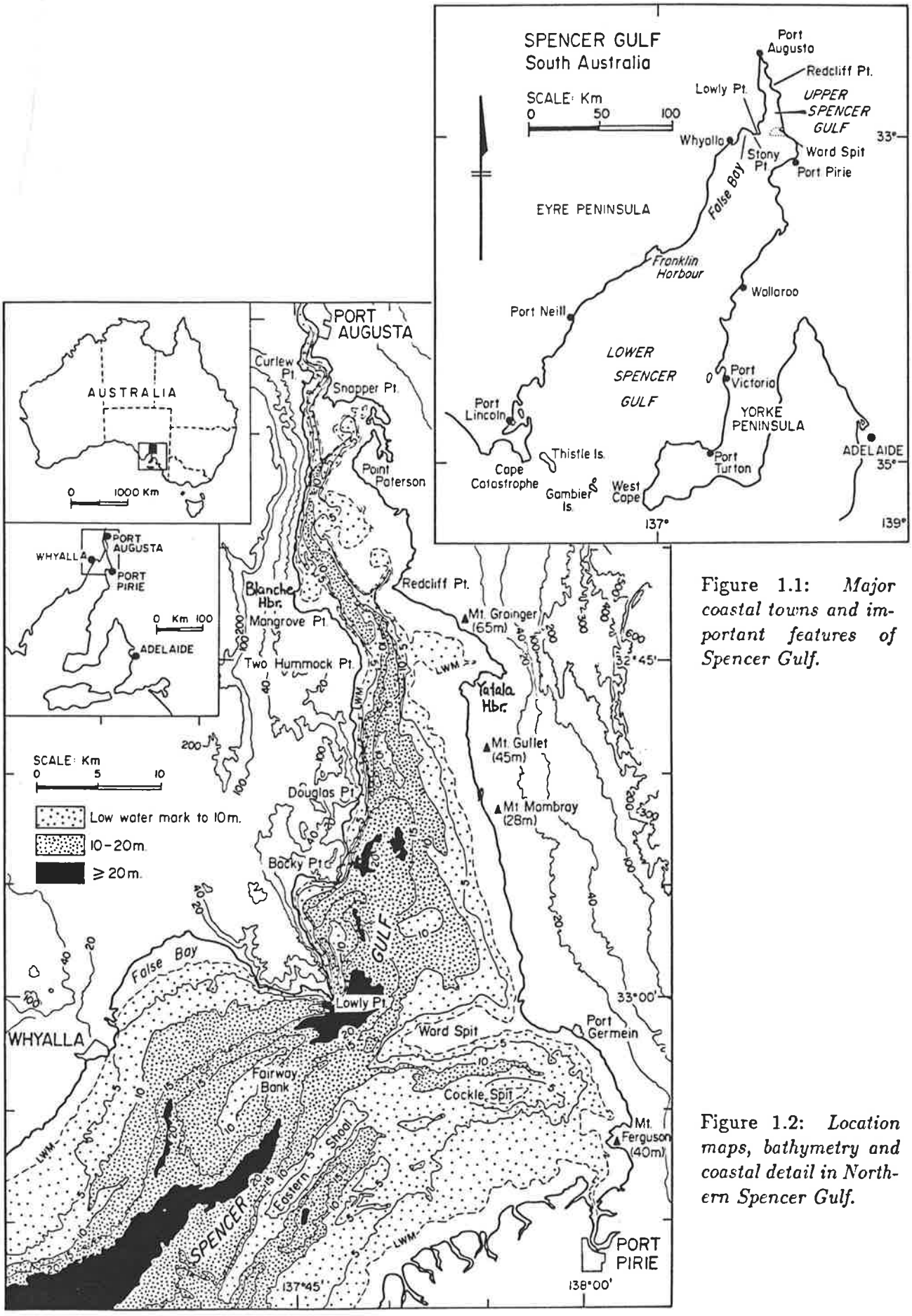


Figure 1.1: *Major coastal towns and important features of Spencer Gulf.*

Figure 1.2: *Location maps, bathymetry and coastal detail in Northern Spencer Gulf.*

Noye (1984c) refers to it being "seen on aerial photographs as a narrow band of lighter coloured water" (ibid., p.206). Numerical prediction of the gyre, and a complementary gyre north of Lowly Point, is achieved in Chapter 8.

On a larger scale, the strength of the semi-diurnal S_2 component in South Australian tides guarantees the return of high and low tides at almost the same time each day, something taken for granted by the local population. Since S_2 is of similar strength to M_2 in these waters, the semi-diurnals cancel at springs producing a phenomenon locally termed the "dodge" tide, when the only perceptible movement in tide height is due to the diurnals or to the minor constituents. This points to a vibrant spring-neap cycle, a phenomenon which is responsible for other interesting features of the Gulf's circulation.

It is with this background of environmental and scientific interest that the present modelling of the tides in Spencer Gulf has been approached. Notwithstanding the work of earlier researchers, could the particular features of tidal flow in Spencer Gulf be more accurately reproduced by a new numerical approach? If so, perhaps new features might be predicted leading to a greater understanding of the tides in this region. With enhanced understanding there might emerge a firmer basis for the more intelligent use of, and greater concern and respect for, the waters of Spencer Gulf.

The models developed ought to be stable and flexible. As the need arises to investigate different aspects of the Gulf's tidal dynamics, the models should be able to be extended and applied easily. The programs should also be able to be used to model other coastal regions.

In the process of developing the numerical models described herein, some contributions to the overall science of computer modelling and to the art of its application have been made. These are reported in the remaining chapters.

Chapter 2 contains the mathematical formulations of the tidal equations. These are the barotropic Reynolds-averaged Navier Stokes equations for long waves. The so-called σ-transformation is used; this maps the surface and bottom levels onto flat surfaces in the transformed frame of reference. Eleven depth levels are used, with the relative spacing between the levels varying smoothly from fine to coarse and back to fine as one moves up or down the water column. Although Spencer Gulf can be classified as an "inverse estuary", indicating that salinity decreases noticeably from the northern end along the axis of the Gulf, saline concentration and consequent changes in water density are not significant driving mechanisms of Gulf circulation on tidal time scales. Likewise, although water temperature varies noticeably from the mouth of the Gulf to its tip near Port Augusta, this variation takes place mostly in the region nearest the tip and is therefore a minor influence in the context of the models developed here.

Provis and Lennon (1983) point out that temperature and salinity effects may be important components of the *residual* current during neaps in the South Australian Gulfs. At all other times "observations of temperature and salinity together with the records from moored current meters have shown the Gulfs to be well mixed in the vertical sense" (ibid., pp. 352–353).

It is not the intent of this thesis to address the accuracy of the mathematical formulation describing the tidal phenomenon in Spencer Gulf. The formulation given is believed to be reasonably accurate; the general equations used are well known and standard throughout tidal modelling literature. In this thesis we are concerned with a flexible numerical approach to their stable and accurate solution.

In **Chapter 3** the finite difference scheme used to solve the mathematical equations

of Chapter 2 is presented. This is a new scheme, with similarities to both the classical leap-frog and forward-time schemes in the time discretisation sense. In order to make forward time calculations of the horizontal velocity components as accurate as possible, intermediate calculation of elevation is used to give estimates of total depth at half time steps. A major interest in developing this scheme has been to maximize accuracy whilst involving the minimum number of spatial gridpoints in computations. Another interest has been to write program code which is general, so that the same subroutines can be applied to any coastal region. Once the user has classified each element of the model as one of only four distinct types, the subroutines automatically select the correct form of each finite difference equation for each element of the model.

It is hoped that the computer programs described here will be used to provide important tidal, navigational, marine species management, environmental and engineering information at other coastal sites. They can also be used to provide this information at oil-rig sites on a continental shelf.

Chapter 4 is devoted to the numerical and analytical checking of program code. Because the subroutines are designed to be independent of the region being modelled, it can be expected that the program code is intricate and therefore thorough checking is necessary. Various numerical tests are used to check the coding of all major terms of the equations, whether differenced horizontally or vertically. Using constant Coriolis force, equivalence of results is required when applying the program code to a rectangular bay which is rotated through eight basic orientations. Wave propagation characteristics are derived for linear cases. In the vertical, numerical tests are carried out using a realistic vertical eddy viscosity coefficient.

In **Chapter 5** a depth-averaged model of Spencer Gulf is developed. This model is forced at the open boundary by the four major tidal constituents O_1, K_1, M_2 and S_2. The "height specified" open boundary condition is used. The direct effect of the tide generating forces on the waters of the Gulf is ignored. Simulations of 32 days are conducted in order to obtain the predicted data sets of 29 days duration required as input to our tidal analysis programs. Results using various forms for bed friction parameterization are compared. A linear form of the program is implemented and results are compared with those obtained using the non-linear formulation.

The results obtained by previous modellers of this Gulf are checked and clarified. An interesting new feature of tidal flow predicted is the formation and dissipation of large scale tidal gyres in the region near Wallaroo in the closing stages of both the ebb and flood tide.

In **Chapter 6** various open boundary conditions are investigated by applying them to the Spencer Gulf model. It is demonstrated that for tidal modelling in this gulf, radiation open boundary conditions are not necessary — the height specified condition performs well for this model.

While wind effects have been included in the equations, only tidal effects are examined and presented in this thesis. An important "future project" will be to incorporate wind effects in the modelling of the tidal flat regions of Northern Spencer Gulf (see Chapter 8). Wind effects in the case of the movement of prawn larvae are also important and are currently being examined by Nixon (1992) using a three-dimensional form of this model.

Using a depth-averaged model, one may obtain tidal elevations and depth-averaged currents in a relatively short computational time. The results for this model are accurate so long as the corresponding horizontal depth-dependent currents do not vary significantly

in the vertical. In the large scale sense, this is a fair assumption for Spencer Gulf tides.

In order to predict detailed current structure over depth, a three-dimensional model is required (and is useful as an independent check of the general trends suggested by the depth-averaged model). A knowledge of surface velocity is important for determining the route and spread of surface pollutants. A knowledge of depth-dependent current at all levels is needed for studying the movement of prawn larvae, for which various biological models of daily vertical motion have been proposed; the prawn industry in Spencer Gulf contributes about $20 million annually to the South Australian economy. Vertical current profiles may also be used to calculate tidal stresses acting on berthing structures.

Chapter 7 reports the predictions of a three-dimensional model of the Gulf. In particular the model is used to demonstrate that the gyres reported in Chapter 5 are numerical predictions of a real phenomenon and are not just by-products of the depth-averaging process. Once again the predictions of previous three-dimensional models of the Gulf are checked and clarified.

The depth-averaged model of Spencer Gulf requires 2.5 hours of central processor time on a DEC VAX 11/785 to perform a 32 day tidal simulation. (The same simulation carried out recently took 1 hr 18 min on a PYRAMID-9820, 43 min on a SUN Microsystems SPARCstation 1+ and only 9 min on an IBM RISC System/6000 POWERserver 530.) If 11 depth levels are used in the three-dimensional model of Spencer Gulf, 18 hours of processing time are required on the VAX 11/785 to carry out the 32 day simulation. (Again, the same simulation carried out recently took 4 hr 20 min on the SUN SPARCstation 1+ and only 4 min on a Cray Y-MP 2D 2-16. In the latter case, the numerical scheme was modified so as to be able to obtain vectorizable code (Nixon, 1992).)

These computing times represent costs which are inexpensive relative to the much greater outlays that would be required to establish sufficient observation stations in the region to obtain equivalent information. To obtain observational data one generally needs to deploy gauges for at least a month, preferably 6 or 12 months, at any particular site — and it is simply not practical to obtain the amount of information at the "sites" routinely "monitored" by the computer model. The computer model acts as a means of large scale spatial and temporal interpolation taking into account the approximate bathymetry and coastline of the region. To calibrate the model and verify its predictions, some quantitative observations of tidal phenomena are required for the given study region.

In **Chapter 8** a modification of the method for incorporating tidal flats due to Flather and Heaps (1975) is presented. A fine-grid depth-averaged model of Northern Spencer Gulf is developed with an open boundary two-thirds the way north along the axis of the Gulf. Open boundary forcing for this model is taken from the predictions of the model of Chapter 5. The resulting program predicts that Ward Spit, a 10 km × 2 km sandbar to the east of Port Bonython, is uncovered only at low springs. This prediction is supported by annotation placed on an old map of the region. The Northern Spencer Gulf model is also used to seek numerical evidence for the existence of a gyre in tidal circulation south of Port Bonython. This gyre is predicted on the ebb tide, and a complementary gyre is predicted north of Lowly Point on the flood.

In conclusion, it may be stated that a new accurate and stable finite difference formulation of the long wave equations for shallow seas has been achieved. The resulting programs have been applied to depth-averaged and three-dimensional models of Spencer Gulf, and to a depth-averaged model of Northern Spencer Gulf. A modified tidal flats scheme based on concepts present in the literature has been incorporated and the resulting program

produces stable predictions from a 32 day simulation. New features of tidal circulation in Spencer Gulf have been predicted; greater detail has been provided concerning already known features.

The three-dimensional tidal program has been applied by Mitchell et al. (1984) to a study of tide and wind induced circulation in the Gulf of Carpentaria. The same program has also been used by Arnold and Noye (1986b) to investigate the three-dimensional structure of tide and wind induced currents in Bass Strait. These applications demonstrate the flexibility and generality of the element coding procedure developed.

Further to these applications, both depth-averaged and depth-dependent tidal and tidal plus wind induced currents predicted by these models have been used by I'Anson (1989) and Wong (1990) as input to advection-diffusion schemes for prawn larvae movement in the Spencer Gulf region. This work is summarized in Noye et al. (1992). Nixon (1992) has restructured the numerical scheme of the three-dimensional program in order to obtain program code that runs at vector speeds on a Cray. The long-term aim of this work is to conduct six month tidal and tidal plus wind simulations of the entire spawning season of the prawns, spanning peak spawning and settlement periods, as part of developing sound management strategies for the prawn fishery in Spencer Gulf.

Chapter 2

Mathematical Formulation

2.1 Introduction

In this chapter the equations describing barotropic tidal motion are presented for three-dimensional and depth-averaged flows. The associated boundary conditions and initial conditions are also formulated.

For the three-dimensional equations, closure is obtained by prescribing a functional form for the vertical eddy viscosity coefficient. An alternative method of closure, namely solving for the vertical eddy viscosity directly by incorporating the equations for transport and dissipation of turbulent kinetic energy, is not used because firstly, the computational time required by such schemes is appreciably greater (Arnold, 1985, p.144) and secondly, because of difficulties encountered in solving these equations to obtain positive definite results.

The functional form chosen for the vertical eddy viscosity coefficient is given in Chapter 7. It is one of many forms available. Stevens (1990) lists some of these for the tidal case, Arnold (1985) investigates appropriate forms in the case of wind driven flow in lakes and Davies (1985a) considers their form for wind and tide driven flows; these are just a few of the many authors who have written on this subject. The form chosen here fits the basic criteria and performs well in application to Spencer Gulf. Likewise, the form of the coefficient used to relate wind speed to surface stress is taken in good faith from other authors, as are the various forms considered for bottom stress formulation in the depth-averaged flow case.

It is not the primary intent of this thesis to discuss or compare the merits of the various mathematical formulations available, although some discussion and comparison does take place in later chapters. Relatively standard formulations have been chosen and we seek the best method of solution of the governing equations in the light of these choices.

This work has appeared in research progress reports to the author's scholarship disbursement body (Bills, 1981, 1982).

2.2 The three-dimensional equations

The three-dimensional equations that describe tidal motion are well known and will only be stated here. For a derivation using basic considerations of forces acting on an element of fluid see Nihoul (1975). The equations are written for barotropic conditions where

stratification in the horizontal and vertical due to temperature and density differences is neglected over tidal time scales.

In the orthogonal cartesian (x, y, z, t) system, the equations consist of the mass conservation equation for incompressible flow (the continuity equation):

$$\frac{\partial u}{\partial x} + \frac{\partial v}{\partial y} + \frac{\partial w}{\partial z} = 0\,, \tag{2.1}$$

and the three components of the momentum conservation equation (the momentum equations):

$$\begin{aligned}\frac{\partial u}{\partial t} + u\frac{\partial u}{\partial x} + v\frac{\partial u}{\partial y} + w\frac{\partial u}{\partial z} - fv = &-\frac{1}{\rho}\frac{\partial p}{\partial x} \\ &+\frac{\partial}{\partial x}\left(N_x\frac{\partial u}{\partial x}\right) + \frac{\partial}{\partial y}\left(N_y\frac{\partial u}{\partial y}\right) + \frac{\partial}{\partial z}\left(N_z\frac{\partial u}{\partial z}\right),\end{aligned} \tag{2.2}$$

$$\begin{aligned}\frac{\partial v}{\partial t} + u\frac{\partial v}{\partial x} + v\frac{\partial v}{\partial y} + w\frac{\partial v}{\partial z} + fu = &-\frac{1}{\rho}\frac{\partial p}{\partial y} \\ &+\frac{\partial}{\partial x}\left(N_x\frac{\partial v}{\partial x}\right) + \frac{\partial}{\partial y}\left(N_y\frac{\partial v}{\partial y}\right) + \frac{\partial}{\partial z}\left(N_z\frac{\partial v}{\partial z}\right),\end{aligned} \tag{2.3}$$

$$\begin{aligned}\frac{\partial w}{\partial t} + u\frac{\partial w}{\partial x} + v\frac{\partial w}{\partial y} + w\frac{\partial w}{\partial z} - F_z = &-\frac{1}{\rho}\frac{\partial p}{\partial z} \\ &+\frac{\partial}{\partial x}\left(N_x\frac{\partial w}{\partial x}\right) + \frac{\partial}{\partial y}\left(N_y\frac{\partial w}{\partial y}\right) + \frac{\partial}{\partial z}\left(N_z\frac{\partial w}{\partial z}\right).\end{aligned} \tag{2.4}$$

These equations are to be solved in conjunction with the free surface condition

$$w|_{z=\zeta} = \frac{D\zeta}{Dt}, \qquad \text{i.e.,} \qquad w|_{z=\zeta} = \frac{\partial \zeta}{\partial t} + (u|_{z=\zeta})\frac{\partial \zeta}{\partial x} + (v|_{z=\zeta})\frac{\partial \zeta}{\partial y}, \tag{2.5}$$

and the bottom condition

$$w|_{z=-h} = \frac{D(-h)}{Dt} = 0, \qquad \text{i.e.,} \qquad w|_{z=-h} = -(u|_{z=-h})\frac{\partial h}{\partial x} - (v|_{z=-h})\frac{\partial h}{\partial y} = 0. \tag{2.6}$$

The symbols used in the above equations have the following meaning:

t	is the time, here chosen to be measured relative to the start of the epoch (00:00 hr on 1/1/1900, Greenwich Mean Time (G.M.T.)),
x, y, z	are the rectangular cartesian co-ordinates with the x and y axes in the plane of mean sea level and the z axis directed vertically upwards,
u, v, w	are the respective depth-dependent x, y, z velocity components,
p	is the pressure, resulting from the head of the fluid and atmospheric pressure,
f	is the Coriolis parameter, and has the form $2\Omega \sin\Phi$ where Ω is the Earth's angular velocity of rotation and is taken to be $\Omega = 2\pi/(3600 \times 23.9333)\,\text{sec}^{-1}$, and Φ is latitude north (Φ is negative in the southern hemisphere),
ρ	is the density of sea water, assumed constant at $1027\,\text{kg/m}^3$,

F_z is the z-component of the external forces, attributed to acceleration due to gravity g, taken as $9.81\,\mathrm{m/sec^2}$,

N_x, N_y, N_z are the eddy viscosity coefficients in the indicated directions (N_x and N_y are often taken as constants, as in the work on Spencer Gulf done by Noye et al. (1981, 1982) — however, in the present work, a formulation based on that used by Schwiderski (1980) is used (see Chapters 3 and 5); N_z is given a variable form (see Chapter 7)),

ζ is the free surface elevation measured in the direction of increasing z relative to mean sea level,

h is the distance of the sea bed below mean sea level, and

$q|_{z=z^*}$ is notation meaning that q is evaluated at (depth level) $z = z^*$.

In equations (2.2)–(2.4), the Boussinesq form of the Reynolds stresses is used. Since Spencer Gulf is less than 350 km long and half that in width, spherical co-ordinates introducing the effect of the Earth's curvature are not used.

Because the vertical fluid acceleration is generally negligible compared with the acceleration due to gravity, equation (2.4) can be approximated by the hydrostatic equation for pressure, viz.

$$\frac{\partial p}{\partial z} = -\rho g. \tag{2.7}$$

On integration over depth from some level z to the surface ζ we obtain

$$p = p_a + \rho g\,(\zeta - z)\,, \tag{2.8}$$

where p_a is the atmospheric pressure. This equation is used to eliminate p from equations (2.2) and (2.3).

To solve the equations more easily using finite difference techniques, a transformation of the depth co-ordinate is introduced. The transformation is one of a class of σ-transformations. This approach was initiated by Phillips (1957) for numerical weather forecasting and has subsequently been employed in tidal modelling where it has been used by many authors, e.g. Freeman (1970), Freeman et al. (1972), Spaulding (1974), Noye et al. (1981, 1982), Davies and Stephens (1983), Wolf (1983), Davies (1985a,b,c) and Johns and Oguz (1987). We define

$$\eta = \frac{\zeta - z}{\zeta + h} = \frac{\zeta - z}{H}, \tag{2.9}$$

where $H = \zeta + h$ is the total depth. The transformation maps the sea surface $z = \zeta(x, y, t)$ and the sea bed $z = -h(x, y)$ onto the flat surfaces $\eta = 0$ and $\eta = 1$, respectively (see Figure 2.1), and has the additional advantage of providing greater resolution per unit depth for shallow water. Under the transformation the u and v components of velocity are computed directly. However, the w component is computed indirectly by calculating a new velocity component ω, defined to be normal to the planes $\eta = \textit{constant}$ by

$$\omega = \frac{D\eta}{Dt}. \tag{2.10}$$

Expanding (2.10) using (2.9) gives

$$\omega = \frac{1}{H}\left(-w + (1-\eta)\left[\frac{\partial \zeta}{\partial t} + u\frac{\partial \zeta}{\partial x} + v\frac{\partial \zeta}{\partial y}\right] - \eta\left[u\frac{\partial h}{\partial x} + v\frac{\partial h}{\partial y}\right]\right). \tag{2.11}$$

Transformed versions of equations (2.1)–(2.4) can be obtained using (2.9). These are a particular case of the general equations used by Noye et al. (1982) for transformations of all three spatial co-ordinates.

For the continuity equation, a depth-averaged form is obtained:

$$\frac{\partial \zeta}{\partial t} = -\frac{\partial (HU)}{\partial x} - \frac{\partial (HV)}{\partial y}, \tag{2.12}$$

where U and V are the depth-averaged horizontal velocities:

$$U = \int_0^1 u \, d\eta \quad \text{and} \quad V = \int_0^1 v \, d\eta. \tag{2.13}$$

The respective forms of the transformed x and y momentum equations are

$$\begin{aligned} \frac{\partial u}{\partial t} + u\frac{\partial u}{\partial x} + v\frac{\partial u}{\partial y} + \omega\frac{\partial u}{\partial \eta} - fv = &-g\frac{\partial \zeta}{\partial x} - \frac{1}{\rho}\frac{\partial p_a}{\partial x} \\ &+ N_x\frac{\partial^2 u}{\partial x^2} + N_y\frac{\partial^2 u}{\partial y^2} + \frac{1}{H^2}\frac{\partial}{\partial \eta}\left(N_\eta \frac{\partial u}{\partial \eta}\right), \end{aligned} \tag{2.14}$$

and

$$\begin{aligned} \frac{\partial v}{\partial t} + u\frac{\partial v}{\partial x} + v\frac{\partial v}{\partial y} + \omega\frac{\partial v}{\partial \eta} + fu = &-g\frac{\partial \zeta}{\partial y} - \frac{1}{\rho}\frac{\partial p_a}{\partial y} \\ &+ N_x\frac{\partial^2 v}{\partial x^2} + N_y\frac{\partial^2 v}{\partial y^2} + \frac{1}{H^2}\frac{\partial}{\partial \eta}\left(N_\eta \frac{\partial v}{\partial \eta}\right). \end{aligned} \tag{2.15}$$

The equation for the calculation of ω is

$$\omega = -\frac{1}{H}\frac{\partial}{\partial x}\{H\,(U(\eta) - \eta U)\} - \frac{1}{H}\frac{\partial}{\partial y}\{H\,(V(\eta) - \eta V)\}, \tag{2.16}$$

and the supplementary equation for the calculation of w is obtained by rearranging (2.11):

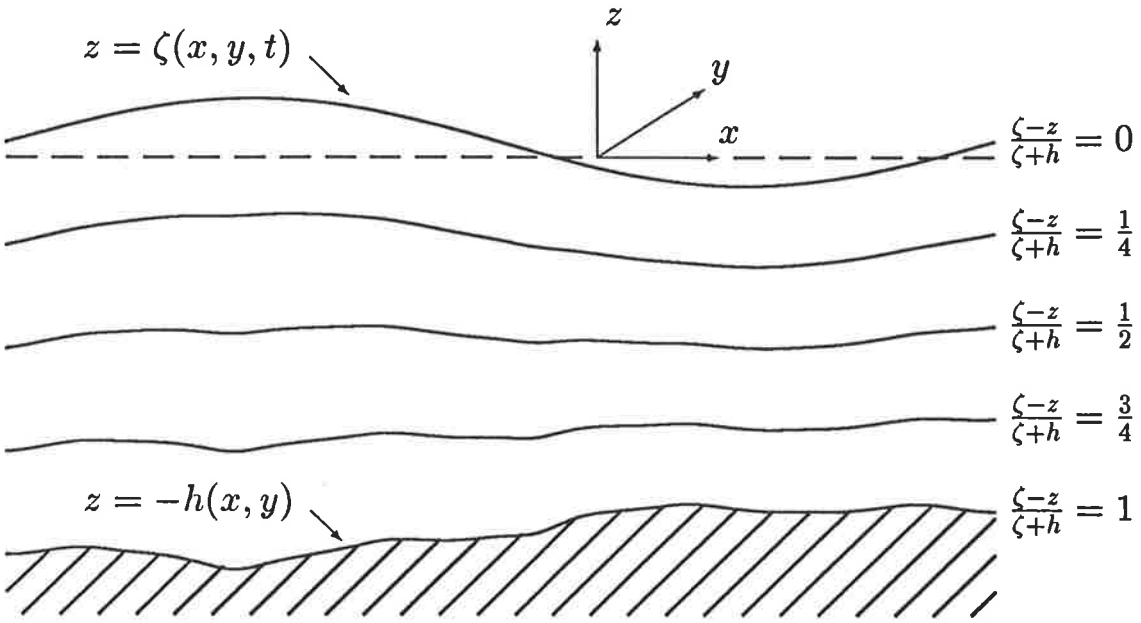
$$w = -H\omega + (1-\eta)\left\{\frac{\partial \zeta}{\partial t} + u\frac{\partial \zeta}{\partial x} + v\frac{\partial \zeta}{\partial y}\right\} - \eta\left\{u\frac{\partial h}{\partial x} + v\frac{\partial h}{\partial y}\right\}. \tag{2.17}$$

Only the leading term in the transformation of each horizontal diffusive term has been retained in equations (2.14)–(2.15). The remaining terms are omitted because Teubner (1976) found they have negligible effect on the predicted displacements and velocities in tidal modelling; these terms were also omitted by Freeman (1970) and Spaulding (1974) in their work. The form used for the vertical eddy viscosity coefficient N_η is

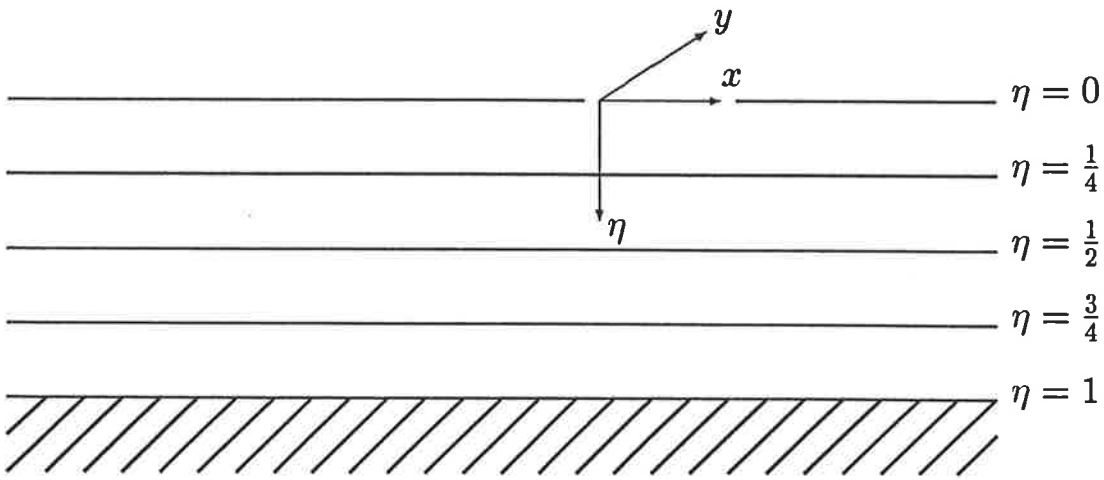
$$N_\eta(x, y, \eta, t) = \alpha + \beta F(\eta) H \sqrt{U^2 + V^2}, \tag{2.18}$$

where

- α is a minimum (or background) absolute value for N_η; for tidal flows it is greater than or equal to molecular eddy viscosity, but is typically $0.0005\,\mathrm{m}^2/\mathrm{sec}$ (as used by Noye et al. 1981, 1982) and for tidal plus wind induced flows it is larger, typically $0.02\,\mathrm{m}^2/\mathrm{sec}$ (as used by Davies 1985b),
- $F(\eta)$ is some prescribed variation of the vertical eddy viscosity coefficient in the η direction, and
- β is a dimensionless constant, determined numerically as the optimal value required to minimize errors between observed and predicted results. The form chosen for $F(\eta)$ influences the optimal choice for β.



(a) The x, y, z system showing surfaces given by $(\zeta - z)/(\zeta + h) = \textit{constant}$.



(b) The x, y, η system showing the transformed surfaces as level surfaces given by $\eta = \textit{constant}$.

Figure 2.1: The equi-spaced curved surfaces $(\zeta - z)/(\zeta + h) = \textit{constant}$ are mapped onto the level surfaces $\eta = \textit{constant}$ by the vertical transformation.

Expressions like (2.18) for the vertical eddy viscosity coefficient have been used by Owen (1980), Noye et al. (1981, 1982) and Wolf (1983).

The terms $U(\eta)$ and $V(\eta)$ of equation (2.16) are depth-averaged velocities over a layer of vertical thickness η extending downwards from the surface, namely

$$U(\eta) = \int_0^\eta u \, d\eta' \quad \text{and} \quad V(\eta) = \int_0^\eta v \, d\eta'. \tag{2.19}$$

Equations (2.13) are equivalent to equations (2.19) for $\eta = 1$, i.e. $U = U(1)$ and $V = V(1)$.

Equations (2.12)–(2.16) are the basic equations used in this work to solve for the barotropic flow variables ζ, u, v, ω, U and V. Equation (2.18) provides an expression for N_η and closes the system of equations. Equations (2.13) and (2.19) define the required depth-averaged velocity quantities. Equation (2.17) is not necessary to the overall computation, but it may be used to calculate the cartesian vertical velocity w if required.

Appropriate boundary and initial conditions are required to apply the model to a particular region.

In the finite difference approach, the actual boundary of the plan of the sea region is approximated by horizontal orthogonal line segments parallel to the x and y axes and it is assumed that the sides of the model can be approximated by rectangular vertical surfaces. The latter approximation is required by the nature of the vertical transformation and it also follows from the way the interior sea region is modelled by a connected set of flat-bottomed rectangular boxes.

Consider the following boundary conditions:

1. Assuming the model coastline is "solid", a condition of impermeability is set, viz.

$$(u, v) \cdot \underline{n} = 0 \quad \text{on the coastline,} \tag{2.20}$$

   where $\underline{n}$ is a vector normal to the "coastline". If it is assumed that the coastline is constructed of straight line segments passing only through u or v gridpoints on a rectangular staggered grid (see Figure 3.1) then (2.20) leads to the numerical conditions that, where the coastline runs parallel to the

   (i) x-axis, $v = 0$ at v gridpoints on the coast,

   (ii) y-axis, $u = 0$ at u gridpoints on the coast.

2. A condition of no-slip is used at the sea bed so that

$$u = v = \omega = w = 0 \quad \text{at} \quad \eta = 1. \tag{2.21}$$

3. Application of the free surface condition (2.5) in (2.17) with $\eta = 0$ shows that

$$\omega = 0 \quad \text{at} \quad \eta = 0, \tag{2.22}$$

   for all time t.

4. If only tidal forcing is considered, the surface η-gradients of the horizontal velocity components at the sea surface are zero; i.e.

$$\left.\frac{\partial u}{\partial \eta}\right|_{\eta=0} = 0 \quad \text{and} \quad \left.\frac{\partial v}{\partial \eta}\right|_{\eta=0} = 0. \tag{2.23}$$

If there is wind forcing it is assumed that the horizontal components S_x, S_y of surface stress are proportional to the η-gradient of surface current in the following way:

$$S_x = -\frac{\rho}{H}\left(N_\eta \frac{\partial u}{\partial \eta}\right)\Big|_{\eta=0}, \tag{2.24}$$

$$S_y = -\frac{\rho}{H}\left(N_\eta \frac{\partial v}{\partial \eta}\right)\Big|_{\eta=0}. \tag{2.25}$$

The surface stress components may also be expressed in terms of the wind velocity field using the following quadratic law:

$$S_x = \rho_a c_{10} u_{10}\sqrt{(u_{10})^2 + (v_{10})^2}, \tag{2.26}$$

$$S_y = \rho_a c_{10} v_{10}\sqrt{(u_{10})^2 + (v_{10})^2}. \tag{2.27}$$

Here,

ρ_a is the density of air (assumed constant at $1.225\,\mathrm{kg/m^3}$),

(u_{10}, v_{10}) are the horizontal components of wind velocity recorded 10 m above mean sea level (MSL), and

c_{10} is a dimensionless drag coefficient which depends on the wind speed according to some empirical formula. Bode and Sobey (1985) suggest that perhaps the simplest and most widely applicable is that proposed by Wu (1982), viz.

$$c_{10} = \left(0.8 + 0.065\sqrt{(u_{10})^2 + (v_{10})^2}\right) \times 10^{-3}, \tag{2.28}$$

for light to hurricane force winds.

The wind field may be specified from meteorological data, or may take some idealized time and space dependent form, or may be specified as steady and homogeneous for the entire simulation.

5. The atmospheric pressure p_a may be specified from meteorological data, or may take an idealized form, or may be assumed to be constant.

6. The open boundaries of the model pass through elevation points and gridpoints at which the velocity is tangential to these boundaries. Data is not available to provide information about the velocity normal to the open boundary in this work. In the case of tide-only forcing, tidal elevation ζ_b at position b on the open boundary is specified for all time as the sum of the contributions of the dominant tidal constituents. The four major astronomical constituents are used and

$$\zeta_b = \sum_{m=1}^{4} f_m a_m \cos(\omega_m t + V_0 + \mu_m - \gamma_m), \tag{2.29}$$

$a_m \to a_{m,b}$ $\quad V_0 \to V_{0,m}$ $\quad \gamma_m \to \gamma_{m,b}$

where

a_m, γ_m are the **tide-height constants** (amplitude and phase, respectively) for constituent m,

ω_m is the angular frequency of the constituent (corresponding to idealized motions of the sun and/or moon with period less than one year),

f_m, μ_m are amplitude and phase correction factors, respectively, taking into account the longer period changes in the celestial positions, and

$V_{0,m}$ is the phase of constituent m at Greenwich at the start of the epoch.

Two of the constituents are diurnal (O_1,K_1) and two are semi-diurnal (M_2,S_2). Condition (2.29) is applied at every elevation gridpoint of the open boundaries and the specifications of a_m and γ_m vary with position from element to element. This type of condition is commonly referred to as a "height specified" open boundary condition. The direct effect of the tide generating forces on the waters of Spencer Gulf is not included.

With tide and meteorological forcing it is not appropriate to constrain the movement of the surface at the open boundaries. The open boundaries must be able to both accommodate tidal forcing and be free to move in response to the interior solution. The boundary condition used should allow the outward passage of waves (transients produced when modelling commences, meteorologically generated waves and tidally induced outgoing waves) as well as allow the inward passage of waves (meteorologically or tidally induced). An appropriately discretised Sommerfeld condition may be used, viz.

$$\frac{\partial \zeta_b}{\partial t} + c\frac{\partial \zeta_b}{\partial n} = 0, \tag{2.30}$$

where phase speed c is calculated in the Orlanski (1976) manner (see Chapter 6), n is measured in the outward normal direction $\underline{n}$, and meteorological and tidal forcing are specified through the open boundary elevation ζ_b.

The initial conditions used are:

$$\zeta = u = v = \omega = w = U = V = 0 \quad \text{at time} \quad t = 0. \tag{2.31}$$

Consequently, total depth H is initially set as mean sea level depth h. Along the open boundaries elevation ζ_b at time $t = 0$ is given by (2.29) for models forced by both tide and mixed tide and meteorological inputs. The total depth at the open boundaries is therefore given by

$$H_b = h_b + \zeta_b \quad \text{at time} \quad t = 0, \tag{2.32}$$

at each open boundary elevation gridpoint b.

For numerical solution, the elevation equation (2.12) requires one initial condition for every ζ, U and V gridpoint of the model — this is provided by expressions (2.29) and (2.31). Coastal boundary conditions are also required for each of the depth-averaged horizontal velocity fields U and V — these are provided by the depth-averaged form of the impermeability condition (2.20) (see condition (2.37)) at coastal velocity gridpoints.

The momentum equations (2.14) and (2.15) require one initial condition for every ζ, u, v and ω gridpoint of the model — this is provided by expression (2.31). They require coastal boundary conditions for the horizontal u and v fields — these are provided by the impermeability condition (2.20); they also require conditions on flow at the bed and at the free surface — these are provided by the no-slip condition (2.21), the free surface condition (2.22) and the appropriate horizontal surface conditions (2.23)–(2.28).

The initial conditions for equations (2.16) and (2.17) are given by (2.31); the horizontal boundary conditions are those given by the impermeability expression (2.20) and the vertical boundary conditions used are the conditions of no slip (2.21) and the free surface condition (2.22).

2.3 The depth-averaged equations

The depth-averaged equations are obtained by integrating equations (2.12) and (2.14)–(2.15) from $\eta = 0$ to $\eta = 1$.

Using notation with the same meaning as before, the continuity equation remains

$$\frac{\partial \zeta}{\partial t} = -\frac{\partial (HU)}{\partial x} - \frac{\partial (HV)}{\partial y}. \tag{2.33}$$

Using a quadratic form for bottom friction to parameterize the vertical turbulence, the momentum equations for the depth-averaged horizontal velocity components U,V are, respectively,

$$\begin{aligned} \frac{\partial U}{\partial t} + U\frac{\partial U}{\partial x} + V\frac{\partial U}{\partial y} - fV = &-g\frac{\partial \zeta}{\partial x} - \frac{1}{\rho H}\frac{\partial p_a}{\partial x} \\ &+N_x\frac{\partial^2 U}{\partial x^2} + N_y\frac{\partial^2 U}{\partial y^2} + \frac{\rho_a}{\rho H}c_{10}u_{10}\sqrt{(u_{10})^2 + (v_{10})^2} - C_b\frac{1}{H}U\sqrt{U^2+V^2}, \end{aligned} \tag{2.34}$$

and

$$\begin{aligned} \frac{\partial V}{\partial t} + U\frac{\partial V}{\partial x} + V\frac{\partial V}{\partial y} + fU = &-g\frac{\partial \zeta}{\partial y} - \frac{1}{\rho H}\frac{\partial p_a}{\partial y} \\ &+N_x\frac{\partial^2 V}{\partial x^2} + N_y\frac{\partial^2 V}{\partial y^2} + \frac{\rho_a}{\rho H}c_{10}v_{10}\sqrt{(u_{10})^2 + (v_{10})^2} - C_b\frac{1}{H}V\sqrt{U^2+V^2}. \end{aligned} \tag{2.35}$$

The form given for the advective terms in (2.34)–(2.35) assumes that the depth-dependent currents do not vary significantly in the vertical (Flather and Heaps, 1975; Johns, 1978), so that

$$\int_0^1 u^2\,d\eta = U^2, \quad \int_0^1 uv\,d\eta = UV, \quad \int_0^1 v^2\,d\eta = V^2. \tag{2.36}$$

The coefficient of quadratic bottom friction C_b may take a constant or depth-dependent form (see Chapter 5). In either case a dimensionless constant must be determined for particular flow conditions by numerical experiments seeking to minimize the differences between observed and predicted results; a typical value, if C_b takes a globally constant form, is $C_b = 0.0025$ for coastal seas.

The boundary conditions for depth-averaged flow are analogous to those used for three-dimensional flow:

1. A condition of zero flow normal to the coastline is set:

$$(U, V) \cdot \underline{n} = 0 \quad \text{on the coastline,} \tag{2.37}$$

where $\underline{n}$, as in (2.20), is a vector normal to the "coastline". If the coastline is constructed of straight line segments passing only through U or V gridpoints on a rectangular staggered grid this leads to the numerical conditions that, where the coastline runs parallel to the

(i) x-axis, $V = 0$ at V gridpoints on the coast,

(ii) y-axis, $U = 0$ at U gridpoints on the coast.

If the wetting and drying of tidal flats is incorporated into the modelling, (2.37) is applied only at the permanent coastal boundary (see Chapter 8).

2. It is assumed that the wind stress components may be expressed in terms of the wind velocity field using the quadratic law given in equations (2.26) and (2.27).

The wind field may be specified from meteorological data, or may take an idealized time and space dependent form, or may be specified as steady and homogeneous throughout the simulation.

3. Atmospheric pressure may be specified from meteorological data, or may take an idealized form, or may be assumed to be constant.

4. At the open boundaries of the model, tidal elevation is specified as discussed in the previous section.

The initial conditions used in the interior of the model are:

$$\zeta = U = V = 0 \quad \text{at time} \quad t = 0. \tag{2.38}$$

Thus the total depth H in the interior is initially mean sea level depth h. Along the open boundaries elevation ζ_b at time $t = 0$ is given by (2.29) for models forced by both tidal and mixed tidal and meteorological inputs. Total depth at the open boundaries is therefore given by (2.32) at time $t = 0$.

A discussion of the specific initial and boundary conditions required for the numerical solution of each of the equations (2.33)–(2.35) parallels that given above for equations (2.12), (2.14) and (2.15).

2.4 Summary

In this chapter we have stated the mathematical equations that describe tidal flow in shallow seas. A standard transformation of the depth co-ordinate has been used to map the sea surface and sea bed onto flat planes in the depth-dependent case.

In Chapter 3 we outline a new finite difference approach to the numerical solution of the depth-dependent and depth-averaged equations. A method is described for automatically generating program code to take account of all plausible coastal and open sea boundary configurations.

Chapter 3

Finite Difference Formulation

3.1 Introduction

The finite difference method is used to approximately solve the set of simultaneous partial differential equations described in Chapter 2.

In this chapter, the finite difference grid and its component parts are defined, the finite difference expressions developed are stated and the steps taken in the computational procedure are described. The programming language used is VAX Fortran.

The equations are discretised on a rectangular staggered grid. The differencing of each term in each equation is formulated with a view to maximizing the accuracy of the approximations whilst confining the difference expressions to a "9-element" block — the computational element and its eight immediate neighbours.

By assigning one of only four characteristic integer codes to each element, based principally on whether the element represents land, sea (inside or outside the model) or part of the open boundary of the model, it is possible to write down a single generalized computer code for each finite difference equation for application to any realistic 9-element configuration. In Section 3.6 strategic decisions on the application of the finite differencing for advective and diffusive terms effectively leads to a simpler element code assignment where only three codes are actually used and the fourth, assigned to sea elements outside the model, is for presentation purposes only. Using the integer codes in simple arithmetic switches, the program automatically selects, by reason of the configuration of the neighbouring elements, the right form of the equations applying to the computational element. This is done with the minimum use of the IF statement. A general and portable computer code for application to tidal models of any coastal sea region with realistic open boundaries is obtained.

Provision for river discharge or the inclusion of barriers is also possible. Although not part of the general code, these phenomena can be included at specific sites.

The computer code was developed on a DEC VAX 11/785. The computational procedures outlined here are designed for use on such minicomputers. Access to supercomputers using vector and/or parallel architectures was not available for this work. Thus all algorithms were written so as to minimize demands on computer storage and central processor time, particularly given the heavy use of the machine by other postgraduates and a large number of undergraduates. Since most government departments, research institutions and consulting engineers at the present time only have ready access to scalar processors of the minicomputer type, the development of these computer programs in the stated

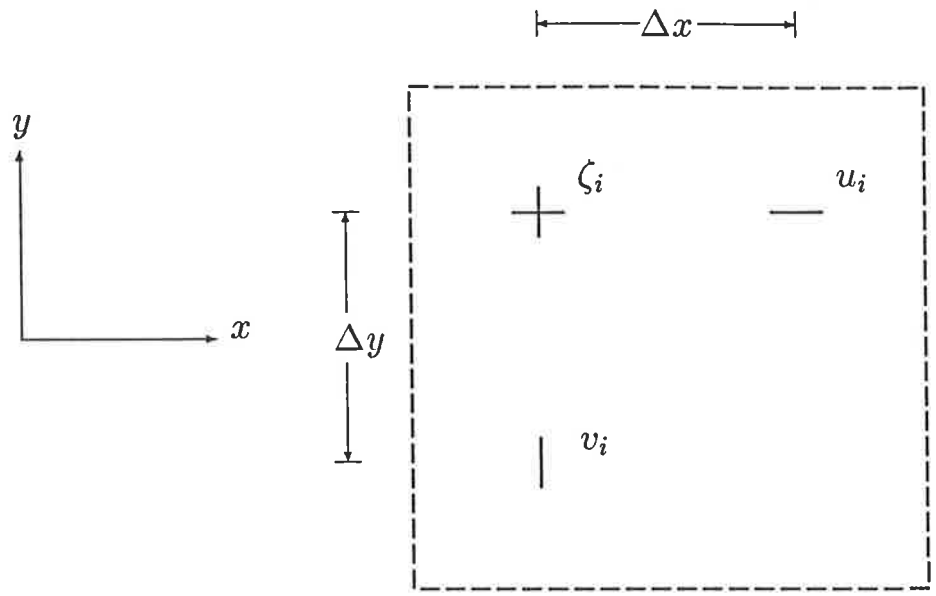


Figure 3.1: *Plan view of the ith grid element showing the ζ_i, u_i and v_i gridpoints, and the horizontal grid step sizes. The dashed lines show the boundaries of the element. This definition of a grid element is identical to that used by Flather (1972, Figure 31).*

manner should enable them to be readily adapted for use on the most commonly available machines.

On the other hand, the program code has proven to be readily vectorizable. Some thoughts regarding vectorizing the program code for a Cray machine are presented in Noye and Bills (1990). Nixon (1992) has successfully completed this task. The code may in fact be ideally suited for running on the new generation of massively parallel machines: in that case one would assign one CPU (central processing unit) to each computational element.

The material presented here, in original concept, was included in research progress reports to the author's scholarship disbursing body (Bills, 1981, 1982). More recently, discussions of the finite difference scheme have appeared in Noye and Bills (1990, 1992).

3.2 The finite difference grid

The finite difference grid used is known as the "Arakawa C" grid or the "Richardson lattice" (see, for example, Arakawa and Lamb, 1977). The advantages of using such a grid are given in detail by Flather (1972, pp. 129–131). Briefly, it allows spatial derivatives to be conveniently approximated and land boundaries to be simply represented. Batteen and Han (1981) have shown that the C-scheme is appropriate for fine-scale ($< 50\,\mathrm{km}$) ocean models. The grid is widely accepted and has been used by Platzmann (1958), Hansen (1962), Leendertse (1967, 1970), Leendertse et al. (1973), Flather and Heaps (1975), Blumberg (1977), Webber (1980), Greenberg (1981), Henry (1982), Stevens and Noye (1984), Davies (1985c) and Dube et al. (1986), to name just a few.

The basic unit of the grid is the grid *element*. Each element contains three *gridpoints*, one for the free surface elevation ζ and one for each of the two horizontal velocity compo-

nents u, v as indicated in Figure 3.1. At the elevation point, it is also convenient to define the transformed vertical velocity ω, cartesian vertical velocity w, mean sea level depth h, total depth H, Coriolis parameter f and atmospheric pressure p_a. Because the wind velocity components u_{10}, v_{10} are prescribed values and are not calculated by these programs, they are also defined at the ζ-point, but the depth-averaged velocity components U, V are defined at the respective u and v gridpoints. The spacing between gridpoints in the x-direction is Δx and in the y-direction, Δy. The size of the element, in plan, is therefore $2\Delta x \times 2\Delta y$.

The configuration of rectangular elements chosen as the best representation of the actual sea region is called the *model.* The boundary of the model in plan view is made up of the *coastline* and the *open boundary.* The coastline consists of line segments which, in the x-direction, pass only though v-points and in the y-direction pass only through u-points, and at the same time approximate most nearly the actual coastline whilst locally preserving the hydrodynamics of the sea region on the scale at which it is being modelled. The open boundary consists of line segments which pass through or change direction at ζ-points in either the x or y-directions — it also passes through tangential velocity points. The open boundary connects the interior model region with the open ocean beyond. This description differs only slightly to that given by Flather (1972).

River discharges may be incorporated in the model by suitably specifying the discharge velocity at appropriate velocity points. Likewise, barriers to tidal flow may be incorporated by setting the appropriate velocity component(s) to zero at the given sites. Barriers may be set where islands, too small to warrant representation by an entire grid element, are considered to offer sufficient resistance to flow in a particular direction(s).

On the VAX it is economical of computer time and storage space to select out the sea elements comprising the model and perform computations on them only. Such elements will be called *computational elements* and are of two types: Type 1 computational elements are those which have their ζ gridpoint lying within the model boundaries and Type 2 computational elements are those which have their ζ gridpoint lying on the open boundary. The ζ, u and v gridpoints within these computational elements are called *computational gridpoints* or, more briefly, *computational points.* Their values are assigned to one-dimensional ζ, u and v lists, again of two types. Computations are attempted at the ζ, u and v gridpoints of the Type 1 computational elements but not at u and/or v gridpoints of Type 2 computational elements if they lie on or outside the model's open boundary. The positions of the computational elements/points within the original two-dimensional lattice are obtained by means of cross reference lists established at the commencement of modelling. Thus, rather than basing the computational scheme on a two-dimensional lattice, calculations are carried out on one-dimensional lists.

This approach is computationally efficient since Fortran internal representation of two-dimensional arrays is one-dimensional: a two-dimensional array is internally stored as a list constructed by concatenating each successive column to the bottom of the previous column.

See Section 3.5 for an example of the cross-referencing required in the case of a model containing just a few grid elements. A discussion of the methods used by other researchers to perform grid calculations is also contained in Section 3.5.

Consider the ith computational element and its eight neighbours. Figure 3.2 shows the relative indexing system used. Individual gridpoints within each neighbour element carry the index label of the parent element (as in Figure 3.1). The element above the ith

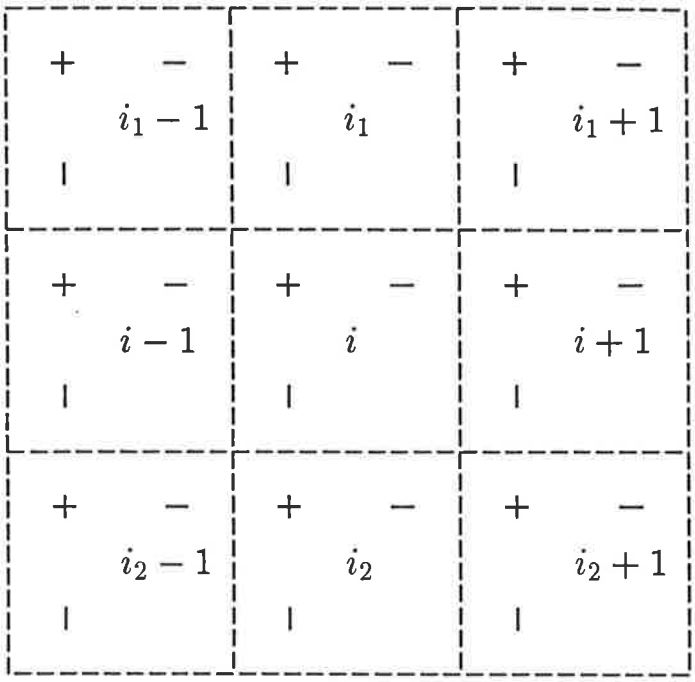


Figure 3.2: *Plan view of the ith element and the relative index labels used for its 8 immediate neighbours. The dashed lines represent element boundaries. Each quantity defined at the gridpoints of a given element is indexed according to the index of the parent element.*

is indexed the i_1th element, and the element below is indexed the i_2th. Elements to the left and right of these are indexed accordingly. In order to reference elements in the next nearest 16 neighbours of the ith element, this indexing can be generalized by indexing the element above the i_1th as the i_{11}th, and the element below the i_2th as the i_{22}th, and so on — thus providing indices for each element in a 25-element block centred on element i. In the work that follows, the central element will be labelled the ith and may at times be referred to as the *central* computational element.

During a time step of the computational process, calculations are carried out in sequential order on the list of computational elements. This corresponds to passing from one computational element to the next across each model row from left to right and down the rows from top to bottom.

In the η direction, a sequence of smoothly varying non-uniform depth level spacings is generated using the Kappa method described by Noye (1984a) (see also Sundqvist and Veronis, 1970). The spacings satisfy the relation

$$\Delta\eta_k = \Delta\eta_{k-1}(1 + \kappa\Delta\eta_{k-1}), \tag{3.1}$$

for a given parameter κ. The terms $\Delta\eta_k$, $\Delta\eta_{k-1}$ are defined in Figure 3.3; for example, $\Delta\eta_k$ is the distance between the η_k and η_{k+1} depth levels. Uniform spacings correspond to the value $\kappa = 0$. For non-zero κ, the structure of the spacings is chosen to vary symmetrically from fine near the sea bed, to coarse at mid levels and back to fine near the surface. This "fine-coarse-fine" structure allows greater resolution both near the sea bed, where vertical gradients in the horizontal velocity components can be large, and near the sea

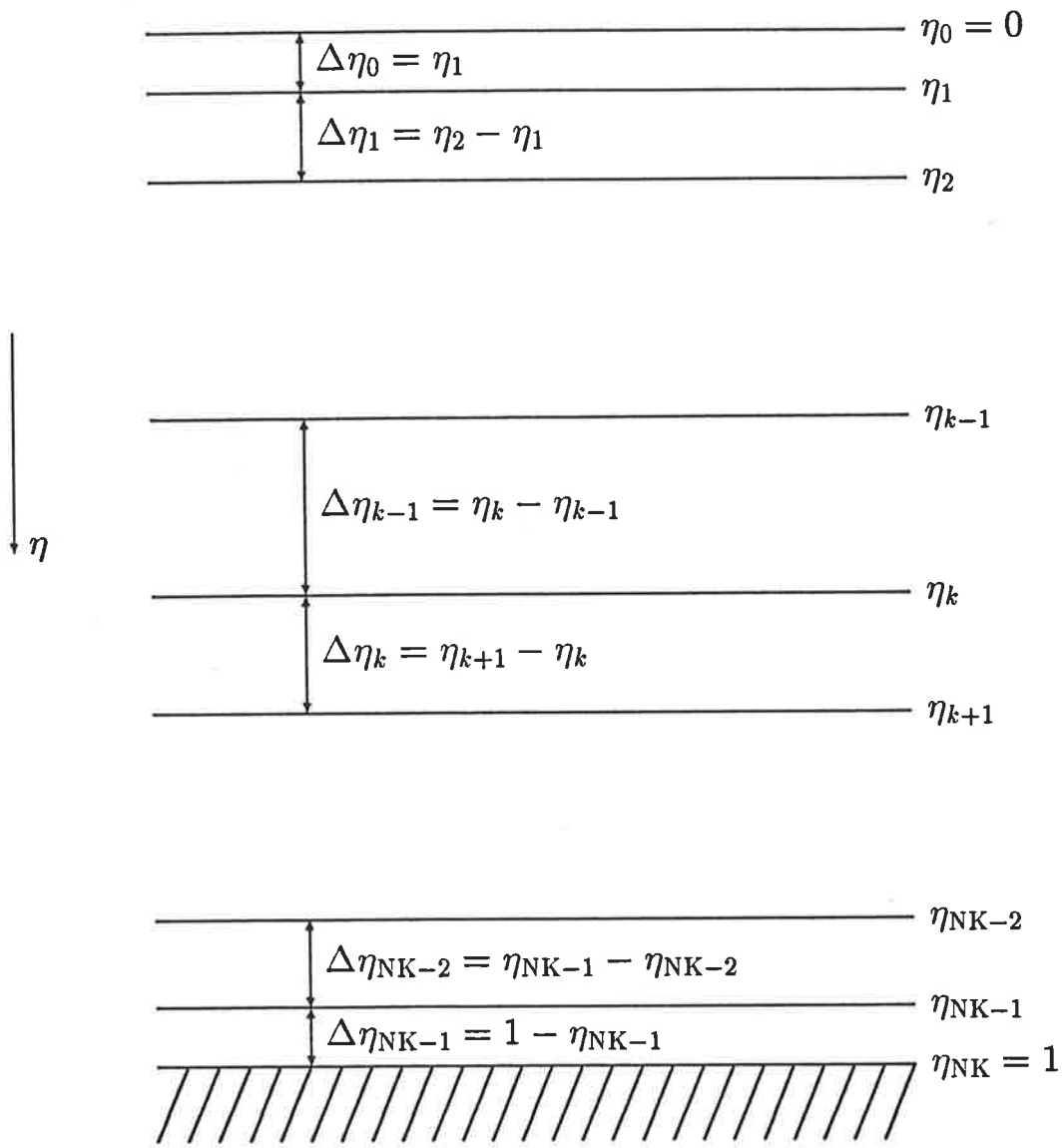


Figure 3.3: *An η cross-section of the transformed vertical region indicating the unequal depth levels and spacings. There are (NK+1) depth levels and NK depth intervals.*

surface, where the fine vertical grid structure leads to more accurate extrapolations for the horizontal surface velocity values (see Section 3.4). In the latter case, a wind stress may give rise to large near-surface gradients in the horizontal velocity components, so a fine near-surface grid also gives better resolution of this phenomenon.

In order to generate the symmetrical fine-coarse-fine structure of the grid spacings, equation (3.1) is solved iteratively over the interval $\eta \in [0, 0.5]$ and the solution for $\eta \in [0.5, 1]$ is obtained as the reflection about $\eta = 0.5$. The values of η required at each depth level are determined from the spacings.

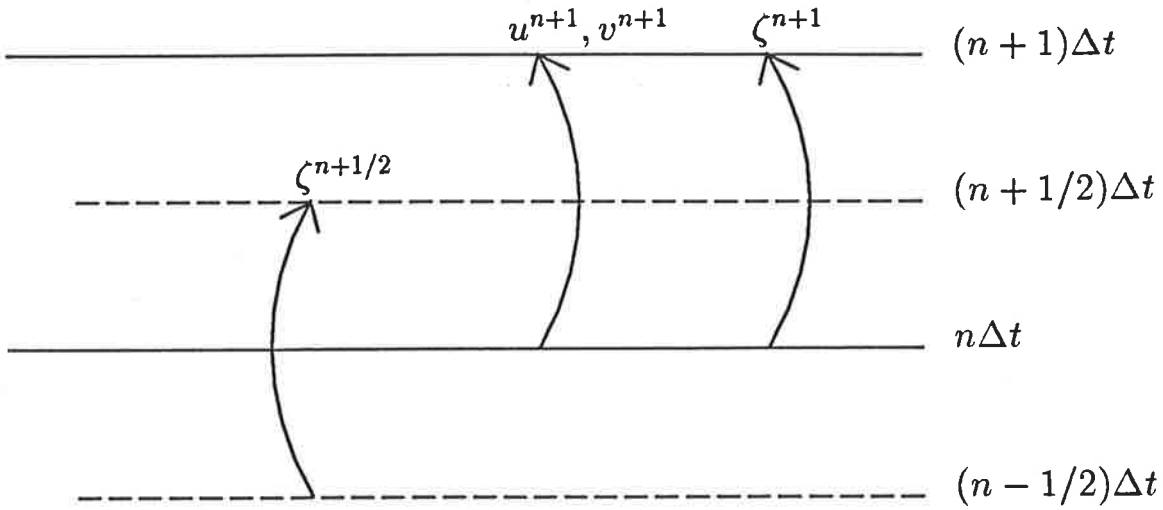


Figure 3.4: *The overall finite difference scheme is dominated by the momentum calculations which use time centred elevation values from intermediate calculations of elevation.*

3.3 The computational scheme

The computational scheme will be presented before the finite difference expressions are given. An overview of the scheme at this point should make the reasons for choosing the stated finite difference expressions of the next section more immediately evident.

The overall finite difference scheme used is three-level in time. That is, each time step involves three time levels: the entry level, the half time step level and the full time step level. For each set of calculations of u and v over one time step, there are two calculations of ζ. These are interleaved so that while the first provides direct calculation of a time centred value of ζ for the momentum equations, the second advances this calculation to the full time step (see Figure 3.4). There is no need for a forward time initiation of the scheme since it is commenced by the first ζ calculation which is half a time step out of phase with the remaining u, v and ζ calculations — in this way it differs from the usual "leap-frog" scheme which does require initiation.

On this basis, the present scheme can be distinguished from the three-dimensional vertically layered model of Backhaus et al. (1987) who solve the equations of continuity and momentum half a time step apart with a scheme which is "essentially of the leap-frog type, although it does not explicitly involve three time levels" (ibid., p.154). The depth-averaged scheme used by Blumberg (1977) is purely leap-frog and is initiated using a forward time step. There is only one ζ calculation per time step. "The frictional terms are lagged one time step to avoid numerical instability" (ibid., p.4). Blumberg states that his scheme is second order accurate in space and first order in time.

The time stepping procedure of the present scheme is schematically illustrated in Figure 3.4. During the nth time step, the elevation field at time $(n+1/2)\Delta t$ is calculated explicitly using values from the two preceding half time steps. With the updated values of elevation and of total depth, the horizontal velocity fields at time $(n+1)\Delta t$ are calculated — in the case of the three-dimensional model, this calculation is implicit in the vertical and explicit in the horizontal, while for the depth-averaged model, this calculation is explicit. Elevation is then calculated at time $(n+1)\Delta t$ using an explicit scheme.

For three-dimensional flows, transformed vertical velocity ω and cartesian vertical velocity w are then obtained using explicit expressions employing values entirely from time level $(n+1)$.

All difference expressions in the horizontal are space centred and are therefore second order accurate in space. In three-dimensional modelling, the difference expressions in the vertical are second order accurate because of the use of the Kappa method.

The difference expressions corresponding to the ζ calculations are second order accurate in time and those corresponding to the momentum calculations are approximately second order accurate in time. The expressions for ω and w introduce no time discretisation error.

The steps of the computational procedure for three-dimensional modelling are:

1. Input model data.
   Set model time to $t = n\Delta t = 0$.
   Set initial values.

2. Update model time to level $(n + 1/2)$. Time $t = (n + 1/2)\Delta t$.
   Update open boundary elevation specifications to time level $(n + 1/2)$.
   Calculate elevation field $\zeta^{n+1/2}$ and total depth field $H^{n+1/2}$.

3. Update model time to level $(n + 1)$. Time $t = (n + 1)\Delta t$.
   Update atmospheric pressure and wind field specifications to time level $(n + 1)$.
   Calculate depth-dependent horizontal velocity fields u^{n+1}, v^{n+1} and from these calculate the depth-averaged horizontal velocity fields U^{n+1}, V^{n+1}.

4. Update open boundary elevation specifications to time level $(n + 1)$.
   Calculate elevation field ζ^{n+1} and total depth field H^{n+1}.

5. Calculate the transformed vertical velocity field ω^{n+1} and, if required, the cartesian velocity field w^{n+1}.

6. Return to step 2 and repeat until the simulation is completed.

The steps of the computational procedure for depth-averaged modelling are analogous to the above.

At step 3, first u and then v horizontal velocity values are calculated at a given element before proceeding to the next computational element. Since computations proceed row by row, the values u^{n+1} and v^{n+1} calculated in the previous row and in the previous element can be used to achieve time centring for the Coriolis and other terms of the momentum equations in the present row.

In a computational sweep across a row, only elements of that row and the rows both preceding and succeeding it are used. Therefore, a computational window of just three rows is required and it is not necessary to retain complete lists for the velocity fields at both time levels n and $(n+1)$. Instead, the "old" list is used in conjunction with temporary storage lists which hold the "new" values of the present and preceding rows until the corresponding rows of old values are no longer needed. When computations step from the present to the next row, the temporary list of new values held for the preceding row replaces the corresponding values in the velocity lists. The old list is thereby gradually transformed into a list of updated values. This procedure represents a significant saving in computer storage in the case of three-dimensional modelling.

3.4 The finite difference expressions

In this section, the finite difference expressions used to compute the elevation and velocity variables at a general computational element i are stated. The approximations used are the most accurate formulations found that involve only the immediate eight neighbouring elements. In Chapter 4, their accuracy is demonstrated by comparing numerical results to analytical solutions for simplified model geometries.

Attention is firstly given to the finite difference expressions for the three-dimensional equations (2.12), (2.14)–(2.17). The difference expressions for the depth-averaged equations (2.33)–(2.35) follow by analogy and only receive brief comment at the end of this section.

Referring to Figures 3.1 and 3.2, the differencing used for the continuity equation is centred about the ζ_i gridpoint of the ith element. The momentum equations are differenced about their respective gridpoints, u_i and v_i, at the kth depth level. The equations for the calculation of transformed vertical velocity and cartesian vertical velocity are also differenced about the ζ_i gridpoint. For the moment, it will be assumed that coastal and open sea boundaries do not pass through elements within the immediate neighbourhood of the ith element. The effect of boundaries upon the differencing will be considered in Sections 3.5 and 3.6.

Proceeding in the computational order outlined in the previous section, consider the construction of a finite difference analog of equation (2.12) centred about the nth level in discrete time and the ζ_i gridpoint in discrete (horizontal) space. An expression for this statement is:

$$\left\{\frac{\partial \zeta}{\partial t}\right\}^n_{\zeta_i} = -\left\{\frac{\partial (HU)}{\partial x}\right\}^n_{\zeta_i} - \left\{\frac{\partial (HV)}{\partial y}\right\}^n_{\zeta_i} \tag{3.2}$$

where curly braces used in this context denote centring about the time level and the spatial position indicated. The difference expressions chosen for each term are:

$$\left\{\frac{\partial \zeta}{\partial t}\right\}^n_{\zeta_i} \simeq \frac{1}{\Delta t}\left(\zeta_i^{n+\frac{1}{2}} - \zeta_i^{n-\frac{1}{2}}\right), \tag{3.3}$$

$$\left\{\frac{\partial (HU)}{\partial x}\right\}^n_{\zeta_i} \simeq \frac{1}{4\Delta x}\left[\left(H_i^n + H_{i+1}^n\right) U_i^n - \left(H_{i-1}^n + H_i^n\right) U_{i-1}^n\right], \tag{3.4}$$

$$\left\{\frac{\partial (HV)}{\partial y}\right\}^n_{\zeta_i} \simeq \frac{1}{4\Delta y}\left[\left(H_i^n + H_{i_1}^n\right) V_{i_1}^n - \left(H_{i_2}^n + H_i^n\right) V_i^n\right]. \tag{3.5}$$

The first of these is second order accurate in time and contains no spatial discretisation error; the second and third expressions are second order accurate in space and contain no time discretisation error. The explicit expression used to calculate $\zeta_i^{n+1/2}$ is:

$$\begin{aligned}\zeta_i^{n+\frac{1}{2}} = \zeta_i^{n-\frac{1}{2}} &- \frac{\Delta t}{4\Delta x}\left[\left(H_i^n + H_{i+1}^n\right) U_i^n - \left(H_{i-1}^n + H_i^n\right) U_{i-1}^n\right] \\ &- \frac{\Delta t}{4\Delta y}\left[\left(H_i^n + H_{i_1}^n\right) V_{i_1}^n - \left(H_{i_2}^n + H_i^n\right) V_i^n\right],\end{aligned} \tag{3.6}$$

and is second order accurate in both space and time. The corresponding computational "molecule" is shown in Figure 3.5.

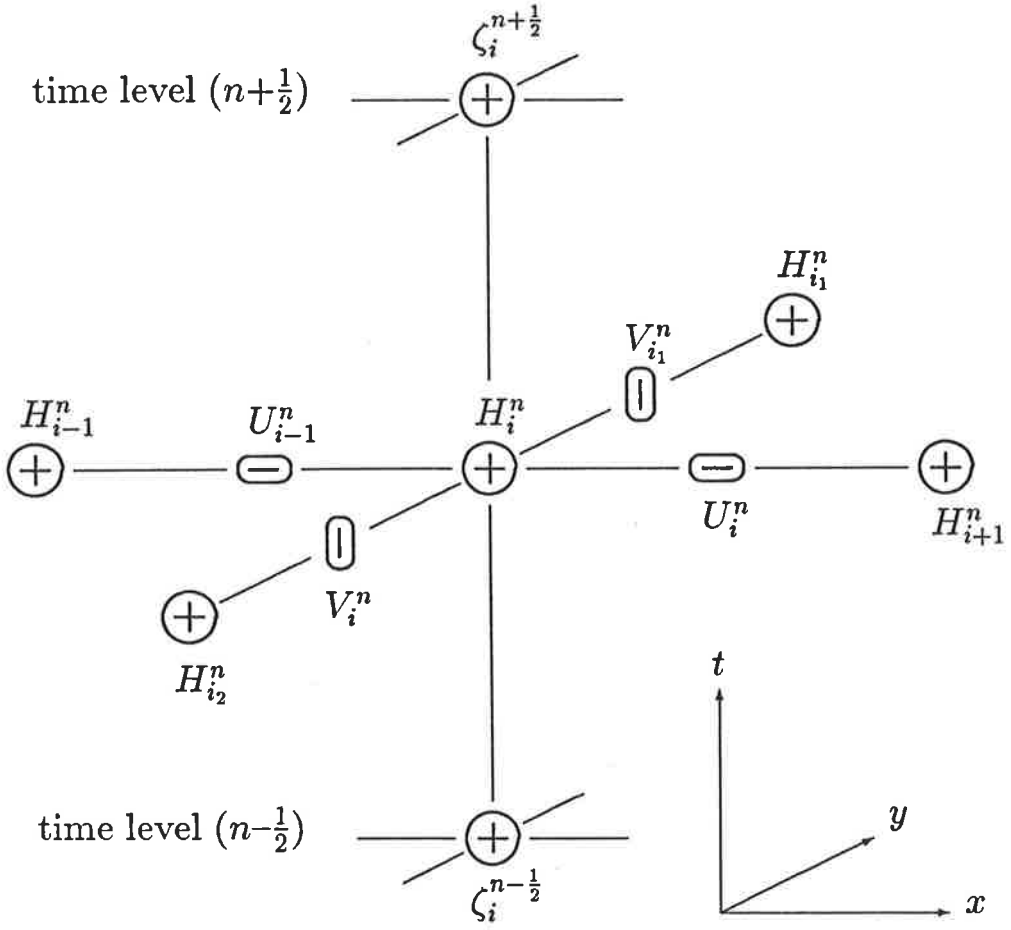


Figure 3.5: *The computational molecule corresponding to the first finite difference form of the continuity equation.*

Total depth at time $(n+1/2)\Delta t$ is calculated as:

$$H_i^{n+\frac{1}{2}} = \zeta_i^{n+\frac{1}{2}} + h_i. \tag{3.7}$$

Now consider the finite difference analog of equation (2.14) centred about the $(n+1/2)$ level in time and the $u_{i,k}$ gridpoint in (three-dimensional) space:

$$\begin{aligned}
&\left\{\frac{\partial u}{\partial t}\right\}_{u_{i,k}}^{n+\frac{1}{2}} + \left\{u\frac{\partial u}{\partial x}\right\}_{u_{i,k}}^{n+\frac{1}{2}} + \left\{v\frac{\partial u}{\partial y}\right\}_{u_{i,k}}^{n+\frac{1}{2}} + \left\{\omega\frac{\partial u}{\partial \eta}\right\}_{u_{i,k}}^{n+\frac{1}{2}} - \{fv\}_{u_{i,k}}^{n+\frac{1}{2}} \\
&= -g\left\{\frac{\partial \zeta}{\partial x}\right\}_{u_{i,k}}^{n+\frac{1}{2}} - \frac{1}{\rho}\left\{\frac{\partial p_a}{\partial x}\right\}_{u_{i,k}}^{n+\frac{1}{2}} \\
&\quad + \left\{N_x\frac{\partial^2 u}{\partial x^2}\right\}_{u_{i,k}}^{n+\frac{1}{2}} + \left\{N_y\frac{\partial^2 u}{\partial y^2}\right\}_{u_{i,k}}^{n+\frac{1}{2}} + \left\{\frac{1}{H^2}\frac{\partial}{\partial \eta}\left(N_\eta\frac{\partial u}{\partial \eta}\right)\right\}_{u_{i,k}}^{n+\frac{1}{2}}.
\end{aligned} \tag{3.8}$$

The following difference expressions for the terms of (3.8) are second order accurate in space. Their accuracy in terms of the time discretisation varies from being better than

first order accurate to being second order accurate. The difference expressions for each term are:

$$\left\{\frac{\partial u}{\partial t}\right\}_{u_{i,k}}^{n+\frac{1}{2}} \simeq \frac{1}{\Delta t}\left(u_{i,k}^{n+1} - u_{i,k}^{n}\right), \tag{3.9}$$

which is second order accurate in time;

$$\left\{u\frac{\partial u}{\partial x}\right\}_{u_{i,k}}^{n+\frac{1}{2}} \simeq u_{i,k}^{n+1}\left\{\frac{\partial u}{\partial x}\right\}_{u_{i,k}}^{n} \simeq \frac{1}{4\Delta x}u_{i,k}^{n+1}\left(u_{i+1,k}^{n} - u_{i-1,k}^{n}\right), \tag{3.10}$$

which is approximately second order accurate in time;

$$\left\{v\frac{\partial u}{\partial y}\right\}_{u_{i,k}}^{n+\frac{1}{2}} \simeq \{v\}_{u_{i,k}}^{n+\frac{1}{2}}\left\{\frac{\partial u}{\partial y}\right\}_{u_{i,k}}^{n} \simeq \frac{1}{16\Delta y}\left(v_{i_1,k}^{n+1} + v_{i_1+1,k}^{n+1} + v_{i,k}^{n} + v_{i+1,k}^{n}\right)\left(u_{i_1,k}^{n} - u_{i_2,k}^{n}\right), \tag{3.11}$$

which is approximately second order accurate in time;

$$\begin{aligned}\left\{\omega\frac{\partial u}{\partial \eta}\right\}_{u_{i,k}}^{n+\frac{1}{2}} &\simeq \frac{1}{2}\left(\omega_{i,k}^{n} + \omega_{i+1,k}^{n}\right)\frac{1}{2}\left(\left\{\frac{\partial u}{\partial \eta}\right\}_{u_{i,k}}^{n} + \left\{\frac{\partial u}{\partial \eta}\right\}_{u_{i,k}}^{n+1}\right)\\ &\simeq \frac{1}{4}\left(\omega_{i,k}^{n} + \omega_{i+1,k}^{n}\right)\frac{1}{r_k(\Delta\eta_{k-1} + \Delta\eta_k)}\\ &\quad\left[(r_k)^2 u_{i,k+1}^{n} + (1-(r_k)^2)u_{i,k}^{n} - u_{i,k-1}^{n}\right.\\ &\quad\left.+(r_k)^2 u_{i,k+1}^{n+1} + (1-(r_k)^2)u_{i,k}^{n+1} - u_{i,k-1}^{n+1}\right],\end{aligned} \tag{3.12}$$

where $r_k = \Delta\eta_{k-1}/\Delta\eta_k$, the expression being approximately second order accurate in time;

$$\{fv\}_{u_{i,k}}^{n+\frac{1}{2}} \simeq \frac{1}{8}\left(f_i + f_{i+1}\right)\left(v_{i_1,k}^{n+1} + v_{i_1+1,k}^{n+1} + v_{i,k}^{n} + v_{i+1,k}^{n}\right), \tag{3.13}$$

which is second order accurate in time;

$$\left\{\frac{\partial \zeta}{\partial x}\right\}_{u_{i,k}}^{n+\frac{1}{2}} \simeq \frac{1}{2\Delta x}\left(\zeta_{i+1}^{n+\frac{1}{2}} - \zeta_{i}^{n+\frac{1}{2}}\right), \tag{3.14}$$

which has no time discretisation error;

$$\left\{\frac{\partial p_a}{\partial x}\right\}_{u_{i,k}}^{n+\frac{1}{2}} \simeq \frac{1}{4\Delta x}\left(\left[p_{a_{i+1}}^{n+1} - p_{a_i}^{n+1}\right] + \left[p_{a_{i+1}}^{n} - p_{a_i}^{n}\right]\right), \tag{3.15}$$

which has no time discretisation error;

$$\begin{aligned}\left\{N_x\frac{\partial^2 u}{\partial x^2}\right\}_{u_{i,k}}^{n+\frac{1}{2}} &\simeq \frac{a}{2}(2\Delta x)\{H\}_{u_{i,k}}^{n+\frac{1}{2}}\left\{\frac{\partial^2 u}{\partial x^2}\right\}_{u_{i,k}}^{n}\\ &\simeq \frac{a}{8\Delta x}\left(H_i^{n+\frac{1}{2}} + H_{i+1}^{n+\frac{1}{2}}\right)\left(u_{i+1,k}^{n} - 2u_{i,k}^{n} + u_{i-1,k}^{n}\right),\end{aligned} \tag{3.16}$$

which is approximately second order accurate in time — here, the Schwiderski (1980) reduced eddy viscosity formulation for the horizontal diffusive coefficient is used (see Chapter 5); similarly,

$$\begin{aligned}\left\{N_y\frac{\partial^2 u}{\partial y^2}\right\}_{u_{i,k}}^{n+\frac{1}{2}} &\simeq \frac{a}{2}(2\Delta x)\{H\}_{u_{i,k}}^{n+\frac{1}{2}}\left\{\frac{\partial^2 u}{\partial y^2}\right\}_{u_{i,k}}^{n} \\ &\simeq \frac{a\Delta x}{8(\Delta y)^2}\left(H_i^{n+\frac{1}{2}}+H_{i+1}^{n+\frac{1}{2}}\right)\left(u_{i_1,k}^n-2u_{i,k}^n+u_{i_2,k}^n\right), \qquad (3.17)\end{aligned}$$

which is approximately second order accurate in time — again, the Schwiderski (1980) formulation for the horizontal diffusive coefficient is used;

$$\begin{aligned}&\left\{\frac{1}{H^2}\frac{\partial}{\partial\eta}\left(N_\eta\frac{\partial u}{\partial\eta}\right)\right\}_{u_{i,k}}^{n+\frac{1}{2}} \\ &\simeq \left(\frac{1}{2}\left[H_i^{n+\frac{1}{2}}+H_{i+1}^{n+\frac{1}{2}}\right]\right)^{-2}\frac{1}{2}\left(\left\{\frac{\partial}{\partial\eta}\left(N_\eta\frac{\partial u}{\partial\eta}\right)\right\}_{u_{i,k}}^{n}+\left\{\frac{\partial}{\partial\eta}\left(N_\eta\frac{\partial u}{\partial\eta}\right)\right\}_{u_{i,k}}^{n+1}\right) \\ &\simeq \frac{2}{r_k(\Delta\eta_{k-1}+\Delta\eta_k)}\left(H_i^{n+\frac{1}{2}}+H_{i+1}^{n+\frac{1}{2}}\right)^{-2} \\ &\quad\left(\left[\frac{(r_k)^2}{\Delta\eta_k}\left(N_{i,k}^n+N_{i,k+1}^n\right)\left(u_{i,k+1}^n-u_{i,k}^n\right)\right.\right. \\ &\quad+\frac{2(1-(r_k)^2)}{r_k(\Delta\eta_{k-1}+\Delta\eta_k)}N_{i,k}^n\left((r_k)^2u_{i,k+1}^n+(1-(r_k)^2)u_{i,k}^n-u_{i,k-1}^n\right) \\ &\quad\left.-\frac{1}{\Delta\eta_{k-1}}\left(N_{i,k-1}^n+N_{i,k}^n\right)\left(u_{i,k}^n-u_{i,k-1}^n\right)\right] \\ &\quad+\left[\frac{(r_k)^2}{\Delta\eta_k}\left(N_{i,k}^n+N_{i,k+1}^n\right)\left(u_{i,k+1}^{n+1}-u_{i,k}^{n+1}\right)\right. \\ &\quad+\frac{2(1-(r_k)^2)}{r_k(\Delta\eta_{k-1}+\Delta\eta_k)}N_{i,k}^n\left((r_k)^2u_{i,k+1}^{n+1}+(1-(r_k)^2)u_{i,k}^{n+1}-u_{i,k-1}^{n+1}\right) \\ &\quad\left.\left.-\frac{1}{\Delta\eta_{k-1}}\left(N_{i,k-1}^n+N_{i,k}^n\right)\left(u_{i,k}^{n+1}-u_{i,k-1}^{n+1}\right)\right]\right), \qquad (3.18)\end{aligned}$$

where $N_{i,k}^n$ is the value of N_η evaluated at the $u_{i,k}^n$ gridpoint:

$$N_{i,k}^n=\alpha+\frac{\beta}{2}(H_i^{n+\frac{1}{2}}+H_{i+1}^{n+\frac{1}{2}})F(\eta_k)\sqrt{(U_i^n)^2+\frac{1}{16}\left(V_{i_1}^{n+1}+V_{i_1+1}^{n+1}+V_i^n+V_{i+1}^n\right)^2}. \qquad (3.19)$$

Expressions (3.18) and (3.19) are approximately second order accurate in time.

In summary, the overall finite difference expression for the u momentum equation is approximately second order accurate in time. The expression used to time centre v in (3.11) is also used in (3.13) but is only calculated once. An analogous time centred expression for V is used in (3.19).

When all the approximations (3.9)–(3.18) are substituted into (3.8), values at the new time level $(n+1)$ and the old time level n are separated out and the overall finite difference expression takes the implicit form:

$$a_k u_{i,k-1}^{n+1}+b_k u_{i,k}^{n+1}+c_k u_{i,k+1}^{n+1}=d_k, \quad k=1,\ldots,\mathrm{NK}-1 \qquad (3.20)$$

where the coefficients a_k, b_k, c_k, d_k, $k = 1, \ldots, \text{NK}-1$, are known. A total of NK–1 such linear equations for depth levels $k = 1, 2, \ldots, \text{NK}-1$ are obtained. This system can be written in tri-diagonal form by replacing $u_{i,0}^{n+1}$ in the equation corresponding to $k = 1$ and $u_{i,\text{NK}}^{n+1}$ in the equation corresponding to $k = \text{NK}-1$ using discretisations of the surface and bottom boundary conditions, respectively.

In the case of no wind stress, the expression for $u_{i,0}^{n+1}$ is obtained by using the following second order approximation of the surface derivative boundary condition (2.23):

$$u_{i,0}^{n+1} \simeq \frac{(\Delta\eta_0 + \Delta\eta_1)^2}{\Delta\eta_1(\Delta\eta_1 + 2\Delta\eta_0)} u_{i,1}^{n+1} - \frac{(\Delta\eta_0)^2}{\Delta\eta_1(\Delta\eta_1 + 2\Delta\eta_0)} u_{i,2}^{n+1}, \tag{3.21}$$

where $\Delta\eta_0$, $\Delta\eta_1$ are defined in Figure 3.3. Because the truncation error in (3.21) depends on the factor $(\Delta\eta_0)^2(\Delta\eta_0+\Delta\eta_1)^2/(\Delta\eta_1+2\Delta\eta_0)$, (3.21) is more accurate if a fine depth level spacing is used near the surface. This is the reason for the use of a finely spaced vertical structure in the depth levels near the surface even in the absence of wind stress. In the presence of wind stress, a one-sided approximation of the derivative boundary condition (2.24) is used, in conjunction with (2.26), yielding

$$\begin{aligned} u_{i,0}^{n+1} \simeq\ & \frac{(\Delta\eta_0 + \Delta\eta_1)^2}{\Delta\eta_1(\Delta\eta_1 + 2\Delta\eta_0)} u_{i,1}^{n+1} - \frac{(\Delta\eta_0)^2}{\Delta\eta_1(\Delta\eta_1 + 2\Delta\eta_0)} u_{i,2}^{n+1} \\ & - \frac{\Delta\eta_0(\Delta\eta_0 + \Delta\eta_1)}{(\Delta\eta_1 + 2\Delta\eta_0)} \frac{S_{u_i}^{n+1} H_{u_i}^{n+1}}{\rho N_{i,0}^{n+1}}, \end{aligned} \tag{3.22}$$

where

$$S_{u_i}^{n+1} = \rho_a c_{10} \frac{1}{4}(u_{10}|_i^{n+1} + u_{10}|_{i+1}^{n+1}) \sqrt{(u_{10}|_i^{n+1} + u_{10}|_{i+1}^{n+1})^2 + (v_{10}|_i^{n+1} + v_{10}|_{i+1}^{n+1})^2}, \tag{3.23}$$

$$H_{u_i}^{n+1} = H_i^{n+\frac{1}{2}} + H_{i+1}^{n+\frac{1}{2}} - \frac{1}{2}\left(\zeta_i^n + h_i + \zeta_{i+1}^n + h_{i+1}\right), \tag{3.24}$$

and

$$N_{i,0}^{n+1} = \alpha + \beta H_{u_i}^{n+1} F(0) \sqrt{(U_i^n)^2 + \frac{1}{16}\left(V_{i_1}^{n+1} + V_{i_1+1}^{n+1} + V_i^n + V_{i+1}^n\right)^2}. \tag{3.25}$$

The value $S_{u_i}^{n+1}$ is an estimate of surface stress at the u_i point at time level $(n+1)$. The value $H_{u_i}^{n+1}$ is an extrapolation for total depth at the u_i point at time level $(n+1)$ using values from the two preceding half time levels.

From boundary condition (2.21), the value of u at the sea bed is zero; thus $u_{i,\text{NK}}^{n+1} = 0$ is used in equation (3.20) for depth level $k = \text{NK}-1$.

With these approximations for the surface and bed velocities, the system of linear equations (3.20) is converted to a tri-diagonal form which is rapidly solved using the Thomas (1949) algorithm.

The v momentum equation (2.15) is differenced and solved in a similar way.

After the updated depth-dependent velocity fields are obtained, the corresponding depth-averaged fields defined by equation (2.13) are evaluated. The numerical integration is carried out using the composite Simpson's rule for non-uniformly spaced intervals. For

the u-integration, the approximation at the u_i gridpoint at time level $(n+1)$ for depth-averaged velocity is

$$\begin{aligned} U_i^{n+1} &= \left\{\int_0^1 u\,d\eta\right\}_{u_i}^{n+1} \\ &\simeq \frac{1}{6}\sum_{k=1(2)}^{NK-1}(\Delta\eta_{k-1}+\Delta\eta_k)\left[\left(2-\frac{1}{r_k}\right)u_{i,k-1}^{n+1}+\left(2+\frac{1}{r_k}+r_k\right)u_{i,k}^{n+1}+(2-r_k)u_{i,k+1}^{n+1}\right], \end{aligned} \tag{3.26}$$

where the dummy index k is incremented by two at each step of the summation. This approximation is third order accurate and requires the use of an even number of intervals. For the three-dimensional model of Spencer Gulf, NK = 10 is used, defining 10 intervals between 11 consecutive depth levels.

Using the depth-averaged velocity fields now available at both the $(n+1)$ and n time levels, a difference scheme centred about the $(n+1/2)$ time level and the ζ_i gridpoint can be constructed to obtain the updated elevation field at the time $(n+1)\Delta t$:

$$\left\{\frac{\partial\zeta}{\partial t}\right\}_{\zeta_i}^{n+\frac{1}{2}} = -\left\{\frac{\partial(HU)}{\partial x}\right\}_{\zeta_i}^{n+\frac{1}{2}} - \left\{\frac{\partial(HV)}{\partial y}\right\}_{\zeta_i}^{n+\frac{1}{2}}. \tag{3.27}$$

The explicit expression used to evaluate ζ_i^{n+1} is:

$$\begin{aligned} \zeta_i^{n+1} &= \zeta_i^n - \frac{\Delta t}{8\Delta x}\left[\left(H_i^{n+\frac{1}{2}}+H_{i+1}^{n+\frac{1}{2}}\right)\left(U_i^{n+1}+U_i^n\right)\right. \\ &\qquad \left.-\left(H_{i-1}^{n+\frac{1}{2}}+H_i^{n+\frac{1}{2}}\right)\left(U_{i-1}^{n+1}+U_{i-1}^n\right)\right] \\ &\quad -\frac{\Delta t}{8\Delta y}\left[\left(H_i^{n+\frac{1}{2}}+H_{i_1}^{n+\frac{1}{2}}\right)\left(V_{i_1}^{n+1}+V_{i_1}^n\right)\right. \\ &\qquad \left.-\left(H_{i_2}^{n+\frac{1}{2}}+H_i^{n+\frac{1}{2}}\right)\left(V_i^{n+1}+V_i^n\right)\right]. \end{aligned} \tag{3.28}$$

This expression is second order accurate in both space and time. The corresponding computational molecule is shown in Figure 3.6.

Total depth at time $(n+1)\Delta t$ is found using:

$$H_i^{n+1} = \zeta_i^{n+1} + h_i. \tag{3.29}$$

The ω^{n+1} field is obtained by centrally differencing (2.16) about the ω_i gridpoint (which occupies the same horizontal position as the ζ_i gridpoint) at the kth depth level:

$$\omega_{i,k}^{n+1} = -\left\{\frac{1}{H}\frac{\partial}{\partial x}\left[H(U(\eta)-\eta U)\right]\right\}_{\omega_{i,k}}^{n+1} - \left\{\frac{1}{H}\frac{\partial}{\partial y}\left[H(V(\eta)-\eta V)\right]\right\}_{\omega_{i,k}}^{n+1}. \tag{3.30}$$

No time derivatives are involved, so this scheme contains no time discretisation error. The explicit expression for $\omega_{i,k}^{n+1}$ is obtained entirely in terms of values at time level $(n+1)$:

$$\begin{aligned} \omega_{i,k}^{n+1} &= -\frac{1}{4\Delta x}\frac{1}{H_i^{n+1}}\left[\left(H_i^{n+1}+H_{i+1}^{n+1}\right)\left(U(\eta_k)_i^{n+1}-\eta_k U_i^{n+1}\right)\right. \\ &\qquad \left.-\left(H_{i-1}^{n+1}+H_i^{n+1}\right)\left(U(\eta_k)_{i-1}^{n+1}-\eta_k U_{i-1}^{n+1}\right)\right] \\ &\quad -\frac{1}{4\Delta y}\frac{1}{H_i^{n+1}}\left[\left(H_i^{n+1}+H_{i_1}^{n+1}\right)\left(V(\eta_k)_{i_1}^{n+1}-\eta_k V_{i_1}^{n+1}\right)\right. \\ &\qquad \left.-\left(H_{i_2}^{n+1}+H_i^{n+1}\right)\left(V(\eta_k)_i^{n+1}-\eta_k V_i^{n+1}\right)\right], \end{aligned} \tag{3.31}$$

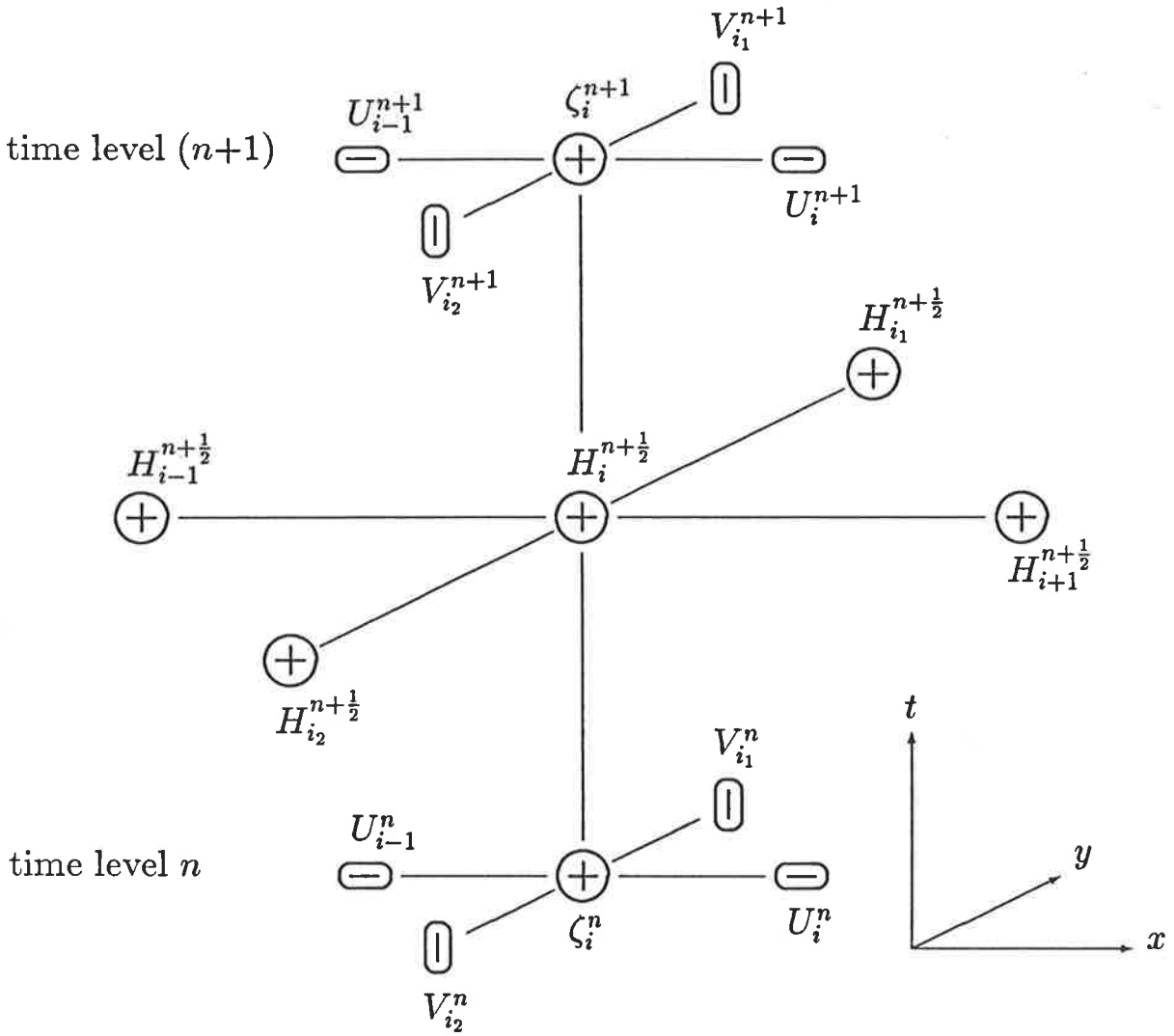


Figure 3.6: *The computational molecule corresponding to the second difference form of the continuity equation.*

and is second order accurate in space.

The depth-averaged velocity quantities $U(\eta_k)$, $V(\eta_k)$ are the numerical analogs of equations (2.19). That is,

$$U(\eta_k) = \int_0^{\eta_k} u\, d\eta \quad \text{and} \quad V(\eta_k) = \int_0^{\eta_k} v\, d\eta. \tag{3.32}$$

The integrals are numerically evaluated using the composite trapezoidal rule for non-uniform spacing, which is second order accurate. In the program, the values $\omega_{i,k}^{n+1}$, $k = 1, 2, \ldots,$ NK–1 are calculated successively and so some computational saving is gained by performing the integrations cumulatively. For instance, the value $U(\eta_k)$ is obtained using $U(\eta_{k-1})$:

$$U(\eta_k) = U(\eta_{k-1}) + \int_{\eta_{k-1}}^{\eta_k} u\, d\eta, \tag{3.33}$$

which has the discrete form:

$$U(\eta_k) = U(\eta_{k-1}) + \frac{\Delta\eta_{k-1}}{2}\left(u_{k-1} + u_k\right), \tag{3.34}$$

at horizontal position u_i and time level $(n+1)$. The use of the composite trapezoidal rule is therefore very convenient since it only requires a summation step of one interval.

The computation of the w field is not necessary to the advancement of the overall numerical solution, but if knowledge of the w field is required, an explicit formulation can be obtained as follows. Firstly, equation (2.17) is written in the form

$$w = -H\omega + (1-\eta)\left(-\frac{\partial(HU)}{\partial x} - \frac{\partial(HV)}{\partial y} + u\frac{\partial\zeta}{\partial x} + v\frac{\partial\zeta}{\partial y}\right) - \eta\left(u\frac{\partial h}{\partial x} + v\frac{\partial h}{\partial y}\right), \tag{3.35}$$

where the time derivative $\partial\zeta/\partial t$ has been replaced by spatial gradients using the continuity equation (2.12). The w^{n+1} field is obtained by centrally differencing (3.35) about the w_i gridpoint (i.e. the ζ_i position) at the kth depth level:

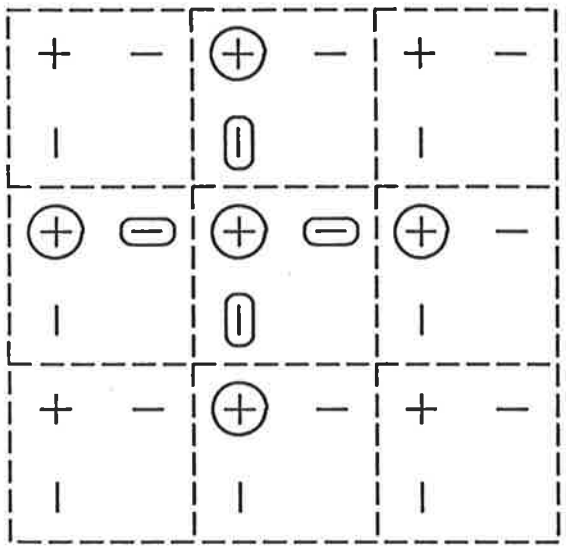
$$\begin{aligned} w_{i,k}^{n+1} \;=\; & -\{H\omega\}_{w_{i,k}}^{n+1} - (1-\eta_k)\left(\left\{\frac{\partial(HU)}{\partial x}\right\}_{w_{i,k}}^{n+1} + \left\{\frac{\partial(HV)}{\partial y}\right\}_{w_{i,k}}^{n+1}\right) \\ & +(1-\eta_k)\left(\left\{u\frac{\partial\zeta}{\partial x}\right\}_{w_{i,k}}^{n+1} + \left\{v\frac{\partial\zeta}{\partial y}\right\}_{w_{i,k}}^{n+1}\right) \\ & -\eta_k\left(\left\{u\frac{\partial h}{\partial x}\right\}_{w_{i,k}}^{n+1} + \left\{v\frac{\partial h}{\partial y}\right\}_{w_{i,k}}^{n+1}\right). \end{aligned} \tag{3.36}$$

The explicit expression used for $w_{i,k}^n$ is obtained entirely in terms of values at time level $(n+1)$:

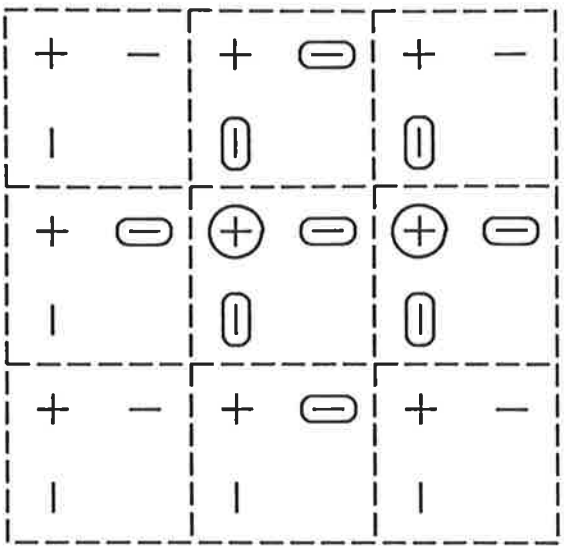
$$\begin{aligned} w_{i,k}^{n+1} \;=\; & -H_i^{n+1}\,\omega_{i,k}^{n+1} \\ & +(1-\eta_k)\left(-\frac{1}{4\Delta x}\left[\left(H_i^{n+1} + H_{i+1}^{n+1}\right)U_i^{n+1} - \left(H_{i-1}^{n+1} + H_i^{n+1}\right)U_{i-1}^{n+1}\right]\right. \\ & \quad -\frac{1}{4\Delta y}\left[\left(H_i^{n+1} + H_{i_1}^{n+1}\right)V_{i_1}^{n+1} - \left(H_{i_2}^{n+1} + H_i^{n+1}\right)V_i^{n+1}\right] \\ & \quad +\frac{1}{8\Delta x}\left(u_{i-1,k}^{n+1} + u_{i,k}^{n+1}\right)\left(\zeta_{i+1}^{n+1} - \zeta_{i-1}^{n+1}\right) \\ & \quad \left.+\frac{1}{8\Delta y}\left(v_{i,k}^{n+1} + v_{i_1,k}^{n+1}\right)\left(\zeta_{i_1}^{n+1} - \zeta_{i_2}^{n+1}\right)\right) \\ & -\eta_k\left(\frac{1}{8\Delta x}\left(u_{i-1,k}^{n+1} + u_{i,k}^{n+1}\right)\left(h_{i+1} - h_{i-1}\right)\right. \\ & +\quad \left.\frac{1}{8\Delta y}\left(v_{i,k}^{n+1} + v_{i_1,k}^{n+1}\right)\left(h_{i_1} - h_{i_2}\right)\right), \end{aligned} \tag{3.37}$$

and is second order accurate in space.

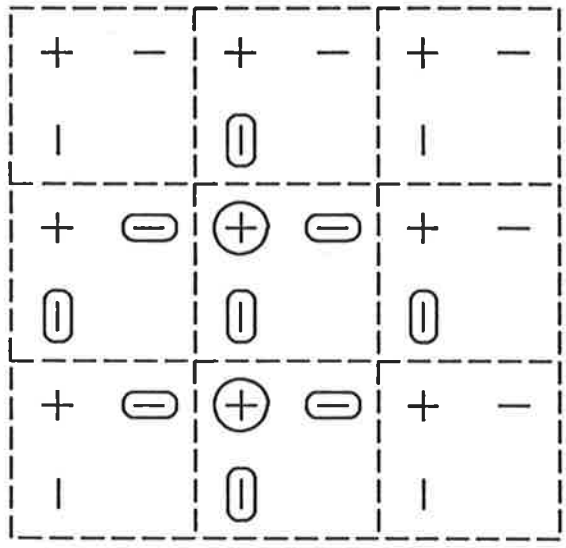
Now consider Figures 3.7 which show the horizontal or plan structure of the computational "molecules" of the above finite difference equations. Figures 3.7 will be referred to as the associated "stencils" of the corresponding computational molecules since the word "stencil" implies no vertical structure whereas the word "molecule" implies three-dimensionality. Figure 3.7(a) is the computational stencil for either of the finite difference forms for the elevation equation, viz. equations (3.6) or (3.28). Equivalently, Figure 3.7(a) is the horizontal structure of the computational molecules of Figures 3.5 or 3.6.



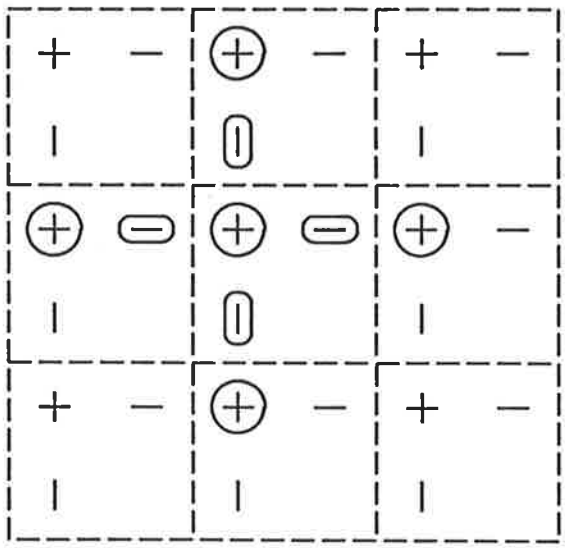
(a) ζ_i computational stencil



(b) u_i computational stencil



(c) v_i computational stencil



(d) ω_i, w_i computational stencil

Figure 3.7: *Computational stencils, in plan view, for the finite difference approximations for (a) the continuity equation, (b) the u momentum equation, (c) the v momentum equation and (d) the ω and w equations.*

Figure 3.7(a) is identical to Figure 3.7(d), the stencil for the ω and w finite difference equations. Figures 3.7(b),(c) are the stencils for the u and v momentum finite difference equations, respectively.

Since chemical molecules are composed of atoms, let us use the term "atom" to refer to a constituent gridpoint of a computational molecule or stencil. In Figure 3.7 the "atoms" of the stencils are the ringed gridpoints. The symmetry of each stencil about its corresponding central gridpoint reflects the fact that the finite difference schemes are space centred.

This completes the consideration of the finite difference expressions for the three-dimensional set of equations.

The finite difference expressions for the depth-averaged equations (2.33)–(2.35) are analogous to the above. Briefly, equation (3.6) is used to update the elevation field to the $(n+1/2)$ time level and (3.7) is used to calculate total depth. The U momentum equation (2.34) is differenced about the $(n+1/2)$ time level and the U_i gridpoint (in the same position as the u_i gridpoint), and the differencing employed for each term has the same form as the differencing used for the corresponding terms of (3.8). The quadratic friction term of (2.34), viz.

$$C_b \frac{1}{H} U \sqrt{U^2 + V^2}, \tag{3.38}$$

is differenced as

$$\frac{2C_b}{\left(H_i^{n+\frac{1}{2}} + H_{i+1}^{n+\frac{1}{2}}\right)} U_i^{n+1} \sqrt{(U_i^n)^2 + \frac{1}{16}\left(V_{i_1}^{n+1} + V_{i_1+1}^{n+1} + V_i^n + V_{i+1}^n\right)^2}, \tag{3.39}$$

and employs the same differencing for the V value as is used in differencing the V-advective and Coriolis terms of (2.34). The wind stress term of (2.34), viz.

$$\frac{\rho_a}{\rho H} c_{10} u_{10} \sqrt{(u_{10})^2 + (v_{10})^2}, \tag{3.40}$$

is differenced as

$$\frac{\rho_a c_{10}}{2\rho} \left(\frac{u_{10}|_i^{n+1} + u_{10}|_{i+1}^{n+1}}{H_i^{n+\frac{1}{2}} + H_{i+1}^{n+\frac{1}{2}}} \right) \sqrt{\left(u_{10}|_i^{n+1} + u_{10}|_{i+1}^{n+1}\right)^2 + \left(v_{10}|_i^{n+1} + v_{10}|_{i+1}^{n+1}\right)^2}. \tag{3.41}$$

Similar comments apply for the differencing of the V momentum equation (2.35). Finally, equation (3.28) is used to update the elevation field at the $(n+1)$ time level and (3.29) is used to update total depth.

The computational stencils, in plan view, for the finite difference equations for depth-averaged flow are analogous to those given in Figure 3.7.

3.5 The element classification scheme

It is both instructive and historically interesting to observe something of the evolution of schemes for solving the finite difference equations used in numerical tidal modelling.

Heaps (1969) uses a grid element consisting of two gridpoints. At one is defined the elevation; at the other are defined the "stream" values hU and hV (m^2/sec). The model of the sea basin, representing the actual basin, is marked out on grid lines (lines joining similar gridpoints) — open sea boundaries consist of line segments connecting elevation points, coastal boundaries consist of line segments connecting stream points. An elevation point is located either outside the model sea region, on one of its open boundaries, or within the model sea; a stream point is located outside the model sea, on one of the coastal boundaries or within the model sea. Values of ζ, hU, hV "at gridpoints lying outside the sea are purely fictitious and have no physical significance; they are allocated to control the output format of the computed elevations and streams" (ibid., p.101).

Heaps uses the integers 1 to 22 to define 22 different types of gridpoint location: integers $1, 2, 3$ identify the different types of location of elevation point and integers $4, \ldots, 22$ identify different types of location of stream point. Labelling each gridpoint with the integer appropriate to its location yields an integer array which implicitly defines the model region. Because advective and diffusive terms are omitted, the computational stencils involved are very compact and consist of either the elevation point and its four nearest stream point neighbours, or the stream point and its four nearest elevation point neighbours. Starting with the most general form of the finite difference expressions for the stream component equations, Heaps systematically produces modified forms of those parts of the expressions which depend on neighbouring gridpoints, for each different type of stream point. During the iterative procedure the integer label of each stream point directs program control to the corresponding section of modified program code.

Flather (1972), as we have noted, uses the Arakawa "C" grid element (Figure 3.1) consisting of three gridpoints. He proposes a classification not of gridpoints, but of grid elements, and bases it on the location of each element's constituent gridpoints relative to the model sea and its boundaries. By considering the range of possible and realistic configurations, he settles on 17 classes of element to each of which is assigned an integer label. Again, the resultant integer array implicitly defines the model region. Like Heaps (1969), values are allocated to ζ, U, V gridpoints outside the model sea but "serve only in controlling the output format of elevation and flow-component fields, and in no way do they affect the calculations" (Flather, 1972, p.132). At each of the three types of gridpoint in an element, he gives the modified form of the corresponding finite difference expression based on the element classification.

The work of Heaps (1969) and Flather (1972) may be seen as an early step toward automatic program modification of the general finite difference expressions to take into account the various different forms of these expressions applying to gridpoints near boundaries of the model sea. Because the same type of calculation is required at boundary points of a similar nature, regardless of position on the grid, they observed it was possible to classify gridpoints or grid elements into groupings for which calculations were the same.

Henry (1982a) took this approach a step further by using a program to classify the gridpoints into such groupings based on the assignment of a much simpler set of integer gridpoint labels. Again using the Arakawa "C" (or Richardson) lattice, Henry assigns two "primary codes" to elevation points: either they are on open sea boundaries or they are not; he assigns five "primary codes" to each of the velocity points: these codes correspond to (1) a velocity point on a coastal boundary, (2) a velocity point on a spit or causeway, (3) a specified velocity at an open sea boundary, (4) a radiation velocity at an open sea boundary or (5) a velocity point which is none of these but is "elsewhere".

Although now only 12 (primary) codes are used, the procedure is still fairly complex and a graphical check of the primary coding is employed to ensure that the model geometry has been coded correctly. This "independent" verification of the primary coding of gridpoints is seen as a definite advantage over the hand coding used by Heaps (1969) and Flather (1972), which seems more prone to errors in user implementation.

Having verified the primary codes by graphical means, they are converted to "intermediate" codes: "In order to carry out the correct finite-difference calculations, the time-stepping subroutine must distinguish between boundaries at opposite sides of the model e.g. between land/sea and sea/land boundaries, both of which have the same primary code. For this reason the primary codes are translated automatically by a conversion program to a more varied set, termed 'intermediate codes', which contain all the necessary information. The conversion program also labels all variable points outside the model as null points requiring no computation and defines the minimum area of the grid which need be scanned at each time step" (Henry, 1982b, p.115). At least 25 intermediate codes are identified for internal use by the program subroutines, but the user need not be concerned with these.

A important point made by Henry (1982a,b) is that the development of new models is potentially accelerated by the use of such a system of (primary and subsequent) codes. The modeller merely provides the set of codes describing a model of a sea region, as well as depth, initialization and forcing information. Calculations are automated by use of the codes in pre-developed subroutines. Numerical modelling of a range of long-wave phenomena such as tides, storm surges and tsunamis can be carried out in this way as the governing shallow water equations may be represented by means of a common finite difference scheme.

Henry (1982a,b) has applied this approach to the semi-linearized shallow water equations, the only nonlinearity admitted being the inclusion of quadratic friction. The inclusion of advection in possible subsequent work is seen as requiring an even more diversified set of "secondary codes" capable of distinguishing all the various additional combinations of boundary formulae that thereby arise, but as with the intermediate codes, the secondary codes will be produced automatically by a conversion program from the primary codes.

In this work, there has been considerable interest in simplifying the procedure of element classification for the modeller and in generalizing the computer algorithms so that any model region can be handled by the program.

What follows will be a description of a way of programming the finite difference expressions so that the correct form applying to a given computational gridpoint is automatically selected. The method evolves organically from considering the computational stencils of each finite difference expression. It is based on the location of the elevation points of grid elements and assumes the use of the Arakawa "C" lattice.

Examining the plan views of the computational stencils of Figure 3.7, it can be seen that in each case values from all three gridpoints of the central computational element are used in the corresponding finite difference expression, but only selected gridpoints of the neighbouring elements are used. If an "atom" of a computational stencil lies on a coastal boundary, or beyond it on land, or on an open sea boundary or beyond it, the finite difference expression needs to be modified. Since there are many different possibilities in this regard, a long list of possible types of 9-element blocks and accompanying modified finite difference equations could be constructed. Certainly, some of these will be equivalent and so some economy is obtained by grouping equivalent configurations. This was essentially

the approach of Heaps (1969) and Flather (1972).

But a much more compact method is available. Suppose that each element is assigned one of just four integer codes according to the position of its elevation gridpoint. An element is coded

- "0", and denoted "Type 0", if its elevation point lies on land,
- "1", and denoted "Type 1", if its elevation point lies on water within the model,
- "2", and denoted "Type 2", if its elevation point lies on an open boundary, and
- "4", and denoted "Type 4", if its elevation point lies on water outside the model region.

(In Section 3.6, a more careful application of the finite difference code for advective and diffusive terms leads to the redundancy of code "4", whence it is only used for presentation purposes. This assignment is what is finally used for the models of Spencer Gulf described in Chapters 5, 7 and 8.)

The modeller need only be aware of the definition of these four types of element in order to precisely define the model region for the program. But as this is a thesis on the subject, the "how" and "why" of the automation mechanism will be described in the rest of this section and a specific simplification will be outlined in the next section.

The codes 0,1,2,4 can be thought of as "neighbour codes" with respect to a computational element. The use of the values "0" and "1" is immediately a potential "off-on" switch to facilitate the development of automatic program code. The additional inclusion of a "2" code simply acts as another form of "on" switch.

The immediate family of eight neighbour codes of the central computational element is labelled as in Figure 3.8. The codes are numbered clockwise from the top-left element of the innermost ring of neighbour elements. Only a selection of neighbour codes is needed to automate the program code of a given finite difference equation — as is suggested by inspecting the computational stencil of Figure 3.7.

Because of the special treatment of the advective and diffusive terms (to be discussed further in the next section), two neighbour codes from the next neighbouring ring of elements are also determined. The codes in this ring are also numbered clockwise starting from the top-left element. The two extra codes required are the codes of elements $(i+2)$ and i_{22}. Because of the neighbour numbering system used, these are respectively labelled NC15 and NC19. They are needed to determine if a land boundary passes through the u-point of the $(i+1)$th element, or the v-point of the i_2th element, respectively. Code NC15 is used in the automation of the u finite difference equation and code NC19 is used in the automation of the v finite difference equation.

The reason why these codes are needed is more readily seen if the computational stencils are drawn as in Figures 3.9. Figure 3.9(a) represents the computational molecule for the ζ, ω and w finite difference equations, and Figures 3.9(b) and 3.9(c) respectively represent the computational stencils for the u and v finite difference equations. In each of the figures, each solid line segment is potentially part of a coastal boundary since coastal boundaries pass only through velocity gridpoints. Besides showing the gridpoints comprising the respective computational stencils (ringed), Figures 3.9(b),(c) show additional ζ gridpoints. Recalling that the neighbour code of an element is defined according to the location of its ζ gridpoint, and noting that elements containing coastal boundary segments are always sandwiched between Type 0 and Type 1 elements, it can be seen that knowing the

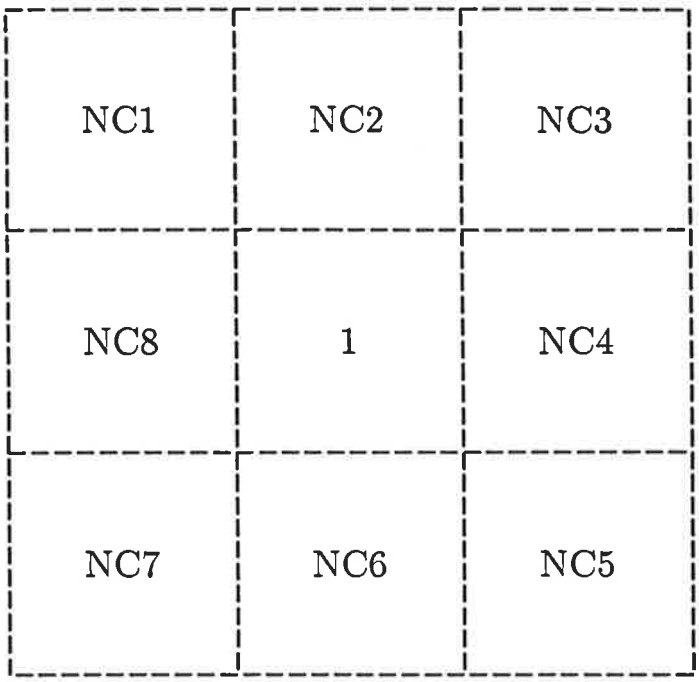
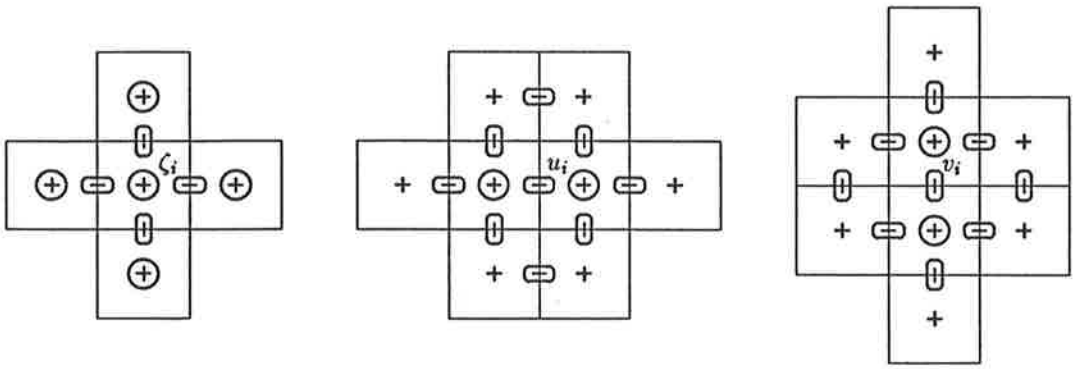


Figure 3.8: *Labelling convention for the immediate eight generic neighbour codes of the central element i which here is taken to be Type 1.*

location of these additional elevation gridpoints, i.e. knowing the neighbour codes of the corresponding elements, is necessary and sufficient information from which to determine whether coastal boundaries pass through the outlying velocity gridpoints of the u and v computational stencils.



(a) ζ, ω, w stencil (b) u stencil (c) v stencil

Figure 3.9: *The ζ, u, v, ω, w computational stencils drawn on a background network of line segments, any realistic grouping of which may represent a coastal boundary passing through or near the respective computational gridpoint. Gridpoints not ringed are not part of the respective computational stencil.*

Figure 3.9(a) shows that the ζ gridpoints of the ζ computational stencil are sufficient

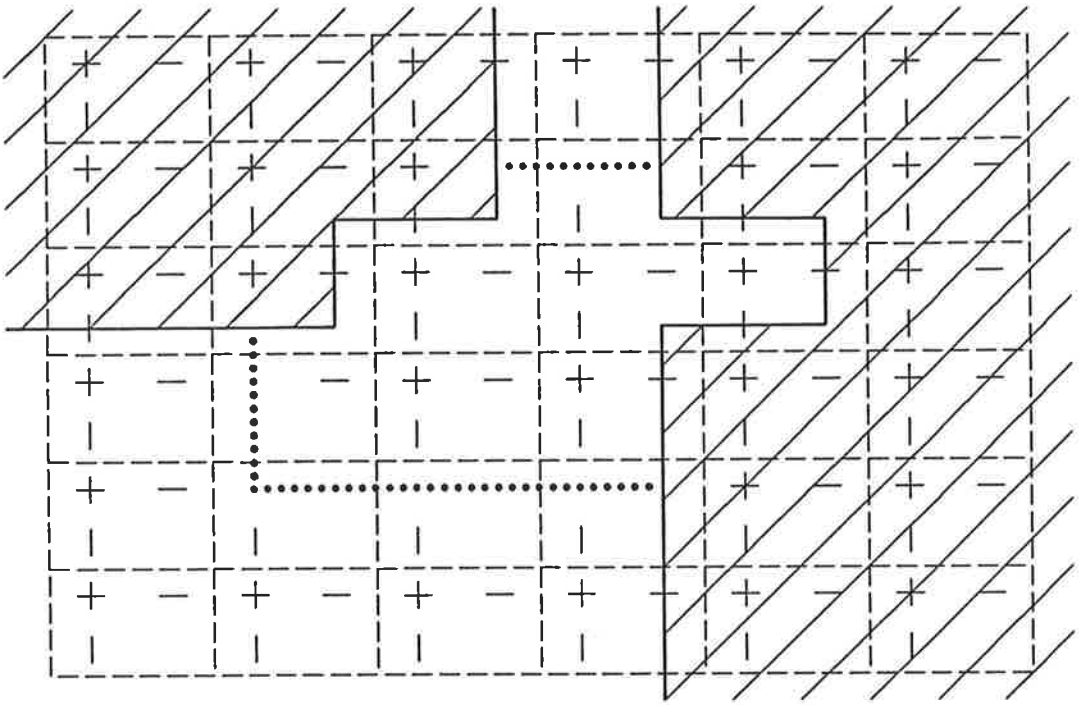


Figure 3.10: *A simple model region bounded by coastal boundaries (solid line segments) and open sea boundaries (dotted line segments). The hatched regions are land areas.*

to ascertain whether any of its constituent velocity gridpoints lies on a coastal boundary. That is, knowing the values of the codes NC2, NC4, NC6 and NC8 is all that is required in order to precisely determine if the ζ computational stencil is to be applied to a coastal configuration of neighbours surrounding the corresponding computational ζ gridpoint.

On the other hand Figure 3.9(b) shows that one additional neighbour code outside those of the 9-element block shown in Figure 3.7(b) is required to determine if a coastline passes through gridpoint u_{i+1}. That is, besides requiring the values of the codes NC2, NC3, NC4, NC5, NC6 and NC8 of the 9-element block, the additional code NC15 is required. These codes give the location of all the elevation gridpoints marked in the figure — the code of the central computational element is a "given" — and from these it can be determined if any of the outlying velocity gridpoints of the u computational stencil lie on a coastline.

Similarly, Figure 3.9(c) shows that in addition to the neighbour codes NC2, NC4, NC5, NC6, NC7 and NC8 which are all within the 9-element block, code NC19 is also required. Together with the given code of the central computational element, these seven neighbour codes are sufficient to determine if there is a coastal configuration of neighbours surrounding the computational v gridpoint.

The central computational element is usually a Type 1 element, but in cases where the elevation point of the computational element lies on an open boundary in such a way that its u-point and/or v-point lies within the model region, it is a Type 2 element. Thus either the computational element is Type 1, or it is Type 2 in which case it has an open boundary to the left or above — "west" or "north" — of the interior of the model region.

A neighbourhood code array is constructed by the modeller from the way the ζ grid-

points of a rectangular Arakawa "C" lattice lie over the plan of the region being studied. The array in its entirety clearly locates the model region, the model coastline, the position of the open boundary lines and the location of any exterior "water" elements. It is supplied to the computer program as part of the input data. The same array is later passed to the graphics routines that produce contour plots and so forth, from predictions generated by the program. These routines use the array to draw the model region and its boundaries and so provide a visual check on the accuracy of the input neighbourhood code array.

For computations, the programmed expressions for each of the finite difference equations at the gridpoints of each computational element require the neighbour codes of the neighbouring elements involved. Instead of determining these codes at each time step as computations occur, they are determined once at the commencement of modelling for each Type 1 and Type 2 element and stored in lists for later retrieval.

As an example of a study region to which neighbourhood codes are assigned, and to illustrate how these codes are stored and later retrieved, consider Figure 3.10. The model region is the central portion bounded by solid lines (coastal boundaries) and dotted lines (open sea boundaries). The hatched regions are land areas.

Using the definitions of the four element types given above, the neighbourhood code array corresponding to the study region of Figure 3.10 is given in Figure 3.11.

Elevation ζ and velocity components ω, w are updated only at Type 1 elements. Elevation ζ is prescribed as a time series at Type 2 elements. Velocity components u, v are updated at Type 1 elements and are updated at Type 2 elements if the corresponding gridpoints lie over the model sea.

For ζ computations, neighbour codes NC2, NC4, NC6 and NC8 are required by the program code, so the corresponding neighbour elements must be available at every Type 1 element. This is achieved if every Type 1 element is at the centre of a 9-element block. Therefore the first and last rows and columns of the array must not contain Type 1 elements. If necessary the array is expanded so as to achieve this. In addition, because codes NC15 and NC19 are required in the program code for the u and v finite difference equations, respectively, there must be two columns in the neighbourhood code array to the right of the most easterly computational u-point (but not a coastal u-point), and two rows in the array below the most southerly computational v-point (but not a coastal v-point); u-points and v-points on coastal boundaries are excluded from this since their value is set by the coastal boundary condition. Thus the outermost rows and columns of the array of Figure 3.11 are necessary to the program code even though at first sight they may appear superfluous to a model of the region.

For the purposes of computation, several permanent one-dimensional lists are immediately constructed from the neighbourhood code array. Computer expressions using lists are computationally quicker to execute than expressions using arrays. However, in order to relate a Type 1 or Type 2 element in a list back to its neighbourhood context in the array, two cross-referencing lists have to be defined, though these are only as long as the number of Type 1 and Type 2 elements declared. The lists are:

- **L**, the list form of the neighbourhood code array, generated by listing the entries of the array moving from left to right across the rows taken in order from top to bottom.

- **LR**, a list based on the L list wherein each Type 1 element is **ranked** as a Natural number in terms of the order of its appearance in list L and each Type 2 element is

0	0	0	4	0	0
0	0	0	2	0	0
0	0	1	1	1	0
4	2	1	1	0	0
4	2	2	2	0	0
4	4	4	4	0	0

Figure 3.11: *The array of neighbourhood codes assigned to the elements of the rectangular study region given in the simple model of the previous figure. Elements coded "4" are water elements outside the model.*

likewise ranked in increasing order of its appearance. Type 0 and Type 4 elements are assigned rank zero.

- **L1**, cross-reference list of Type 1 elements which uses their rank to determine their position in the L list.
- **L2**, cross-reference list of Type 2 elements which uses their rank to determine their position in the L list.

Using the array of Figure 3.11 as the example, the elements of the above lists are, respectively:

- L(1)=0, L(2)=0, L(3)=0, L(4)=4, L(5)=0, L(6)=0,
  L(7)=0, L(8)=0, L(9)=0, L(10)=2, L(11)=0, L(12)=0,
  ⋮
  L(31)=4, L(32)=4, L(33)=4, L(34)=4, L(35)=0, L(36)=0.
- LR(1)=0, LR(2)=0, LR(3)=0, LR(4)=0, LR(5)=0, LR(6)=0,
  LR(7)=0, LR(8)=0, LR(9)=0, LR(10)=1, LR(11)=0, LR(12)=0,
  LR(13)=0, LR(14)=0, LR(15)=1, LR(16)=2, LR(17)=3, LR(18)=0,
  LR(19)=0, LR(20)=2, LR(21)=4, LR(22)=5, LR(23)=0, LR(24)=0,
  LR(25)=0, LR(26)=3, LR(27)=4, LR(28)=5, LR(29)=0, LR(30)=0,
  LR(31)=0, LR(32)=0, LR(33)=0, LR(34)=0, LR(35)=0, LR(36)=0.
- L1(1)=15, L1(2)=16, L1(3)=17, L1(4)=21, L1(5)=22.

- L2(1)=10, L2(2)=20, L2(3)=26, L2(4)=27, L2(5)=28.

Having calculated the entries of these four lists, the neighbour codes, the "neighbourhood configuration" (which will be explained shortly), and the Type 1 list index or Type 2 list index of each neighbour are calculated and stored for each Type 1 element, in turn. Then, the neighbour codes and the indices of each neighbour for each Type 2 element, in turn, is calculated and stored.

While the neighbour codes and corresponding indices so calculated for some of the Type 1 and Type 2 elements will not be used in later computations, there is no advantage in trying to be selective at this stage. To illustrate this point, in Figure 3.10 it is clear that at the third Type 1 element the only active computational gridpoint is the ζ-point — both the u and v-points receive zero value by applying the coastal boundary condition. Therefore only the neighbour codes NC2, NC4, NC6 and NC8 and the corresponding index values are actually required. Knowing that, it might be argued it is a waste of computational time to calculate the remaining codes and indices of the neighbours of this element, but on the other hand it would be wasteful to attempt to be selective: the computational time used to calculate all the codes and indices of the neighbours of computational elements is sure to be less than the time required to search each neighbourhood in order to calculate the minimum number of such codes and indices. The computational subroutines select the codes and indices they require according to the corresponding design of the respective computational stencil. Besides the sheer simplicity of calculating all the codes and indices of the immediate neighbours (and codes NC15 and NC19) without being selective at this stage, their availability leaves the way open at the subroutine level for more easily modifying the program code should this be useful at a future point.

For Type 1 elements, the procedure is as follows. For element i its position IPOS in the list L is determined using the Fortran statement

```
IPOS =  L1(I)
```

where I is the program variable name of "i". Thus, for example, the position of the fourth Type 1 element in list LR for the model array of Figure 3.11 is L1(4)=21.

The neighbour codes are then calculated and stored in generic neighbour code lists using program statements which follow the pattern

```
Neigh_Code_1(I) = L(IPOS - NC - 1)
Neigh_Code_2(I) = L(IPOS - NC    )
      ⋮
Neigh_Code_8(I) = L(IPOS      - 1)
```

where NC is the number of columns in the array. Later, during computations, the codes of the neighbours of a Type 1 element i are retrieved using the statements

```
NC1 = Neigh_Code_1(I)
NC2 = Neigh_Code_2(I)
      ⋮
NC8 = Neigh_Code_8(I)
```

The special neighbourhood codes NC15 and NC19 are calculated and retrieved in similar ways.

Having calculated the neighbour codes of Type 1 element i, numbers which characterize the computational neighbour configuration of the element with respect to each of the basic computational stencils, are calculated and stored for later retrieval. During computations to update each of the ζ, u, v, ω, w fields for each subroutine, these neighbourhood configuration numbers (NCN's) are used to direct program control to one of three sections of program code, each section written for one of the following configurations of neighbourhood:

- "open sea neighbourhoods", where the computational neighbour codes of element i are all of value "1" — for brevity, this is referred to as a "**1**'s" neighbourhood (configuration),
- "coastal neighbourhoods", where the computational neighbour codes of element i are a mixture of "0" and "1" values — this is referred to as a "**0–1**'s" neighbourhood (configuration), and
- "open boundary neighbourhoods", where the computational neighbour codes of element i are a mixture of "0", "1" and "2" values — this is referred to as a "**0–1–2**'s" neighbourhood (configuration).

It must be emphasized that the neighbourhood configuration numbers use only the codes of the neighbour elements used by the corresponding computational stencils and they do not use the codes NC15 or NC19. They are therefore formed from a **selection** of the 8 immediate neighbours of the central (Type 1) computational element. Thus an open sea neighbourhood, for example, does not refer to the codes of all 8 immediate neighbours of the element, but only the neighbours involved in computations — furthermore, the open sea neighbourhood for which the u finite difference equation is being solved may be different to the open sea neighbourhood for which the v equation is solved. An important consequence of the fact that not all 8 immediate neighbours are involved in these categories of neighbourhood is that more 9-element blocks with a central "1" element may be classified as open sea neighbourhoods than would be the case if all 8 neighbours were involved. Since the program code associated with this type of neighbourhood is the least complicated, it is efficient to process as many computational elements through this section of program code as possible.

There are three neighbourhood configuration numbers for each Type 1 element and these correspond to the three basic patterns exhibited by the ζ, u, v, ω, w computational stencils of Figure 3.7. Thus, for Type 1 element i, and for the ζ finite difference equation, we define the neighbourhood configuration number

```
NCN_Z(I) =                          Neigh_Code_2(I)**3
          +Neigh_Code_8(I)**3                          +Neigh_Code_4(I)**3
                              +Neigh_Code_6(I)**3
```

where the operation of summing the cubes of the corresponding neighbour codes is a simple way to distinguish between the three basic configurations of neighbourhood. The statement is "shaped" like the ζ computational stencil for no other reason than to emphasize the fact that the neighbour codes used are only those of the neighbours that the ζ computational stencil accesses. This NCN value is also used in the subroutine for the calculation of ω and w because the computational stencils of the corresponding finite difference

equations have the same shape. For the u finite difference equation, the neighbourhood configuration number is defined to be

```
NCN_U(I) = NCN_Z(I) + Neigh_Code_3(I)**3 + Neigh_Code_5(I)**3
```

and for the v finite difference equation, it is defined to be

```
NCN_V(I) = NCN_Z(I) + Neigh_Code_7(I)**3 + Neigh_Code_5(I)**3
```

Examining the possible values of NCN_U, for example, it can be seen that

- NCN_U = 6 if the neighbour codes of the u computational stencil are all 1's,
- NCN_U < 6 if the neighbour codes of the u computational stencil are a mixture of 0's and 1's, and
- NCN_U > 6 if the neighbour codes of the u computational stencil are a mixture of 0's, 1's and 2's.

For the u equation (and for the v equation) the value 6 is critical in assigning program control to the appropriate section. For the ζ equation (and ω, w equations) the value 4 is the critical control value.

Finally, and in the same DO loops in which the neighbour codes and neighbourhood configuration numbers are calculated at the commencement of modelling, the Type 1 and Type 2 index values of the neighbours of each Type 1 element i are also calculated and stored. The pattern of statements used is

```
Index_Value_I1M1(I) = LR(IPOS - NC - 1)
Index_Value_I1  (I) = LR(IPOS - NC    )
 :
Index_Value_IM1 (I) = LR(IPOS      - 1)
```

Recalling that in list LR, Type 1 and Type 2 elements are ranked in ascending order of their appearance in the neighbourhood code array L, and Type 0 and Type 4 elements are given zero rank, the index values of neighbour elements can either be zero or can be non-zero and refer to Type 1 or Type 2 elements. Indices having zero value — indicating that the parent elements are of Type 0 or Type 4 and have no contribution to make to the finite difference equations — access the zeroth entries of the variable lists, which are programmed to have zero value. Since non-zero entries refer to Type 1 or Type 2 elements, some means of distinguishing between these is required. For instance, does an index value of 3 refer to the third member of the u velocity list for Type 1 elements (whose program variable name is U) or to the third member of the u velocity list for Type 2 elements (whose program variable name is U2)? The choice is resolved by making use of the corresponding neighbour code values. Thus suppose the indices of the neighbours of a Type 1 element i are to be retrieved at some point during computations. As a first step, the index variables are filled using the commands

```
I1M1 = Index_Value_I1M1(I)
I1   = Index_Value_I1  (I)
 :
IM1  = Index_Value_IM1 (I)
```

If the NCN of the element is such that its neighbourhood is either a "1's" or "0–1's" configuration, then the index values are either all 1's or a mixture of 0's and 1's. In either case there are no Type 2 elements referenced, the index values are already correctly set and computations may proceed. However, if the NCN of the element indicates a "0–1–2's" configuration, at least one of these index values will refer to a Type 2 element. In order to select out the Type 2 element indices, a multiplicative factor of the form $(\mathrm{NC}i/2)$, $i = 1, 2, \ldots, 8$, whose value is determined by Fortran integer arithmetic, is introduced as follows:

```
II1M1 = (NC1/2) * I1M1
II1   = (NC2/2) * I1
  ⋮
IIM1  = (NC8/2) * IM1
```

where the double-I at the beginning of each index name is a convention used to denote the index of a Type 2 element. It can be seen from these commands that only indices corresponding to Type 2 elements will be non-zero — if the neighbour code is 0 or 1 the factor $(\mathrm{NC}i/2)$, $i = 1, 2, \ldots, 8$ has the value zero. Index values of Type 1 neighbours are retrieved by introducing a different factor as in the commands:

```
I1M1 = (NC1*(2-NC1)) * I1M1
I1   = (NC2*(2-NC2)) * I1
  ⋮
IM1  = (NC8*(2-NC8)) * IM1
```

Here, because the multiplicative factor now returns the value zero if the neighbour code is 0 or 2, only indices corresponding to Type 1 elements will be non-zero. By this process of elimination, index values of neighbour elements for "0–1–2's" configurations can be precisely set. Because "0–1–2" configurations represent only a small percentage of the total number of computational configurations, the extra statements executed in this elimination procedure do not significantly increase computational cost.

Although the process of retrieval of codes and index values of neighbours of a Type 1 computational element has been illustrated as being applied to all the near neighbours of the element, in actual implementation for a subroutine solving a given finite difference equation, only the codes and index values of the set of neighbours required by the corresponding computational stencil are retrieved.

Codes and index values for the neighbours of Type 2 computational elements are calculated and stored at the commencement of simulations, and are later retrieved, in a similar manner. Computations at Type 2 elements are only carried out for the u and v finite difference equations. For both the u and v subroutines, a further section of program code — in addition to that written for "1's", "0–1's" and "0–1–2's" configurations of neighbours of Type 1 elements — is written for these "Type 2 neighbourhoods". These sections of program code are similar to the sections written for "0–1–2's" neighbourhoods but assume the central element is of Type 2 rather than Type 1. Of course, being for the u and v-points (of Type 2 elements) that lie over the model sea, these sections are rarely used compared with the frequency of use of the code written for "1's" and "0–1's" configurations. Figure 3.12 shows the u computational stencil applied at the u-point of a Type 2 element of a western open boundary. The Spencer Gulf models of Chapters 5,

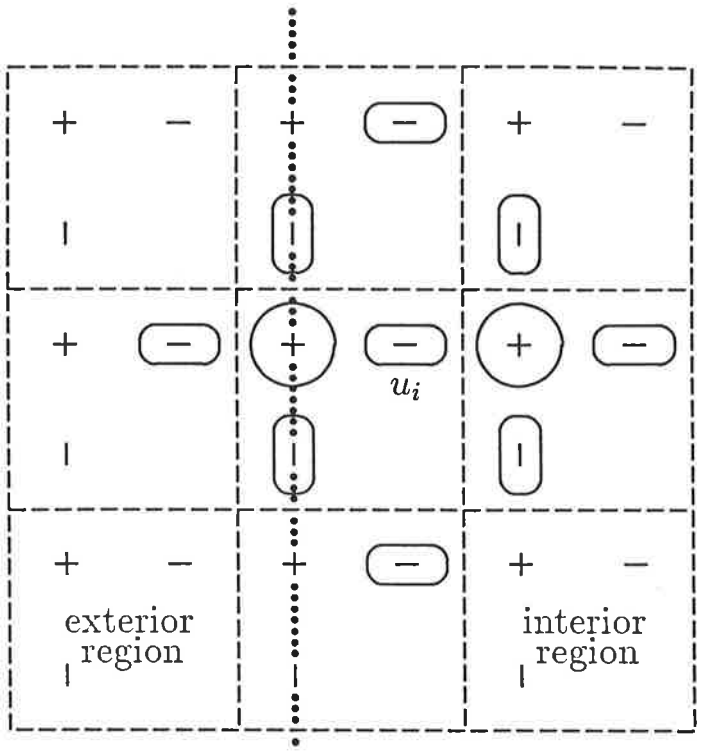


Figure 3.12: *Plan view of the u_i computational stencil with central element of Type 2. The open boundary line is dotted.*

7 and 8 do not use Type 2 computational elements at all since the open boundaries are exclusively to the "south" and "east" of the model region. The program code for "Type 2 neighbourhoods" was developed for the sake of generality of application of the programs and has found application in the Gulf of Carpentaria model of Mitchell et al. (1984) and the Bass Strait model of Arnold and Noye (1986b).

The principles of automation of program code in this work will now be illustrated.

Automated program code for the first form of the elevation finite difference equation, viz.

$$\begin{aligned}\zeta_i^{n+\frac{1}{2}} = \zeta_i^{n-\frac{1}{2}} &- \frac{\Delta t}{4\Delta x}\left[\left(H_i^n + H_{i+1}^n\right) U_i^n - \left(H_{i-1}^n + H_i^n\right) U_{i-1}^n\right] \\ &- \frac{\Delta t}{4\Delta y}\left[\left(H_i^n + H_{i_1}^n\right) V_{i_1}^n - \left(H_{i_2}^n + H_i^n\right) V_i^n\right], \qquad (3.42)\end{aligned}$$

will be given for the three general configurations of ζ computational neighbourhood, viz. "1's", "0–1's" and "0–1–2's" configurations. After a discussion of how this works, certain simplifications to the code will be observed in the case of the latter two configurations.

1. For a ζ computational neighbourhood configuration of Type 1 elements, the program code is

```
Z(I) = Z(I) - DTR4DX * (   ( H(I) + H(IP1) ) * UA(I  )
                         - ( H(I) + H(IM1) ) * UA(IM1) )
            - DTR4DY * (   ( H(I) + H(I1 ) ) * VA(I1 )
                         - ( H(I) + H(I2 ) ) * VA(I  ) )
```

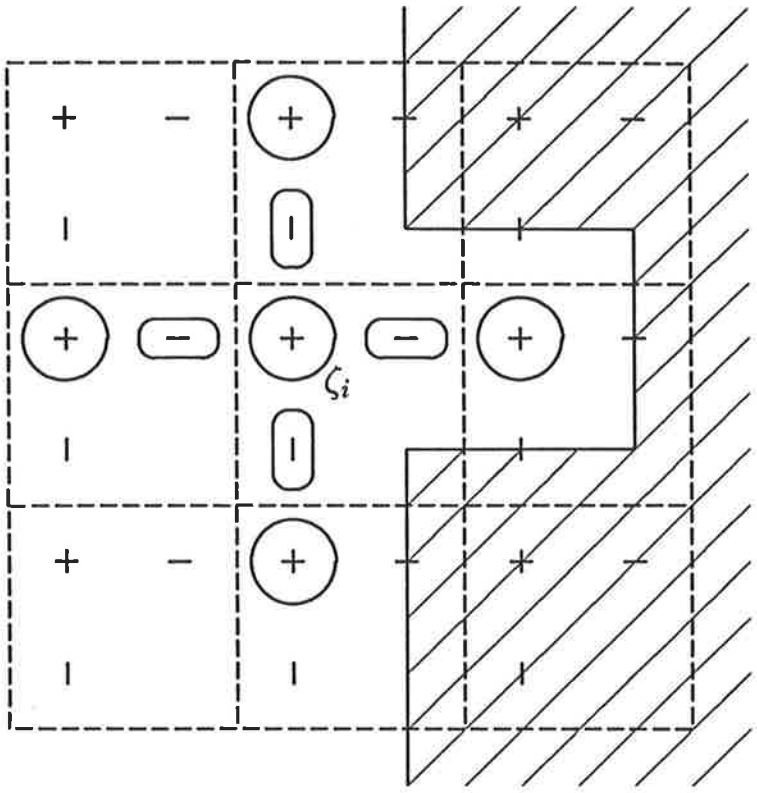


Figure 3.13: *Plan view of the ζ_i computational stencil near a coastal region of a model. In this situation the ζ computational neighbourhood is a "1's" neighbourhood configuration.*

where	`Z`	on the left hand side of the expression is the program variable name of the updated list of elevation values for Type 1 elements at time $(n+1/2)\Delta t$, and on the right hand side is for "old" list of values at time $(n-1/2)\Delta t$
	`DTR4DX`	is the program variable name of $\Delta t/(4\Delta x)$
	`DTR4DY`	is the program variable name of $\Delta t/(4\Delta y)$
	`H`	is the program variable name of the list of total depth values for Type 1 elements at time $n\Delta t$
	`UA`	is the program variable name of the list of U components of depth-averaged velocity for Type 1 elements at time $n\Delta t$
	`VA`	is the program variable name of the list of V components of depth-averaged velocity for Type 1 elements at time $n\Delta t$
	`IP1`	is the program variable name of index $(i+1)$ for a Type 1 element
	`IM1`	is the program variable name of index $(i-1)$ for a Type 1 element
	`I1`	is the program variable name of index i_1 for a Type 1 element
	`I2`	is the program variable name of index i_2 for a Type 1 element

The program code for this configuration is straightforward. It does not involve the use of neighbour codes and so is the least complicated, and is also the most frequently used since, in general, most computational elements will have such a neighbourhood configuration.

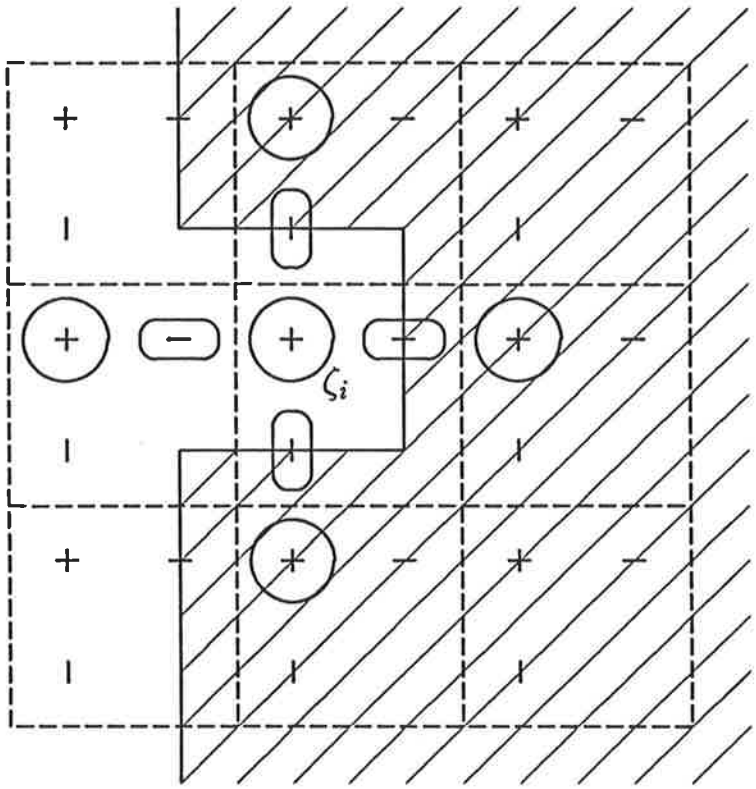


Figure 3.14: *Plan view of the ζ_i computational stencil near a coastal boundary of a model. In this case the ζ computational neighbourhood configuration is a "0–1's" configuration.*

This program code applies to neighbourhood configurations where NC2=1, NC4=1, NC6=1, NC8=1 and therefore is applicable in the situation depicted by Figure 3.13 where, although NC3=NC5=0, the ζ-points of the four neighbours in the ζ computational stencil of element i are all Type 1 elements.

2. For a ζ computational neighbourhood configuration which is a mixture of Type 0 and Type 1 elements, a possible program code is

```
Z(I) = Z(I) - DTR4DX * (   NC4 * ( H(I) + H(IP1) ) * UA(I  )
                         - NC8 * ( H(I) + H(IM1) ) * UA(IM1) )
            - DTR4DY * (   NC2 * ( H(I) + H(I1 ) ) * VA(I1 )
                         - NC6 * ( H(I) + H(I2 ) ) * VA(I  ) )
```

Here, elements i_1, $(i+1)$, i_2, $(i-1)$ may be Type 0 or Type 1 and so the neighbour codes NC2, NC4, NC6, NC8 may have the values "0" or "1". Generally, the program code for the "0–1's" configurations is more complicated than that for the "1's" configuration and less complicated than that for the "0–1–2's" configuration. In terms of frequency of use, it is also sandwiched between the other configurations — generally less frequently used than the "1's" program code and more frequently used than the "0–1–2's" code, for a typical model.

Figure 3.14 shows the ζ computational stencil in the vicinity of a coastal boundary, and here NC2=NC4=NC6=0 while NC8=1, and so the computational configuration

is a "0–1's" configuration. Gridpoints V_{i_1}, U_i and V_i all lie on the coastal boundary and, by the coastal boundary condition (2.20), are set to zero. This zero contribution is passed to the scheme by the corresponding value of the neighbour code multipliers NCi, $i = 2,4,6,8$. These codes act as algebraic "off-on" switches with respect to the terms of the overall finite difference expression in which they are factors. The values NC2=0, NC4=0, NC6=0 switch off the contributions from the respective terms; the value NC8=1 does not alter the contribution from the term involving U_{i-1}.

Hence the effective statement executed in the situation depicted in Figure 3.14 is

```
Z(I) = Z(I) - DTR4DX * ( - ( H(I) + H(IM1) ) * UA(IM1) )
```

and is precisely what would be obtained on the basis of applying the coastal boundary conditions and using the fact that each of `VA(I1)`, `UA(IP1)` and `VA(I)` are zero.

3. For a ζ computational neighbourhood configuration which is a mixture of Type 0, Type 1 and Type 2 elements, a possible program code is

```
Z(I) = Z(I) - DTR4DX * ( ((NC4+1)/2) * ( H(I) + H(IP1) + H2(IIP1) )
                                      *   UA(I)
                         -((NC8+1)/2) * ( H(I) + H(IM1) + H2(IIM1) )
                                      * ( UA(IM1) + UA2(IIM1) )
             - DTR4DY * ( ((NC2+1)/2) * ( H(I) + H(I1 ) + H2(II1 ) )
                                      * ( VA(I1) + VA2(II1) )
                         -((NC6+1)/2) * ( H(I) + H(I2 ) + H2(II2 ) )
                                      *   VA(I) )
```

where
- `H2` is the program variable name of the list of total depth values for Type 2 elements at time $n\Delta t$
- `UA2` is the program variable name of the list of U components of depth-averaged velocity for Type 2 elements at time $n\Delta t$
- `VA2` is the program variable name of the list of V components of depth-averaged velocity for Type 2 elements at time $n\Delta t$
- `IIP1` is the program variable name of index $(i+1)$ for a Type 2 element
- `IIM1` is the program variable name of index $(i-1)$ for a Type 2 element
- `II1` is the program variable name of index i_1 for a Type 2 element
- `II2` is the program variable name of index i_2 for a Type 2 element

This program code is the most general as it will handle all the possible element types — 0,1,2 — at the four neighbour positions of the ζ computational stencil. It is used for Type 1 elements alongside an open boundary. Being the most general program code and requiring many extra arithmetic operations and list accesses due to its generality, it is the most complicated and takes the longest time to execute but in a typical model where the number of open boundary elements (and hence the number of "0–1–2" configurations) is a small percentage of the total number of model elements, it is relatively seldom used.

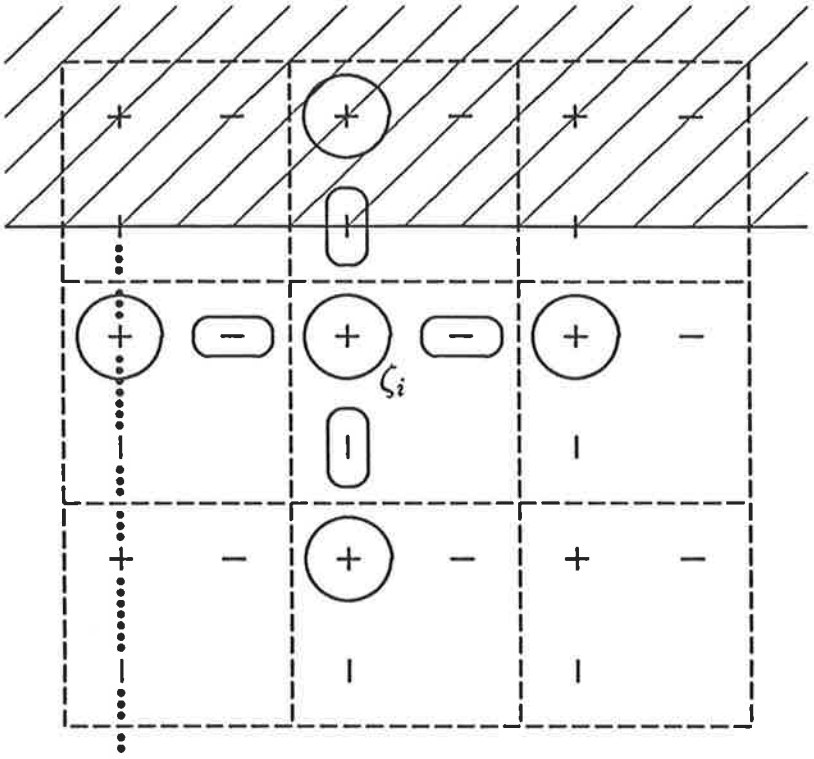


Figure 3.15: *The ζ computational stencil near a junction of a coastal and open sea boundary of a model. Here, the ζ computational neighbourhood configuration is a "0-1-2's" configuration.*

Consider the application of this statement in the situation of Figure 3.15. Element i_1 is Type 0 and gridpoint V_{i_1} lies on a coastal boundary. The former fact conveys the implication of the latter information by means of the factor `((NC2+1)/2)` which is 0 when NC2=0, using Fortran integer arithmetic; i.e. the term involving V_{i_1} is "switched off" because NC2=0. Elements $(i+1)$ and i_2 are Type 1 and their respective terms are included; i.e. the terms involving U_i and V_i are "switched on" because NC4=NC6=1. Since these elements are of Type 1, indices `IIP1` and `II2` are both 0 thus eliminating the quantities `H2(IIP1)` and `H2(II2)`. Element $(i-1)$ is Type 2 and the factor `((NC8+1)/2)` has value 1 when NC8=2, so there is a contribution from the associated term. Because element $(i-1)$ is Type 2, index `IM1` is 0 and so the quantities `H(IM1)` and `UA(IM1)` are eliminated, but index `IIM1` is non-zero and quantities `H2(IIM1)` and `UA2(IIM1)` are substituted.

For completeness, because NC2=0 index `I1` is 0 and so `H(I1)` is 0 and `VA(I1)` is 0; similarly, index `II1` is 0 and so `H2(II1)` is 0 and `VA2(II1)` is 0.

Hence the effective statement executed in the situation of Figure 3.15 is

```
Z(I) = Z(I) - DTR4DX * (   ( H(I) + H(IP1)   ) * UA(I)
                         - ( H(I) + H2(IIM1) ) * UA2(IIM1) )
            - DTR4DY * ( - ( H(I) + H(I2 )   ) * VA(I)     )
```

which is what is required. The elimination of the term in `VA(I1)` is again what is

required on the basis of applying the coastal boundary condition to the value `VA(I1)`.

The above program code will handle all physically realistic boundary configurations of elements for the ζ computational stencil. The program code for the "0–1–2's" configuration could be used for all configurations but the extra computer operations and list look-ups involved makes it worthwhile to use the NCN_Z value to divert program control to the most efficient computer code for each case. To illustrate this point, the depth-averaged model of Chapter 5 was run forcing every configuration to be processed using the "0–1–2's" code in each subroutine — program execution time nearly doubled and the same answers were obtained. The same answers are expected, and from the point of view of validating the program code, this experiment at least demonstrates agreement between all three sections of code. Because the program code for "0–1–2" neighbourhoods is complicated, rigorous testing for error is necessary. The tests carried out are summarized in Chapter 4, and are intended to test as much of the program code as possible.

A further advantage of dividing the program code into sections in this way is that the different categories of elements can be treated in different ways. For example, advective terms could be easily omitted from the programming code of "0–1–2's" configurations if it were desired to exclude the advective effect from computations near the open boundary; special formulations for the Coriolis terms could be introduced along the coastline by including them in "0–1's" programming code; and so on.

Returning to the program code for the "0–1's" configuration, a simplification may be observed. Element i_1 in Figure 3.14 is Type 0 and so index `I1` will be 0 since index values of Type 0 elements are zero, as explained previously. Likewise, in this example, indices `IP1` and `I2` are 0. This suggests that the corresponding multiplicative factors are not needed as their effect is implicitly conveyed by the indices of the respective velocity quantities. This leads to the discovery that program code for "0–1's" configurations for the ζ computational stencil is effectively identical to that for "1's" configurations.

A similar simplification can be made to the stated program code for "0–1–2's" configurations. The fact that in Figure 3.15 element i_1 is Type 0 leads to indices `I1` and `II1` having value 0 and thus the factor `((NC2+1)/2)` is superfluous as a means of eliminating the corresponding term. Regarding element $(i-1)$, index `IM1` is 0 because the element is not Type 1, and index `IIM1` is non-zero because the element is Type 2. Hence the factor `((NC8+1)/2)` is superfluous as a means of retaining the associated term as part of computations. This leads to the conclusion that program code for "0–1–2's" configurations for the ζ computational stencil can be simplified by removing all the factors of the form $((\mathrm{NC}i+1)/2)$, $i = 2, 4, 6, 8$.

This completes our study of the automated program code for the first finite difference form of the elevation equation. Automation of the program code for the second form of the ζ finite difference equation follows in an analogous way.

Automation of the program code for the u and v finite difference equations proves to be more complicated, but is achieved by treating each term (3.9)–(3.19) separately rather than lumping them all together into a single expression and trying to automate that.

As an illustration of the processes involved in automating the terms of the u and v finite difference equations, consider the derivative factor $\partial u/\partial x$ of the x-advective term $u\partial u/\partial x$ of the u equation. The finite difference expression for this factor is, from (3.10):

$$\left\{\frac{\partial u}{\partial x}\right\}^n_{u_{i,k}} \simeq \frac{1}{4\Delta x}\left(u^n_{i+1,k} - u^n_{i-1,k}\right). \tag{3.43}$$

The program code written for (3.43), for each of the three general configurations of neighbour elements for the u computational stencil with a central Type 1 element, is as follows:

1. For a neighbour configuration of Type 1 elements,

```
DuDx = R4DX * (U(K,IP1) - U(K,IM1))
```

where `DuDx` is the program variable name of the result
`R4DX` is the program variable name of $1/(4\Delta x)$
`U` is the program variable name of the array of u components of depth-dependent velocity for Type 1 elements
`K` is the program variable name of depth level k

For this configuration, element $(i-1)$ is Type 1 so u-point u_{i-1} is readily available to the numerical scheme. Element $(i+1)$ is also Type 1, so u-point u_{i+1} is also available. If the ζ-point to its right lies on land, in which case NC15=0, u_{i+1} lies on a coastal boundary and $u_{i+1,k} = 0$, for all levels k, is the actual value of this quantity.

In Section 3.6 it will be argued that this term ought to be deleted if NC15=0.

2. For a neighbour configuration of Type 0 and Type 1 elements, the program code is

```
DuDx = R4DX * (U(K,IP1) - U(K,IM1))
```

which is the same code as for the "1's" configuration above. If both elements $(i-1)$ and $(i+1)$ are Type 1, then the same situation as above holds, and so identical code is anticipated. If element $(i-1)$ is Type 0, then u_{i-1} lies on a coastal boundary and its contribution is zero. This information is implicitly conveyed to the expression by means of index `IM1` which is 0 if element $(i-1)$ is Type 0. Element $(i+1)$ cannot be Type 0 at this stage. If it were, computations would not have proceeded this far in the u subroutine since a check is made on the value of NC4 immediately the neighbour codes, configuration number and indices are retrieved for element i. If NC4=0 the subroutine sets $u_{i,k}^{n+1} = 0$ for all levels k since this u-point lies on a coastal boundary; program control then passes to the next computational u-point. Thus program code for the "0–1's" configuration is indeed the same as for the "1's" configuration for the finite difference form of the $\partial u/\partial x$ factor.

In the next section it will be argued that this term should be deleted if either NC8=0 or NC15=0.

3. For a neighbour configuration of Type 0, Type 1 and Type 2 elements, the program code is

```
DuDx = R4DX*( U(K,IP1)+(NC4/2)*((NC15+2)/4)*(2.0*U(K,I)-U(K,IM1))
             -U(K,IM1)-U2(K,IIM1) )
```

Let us examine this code to see if it takes into account the possibility that element $(i-1)$ may be Type 0, 1 or 2 and that element $(i+1)$ may be Type 1 or 2 (it is not Type 0 for reasons already stated). Since we have already examined the cases where element $(i-1)$ is Type 0 or 1 and element $(i+1)$ is Type 1, it simply remains to show that this general code reduces to the code of the previous configurations if NC4≠2 and NC8≠2, and that it gives sensible results if either NC4=2 or NC8=2. It can be seen that since the central element i is Type 1, it is not realistically possible for both elements $(i-1)$ and $(i+1)$ to be Type 2. If neither NC4 nor NC8 are 2 then the above expression does reduce to that of the previous configurations since then `(NC4/2)`=0 and index `IIM1`=0.

Now suppose NC8=2, and hence NC4≠2:

- This implies element $(i-1)$ is Type 2 and so `IM1`=0 and there is no contribution from the two terms `U(K,IM1)`, while `IIM1` is non-zero and there is a contribution from the term `U2(K,IIM1)`.
- At the same time, since NC4≠0,2 then NC4=1 and there is a contribution from the `U(K,IP1)` term.

Finally, suppose NC4=2, and hence NC8≠2:

- This implies element $(i+1)$ is Type 2 and so `IP1`=0 and there is no contribution from the term `U(K,IP1)`.
- Element $(i+1)$ being Type 2 implies that an open sea boundary passes through the ζ-point of element $(i+1)$ in some fashion — either from ζ_{i_2+1} via ζ_{i+1} to ζ_{i_1+1} (as in Figure 3.16), or from ζ_{i_2+1} via ζ_{i+1} to ζ_{i+2}, or from ζ_{i_1+1} via ζ_{i+1} to ζ_{i+2}. In any of these three possibilities, u_{i+1} is either on the open boundary line and as such is not calculated and an approximation for it is required, or it lies on water outside the model region (as in Figure 3.16) and an approximation for it is required. The approximation used is the second order accurate extrapolation

$$u_{i+1} = 2u_i - u_{i-1} + O(\Delta x)^2 \tag{3.44}$$

  which is guaranteed to be available because element i is Type 1 and element $(i-1)$ is either Type 0 or 1.
- The factor `((NC15+2)/4)` is included to take care of the possibility that NC15=0 when NC4=2. In this case u_{i+1} lies on a coastline beyond the open boundary and has the value zero. In this case the program statement should produce a zero value — which it does because when NC15=0, ((NC15+2)/4)=0. Now, if NC4=2, it is not realistically possible for NC15 to be 1. If NC15=2, signifying that the open boundary connects ζ_{i+1} and ζ_{i+2}, then extrapolation (3.44) is used because ((NC15+2)/4)=1. If NC15=4, the extrapolation is still used since again ((NC15+2)/4)=1.

In the next section it will be argued that the term should be deleted if NC4=2 (or if NC8=0 or NC15=0) since that forces extrapolation (3.44) to be used for the unknown value u_{i+1}, and leads to only a first order accurate gradient approximation.

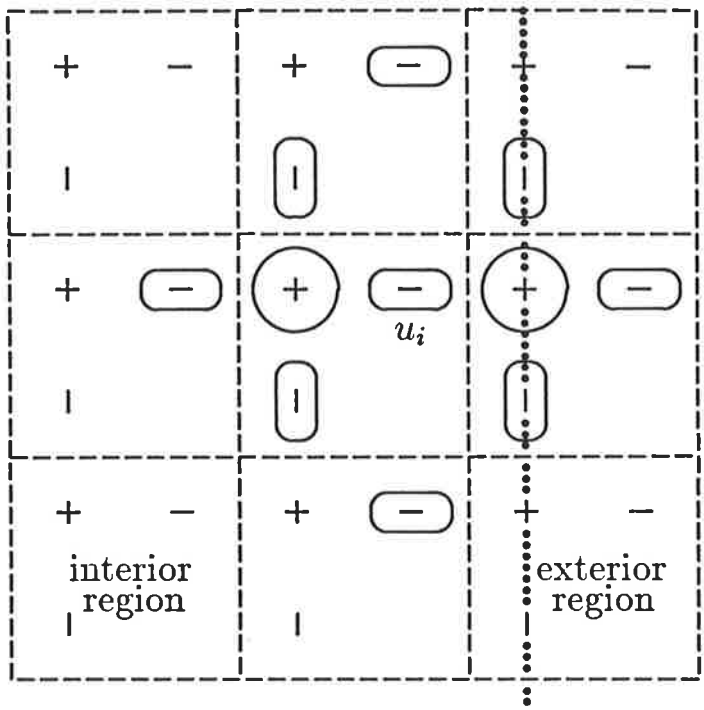


Figure 3.16: *Plan view of the u_i computational stencil in the vicinity of an open sea boundary.*

This completes a consideration of the form of the u finite difference program code for the gradient factor $\partial u/\partial x$ for all the possible realistic configurations of neighbours that element i may have. The given three computer expressions illustrate the style of programming with which the generalized code for the u finite difference equation has been developed — thoughtful consideration of all possible configurations of neighbours as they relate to each term of the u finite difference equation leads to appropriate program code. Such code has been developed for updating each of v, ω and w as well as ζ and u.

The program code written is at once both complicated — for the "0–1–2's" configurations particularly — and yet surprisingly succinct given the large range of neighbour configurations it handles. Much time was invested in developing the code, but the result is a program capable of handling any realistic boundary configuration, including "stepped" open boundaries, complicated coastal boundary configurations and combinations of these. Rigorous checking of the program code has been necessary. The one restriction imposed on the placement of open boundaries is that they must be realistic. They must not run parallel to the coast to within two rows of elements — this is very unlikely to occur in a realistic model. Thus neighbourhoods such as those depicted in Figure 3.17 are not catered for.

Likewise, distortions of the open boundary line that give rise to element triples such as in Figure 3.18 are not catered for by the programming code as they would not occur in a realistic model.

There are no restrictions placed on coastal boundary configurations.

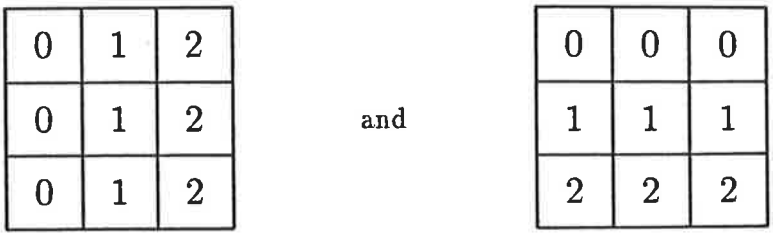


Figure 3.17: *Neighbourhoods such as these are not catered for in the present program — they are not realistic.*

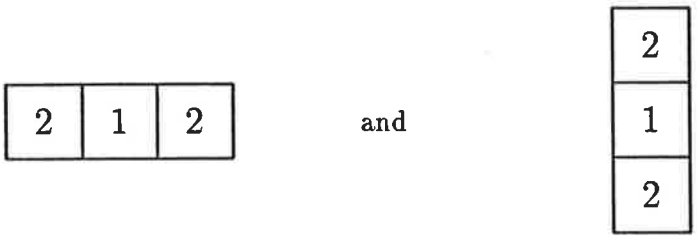


Figure 3.18: *Element strips such as these are also not catered for in the present program — they represent unrealistic wiggles in the open boundary line.*

3.6 Subordinate approximation for advective and diffusive terms near boundaries

The finite difference expressions developed in Section 3.4 can be applied in a straightforward manner to interior model elements (those elements centring computational stencils each of whose "atoms" lie over water within the model basin i.e. "1's" configurations), but in this section it will be shown that care must be taken in their application to elements bordered by coastal and/or open sea boundaries.

In the last section it was indicated how it is possible to automate program selection of the appropriate forms of the finite difference expressions to apply to a computational gridpoint when one or more of the computational "atoms" lies on a coastal and/or open sea boundary. This can be done using the neighbourhood codes (NCi) in arithmetic on-off "switches" used either directly in multiplicative factors or indirectly to modify list indices.

The NCi codes were also used in automated development of what could be termed "subordinate" approximations where, if a value in the finite difference expressions of Section 3.4 was not available, an approximation for it was developed. An example of this was the use of the extrapolation (3.44) in the "0–1–2's" program code for the $\partial u/\partial x$ gradient of the x-advective term of the u equation.

It is clearly important that such subordinate approximations do not corrupt the overall accuracy of the finite difference scheme. Specifically, spatial accuracy ought to continue to be second order and temporal accuracy ought to continue to be better than first order, following the use of these subordinate approximations.

It is found that in the application of the elevation finite difference equation to any computational ζ gridpoint there is never a need for subordinate approximation. Modification of the elevation finite difference equation to accommodate a coastal boundary is effected at the velocity gridpoint(s) through which the model coastline passes. At such a grid-

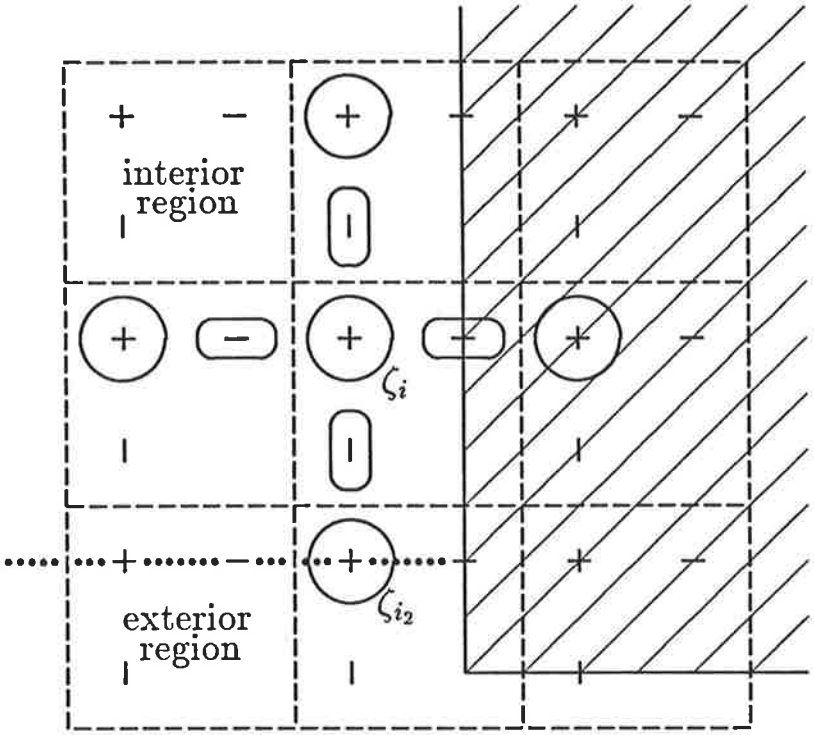


Figure 3.19: *Plan view of the ζ_i computational stencil at the junction of a coastal and open sea boundary. The open boundary is indicated by the dotted line. The shaded region represents land, and its border represents a coastal boundary.*

point(s) the velocity value is zero. Modification to accommodate an open sea boundary is effected at the respective elevation gridpoint(s) by switching in the prescribed elevation value at that point(s) and simultaneously switching out the iterated elevation value(s) (see the discussion in Section 3.5, concerning the "0–1–2's" program code for the elevation equation).

Consider the application of the elevation finite difference equation at the junction of the coastal and open sea boundary depicted in Figure 3.19. Applying condition (2.20), we have $U_i = 0$ for all time levels, which correctly simplifies equations (3.6) and (3.28); the unavailability of the quantity H_{i+1} for these equations is of no relevance. Thus the coastal boundary through gridpoint U_i is accommodated by simply using the boundary condition $U_i = 0$. This is invoked through the value of NC4, which is 0 in this instance. Values at the remaining gridpoints referenced in (3.6) and (3.28) for the situation of Figure 3.19 are available directly. The quantity H_{i_2} is available by reason of the application of boundary condition (2.29), and the equations for total depth (3.7) and (3.29). That is, the open sea boundary through gridpoint ζ_{i_2} is accommodated by using the prescribed value of elevation at that point instead of the iterated value. This is achieved by means of the value of NC6, which is 2 in this instance.

Since the structure of the computational stencil for the calculation of ω has the same form as that for the calculation of ζ, similar points can be made for the evaluation of ω_i in the vicinity of coastal and open sea boundaries.

However the situation is more complicated in the case of the momentum finite difference equations. This is partly because there are non-derivative and second order derivative

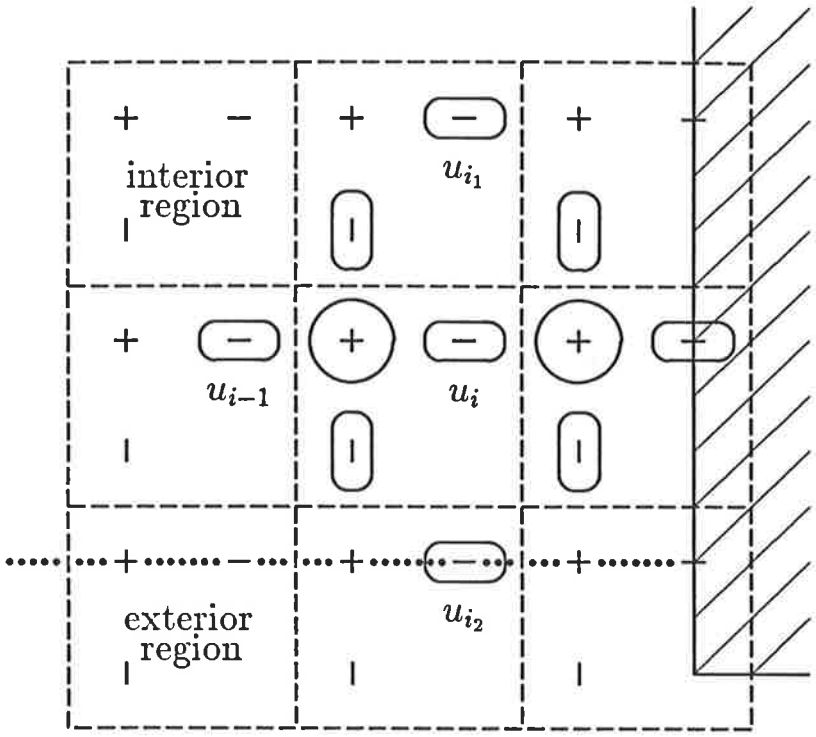


Figure 3.20: *Plan view of the u_i computational stencil near the junction of a coastal and open sea boundary.*

terms in these equations in addition to first order derivative terms, and partly because the u, v computational stencils consist of more gridpoints. Thus subordinate approximation of one or more values in the Section 3.4 finite difference expressions for the advective, Coriolis and diffusive terms may be required.

Provided the subordinate approximations are carried out so that the net effect is to maintain spatial symmetry with respect to the computational gridpoint, second order spatial accuracy will be maintained for the zeroth derivatives, viz. the Coriolis terms and u, v, ω factors of the advective terms.

But, as will be demonstrated, spatially second order accurate subordinate approximations cannot be found for the first and second order derivatives if the requirement to not go outside the 9-element block (for the approximations) is adhered to. Going outside the 9-element block would, because it is intended to develop a general program code, force going to at least a 25-element block which would result in much more complicated program code.

Consider the application of the u momentum finite difference equation near the junction of the coastal and open sea boundary depicted in Figure 3.20.

The finite difference expression for the y-advective term of the u equation is given in full by (3.11). The gradient component of this is:

$$\left\{\frac{\partial u}{\partial y}\right\}^n_{u_{i,k}} \simeq \frac{1}{4\Delta y}\left(u^n_{i_1,k} - u^n_{i_2,k}\right). \tag{3.45}$$

Because values are not calculated for velocity gridpoints on the open boundary, a subordinate approximation for $u^n_{i_2,k}$ is required. A linear extrapolation based on interior values,

viz.

$$u^n_{i_2,k} = 2u^n_{i,k} - u^n_{i_1,k} + O(\Delta y)^2, \tag{3.46}$$

leads to

$$\left\{\frac{\partial u}{\partial y}\right\}^n_{u_i,k} = \frac{1}{2\Delta y}\left(u^n_{i_1,k} - u^n_{i,k}\right) + O(\Delta y), \tag{3.47}$$

and is only first order accurate in space.

Obtaining a spatially second order accurate subordinate approximation requires replacing $u^n_{i_2,k}$ by a linear combination of u values (all from within the 9-element block), expanding each as a Taylor series about the value $u^n_{i,k}$ and then deriving sufficient algebraic equations that unwanted zeroth, first and second order terms can be eliminated. There are six zeroth, first and second order terms in the Taylor expansion of a function of two independent variables, so in general we need to find six algebraic equations. Solving these equations should give the desired linear combination. An approximation that will clearly do the job (but is unacceptable) is the quadratic extrapolation:

$$u^n_{i_2,k} = 3u^n_{i,k} - 3u^n_{i_1,k} + u^n_{i_{11},k} + O(\Delta y)^3. \tag{3.48}$$

Because the value $u^n_{i_{11},k}$ lies outside the 9-element block (3.48) cannot be used.

Confining attention to the 9-element block, let us seek a second order accurate subordinate approximation for $\partial u/\partial y$ using the six u values available (see Figure 3.20). Setting

$$u^n_{i_2,k} = au^n_{i_1-1,k} + bu^n_{i_1,k} + cu^n_{i_1+1,k} + du^n_{i-1,k} + eu^n_{i,k} + fu^n_{i+1,k}, \tag{3.49}$$

for unknowns a, b, c, d, e, f and substituting this expression into (3.45) leads to:

$$\left\{\frac{\partial u}{\partial y}\right\}^n_{u_i,k} \simeq \frac{1}{4\Delta y}\left(-au^n_{i_1-1,k} + (1-b)u^n_{i_1,k} - cu^n_{i_1+1,k} - du^n_{i-1,k} - eu^n_{i,k} - fu^n_{i+1,k}\right). \tag{3.50}$$

Expanding each u value on the right hand side about the gridpoint $u^n_{i,k}$, and imposing the condition that the derivative approximation be second order accurate in space, leads to the following set of 6 algebraic equations in the 6 unknowns a, b, c, d, e, f:

$$\begin{aligned}
-a + (1-b) - c - d - e - f &= 0,\\
a \qquad\quad - c + d \qquad - f &= 0,\\
-a + (1-b) - c \qquad\quad\ \ &= 2,\\
-a \qquad\quad - c - d \qquad - f &= 0,\\
a \qquad\quad - c \qquad\quad\ \ &= 0,\\
-a + (1-b) - c \qquad\quad\ \ &= 0.
\end{aligned} \tag{3.51}$$

This system is inconsistent — the third and sixth equations in the set contradict. That is, using the six available u values of the 9-element block shown in Figure 3.20 does not lead to a second order accurate subordinate approximation for $\partial u/\partial y$: one must go beyond the 9-element block to obtain such accuracy.

Because a spatially second order accurate subordinate approximation is not available within the preferred framework of the 9-element block, the y-advective term is omitted from the u equation in the situation depicted in Figure 3.20.

A similar conclusion is reached for the y-diffusive term of the u equation for the instance depicted in Figure 3.20. The full finite difference expression for this term is given in (3.17). The approximation for the second derivative is:

$$\left\{\frac{\partial^2 u}{\partial y^2}\right\}^n_{u_{i,k}} \simeq \frac{1}{4(\Delta y)^2}\left(u^n_{i_1,k} - 2u^n_{i,k} + u^n_{i_2,k}\right). \tag{3.52}$$

Replacing the unknown value $u^n_{i_2,k}$ with the linear extrapolation (3.46) gives a subordinate second derivative approximation of zero value. This is because the replacement is equivalent to assuming a straight line connects $u^n_{i_2,k}$, $u^n_{i,k}$ and $u^n_{i_1,k}$, and a straight line has zero second derivative. It is therefore pointless to retain this diffusive term where a linear extrapolation is used at the boundary.

It may be asked whether it is possible to replace $u^n_{i_2,k}$ with a higher order extrapolation based on available u values within the 9-element block in such a way that the resulting second derivative approximation is second order accurate. The answer is no. There are simply not enough gridpoints within the 9-element block to ensure that the truncation error of the Taylor expansion is sufficiently small. The y-diffusive term of the u equation is therefore omitted in this instance.

Consider now the x-advective and x-diffusive finite difference expressions of the u equation, (3.10) and (3.16) respectively, applied to the u_i gridpoint of Figure 3.20.

The approximation for the x-gradient of the x-advective term is

$$\left\{\frac{\partial u}{\partial x}\right\}^n_{u_{i,k}} \simeq \frac{1}{4\Delta x}\left(u^n_{i+1,k} - u^n_{i-1,k}\right). \tag{3.53}$$

Using the coastal boundary condition, $u^n_{i+1,k} = 0$ and we have

$$\left\{\frac{\partial u}{\partial x}\right\}^n_{u_{i,k}} = -\frac{1}{4\Delta x}u^n_{i-1,k} + O(\Delta x)^2, \tag{3.54}$$

which requires no subordinate approximation.

The approximation for the second derivative of the x-diffusive term is

$$\left\{\frac{\partial^2 u}{\partial x^2}\right\}^n_{u_{i,k}} \simeq \frac{1}{4(\Delta x)^2}\left(u^n_{i+1,k} - 2u^n_{i,k} + u^n_{i-1,k}\right). \tag{3.55}$$

Again using the coastal boundary condition, $u^n_{i+1,k} = 0$ and we have

$$\left\{\frac{\partial^2 u}{\partial x^2}\right\}^n_{u_{i,k}} = -\frac{1}{4(\Delta x)^2}\left(2u^n_{i,k} - u^n_{i-1,k}\right) + O(\Delta x)^2, \tag{3.56}$$

which requires no subordinate approximation.

Another group of important approximations arises in cases such as in Figure 3.21, where the v momentum finite difference equation is applied near the junction of a coastal and open sea boundary.

The gradient part of the y-advective term at the v_i gridpoint is:

$$\left\{\frac{\partial v}{\partial y}\right\}^n_{v_{i,k}} \simeq \frac{1}{4\Delta y}\left(v^n_{i_1,k} - v^n_{i_2,k}\right) \tag{3.57}$$

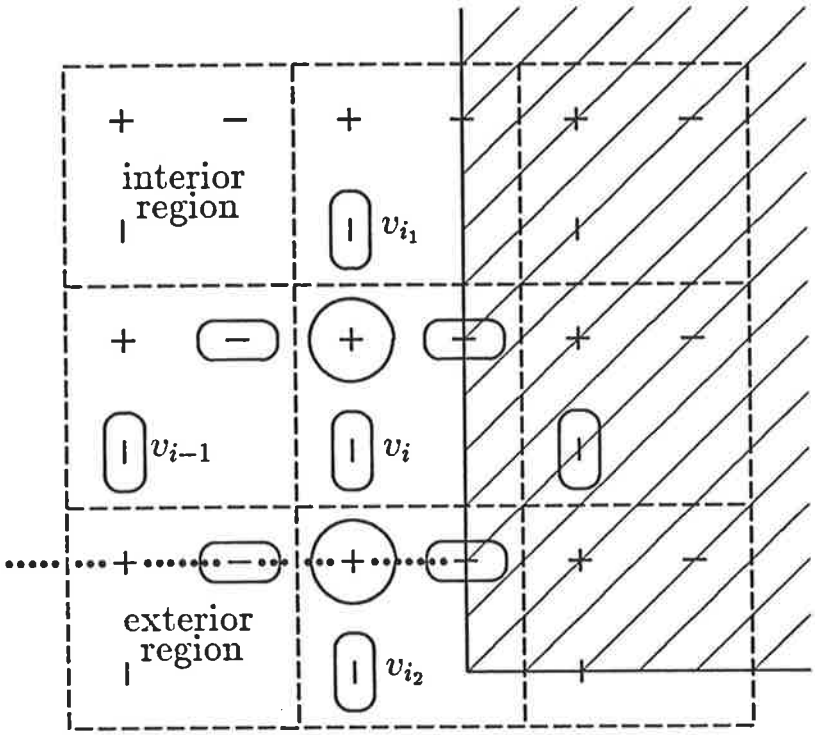


Figure 3.21: *Plan view of the v_i computational stencil at the junction of a coastal and open sea boundary.*

and clearly requires subordinate approximation for the $v^n_{i_2,k}$ value. As in the case of the y-advective term (3.45) applied at the u_i gridpoint of Figure 3.20, a linear extrapolation of the form (3.46) will lead to an unsuitable first order subordinate approximation, and it is not possible to find a spatially second order accurate expression for the gradient using the four available v values of the 9-element block. The y-advective term is therefore omitted from the v finite difference expression in this instance.

The expression for the second derivative of the y-diffusive term at the v_i gridpoint is:

$$\left\{\frac{\partial^2 v}{\partial y^2}\right\}^n_{v_{i,k}} \simeq \frac{1}{4(\Delta y)^2}\left(v^n_{i_1,k} - 2v^n_{i,k} + v^n_{i_2,k}\right). \tag{3.58}$$

Again, as in the case of the y-diffusive term (3.52) applied at the u_i gridpoint of Figure 3.20, linear extrapolation for $v^n_{i_2,k}$ yields a zero valued subordinate approximation, and it is not otherwise possible to find a spatially second order accurate subordinate approximation. The y-diffusive term is therefore also omitted in this instance.

The gradient part of the x-advective term at the v_i gridpoint is:

$$\left\{\frac{\partial v}{\partial x}\right\}^n_{v_{i,k}} \simeq \frac{1}{4\Delta x}\left(v^n_{i+1,k} - v^n_{i-1,k}\right). \tag{3.59}$$

The one-sided derivative approximation

$$\left\{\frac{\partial v}{\partial x}\right\}^n_{v_{i,k}} = \frac{1}{2\Delta x}\left(v^n_{i,k} - v^n_{i-1,k}\right) + O(\Delta x) \tag{3.60}$$

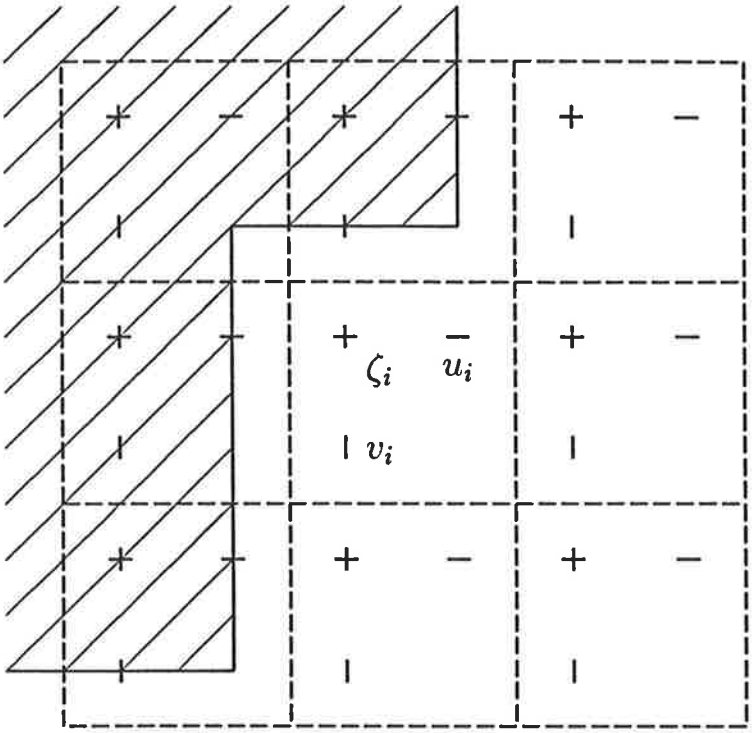


Figure 3.22: *Plan view of the ith computational element in the vicinity of a corner in the coastal boundary.*

is only first order accurate and hence unsuitable, and a second order accurate approximation is not available within the context of the 9-element block, so the term is omitted in this instance.

The expression for the second derivative of the x-diffusive term at the v_i gridpoint is:

$$\left\{\frac{\partial^2 v}{\partial x^2}\right\}^n_{v_{i,k}} \simeq \frac{1}{4(\Delta x)^2}\left(v^n_{i+1,k} - 2v^n_{i,k} + v^n_{i-1,k}\right). \tag{3.61}$$

Linear extrapolation for the value $v^n_{i+1,k}$ yields zero value for the approximation and once again, a second order accurate approximation is not available within the context of the 9-element block, so the term is omitted in this instance.

Care must also be exercised at gridpoints near purely coastal boundaries, particularly where there is a corner in the boundary such as in Figure 3.22.

Applying the u computational stencil at the u_i gridpoint, it is seen that all values required for computation are available — three of them $(u_{i_1}, v_{i_1}, u_{i-1})$ lie on the coastline and are assumed known precisely as zero values, by reason of the coastal boundary conditions.

Applying the v computational stencil at the v_i gridpoint, it can be seen that the x-wise advective and diffusive terms ought to be omitted. The y-advective and y-diffusive terms may be included if use is made of the prescribed boundary value $v^n_{i_1,k} = 0$.

There are so many different ways in which coastal and open sea boundaries can impinge on the neighbourhood of a computational u or v gridpoint that checking for these seems at first thought to be a huge task. However, it is possible to devise simple arithmetic switches that include/exclude the advective and diffusive terms in all appropriate cases, with or

without the use of IF statements. Basically, we only wish to exclude these terms when subordinate approximation for one or more of the referenced values in the expressions for the terms is necessary. Otherwise, these terms will be included in the overall numerical scheme.

Let's illustrate how automation of the program code is achieved for the advective and diffusive terms of the u momentum equation. We will assume a "0–1–2's" computational configuration. For a "1's" or "0–1's" computational configuration the program code is correspondingly simpler.

1. The program code for the gradient factor $\partial u/\partial x$ in the x-advective term is now

```
DuDx = (1-NC4TWO) * R4DX * (U(K,IP1) - U(K,IM1) - U2(K,IIM1))
```

   where NC4TWO=(1–(NC4/2)) and is zero only if NC4=2. All other program variable names in this expression have meaning as already defined. Comparing this expression with that on page 51 (part 3.) it can be seen that the subordinate approximation option for gridpoint u_{i+1} has been removed.

   The term is automatically deleted if NC4=2. In such a case the gridpoint u_{i+1} is either on an open boundary or lies outside the model basin; subordinate approximation within the 9-element block cannot provide a second order accurate approximation for this gradient so the term is omitted.

   If an open sea boundary passes through the ζ gridpoint of element $(i-1)$ the value $u^n_{i-1,k}$ will be found in list U2. At the same time the value of the index IM1 will be zero, thus effectively deleting the term U(K,IM1) from the expression.

   There are no other physically realistic ways in which a coastal and/or open sea boundary can lead to modification of the expression. Referring to the situation depicted in Figure 3.20 it can be verified that this term will be included in that case.

2. The program code for the gradient factor $\partial u/\partial y$ in the y-advective term is now

```
DuDy =   (1-NC23_both_0) * (1-NC65_both_0)
       * (1-NC23_both_2) * (1-NC65_both_2)
       * R4DY * (U(K,I1) + U2(K,II1) - U(K,I2) - U2(K,II2))
```

   where

where	DuDy	is the program variable name of the result
	NC23_both_0	is the program variable name of (1–((1+NC2)/2))*(1–((1+NC3)/2))
	NC65_both_0	is the program variable name of (1–((1+NC6)/2))*(1–((1+NC5)/2))
	NC23_both_2	is the program variable name of (NC2/2)*(NC3/2)
	NC65_both_2	is the program variable name of (NC6/2)*(NC5/2)
	R4DY	is the program variable name of $1/(4\Delta y)$

   The term is automatically deleted if either u_{i_1} or u_{i_2} or both lie over land, or over water outside the model, or on the open boundary. For example, if both NC2 and NC3 are zero then NC23_both_0=1: this corresponds to gridpoint u_{i_1} being over land — the term is deleted.

If an open boundary passes through element i_1 or i_2 in such a way as to leave the associated u value inside the model basin, then that value is taken from the U2 list.

This takes care of all physically realistic boundary cases. Again with reference to Figure 3.20, because NC6=NC5=2, this term will be omitted in that situation (because of the unavailability of the value u_{i_2}).

3. The program code for the x-diffusive term $\partial^2 u/\partial x^2$ is now

```
D2uDx2 = (1-NC4TWO)*R4DXS*(U(K,IP1)-2.0*U(K,I)+U(K,IM1)+U2(K,IIM1))
```

where D2uDx2 is a variable name for the result, R4DXS= $1/(4(\Delta x)^2)$ and the remaining variables are as before. The term is automatically deleted if NC4=2 since then the gridpoint u_{i+1} is either on an open sea boundary or outside the model basin. This term is programmed in a similar way to the gradient factor $\partial u/\partial x$ of the x-advective term. Referring to the situation of Figure 3.20, this term is retained in that case.

4. The program code for the y-diffusive term $\partial^2 u/\partial y^2$ is now

```
D2uDy2 =   (1-NC23_both_0) * (1-NC65_both_0)
         * (1-NC23_both_2) * (1-NC65_both_2)
         * R4DYS*(U(K,I1)+U2(K,II1)-2.0*U(K,I)+U(K,I2)+U2(K,II2))
```

where D2uDy2 is a variable name for the result, R4DYS= $1/(4(\Delta y)^2)$ and the remaining variables are as before. The discussion of the inclusion/exclusion of this term follows that concerning the gradient factor $\partial u/\partial y$ in the y-advective term above. For the situation depicted in Figure 3.20, this term is, of course, deleted.

Summarizing this section thus far, subordinate approximations of values in the finite difference expressions for the zeroth order derivative terms and factors seem valid. But subordinate approximation of values in the advective and the diffusive terms is only possible to first order accuracy using the resources of the 9-element block and therefore such terms should be discarded on the basis that it is better not to attempt to model a term when such attempts may corrupt the (more accurate) modelling of the remaining terms of the u, v equations. Wherever subordinate approximations of values in advective and diffusive terms is not required, even parallel to coastal and open sea boundaries, these terms are retained. The implementation of the coastal boundary condition in the way stated in Chapter 2 may not be realistic for modelling advective and diffusive terms whose values lie on the prescribed rectangular coastline.

Consider now the effects of total and selective inclusion of the advective and diffusive terms close to the coastal and open sea boundaries. Three numerical experiments are conducted. In each experiment the same one-month tidal simulation is carried out using the model that will be discussed in detail in Chapter 5. Averaged velocity residuals (in m/sec$\times 10^{-2}$) (see Section 5.5 for an explanation of how these residuals are determined) and averaged stream residuals (in m^2/sec) over a period of 29 days are obtained and plotted in Figures 3.23(a),(b),(c) and Figures 3.24(a),(b),(c), respectively. Because the residuals are based on an average over 29 days of predictions, the stream vectors of Figures 3.24 are obtained by multiplying the averaged velocity vectors of Figures 3.23 by the local

mean sea level depth values. The stream values represent the rate of volumetric flow at each gridpoint. The three graphs in each figure correspond respectively to the following strategies of inclusion of advective and diffusive terms near the coastal and open sea boundaries:

(a) Firstly, a simulation is conducted in which all advective and diffusive terms are retained, even if subordinate approximation renders their contribution to be only first order accurate. The average velocity residuals and average stream residuals resulting from this simulation are plotted in Figures 3.23(a) and 3.24(a).

(b) Secondly, a simulation is carried out in which all instances of first order subordinate approximation in advective and diffusive terms near the coastal and open sea boundaries are suppressed by omitting the respective terms at the corresponding computational elements. The velocity and stream residuals for this case are given in Figures 3.23(b) and 3.24(b).

(c) Thirdly, a simulation is conducted in which not only are advective and diffusive terms omitted when subordinate approximation yields first order accurate finite difference expressions, but also all advective and diffusive terms which use a coastal boundary value such as $u = 0$ and $v = 0$ are deleted. This does not lead to the deletion of all advective and diffusive terms at velocity points adjacent to the coastal and open sea boundaries since many of them have a gradient parallel to the boundary line and hence may be included if each of the values in their finite difference expressions lies over water within the model basin. The resultant velocity and stream residuals are given in Figures 3.23(c) and 3.24(c).

Figure 3.23(a) clearly shows the "noisiest" velocity residual pattern of Figures 3.23 — many of the residuals at the open boundary seem physically unrealistic. This shows up more clearly by looking at the streams, i.e. at Figure 3.24(a). Defining north to be up the page, there is a strong "NNW" directed velocity residual vector emanating from the bottom right hand corner of Figure 3.23(a). This vector arises from first order approximation of the derivative factor of the y-advective term of the v equation, viz. the use of an approximation such as (3.47) applied at the v_i gridpoint of Figure 3.21. Although harder to detect, a similar residual vector can be seen to the left of Thistle Island (see Figure 1.1) in a similar relative location. These vectors also show up in the stream plot, but are not as noticeable because of the presence of larger stream residuals in the vicinity of the open boundary.

Also in Figure 3.23(a), halfway northwards and alongside the western boundary where the coastline is very "stepped", there are a series of grid-scale clockwise rotating gyres; these can be seen in Figures 3.24(a) as well. This also seems an unrealistic phenomenon and to be a consequence of the interplay between the numerical scheme and the stepping in the coastal boundary. Note the presence of a series of strongly onshore directed and strongly offshore directed residual vectors along this portion of the model coastline.

Figure 3.23(b) shows immediate settling down and a more controlled and physically realistic set of velocity residuals. The corresponding stream plot of Figure 3.24(b) likewise shows a more controlled and realistic pattern. The spuriously large and seemingly randomly directed vectors across the open boundary of Figures 3.23(a) and 3.24(a) have been replaced by an orderly outward flow across the open boundary in the centre. The large vectors emanating from the two aforementioned junctions of the open sea boundary and

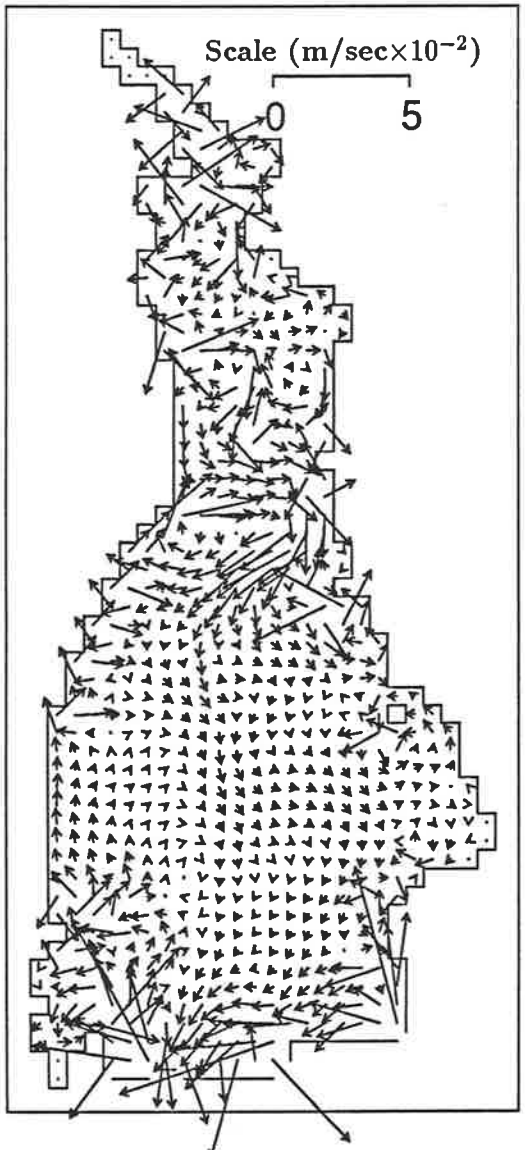


Figure 3.23(a): *Residuals for depth-averaged velocity generated by the numerical scheme outlined in the text as option (a).*

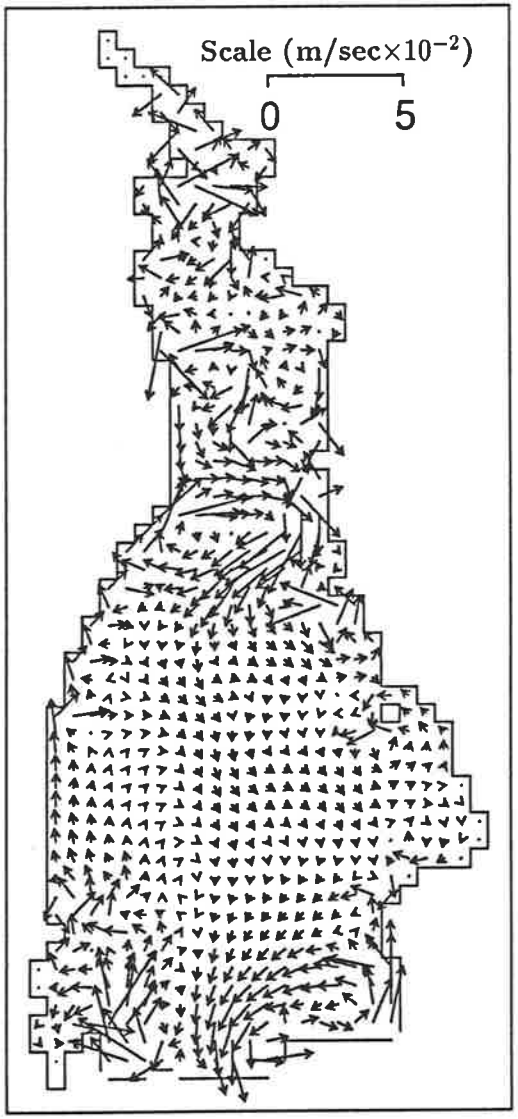


Figure 3.23(b): *Residuals for depth-averaged velocity generated by the numerical scheme outlined in the text as option (b).*

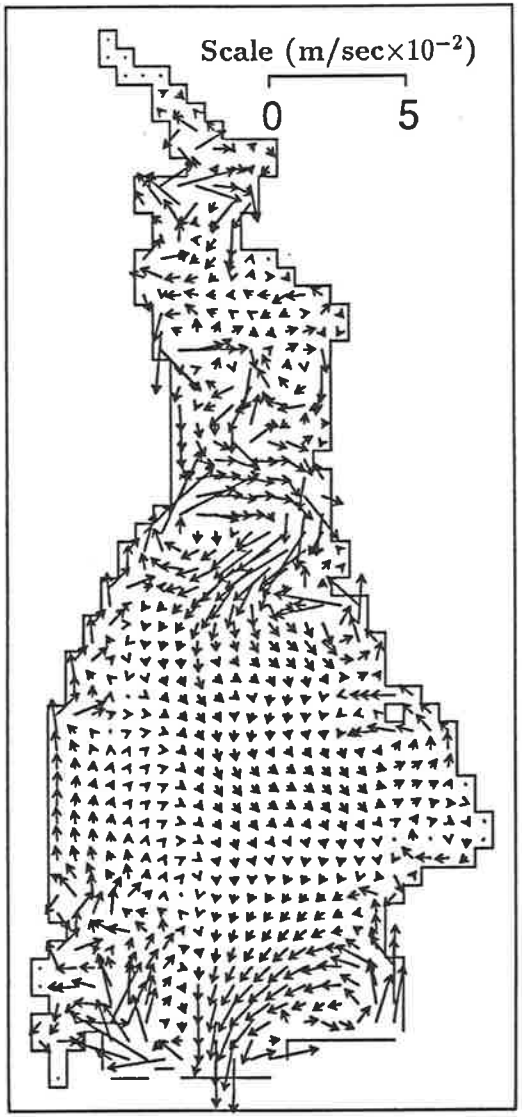


Figure 3.23(c): *Residuals for depth-averaged velocity generated by the numerical scheme outlined in the text as option (c).*

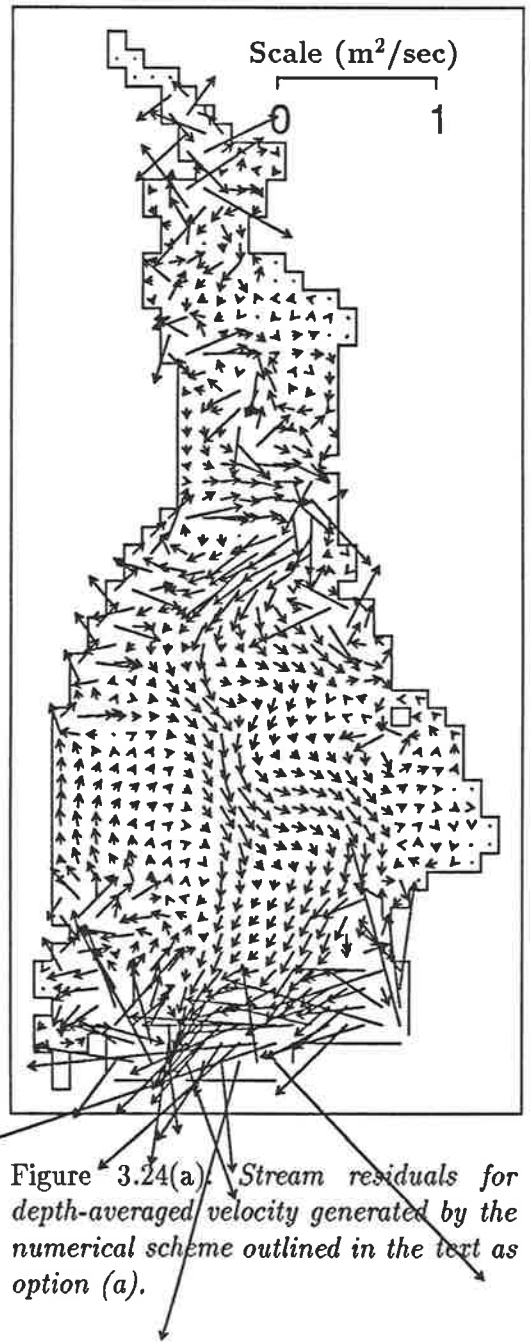


Figure 3.24(a): *Stream residuals for depth-averaged velocity generated by the numerical scheme outlined in the text as option (a).*

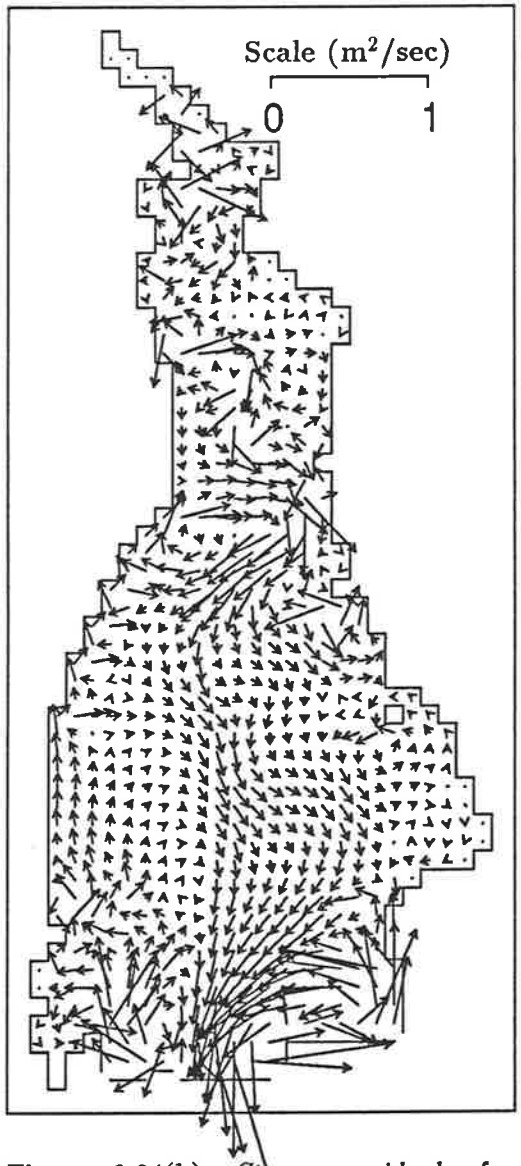


Figure 3.24(b): *Stream residuals for depth-averaged velocity generated by the numerical scheme outlined in the text as option (b).*

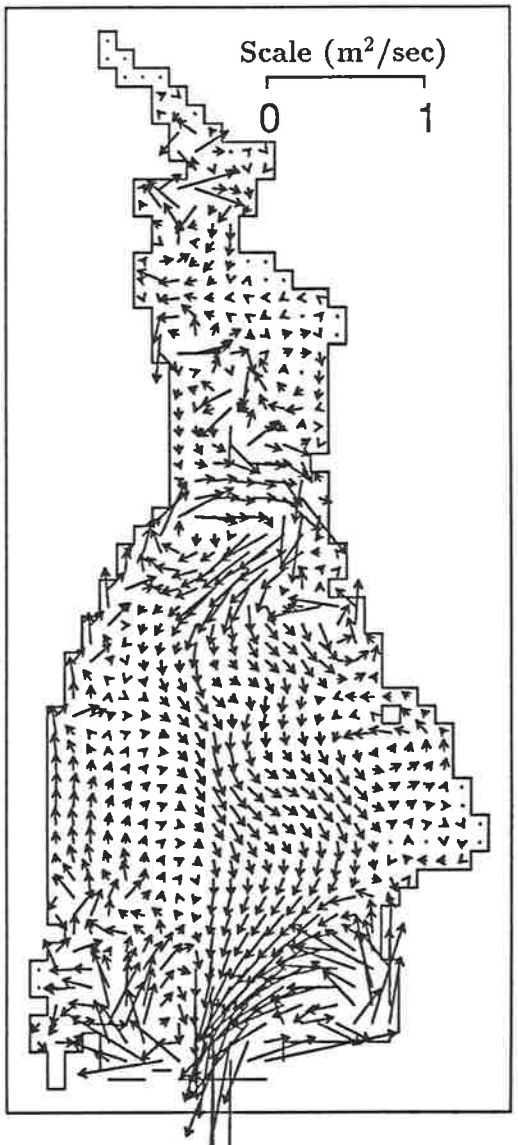


Figure 3.24(c): *Stream residuals for depth-averaged velocity generated by the numerical scheme outlined in the text as option (c).*

coastal boundary no longer exist, and flow along the western coastline past the steps in the boundary has settled down, but there is still evidence of the presence of model/scheme generated grid-scale gyres there.

Figures 3.23(c) and 3.24(c) are even smoother in their residual flow patterns. There are no grid-scale gyres along the stepped region of the western coastal boundary and flow along that coastline looks even smoother than that in Figures 3.23(b) and 3.24(b). There is now very little westerly directed component in the residual vectors in this region.

The absence of gyres adjacent to the stepped boundary of the western coastline is clearly linked to the absence of the implementation of the u=0, v=0 interpretation of the coastal boundary condition in the advective and diffusive terms. One therefore cannot suppose that it should be numerically reasonable to find gyres there because of the stepped nature of the coastline. Rather, the presence or absence of gyres in this region is a consequence of the particular numerical scheme used. Since there is no known report of the existence of such gyres, it makes sense to choose the numerical scheme (from options (a),(b) or (c)) that most suppresses them, i.e. that is least likely to give rise to their numerical creation. It may be that some other numerical scheme will achieve improved results — for example, a scheme arising out of an examination of the implementation of the Coriolis finite difference forms at coastal and open sea boundaries in conjunction with the present advective/diffusive measures — but a more thorough investigation of this phenomenon is outside the scope of this thesis.

There are other gyral events which are common to all three numerical options. These, being independent of the choice of option, and also being larger than grid scale, seem to be associated with real gyral events. They will be discussed fully in subsequent chapters. Briefly, there is a large clockwise rotating gyre at the entrance to the narrowing part of the Gulf, as one goes northward, opposite Wallaroo (Figure 1.1) — there is a smaller gyre of opposite direction of rotation south-east of it along the coastline (see Chapter 5). As well, there are gyres to the south and north of Lowly Point (Figures 1.1 and 1.2) (see Chapter 8).

The program code modifications required to implement option (c), which may be compared to those already outlined for implementing option (b), are the following if again a "0–1–2's" computational configuration is assumed and the advective and diffusive terms of the u equation are considered:

1. The gradient factor $\partial u/\partial x$ in the x-advective term may now be coded as

```
DuDx =   ((NC8+1)/2) * ((NC15+1)/2) * (1-NC4TWO)
       * R4DX * (U(K,IP1) - U(K,IM1) - U2(K,IIM1))
```

   This expression should be compared with the corresponding option (a) differencing on page 51 and option (b) differencing on page 61. If NC8=0 or NC15=0, or both, then one or both of the gridpoints u_{i-1} and u_{i+1} lie on coastlines and so the term is deleted, by option (c). If NC8 is 1 or 2 then the integer expression ((NC8+1)/2) returns the value 1; similarly for NC15.

   If NC4=2 a subordinate approximation for u_{i+1} is needed, but cannot be supplied, so again the term is deleted.

   A computationally more efficient program code for this term using IF statements is:

```
IF (NC8*NC15*(1-NC4TWO) .Eq. 0) THEN
  DuDx = 0.0
ELSE
  DuDx = R4DX * (U(K,IP1) - U(K,IM1) - U2(K,IIM1))
ENDIF
```

The computational saving here is in the fact that there are two less divisions to carry out, two fewer additions and if the product of integer codes is zero, there is an additional saving of two multiplications, two subtractions and three list look-ups.

2. The gradient factor $\partial u/\partial y$ in the y-advective term may now be coded as

```
DuDy =   ((NC2+1)/2) * ((NC3+1)/2) * ((NC6+1)/2) * ((NC5+1)/2)
       * (1-NC23_both_2) * (1-NC65_both_2)
       * R4DY * (U(K,I1) + U2(K,II1) - U(K,I2) - U2(K,II2))
```

where if any one of NC2,NC3,NC6,NC5 is zero, then one or both of u_{i_1} and u_{i_2} lie on a coastline so the term is deleted. If an open boundary places either of u_{i_1} or u_{i_2} outside the model, subordinate approximation is required and since it cannot provide second order accuracy within the 9-element block, the term is deleted — this is effected by the factors (1-NC23_both_2) and (1-NC65_both_2).

A computationally more efficient program code for this term is:

```
IF (NC2*NC3*NC6*NC5*(1-NC23_both_2)*(1-NC65_both_2) .Eq. 0) THEN
  DuDy = 0.0
ELSE
  DuDy = R4DY * (U(K,I1) + U2(K,II1) - U(K,I2) - U2(K,II2))
ENDIF
```

3. The program code for the x-diffusive term $\partial^2 u/\partial x^2$ may now be coded as

```
D2uDx2 =   ((NC8+1)/2) * ((NC15+1)/2) * (1-NC4TWO)
         * R4DXS * (U(K,IP1) - 2.0*U(K,I) + U(K,IM1) + U2(K,IIM1))
```

As for the advective term discussed above, the term is automatically deleted if either NC8=0 or NC15=0, or if NC4=2.

A more efficient program code for this term is:

```
IF (NC8*NC15*(1-NC4TWO) .Eq. 0) THEN
  D2uDx2 = 0.0
ELSE
  D2uDx2 = R4DXS * (U(K,IP1) - 2.0*U(K,I) + U(K,IM1) + U2(K,IIM1))
ENDIF
```

4. The program code for the y-diffusive term $\partial^2 u/\partial y^2$ may now be coded as

```
D2uDy2 =   ((NC2+1)/2) * ((NC3+1)/2) * ((NC6+1)/2) * ((NC5+1)/2)
         * (1-NC23_both_2) * (1-NC65_both_2)
         * R4DYS*(U(K,I1)+U2(K,II1)-2.0*U(K,I)+U(K,I2)+U2(K,II2))
```

and again, as for the y-advective term discussed above, the term is deleted if any of NC2,NC3,NC6,NC5 is zero, since then either one of the velocity component values is on a coastline or lies over land requiring a subordinate approximation; the term is likewise deleted if an open sea boundary places u_{i_1} or u_{i_2} on or outside the boundary and hence requiring subordinate approximation.

A more efficient program code for this term is:

```
IF (NC2*NC3*NC6*NC5*(1-NC23_both_2)*(1-NC65_both_2) .Eq. 0) THEN
  D2uDy2 = 0.0
ELSE
  D2uDy2 = R4DYS*(U(K,I1)+U2(K,II1)-2.0*U(K,I)+U(K,I2)+U2(K,II2))
ENDIF
```

On the basis of the apparent fact that the scheme used to generate Figures 3.23(c) and 3.24(c) produces a smoother and seemingly more realistic residual flow field, the option (c) numerical scheme has been adopted throughout this thesis, for both two and three-dimensional models of Spencer Gulf, and also in the tidal flat modelling of Chapter 8.

Some authors do not include the horizontal diffusive terms in the momentum equations for tidal flow (e.g. Leendertse, 1967). For whatever reasons this is done, the problems of approximation of these terms near boundaries as discussed above are avoided. Since the significance of these terms is at best slight in shallow seas relative to other more dominant effects, this may be of small consequence.

For the advective terms, Leendertse (1967) in a detailed description of his computational method, seems to adopt the same approach as used here: "if the spatial derivative in the convective-inertia terms cannot be computed, the linear approximation results in omitting these terms. The use of non-central spatial derivatives ... (extrapolation from the interior field) is not feasible for reasons of instability" (ibid., p.67). That is, he omits the advective term if one of the values in the finite difference expression for the gradient lies outside the available field of values because subordinate approximations like (3.47) and (3.60) lead to instability in his model.

Flather and Heaps (1975) are interested in accurately representing the wetting and drying of tidal flats and "Since the non-linear advective acceleration should be important in shallow water, schemes for incorporating these terms are examined" (ibid., p.489). They find that "since not all values of current needed ... at flow points adjacent to open-sea boundaries are defined, it is necessary to omit the advective schemes within a distance s [one element] of these boundaries" (ibid., p.499). Even so, grid scale oscillations were observed to originate from a corner in the open boundary, so they decided upon a strategy of "Leaving out the advective accelerations within $3s$ [3 elements] of the boundary, so that the treatment of advection and of open-sea boundaries are decoupled, [removing] the instability" (ibid., p.499). Such decoupling has *not* been necessary in the present work.

They continue: "Although this omission is less than ideal, it is perhaps more acceptable than restrictions imposed by some other schemes: for example, Leendertse (1967) excludes advective accelerations within a distance s of *land* boundaries, where the water is likely to be shallow and therefore, according to dimensional analysis non-linear terms important" (ibid., p.499). Flather and Heaps seem to have misinterpreted Leendertse on this point — Leendertse only omits advective terms within a distance s of land boundaries if not all values of the approximations are available. For the advective term at the same flow

point for which all values of the approximations are available (e.g. the advective gradient is parallel to the coastline), the term is retained by Leendertse.

Greenberg (1983) acknowledges that "the practical problem of stability has required that ... the advective terms not be included in the momentum equations at all points adjacent to this [open] boundary" (ibid., p.900). In the present work, the only advective terms excluded in the momentum equations at points adjacent to the open boundary are those whose gradients are normal to it.

Black (1987) says: "One of the most important generators of instability in the explicit scheme model is a poor representation of the convective momentum terms near land/sea boundaries, particularly where adjacent currents are fast, such as in an estuary entrance gorge". "Poor treatment of these terms results in an instability called 'zig-zagging' " (ibid., p.6). When using central difference expressions such as (3.10) and (3.11), "the finite difference approximation becomes excessively large when one of the two nodes is on land (then $U = 0$) and the other is in fast current flows". "The simplest prevention identified was to offset the derivative forward or backward so that the $U = 0$ term on land is not included" (ibid., p.7). This approach is not favoured in the present work because even if, as Black reports, this smooths the instantaneous velocity field, it introduces first order errors which may show up as unrealistic residual vectors (possibly even gyres) over a long simulation. Indeed Black concedes that "on the very shallow intertidal zones, offset derivatives caused instability that often led to the collapse of the numerical solution" (ibid., p.7).

The fact that the above authors have explicitly stated their problems with advective terms near boundaries is to be applauded, since it is the basis upon which some clarification of the matter has more easily proceeded.

As an historical note, this section of work was initially motivated by an investigation of what seemed an unrealistically large residual velocity vector at the gridpoint in the south-eastern corner of the Spencer Gulf model of Chapter 5 near the junction of the open sea and coastal boundary (specifically, gridpoint v_i of Figure 3.21). The residual plot first produced was that of Figure 3.23(a). Concern that something was amiss seemed justified as another similarly large and also seemingly unrealistic residual vector was noticed in a numerically similar position at the junction of the open sea and coastal boundary to the left of Thistle Island in the same figure. Furthermore, in some simulations in which steady winds were blown across the model from the south and the SSE, both these residual vectors grew disproportionately large relative to the rest of the residual vector field.

The option (c) differencing, whose effect is displayed in Figures 3.23(c) and 3.24(c), seems satisfactory in providing a residual circulation that is relatively smooth and physically realistic.

3.7 Summary

The method of automatic program code modification outlined in Section 3.5 is based on the plan layout of element codes. It is therefore as easy to use in three-dimensional applications as in two-dimensional applications.

The method allows models of sea regions to be constructed quickly, since it only requires the accurate specification of the codes "0", "1" and "2" to all elements of the study region. The appropriate forms of the finite difference equations to be applied at each computational gridpoint within the model region are then automatically generated by the program. With

the adoption of strategy (c) of the last section, the use of code "4" is relegated to only presentational importance, distinguishing water elements outside the model from those inside. It's use could be replaced by the alternative use of code "0" — which would then be defined as the code for both land elements and outside water elements.

The advective and diffusive gradients of the u and v equations are differenced across a two-element span and in that sense are the most precarious finite difference approximations of the numerical scheme — all other gradients in these equations are performed across the span of a single element. It is therefore not surprising that for optimal performance these difference approximations should be used in optimal conditions, free from any need to use subordinate approximation or assumption in providing the values required by their finite difference expression. If these conditions are not present it is better to delete the terms, as necessary, in order to prevent contamination of the solution field.

The present numerical scheme has been used for three-dimensional models of the Gulf of Carpentaria (by Mitchell et al., 1984) and Bass Strait (Arnold and Noye, 1986b) as well as the present depth-averaged and three-dimensional models of Spencer Gulf.

In the next chapter tests carried out on the major components of the numerical scheme are reported. These were useful in establishing the finite difference approximations used, and were essential in verifying that the automatic method of program code modification works.

Chapter 4

Analytical and numerical verification of program code

4.1 Introduction

In this work it is assumed that the physical characteristics of tidal motion in sea water are adequately modelled by the mathematical equations described in Chapter 2. No attempt is made to modify the equations except in the case of the modelling of tidal flats (see Chapter 8).

In this chapter an assessment of the accuracy and stability of the finite difference expressions given in Chapter 3 is presented. In the case of non-linear terms, the selection of the most accurate finite difference approximations is often not immediately clear, so a set of likely formulations is considered in order to give some justification for the choices made in Chapter 3.

It may be noted that while the equations of Chapter 2 are non-linear, the finite difference expressions used to approximate them are locally linear. Within sufficiently small neighbourhoods, in both time and space, such linear finite difference analogues prove to be accurate approximations to the non-linear mathematical equations. In Chapter 5, for the depth-averaged Spencer Gulf model, we will see that the non-linear formulation produces lower calibration errors than does the linear formulation, and the circulation patterns produced are physically realistic.

One way to assess the accuracy and stability of a given finite difference formulation of the given equations and to verify the corresponding program code is to compare numerical and analytical solutions for flow in estuaries of simple geometry. Both the numerical and analytical solutions must be solutions of the same (generally simplified) set of partial differential equations. Another approach is to analytically examine the wave propagation characteristics of the finite difference scheme, but this is possible only in the case of linear systems of differential equations. An advantage of the former approach over the latter is that the former includes boundary effects — both at the coast and the open boundary — while the latter does not. However, it is possible to examine the propagation characteristics of a boundary difference scheme, although not in conjunction with the corresponding interior scheme. Both approaches are used in this chapter.

Some of this work was originally presented in a progress report to the author's scholarship disbursing body (Bills, 1982). Some basic tests were reported in a conference paper

by Bills and Noye (1984), and were further developed in papers by Jung, Bills and Noye (1986) and Jung, Bills, Stevens and Noye (1987).

4.2 Lynch and Gray 1D linear solutions

Lynch and Gray (1978) provide several analytical solutions of the equations

$$\frac{\partial \zeta}{\partial t} = -\frac{\partial (hU)}{\partial x}, \tag{4.1}$$

$$\frac{\partial U}{\partial t} = -g\frac{\partial \zeta}{\partial x} - \tau U, \tag{4.2}$$

for one-dimensional estuaries with depth profiles described by $h(x) = h_p x^p$, where h_p and p are constants. The estuaries are closed at one end and open at the other to external tidal forcing. In (4.2), τ is a constant linear friction coefficient with units $\sec^{-1}$; more usually, the linear friction coefficient is written k ($= \tau h_0$, implicitly) with units m/sec (e.g. see Section 4.4 and expression (5.15) in the next chapter) and the friction term explicitly consists of an averaging over depth. The remaining variables are as defined in Chapter 2.

4.2.1 Case 1: Estuary with constant depth

If the estuary has constant depth $h = h_0$, one set of solutions of equations (4.1)–(4.2) is (Lynch and Gray, 1978, p.1422):

$$\zeta = \Re e\left\{\zeta_0 \frac{\cos[\beta(x - x_1)]}{\cos[\beta(x_2 - x_1)]}\, e^{\imath\sigma t}\right\}, \tag{4.3}$$

$$U = \Re e\left\{\frac{-\imath\sigma\zeta_0}{\beta h_0}\frac{\sin[\beta(x - x_1)]}{\cos[\beta(x_2 - x_1)]}\, e^{\imath\sigma t}\right\}, \tag{4.4}$$

where the head of the estuary is at $x = x_1$ and the open boundary is set at $x = x_2$ as shown in Figure 4.1. In (4.3)–(4.4), ζ_0 is the real amplitude of tidal forcing at the open boundary,

$$\beta = [(\sigma^2 - \imath\sigma\tau)/(gh_0)]^{1/2} \tag{4.5}$$

is the complex wavenumber with units m^{-1}, σ is the angular frequency of forcing and $\imath = \sqrt{-1}$.

From equation (4.3) it can be seen that tidal forcing at the open boundary is described in terms of the oscillation at the boundary as

$$\zeta(t) = \Re e\left\{\zeta_0 e^{\imath\sigma t}\right\} = \zeta_0 \cos\sigma t. \tag{4.6}$$

A sum of four components of this form, with appropriate phase shifting, is used to specify the forcing at the open boundaries of the Spencer Gulf models of Chapters 5 and 8, and is commonly known as a "height specified" open boundary condition.

Solving equations (4.1)–(4.2) numerically and comparing the results with the solutions (4.3)–(4.4) is a simple basic test of both the differencing used for some of the major terms in the equations of Chapter 2 and the computer code used to solve the corresponding finite difference expressions. By orienting the estuary so that the open boundary faces toward the

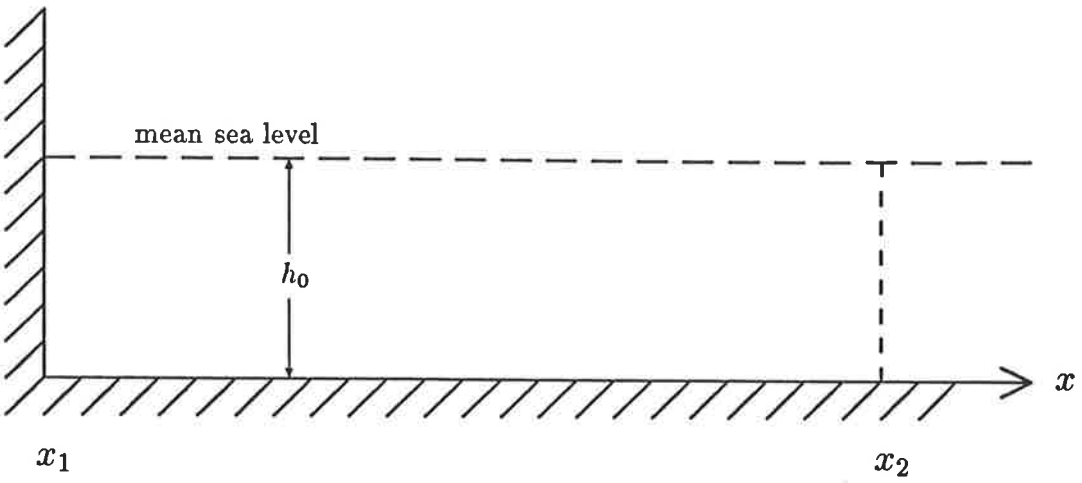


Figure 4.1: *Diagram illustrating the notation used to describe the constant depth ($h = h_0$) Lynch and Gray estuary. The head of the estuary is at $x = x_1$ and the open boundary is at $x = x_2$.*

positive-y (or "north"), negative-y ("south"), positive-x ("east") and negative-x ("west") directions, the use of the element classification scheme of Section 3.5 in the program code can also be tested. One expects identical results from the numerical simulations regardless of estuary orientation, if the program code is correct.

The finite difference scheme for the system (4.1)–(4.2), based on the differencing given in Chapter 3, is presented in the following computational procedure:

1. Input model data and set initial values. Time $t = n\Delta t = 0$.

2. Update model time to level $(n+1/2)$. Time $t = (n + 1/2)\Delta t$.
   Input the open boundary elevation specification at time level $(n + 1/2)$.
   Calculate elevation field $\zeta^{n+1/2}$ using

$$\frac{\zeta_i^{n+\frac{1}{2}} - \zeta_i^{n-\frac{1}{2}}}{\Delta t} = -h_0 \left(\frac{U_i^n - U_{i-1}^n}{2\Delta x} \right). \tag{4.7}$$

3. Update model time to level $(n + 1)$. Time $t = (n + 1)\Delta t$.
   Calculate depth-averaged velocity field U^{n+1} using

$$\frac{U_i^{n+1} - U_i^n}{\Delta t} = -g \left(\frac{\zeta_{i+1}^{n+\frac{1}{2}} - \zeta_i^{n+\frac{1}{2}}}{2\Delta x} \right) - \frac{\tau}{2} \left(U_i^{n+1} + U_i^n \right). \tag{4.8}$$

4. Input the open boundary elevation specification at time level $(n + 1)$.
   Calculate elevation field ζ^{n+1} using

$$\frac{\zeta_i^{n+1} - \zeta_i^n}{\Delta t} = -\frac{h_0}{2\Delta x} \left(\frac{1}{2} \left[U_i^{n+1} + U_i^n \right] - \frac{1}{2} \left[U_{i-1}^{n+1} + U_{i-1}^n \right] \right). \tag{4.9}$$

5. Return to Step 2 and repeat until the simulation is completed.

Although the second elevation calculation (4.9) is not needed for the numerical solution of equations (4.1)–(4.2), it is included to give elevation results for the same time levels as the velocity results. In so doing, the accuracy of the second elevation calculation is tested.

The accuracy of the overall finite difference scheme (4.7)–(4.9) can be checked by either a series of numerical tests using parameters representative of the region being studied, or by a mathematical investigation of the wave propagation characteristics of the scheme.

4.2.2 Case 1: Numerical tests

In order to test the performance of the numerical simulation for a range of parameters, it is convenient to non-dimensionalize equations (4.1) and (4.2) by introducing the dimensionless variables

$$x^* = x/L, \quad t^* = t/T, \quad \zeta^* = \zeta/\zeta_0 \text{ and } U^* = U/U_0, \tag{4.10}$$

where $L = x_2 - x_1$ is the length of the estuary, $T = 2\pi/\sigma$ is the period of oscillation and $U_0 = g\zeta_0 T/L$ is a characteristic value of horizontal velocity.

With these changes of variable, equations (4.1) and (4.2) become

$$\frac{\partial \zeta^*}{\partial t^*} = -\alpha_0^2 \frac{\partial U^*}{\partial x^*}, \tag{4.11}$$

$$\frac{\partial U^*}{\partial t^*} = -\frac{\partial \zeta^*}{\partial x^*} - KU^*, \tag{4.12}$$

where $\alpha_0 = T\sqrt{gh_0}/L$ is the ratio of constituent wavelength to estuary length and $K = \tau T$ is a friction number that depends on the period of the tidal constituent, i.e. it is a "constituent friction number". The dimensionless numbers α_0 and K, together with ζ_0/h_0 (the ratio of amplitude of oscillation to mean depth), summarize the main features of the (bounded) physical problem.

Introducing the numerical parameters

$$N_\lambda = \frac{\lambda}{2\Delta x} = \text{number of grid spacings in a wavelength } \lambda, \text{ and} \tag{4.13}$$

$$N_L = \frac{L}{2\Delta x} = \text{number of grid spacings in the length } L, \tag{4.14}$$

an alternative expression for α_0 is

$$\alpha_0 = \frac{T\sqrt{gh_0}}{L} = \frac{\lambda}{L} = \left(\frac{\lambda}{2\Delta x}\right) \Big/ \left(\frac{L}{2\Delta x}\right) = \frac{N_\lambda}{N_L}. \tag{4.15}$$

Since N_L is the number of grid elements between a u gridpoint at the head of the estuary and a ζ gridpoint at the open boundary, it is always an integer and a half, i.e.,

$$N_L = NL1 + 0.5, \tag{4.16}$$

where $NL1$ is the number of Type 1 elements used in the given one-dimensional model.

The dimensionless numbers N_λ, N_L and the Courant number C_x, where

$$C_x = \frac{\Delta t\sqrt{gh_0}}{2\Delta x}, \tag{4.17}$$

summarize the main features of numerical solution of the present problem. The Courant number can be interpreted as the ratio of the distance travelled by the wave in one time step to the length of the grid element used.

In Chapter 5 a coarse-grid depth-averaged model of Spencer Gulf (denoted "SG") is described. Numerical tests using parameters representative of this model are now considered.

The average depth of the SG model is about 25 m. The length of the model Gulf along its axis is $L = 340042.5$ m and it is made up of $N_L = 59.5$ grid elements of dimension $2\Delta x = 5715$ m. Using a semi-diurnal period of 12 hr, this suggests that a value of α_0 representative of the SG model for this wave is about 2. If the value of h_0 is taken as

$$h_0 = \frac{1}{g}\left(2 \times \frac{340042.5}{43200}\right)^2 \simeq 25.3\,\text{m}, \tag{4.18}$$

the formulation being based on a rearrangement of the definition for α_0, then $\alpha_0 = 2.0$, leading to the simple relationship

$$N_\lambda = 2N_L \tag{4.19}$$

for a semi-diurnal tidal constituent.

By using one-dimensional models with different values N_L for the number of grid spacings in the length, error curves for a selection of values of Courant number may be plotted against the parameter N_λ for fixed values of α_0 and K.

The error measure used, for either dimensionless elevation ζ^* or dimensionless depth-averaged velocity U^* is a relative percentage error based on the quotient of the average absolute difference between analytical and numerical solutions over one cycle of oscillation, and the characteristic value (ζ_0 or U_0) of the variable for the particular test. For example, the error measure used for the dimensionless elevation ζ^* is

$$\varepsilon^*_\zeta = 100\frac{(1/\zeta_0)}{N_T NL1}\sum_{n=1}^{N_T}\sum_{i=1}^{NL1}|a_i^n - \zeta_i^n|\ \%, \tag{4.20}$$

where

- ε^*_ζ is the dimensionless elevation error expressed as a percentage,
- ζ_0 is the characteristic value of the elevation ζ, viz. the forcing amplitude,
- $NL1$ is the number of spatial sampling positions along the model estuary and is the number of Type 1 elements used in the model,
- N_T is the number of time steps in a period (an integer in these tests),
- a_i^n is the analytical solution for elevation at position i, time level n,
- ζ_i^n is the numerical solution for elevation at position i, time level n.

The use of ζ_0 as a normalizing value in (4.20) follows from the definition of ζ^* and has the effect of removing the influence of ζ_0 from the error plots in the (linear) numerical tests. An alternative expression for ε^*_ζ might use, as the normalizing factor, the maximum absolute analytical value taken from the set of spatial and temporal gridpoints during a cycle of oscillation within the estuary, but this value varies from model to model since each uses a different set of gridpoints; the variation is greatest for small $NL1$ when there are few spatial and temporal gridpoints modelling the cycle of oscillation.

All tests are commenced with a "cold" start (elevation and velocity values initially set to zero) and error values are calculated for each tidal cycle. The presented errors are those obtained when the difference between values of ε_ζ^* from one cycle to the next is less than or equal to 10^{-7} m. For tests with the semi-diurnal constituent, this occurs at about the 15th cycle of oscillation using Double Precision in VAX Fortran.

It is important that N_T be an integer. Given that Δt is fixed for a given numerical test, an integer value for N_T ensures that values of the same analytical and numerical fields are compared from one cycle to the next. For a given Courant number C_x the value of the time step Δt is obtained from

$$\Delta t = 2\Delta x\, C_x \frac{1}{\sqrt{g h_0}} = \frac{C_x T}{N_\lambda}. \tag{4.21}$$

Therefore,

$$N_T = \frac{T}{\Delta t} = \frac{\alpha_0 N_L}{C_x} = \frac{N_\lambda}{C_x}. \tag{4.22}$$

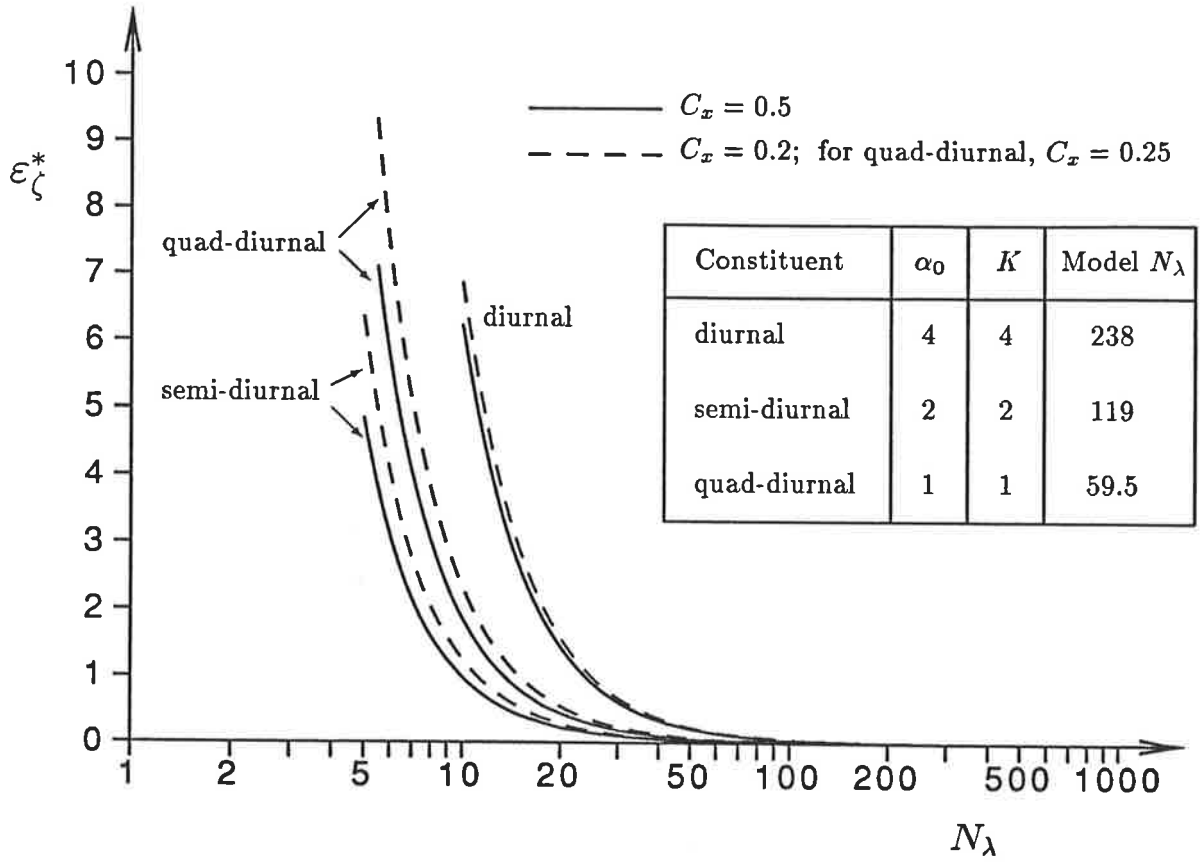
Since $N_L = NL1 + 0.5$ and $\alpha_0 = 2.0$ (for the semi-diurnal SG tests), N_T is an integer for $C_x = 0.2$ and $C_x = 0.5$. The average value of C_x for the depth-averaged Spencer Gulf model of Chapter 5 is about $C_x = 0.3$, so generating results for $C_x = 0.2$ and $C_x = 0.5$ covers a range of operating values — the actual value in the SG model varies from gridpoint to gridpoint depending on local depth.

Figure 4.2 shows plots of ε_ζ^* versus N_λ for SG model tests using diurnal (24 hr), semi-diurnal (12 hr) and quad-diurnal (6 hr) constituents. Because the error in ζ^* is found to be generally more than or about the same as the error in U^*, only the former error values are plotted. (This arises because of the particular definition of error measure used. In calculating ε_ζ^* we divide through by ζ_0 whose value is set at 0.75 m for each constituent in these tests; to calculate a similarly defined error measure ε_U^* we would divide through by $U_0 = (g\zeta_0 T/L)$ which is 1.87 m/sec for the diurnal constituent, 0.93 m/sec for the semi-diurnal constituent and 0.47 m/sec for the quad-diurnal constituent in these tests. In dimensional terms, it is observed that generally $\varepsilon_U \simeq 1.3\varepsilon_\zeta$ in the case of each constituent test.) As well, since N_L takes integer and a half values, only discrete points of the ε_ζ^*–N_λ graphs can be generated, so the curves have been completed by interpolation. Each curve represents a significant computational effort since for each value of N_L used, a model of the estuary using a different number of gridpoints is required to perform the simulations.

The figure is accompanied by a table of values of α_0 and K for each constituent and the corresponding operating values of N_λ as used in the SG model, based on $N_L = 59.5$. The value used for K in each case gives the same value for τh_0 ($\simeq 0.0012$ m/sec) (see expression (5.15)).

The linear Spencer Gulf model of Chapter 5 is driven by the four major constituents O_1, K_1, M_2 and S_2, so the calibrated friction coefficient used in that model is a model average of the constituent friction coefficients. The value of τh_0 used here is approximately that value. Of course, the use of several constituents to drive a tidal model leads naturally to the use of the non-linear tidal equations, given the potential for generation of other constituents by reason of constituent interaction — that is the major emphasis of Chapter 5.

In practice, the O_1 and K_1 constituents have about the same amplitude and together account for about half the tidal energy at the mouth of the Gulf; similarly, M_2 and S_2 are approximately equal and account for the other half. The combined amplitude of the



Constituent	α_0	K	Model N_λ
diurnal	4	4	238
semi-diurnal	2	2	119
quad-diurnal	1	1	59.5

Figure 4.2: *Percentage error in dimensionless elevation ε^*_ζ versus number of grid spacings per wavelength N_λ for fixed depth one-dimensional Spencer Gulf model tests using diurnal, semi-diurnal and quad-diurnal tidal constituents. The table shows the values used for α_0 and K for each constituent, along with the corresponding operating values of N_λ based on $N_L = 59.5$ for the Spencer Gulf model of Chapter 5. For each wave the input amplitude is 0.75 m. Runs using two values of Courant number C_x are made. At the given model values for N_λ, error values are very low for each constituent considered (see text).*

quad-diurnal constituents at the mouth of the Gulf is less than 2% of the total. The value $C_x = 0.25$ is used for the quad-diurnal wave instead of $C_x = 0.2$ because the former gives an integer value for N_T while the latter does not.

At the operating model values of N_λ for these constituents, the percentage errors ε^*_ζ to two decimal places are:

(1) diurnal (N_λ=238) — at C_x=0.5, ε^*_ζ=0.01%; at C_x=0.2, ε^*_ζ=0.01%

(2) semi-diurnal (N_λ=119) — at C_x=0.5, ε^*_ζ=0.00%; at C_x=0.2, ε^*_ζ=0.01%

(3) quad-diurnal (N_λ=59.5) — at C_x=0.5, ε^*_ζ=0.05%; at C_x=0.25, ε^*_ζ=0.06%

These errors are very low for each constituent, having taken into account the relative contribution of each constituent to the overall tidal energy of Spencer Gulf.

4.2.3 Case 1: Wave propagation characteristics

Following Noye (1984b), consider the performance of the system of finite difference equations (4.7)–(4.9) in propagating Fourier modes.

For the purposes of deriving wave propagation characteristics, the analysis is simplified by assuming that the propagation takes place in an infinite domain consisting of computational elements. Therefore, only the interior differencing used by the scheme is checked by this analysis. Furthermore, since the original system of equations (4.1)–(4.2) is linear for the case $p = 0$, superposition of modes is valid and the propagation of only one Fourier component need be considered. As well, the initial amplitude and phase of the component are not of interest — only relative changes in amplitude and phase will be examined.

Equation (4.7) may be rewritten as

$$\zeta_i^{n+\frac{1}{2}} - \zeta_i^{n-\frac{1}{2}} = -rh_0 \left(U_i^n - U_{i-1}^n\right), \tag{4.23}$$

where $r = \Delta t/(2\Delta x)$ and ζ, in this context, denotes the solution for elevation using the first elevation calculation at Step 2 of the computational procedure. Equation (4.8) is rewritten as

$$U_i^{n+1} - U_i^n = -rg\left(\zeta_{i+1}^{n+\frac{1}{2}} - \zeta_i^{n+\frac{1}{2}}\right) - \frac{1}{2}\Delta t\, \tau \left(U_i^{n+1} + U_i^n\right), \tag{4.24}$$

and equation (4.9) is written as

$$Z_i^{n+1} - Z_i^n = -\frac{1}{2}rh_0 \left(\left[U_i^{n+1} + U_i^n\right] - \left[U_{i-1}^{n+1} + U_{i-1}^n\right]\right), \tag{4.25}$$

where Z denotes the numerical solution for elevation using the second elevation calculation.

Solutions to (4.23)–(4.25) of the form

$$\zeta_i^n = \zeta_a \exp\left\{\imath\left(k_t n\Delta t + k_x i\, 2\Delta x\right)\right\}, \tag{4.26}$$

$$U_i^n = U_a \exp\left\{\imath\left(k_t n\Delta t + k_x i\, 2\Delta x\right)\right\}, \tag{4.27}$$

$$Z_i^n = Z_a \exp\left\{\imath\left(k_t n\Delta t + k_x i\, 2\Delta x\right)\right\}, \tag{4.28}$$

are sought, where ζ_a, U_a and Z_a are the (possibly complex) amplitudes of the particular Fourier component being studied, which has complex frequency k_t and real wavenumber k_x. Equations (4.26)–(4.28) indicate that at time $t = 0$ the wave is of purely travelling form, extending infinitely along the spatial axis. Since k_t is complex, the computed wave may alter in both amplitude and phase with the passage of time, these changes being caused by the combined effect of the spatial and temporal approximations used in the finite difference expressions. In the present case, one expects the computed wave to be attenuated and lagged because of the inclusion of friction.

Substituting (4.26) and (4.27) into (4.23) gives

$$\zeta_a(\xi - 1) + U_a\sqrt{\xi}\, 2\imath r h_0 \sin\left(k_x\Delta x\right) = 0, \tag{4.29}$$

where $\xi = \exp\{\imath k_t \Delta t\}$; substituting (4.26) and (4.27) into (4.24) gives

$$\zeta_a\sqrt{\xi}\, 2\imath g r \sin\left(k_x\Delta x\right) + U_a\left(\xi - 1 + \frac{1}{2}\Delta t\, \tau[\xi + 1]\right) = 0, \tag{4.30}$$

and substituting (4.27) and (4.28) into (4.25) gives

$$U_a(\xi+1)rh_0\,\imath\sin(k_x\Delta x)+Z_a(\xi-1)=0. \tag{4.31}$$

In expressions (4.23)–(4.25), recall that the i subscript in ζ_i and Z_i refers to the ith ζ-point and the i subscript in U_i refers to the ith U-point — gridpoints ζ_i and U_i are actually separated by a distance Δx. These conventions have been taken into account in deriving expressions (4.29)–(4.31).

Equations (4.29)–(4.31) can be expressed in matrix form as

$$\begin{bmatrix} \xi-1 & \sqrt{\xi}\,2\imath rh_0\sin(k_x\Delta x) & 0 \\ \sqrt{\xi}\,2\imath gr\sin(k_x\Delta x) & \xi-1+\frac{1}{2}\Delta t\,\tau[\xi+1] & 0 \\ 0 & (\xi+1)rh_0\,\imath\sin(k_x\Delta x) & \xi-1 \end{bmatrix}\begin{bmatrix} \zeta_a \\ U_a \\ Z_a \end{bmatrix}=\begin{bmatrix} 0 \\ 0 \\ 0 \end{bmatrix}, \tag{4.32}$$

and non-trivial solutions of the form (4.26)–(4.28) exist if and only if the coefficient matrix is singular. Setting the determinant of the coefficient matrix to zero therefore yields possible solutions for ξ.

Solving the determinant equation by expanding down the third column leads to

$$(\xi-1)\begin{vmatrix} \xi-1 & \sqrt{\xi}\,2\imath rh_0\sin(k_x\Delta x) \\ \sqrt{\xi}\,2\imath gr\sin(k_x\Delta x) & \xi-1+\frac{1}{2}\Delta t\,\tau[\xi+1] \end{vmatrix}=0. \tag{4.33}$$

Now, equations (4.7)–(4.9) remain a stable system as long as $|\xi|\leq 1$ for every solution ξ. It is clear from (4.33) that $\xi=1$ is a solution, indicating that equation (4.9) has a neutral effect on the stability of the overall scheme. The stability of the overall scheme is therefore determined by the stability of the simpler system (4.7)–(4.8), this being a consequence of the fact that (4.9) is not needed for the numerical solution of equations (4.1) and (4.2), due in turn to the fact that (4.1) is linear.

The critical solutions for ξ are obtained by setting the 2×2 determinant of (4.33) to zero, giving

$$\xi^2\left(1+\frac{1}{2}\frac{C_x}{N_\lambda}K\right)+\xi\left(-2+4C_x^2\sin^2\frac{\pi}{N_\lambda}\right)+\left(1-\frac{1}{2}\frac{C_x}{N_\lambda}K\right)=0, \tag{4.34}$$

where the following substitutions have been made:

$$r^2gh_0=C_x^2,\quad k_x\Delta x=\frac{\pi}{N_\lambda}\quad\text{and}\quad\Delta t\,\tau=\frac{C_x}{N_\lambda}K. \tag{4.35}$$

Although equations (4.7) and (4.8) are a stable system as long as every $|\xi|\leq 1$, this does not guarantee that the numerical solutions are an accurate approximation to the solution of the original system (4.1)–(4.2).

In order to assess accuracy, solutions of (4.1) and (4.2) analogous to (4.26) and (4.27), and with the same initial conditions, are developed against which to compare the computed solutions. Thus, solutions of (4.1) and (4.2) of the form

$$\widehat{\zeta} = \zeta_a\exp\left\{\imath\left(\widehat{k}_t t+k_x x\right)\right\}, \tag{4.36}$$

$$\widehat{U} = U_a\exp\left\{\imath\left(\widehat{k}_t t+k_x x\right)\right\}, \tag{4.37}$$

are sought, and are referred to as the true wave solutions. Here ζ_a, U_a and k_x are as before and $\widehat{k}_t$ is the complex frequency of the true wave.

Substitution of (4.36)–(4.37) into (4.1)–(4.2) yields the matrix equation

$$\begin{bmatrix} \widehat{k}_t & h_0 k_x \\ g k_x & \widehat{k}_t - \imath\tau \end{bmatrix} \begin{bmatrix} \zeta_a \\ U_a \end{bmatrix} = \begin{bmatrix} 0 \\ 0 \end{bmatrix}, \tag{4.38}$$

which has non-trivial solutions when the determinant of the coefficient matrix is zero. Setting the determinant to zero leads to

$$\widehat{k}_t = \left(\imath\tau \pm \sqrt{4\sigma^2 - \tau^2}\right)/2, \tag{4.39}$$

where the following substitution has been made:

$$g h_0 k_x^2 = \sigma^2. \tag{4.40}$$

Equation (4.39) shows that there are two solutions $\widehat{k}_t$ for the true wave. These solutions have equal but opposite real parts and correspond to left and right going waves of equal magnitude in the real domain; their imaginary part is due entirely to the inclusion of friction.

The true wave frequency $\widehat{k}_t$ for, say, the right going wave, is now compared with the computed wave frequency k_t (for the right going wave), where

$$k_t = -(\imath/\Delta t)\ln\xi. \tag{4.41}$$

Two parameters which summarize the differences between the true wave and the computed wave are the ratios of the amplitudes and speeds of the waves. Putting

$$\widehat{\nu} = -\Re e\left\{\widehat{k}_t\right\} \quad \text{and} \quad \widehat{\eta} = \Im m\left\{\widehat{k}_t\right\}, \tag{4.42}$$

where $\widehat{\nu} > 0$ (ensuring the right going wave) and by inspection (and from physical considerations) $\widehat{\eta} > 0$, the right going solution of (4.39) may be written in the form

$$\widehat{k}_t = -\widehat{\nu} + \imath\widehat{\eta}. \tag{4.43}$$

Further, if the amplitude of the wave is described by

$$\zeta_a = \widehat{a}e^{\imath\widehat{\epsilon}}, \tag{4.44}$$

where $\widehat{a}$, $\widehat{\epsilon}$ are real, then (using (4.36))

$$\widehat{\zeta} = \widehat{a}e^{-\widehat{\eta}t}\exp\left\{\imath\left(k_x x - \widehat{\nu}t + \widehat{\epsilon}\right)\right\}, \tag{4.45}$$

so that

$$\Re e\left\{\widehat{\zeta}\right\} = \widehat{a}e^{-\widehat{\eta}t}\cos\left(k_x x - \widehat{\nu}t + \widehat{\epsilon}\right). \tag{4.46}$$

From this, it is seen that the inclusion of friction damps the wave (since $\widehat{\eta} > 0$).

The true wave is travelling with speed

$$\widehat{q} = \widehat{\nu}/k_x \tag{4.47}$$

in the positive x direction (since $\widehat{\nu} > 0$) in the real domain.

After one wave period of duration $2\pi/\widehat{\nu}$, the amplitude $\widehat{a}$ of the true wave is multiplied by the factor

$$\widehat{\alpha} = \exp\left(-2\pi\widehat{\eta}/\widehat{\nu}\right). \tag{4.48}$$

Similarly, if $k_t = -\nu + \imath\eta$, where ν, η are real and positive, the computed wave is travelling with speed

$$q = \nu/k_x \tag{4.49}$$

in the positive x direction, and after one wave period of duration $2\pi/\nu$, its amplitude is multiplied by the factor

$$\alpha = \exp\left(-2\pi\eta/\nu\right). \tag{4.50}$$

Note that the expressions for $\widehat{\alpha}$ and α are based on the fact that the wavelength of both the true and computed waves is the same, viz. $2\pi/k_x$.

The ratio of the amplitudes of the computed and true waves is therefore

$$\chi = \alpha/\widehat{\alpha} = \exp\left\{-2\pi\left(\eta/\nu - \widehat{\eta}/\widehat{\nu}\right)\right\}. \tag{4.51}$$

This is called the amplitude response of the method, viz.

$$\chi = \exp\left\{2\pi\left(\frac{\Im m\left\{k_t\right\}}{\Re e\left\{k_t\right\}} - \frac{\Im m\left\{\widehat{k}_t\right\}}{\Re e\left\{\widehat{k}_t\right\}}\right)\right\}. \tag{4.52}$$

The relative wave speed is

$$\mu = \frac{q}{\widehat{q}} = \frac{\nu}{\widehat{\nu}} = \frac{\Re e\left\{k_t\right\}}{\Re e\left\{\widehat{k}_t\right\}}. \tag{4.53}$$

Values of χ and μ can be computed for given values of K and T and expressed as functions of N_λ and C_x. Ideally, χ and μ are 1.0 for all values of N_λ and C_x if the computed wave is identical to the true wave.

Figures 4.3(a),(b) show these wave propagation characteristics of the numerical scheme using parameters representative of the Spencer Gulf model, for the same three tidal constituents as considered in the previous sub-section. The value used for the Courant number is $C_x = 0.3$ for each curve. According to these results, longer period constituents are propagated with less accuracy than shorter period waves when the same number of grid elements are used to represent one wavelength. However, at the operating values of N_λ for these constituents, it is evident that the longer period waves are modelled with greater accuracy than shorter period waves (see table insert). Nevertheless, at model values of N_λ the scheme propagates all three waves accurately — within an error of less than 10^{-3}.

Note that the parameters α_0, N_L and ζ_0 of the previous sub-section have been absent from this discussion. Parameters α_0 and N_L are defined in the context of the bounded problem — the derivation of wave propagation characteristics assumes there are no bounds to fluid flow. The parameter ζ_0 is not important here, as before, since it is the relative change in amplitude — computed wave to true wave — that is being considered.

Figure 4.3 is only qualitatively comparable with Figure 4.2 obtained for the numerical tests of the previous sub-section. It is not possible to compare the two sets of results directly for the following reasons:

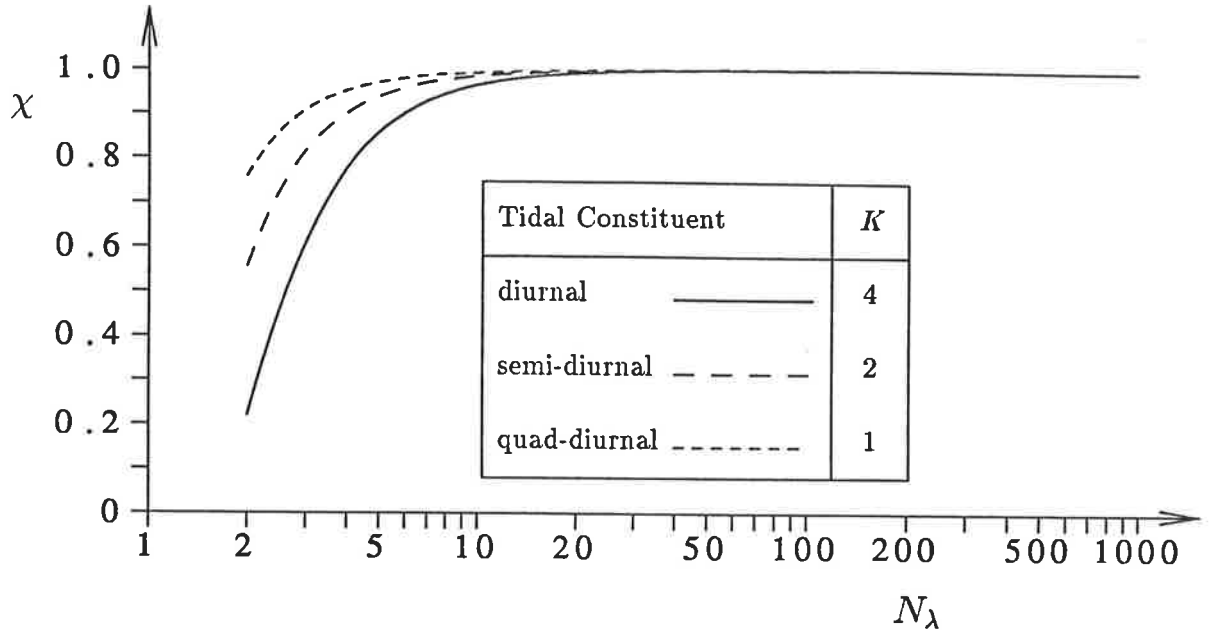
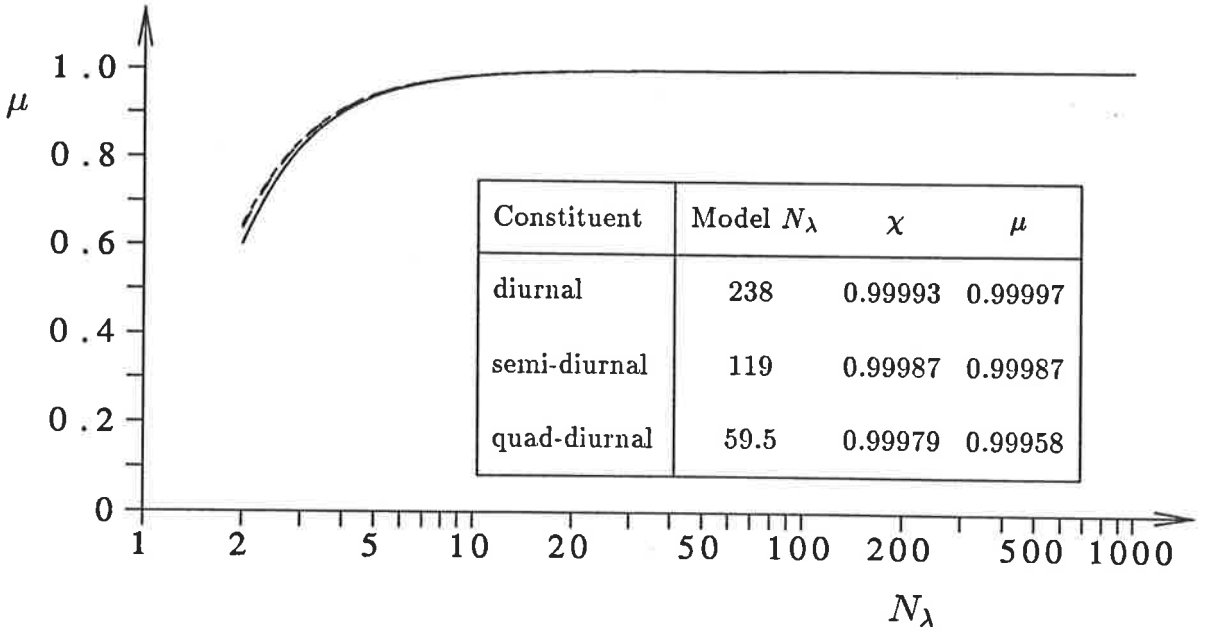


Figure 4.3(a): *Amplitude response χ versus number of grid spacings per wavelength N_λ for the numerical scheme using parameters representative of the Spencer Gulf model. Curve identification and parameters used are given in the table above. Operational values of χ for each constituent are given in the table below.*



Constituent	Model N_λ	χ	μ
diurnal	238	0.99993	0.99997
semi-diurnal	119	0.99987	0.99987
quad-diurnal	59.5	0.99979	0.99958

Figure 4.3(b): *Relative wave speed μ versus number of grid spacings per wavelength N_λ for parameters representative of the Spencer Gulf model. Parameter values used are given in the top table; Courant number $C_x = 0.3$. Values of χ and μ for each constituent at model values of N_λ are given in the table immediately above; at these values of N_λ the scheme propagates each wave with high accuracy — longer waves with greater accuracy than shorter waves.*

(i) the numerical tests correspond to tests with standing wave solutions while the wave propagation characteristics are derived from theoretical performances of the numerical scheme in propagating travelling waves;

(ii) the numerical tests include the effects of boundary conditions applied at both the head and the open boundary of the estuary, while the plots of wave propagation characteristics include no boundary effects;

(iii) the error measure used in the numerical tests is a simple comparison between numerical and analytical values and does not separate out error in amplitude and phase at the various testing stations, whereas the wave propagation characteristics are derived for a single typical station and compare the amplitude and wave speed (and hence phase, indirectly) of a component propagated by the numerical scheme relative to its exact propagation as obtained by solution of the original mathematical equations.

4.2.4 Case 2: Estuary with parabolic depth profile

If the estuary has bathymetry given by $h = h_2 x^2$, where h_2 is a constant with dimensions $(\text{Length})^{-1}$, a set of solutions of equations (4.1)–(4.2) is (Lynch and Gray, 1978, p. 1422):

$$\zeta = \Re e\left\{[Ax^{s_1} + Bx^{s_2}]\, e^{\imath\sigma t}\right\}, \tag{4.54}$$

$$U = \Re e\left\{\frac{\imath\sigma}{\beta^2 h_2}\left[As_1 x^{s_1-1} + Bs_2 x^{s_2-1}\right] e^{\imath\sigma t}\right\}, \tag{4.55}$$

where

$$s_1 = -\frac{1}{2} + \sqrt{\frac{1}{4} - \beta^2}\,, \qquad s_2 = -\frac{1}{2} - \sqrt{\frac{1}{4} - \beta^2}\,, \tag{4.56}$$

$$A = \frac{\zeta_0 s_2 x_1^{s_2}}{s_2 x_1^{s_2} x_2^{s_1} - s_1 x_1^{s_1} x_2^{s_2}}\,, \qquad B = \frac{-\zeta_0 s_1 x_1^{s_1}}{s_2 x_1^{s_2} x_2^{s_1} - s_1 x_1^{s_1} x_2^{s_2}}\,, \tag{4.57}$$

and again the head of the estuary is at $x = x_1$, and the open boundary is at $x = x_2$ (see Figure 4.4). The dimensionless complex wavenumber is $\beta = [(\sigma^2 - \imath\sigma\tau)/(gh_2)]^{1/2}$.

From equation (4.54), it can be seen that the elevation at the open boundary is

$$\zeta(t) = \Re e\left\{\zeta_0 e^{\imath\sigma t}\right\} = \zeta_0 \cos\sigma t. \tag{4.58}$$

The finite difference expressions used to solve equations (4.1)–(4.2) in this case are given in the following computational procedure:

1. Input model data and set initial values. Time $t = n\Delta t = 0$.

2. Update model time to level $(n + 1/2)$. Time $t = (n + 1/2)\Delta t$.
   Input the open boundary elevation specification at time level $(n + 1/2)$.
   Calculate elevation field $\zeta^{n+1/2}$ using

$$\frac{\zeta_i^{n+\frac{1}{2}} - \zeta_i^{n-\frac{1}{2}}}{\Delta t} = \frac{-1}{2\Delta x}\left(\frac{1}{2}\left[h_i + h_{i+1}\right] U_i^n - \frac{1}{2}\left[h_{i-1} + h_i\right] U_{i-1}^n\right). \tag{4.59}$$

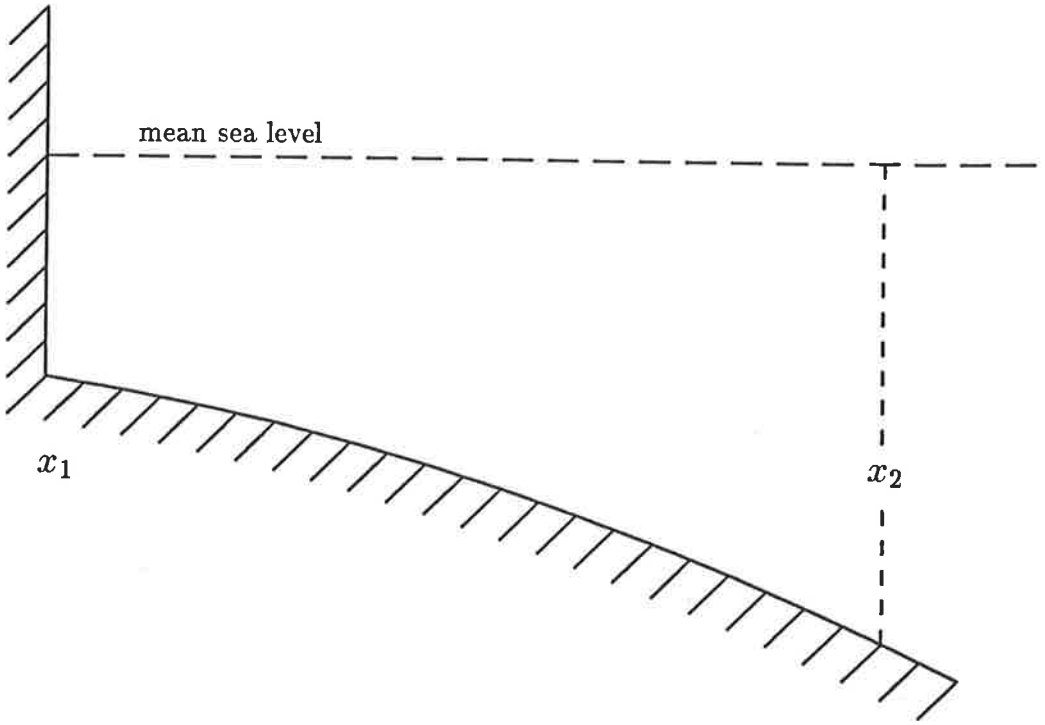


Figure 4.4: *Diagram illustrating the notation used to describe the Lynch and Gray idealized estuary with parabolic depth profile* $h(x) = h_2 x^2$. *The head of the estuary is at* $x = x_1$ *and the open boundary is at* $x = x_2$.

3. Update model time to level $(n+1)$. Time $t = (n+1)\Delta t$.
   Calculate depth-averaged velocity field U^{n+1} using

$$\frac{U_i^{n+1} - U_i^n}{\Delta t} = -g\left(\frac{\zeta_{i+1}^{n+\frac{1}{2}} - \zeta_i^{n+\frac{1}{2}}}{2\Delta x}\right) - \frac{\tau}{2}\left(U_i^{n+1} + U_i^n\right). \tag{4.60}$$

4. Input the open boundary elevation specification at time level $(n+1)$.
   Calculate elevation field ζ^{n+1} using

$$\frac{\zeta_i^{n+1} - \zeta_i^n}{\Delta t} = \frac{-1}{8\Delta x}\left([h_i + h_{i+1}]\left[U_i^{n+1} + U_i^n\right] - [h_{i-1} + h_i]\left[U_{i-1}^{n+1} + U_{i-1}^n\right]\right). \tag{4.61}$$

5. Return to Step 2 and repeat until the simulation is completed.

The linear approximations for depth used in (4.59) and (4.61) are taken from the program. The tests with a parabolic depth profile provide an opportunity to check these depth approximation expressions. In the case of the constant depth estuary the linear depth approximations are exact, so in equations (4.7) and (4.9) the value h_0 was substituted in their place.

The accuracy of the finite difference scheme in this case can be again checked by a series of numerical tests using parameters representative of the Spencer Gulf model.

4.2.5 Case 2: Numerical tests

Using the same set of dimensionless variables as used in Section 4.2.2, equations (4.1) and (4.2) may be written as

$$\frac{\partial \zeta^*}{\partial t^*} = -\alpha_2^2 \frac{\partial (x^*)^2 U^*}{\partial x^*}, \tag{4.62}$$

$$\frac{\partial U^*}{\partial t^*} = -\frac{\partial \zeta^*}{\partial x^*} - KU^*, \tag{4.63}$$

where $K = \tau T$ as before, and $\alpha_2 = T\sqrt{gh_2}$.

A degree of comparison with the numerical tests of Case 1 is possible if h_2 is related to h_0 in the following manner:

$$h_2 = h_0/L^2 \text{ m}^{-1}, \tag{4.64}$$

where h_0 and L are as before. Then the values assigned to α_0 in the Case 1 tests may be assigned to α_2. As well, the length and the average depth of the estuaries considered here will be taken to be the same as in the Case 1 numerical tests. Using these criteria, appropriate values for x_1 and x_2, the horizontal extents of the estuary, can be determined. Since the average depth h_a over the interval $[x_1, x_2]$ is

$$\begin{aligned} h_a &= \frac{1}{(x_2 - x_1)} \int_{x_1}^{x_2} h_2 x^2 \, dx \\ &= \frac{h_0}{L^3} \int_{x_1}^{x_1+L} x^2 \, dx \\ &= \frac{1}{3} \frac{h_0}{L^2} \left(x_1^2 + x_1[x_1 + L] + [x_1 + L]^2 \right), \end{aligned} \tag{4.65}$$

and if the substitution

$$h_a = h_0 \tag{4.66}$$

is made, then

$$x_1 = L\sqrt{\frac{5}{12}} \quad \text{and} \quad x_2 = L\sqrt{\frac{17}{12}}. \tag{4.67}$$

Using, for example, $L = 340042.5$m from the Spencer Gulf model tests of Section 4.2.2, $x_1 \simeq 155545$m and $x_2 \simeq 495587$ m, and the depths at these positions are, respectively, $h(x_1) \simeq 5.29$m and $h(x_2) \simeq 53.7$m; the average depth is $h_a = h_0 \simeq 25.3$m as before.

An average Courant number can be defined as

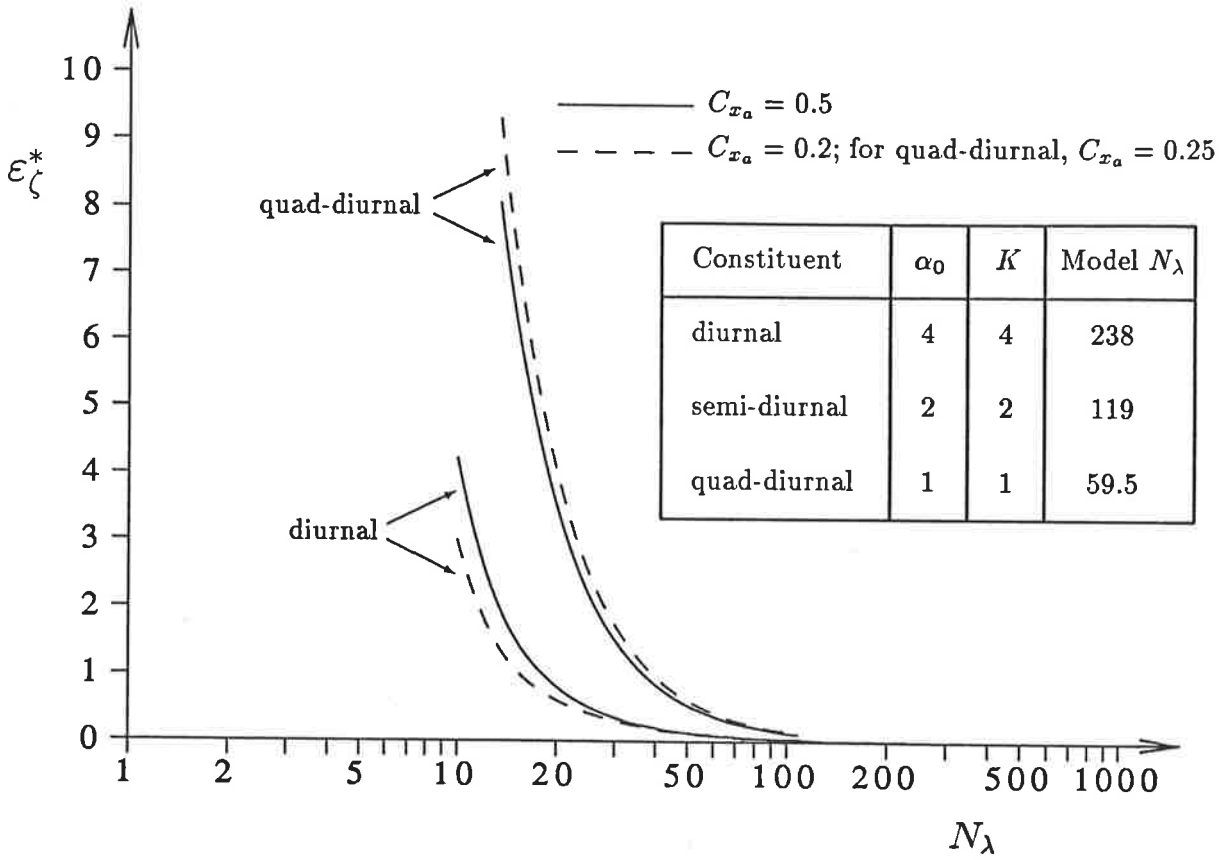
$$C_{x_a} = \Delta t \sqrt{g h_a}/(2\Delta x), \tag{4.68}$$

and has the same values as in Case 1 if $h_a = h_0$.

Since the substitutions (4.64) and (4.66) allow the same set of dimensionless numbers to be used in the Case 2 tests as are used in the Case 1 tests, one outcome of the present tests is to check the effect of the linear interpolations of the depth field at the velocity gridpoints in equations (4.59) and (4.61).

Figure 4.5 shows the results of numerical tests using parameters representative of Spencer Gulf. Only the diurnal and quad-diurnal results are plotted, the semi-diurnal results being indistinguishable from the diurnal results.

At the operating model values of N_λ for these constituents, the percentage errors ε_ζ^* to two decimal places are:



Constituent	α_0	K	Model N_λ
diurnal	4	4	238
semi-diurnal	2	2	119
quad-diurnal	1	1	59.5

Figure 4.5: *Percentage error in dimensionless elevation ε^*_ζ versus number of grid spacings per wavelength N_λ for the parabolic depth profile Spencer Gulf model tests for diurnal and quad-diurnal constituents. Because the plots for the semi-diurnal wave overlay those for the diurnal, the diurnal plots are given in representation of both. For each wave the input amplitude is $\zeta_0 = 0.75$ m and curves for two values of Courant number C_{x_a} are shown. The table shows the values used for α_0 and K for each constituent, along with the corresponding operating values of N_λ for the Spencer Gulf model of Chapter 5 (error values at these N_λ are given in the text).*

(1) diurnal (N_λ=238) — at C_x=0.5, ε^*_ζ=0.00%; at C_x=0.2, ε^*_ζ=0.00%

(2) semi-diurnal (N_λ=119) — at C_x=0.5, ε^*_ζ=0.03%; at C_x=0.2, ε^*_ζ=0.03%

(3) quad-diurnal (N_λ=59.5) — at C_x=0.5, ε^*_ζ=0.38%; at C_x=0.25, ε^*_ζ=0.43%

These errors are still low for the diurnal and semi-diurnal constituents. However, the errors for the semi-diurnal and quad-diurnal waves are noticeably higher than for the constant depth estuary. In dimensional terms, it is observed that $\varepsilon_U \simeq 1.3\varepsilon_\zeta$ for these tests also.

While in the Case 1 tests the numerical scheme is stable to $C_x = 1.0$, the scheme used for the tests with the parabolic depth profile is stable for $C_{x_a} \leq 0.85$. The latter restriction is unlikely to be influential in the case of the SG model since the operational Courant number is about 0.3, and the Gulf has a relatively gently sloping bathymetry.

4.3 Knight 1D approximate non-linear solution

Knight (1973) provides a second order perturbation solution for the one-dimensional non-linear equations:

$$\frac{\partial \zeta}{\partial t} = -\frac{\partial (h_0 + \zeta) U}{\partial x}, \tag{4.69}$$

$$\frac{\partial U}{\partial t} + U\frac{\partial U}{\partial x} = -g\frac{\partial \zeta}{\partial x} - \frac{d}{2r_1}\frac{1}{h_0}U|U|, \tag{4.70}$$

where d is the Darcy coefficient, r_1 is a coefficient relating the hydraulic radius to the mean depth and $r_1 = R/h_0 = 1/(1 + 2/r_2)$, in which R is the hydraulic radius and $r_2 = B/h_0$, the (breadth)/(mean depth) ratio of the estuary, B is the (fixed) breadth and h_0 is the mean depth of the idealized estuary. The remaining quantities are as defined in Chapter 2. For the purposes of the numerical experiments conducted here, we could define $C_b = d/(2r_1)$ and regard C_b as a dimensionless coefficient of quadratic friction for one-dimensional flow. (For an estuary of essentially infinite breadth, $r_1 \to 1$ as $B \to \infty$ and in that case $C_b \to d/2$ — the breadth is so wide that it is of no importance in setting a value for the coefficient of friction.) Knight's work is based on general second order solutions originally developed by Proudman (1957) for an idealized estuary with horizontal bed and constant rectangular cross-section; the estuary is closed at one end and open at the other to external tidal influence. The situation is portrayed schematically in Figure 4.6.

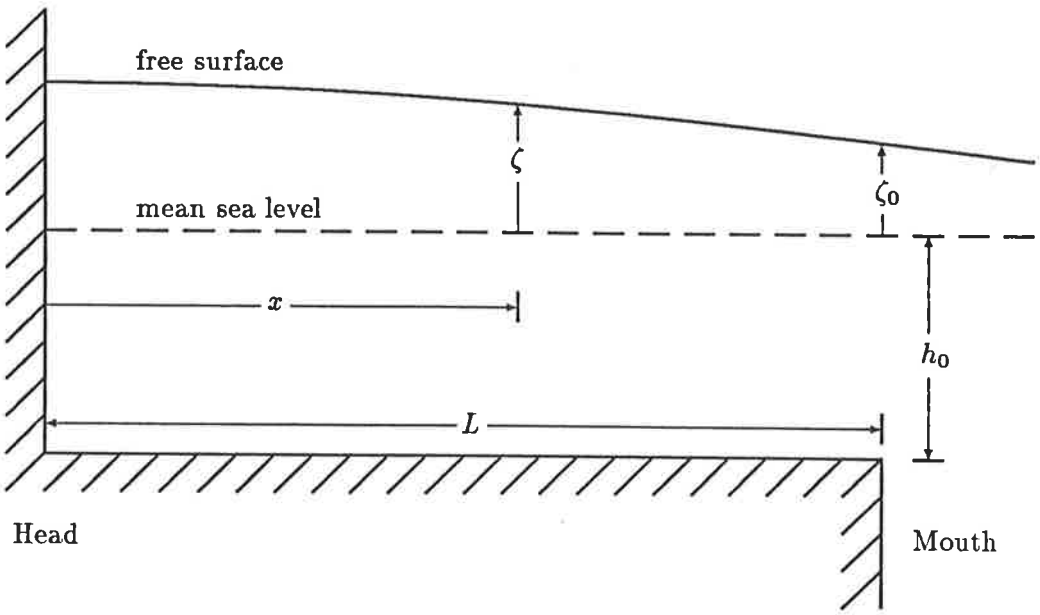


Figure 4.6: *Diagram illustrating the notation used to describe the idealized estuary. The amplitude of the first order tide at the estuary mouth is ζ_0 and the estuary length is L. Distance along the estuary from the head is x. (After Figure 1, Knight (1973).)*

The second order solution for (elevation)/(mean depth) at any point along the estuary is (Knight, 1973, pp. 996–997)

$$
\begin{aligned}
\frac{\zeta}{h_0} &= 2A\cos\sigma t\cos\frac{\sigma x}{c} \\
&\quad +\frac{A^2}{8}\left\{\cos^2\sigma\left(t+\frac{x}{c}\right)+\cos^2\sigma\left(t-\frac{x}{c}\right)\right. \\
&\quad \left.-\cos^2\sigma\left(t+\frac{x}{c}-\frac{2L}{c}\right)-\cos^2\sigma\left(t-\frac{x}{c}-\frac{2L}{c}\right)\right\} \\
&\quad -\frac{3A^2}{4}\frac{\sigma(L-x)}{c}\sin 2\sigma\left(t+\frac{x}{c}\right)-\frac{3A^2}{4}\frac{\sigma(L+x)}{c}\sin 2\sigma\left(t-\frac{x}{c}\right) \\
&\quad -\frac{A^2}{2}\cos\frac{2\sigma L}{c}+\frac{A^2}{2}\cos\frac{2\sigma x}{c} \\
&\quad -\frac{dcA^2}{8r_1h_0}\left\{\int_{t+x/c-2L/c}^{t-x/c}\left|\cos\sigma\left(t+\frac{x}{c}\right)-\cos\sigma\theta\right|\left[\cos\sigma\left(t+\frac{x}{c}\right)-\cos\sigma\theta\right]d\theta\right. \\
&\quad \left.+\int_{t-x/c-2L/c}^{t+x/c}\left|\cos\sigma\left(t-\frac{x}{c}\right)-\cos\sigma\theta\right|\left[\cos\sigma\left(t-\frac{x}{c}\right)-\cos\sigma\theta\right]d\theta\right\}, \qquad (4.71)
\end{aligned}
$$

and for (tidal velocity)/(wave celerity) at any point, is

$$
\begin{aligned}
\frac{U}{c} &= 2A\sin\sigma t\sin\frac{\sigma x}{c} \\
&\quad +\frac{A^2}{8}\left\{\cos^2\sigma\left(t+\frac{x}{c}\right)-\cos^2\sigma\left(t-\frac{x}{c}\right)\right. \\
&\quad \left.+\cos^2\sigma\left(t+\frac{x}{c}-\frac{2L}{c}\right)-\cos^2\sigma\left(t-\frac{x}{c}-\frac{2L}{c}\right)\right\} \\
&\quad +\frac{3A^2}{4}\frac{\sigma(L-x)}{c}\sin 2\sigma\left(t+\frac{x}{c}\right)-\frac{3A^2}{4}\frac{\sigma(L+x)}{c}\sin 2\sigma\left(t-\frac{x}{c}\right) \\
&\quad +\frac{dcA^2}{8r_1h_0}\left\{\int_{t+x/c-2L/c}^{t-x/c}\left|\cos\sigma\left(t+\frac{x}{c}\right)-\cos\sigma\theta\right|\left[\cos\sigma\left(t+\frac{x}{c}\right)-\cos\sigma\theta\right]d\theta\right. \\
&\quad \left.-\int_{t-x/c-2L/c}^{t+x/c}\left|\cos\sigma\left(t-\frac{x}{c}\right)-\cos\sigma\theta\right|\left[\cos\sigma\left(t-\frac{x}{c}\right)-\cos\sigma\theta\right]d\theta\right\}. \qquad (4.72)
\end{aligned}
$$

Here, A is a constant given by

$$
A=\frac{\zeta_0/h_0}{2\cos(\sigma L/c)}, \qquad (4.73)
$$

where ζ_0 is the amplitude of the first order tide at the estuary mouth (at $x = L$), x is the distance along the estuary from the head, σ is given by $2\pi/T$, T is the tidal period and $c = \sqrt{gh_0}$ is the wave celerity. Note that the solutions given by equations (4.71) and (4.72) are periodic, making them very useful in numerical testing since analytical values for the computational points of only the first cycle need to be calculated and stored for comparison with the numerically generated results from the first and subsequent cycles.

Knight provides a graph showing the limits of application of Proudman's solution (Knight, 1973, Figure 8). It is valid when the second order terms are small compared with the first order terms. Knight explains that in practice this means the dimensionless group $\sigma L/c$ should be small and that the product of three other dimensionless groups d/r_1, ζ_0/h_0 and $c/(h_0\sigma)$ should also be small: "The magnification of the tidal range from

the estuary mouth to head is very largely governed by the value of $\sigma L/c$, and for a given value of $\sigma L/c$ the deviation from the first order solution is entirely governed by the value of $(d/r_1)(\zeta_0/h_0)[c/(h_0\sigma)]$" (Knight, 1973, p.1001).

Knight graphs the solution for the well conditioned case when $T = 120\,\text{sec}$, $h_0 = 0.15\,\text{m}$, $\zeta_0 = 0.02\,\text{m}$, $B = 0.15\,\text{m}$, $L = 20\,\text{m}$ and $d = 0.005$. Using these values,

$$\frac{\sigma L}{c} = X \simeq 0.863 \quad \text{and} \quad \frac{d}{r_1}\frac{\zeta_0}{h_0}\frac{c}{h_0\sigma} = Y \simeq 0.309, \tag{4.74}$$

and the point $(X, Y) = (0.863, 0.309)$ lies just inside the region specified for accurate solutions. The values used here are taken from a laboratory project in which the scale of the model estuary is necessarily small.

The laboratory values give $C_b = 0.0075$ which is three times the value normally assigned to the coefficient of quadratic friction for estuaries; on the other hand, the ratio $\zeta_0/h_0 = 2/15$ is high. In the numerical experiments that follow, first values similar to the laboratory values will be used, and then values taken from the Northern Spencer Gulf model will be used in two further tests.

In equations (4.69) and (4.70), it is only the advective and friction terms of the momentum equation which pose some difficulty in finite difference approximation. The other terms take the straightforward time and space centred approximations given in the following computational procedure:

1. Input model data and set initial values. Time $t = n\Delta t = 0$.

2. Update model time to level $(n + 1/2)$. Time $t = (n + 1/2)\Delta t$.
   Input the open boundary elevation specification at time level $(n + 1/2)$.
   Calculate elevation field $\zeta^{n+1/2}$ using

$$\frac{\zeta_i^{n+\frac{1}{2}} - \zeta_i^{n-\frac{1}{2}}}{\Delta t} = -\frac{1}{2\Delta x}\left[\frac{1}{2}\left(H_i^n + H_{i+1}^n\right)U_i^n - \frac{1}{2}\left(H_{i-1}^n + H_i^n\right)U_{i-1}^n\right]. \tag{4.75}$$

3. Calculate total depth field $H^{n+1/2}$ using

$$H_i^{n+\frac{1}{2}} = \zeta_i^{n+\frac{1}{2}} + h_0. \tag{4.76}$$

4. Update model time to level $(n + 1)$. Time $t = (n + 1)\Delta t$.
   Calculate depth-averaged velocity field U^{n+1} using a scheme of the form

$$\frac{U_i^{n+1} - U_i^n}{\Delta t} + \left\{U\frac{\partial U}{\partial x}\right\}_i^{n+\frac{1}{2}} = -g\left(\frac{\zeta_{i+1}^{n+\frac{1}{2}} - \zeta_i^{n+\frac{1}{2}}}{2\Delta x}\right) - \frac{d}{2r_1}\frac{1}{h}\left\{U|U|\right\}_i^{n+\frac{1}{2}}, \tag{4.77}$$

   where various ways of approximating the advective and friction terms are considered below.

5. Input the open boundary elevation specification at time level $(n + 1)$.
   Calculate elevation field ζ^{n+1} using

$$\begin{aligned}\frac{\zeta_i^{n+1} - \zeta_i^n}{\Delta t} \;=\; -\frac{1}{2\Delta x}\Bigg[&\frac{1}{2}\left(H_i^{n+\frac{1}{2}} + H_{i+1}^{n+\frac{1}{2}}\right)\frac{1}{2}\left(U_i^n + U_i^{n+1}\right) \\ &-\frac{1}{2}\left(H_{i-1}^{n+\frac{1}{2}} + H_i^{n+\frac{1}{2}}\right)\frac{1}{2}\left(U_{i-1}^n + U_{i-1}^{n+1}\right)\Bigg].\end{aligned} \tag{4.78}$$

6. Calculate total depth field H^{n+1} using

$$H_i^{n+1} = \zeta_i^{n+1} + h_0. \tag{4.79}$$

7. Return to Step 2 and repeat until the simulation is completed.

Proudman's solution not only gives a means of testing various finite difference approximations for the advective and friction terms of the momentum equation, but also tests the interlaced calculation of elevation. The solution checks the ability of the program to model three sources of non-linearity: (i) the inclusion of elevation in the depth expression on the right hand side of continuity equation (4.69), and the inclusion of (ii) the advective and (iii) the quadratic friction terms in equation (4.70).

There are several relatively simple ways of approximating the advective term of equation (4.77) which are easily tested using the program. These are

A1. $\{U\partial U/\partial x\}_i^{n+\frac{1}{2}} = \{\partial U^2/\partial x\}_i^{n+\frac{1}{2}}/2 \simeq \left[(U_{i+1}^n)^2 - (U_{i-1}^n)^2\right]/(8\Delta x),$

A2. $\{U\partial U/\partial x\}_i^{n+\frac{1}{2}} = \{\partial U^2/\partial x\}_i^{n+\frac{1}{2}}/2 \simeq \left[(U_i^n + U_{i+1}^n)^2 - (U_{i-1}^n + U_i^n)^2\right]/(16\Delta x),$

A3. $\{U\partial U/\partial x\}_i^{n+\frac{1}{2}} \simeq U_i^n\{\partial U/\partial x\}_i^n \simeq U_i^n\,(U_{i+1}^n - U_{i-1}^n)/(4\Delta x),$

A4. $\{U\partial U/\partial x\}_i^{n+\frac{1}{2}} \simeq U_i^{n+\frac{1}{2}}\{\partial U/\partial x\}_i^n \simeq \left(U_i^{n+1} + U_i^n\right)(U_{i+1}^n - U_{i-1}^n)/(8\Delta x),$

A5. $\{U\partial U/\partial x\}_i^{n+\frac{1}{2}} \simeq U_i^{n+1}\{\partial U/\partial x\}_i^n \simeq U_i^{n+1}\,(U_{i+1}^n - U_{i-1}^n)/(4\Delta x).$

Various other approximations such as the explicit upwind schemes and the "angled-derivative" of Roberts and Weiss (1966) have not been tried. The upwind schemes are known to damp the solution field and the "angled-derivative" reduces wave speed leading to significantly lagged predictions — see Noye (1986) for a discussion of these schemes.

Three methods for approximating the quadratic friction term are:

F1. $\{U|U|\}_i^{n+\frac{1}{2}} \simeq \{U\}_i^n\{|U|\}_i^n = U_i^n|U_i^n|,$

F2. $\{U|U|\}_i^{n+\frac{1}{2}} \simeq \{U\}_i^{n+\frac{1}{2}}\{|U|\}_i^n = \left(U_i^{n+1} + U_i^n\right)|U_i^n|/2,$

F3. $\{U|U|\}_i^{n+\frac{1}{2}} \simeq \{U\}_i^{n+1}\{|U|\}_i^n = U_i^{n+1}|U_i^n|.$

The five options for the advective term combined with the three options for the friction term generate 15 different schemes.

Because the governing mathematical equations (4.69)–(4.70) are non-linear, it is not possible to carry out a wave propagation analysis of the finite difference schemes (4.75)–(4.79). However, numerical comparisons of the 15 finite difference options for the momentum difference equation (4.77) have been carried out for fixed values of the number of grid spacings per wavelength N_λ and, selecting the most favourable momentum difference scheme, tests covering a range of values of N_λ are then performed.

4.3.1 Numerical tests

Defining dimensionless variables in the usual way, equations (4.69) and (4.70) may be written as

$$\frac{\partial \zeta^*}{\partial t^*} = -\alpha_0^2 \frac{\partial (1+\epsilon\zeta^*)U^*}{\partial x^*}, \tag{4.80}$$

$$\frac{\partial U^*}{\partial t^*} + \alpha_0^2 \epsilon U^* \frac{\partial U^*}{\partial x^*} = - \frac{\partial \zeta^*}{\partial x^*} - C_b \left(\frac{L}{h_0}\right) \alpha_0^2 \epsilon U^* |U^*|, \tag{4.81}$$

where $\alpha_0 = T\sqrt{gh_0}/L$ as before, $\epsilon = \zeta_0/h_0$ is a measure of the degree of non-linearity as defined, for instance, in McCowan and Blackman (1988) and $C_b = d/(2r_1)$.

Consider now three experiments which compare the performance of the chosen 15 finite difference schemes with the analytical solution. Because the limits of application of Proudman's solution are restrictive, it is not possible to run numerical experiments with all parameters taken directly from the Spencer Gulf model as was done in the previous sections. However, some essential parameters such as a realistic value for mean depth and a tidal component of realistic amplitude are included in two of the three tests.

In the first test, values similar to the laboratory parameters from Knight (1973) are used. Here, the amplitude of oscillation is about 14% of the value of mean depth; in fact, $\epsilon \simeq 0.136$. In the second and third tests the propagation of a diurnal tidal constituent along one-dimensional estuaries is considered. The reason for the use of the diurnal constituent and not a wave of shorter period, such as the semi-diurnal, is that the criteria of application of Proudman's solution would force the amplitude of a semi-diurnal wave to be unrealistically small compared to the mean depth value.

In each test, simulations are started from "cold" and are run until the value of ε_ζ^* over a cycle of oscillation is less than 10^{-5} m different from its value over the preceding cycle. For the runs of Test 1, about 20 cycles are required to achieve this degree of convergence, but for the runs of Tests 2 and 3, less than 10 cycles are required. Error values taken from the last cycle of each test are presented. The error measure used is again the average absolute difference between numerical and analytical values calculated over all the computational space and time points for a cycle, relative to a corresponding characteristic value and expressed as a percentage, as defined in Section 4.2.2. Errors in the elevation field calculated at Step 5 of the computational procedure are given. The dimensionless elevation errors are higher than the dimensionless velocity errors mainly because of scaling with respect to characteristic value as required by the definition of the error measure.

Test 1: Pseudo-laboratory parameters

In this test, parameters based on the laboratory values given above, are used. The values chosen are

$$T = 120\,\text{sec}, \quad \zeta_0 = 0.02\,\text{m}, \quad d = 0.005, \quad L = 20\,\text{m}, \tag{4.82}$$

all of which are laboratory values; however, h_0 and B are chosen as

$$h_0 = B = \frac{1}{g}\left(7.2 \times \frac{20}{120}\right)^2 \simeq 0.147\,\text{m}, \tag{4.83}$$

slightly different to those given by Knight, but allowing the number of time steps per period N_T to be an integer for all values of N_L used, while the Courant number is fixed at $C_x = 0.3$.

Using (4.83), $\alpha_0 = 7.2$ and $N_\lambda = 7.2N_L$; choosing $C_x = 0.3$ gives $N_T = 24N_L$. Furthermore, the value of the pair of dimensionless groups is $(X, Y) \simeq (0.873, 0.319)$, again slightly different to Knight's laboratory values but still inside the region specified for accurate solutions.

		A1	A2	A3	A4	A5
F1	ε^*_ζ:	2.556	2.554	2.552	2.516	2.481
	ε^*_U:	0.366	0.366	0.366	0.360	0.355
F2	ε^*_ζ:	2.546	2.544	2.533	2.507	2.471
	ε^*_U:	0.365	0.365	0.363	0.359	0.354
F3	ε^*_ζ:	2.537	2.535	2.524	2.497	2.461
	ε^*_U:	0.364	0.364	0.362	0.358	0.353

Table 4.1: *Percentage errors in dimensionless elevation ε^*_ζ and dimensionless depth-averaged velocity ε^*_U for 15 different schemes approximating equations (4.69) and (4.70). The error measure is explained in the text. F1, ..., F3 are selected finite difference forms for the quadratic friction term and A1, ..., A5 are selected difference forms for the advective term. The parameters used are the Test 1 values given in the text; these values correspond to $C_x = 0.3$, $N_\lambda = 104.4$, $N_L = 14.5$, $N_T = 348$ and $(X, Y) \simeq (0.873, 0.319)$. (Dimensional errors are obtained using the formulae $\varepsilon_\zeta = \varepsilon^*_\zeta \times 0.02/100$ m and $\varepsilon_U = \varepsilon^*_U \times 1.1772/100$ m/sec.)*

Percentage errors in dimensionless elevation and velocity for each of the 15 combinations of schemes are presented in Table 4.1 for $N_\lambda = 104.4$. At this value, $N_L = 14.5$ and $N_T = 348$. From the table, it seems that the combination of schemes (F3, A5) produces the most accurate results at the given value of N_λ. Because $\zeta_0 = 0.02$ m and $U_0 = (g\zeta_0 T/L) = 1.1772$ m/sec, the dimensional errors corresponding to combination (F3, A5) are $\varepsilon_\zeta = 4.92 \times 10^{-4}$ m and $\varepsilon_U = 4.146 \times 10^{-3}$ m/sec.

One expects the performance of the schemes to show less difference at higher values of N_λ and this is illustrated in the comparison of results from Tests 2 and 3.

Test 2: Diurnal wave of amplitude $\zeta_0 = 0.4$ m in a 90 km estuary

In this test, a diurnal wave of realistic amplitude in an estuary of mean depth approximating that of Northern Spencer Gulf is modelled. The values used are

$$T = 86400 \text{ sec}, \quad \zeta_0 = 0.40 \text{ m}, \quad C_b = 0.0025, \quad L = 90000 \text{ m}, \tag{4.84}$$

and

$$h_0 = \frac{1}{g}\left(10.2 \times \frac{90000}{86400}\right)^2 \simeq 11.5 \text{ m}. \tag{4.85}$$

The value $C_b = 0.0025$ arises if $d = 0.005$ and an estuary of infinite width is considered in which the flow is nevertheless one-dimensional.

Using (4.85), $\alpha_0 = 10.2$ and $N_\lambda = 10.2 N_L$; choosing $C_x = 0.3$ gives $N_T = 34 N_L$, which is an integer for all values $N_L = 1.5, 2.5, 3.5, \ldots$ The value of the pair of dimensionless groups is $(X, Y) \simeq (0.616, 2.21)$ and this point lies within the region where the analytical solution is "well conditioned".

Percentage errors in dimensionless elevation and velocity for each of the 15 chosen finite difference schemes are presented in Table 4.2 for $N_\lambda = 107.1$. At this value, $N_L = 10.5$ and $N_T = 357$. From the table, it again seems that the combination of schemes (F3, A5) produces the most accurate results at the given value of N_λ. Because $\zeta_0 = 0.40$ m and

$U_0 = 3.767\,\mathrm{m/sec}$ in this case, the dimensional errors corresponding to schemes (F3, A5) are $\varepsilon_\zeta = 5.164 \times 10^{-3}\,\mathrm{m}$ and $\varepsilon_U = 3.315 \times 10^{-3}\,\mathrm{m/sec}$.

		A1	A2	A3	A4	A5
F1	ε^*_ζ:	1.325	1.325	1.326	1.324	1.322
	ε^*_U:	0.092	0.092	0.092	0.092	0.092
F2	ε^*_ζ:	1.310	1.310	1.310	1.308	1.307
	ε^*_U:	0.090	0.090	0.090	0.090	0.090
F3	ε^*_ζ:	1.294	1.294	1.294	1.293	1.291
	ε^*_U:	0.088	0.088	0.088	0.088	0.088

Table 4.2: *Percentage dimensionless error values arising from Test 2 which uses parameters as given in the text; these values correspond to $C_x = 0.3$, $N_\lambda = 107.1$, $N_L = 10.5$, $N_T = 357$ and $(X, Y) \simeq (0.616, 2.21)$. (Dimensional errors are obtained using: $\varepsilon_\zeta = \varepsilon^*_\zeta \times 0.40/100\,m$ and $\varepsilon_U = \varepsilon^*_U \times 3.767/100\,m/sec.$)*

Using scheme (F3, A5), error values covering a range of values of N_λ are plotted in Figure 4.7 and are discussed following the next sub-section.

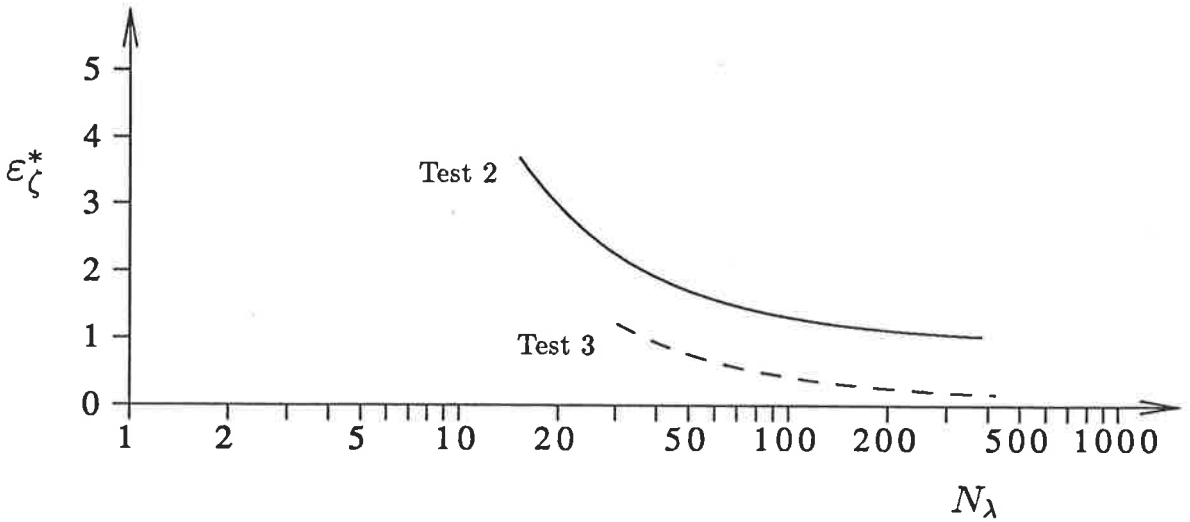


Figure 4.7: *Percentage error in dimensionless elevation ε^*_ζ versus number of grid spacings per wavelength N_λ for Tests 2 and 3 using scheme (F3, A5) to model diurnal waves of different amplitudes at Courant number $C_x = 0.3$. For Test 2, $\alpha_0 = 104.04$; since the simplest model uses $N_L = 1.5$, the curve starts at $N_\lambda = 15.3$; for Test 3, $\alpha_0 = 416.16$ and the curve starts at $N_\lambda = 30.6$. At the operating value $N_\lambda = 436$ for a diurnal wave in the Northern Spencer Gulf model the errors are low for Test 3 where input amplitude is $\zeta_0 = 0.8\,m$, but higher for Test 2 where $\zeta_0 = 0.4\,m$. This result is considered under the title "Discussion of test results" at the end of this section.*

Test 3: Diurnal wave of amplitude $\zeta_0 = 0.8\,\mathrm{m}$ in a 45 km estuary

For this test, the amplitude of the diurnal oscillation is doubled and now corresponds to the maximum O_1 plus K_1 amplitudes of Northern Spencer Gulf. In order to keep the value of (X, Y) within the "well conditioned" region, the estuary length is correspondingly halved. The mean depth remains the same as in Test 2. The values used are

$$T = 86400\,\mathrm{sec}, \quad \zeta_0 = 0.80\,\mathrm{m}, \quad C_b = 0.0025, \quad L = 45000\,\mathrm{m}, \tag{4.86}$$

and

$$h_0 = \frac{1}{g}\left(20.4 \times \frac{45000}{86400}\right)^2 \simeq 11.5\,\mathrm{m}. \tag{4.87}$$

Using (4.87), $\alpha_0 = 20.4$ and $N_\lambda = 20.4 N_L$; choosing $C_x = 0.3$ gives $N_T = 68 N_L$, which is always an integer for $N_L = 1.5, 2.5, 3.5, \ldots$ The value of the pair of dimensionless groups is $(X, Y) \simeq (0.308, 4.41)$ and lies off Knight's Figure 8 (Knight, 1973, p.1000), though it is presumably still within the "well conditioned" region.

Percentage errors in dimensionless elevation and velocity for each of the 15 combinations of schemes are presented in Table 4.3 for $N_\lambda = 418.2$. At this value, $N_L = 20.5$ and $N_T = 1394$. From the table, scheme (F3, A5) produces results at least as accurate as the other schemes at the given value of N_λ and, as anticipated, there is very little difference in performance of the schemes at this high value of N_λ (c.f. Tests 1 and 2). Using $\zeta_0 = 0.80\,\mathrm{m}$ and $U_0 = 15.07\,\mathrm{m/sec}$, the dimensional errors corresponding to schemes (F3, A5) are $\varepsilon_\zeta = 1.392 \times 10^{-3}\,\mathrm{m}$ and $\varepsilon_U = 6.03 \times 10^{-4}\,\mathrm{m/sec}$.

		A1	A2	A3	A4	A5
F1	ε^*_ζ:	0.176	0.176	0.176	0.176	0.176
	ε^*_U:	0.004	0.004	0.004	0.004	0.004
F2	ε^*_ζ:	0.175	0.175	0.175	0.175	0.175
	ε^*_U:	0.004	0.004	0.004	0.004	0.004
F3	ε^*_ζ:	0.174	0.174	0.174	0.174	0.174
	ε^*_U:	0.004	0.004	0.004	0.004	0.004

Table 4.3: *Percentage dimensionless error values arising from Test 3 which uses the same parameter values as Test 2 except that amplitude is doubled and length is halved. Thus $C_x = 0.3$, $N_\lambda = 418.2$, $N_L = 20.5$, $N_T = 1394$ and $(X, Y) \simeq (0.308, 4.41)$. (Dimensional errors are obtained using: $\varepsilon_\zeta = \varepsilon^*_\zeta \times 0.80/100\,\mathrm{m}$ and $\varepsilon_U = \varepsilon^*_U \times 15.07/100\,\mathrm{m/sec}$.)*

Using scheme (F3, A5), error values are plotted for a range of values of N_λ in Figure 4.7. A typical value of N_λ for the diurnal wave in Northern Spencer Gulf is $N_\lambda = 436$; at this value, scheme (F3, A5) performs well.

Discussion of test results

In each of the three tests conducted, scheme (F3, A5) performed with either the smallest error (Tests 1 and 2) or shared the lowest error (Test 3) of the 15 schemes considered.

As may be expected, differences in performance of the various schemes is greatest for small N_λ and least for large N_λ. For large N_λ, there is almost no difference in performance

among the schemes. Because of the consistently accurate performance of scheme (F3, A5), it is preferred. Furthermore, it is one of the simplest to program and the fastest to execute of the 15 possibilities presented.

Figure 4.7 shows that for the diurnal wave, scheme (F3, A5) performs accurately near the operational value of $N_\lambda = 436$ for the Northern Spencer Gulf model. It is interesting to note that the results of Test 2 show greater error than those of Test 3 even though the degree of non-linearity, as measured by the parameter ϵ, is half that used in the latter test. It seems likely that this reflects the fact that the analytical solution for Test 2, represented by the values $(X, Y) \simeq (0.616, 2.21)$, is closer to Knight's breakdown curve (Figure 8, Knight, 1973) than the solution for Test 3 with values $(X, Y) \simeq (0.308, 4.41)$; that is, Proudman's solution for Test 2 is less accurate than that for Test 3. Thus the error values ε_ζ^* recorded in Figure 4.7 are a composite of errors in both the perturbation solution and the finite difference scheme.

In the same manner in which the diurnal curves of Figure 4.7 are constructed for parameters of Tests 2 and 3, runs for a range of values of N_λ with scheme (F3, A5) using parameters of Test 1 can also be made but are found to be unstable for $N_\lambda \geq 25$. The curve connecting the results up to $N_\lambda = 20$ is oscillatory, indicating the presence of instability in the results for $N_\lambda < 25$. This suggests that the point $(X, Y) \simeq (0.873, 0.319)$ (Test 1) is very near to the breakdown curve of Proudman's solution. Indeed, it seems plausible to replace Knight's breakdown curve by a "breakdown region" where there is a gradual loss of accuracy in Proudman's solution. Thus, again, it is likely that the relatively large size of the error values of Table 4.1 simply reflects the probability that the analytical solution generated for the Test 1 parameters is itself inaccurate, rather than being due entirely to an inability of the finite difference scheme to model the situation.

It seems that the limitation in this comparison is the perturbation solution itself, not the finite difference scheme.

In agreement with Knight's conclusions, it can be stated that further work is needed to assess the accuracy of Proudman's solution especially if, as Knight proposes, it is to be useful in the assessment of numerical finite difference schemes. With the increased availability of powerful symbolic manipulation packages such as MACSYMA (1982), the development and verification of higher order analytical solutions may now be easier to obtain, but this is outside the scope of the present work.

4.4 Rienecker and Teubner 2D horizontal linear solution

Rienecker and Teubner (1980) provide a truncated series solution for the propagation and reflection of a Kelvin wave in the closed end of a rotating semi-infinite rectangular bay; their solution includes the effect of friction. The equations solved are

$$\frac{\partial \zeta}{\partial t} = -h_0 \frac{\partial U}{\partial x} - h_0 \frac{\partial V}{\partial y}, \tag{4.88}$$

$$\frac{\partial U}{\partial t} - fV = -g \frac{\partial \zeta}{\partial x} - \frac{k}{h_0} U, \tag{4.89}$$

$$\frac{\partial V}{\partial t} + fU = -g \frac{\partial \zeta}{\partial y} - \frac{k}{h_0} V, \tag{4.90}$$

where h_0 is the depth, f is the Coriolis parameter with units sec^{-1} and k is the coefficient of linear friction with units m/sec. The parameters h_0, f and k are assumed constant. The

remaining variables are defined as before. These equations are solved in conjunction with boundary conditions of zero perpendicular flow at coastal boundaries (see Figure 4.8), viz.

$$V(x,y) = 0 \quad \text{at} \quad y = 0 \quad \text{and} \quad y = B \quad \text{for} \quad x \geq 0, \tag{4.91}$$

$$U(0,y) = 0 \quad \text{for} \quad 0 \leq y \leq B, \tag{4.92}$$

where the breadth of the bay is B, and a condition that ensures that the input wave is uni-directional, viz.

$$V(L,y) = 0 \quad \text{for} \quad 0 \leq y \leq B, \tag{4.93}$$

where the length of the bay is L.

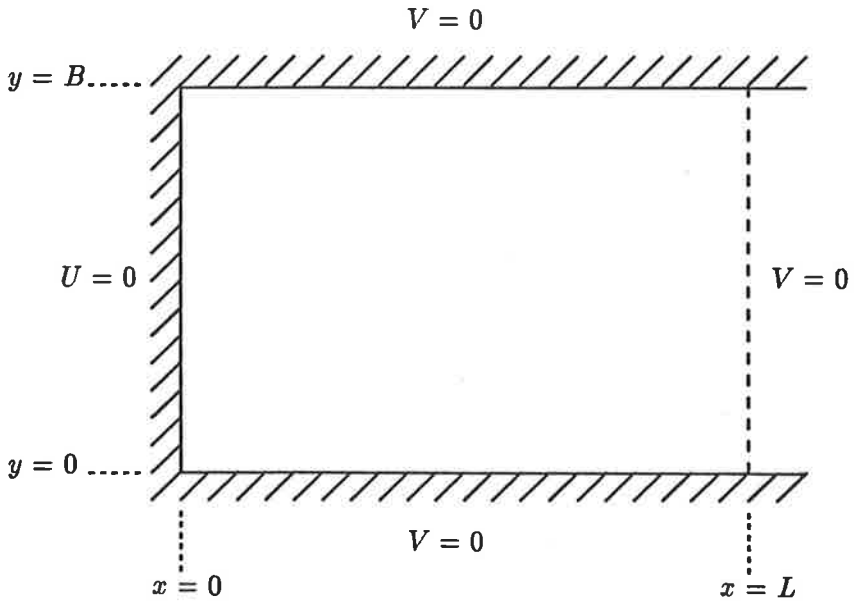


Figure 4.8: *Diagram illustrating the rectangular bay and boundary conditions used in the Rienecker and Teubner (1980) study. The length of the bay is L and the breadth is B.*

Details of the series solution are given in Rienecker and Teubner (1980), and Webber (1980) — they are not reproduced here because of their length.

Time and space centred finite difference approximations for equations (4.88)–(4.90) are presented in the following computational procedure:

1. Input model data and set initial values. Time $t = n\Delta t = 0$.

2. Update model time to level $(n + 1/2)$. Time $t = (n + 1/2)\Delta t$.
   Input the open boundary elevation specification at time level $(n + 1/2)$.
   Calculate elevation field $\zeta^{n+1/2}$ using

$$\frac{\zeta_i^{n+\frac{1}{2}} - \zeta_i^{n-\frac{1}{2}}}{\Delta t} = -h_0 \left(\frac{U_i^n - U_{i-1}^n}{2\Delta x} \right) - h_0 \left(\frac{V_{i_1}^n - V_i^n}{2\Delta y} \right). \tag{4.94}$$

3. Update model time to level $(n+1)$. Time $t = (n+1)\Delta t$.
Calculate depth-averaged velocity fields U^{n+1}, V^{n+1} using

$$\begin{aligned}\frac{U_i^{n+1} - U_i^n}{\Delta t} &- \frac{f}{4}\left(V_{i_1}^{n+1} + V_{i_1+1}^{n+1} + V_i^n + V_{i+1}^n\right) \\ &= -g\left(\frac{\zeta_{i+1}^{n+\frac{1}{2}} - \zeta_i^{n+\frac{1}{2}}}{2\Delta x}\right) - \frac{k}{2h_0}\left(U_i^{n+1} + U_i^n\right). \qquad (4.95)\end{aligned}$$

$$\begin{aligned}\frac{V_i^{n+1} - V_i^n}{\Delta t} &+ \frac{f}{4}\left(U_{i-1}^{n+1} + U_i^{n+1} + U_{i_2-1}^n + U_{i_2}^n\right) \\ &= -g\left(\frac{\zeta_i^{n+\frac{1}{2}} - \zeta_{i_2}^{n+\frac{1}{2}}}{2\Delta y}\right) - \frac{k}{2h_0}\left(V_i^{n+1} + V_i^n\right). \qquad (4.96)\end{aligned}$$

4. Input the open boundary elevation specification at time level $(n+1)$.
Calculate elevation field ζ^{n+1} using

$$\begin{aligned}\frac{\zeta_i^{n+1} - \zeta_i^n}{\Delta t} = &- \frac{h_0}{2\Delta x}\left(\frac{1}{2}\left[U_i^{n+1} + U_i^n\right] - \frac{1}{2}\left[U_{i-1}^{n+1} + U_{i-1}^n\right]\right) \\ &- \frac{h_0}{2\Delta y}\left(\frac{1}{2}\left[V_{i_1}^{n+1} + V_{i_1}^n\right] - \frac{1}{2}\left[V_i^{n+1} + V_i^n\right]\right). \qquad (4.97)\end{aligned}$$

5. Return to Step 2 and repeat until the simulation is completed.

The time centred differencing used in (4.95) and (4.96) to approximate the Coriolis terms is made possible by reason of the calculation of first the U velocity value and then the V velocity value in each computational element as the scheme sweeps across each row of elements from left to right and down the rows from top to bottom. Thus in (4.95) the values $V_{i_1}^{n+1}$ and $V_{i_1+1}^{n+1}$ are known at the time of calculation of U_i^{n+1}, and the values U_{i-1}^{n+1} and U_i^{n+1} are available for the time centred Coriolis approximation in (4.96).

As in Section 4.2.1, the second elevation calculation does not contribute to the overall finite difference solution for the ζ, U and V fields, but is included in order to give elevation results at the same time levels as the velocity results and to check the accuracy of the second elevation calculation.

The accuracy of the overall scheme (4.94)–(4.97) can be checked by numerical experiments using parameters representative of the region being studied and by investigating the wave propagation characteristics of the scheme.

4.4.1 Numerical tests

Introducing the dimensionless variables

$$x^* = x/L, \quad y^* = y/B, \quad t^* = t/T, \quad \zeta^* = \zeta/\zeta_0, \quad U^* = U/U_0 \quad \text{and} \quad V^* = V/V_0, \quad (4.98)$$

where L is the length of the bay, B is its breadth, T is the period of oscillation, ζ_0 is the input amplitude, $U_0 = g\zeta_0 T/L$ is a characteristic value of horizontal velocity in the x direction and $V_0 = g\zeta_0 T/B$ is a characteristic horizontal velocity in the y direction,

equations (4.88)–(4.90) become:

$$\frac{\partial \zeta^*}{\partial t^*} = -\alpha_0^2 \frac{\partial U^*}{\partial x^*} - \beta_0^2 \frac{\partial V^*}{\partial y^*}, \tag{4.99}$$

$$\frac{\partial U^*}{\partial t^*} - \left(\frac{L}{B}\right) FV^* = -\frac{\partial \zeta^*}{\partial x*} - KU^*, \tag{4.100}$$

$$\frac{\partial V^*}{\partial t^*} + \left(\frac{B}{L}\right) FU^* = -\frac{\partial \zeta^*}{\partial y*} - KV^*, \tag{4.101}$$

where $\alpha_0 = T\sqrt{gh_0}/L$ is the ratio of wavelength to length of the bay, $\beta_0 = T\sqrt{gh_0}/B$ is the ratio of wavelength to breadth of the bay, $K = (k/h_0)T$ is a constituent friction number and $F = fT$ is a constituent Coriolis number. The dimensionless numbers α_0, β_0, K and F, together with the ratio ζ_0/h_0, summarize the physical properties of the problem.

In the context of numerical testing, it is the Coriolis term which is of most interest here. Coriolis force is most influential in the expansive southern half of Spencer Gulf, where tidal flow is less constrained by coastal topography and the bottom bathymetry is relatively smooth (see Chapter 5). This region is approximately square, so for convenience an area of dimension $L \times B = 114300\,\mathrm{m} \times 114300\,\mathrm{m}$, consisting of 400 coarse grid elements (of individual size $5715\,\mathrm{m} \times 5715\,\mathrm{m}$), will be used as the test region. Writing $L = B = S$ simplifies equations (4.99)–(4.101) and reduces the set of effective dimensionless numbers to three, viz. α_0, K and F.

Furthermore, adopting square elements with sides $2\Delta x = 2\Delta y = 2\Delta s$, we may define

$$N_S = \frac{S}{2\Delta s} = \text{number of grid spacings in the side } S \tag{4.102}$$

of the square test region.

The length of the bay is measured from a velocity point at the head of the bay to a similar velocity point just beyond the open boundary. In the numerical tests, therefore, tidal forcing is supplied along the line of elevation gridpoints to the left of the open boundary of the numerical model, such as is depicted in Figure 4.8.

Defining the number of grid spacings per wavelength as

$$N_\lambda = \frac{\lambda}{2\Delta s}, \tag{4.103}$$

α_0 can be written as

$$\alpha_0 = \frac{T\sqrt{gh_0}}{S} = \frac{\lambda}{S} = \left(\frac{\lambda}{2\Delta s}\right) \Big/ \left(\frac{S}{2\Delta s}\right) = \frac{N_\lambda}{N_S}, \tag{4.104}$$

for a square region made up of square elements. The Courant number C_r is defined as

$$C_r = \frac{\Delta t\sqrt{gh_0}}{\sqrt{(2\Delta x)^2 + (2\Delta y)^2}} = \frac{\Delta t\sqrt{gh_0}}{2\Delta s\sqrt{2}}. \tag{4.105}$$

The dimensionless numbers N_λ, N_S and C_r summarize the aspects of numerical solution of the problem.

The average depth of the test region is about 30 m. Using the semi-diurnal period of 12 hr, this suggests a value for α_0^2 of about 40. For convenience, the value of h_0 is taken as

$$h_0 = \frac{40.5}{g}\left(\frac{114300}{43200}\right)^2 \simeq 28.9\,\mathrm{m}, \tag{4.106}$$

which sets $\alpha_0 = \sqrt{40.5}$ and gives the relationship

$$N_\lambda = 4.5\sqrt{2}\, N_S\,. \tag{4.107}$$

For a given value of Courant number C_r, the value of time step Δt is obtained from

$$\Delta t = \sqrt{2}(2\Delta s)\frac{C_r}{\sqrt{gh_0}} = \frac{\sqrt{2}\,C_r\,T}{N_\lambda} = \frac{C_r\,T}{4.5N_S}\,, \tag{4.108}$$

and so the number of time steps per period is

$$N_T = \frac{T}{\Delta t} = \frac{4.5N_S}{C_r}\,. \tag{4.109}$$

For the values $C_r = 0.15$ and $C_r = 0.45$, N_T is an integer as required by the error measure of Section 4.2.2. Since the operating average value of C_r is 0.3 for the Gulf models, these choices of C_r for the present tests provide a useful range of values.

For the semi-diurnal tests, an appropriate value for the constituent friction number is $K = 1.5$. This sets $k \simeq 0.0011\,\mathrm{m/sec}$ which is close to the optimal value of the linear coefficient of friction for the linear Spencer Gulf model of Chapter 5. Since the present test basin lies on about latitude $\Phi = -34°\,\mathrm{S}$, an appropriate value for the constituent Coriolis number is $F = -3.5$.

Figure 4.9 shows the error curves obtained for both semi-diurnal and quad-diurnal tests using Courant numbers $C_r = 0.15$ and $C_r = 0.45$. Curves for diurnal tests lie between these and since the three sets are not easily distinguished, they have been omitted.

At the operating values of N_λ given for each constituent, the percentage errors ε^*_ζ to two decimal places are:

(1) diurnal ($N_\lambda \simeq 255$) — at C_x=0.45, ε^*_ζ=0.03%

(2) semi-diurnal ($N_\lambda \simeq 127$) — at C_x=0.45, ε^*_ζ=0.04%

(3) quad-diurnal ($N_\lambda \simeq 64$) — at C_x=0.45, ε^*_ζ=0.16%; at C_x=0.15, ε^*_ζ=0.20%

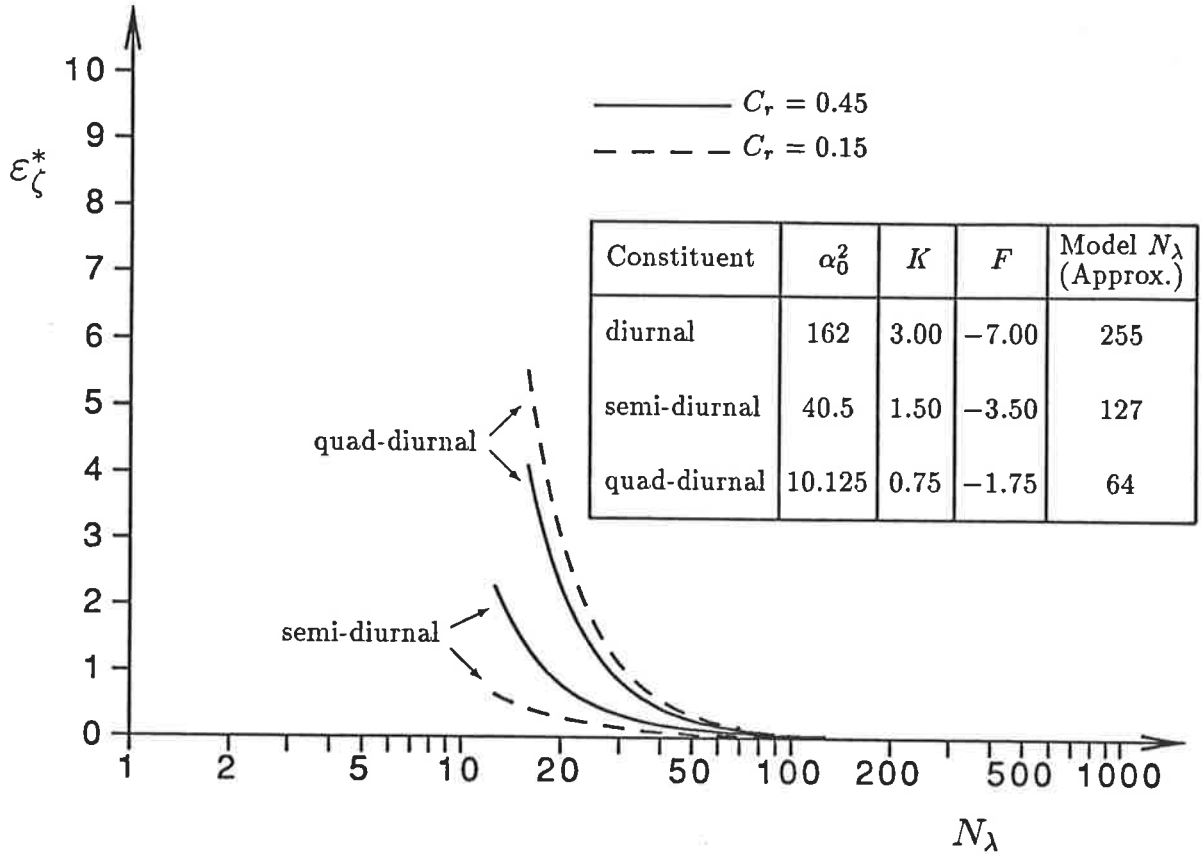
The corresponding dimensional errors are calculated using $\varepsilon_\zeta = \varepsilon^*_\zeta \times 0.75/100\,\mathrm{m}$ and for each constituent are at least twice as large as the associated dimensional velocity errors. At the operational values of N_λ, both diurnal and semi-diurnal constituents are propagated with high accuracy.

4.4.2 Wave propagation characteristics

The derivation of wave propagation characteristics outlined in Section 4.2.3 is now applied to the finite difference system (4.94)–(4.97).

Although the input wave in the bounded case is uni-directional at the open boundary, it is rotated by the Coriolis force in the body of the bay, and so in order to generalize the present analysis, the pth (say) Fourier component travelling at an angle θ to the positive x direction (defined as $\theta = 0°$) at the ith element is considered. If the wavenumber of this component is k_p, the components of real wavenumber in the x and y directions are

$$k_x = k_p \cos\theta \quad \text{and} \quad k_y = k_p \sin\theta\,. \tag{4.110}$$



Constituent	α_0^2	K	F	Model N_λ (Approx.)
diurnal	162	3.00	−7.00	255
semi-diurnal	40.5	1.50	−3.50	127
quad-diurnal	10.125	0.75	−1.75	64

Figure 4.9: *Percentage error in dimensionless elevation ε^*_ζ versus number of grid spacings per wavelength N_λ for constant depth rectangular bay model tests using semi-diurnal and quad-diurnal constituents. Curves for the diurnal wave overlay the plotted curves and so are not given. The table shows the values used for α_0^2, K and F for each wave, along with the corresponding operating value of N_λ for the coarse grid model of the southern Spencer Gulf region, which uses $N_S = 20$. For each wave, the input amplitude is $\zeta_0 = 0.75$ m and curves for two values of Courant number C_r are shown.*

Thus solutions to (4.94)–(4.97) of the form

$$\zeta_i^n = \zeta_a \exp\{\imath(k_t n\Delta t + k_x i2\Delta x + k_y i2\Delta y)\}, \quad (4.111)$$

$$U_i^n = U_a \exp\{\imath(k_t n\Delta t + k_x i2\Delta x + k_y i2\Delta y)\}, \quad (4.112)$$

$$V_i^n = V_a \exp\{\imath(k_t n\Delta t + k_x i2\Delta x + k_y i2\Delta y)\}, \quad (4.113)$$

$$Z_i^n = Z_a \exp\{\imath(k_t n\Delta t + k_x i2\Delta x + k_y i2\Delta y)\}, \quad (4.114)$$

are sought, where ζ_a, U_a, V_a and Z_a are the (possibly complex) amplitudes of the component, which has complex frequency k_t. ζ_a is the amplitude of the solution for elevation at the first elevation calculation (4.94) and Z_a is the amplitude of the solution for elevation at the second elevation calculation (4.97). Note that i here specifies the ith computational element and hence correctly situates both the x and y components of the position of the element.

Substituting (4.111)–(4.114) into (4.94)–(4.97) leads to the following determinant equa-

UNIVERSITY OF ADELAIDE LIBRARY

tion, which is valid for rectangular elements, and from which solutions for ξ can be obtained:

$$\begin{vmatrix} \xi-1 & \sqrt{\xi}\,2\imath r_x h_0 \sin(k_x\Delta x) & \sqrt{\xi}\,2\imath r_y h_0 \sin(k_y\Delta y) & 0 \\ \sqrt{\xi}2\imath g r_x \sin(k_x\Delta x) & \xi\left(1+\frac{k\Delta t}{2h_0}\right)-\left(1-\frac{k\Delta t}{2h_0}\right) & -\frac{f\Delta t}{2}\cos(k_x\Delta x)\left(\xi e^{\imath k_y\Delta y}+e^{-\imath k_y\Delta y}\right) & 0 \\ \sqrt{\xi}2\imath g r_y \sin(k_y\Delta y) & \frac{f\Delta t}{2}\cos(k_x\Delta x)\left(\xi e^{\imath k_y\Delta y}+e^{-\imath k_y\Delta y}\right) & \xi\left(1+\frac{k\Delta t}{2h_0}\right)-\left(1-\frac{k\Delta t}{2h_0}\right) & 0 \\ 0 & r_x h_0(1+\xi)\imath \sin(k_x\Delta x) & r_y h_0(1+\xi)\imath \sin(k_y\Delta y) & \xi-1 \end{vmatrix} = 0,$$

where $\xi = \exp(\imath k_t \Delta t)$, $r_x = \Delta t/(2\Delta x)$ and $r_y = \Delta t/(2\Delta y)$. Expanding the determinant down the fourth column immediately gives the solution $\xi = 1$ which, as in Section 4.2.3, indicates that equation (4.97) does not influence the overall stability of the system (4.94)–(4.97), a consequence of the fact that (4.97) is not needed to solve equations (4.88)–(4.90), since (4.88) is linear.

The critical solutions for ξ are therefore the solutions of the following cubic equation

$$\begin{aligned}
&\xi^3\left[\left(1+\frac{1}{\sqrt{2}}\frac{C_r}{N_\lambda}K\right)^2+\left(\frac{1}{\sqrt{2}}\frac{C_r}{N_\lambda}F\cos\left\{\frac{\pi}{N_\lambda}\cos\theta\right\}\right)^2\exp\left\{\imath\frac{2\pi}{N_\lambda}\sin\theta\right\}\right] \\
&+\xi^2\left[\left(\frac{1}{\sqrt{2}}\frac{C_r}{N_\lambda}F\cos\left\{\frac{\pi}{N_\lambda}\cos\theta\right\}\right)^2\left(2-\exp\left\{\imath\frac{2\pi}{N_\lambda}\sin\theta\right\}\right)-\left(1+\frac{1}{\sqrt{2}}\frac{C_r}{N_\lambda}K\right)\left(3-\frac{1}{\sqrt{2}}\frac{C_r}{N_\lambda}K\right)\right. \\
&\left.+8C_r^2\left(\sin^2\left\{\frac{\pi}{N_\lambda}\cos\theta\right\}+\sin^2\left\{\frac{\pi}{N_\lambda}\sin\theta\right\}\right)\left(1+\frac{1}{\sqrt{2}}\frac{C_r}{N_\lambda}K\right)\right] \\
&+\xi\left[\left(\frac{1}{\sqrt{2}}\frac{C_r}{N_\lambda}F\cos\left\{\frac{\pi}{N_\lambda}\cos\theta\right\}\right)^2\left(\exp\left\{-\imath\frac{2\pi}{N_\lambda}\sin\theta\right\}-2\right)+\left(1-\frac{1}{\sqrt{2}}\frac{C_r}{N_\lambda}K\right)\left(3+\frac{1}{\sqrt{2}}\frac{C_r}{N_\lambda}K\right)\right. \\
&\left.-8C_r^2\left(\sin^2\left\{\frac{\pi}{N_\lambda}\cos\theta\right\}+\sin^2\left\{\frac{\pi}{N_\lambda}\sin\theta\right\}\right)\left(1-\frac{1}{\sqrt{2}}\frac{C_r}{N_\lambda}K\right)\right] \\
&-\left[\left(1-\frac{1}{\sqrt{2}}\frac{C_r}{N_\lambda}K\right)^2+\left(\frac{1}{\sqrt{2}}\frac{C_r}{N_\lambda}F\cos\left\{\frac{\pi}{N_\lambda}\cos\theta\right\}\right)^2\exp\left\{-\imath\frac{2\pi}{N_\lambda}\sin\theta\right\}\right]=0\,, \qquad (4.115)
\end{aligned}$$

where the expression has been simplified by considering only square elements, so that $r_x = r_y = r$, and the following substitutions have been made:

$$r^2 g h_0 = 2C_r^2, \quad \frac{k\Delta t}{2h_0} = \frac{1}{\sqrt{2}}\frac{C_r}{N_\lambda}K, \quad \frac{f\Delta t}{2} = \frac{1}{\sqrt{2}}\frac{C_r}{N_\lambda}F\,, \qquad (4.116)$$

and

$$k_x\Delta s = k_p\Delta s\cos\theta = \frac{\pi}{N_\lambda}\cos\theta\,, \quad k_y\Delta s = k_p\Delta s\sin\theta = \frac{\pi}{N_\lambda}\sin\theta\,. \qquad (4.117)$$

Courant number C_r, friction number K, Coriolis number F and grid spacings per wavelength N_λ are defined in the present context as

$$C_r = \frac{\sqrt{gh_0}\Delta t}{\sqrt{(2\Delta x)^2+(2\Delta y)^2}} = \frac{\sqrt{gh_0}\Delta t}{2\Delta s\sqrt{2}},\ K = T\frac{k}{h_0},\ F = Tf \text{ and } N_\lambda = \frac{\pi}{k_p\Delta s}. \qquad (4.118)$$

Given values for C_r, K, F, N_λ and an angle of incidence θ, solutions for ξ may be obtained. The numerical scheme (4.94)–(4.96) is stable if for every ξ, $|\xi| \le 1$.

To determine the accuracy of the answers generated by the numerical scheme, solutions of equations (4.88)–(4.90) analogous to (4.111)–(4.113) are developed, against which a comparison can be made. Thus true wave solutions of the form

$$\widehat{\zeta} = \zeta_a \exp\left\{\imath\left(\widehat{k}_t t + k_x x + k_y y\right)\right\}, \tag{4.119}$$

$$\widehat{U} = U_a \exp\left\{\imath\left(\widehat{k}_t t + k_x x + k_y y\right)\right\}, \tag{4.120}$$

$$\widehat{V} = V_a \exp\left\{\imath\left(\widehat{k}_t t + k_x x + k_y y\right)\right\}, \tag{4.121}$$

are sought. The amplitudes ζ_a, U_a and V_a, and the wavenumbers k_x and k_y are as before, and $\widehat{k}_t$ is the complex frequency of the true wave.

Substitution of (4.119)–(4.121) into (4.88)–(4.90) leads to the following determinant equation in $\widehat{k}_t$:

$$\begin{vmatrix} \widehat{k}_t & h_0 k_x & h_0 k_y \\ g k_x & \widehat{k}_t - \imath\frac{k}{h_0} & \imath f \\ g k_y & -\imath f & \widehat{k}_t - \imath\frac{k}{h_0} \end{vmatrix} = 0\,. \tag{4.122}$$

This in turn yields the cubic equation

$$\left(\widehat{k}_t\right)^3 - \left(\widehat{k}_t\right)^2 2\imath\left(\frac{k}{h_0}\right) - \widehat{k}_t\left[\left(\frac{k}{h_0}\right)^2 + f^2 + \sigma^2\right] + \imath\sigma^2\left(\frac{k}{h_0}\right) = 0\,, \tag{4.123}$$

where the following substitution has been made:

$$g h_0 k_p^2 = \sigma^2\,. \tag{4.124}$$

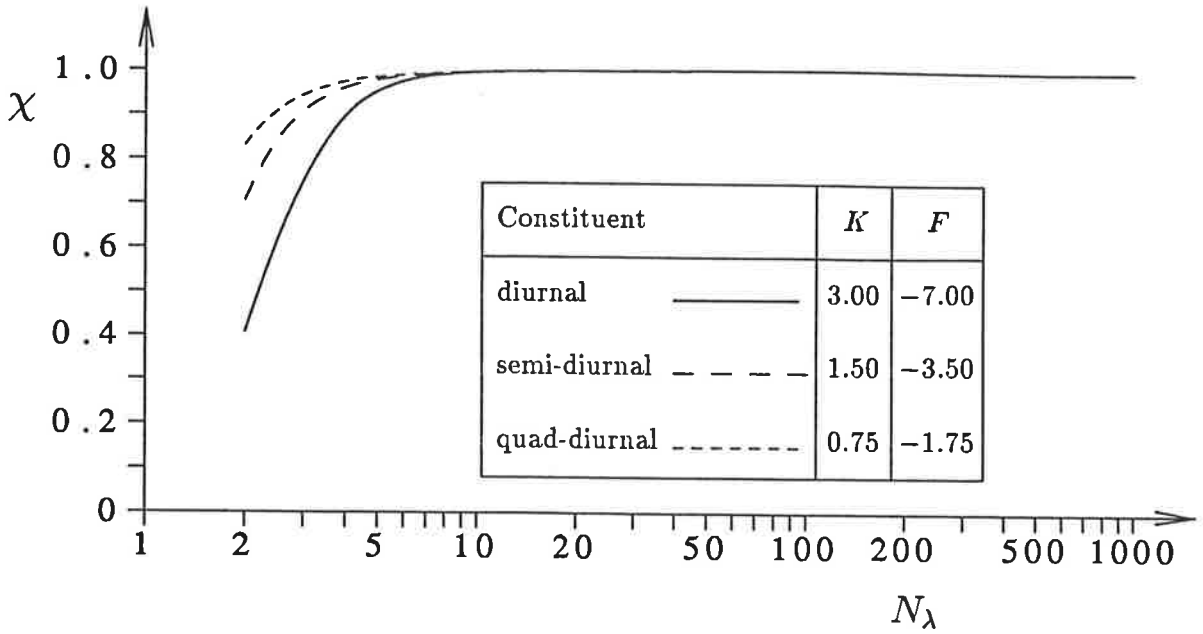
From (4.123) it can be seen that the complex frequency of the true wave solution is independent of the direction of propagation of the Fourier component.

Figures 4.10(a),(b), 4.11(a),(b) and 4.12(a),(b) show the propagation characteristics of diurnal, semi-diurnal and quad-diurnal waves travelling at angles $\theta = 0°$, $\theta = 30°$ and $\theta = 45°$, respectively, to the x-axis. In all three cases, it is clear that the finite difference scheme gives accurate results at the given operational values of N_λ for each wave; in each case, the diurnal wave is modelled the most accurately and the quad-diurnal the least. For increasing angle of incidence, amplitude response is gradually decreased for each constituent, but only slightly, while relative wave speed improves for each constituent.

4.4.3 Wave propagation characteristics for a finite difference scheme used near an open boundary

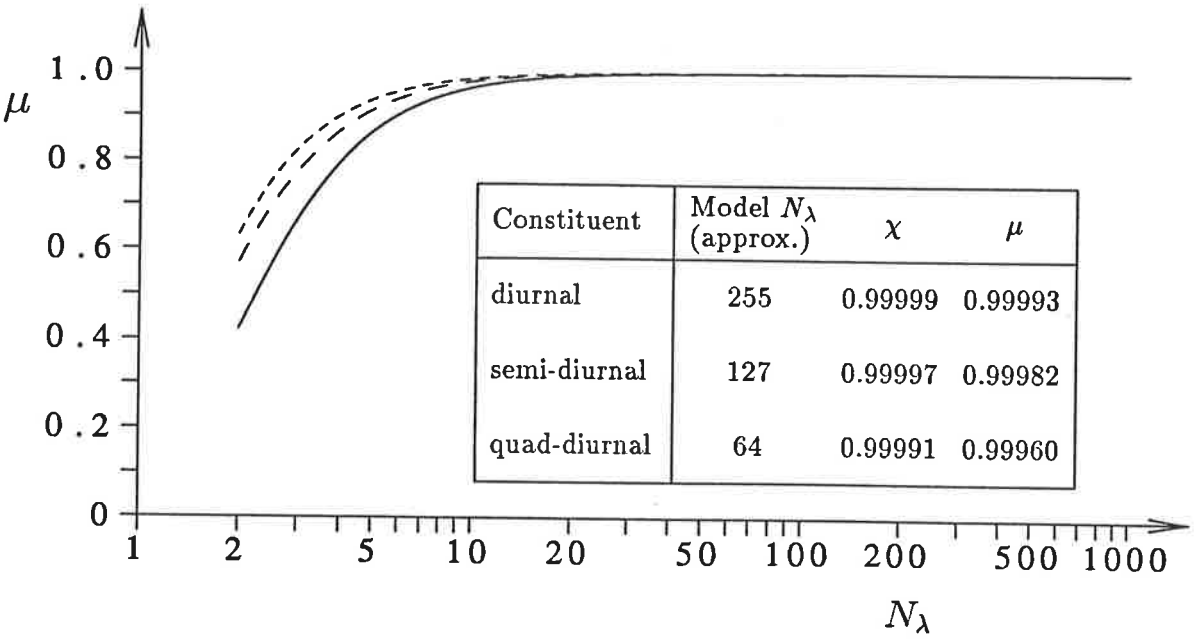
Trapp and Ramshaw (1976) have suggested that the von Neumann stability analysis may be applied to a finite difference scheme used near an open boundary by proceeding as though the boundary scheme applies everywhere in an infinite domain. This is useful in determining the stability of the specific forms of the finite difference expressions used near the boundaries, though it does not lead to the derivation of wave propagation characteristics for a combination of interior and open boundary finite difference expressions.

In the present consideration, the Coriolis effect is included and so various special finite difference forms of the momentum equations are required immediately adjacent to the open boundary. The numerical procedure of Chapter 3 does not incorporate direct calculation



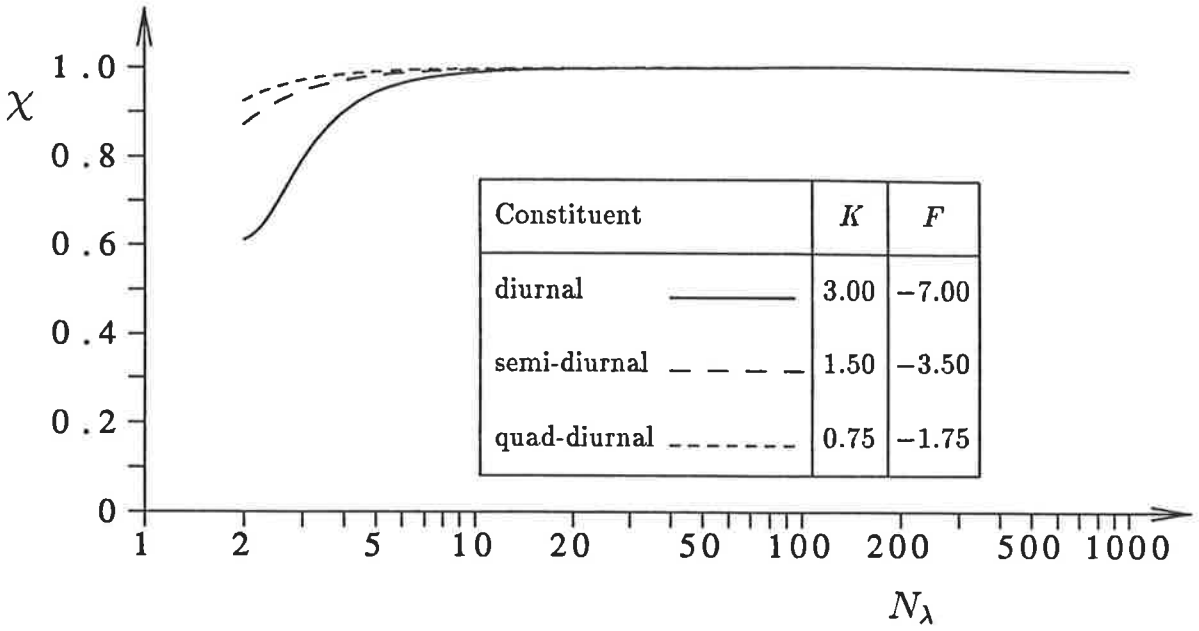
Constituent	K	F
diurnal ———	3.00	−7.00
semi-diurnal — — — —	1.50	−3.50
quad-diurnal -------	0.75	−1.75

Figure 4.10(a): *Amplitude response χ versus number of grid spacings per wavelength N_λ for waves of different frequency propagating along the x-axis ($\theta = 0°$); Courant number is $C_r = 0.3$ and latitude is $\Phi \simeq 34°S$. Curve identification and parameters used are given in the table above. Operational values for χ for each constituent are given in the table below.*



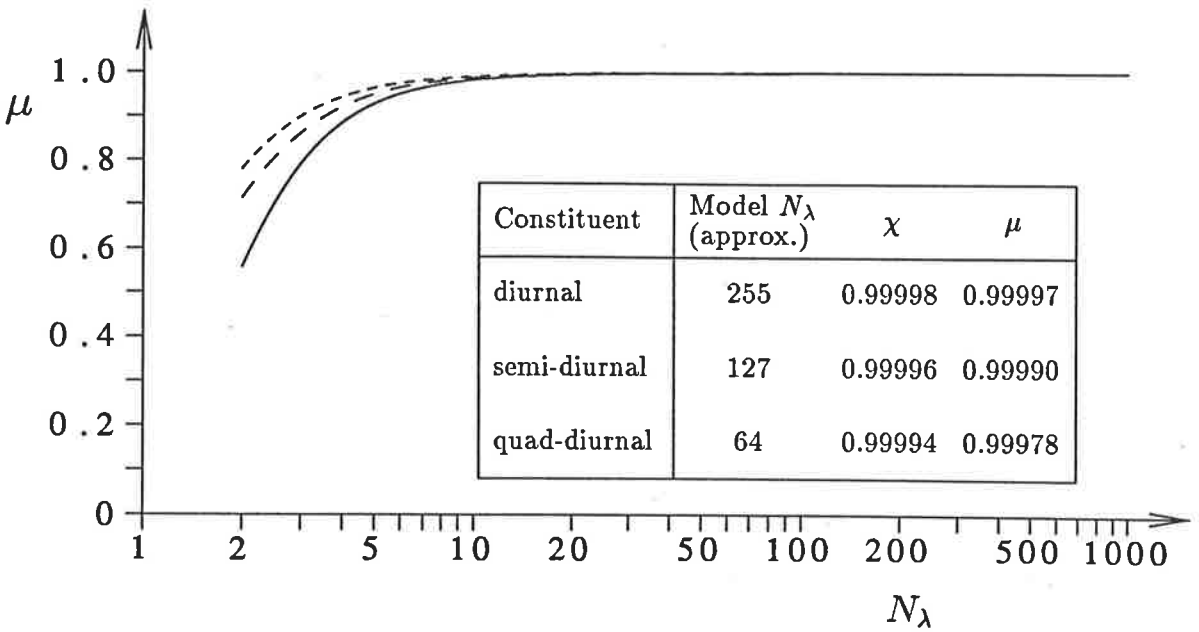
Constituent	Model N_λ (approx.)	χ	μ
diurnal	255	0.99999	0.99993
semi-diurnal	127	0.99997	0.99982
quad-diurnal	64	0.99991	0.99960

Figure 4.10(b): *Relative wave speed μ versus number of grid spacings per wavelength N_λ for waves of different frequency propagating along the x-axis ($\theta = 0°$); Courant number is $C_r = 0.3$ and latitude is $\Phi \simeq 34°S$. Parameter values used are given in the top table and are representative of Southern Spencer Gulf. Operational values for μ for each constituent are given in the table immediately above.*



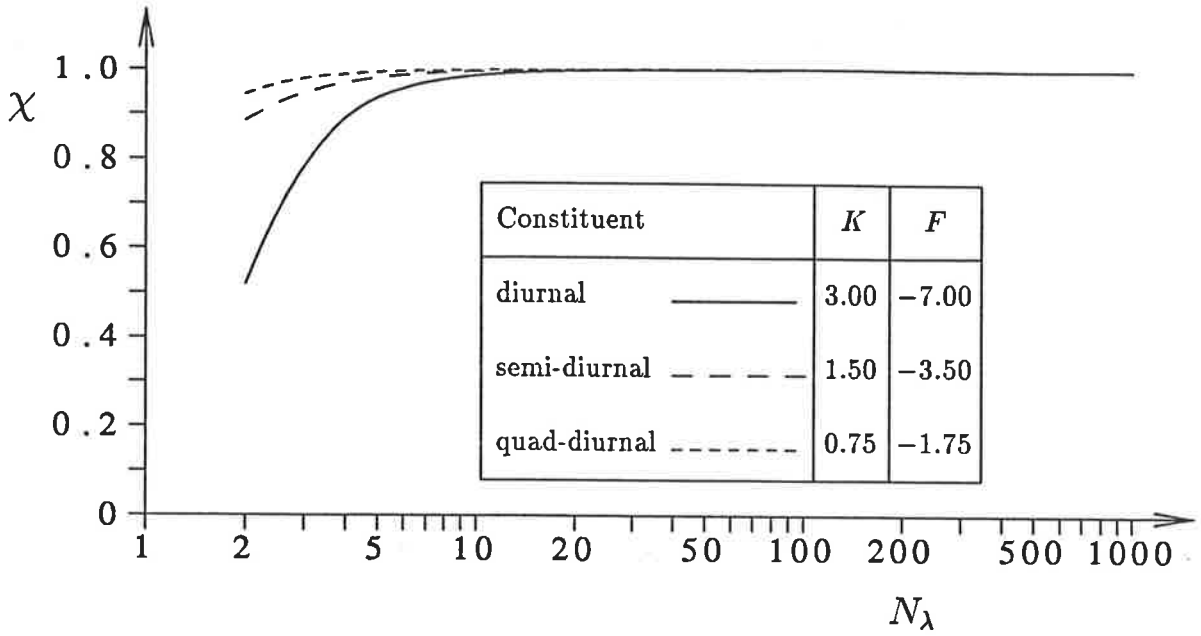
Constituent	K	F
diurnal ———	3.00	−7.00
semi-diurnal — — — —	1.50	−3.50
quad-diurnal -------	0.75	−1.75

Figure 4.11(a): *Amplitude response χ versus number of grid spacings per wavelength N_λ for waves of different frequency propagating obliquely to the x-axis ($\theta = 30°$); Courant number is $C_r = 0.3$ and latitude is $\Phi \simeq 34°S$. Curve identification and parameters used are given in the table above. The initial flattening in the diurnal curve at small N_λ was verified by calculating the amplitude response at intervals of one tenth for $N_\lambda \in [2,4]$. Operational values for χ for each constituent are given in the table below.*



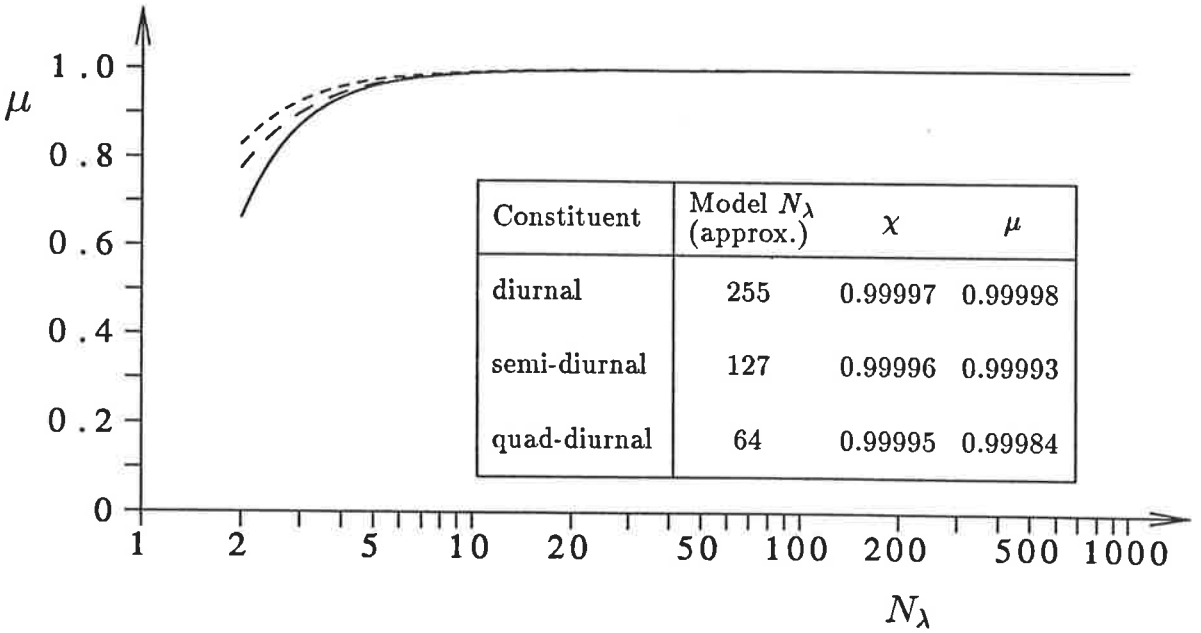
Constituent	Model N_λ (approx.)	χ	μ
diurnal	255	0.99998	0.99997
semi-diurnal	127	0.99996	0.99990
quad-diurnal	64	0.99994	0.99978

Figure 4.11(b): *Relative wave speed μ versus number of grid spacings per wavelength N_λ for waves of different frequency propagating obliquely to the x-axis ($\theta = 30°$); Courant number is $C_r = 0.3$ and latitude is $\Phi \simeq 34°S$. Parameter values used are given in the top table and are representative of Southern Spencer Gulf. Operational values for μ for each constituent are given in the table immediately above.*



Constituent	K	F
diurnal ———	3.00	−7.00
semi-diurnal — — — —	1.50	−3.50
quad-diurnal - - - - - - -	0.75	−1.75

Figure 4.12(a): *Amplitude response χ versus number of grid spacings per wavelength N_λ for waves of different frequency propagating diagonally to the x-axis ($\theta = 45°$); Courant number is $C_r = 0.3$ and latitude is $\Phi \simeq 34°S$. Curve identification and parameter values used are given in the table above. Operational values for χ for each constituent are given in the table below.*



Constituent	Model N_λ (approx.)	χ	μ
diurnal	255	0.99997	0.99998
semi-diurnal	127	0.99996	0.99993
quad-diurnal	64	0.99995	0.99984

Figure 4.12(b): *Relative wave speed μ versus number of grid spacings per wavelength N_λ for waves of different frequency propagating diagonally to the x-axis ($\theta = 45°$); Courant number is $C_r = 0.3$ and latitude is $\Phi \simeq 34°S$. Parameter values used are given in the top table and are representative of Southern Spencer Gulf. Operational values for μ for each constituent are given in the table immediately above.*

of velocities on the open boundary line and such values are found by extrapolation from interior values. Only the approximations for the velocity values in the Coriolis terms require modification.

Figure 4.13 shows the approximations used in the case of open boundaries facing towards the north, south, east and west. In each case, extrapolations from interior points are used to estimate the unknown quantities on the open boundary line. Each expression given is approximately space centred about the starred $(*)$ gridpoint and, apart from the approximation used for the northerly facing open boundary, each expression is time centred.

Using the procedure of Chapter 3, it is not possible to time centre the Coriolis term at a V gridpoint adjacent to a northerly facing open boundary. One way to resolve this is to use an alternating direction sweep procedure for the velocity quantities, but since the Spencer Gulf models do not contain northerly facing open boundaries, this is not an immediate requirement.

Figure 4.14 shows the Coriolis velocity approximations used for U gridpoints adjacent to open boundaries facing the north-west, north-east, south-west and south-east directions. Each of the given expressions is space centred about the starred U gridpoint and each is time centred about the $(n + 1/2)$ time level. Similar diagrams and expressions can be given for the case of V gridpoints adjacent to oblique open boundaries.

The computer expressions used for the Coriolis terms of the U and V momentum equations in a "0–1–2" (open boundary) neighbourhood are single statements capable of automatically generating the appropriate approximation expression for any practical design of open boundary configuration.

To see how this is achieved, consider the task of writing generalized computer code to approximate the Coriolis term

$$f\{U\}_i^{n+\frac{1}{2}} \tag{4.125}$$

of the V momentum equation, where f is constant.

Accompanying the basic approximation expression, given in this case in equation (4.96), are two levels of inner approximation which are activated according to the value of algebraic expressions based on one or more of the associated element codes.

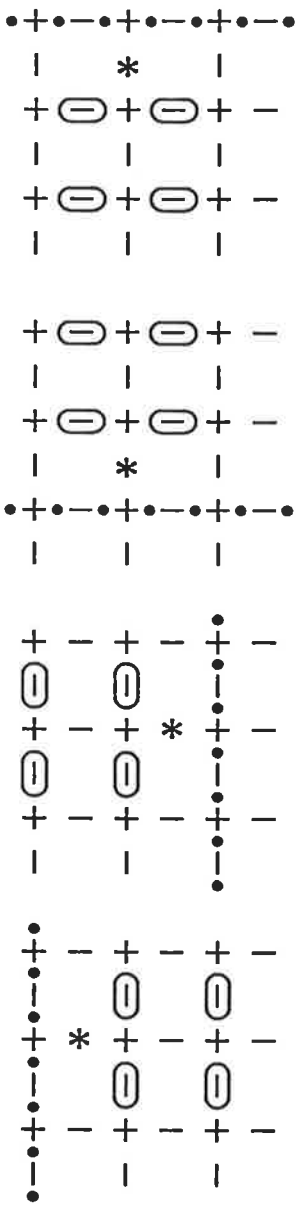
The procedure that invokes the inner levels of approximation is as follows:

- if a U gridpoint of the **basic** approximation expression lies on the open boundary, use a "diagonal" extrapolation to estimate it, where quantities in the row of elements "north" of the starred gridpoint (see, for example, Figures 4.13 and 4.14) are taken at the $(n+1)$th time level and quantities "south" of it are taken at the nth time level, and

- if, in turn, a U gridpoint of the **diagonal** extrapolation lies on the open boundary, use a linear extrapolation to estimate it, with all quantities taken at the nth time level.

Consider the case of the southerly facing open boundary of Figure 4.13. While the basic form of approximation for (4.125) is

$$f\{U\}_i^{n+\frac{1}{2}} \simeq f\left(U_{i-1}^{n+1} + U_i^{n+1} + U_{i_2-1}^n + U_{i_2}^n\right)/4, \tag{4.126}$$



Northerly facing open boundary

$$f\{U\}_i^{n+\frac{1}{2}} \simeq f\left(3U_{i_2-1}^n - U_{i_{22}-1}^n + 3U_{i_2}^n - U_{i_{22}}^n\right)/4$$

Southerly facing open boundary

$$f\{U\}_i^{n+\frac{1}{2}} \simeq f\left(U_{i-1}^{n+1} + U_i^{n+1} + 2U_{i-1}^n - U_{i_1-1}^n + 2U_i^n - U_{i_1}^n\right)/4$$

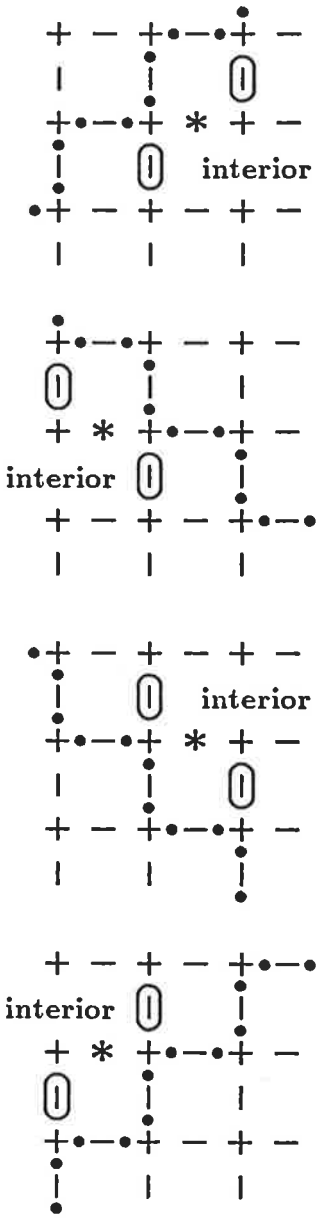
Easterly facing open boundary

$$f\{V\}_i^{n+\frac{1}{2}} \simeq f\left(3V_{i_1}^{n+1} - V_{i_1-1}^{n+1} + 3V_i^n - V_{i-1}^n\right)/4$$

Westerly facing open boundary

$$f\{V\}_i^{n+\frac{1}{2}} \simeq f\left(3V_{i_1+1}^{n+1} - V_{i_1+2}^{n+1} + 3V_{i+1}^n - V_{i+2}^n\right)/4$$

Figure 4.13: *Finite difference approximations used for the Coriolis term of the momentum equation applying at the starred gridpoint in the case of, from top to bottom, open boundaries facing towards the north, south, east and west. Coriolis parameter f is taken as constant. All expressions are approximately space centred about the starred gridpoint and, except for the northerly facing open boundary, all are time centred. Open boundary lines are dotted. The starred velocity gridpoint is labelled the i'th U or V gridpoint in each case and surrounding elements are labelled according to the general pattern, as given in Figure 3.2.*



North-westerly facing open boundary

$$f\{V\}_i^{n+\frac{1}{2}} \simeq f\left(V_{i_1+1}^{n+1} + V_i^n\right)/2$$

North-easterly facing open boundary

$$f\{V\}_i^{n+\frac{1}{2}} \simeq f\left(V_{i_1}^{n+1} + V_{i+1}^n\right)/2$$

South-westerly facing open boundary

$$f\{V\}_i^{n+\frac{1}{2}} \simeq f\left(V_{i_1}^{n+1} + V_{i+1}^n\right)/2$$

South-easterly facing open boundary

$$f\{V\}_i^{n+\frac{1}{2}} \simeq f\left(V_{i_1+1}^{n+1} + V_i^n\right)/2$$

Figure 4.14: *Finite difference approximations used for the Coriolis term of the momentum equation applying at the starred gridpoint in the case of oblique facing open boundaries — from top to bottom, facing north-west, north-east, south-west and south-east. Coriolis parameter f is taken as constant. All expressions are both space and time centred. The starred U gridpoint is labelled the i'th, in each case, and surrounding gridpoints are labelled accordingly. Similar diagrams and expressions may be presented for V gridpoints adjacent to oblique open boundaries.*

gridpoints $U^n_{i_2-1}$ and $U^n_{i_2}$ both lie on the open boundary line. For these two quantities, the next levels of approximation are the "diagonal" extrapolations.

$$U^n_{i_2-1} \simeq U^{n+1}_{i-1} - U^{n+1}_i + U^n_{i_2}, \tag{4.127}$$

$$U^n_{i_2} \simeq U^{n+1}_i - U^{n+1}_{i-1} + U^n_{i_2-1}, \tag{4.128}$$

but in (4.127), the value $U^n_{i_2}$ is unknown while in (4.128), $U^n_{i_2-1}$ is unknown. The innermost levels of approximation are therefore called upon and are, respectively,

$$U^n_{i_2} \simeq 2U^n_i - U^n_{i_1}, \tag{4.129}$$

$$U^n_{i_2-1} \simeq 2U^n_{i-1} - U^n_{i_1-1}, \tag{4.130}$$

where all quantities are taken at the nth time level. Substituting (4.129) into (4.127) and the resulting expression into (4.126) and, similarly, substituting (4.130) into (4.128) and the resulting expression into (4.126), gives the following expression which the computer implements:

$$\begin{aligned} f\{U\}^{n+\frac{1}{2}}_i \simeq\ & f\Big(U^{n+1}_{i-1} + U^{n+1}_i \\ & + U^{n+1}_{i-1} - U^{n+1}_i + (2U^n_i - U^n_{i_1}) \\ & + U^{n+1}_i - U^{n+1}_{i-1} + (2U^n_{i-1} - U^n_{i_1-1})\Big)/4. \end{aligned} \tag{4.131}$$

On simplifying, this becomes

$$f\{U\}^{n+\frac{1}{2}}_i \simeq f\left(U^{n+1}_{i-1} + U^{n+1}_i + 2U^n_{i-1} - U^n_{i_1-1} + 2U^n_i - U^n_{i_1}\right)/4, \tag{4.132}$$

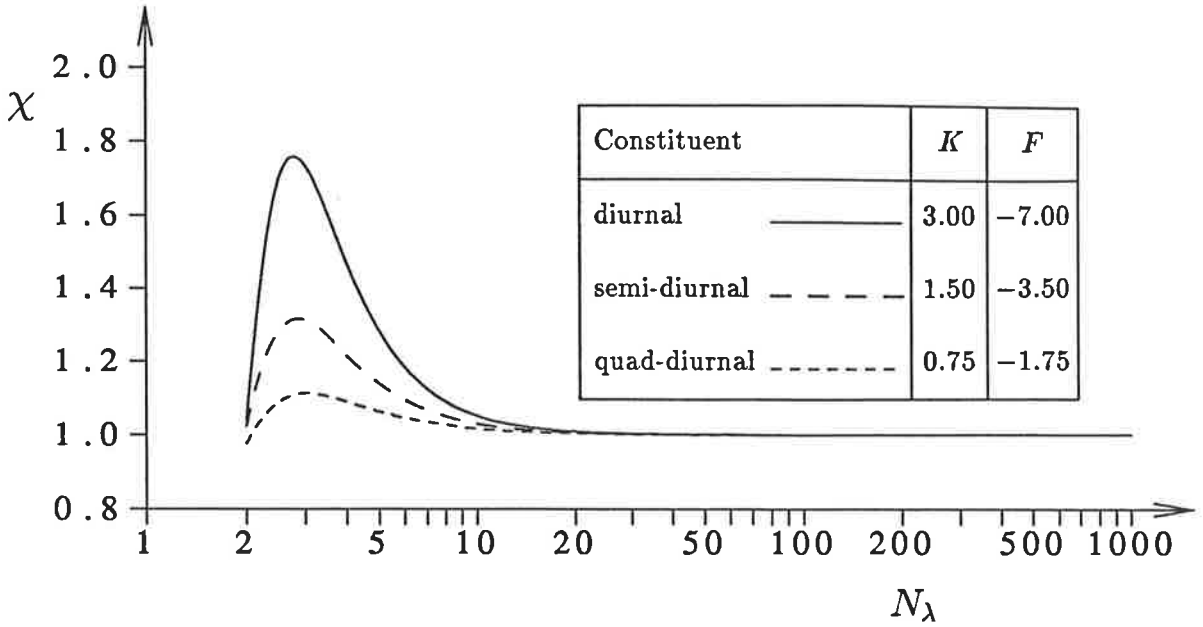
as given in Figure 4.13.

This systematic plan of "levels of approximation within levels of approximation" generates all the expressions of Figures 4.13 and 4.14 as well as the implied expressions for V gridpoints adjacent to oblique open boundaries.

The switches that cause control to pass from the basic level of approximation, typified by expression (4.126), to the diagonal extrapolation level, typified by (4.127) or (4.128), and finally to the linear extrapolation level, typified by (4.129) or (4.130), are composed of the integer element codes used in pairs or alone. Thus in the above example, the gridpoint U_{i_2-1} is flanked by Type 2 elements to its left and to its right. A switch which employs these two pieces of information invokes the diagonal extrapolation (4.127). Associated with the term $U^n_{i_2}$ of (4.127) is a switch which tests whether element i_2 is of Type 0, 1 or 2. In this case it is of Type 2 and so the linear extrapolation (4.129) is used.

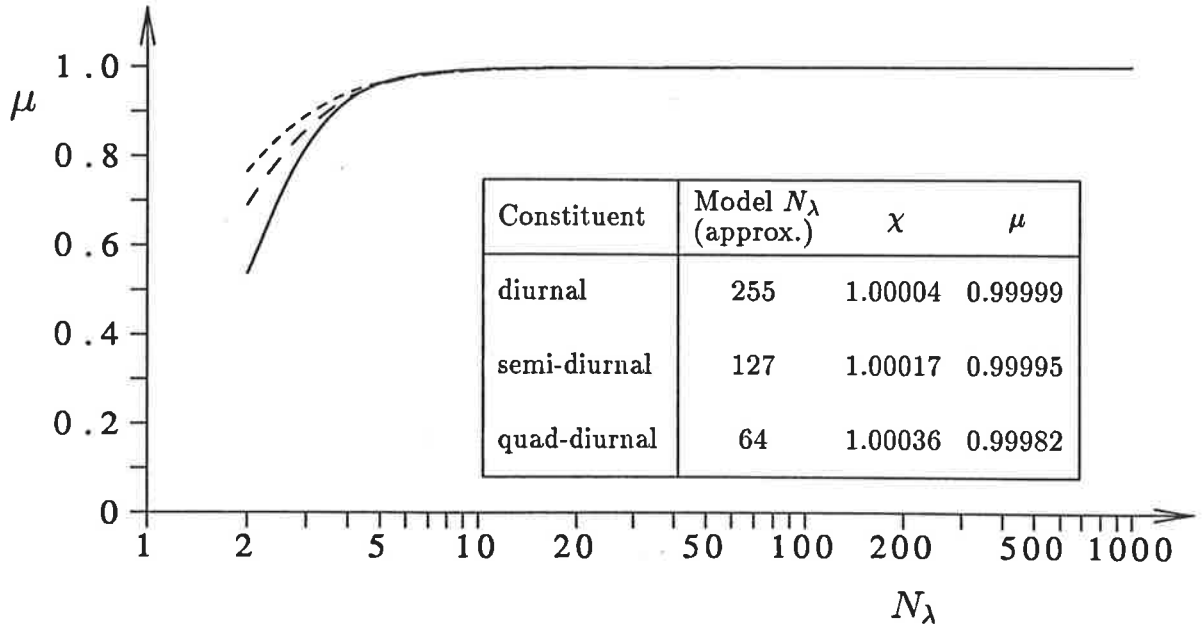
The special finite difference expressions developed here for the velocity factor of the Coriolis terms are also used in approximating the advective terms and, in the two-dimensional case, the quadratic friction terms, but are only calculated once in the program for each horizontal position i, depth level k and time level n.

Returning to the simple linear system (4.88)–(4.90), consider the Trapp and Ramshaw approach to deriving wave propagation characteristics for the finite difference expressions applying to an element adjacent to a southerly facing open boundary, such as is encountered along the open boundaries of the Spencer Gulf models.



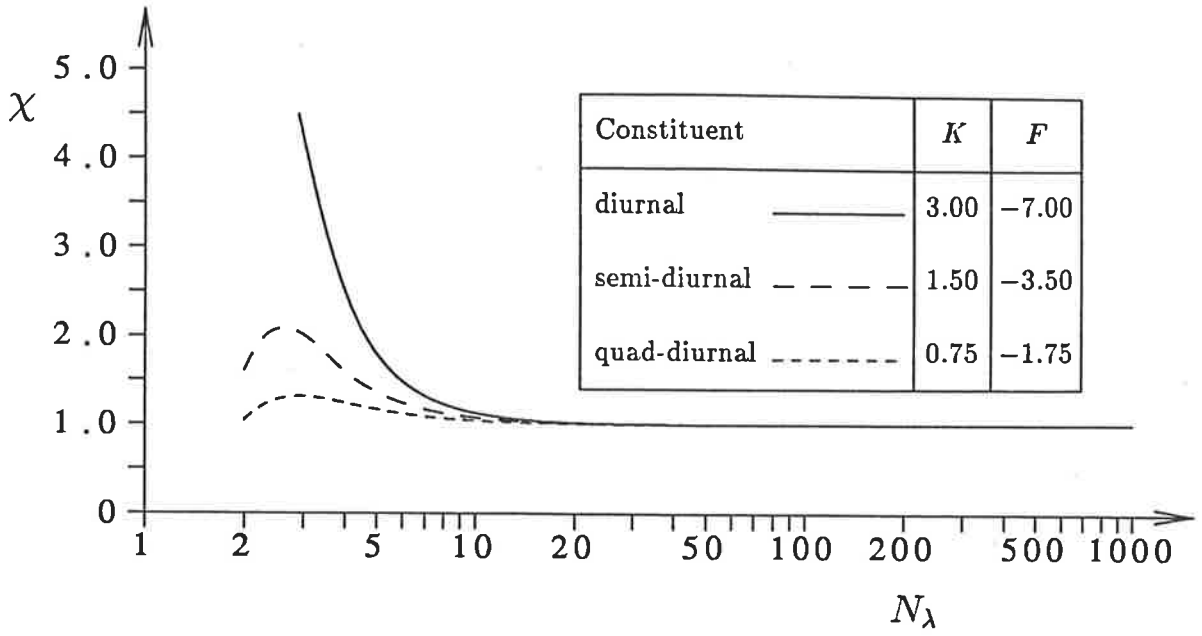
Constituent	K	F
diurnal ———	3.00	−7.00
semi-diurnal – – – –	1.50	−3.50
quad-diurnal - - - - - - -	0.75	−1.75

Figure 4.15(a): *Amplitude response χ versus number of grid spacings per wavelength N_λ for waves of different frequency propagating through the open boundary scheme obliquely to the x-axis ($\theta = 30°$); Courant number is $C_r = 0.3$ and latitude is $\Phi \simeq 34°$ S. Curve identification and parameter values used are given in the table above. Operational values for χ for each constituent are given in the table below.*



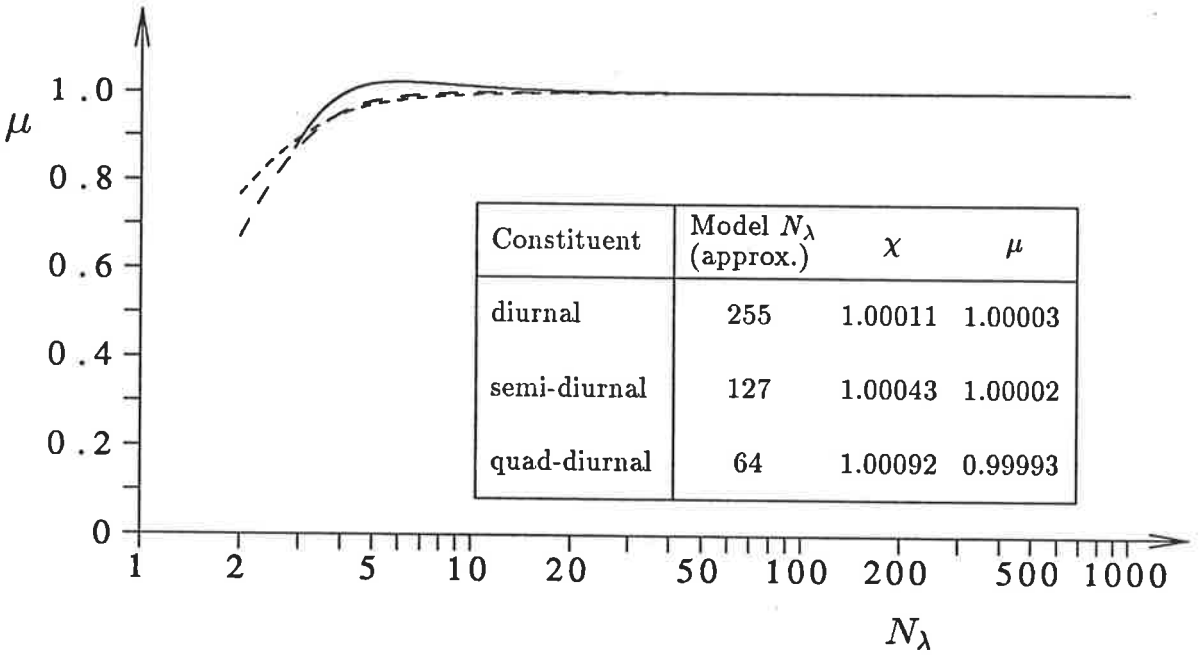
Constituent	Model N_λ (approx.)	χ	μ
diurnal	255	1.00004	0.99999
semi-diurnal	127	1.00017	0.99995
quad-diurnal	64	1.00036	0.99982

Figure 4.15(b): *Relative wave speed μ versus number of grid spacings per wavelength N_λ for waves of different frequency propagating through the open boundary scheme obliquely to the x-axis ($\theta = 30°$); Courant number is $C_r = 0.3$ and latitude is $\Phi \simeq 34°$ S. Parameter values used are given in the top table and are representative of Southern Spencer Gulf. Operational values for μ for each constituent are given in the table immediately above.*



Constituent	K	F
diurnal ———	3.00	−7.00
semi-diurnal – – – –	1.50	−3.50
quad-diurnal - - - - - - -	0.75	−1.75

Figure 4.16(a): *Amplitude response χ versus number of grid spacings per wavelength N_λ for waves of different frequency propagating through the open boundary scheme diagonally to the x-axis ($\theta = 45°$); Courant number is $C_r = 0.3$ and latitude is $\Phi \simeq 34°$ S. Curve identification and parameter values used are given in the table above. Operational values for χ for each constituent are given in the table below.*



Constituent	Model N_λ (approx.)	χ	μ
diurnal	255	1.00011	1.00003
semi-diurnal	127	1.00043	1.00002
quad-diurnal	64	1.00092	0.99993

Figure 4.16(b): *Relative wave speed μ versus number of grid spacings per wavelength N_λ for waves of different frequency propagating through the open boundary scheme diagonally to the x-axis ($\theta = 45°$); Courant number is $C_r = 0.3$ and latitude is $\Phi \simeq 34°$ S. Parameter values used are given in the top table and are representative of Southern Spencer Gulf. Operational values for μ for each constituent are given in the table immediately above.*

By inspection, only expression (4.96) of the finite difference scheme (4.94)–(4.96) is altered. It becomes

$$\begin{aligned}\frac{V_i^{n+1}-V_i^n}{\Delta t} &+ \frac{f}{4}\left(U_{i-1}^{n+1}+U_i^{n+1}+2U_{i-1}^n-U_{i_1-1}^n+2U_i^n-U_{i_1}^n\right)\\ &= -g\left(\frac{\zeta_i^{n+\frac{1}{2}}-\zeta_{i_2}^{n+\frac{1}{2}}}{2\Delta y}\right)-\frac{k}{2h_0}\left(V_i^{n+1}+V_i^n\right),\end{aligned}\tag{4.133}$$

where the Coriolis parameter f is taken as constant. Substituting (4.111)–(4.113) into (4.94), (4.95) and (4.133) leads to the new determinant equation:

$$\begin{vmatrix} \xi-1 & \sqrt{\xi}\,2\imath r_x h_0\sin(k_x\Delta x) & \sqrt{\xi}\,2\imath r_y h_0\sin(k_y\Delta y)\\ \sqrt{\xi}2\imath g r_x\sin(k_x\Delta x) & \xi\left(1+\frac{k\Delta t}{2h_0}\right)-\left(1-\frac{k\Delta t}{2h_0}\right) & -\frac{f\Delta t}{2}\cos(k_x\Delta x)\left(\xi e^{\imath k_y\Delta y}+e^{-\imath k_y\Delta y}\right)\\ \sqrt{\xi}2\imath g r_y\sin(k_y\Delta y) & \frac{f\Delta t}{2}\cos(k_x\Delta x)e^{\imath k_y\Delta y}\left(\xi+2-e^{2\imath k_y\Delta y}\right) & \xi\left(1+\frac{k\Delta t}{2h_0}\right)-\left(1-\frac{k\Delta t}{2h_0}\right)\end{vmatrix}=0.$$

Again, considering only square elements and making the substitutions (4.116)–(4.117), the critical solutions for ξ are found to be the solutions of the cubic equation:

$$\begin{aligned}&\xi^3\left[\left(1+\frac{1}{\sqrt{2}}\frac{C_r}{N_\lambda}K\right)^2+\left(\frac{1}{\sqrt{2}}\frac{C_r}{N_\lambda}F\cos\left\{\frac{\pi}{N_\lambda}\cos\theta\right\}\right)^2\exp\left\{\imath\frac{2\pi}{N_\lambda}\sin\theta\right\}\right]\\
&+\xi^2\left[-\left(1+\frac{1}{\sqrt{2}}\frac{C_r}{N_\lambda}K\right)\left(3-\frac{1}{\sqrt{2}}\frac{C_r}{N_\lambda}K\right)\right.\\
&\quad+\left(\frac{1}{\sqrt{2}}\frac{C_r}{N_\lambda}F\cos\left\{\frac{\pi}{N_\lambda}\cos\theta\right\}\right)^2\left(1+\exp\left\{\imath\frac{2\pi}{N_\lambda}\sin\theta\right\}-\exp\left\{\imath\frac{4\pi}{N_\lambda}\sin\theta\right\}\right)\\
&\quad\left.+8C_r^2\left(\sin^2\left\{\frac{\pi}{N_\lambda}\cos\theta\right\}+\sin^2\left\{\frac{\pi}{N_\lambda}\sin\theta\right\}\right)\left(1+\frac{1}{\sqrt{2}}\frac{C_r}{N_\lambda}K\right)\right]\\
&+\xi\left[\left(1-\frac{1}{\sqrt{2}}\frac{C_r}{N_\lambda}K\right)\left(3+\frac{1}{\sqrt{2}}\frac{C_r}{N_\lambda}K\right)\right.\\
&\quad+\left(\frac{1}{\sqrt{2}}\frac{C_r}{N_\lambda}F\cos\left\{\frac{\pi}{N_\lambda}\cos\theta\right\}\right)^2\left(1-3\exp\left\{\imath\frac{2\pi}{N_\lambda}\sin\theta\right\}+\exp\left\{\imath\frac{4\pi}{N_\lambda}\sin\theta\right\}\right)\\
&\quad\left.-8C_r^2\left(\sin^2\left\{\frac{\pi}{N_\lambda}\cos\theta\right\}+\sin^2\left\{\frac{\pi}{N_\lambda}\sin\theta\right\}\right)\left(1-\frac{1}{\sqrt{2}}\frac{C_r}{N_\lambda}K\right)\right]\\
&+2\sqrt{2}\frac{C_r^3}{N_\lambda}F\sin\left\{\frac{2\pi}{N_\lambda}\cos\theta\right\}\sin\left\{\frac{\pi}{N_\lambda}\sin\theta\right\}\\
&\quad\left(\exp\left\{-\imath\frac{\pi}{N_\lambda}\sin\theta\right\}-2\exp\left\{\imath\frac{\pi}{N_\lambda}\sin\theta\right\}+\exp\left\{\imath\frac{3\pi}{N_\lambda}\sin\theta\right\}\right)\Big]\\
&-\left[\left(1-\frac{1}{\sqrt{2}}\frac{C_r}{N_\lambda}K\right)^2+\left(\frac{1}{\sqrt{2}}\frac{C_r}{N_\lambda}F\cos\left\{\frac{\pi}{N_\lambda}\cos\theta\right\}\right)^2\left(2-\exp\left\{\imath\frac{2\pi}{N_\lambda}\sin\theta\right\}\right)\right]=0,\end{aligned}$$

The true wave solutions are the same as those developed in the previous section, viz. the solutions of the cubic equation (4.123).

Wave propagation characteristics have been plotted for waves of diurnal, semi-diurnal and quad-diurnal frequency with values of the friction and Coriolis parameters used before. For waves travelling at $\theta = 0°$ to the x-axis, the characteristics are identical to those

of Figures 4.10(a),(b), as is readily seen by substituting $\theta = 0°$ into the respective determinants and comparing them. Figures 4.15(a),(b) and 4.16(a),(b) show the characteristics for waves travelling at angles $\theta = 30°$ and $\theta = 45°$ to the x-axis, respectively. Comparing Figures 4.11 and 4.15, it is immediately apparent that while the interior finite difference expressions propagate the waves with attenuated amplitude, the boundary finite difference scheme generally amplifies the signal for the same value of N_λ; relative wave speed is slightly less diminished by the boundary difference scheme compared with the interior scheme. Comparing Figures 4.12 and 4.16, the tendency for the open boundary scheme to amplify the signal is even more marked for the case $\theta = 45°$; the boundary difference scheme also tends to increase the wave speed of the diurnal and semi-diurnal constituents.

Overall, the boundary scheme performs well at the given operating values of N_λ for each wave, and in this sense seems to be compatible with the interior scheme.

4.5 Johns' vertical and horizontal linear solution

Johns (1966) presents a solution to the linearized shallow water equations

$$\frac{\partial \zeta}{\partial t} = -\frac{\partial}{\partial x}\int_{-h_0}^{0} u\,dz, \tag{4.134}$$

$$\frac{\partial u}{\partial t} = -g\frac{\partial \zeta}{\partial x} + \frac{\partial}{\partial z}\left(N_z \frac{\partial u}{\partial z}\right), \tag{4.135}$$

where the vertical eddy viscosity coefficient N_z has the parabolic form (see Figure 4.17):

$$N_z = \gamma_1 \{1 + \gamma_2(1 + z/h_0)\}^2. \tag{4.136}$$

Here, γ_1 is the reference viscosity at the fluid bed and γ_2 is an arbitrary parameter determining the surface viscosity value. The remaining variables are defined as before. Equations (4.134)–(4.136) are solved subject to a condition of no applied surface stress, viz.

$$\partial u/\partial z = 0 \quad \text{at} \quad z = 0, \tag{4.137}$$

and a condition of no-slip at the bed, viz.

$$u = 0 \quad \text{at} \quad z = -h_0. \tag{4.138}$$

In this section Johns' solution is stated for the transformed form of equations (4.134)–(4.136), viz.

$$\frac{\partial \zeta}{\partial t} = -h_0 \frac{\partial U}{\partial x}, \tag{4.139}$$

$$\frac{\partial u}{\partial t} = -g\frac{\partial \zeta}{\partial x} + \frac{1}{h_0^2}\frac{\partial}{\partial \eta}\left(N_\eta \frac{\partial u}{\partial \eta}\right), \tag{4.140}$$

and

$$N_\eta = \gamma_1\{1 + \gamma_2(1 - \eta)\}^2, \tag{4.141}$$

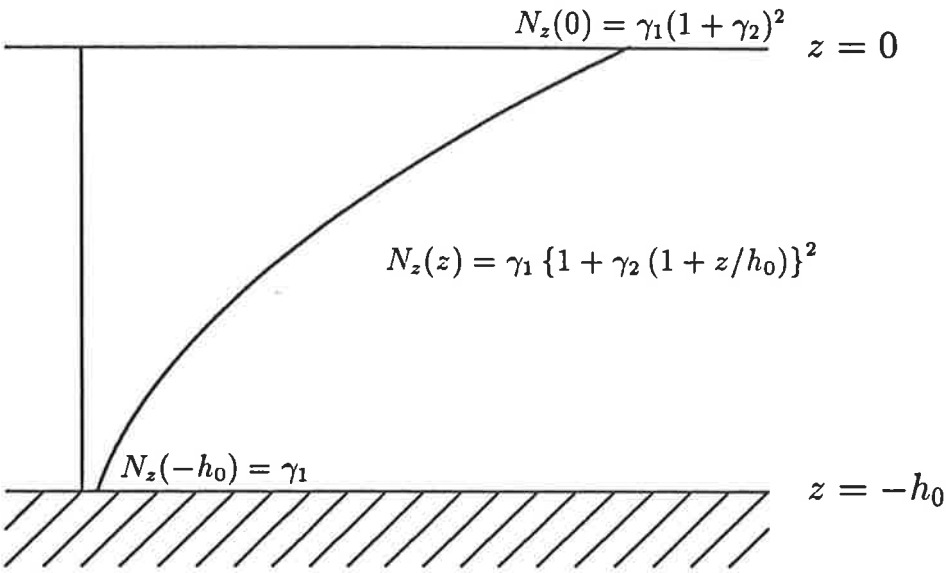


Figure 4.17: *The shape of the vertical eddy viscosity coefficient used by Johns (1966). At the bed, the function takes the value* $\gamma_1\,\mathrm{m}^2/\mathrm{sec}$*; above the bed, the function rises parabolically to a maximum of* $\gamma_1(1+\gamma_2)^2\,\mathrm{m}^2/\mathrm{sec}$ *at the surface.*

together with

$$U = \int_0^1 u\,d\eta, \tag{4.142}$$

where a linear relation between η and z is used (c.f. (2.9)), viz.

$$\eta = -z/h_0. \tag{4.143}$$

The boundary conditions of no applied surface stress and no-slip at the bed become, respectively,

$$\partial u/\partial\eta = 0 \quad \text{at} \quad \eta = 0, \tag{4.144}$$

and

$$u = 0 \quad \text{at} \quad \eta = 1. \tag{4.145}$$

Extending the set of equations solved by Johns, two equations for the explicit calculation of the transformed vertical velocity ω and the cartesian vertical velocity w are (c.f. (2.16) and (2.17))

$$\omega = -\frac{\partial}{\partial x}(U(\eta) - \eta U), \tag{4.146}$$

$$w = -h_0\omega + (1-\eta)\left(\frac{\partial\zeta}{\partial t} + u\frac{\partial\zeta}{\partial x}\right), \tag{4.147}$$

where

$$U(\eta) = \int_0^\eta u\,d\eta'. \tag{4.148}$$

Analytical solutions for ω and w are easily obtained from the solutions for ζ and u. Equations (4.146) and (4.147) are solved in conjunction with the linearized free surface condition (c.f. (2.5))

$$w|_{\eta=0} = \frac{\partial \zeta}{\partial t} + (u|_{\eta=0}) \frac{\partial \zeta}{\partial x} \tag{4.149}$$

and the bottom condition (c.f. (2.6))

$$w|_{\eta=1} = 0. \tag{4.150}$$

Using (4.149) one may verify from (4.147) that

$$\omega = 0 \quad \text{at} \quad \eta = 0, \tag{4.151}$$

and using (4.150) in (4.147) for the bed value shows that

$$\omega = 0 \quad \text{at} \quad \eta = 1. \tag{4.152}$$

Solutions of (4.139) and (4.140) consistent with there being a barrier at the head of the estuary at $x = x_1$ and an open boundary at $x = x_2$ (see Figure 4.18) are:

$$\zeta = \Re e \left\{ \zeta_0 \frac{\cos[m(x - x_1)]}{\cos[m(x_2 - x_1)]} e^{\imath \sigma t} \right\}, \tag{4.153}$$

$$u = \Re e \left\{ \frac{-\imath g \zeta_0 m}{\sigma} \frac{\sin[m(x - x_1)]}{\cos[m(x_2 - x_1)]} F(\eta) e^{\imath \sigma t} \right\}, \tag{4.154}$$

where the angular frequency is $\sigma = 2\pi/T$, T is the period of oscillation and m is the wavenumber of the disturbance; the $F(\eta)$ factor in (4.154) carries the η dependence of the horizontal velocity u; all other symbols are as previously defined. These solutions have been written in a form similar to expressions (4.3) and (4.4) given by Lynch and Gray (1978). An advantage of expression (4.153) over that given by Johns (1966) is that the amplitude of oscillation at the open boundary now takes the familiar form

$$\zeta(t) = \Re e \left\{ \zeta_0 e^{\imath \sigma t} \right\} = \zeta_0 \cos \sigma t. \tag{4.155}$$

Substituting (4.153) and (4.154) into (4.139) gives the dispersion relation

$$\sigma^2 = g h_0 m^2 \int_0^1 F(\eta)\, d\eta. \tag{4.156}$$

Using this result together with (4.154) in (4.142) gives an expression for depth-averaged horizontal velocity, viz.

$$U = \Re e \left\{ \frac{-\imath \sigma \zeta_0}{m h_0} \frac{\sin[m(x - x_1)]}{\cos[m(x_2 - x_1)]} e^{\imath \sigma t} \right\}, \tag{4.157}$$

which has the same form as expression (4.4), developed by Lynch and Gray (1978) for depth-averaged one-dimensional flows. Furthermore, substituting (4.157) into (4.146) and using (4.148) gives the following expression for transformed vertical velocity ω

$$\omega = \Re e \left\{ \imath \sigma \frac{\zeta_0}{h_0} \frac{\cos[m(x - x_1)]}{\cos[m(x_2 - x_1)]} \left[\frac{g h_0 m^2}{\sigma^2} \int_0^\eta F(\eta')d\eta' - \eta \right] e^{\imath \sigma t} \right\}. \tag{4.158}$$

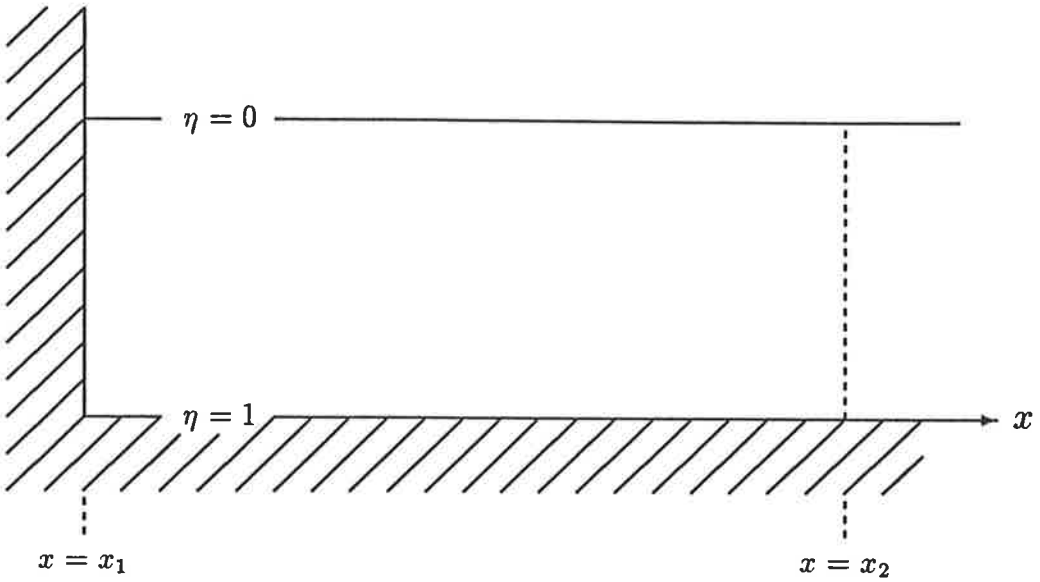


Figure 4.18: *Diagram illustrating the notation used to describe the transformed Johns estuary. The head of the estuary is at $x = x_1$ and the open boundary is at $x = x_2$. The sea surface is described by $\eta = 0$, the sea bed by $\eta = 1$.*

Finally, substituting (4.153), (4.154) and (4.158) into (4.147) gives the following expression for cartesian vertical velocity w:

$$w = \Re e\left\{-\imath\sigma\zeta_0\frac{\cos[m(x-x_1)]}{\cos[m(x_2-x_1)]}\left[\frac{gh_0m^2}{\sigma^2}\int_0^\eta F(\eta' d\eta' - \eta\right]e^{\imath\sigma t}\right.$$
$$\left.+\imath\sigma\zeta_0(1-\eta)\left[\frac{\cos[m(x-x_1)]}{\cos[m(x_2-x_1)]}e^{\imath\sigma t} + \frac{g\zeta_0m^2}{\sigma^2}\left(\frac{\sin[m(x-x_1)]}{\cos[m(x_2-x_1)]}e^{\imath\sigma t}\right)^2 F(\eta)\right]\right\}. \quad (4.159)$$

Explicit solutions for u, ω and w require a suitable formulation for $F(\eta)$.

Using (4.154), the boundary conditions (4.144) and (4.145) become, respectively,

$$dF/d\eta = 0 \quad \text{at} \quad \eta = 0, \quad (4.160)$$
$$F = 0 \quad \text{at} \quad \eta = 1. \quad (4.161)$$

Substituting equations (4.153) and (4.154) into (4.140) gives the following equation for $F(\eta)$:

$$F(\eta) = 1 - \frac{\imath}{\sigma h_0^2}\frac{d}{d\eta}\left(N_\eta\frac{dF}{d\eta}\right), \quad (4.162)$$

which can be solved given a suitable form for N_η. Johns (1966) found that the parabolic form (4.136) (and, implicitly, (4.141)) leads to exact integration of (4.162). To demonstrate this, if the change of independent variable

$$N = 1 + \gamma_2(1-\eta) \quad (4.163)$$

is used, the differential equation (4.162) takes the Euler-Cauchy form

$$N^2\frac{d^2F}{dN^2} + 2N\frac{dF}{dN} - \frac{\imath\sigma h_0^2}{\gamma_1\gamma_2^2}F = -\frac{\imath\sigma h_0^2}{\gamma_1\gamma_2^2}, \quad (4.164)$$

which may be solved using the substitution

$$F = N^n \tag{4.165}$$

and solving the resulting characteristic equation for values n. The solution obtained is

$$F(\eta) = 1 + C_1\{1 + \gamma_2(1-\eta)\}^{n_1} + C_2\{1 + \gamma_2(1-\eta)\}^{n_2}, \tag{4.166}$$

where

$$n_1, n_2 = -\frac{1}{2} \pm \sqrt{\frac{1}{4} + \frac{\imath\sigma h_0^2}{\gamma_1\gamma_2^2}} \tag{4.167}$$

and C_1, C_2 are determined by applying the boundary conditions (4.160) and (4.161). Using (4.160),

$$n_1 C_1(1+\gamma_2)^{n_1} + n_2 C_2(1+\gamma_2)^{n_2} = 0, \tag{4.168}$$

and using (4.161),

$$1 + C_1 + C_2 = 0, \tag{4.169}$$

so that

$$C_1 = \frac{-n_2(1+\gamma_2)^{n_2}}{n_2(1+\gamma_2)^{n_2} - n_1(1+\gamma_2)^{n_1}}, \quad C_2 = \frac{n_1(1+\gamma_2)^{n_1}}{n_2(1+\gamma_2)^{n_2} - n_1(1+\gamma_2)^{n_1}}. \tag{4.170}$$

The time and space centred finite difference expressions used to solve (4.139)–(4.140) and (4.146)–(4.147), subject to the boundary conditions (4.144)–(4.145) and (4.149)–(4.152), and using the form (4.141) for N_η, are contained in the following computational procedure:

1. Input model data and set initial values. Time $t = n\Delta t = 0$.

2. Update model time to level $(n + 1/2)$. Time $t = (n + 1/2)\Delta t$.
   Input the open boundary elevation specification at time level $(n + 1/2)$.
   Calculate elevation field $\zeta^{n+1/2}$ using

$$\frac{\zeta_i^{n+\frac{1}{2}} - \zeta_i^{n-\frac{1}{2}}}{\Delta t} = -h_0\left(\frac{U_i^n - U_{i-1}^n}{2\Delta x}\right). \tag{4.171}$$

3. Update model time to level $(n + 1)$. Time $t = (n + 1)\Delta t$.
   Calculate depth-dependent velocity field u^{n+1} using

$$\begin{aligned}\frac{u_{i,k}^{n+1} - u_{i,k}^n}{\Delta t} &= -g\left(\frac{\zeta_{i+1}^{n+\frac{1}{2}} - \zeta_i^{n+\frac{1}{2}}}{2\Delta x}\right) \\ &+ \frac{1}{h_0^2}\frac{1}{r_k(\Delta\eta_{k-1} + \Delta\eta_k)}\left(\left\{\frac{(r_k)^2}{\Delta\eta_k}(N_k + N_{k+1})\left(u_{i,k+1}^n - u_{i,k}^n\right)\right.\right. \\ &\left.\left. + \frac{2(1-(r_k)^2)}{r_k(\Delta\eta_{k-1} + \Delta\eta_k)}N_k\left((r_k)^2 u_{i,k+1}^n + (1-(r_k)^2)u_{i,k}^n - u_{i,k-1}^n\right)\right.\right.\end{aligned}$$

$$
\begin{aligned}
&-\frac{1}{\Delta\eta_{k-1}}(N_{k-1}+N_k)\left(u^n_{i,k}-u^n_{i,k-1}\right)\Big\} \\
&+\Big\{\frac{(r_k)^2}{\Delta\eta_k}(N_k+N_{k+1})\left(u^{n+1}_{i,k+1}-u^{n+1}_{i,k}\right) \\
&+\frac{2(1-(r_k)^2)}{r_k(\Delta\eta_{k-1}+\Delta\eta_k)}N_k\left((r_k)^2u^{n+1}_{i,k+1}+(1-(r_k)^2)u^{n+1}_{i,k}-u^{n+1}_{i,k-1}\right) \\
&-\frac{1}{\Delta\eta_{k-1}}(N_{k-1}+N_k)\left(u^{n+1}_{i,k}-u^{n+1}_{i,k-1}\right)\Big\}\Big), \quad k=1,2,\ldots,NK-1.
\end{aligned}
\tag{4.172}
$$

These equations are written for a smoothly varying non-uniform grid where the ratio of consecutive grid spacings is $r_k = \Delta\eta_{k-1}/\Delta\eta_k$. The quantity N_k is the value of N_η evaluated at the $u^n_{i,k}$ gridpoint and

$$
N_k = \gamma_1\{1+\gamma_2(1-\eta_k)\}^2, \quad \eta_k \in [0,1], \tag{4.173}
$$

where the value of η_k depends on the parameter κ used in the Kappa method outlined in Chapter 3. Eleven (11) depth levels and hence ten depth intervals are used. The relative spacing of the depth levels varies from fine near the surface to coarse at mid-depths and back to fine near the bed, and is arranged symmetrically about the mid-depth level. The surface velocity value is obtained using an extrapolation in terms of the velocity values at the two levels immediately below it:

$$
u^{n+1}_{i,0} \simeq \frac{(\Delta\eta_0+\Delta\eta_1)^2}{\Delta\eta_1(\Delta\eta_1+2\Delta\eta_0)}u^{n+1}_{i,1} - \frac{(\Delta\eta_0)^2}{\Delta\eta_1(\Delta\eta_1+2\Delta\eta_0)}u^{n+1}_{i,2}, \tag{4.174}
$$

and has a third order discretisation error. The surface condition (4.144) is used in deriving (4.174). The bottom velocity value, from (4.145), is

$$
u^{n+1}_{i,NK} = 0. \tag{4.175}
$$

Using (4.174) and (4.175) in equations (4.172) gives a tri-diagonal system of $(NK-1)$ linear equations for the implicit solution of the horizontal velocity field over the depth column. The system is solved using the Thomas algorithm.

Following this, the depth-averaged horizontal velocity field U^{n+1} is calculated by numerical evaluation of (4.142) using (3.27), the composite Simpson's rule for unequally spaced intervals.

4. Update open boundary elevation specification to time level $(n+1)$.
   Calculate elevation field ζ^{n+1} using

$$
\frac{\zeta^{n+1}_i-\zeta^n_i}{\Delta t} = -\frac{h_0}{2\Delta x}\left(\frac{1}{2}\left[U^{n+1}_i+U^n_i\right]-\frac{1}{2}\left[U^{n+1}_{i-1}+U^n_{i-1}\right]\right). \tag{4.176}
$$

5. Calculate the transformed vertical velocity field ω^{n+1} using

$$
\omega^{n+1}_{i,k} = -\frac{1}{2\Delta x}\left(\left[U(\eta_k)^{n+1}_i-\eta_kU^{n+1}_i\right]-\left[U(\eta_k)^{n+1}_{i-1}-\eta_kU^{n+1}_{i-1}\right]\right), \tag{4.177}
$$

where the integrals $U(\eta_k)_i^{n+1}$ and $U(\eta_k)_{i-1}^{n+1}$ are evaluated using the composite Trapezoidal rule (3.33) applied at each interior depth level.

The cartesian vertical velocity field w^{n+1} is calculated using

$$\begin{aligned} w_{i,k}^{n+1} &= -h_0\omega_{i,k}^{n+1} + (1-\eta)\left(-\frac{h_0}{2\Delta x}\left[U_i^{n+1} - U_{i-1}^{n+1}\right]\right. \\ &\left. + \frac{1}{8\Delta x}\left[u_{i-1,k}^{n+1} + u_{i,k}^{n+1}\right]\left[\zeta_{i+1}^{n+1} - \zeta_{i-1}^{n+1}\right]\right), \end{aligned} \tag{4.178}$$

where the term $\partial\zeta/\partial t$ of (4.147) has been replaced with a spatial gradient using the continuity equation (4.139).

6. Return to Step 2 and repeat until the simulation is completed.

The benefits associated with this numerical test are the following. It tests the accuracy of:

- the numerical approximation used for differencing the vertical eddy viscosity term of the momentum equation,
- the procedure for the implicit solution of equations (4.172),
- the surface velocity approximation,
- the vertical integration methods,
- the approximations used for determining the transformed vertical velocity and cartesian vertical velocity,

and the effect, in each case, of varying the parameter κ which determines the relative sizes of the grid spacings in the vertical.

4.5.1 Numerical tests using Johns' vertical eddy viscosity

Introducing the dimensionless variables

$$x^* = x/L,\ t^* = t/T,\ \zeta^* = \zeta/\zeta_0,\ u^* = u/U_0,\ U^* = U/U_0,\ N_\eta^* = N_\eta/N_{\max}, \tag{4.179}$$

and

$$\omega^* = \omega/\omega_0,\ \ w^* = w/w_0, \tag{4.180}$$

where $L = x_2 - x_1$ is the length of the estuary, T is the period of oscillation, ζ_0 is the forcing amplitude at the open boundary, $U_0 = g\zeta_0 T/L$ is a characteristic value of horizontal velocity, $\omega_0 = U_0/L$ is a characteristic value of ω, $w_0 = h_0\omega_0$ is a characteristic value of w and $N_{\max}$ is a characteristic value of vertical eddy viscosity, taken as the maximum prescribed value in the water column, equations (4.139) and (4.140) become, respectively,

$$\frac{\partial\zeta^*}{\partial t^*} = -\alpha_0^2\frac{\partial U^*}{\partial x^*}, \tag{4.181}$$

$$\frac{\partial u^*}{\partial t^*} = -\frac{\partial\zeta^*}{\partial x^*} + \gamma\frac{\partial}{\partial\eta}\left(N_\eta^*\frac{\partial u^*}{\partial\eta}\right), \tag{4.182}$$

where $\alpha_0 = T\sqrt{gh_0}/L$ as before. The vertical eddy viscosity number $\gamma = N_{\max}T/h_0^2$ may be interpreted as the ratio of vertical momentum exchange rate to inertia of the fluid (Jung et al., 1986, 1987). The dimensionless form of the Johns vertical eddy viscosity coefficient (4.141) is

$$N_\eta^* = \{1 - \gamma_2\eta/(1+\gamma_2)\}^2, \tag{4.183}$$

since $N_{\max} = \gamma_1(1+\gamma_2)^2$ in this case, assuming $\gamma_2 \geq 0$ (ibid.).

The dimensionless forms of equations (4.142) and (4.146)–(4.147) are, respectively,

$$U^* = \int_0^1 u^*\, d\eta, \tag{4.184}$$

$$\omega^* = -\frac{\partial}{\partial x^*}\left(U^*(\eta) - \eta U^*\right), \tag{4.185}$$

where

$$U^*(\eta) = \int_0^\eta u^*\, d\eta', \tag{4.186}$$

and

$$w^* = -\omega^* + (1-\eta)\left(\frac{1}{\alpha_0^2}\frac{\partial \zeta^*}{\partial t^*} + \frac{\zeta_0}{h_0}u^*\frac{\partial \zeta^*}{\partial x^*}\right), \tag{4.187}$$

or using (4.181),

$$w^* = -\omega^* + (1-\eta)\left(-\frac{\partial U^*}{\partial x^*} + \frac{\zeta_0}{h_0}u^*\frac{\partial \zeta^*}{\partial x^*}\right). \tag{4.188}$$

Johns (1966) finds that a suitable value for the kinematic viscosity of the fluid near the bed, for semi-diurnal tidal flows in the lower reaches of the Humber estuary where the depth is approximately 14 m, is $\gamma_1 = 0.0014\,\mathrm{m}^2/\mathrm{sec}$. This choice is theoretically justified by the work of McGregor (1972) who suggests that in the absence of a laminar sub-boundary layer, a high friction is necessary near the bed in order to adequately reproduce the friction length of the empirical logarithmic expression for the horizontal velocity profile. Johns further chooses the surface viscosity value to be $N_{\max} = 0.1\,\mathrm{m}^2/\mathrm{sec}$ (from which $\gamma_2 \simeq 7.5$) and so $\gamma \simeq 22$.

In order to choose values of γ_1 and $N_{\max}$ for the Spencer Gulf (SG) tests, it is observed from the form of the vertical eddy viscosity coefficient (2.18) given in Chapter 2 that the bed and surface values vary with depth H. For the SG tests γ_1 and $N_{\max}$ are chosen as

$$\gamma_1 = 0.0014 \times (h_{\mathrm{SG}}/14) \simeq 0.0025\ \mathrm{m}^2/\mathrm{sec}, \tag{4.189}$$

$$N_{\max} = 0.1 \times (h_{\mathrm{SG}}/14) \simeq 0.18\ \mathrm{m}^2/\mathrm{sec}, \tag{4.190}$$

where h_{SG} is given by (4.18); the corresponding value of γ_2 is about 7.5. The value of γ for the SG tests is

$$\gamma = \gamma_{\mathrm{Johns}} \times (14/h_{\mathrm{SG}}) \simeq 12. \tag{4.191}$$

Thus for SG tests, the values γ_1 and $N_{\max}$ (and hence γ) are proportionally increased according to the relatively greater depth of the SG model compared to that of the Humber

estuary. This is in no way to claim that such choices are accurate for Spencer Gulf, although it is likely they will be of the right order of magnitude for the Johns vertical eddy viscosity coefficient.

The remaining parameter of interest in these tests is κ. For simplicity, only integer values for κ are considered, though κ may take any real value.

For the numerical tests, the semi-diurnal constituent will be used. Figure 4.19 shows plots of dimensionless elevation error ε_ζ^*, expressed as a percentage of characteristic value ζ_0, versus number of grid spacings per wavelength N_λ for SG tests using values of $\kappa = 0(1)7$. Once again, the error in ζ^* is larger than the errors in u^*, U^*, ω^* or w^*, so only the results for ε_ζ^* are shown. The characteristic values for elevation and the velocity components are: $\zeta_0 = 0.75\,\mathrm{m}$, $U_0 \simeq 0.93\,\mathrm{m/sec}$, $\omega_0 \simeq 2.75\times10^{-6}\,\mathrm{sec}^{-1}$, $w_0 \simeq 6.94\times10^{-5}\,\mathrm{m/sec}$. The Courant number used is $C_x = 0.3$. Clearly, $\kappa = 3$ gives best results for the range of integer κ values used. There is considerable difference in performance of the numerical scheme for different values of κ. The results corresponding to the uniform grid, where $\kappa = 0$, are relatively poor but there is immediate improvement as κ is increased and finer resolution near the bed is achieved. This improved performance is maximized at about $\kappa = 3$, whereafter results are poorer partly because, with the number of depth intervals being fixed at 10, the spacings at mid-depths become coarser and lead to decreasing accuracy of representation of the mid-depth activity. When $\kappa = 7$, performance is no better than with a uniform grid. Thus the optimal value of κ for a particular application depends on the number of depth levels used. The term of equations (4.139)–(4.140), whose accuracy of approximation depends upon the choice of κ, is the vertical diffusive term of (4.140). The accuracy of the depth-averaging represented by equation (4.142) also depends on the choice of κ.

At the operational value of $N_\lambda = 119$ for the semi-diurnal wave in the Spencer Gulf model of Chapter 5, it is clear that the numerical scheme performs accurately at $\kappa = 3$ and that there is definite advantage in calibrating with respect to κ.

The variation of performance of the numerical scheme with κ suggests that numerical experimentation will be required in the three-dimensional modelling of Spencer Gulf in order to determine the optimal value of κ for that model.

At this point it is observed that the performance of the numerical scheme for a given value of κ also depends on the accuracy of the discretisation used for the surface velocity value. This dependence is examined in the next section.

4.5.2 The surface velocity approximation

Johns (1969) proposed a numerical scheme for the solution of equation (4.162) in which the surface velocity approximation had second order discretisation error. In this section, more accurate surface velocity discretisations are considered. The numerical scheme given is verified by accurately reproducing $F(\eta)$ in the case of Johns' vertical eddy viscosity (4.141). It may be used to generate benchmark solutions for $F(\eta)$ for any functional form of N_η and is applied for this purpose in the next section.

Expanding the derivative term in (4.162) and using centred differences on a uniform vertical η-grid, one obtains

$$F_k = 1 - \frac{\imath}{\sigma h_0^2}\left.\frac{dN_\eta}{d\eta}\right|_{\eta=k\Delta\eta}\left(\frac{F_{k+1}-F_{k-1}}{2\Delta\eta}\right) - \frac{\imath}{\sigma h_0^2}N_\eta(k\Delta\eta)\left(\frac{F_{k+1}-2F_k+F_{k-1}}{(\Delta\eta)^2}\right), \quad (4.192)$$

for levels $k = 1(2)NK-1$, where F_k is the numerical solution for $F(k\Delta\eta)$. These expressions

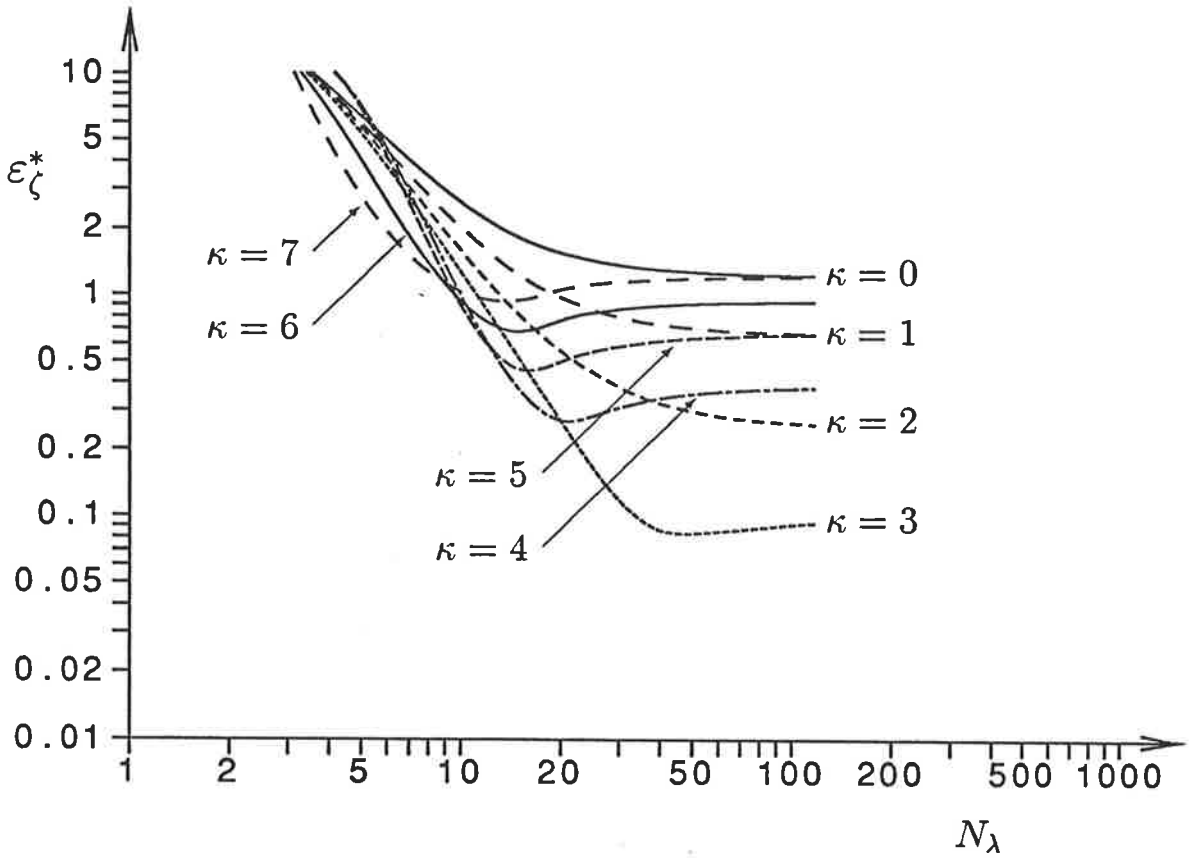


Figure 4.19: *Percentage error in dimensionless elevation ε^*_ζ versus number of grid spacings per wavelength N_λ for constant depth Spencer Gulf numerical tests using a semi-diurnal constituent and Courant number $C_x = 0.3$. The Johns vertical eddy viscosity form is used. The surface velocity approximation used is that of equation (4.174) and has third order discretisation error. In order to investigate the performance of the Kappa method of non-uniform grid spacing, eight integer values of κ are used. At the operational value of $N_\lambda = 119$ for the Spencer Gulf model, $\kappa = 3$ gives best results.*

may be written in implicit form as

$$a_k F_{k-1} + b_k F_k + c_k F_{k+1} = 1, \tag{4.193}$$

where

$$a_k = \frac{\imath}{\sigma h_0^2}\left(-\frac{1}{2\Delta\eta}\left.\frac{dN_\eta}{d\eta}\right|_{\eta=k\Delta\eta} + \frac{1}{(\Delta\eta)^2}N_\eta(k\Delta\eta)\right), \tag{4.194}$$

$$b_k = 1 - \frac{\imath}{\sigma h_0^2}\frac{2}{(\Delta\eta)^2}N_\eta(k\Delta\eta), \tag{4.195}$$

$$c_k = \frac{\imath}{\sigma h_0^2}\left(\frac{1}{2\Delta\eta}\left.\frac{dN_\eta}{d\eta}\right|_{\eta=k\Delta\eta} + \frac{1}{(\Delta\eta)^2}N_\eta(k\Delta\eta)\right), \tag{4.196}$$

and $k = 1(1)NK-1$; because the form for N_η is given, the terms $[dN_\eta/d\eta]|_{\eta=k\Delta\eta}$ and $N_\eta(k\Delta\eta)$ are known. Using the surface boundary condition (4.160), F_0 may be written in

terms of F_1 and F_2 as the third order accurate discretisation

$$F_0 = \frac{4}{3}F_1 - \frac{1}{3}F_2 + O\left((\Delta\eta)^3\right), \tag{4.197}$$

for uniform grid spacing in the vertical. Substituting (4.197) into (4.192), it can be seen that the discretisation obtained for F_1 is only first order accurate, even though (4.197) has discretisation error $O((\Delta\eta)^3)$. However, the discretisation errors for expressions F_k, $k = 2(1)NK-1$ are all second order accurate and the implicit nature of solution spreads the first order inaccuracy of the F_1 expression over all F_k values resulting in an overall solution which is almost second order accurate.

At the bed, the no-slip condition (4.161) is used, and so

$$F_{NK} = 0\,. \tag{4.198}$$

Using (4.197) in the expression for F_1 and (4.198) in the expression for F_{NK-1}, equations (4.192) can be written as the following tri-diagonal system of linear equations which is rapidly solved using the Thomas algorithm:

$$\begin{bmatrix} \frac{4}{3}a_1 + b_1 & -\frac{1}{3}a_1 + c_1 & & & & \\ a_2 & b_2 & c_2 & & & \\ & a_3 & b_3 & c_3 & & \\ & & \ddots & \ddots & \ddots & \\ & & & a_{NK-2} & b_{NK-2} & c_{NK-2} \\ & & & & a_{NK-1} & b_{NK-1} \end{bmatrix} \begin{bmatrix} F_1 \\ F_2 \\ F_3 \\ \vdots \\ F_{NK-2} \\ F_{NK-1} \end{bmatrix} = 1\,. \tag{4.199}$$

A sufficient condition for the solvability of (4.199) is the diagonal dominance of the coefficient matrix (Noye, 1984a). The coefficient matrix is diagonally dominant if along each row the absolute value of the entry on the leading diagonal is greater than or equal to the sum of the absolute values of the remaining coefficients, with strict inequality being the case along at least one row. Thus a solution for the values $F_1, F_2, \ldots, F_{NK-1}$ is guaranteed if N_η satisfies the inequalities

1. $\left|\frac{4}{3}a_1 + b_1\right| \geq \left|-\frac{1}{3}a_1 + c_1\right|$, for level $k = 1$,
2. $|b_k| \geq |a_k| + |c_k|$, for levels $k = 2, 3, \ldots, NK-2$, and
3. $|b_{NK-1}| \geq |a_{NK-1}|$, for level $k = NK-1$.

These three conditions are checked as part of the program written for the numerical solution of (4.192).

In order to optimize the accuracy of benchmark solutions generated using (4.192), the interval $\eta \in [0, 1]$ is divided into as many sub-intervals as is computationally possible. Without optimizing the program code, one may define 50,000 intervals using the storage capacity available on the VAX 11/785 machine. Table 4.4 shows analytical values for $\Re e\{F(\eta)\}$ and $\Re e\{m^*\}$ generated for Johns' vertical eddy viscosity profile (4.183) for a SG semi-diurnal constituent. The quantity m^* is the dimensionless wavenumber defined as

$$m^* = mL. \tag{4.200}$$

In the same table are listed numerical solutions corresponding to Johns' (1969) second order accurate surface velocity discretisation, viz.

$$F_0 = F_1 + O((\Delta\eta)^2), \tag{4.201}$$

for uniform vertical grid level spacing, and the present third order accurate discretisation (4.197). Note that (4.201) leads this time to a local solution for F_1, using (4.192), which is only zeroth order accurate, although this is spread over the remainder of the solution domain, where the local solution for the F_k is second order accurate, by means of the implicit solution procedure. Where the decimal digits of the numerical solution start to differ from the analytical solution they are given bold-faced type. The fact that generally five decimal digits in the results under column (c) in Table 4.4 are bold-faced demonstrates that the inaccuracy of the surface discretisation has been evenly spread over all depths. Under column (b), generally only one decimal place digit is bold-faced. These results verify the numerical scheme using Johns' vertical eddy viscosity and demonstrate that the higher order approximation for surface velocity (4.197) generates results which are generally four orders of magnitude more accurate than Johns' approximation (4.201).

Value	(a) Analytic	(b) 3rd order	(c) 2nd order
$\Re e\{F(0.0)\}$	0.9975246498	0.9975246497	0.9975**228664**
$\Re e\{F(0.1)\}$	0.9966737842	0.9966737**840**	0.9966**721559**
$\Re e\{F(0.2)\}$	0.9936332855	0.9936332**853**	0.9936**318219**
$\Re e\{F(0.3)\}$	0.9873744963	0.9873744**961**	0.9873**732078**
$\Re e\{F(0.4)\}$	0.9762429788	0.9762429**787**	0.9762**418766**
$\Re e\{F(0.5)\}$	0.9574355537	0.9574355**536**	0.9574**346489**
$\Re e\{F(0.6)\}$	0.9258709909	0.9258709**907**	0.9258**702938**
$\Re e\{F(0.7)\}$	0.8714632351	0.8714632**349**	0.8714**627524**
$\Re e\{F(0.8)\}$	0.7714391301	0.7714391**300**	0.7714**388585**
$\Re e\{F(0.9)\}$	0.5630844401	0.5630844**400**	0.5630**843481**
$\Re e\{F(1.0)\}$	0.0000000000	0.0000000000	0.0000000000
$\Re e\{m^*\}$	3.2659929727	3.2659929**733**	3.2659**920660**

Table 4.4: *Values of $\Re e\{F(\eta)\}$, $\eta = 0.0(0.1)1.0$, and $\Re e\{m^*\}$ calculated (a) analytically, (b) numerically, using the third order discretisation for surface velocity and (c) numerically, using the second order surface velocity discretisation. The numerical evaluations use Johns' vertical eddy viscosity coefficient and semi-diurnal Spencer Gulf parameters.*

The numerical estimates for wavenumber m^* are obtained from (4.156) by using the composite Simpson's rule to approximate the integral; for a uniform grid, Simpson's rule is fourth order accurate.

In order to more fully examine the influence of the accuracy of the surface velocity approximation on the performance of the numerical scheme (4.192), a fourth order discretisation for F_0 is also constructed. For a uniform grid, the fourth order estimate for F_0 is

$$F_0 = \frac{18}{11}F_1 - \frac{9}{11}F_2 + \frac{2}{11}F_3 + O\left((\Delta\eta)^4\right), \tag{4.202}$$

where $\Delta\eta$ is the uniform grid level spacing. Expression (4.202) incorporates the surface condition $F'(0) = 0$ and gives solutions for F_k, $k = 1, 2, \ldots, NK{-}1$ which are second order accurate in the overall sense.

Substituting (4.202) into the implicit equation for level $k = 1$ gives

$$(18a_1 + 11b_1)\,F_1 + (11c_1 - 9a_1)\,F_2 + 2a_1 F_3 = 11. \tag{4.203}$$

The equation for level $k = 2$ is used to eliminate F_3 in expression (4.203), giving

$$(18a_1 + 11b_1 - 2a_1a_2/c_2)\,F_1 + (11c_1 - 9a_1 - 2a_1b_2/c_2)\,F_2 = 11 - 2a_1/c_2, \tag{4.204}$$

so that the system of equations (4.193) is tri-diagonal.

The approximations for F_0 with second, third and fourth order discretisation errors are now used in generating, respectively, zeroth, first and second order solutions for F_k, $k = 1, 2, \ldots, NK{-}1$, using Johns' N_η form for a range of choice of number of depth intervals NK. A plot of error, expressed as a percentage and defined as

$$\varepsilon_F^* = \frac{1}{NK} \sum_{k=0}^{NK-1} |F\,(k\Delta\eta) - F_k| \times 100\%, \tag{4.205}$$

where $F(k\Delta\eta)$ is the analytical value for $F(\eta)|_{\eta=k\Delta\eta}$ and F_k is the numerical estimate for the same quantity, is given in Figure 4.20 for each of the surface velocity approximations. The curves for the third and fourth order discretisations almost overlay each other, the results for the latter being only slightly more accurate. This emphasizes that the "first order" solution field for the F_k, $k = 1, 2, \ldots, NK{-}1$ is indeed almost second order. For $NK = 10$ or more, it is clear that using either (4.197) or (4.202) generates results with errors at most half those obtained using Johns' approximation (4.201), though using (4.197) instead of (4.202) is computationally less expensive.

This result is similar to that of Noye (1984a) who found that approximations with discretisation errors of third and fourth order gave essentially equivalent results, almost two orders of magnitude more accurate than results from a second order discretisation, in solving a numerical system with a derivative boundary condition using an explicit marching scheme. Noye says: "Boundary conditions usually involve partial differential equations with derivatives of lower order than those in the partial differential equations which apply to the interior of the scheme. Therefore the truncation errors associated with the boundary equation approximations may need to be of higher order than the truncation error associated with finite difference equations used at interior gridpoints if the discretisation errors are to be of the same order" (ibid., p.178-179).

The accuracy obtained using (4.197) or (4.202) and $NK = 10$ depth intervals is not achieved by using (4.201) unless about $NK = 20$ intervals are used. In the main, the curves are linear on the log-log plot and it is straightforward to derive an expression giving the number of depth intervals required to generate solutions of specified accuracy. This expression is

$$NK \simeq \sqrt[m]{b^{-1}\varepsilon_F^*} \quad \text{for} \quad NK \geq 50, \tag{4.206}$$

where $m \simeq -1.001$ and $b \simeq 15.53$ for the second order discretisation (4.201), $m \simeq -2.002$ and $b \simeq 102.9$ for the third order discretisation (4.197), and $m \simeq -1.996$ and $b \simeq 91.59$ for the fourth order discretisation (4.202).

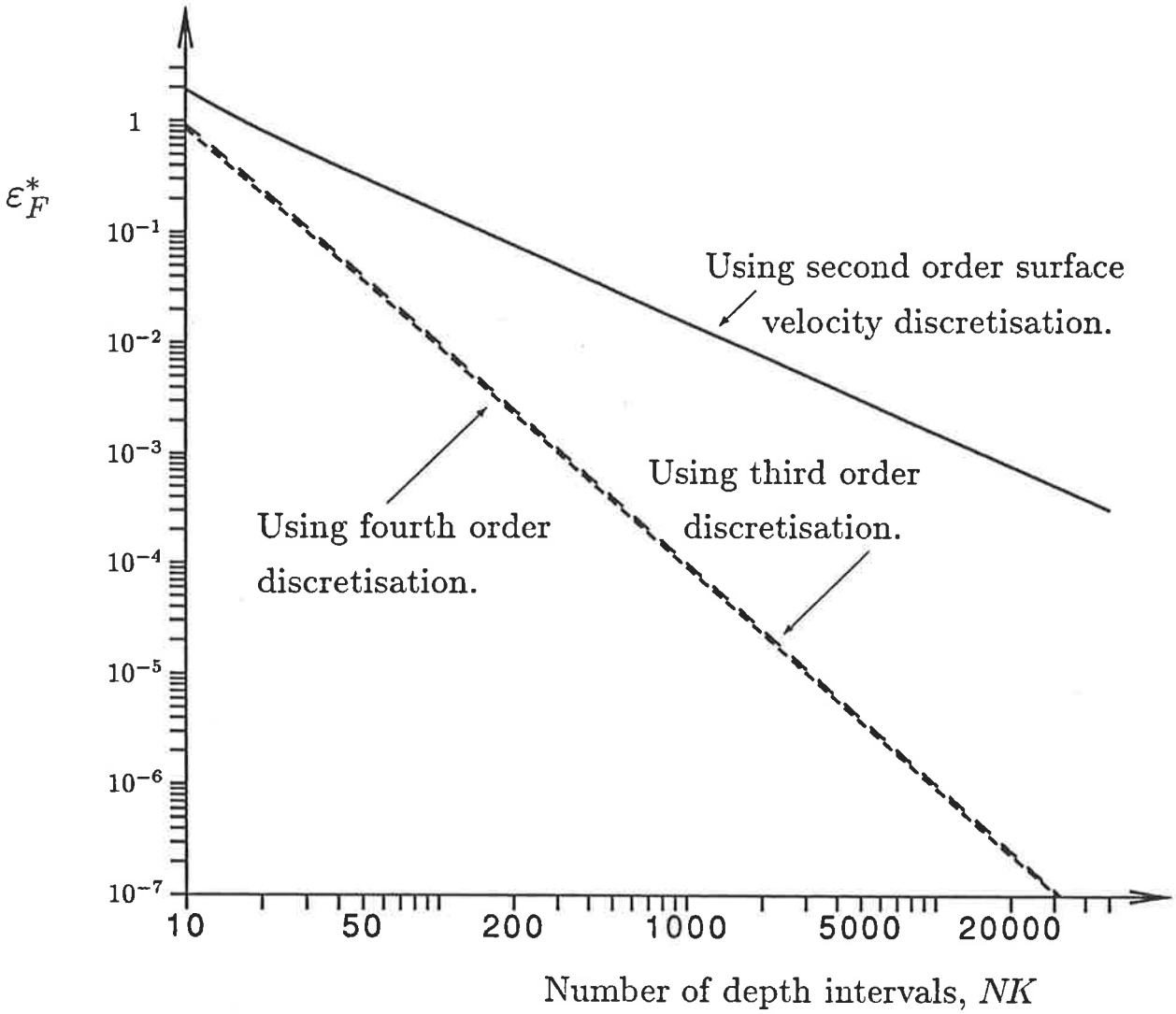


Figure 4.20: *Dimensionless error in $F(\eta)$, ε_F^*, versus number of uniformly spaced depth intervals NK when using various orders of accuracy for the surface velocity discretisation. The curves for the third and fourth order surface velocity discretisations virtually coincide. Johns' vertical eddy viscosity coefficient is used.*

4.5.3 Numerical tests using a symmetric parabolic vertical eddy viscosity coefficient

Besides Johns' solution, there now exist many analytical solutions for (possibly more realistic) different forms of vertical eddy viscosity coefficients. Stevens (1990, p.69, Table 5.1) lists many of these and states their source. He further considers a version of the shallow water equations in which the momentum equation (4.135) is extended to both horizontal coordinates and includes Coriolis terms, horizontal diffusive terms and constant coefficient horizontal advective terms. He then analytically solves these equations for coefficients of the form

- $N_\eta = N_s$ = constant
- $N_\eta = N_s + (N_b - N_s)$ = linear
- $N_\eta = N_b(1 + \gamma_2(1 - \eta))^2$ = Johns' type
- $N_\eta = d(\eta - \alpha)(\eta - \beta)$ = McGregor type
- $N_\eta = \sqrt{N_s^2 + (N_b^2 - N_s^2)\eta}$
- $N_\eta = N_s \exp(\eta \ln(N_b/N_s))$ = exponential type
- $N_\eta = a \sin^2[\pi(\eta - d)/b]$
- N_η = two piece composite (combined linear and parabolic)
- N_η = three piece composite (three piece linear)

thereby bringing all the commonly used analytical solutions "up-to-date" in terms of the inclusion of Coriolis, horizontal diffusive and linearized advective effects. In these expressions, N_s is the surface viscosity value, N_b is the bed value, γ_2 is as before, and the constants a,b,d,α,β are defined as in Stevens (1990) for the respective coefficients. Stevens' work is recommended to the interested reader.

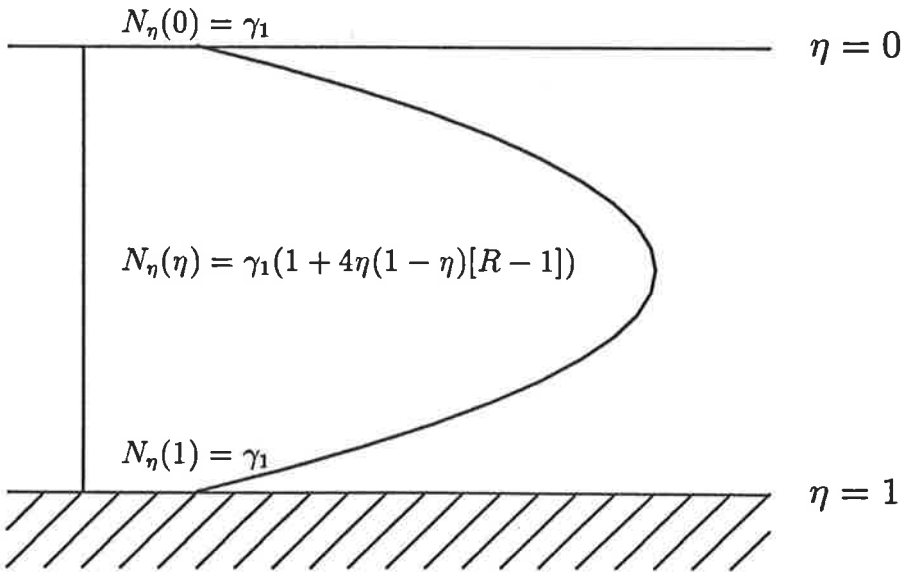
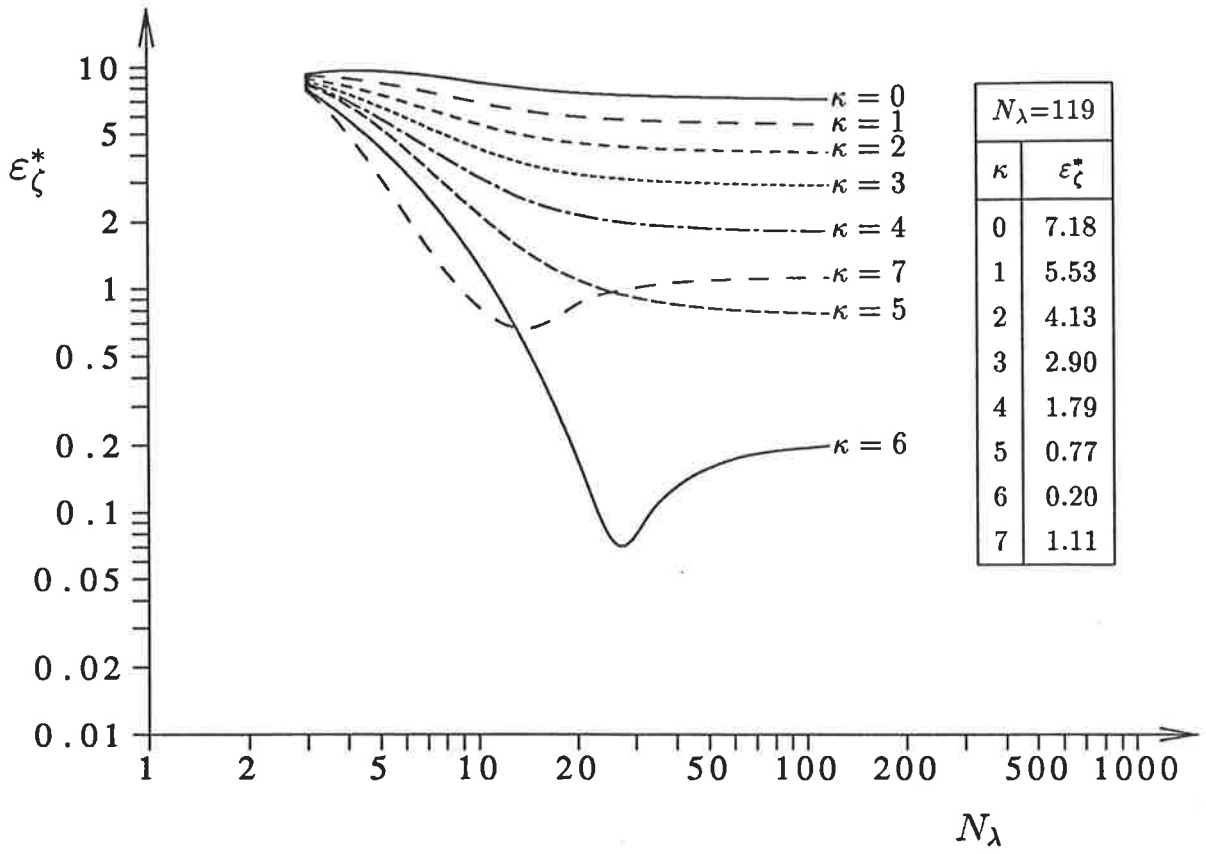


Figure 4.21: *A parabolic vertical eddy viscosity coefficient with equal surface and bed values, i.e.* $N_\eta(0) = N_\eta(1) = \gamma_1$, *and symmetric about the level* $\eta = 0.5$. *Parameter* $R = N_{max}/\gamma_1$.

In this subsection, a "McGregor type" parabolic coefficient (see Figure 4.21) is used in numerical tests with semi-diurnal SG parameters. This coefficient is used in the three-dimensional model of Chapter 7. The coefficient attains a maximum at mid-depth and decreases symmetrically towards the surface and the bed. Johns (1969) numerically derived the horizontal velocity profile corresponding to this coefficient and suggested that it was



N_λ=119	
κ	ε^*_ζ
0	7.18
1	5.53
2	4.13
3	2.90
4	1.79
5	0.77
6	0.20
7	1.11

Figure 4.22: *Percentage error in dimensionless elevation ε^*_ζ versus number of grid spacings per wavelength N_λ for constant depth Spencer Gulf model tests using the semi-diurnal constituent. Courant number $C_x = 0.3$; 10 depth intervals are used. The second order surface velocity discretisation is used together with the symmetric parabolic vertical eddy viscosity form. Each model is run using eight integer values of κ. There is a large range in performance of the numerical scheme for a given N_λ; optimal performance for this selection of κ values occurs at $\kappa = 6$. At the operating value $N_\lambda = 119$ for the Spencer Gulf model, accuracy is good for $\kappa = 6$.*

logarithmic throughout the depth; this was analytically confirmed by McGregor (1972). Bowden and Hamilton (1975) also note that the velocity profile corresponding to this coefficient is logarithmic throughout the depth.

The use of this coefficient thus produces a logarithmic velocity profile near the sea bed, in general agreement with observations reported by Charnock (1959), Bowden et al. (1959) and Bowden (1978). For a theoretical derivation of the logarithmic velocity profile near (but not at) the bed in the case of plane-parallel turbulent flow see, for example, Landau and Lifshitz (1989, p.172).

The vertical eddy viscosity form of Figure 4.21 has the equation

$$N_\eta = \gamma_1(1 + 4\eta(1-\eta)[N_{max}/\gamma_1 - 1]). \tag{4.207}$$

Using this vertical eddy viscosity formulation for the SG tests, along with $\alpha_0 = 2.0$ and the values used for bed viscosity γ_1 ($\simeq 0.0025\,\mathrm{m}^2/\mathrm{sec}$) and maximum viscosity N_{max}

($\simeq 0.18\,\mathrm{m}^2/\mathrm{sec}$) of Subsection 4.5.1, a series of benchmark solutions for $F(\eta)$ using the third order surface velocity discretisation at the 10 depth levels defined by $\kappa = 0(1)7$ are derived, against which numerical comparisons are made. The numerical comparisons are repeated for each of the three discretisations for surface velocity given above.

In terms of a non-uniform grid in the vertical, the second order accurate surface velocity discretisation is

$$u_{i,0}^{n+1} \simeq u_{i,1}^{n+1}\,. \tag{4.208}$$

The third order accurate discretisation is (4.174), viz.

$$u_{i,0}^{n+1} \simeq \frac{(\Delta\eta_0+\Delta\eta_1)^2}{\Delta\eta_1(\Delta\eta_1+2\Delta\eta_0)}\,u_{i,1}^{n+1} - \frac{(\Delta\eta_0)^2}{\Delta\eta_1(\Delta\eta_1+2\Delta\eta_0)}\,u_{i,2}^{n+1}\,, \tag{4.209}$$

and the fourth order accurate discretisation is

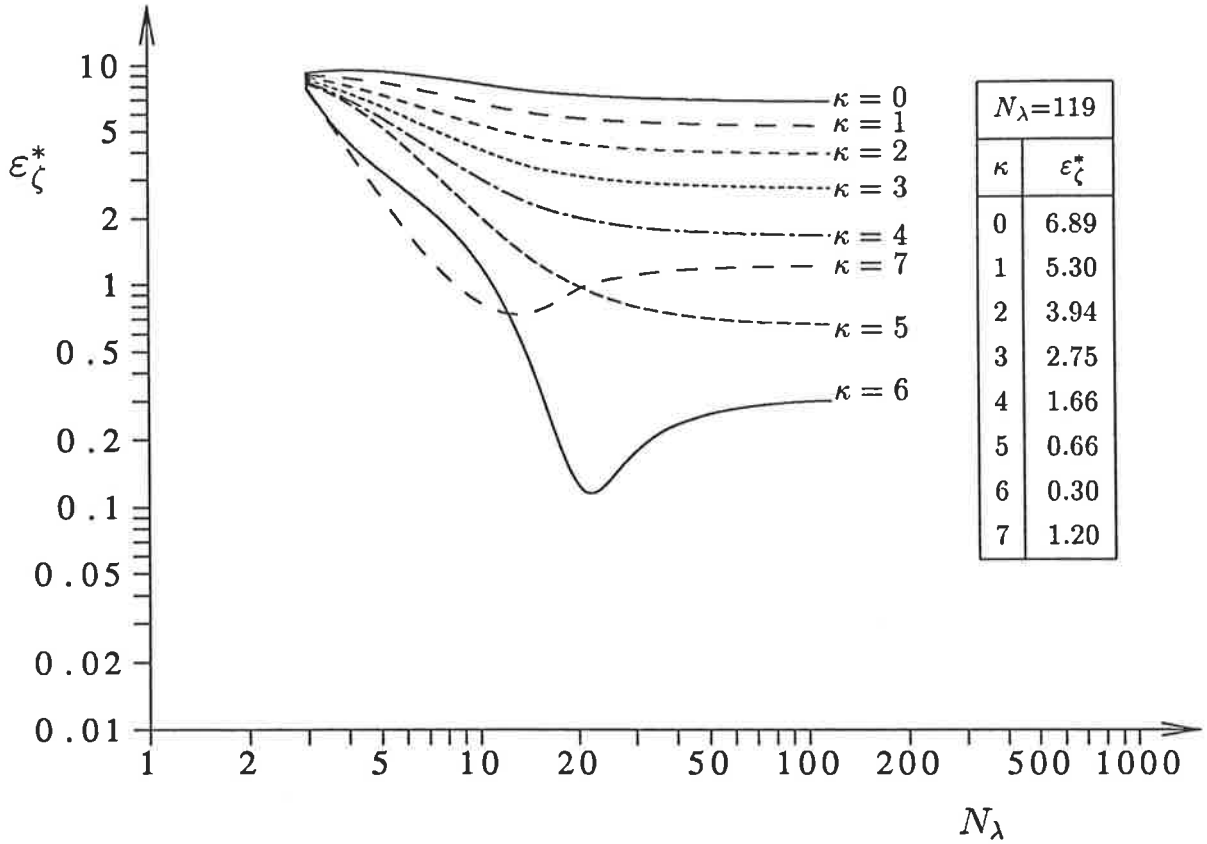
$$\begin{aligned} u_{i,0}^{n+1} \simeq\ & \frac{(\Delta\eta_0+\Delta\eta_1)^2(\Delta\eta_0+\Delta\eta_1+\Delta\eta_2)^2}{\Delta\eta_1(\Delta\eta_1+\Delta\eta_2)(3(\Delta\eta_0)^2+4\Delta\eta_0\Delta\eta_1+2\Delta\eta_0\Delta\eta_2+(\Delta\eta_1)^2+\Delta\eta_1\Delta\eta_2)}\,u_{i,1}^{n+1} \\ & -\frac{(\Delta\eta_0)^2(\Delta\eta_0+\Delta\eta_1+\Delta\eta_2)^2}{\Delta\eta_1\Delta\eta_2(3(\Delta\eta_0)^2+4\Delta\eta_0\Delta\eta_1+2\Delta\eta_0\Delta\eta_2+(\Delta\eta_1)^2+\Delta\eta_1\Delta\eta_2)}\,u_{i,2}^{n+1} \\ & +\frac{(\Delta\eta_0)^2(\Delta\eta_0+\Delta\eta_1)^2}{\Delta\eta_2(\Delta\eta_1+\Delta\eta_2)(3(\Delta\eta_0)^2+4\Delta\eta_0\Delta\eta_1+2\Delta\eta_0\Delta\eta_2+(\Delta\eta_1)^2+\Delta\eta_1\Delta\eta_2)}\,u_{i,3}^{n+1}\,. \end{aligned} \tag{4.210}$$

The results of the tests using SG parameters are presented in Figures 4.22–4.24. From the figures, it can be seen that the discretisation used for the surface velocity value does not seem to influence the (integer) value of κ giving optimal performance of the numerical scheme. The value $\kappa = 6$ gives best results for each discretisation at the operational value of $N_\lambda = 119$ for the Spencer Gulf model. Note that there is a large variation in the results on each plot for $\kappa = 5, 6, 7$, so it is not likely that $\kappa = 6$ is the true optimal value and one cannot say, from these graphs, which of the discretisations produces best results. To determine this, the interval $\kappa \in [5, 7]$ should be subdivided into small non-integer segments, further benchmark solutions derived and numerical tests carried out. These tests need only be conducted at the operational values of N_λ of interest.

Despite the inconclusive nature of evidence from Figures 4.22–4.24 for choosing an optimal surface velocity approximation, the third order accurate discretisation (4.209) will be used since, for non-uniform grids, it is more accurate than the second order discretisation (4.208), and is only slightly less accurate than the fourth order discretisation (4.210) whilst being simpler to program and computationally cheaper to run.

Figures 4.22–4.24 show that the numerical scheme is more sensitive to the value of κ than to the discretisation for surface velocity. That is, the value of κ and hence the vertical grid spacing is a more significant factor contributing to the overall accuracy of the numerical scheme than is the accuracy of discretisation of the surface velocity approximation. This is because of the difficulty in correctly modelling the high shear layer near the bed. Given a fixed number of depth levels, modelling accuracy is improved if more of them can be located in the high shear layer than at mid-levels.

Of course flows in the high shear layer can be more accurately modelled simply by using more depth levels, but for reasons of minimizing both demands on computer storage



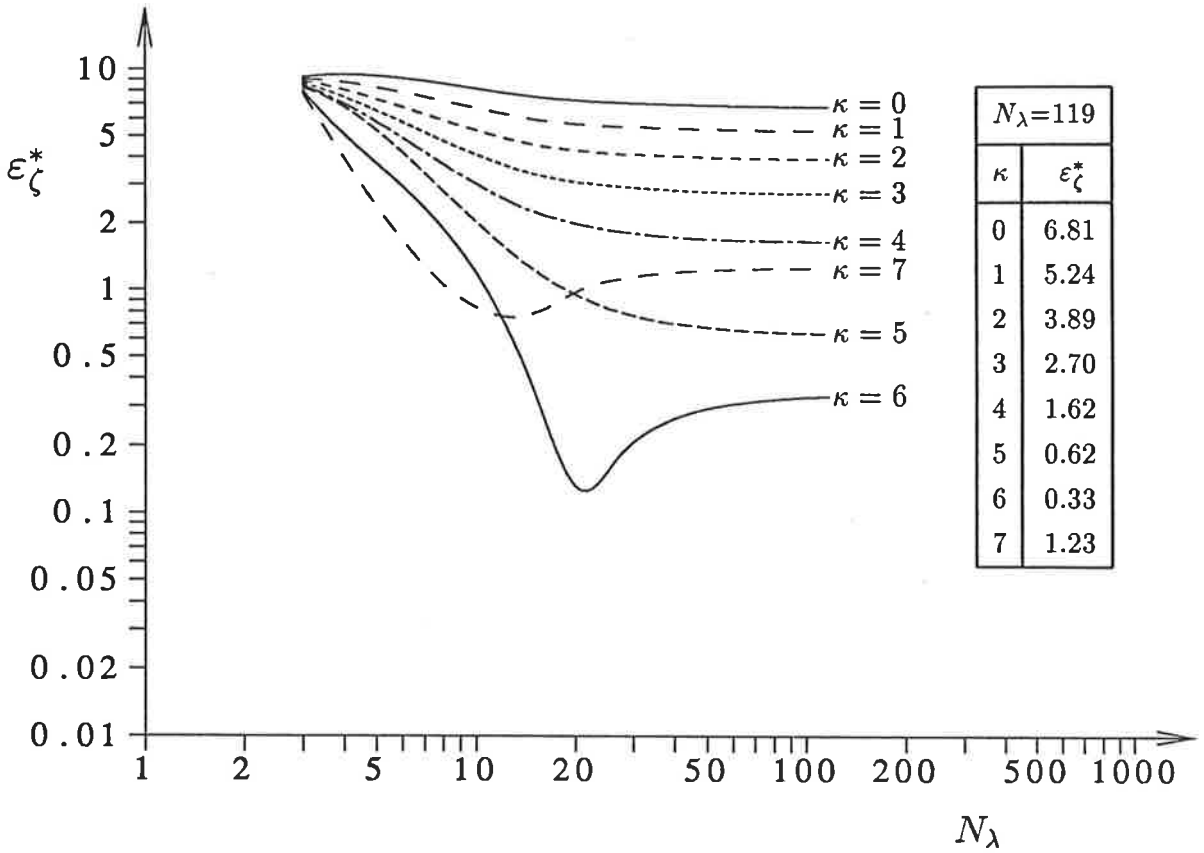
N_λ=119	
κ	ε^*_ζ
0	6.89
1	5.30
2	3.94
3	2.75
4	1.66
5	0.66
6	0.30
7	1.20

Figure 4.23: *Percentage error in dimensionless elevation ε^*_ζ versus number of grid spacings per wavelength N_λ for constant depth Spencer Gulf model tests using the semi-diurnal constituent. Courant number $C_x = 0.3$; 10 depth intervals are used. The third order surface velocity discretisation is used together with the symmetric parabolic vertical eddy viscosity form. Eight integer values of κ are used. Again there is a large range in performance of the numerical scheme for a given N_λ; optimal performance is achieved at $\kappa = 6$. At the operating value $N_\lambda = 119$ for the Spencer Gulf model, accuracy is good for $\kappa = 6$.*

and computational time we have chosen to fix the number of levels at 11 (including the surface and bed levels) and seek their optimal distribution — further discussion of this is given in Section 4.6.

4.5.4 Wave propagation characteristics

The wave propagation analysis carried out here is an extension of the depth-averaged analysis of Section 4.2.3. The vertical profile of horizontal velocity is taken as known and so the analysis does not include the differencing of the vertical diffusive term. However, the κ effect in the Simpson vertical integration is examined, and is found to be negligible. The results presented provide a theoretical best performance of the numerical scheme, at each depth level, in the sense that no errors from the vertical discretisation of the diffusive term are involved. A more general analysis that incorporates the differencing of the vertical diffusive term has been carried out by Stevens (1990).



N_λ=119	
κ	ε^*_ζ
0	6.81
1	5.24
2	3.89
3	2.70
4	1.62
5	0.62
6	0.33
7	1.23

Figure 4.24: *Percentage error in dimensionless elevation ε^*_ζ versus number of grid spacings per wavelength N_λ for constant depth Spencer Gulf model tests using the semi-diurnal constituent. Courant number $C_x = 0.3$; 10 depth intervals are used. The fourth order surface velocity discretisation is used together with the symmetric parabolic vertical eddy viscosity form. Eight integer values of κ are used. There is a large range in performance of the numerical scheme for a given N_λ; again, optimal performance is achieved at $\kappa = 6$. At the operating value $N_\lambda = 119$ for the Spencer Gulf model, accuracy is good for $\kappa = 6$.*

Because the vertical profile is required for the present study, the true wave solution is examined first. In the process, the vertical profile will be established for a given vertical eddy viscosity coefficient.

True wave solutions of the linear equations (4.139)–(4.140) and (4.142) are sought in the horizontally unbounded domain in the form

$$\widehat{\zeta} = \zeta_a \exp\left\{\imath(\widehat{k}_t t + k_x x)\right\}, \tag{4.211}$$

$$\widehat{U} = U_a \exp\left\{\imath(\widehat{k}_t t + k_x x)\right\}, \tag{4.212}$$

$$\widehat{u} = u_a \exp\left\{\imath(\widehat{k}_t t + k_x x)\right\} F(\eta), \tag{4.213}$$

where the amplitudes ζ_a, U_a, u_a may be complex and $F(\eta)$ is a vertical profile of horizontal velocity which satisfies boundary conditions (4.160)–(4.161). Equations (4.146)–(4.147) are not considered since the process of their solution is explicit and does not contribute

to the numerical solutions for elevation and horizontal velocity, and so does not affect numerical stability. For the purposes of studying wave propagation characteristics, $\widehat{k}_t$ must be complex and k_x real.

Substituting (4.213) into (4.142) gives

$$U_a = u_a \int_0^1 F(\eta) d\eta \,, \tag{4.214}$$

and substituting (4.211) and (4.214) into (4.139) gives

$$\zeta_a \widehat{k}_t + u_a h_0 k_x \int_0^1 F(\eta) d\eta = 0 \,. \tag{4.215}$$

Substituting (4.211) and (4.213) into (4.140) gives

$$\zeta_a g k_x + u_a \left(\widehat{k}_t F(\eta) + \frac{\imath}{h_0^2} \frac{d}{d\eta} \left(N_\eta \frac{dF}{d\eta} \right) \right) = 0 \,. \tag{4.216}$$

Combining (4.215) and (4.216) leads to the matrix expression

$$\begin{bmatrix} \widehat{k}_t & h_0 k_x \int_0^1 F(\eta) d\eta \\ g k_x & \widehat{k}_t F(\eta) + \frac{\imath}{h_0^2} \frac{d}{d\eta} \left(N_\eta \frac{dF}{d\eta} \right) \end{bmatrix} \begin{bmatrix} \zeta_a \\ u_a \end{bmatrix} = 0 \,, \tag{4.217}$$

from which it is clear that in order to obtain the true wave solution $\widehat{k}_t$ for a given wavenumber k_x, $F(\eta)$ and N_η must be known. Furthermore, (4.217) is the dispersion relation in matrix form and the equation for finding $F(\eta)$ in the unbounded case (c.f. equations (4.156) and (4.162) for the bounded case). The true wave solution of (4.217) may be obtained by separately solving the two equations that comprise (4.217).

In order to solve (4.215) and (4.216), however, values for the complex amplitudes ζ_a and u_a must be chosen. If the following choices are made:

$$\zeta_a = \zeta_0 \quad \text{and} \quad u_a = -\zeta_0 g k_x / \widehat{k}_t \,, \tag{4.218}$$

the dispersion relation (4.215) becomes

$$\left(\widehat{k}_t \right)^2 = g h_0 (k_x)^2 \int_0^1 F(\eta) d\eta \tag{4.219}$$

and equation (4.216) for $F(\eta)$ becomes

$$F(\eta) = 1 - \frac{\imath}{\widehat{k}_t h_0^2} \frac{d}{d\eta} \left(N_\eta \frac{dF}{d\eta} \right) . \tag{4.220}$$

Comparing (4.219) with (4.156) and (4.220) with (4.162), it is seen that the choice of amplitudes (4.218) leads to the same equations as arise in the bounded case, and so the same solutions apply.

Thus, for example, selecting the Johns vertical eddy viscosity coefficient (4.141), viz.

$$N_\eta = \gamma_1 \{1 + \gamma_2 (1 - \eta)\}^2 \,, \tag{4.221}$$

the solution

$$F(\eta) = 1 + C_1 \{1 + \gamma_2 (1 - \eta)\}^{n_1} + C_2 \{1 + \gamma_2 (1 - \eta)\}^{n_2} \tag{4.222}$$

is obtained. Using (4.222) in (4.219) and simplifying the result with (4.168) leads to

$$\widehat{k}_t = -k_x\sqrt{\frac{gh_0}{\gamma_2}}\sqrt{\frac{(\gamma_2 n_2 - 1)(1+\gamma_2)^{n_2} - (\gamma_2 n_1 - 1)(1+\gamma_2)^{n_1}}{n_2(1+\gamma_2)^{n_2} - n_1(1+\gamma_2)^{n_1}}}, \tag{4.223}$$

where

$$n_1, n_2 = -\frac{1}{2} \pm \sqrt{\frac{1}{4} + \frac{\imath\widehat{k}_t h_0^2}{\gamma_1\gamma_2^2}}. \tag{4.224}$$

Choosing the negative branch of the square root function in (4.223) guarantees a solution for $\widehat{k}_t$ in the second quadrant of the complex plane ($\Re e\{\widehat{k}_t\} < 0, \Im m\{\widehat{k}_t\} > 0$). Equation (4.223) is solved iteratively for $\widehat{k}_t$ using Newton's method. Semi-diurnal SG parameters are used. The (real) wavenumber k_x is calculated from

$$k_x = \frac{2\pi}{\lambda} = \frac{2\pi}{T\sqrt{gh_0}}, \tag{4.225}$$

where h_0 is given by (4.18); γ_1 is given by (4.189) and γ_2 is inferred from (4.190).

Defining

$$f(\widehat{k}_t) = \widehat{k}_t + k_x\sqrt{\frac{gh_0}{\gamma_2}}\sqrt{\frac{(\gamma_2 n_2 - 1)(1+\gamma_2)^{n_2} - (\gamma_2 n_1 - 1)(1+\gamma_2)^{n_1}}{n_2(1+\gamma_2)^{n_2} - n_1(1+\gamma_2)^{n_1}}}, \tag{4.226}$$

we find $\widehat{k}_t$ as a zero of $f(\widehat{k}_t)$ where successive iterates are obtained using the recurrence relation

$$\widehat{k}_t^{[p+1]} = \widehat{k}_t^{[p]} - \frac{f(\widehat{k}_t^{[p]})}{f'(\widehat{k}_t^{[p]})}. \tag{4.227}$$

and $\widehat{k}_t^{[0]} = \sigma$. The derivative is

$$\begin{aligned} f'(\widehat{k}_t) \;=\; 1 - k_x\sqrt{\frac{gh_0}{\gamma_2}}\Big\{&(1+\gamma_2)^{n_1}\left[(1+\gamma_2)^{n_2}\left\{(n_1-n_2)\ln(1+\gamma_2)+1\right\} - (1+\gamma_2)^{n_1}\right]\frac{\partial n_1}{\partial \widehat{k}_t} \\ &-(1+\gamma_2)^{n_2}\left[(1+\gamma_2)^{n_1}\left\{(n_1-n_2)\ln(1+\gamma_2)-1\right\} + (1+\gamma_2)^{n_2}\right]\frac{\partial n_2}{\partial \widehat{k}_t}\Big\} \\ &\Big/\Big\{2\left[n_2(1+\gamma_2)^{n_2} - n_1(1+\gamma_2)^{n_1}\right]^{3/2} \\ &\left[(\gamma_2 n_2 - 1)(1+\gamma_2)^{n_2} - (\gamma_2 n_1 - 1)(1+\gamma_2)^{n_1}\right]^{1/2}\Big\} \end{aligned} \tag{4.228}$$

where

$$\frac{\partial n_1}{\partial \widehat{k}_t}, \frac{\partial n_2}{\partial \widehat{k}_t} = \pm\frac{1}{2}\frac{\imath h^2}{\gamma_1\gamma_2^2}\left(\frac{1}{4} + \frac{\imath\widehat{k}_t h^2}{\gamma_1\gamma_2^2}\right)^{-1/2}. \tag{4.229}$$

Expression (4.228) was obtained using the symbolic algebra/calculus package REDUCE. The method converges rapidly and the error in the zero falls below 10^{-20} on the VAX 11/785 using Double Precision within half a dozen iterations!

Having obtained the true wave solution, consider now the numerical wave solution.

The stability of the overall numerical scheme defined by equations (4.171)–(4.178) is determined by the equations (4.171)–(4.172). Equation (4.171) is written as

$$\zeta_i^{n+\frac{1}{2}} - \zeta_i^{n-\frac{1}{2}} = -rh_0(U_i^n - U_{i-1}^n)\,, \tag{4.230}$$

where $r = \Delta t/(2\Delta x)$ as before, and equation (4.172) is written as

$$\begin{aligned} u_{i,k}^{n+1} - u_{i,k}^n &= -rg(\zeta_{i+1}^{n+\frac{1}{2}} - \zeta_i^{n+\frac{1}{2}}) \\ &+\frac{\Delta t}{2h_0^2}\left[\left\{\frac{\partial}{\partial\eta}\left(N_\eta\frac{\partial u}{\partial\eta}\right)\right\}_{i,k}^n + \left\{\frac{\partial}{\partial\eta}\left(N_\eta\frac{\partial u}{\partial\eta}\right)\right\}_{i,k}^{n+1}\right], \end{aligned} \tag{4.231}$$

where, as stated previously, the differencing of the vertical diffusive term is not considered. The equation for depth-averaging the depth-dependent horizontal velocity is written as

$$U_i^n = \left\{\int_0^1 u d\eta\right\}_i^n, \tag{4.232}$$

and the integration is carried out numerically.

For the present analysis, numerical wave solutions are sought in the horizontally unbounded domain in the form

$$\zeta_i^n = \zeta_a \exp\{\imath(k_t n\Delta t + k_x i 2\Delta x)\}\,, \tag{4.233}$$

$$U_i^n = U_a \exp\{\imath(k_t n\Delta t + k_x i 2\Delta x)\}\,, \tag{4.234}$$

$$u_i^n(\eta_k) = u_a \exp\{\imath(k_t n\Delta t + k_x i 2\Delta x)\}F(\eta_k)\,, \tag{4.235}$$

where $F(\eta_k)$ is known for each level $\eta_k, k = 0, 1, \ldots, NK$, the amplitudes ζ_a, U_a, u_a and wavenumber k_x are as before and k_t is the complex frequency of the numerical wave.

Substituting (4.235) into (4.232) and then the result, together with (4.233), into (4.230) gives

$$\begin{aligned} \zeta_a(\xi - 1) \;+\; & u_a\sqrt{\xi}rh_0 2\imath\sin(k_x\Delta x)\Big[(\Delta\eta_0 + \Delta\eta_1)(2 - r_1^{-1})F(0) \\ &+(\Delta\eta_0 + \Delta\eta_1)(2 + r_1^{-1} + r_1)F(\eta_1) \\ &+\left((\Delta\eta_0 + \Delta\eta_1)(2 - r_1) + (\Delta\eta_2 + \Delta\eta_3)\left(2 - r_3^{-1}\right)\right)F(\eta_2) \\ &+(\Delta\eta_2 + \Delta\eta_3)\left(2 + r_3^{-1} + r_3\right)F(\eta_3) + \ldots \\ &+(\Delta\eta_{NK-2} + \Delta\eta_{NK-1})\left(2 + r_{NK-1}^{-1} + r_{NK-1}\right)F(\eta_{NK-1}) \\ &+(\Delta\eta_{NK-2} + \Delta\eta_{NK-1})(2 - r_{NK-1})F(1)\Big]/6 = 0\,, \end{aligned} \tag{4.236}$$

where Simpson's rule for a non-uniform grid is used, $r_k = \Delta\eta_{k-1}/\Delta\eta_k$ as before, and $\xi = \exp(\imath k_t\Delta t)$. Substituting (4.233) and (4.235) into (4.231) gives the equations

$$\zeta_a\sqrt{\xi}rg2\imath\sin(k_x\Delta x) + u_a\left[F(\eta_k)(\xi - 1) + \Delta t(\xi + 1)\imath\hat{k}_t(1 - F(\eta_k))/2\right], \tag{4.237}$$

for levels $k = 0, 1, \ldots, NK$, where the derivative terms in (4.231) have been replaced with analytical expressions using (4.220). Combining (4.236) and (4.237) gives a matrix equation whose coefficient matrix is 12×12 for $NK = 10$ depth intervals.

The numerical wave solution may be obtained by setting the determinant of the coefficient matrix to zero. However, because the determinant is zero, it may be rearranged into a form which enables the solution to be obtained as one of the eigenvalues of an equivalent eigenvalue/eigenvector problem. One possible rearrangement of the determinant is

$$\begin{vmatrix} \xi-1 & -\xi a S_0 F(0) & -\xi a S_1 F(\eta_1) & \dots & -\xi a S_{NK} F(1) \\ 1 & \mathcal{F}(0) & 0 & \dots & 0 \\ 1 & 0 & \mathcal{F}(\eta_1) & \dots & 0 \\ \vdots & \vdots & \vdots & & \vdots \\ 1 & 0 & 0 & \dots & \mathcal{F}(1) \end{vmatrix} = 0 \tag{4.238}$$

where the functions $\mathcal{F}(\eta_k), k = 0, 1, \dots, NK$ take the form

$$\mathcal{F}(\eta_k) = F(\eta_k)(\xi - 1) + b(\xi + 1)(1 - F(\eta_k)), \tag{4.239}$$

and the Simpson coefficients $S_k, k = 0, 1, \dots, NK$ are

$$\begin{aligned} S_0 &= \frac{1}{6}(\Delta\eta_0 + \Delta\eta_1)\left(2 - \frac{1}{r_1}\right), \\ S_1 &= \frac{1}{6}(\Delta\eta_0 + \Delta\eta_1)\left(2 + \frac{1}{r_1} + r_1\right), \\ &\vdots \\ S_{NK} &= \frac{1}{6}(\Delta\eta_{NK-2} + \Delta\eta_{NK-1})(2 - r_{NK-1}); \end{aligned} \tag{4.240}$$

the constants a and b are

$$a = 4C_x^2 \sin^2\left(\frac{\pi}{N_\lambda}\right), \quad b = \frac{C_x T}{2N_\lambda} \imath \hat{k}_t, \tag{4.241}$$

where the substitutions

$$r^2 g h_0 = C_x^2, \quad k_x \Delta x = \frac{\pi}{N_\lambda} \quad \text{and} \quad \Delta t = \frac{C_x T}{N_\lambda} \tag{4.242}$$

have been used. The determinant (4.238) may now be written in the form

$$|A - \xi B| = 0 \tag{4.243}$$

from which it is clear that solutions ξ are eigenvalues of the eigenvalue/eigenvector equation

$$A\underline{x} = \xi B\underline{x}. \tag{4.244}$$

Here,

$$A = \begin{bmatrix} -1 & 0 & 0 & \dots & 0 \\ 1 & -F(0) + b(1 - F(0)) & 0 & \dots & 0 \\ 1 & 0 & -F(\eta_1) + b(1 - F(\eta_1)) & \dots & 0 \\ \vdots & \vdots & \vdots & & \vdots \\ 1 & 0 & 0 & \dots & -F(1) + b(1 - F(1)) \end{bmatrix} \tag{4.245}$$

and

$$B = \begin{bmatrix} -1 & aS_0F(0) & aS_1F(\eta_1) & \dots & aS_{NK}F(1) \\ 0 & -F(0) - b(1 - F(0)) & 0 & \dots & 0 \\ 0 & 0 & -F(\eta_1) - b(1 - F(\eta_1)) & \dots & 0 \\ \vdots & \vdots & \vdots & & \vdots \\ 0 & 0 & 0 & \dots & -F(1) - b(1 - F(1)) \end{bmatrix} . \quad (4.246)$$

The solutions ξ are obtained using the IMSL package EIGZC which finds the complex zeros of high order complex polynomial functions.

Results for the amplitude response χ and relative wave speed μ are given in Figure 4.25 for SG parameters. In order to test the accuracy of the Simpson integration, non-uniform grids with values $\kappa = 0, 1, \dots, 7$ are used, and the results are all plotted on these figures. Since the results overlay each other, it is clear that the Simpson integration is almost insensitive to the value of κ used and certainly does not account for the large variation in performance of models shown in Figure 4.19. This variation must therefore be attributable to the differencing of the vertical diffusive term and is investigated by Stevens (1990).

Referring to the table of values inserted in Figure 4.25(b) for $N_\lambda = 119$, as κ increases from zero amplitude response decreases although it remains close to unity; relative wave speed first increases but starts to decrease again at high κ, always remaining close to unity. Comparing Figures 4.25 with the semi-diurnal plots in Figures 4.3, there is strong agreement, the operational χ and μ values of that test corresponding to the performance at a κ value in the present test of between 4 and 5.

Rather than use the Johns vertical eddy viscosity coefficient and corresponding vertical profile, the symmetric parabolic coefficient of the previous section could be used to conduct a further analysis. In order to do this, the true wave solution would have to be developed either numerically from equations (4.219) and (4.220), employing many levels in the vertical in order to ensure high accuracy, or analytically using Stevens' (1990) expressions. However, since one anticipates that the results would be qualitatively similar to those given in Figure 4.25, it does not seem useful to pursue this further.

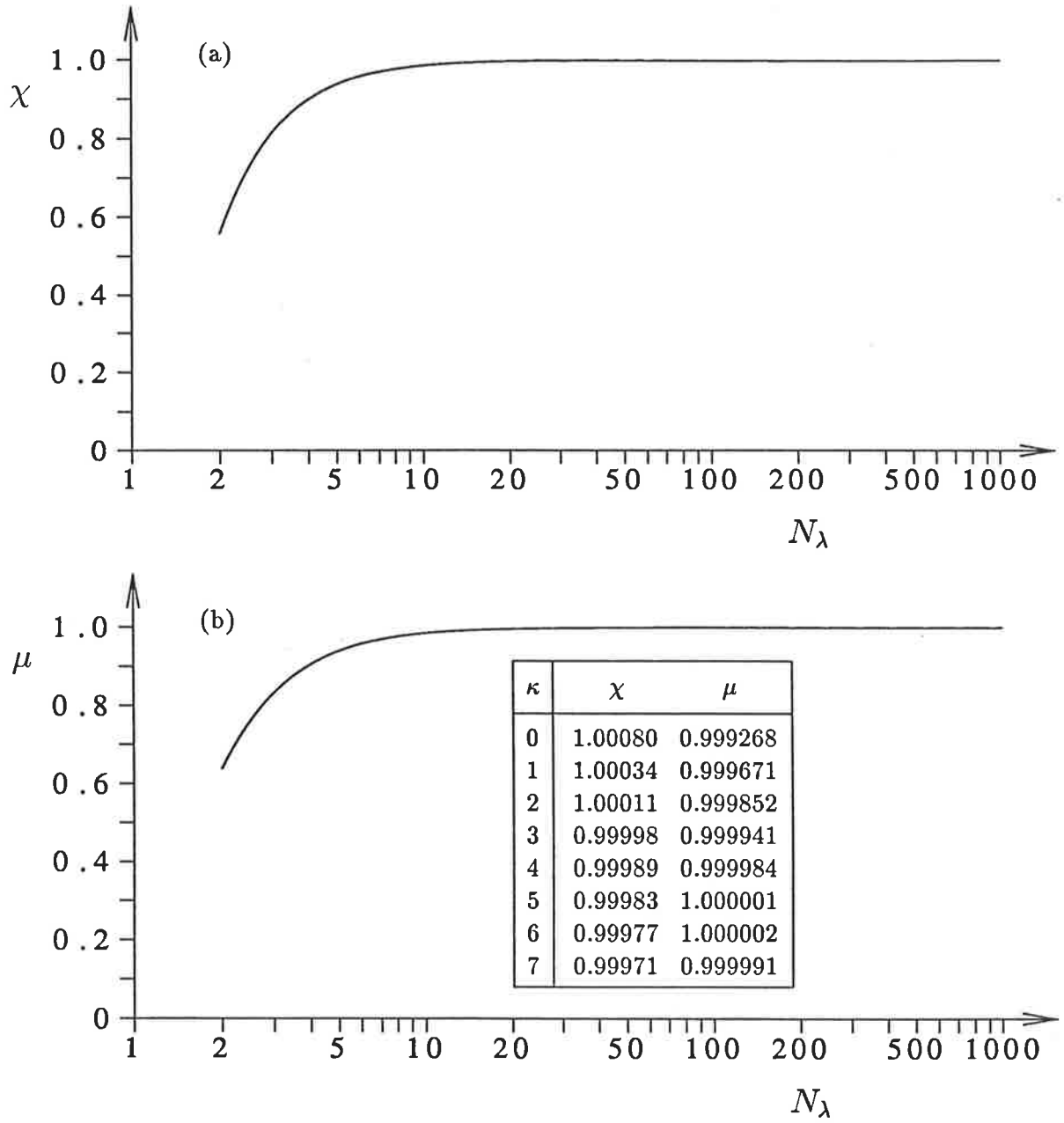
4.6 Summary

The value of comparing numerical and analytical solutions to simplified forms of the governing equations solved in estuaries and bays of simple geometry is that it is part of the process by which more efficient algorithms may be found to perform certain required functions. In this way, model accuracy and algorithm efficiency can be improved.

Because, generally speaking, the linear part of the equations accounts for the bulk of the flow, the results of such experimentation usually apply to the discretised set of fully non-linear equations.

Optimizing the number of depth levels

For a uniform arrangement of depth levels, the accuracy of solution is found to increase as the number of depth levels is increased. However beyond a certain number of levels, improvement is almost negligible, while the cost in terms of computer storage and computational time continues to rise.



κ	χ	μ
0	1.00080	0.999268
1	1.00034	0.999671
2	1.00011	0.999852
3	0.99998	0.999941
4	0.99989	0.999984
5	0.99983	1.000001
6	0.99977	1.000002
7	0.99971	0.999991

Figure 4.25: *(a) (Top) Amplitude response χ versus number of grid spacings per wavelength N_λ and (b) (bottom) relative wave speed μ versus number of grid spacings per wavelength N_λ for semi-diurnal parameters representative of the Spencer Gulf model. The differencing of the vertical diffusion term is not taken into account; however, values of $\kappa = 0,1,\ldots,7$ are used to obtain the Simpson integration and all 8 sets of graphs are plotted, showing that the Simpson integration is virtually insensitive to κ. It can be seen from these figures that provided an accurate differencing for the vertical diffusion term is used, at the operating value of $N_\lambda = 119$ the numerical scheme propagates the semi-diurnal wave with high accuracy (see table).*

Since Spencer Gulf is not deep, the number of depth levels required to determine the vertical current structure accurately does not need to be very large. Each extra depth level used requires computer storage for another three components of velocity for each computational element and must also be taken into account when performing depth-averaging. While the computer available, a VAX 11/785, has a virtual memory facility, there is a limit to the capacity of this facility and as well, time is lost if there is the need to continually swap information in and out of core memory during computation. Furthermore, the machine is shared by many users and quotas apply on computer storage use.

On the other hand, as has been seen, a suitable spacing of the available depth levels can improve the accuracy of solution.

When all these factors are taken into account, 11 depth levels spaced in the optimal fashion suffice to provide greatest accuracy, use least computer memory and give accurate representation of vertical profiles of velocity for a reasonable amount of central processing time.

Optimizing the arrangement of depth levels

Near the bed, the velocity profiles are steep because of the requirement of the no-slip condition at the bed. A vertical grid that is fine near the sea floor and coarse above it is better suited to model the lower region accurately and to convey this information to the upper levels than a uniform grid using the same number of depth levels. Similarly, a fine grid near the surface is better suited to convey information about an applied wind stress into the lower levels of the water column, and allows a more accurate expression for the surface velocity discretisation to be constructed even in the absence of a wind.

It therefore seems best to have a fine grid near the sea bed, graded to coarse at the middle levels and back to fine near the surface.

The actual variation of the grid spacing is smooth and is chosen based on the second order relationship between consecutive grid level spacings governed by the parameter κ as given in equation (3.1) of Chapter 3.

The numerical tests carried out illustrate the necessity of testing for the optimum κ for a given three-dimensional model and vertical eddy viscosity coefficient.

Surface velocity discretisation

Using a surface boundary condition of zero applied stress, second, third and fourth order accurate discretisations for surface velocity are tested. When a uniform grid is used, the third and fourth order discretisations generate results for $F(\eta)$ (see Figure 4.20) which are significantly more accurate than the second order results, for each number of depth levels considered. The uniform grid results of Figures 4.22–4.24 for SG tests show the same trend for a fixed number of 11 depth levels. However, Figures 4.22–4.24 also show that the arrangement of depth levels (i.e. the value of κ) is far more influential on accuracy than is the order of the surface velocity approximation. Considering these factors, it seems best to adopt the third order accurate approximation, it being significantly more accurate than the second order approximation, and while being slightly less accurate than the fourth, it is simpler and quicker to execute.

Integration techniques for depth-averaging the horizontal velocity components

Simpson's rule is a more accurate numerical integration technique than the Trapezoidal rule. Simpson's rule for unequally spaced intervals is third order accurate while the Trapezoidal rule for unequally spaced intervals is second order accurate. Because the finite difference equations are at best second order accurate, it might be expected that a second order numerical integration scheme would provide sufficient accuracy.

In tests, it was found that the two methods of integration give answers that are essentially equivalent, but Simpson's rule always produces slightly more accurate results. Therefore, from the point of view of overall accuracy for models run for at least 29 days of simulated time, Simpson's rule is used. It should be noted, however, that to calculate the ω and w fields the Trapezoidal rule is used rather than Simpson's rule because of the need to compute these fields at every depth level.

Tests with different bay orientations

A major aim of the present tests is to check that the program code for the automatic generation of appropriate boundary approximations is correct. One way of doing this is to check that the results obtained in the case of one-dimensional channel flow are independent of the orientation of the region, and so it is necessary to rotate the models through different angles to verify this requirement. In doing this, errors present in the program code may be located because identical results should be obtained with each orientation.

Initially, the basic orientations with open boundaries facing toward the north, south, east and west, are tested. Then, the oblique (45°) orientations are tested to enable errors in the rest of the code to be detected.

In the case of the two-dimensional depth-averaged models of Section 4.4, the same tests of program code can be carried out and one expects identical results for each orientation when the Coriolis parameter is set to zero. When the Coriolis parameter is a non-zero constant, there are slight differences in results due to the different approximations used for the velocity factor of the Coriolis terms outlined in Subsection 4.4.3 (see Figures 4.13 and 4.14).

Conclusions

In the process of carrying out these tests, confidence in the accuracy and robustness of the numerical scheme has been established, at operational parameter values, for estuaries of simple geometry.

The application of the scheme to the models of greater Spencer Gulf and Northern Spencer Gulf in the remaining chapters will be a further check on the accuracy and stability of the scheme.

Chapter 5

A depth-averaged model of Spencer Gulf

5.1 Introduction

This chapter reports the development of a depth-averaged tidal model of Spencer Gulf, South Australia (Figure 5.1).

Besides re-examining past research and investigating new features of tidal flow in the Gulf, the model is used in Chapter 8 to establish open boundary data for a high resolution tidal model of Northern Spencer Gulf.

An element size appropriate for a Northern Spencer Gulf model is of the order of 2 km × 2 km. Constraints imposed by computing facilities at The University of Adelaide limit the number of computational grid elements in such a model to about 1000. Using this number of elements, the open boundary of the Northern Spencer Gulf model lies across the Gulf approximately halfway between Whyalla and Franklin Harbour on the western side and halfway between Pt. Pirie and Wallaroo on the eastern side (Figure 5.2). There are no nearby tide-height stations to provide accurate forcing data for this open boundary. Ideally, field measurements should be made at positions corresponding to each open boundary elevation gridpoint to obtain the open boundary conditions for the model (McIntosh, 1985), but such data would be too costly and beyond the scope of this work to obtain. Most tide-height data available is for stations around the coastline and at the entrance to the Gulf.

A good open boundary data set for a coarse resolution Spencer Gulf model can be established from four tide-height stations located across the mouth of the Gulf. Boundary data for the smaller model is inferred from the larger. A convenient element size for the coast-grid model is therefore chosen to be three times that of the fine-grid model, in which case all of the gridpoints of the former model coincide with gridpoints of the latter. The total number of coarse-grid elements is then less than 1000.

In the course of reading this chapter, the reader may wish to consult Figures 5.1 and 5.2, or Figures 5.10 and 5.15 for the location of tidal observation stations and certain other features within the Gulf. Unless otherwise indicated, "north" means "up-the-page" and vice versa in the figures that follow. The positive y-direction of the model is referred to as "north" and this is shorthand for the true orientation of the model, viz. 33° T (or NNE).

Much of the work in this chapter has appeared in a research report (Bills, 1985) to the

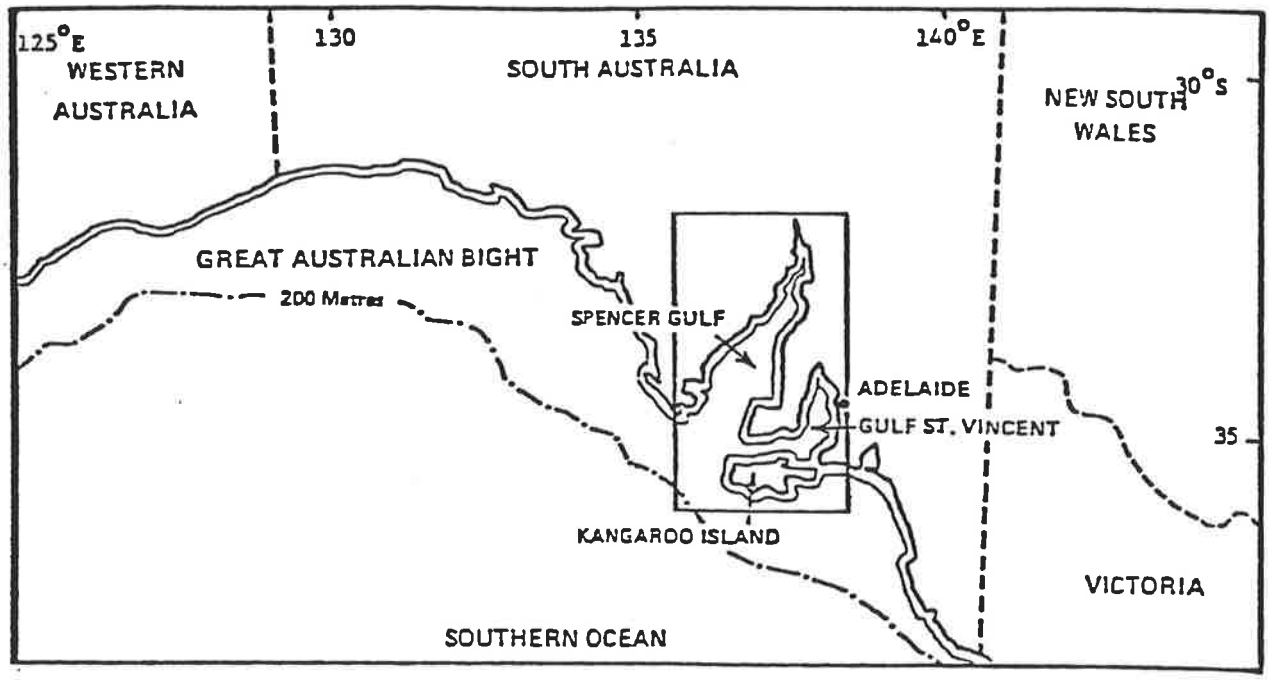


Figure 5.1: *Location of Spencer Gulf within the South Australian Gulf System.*

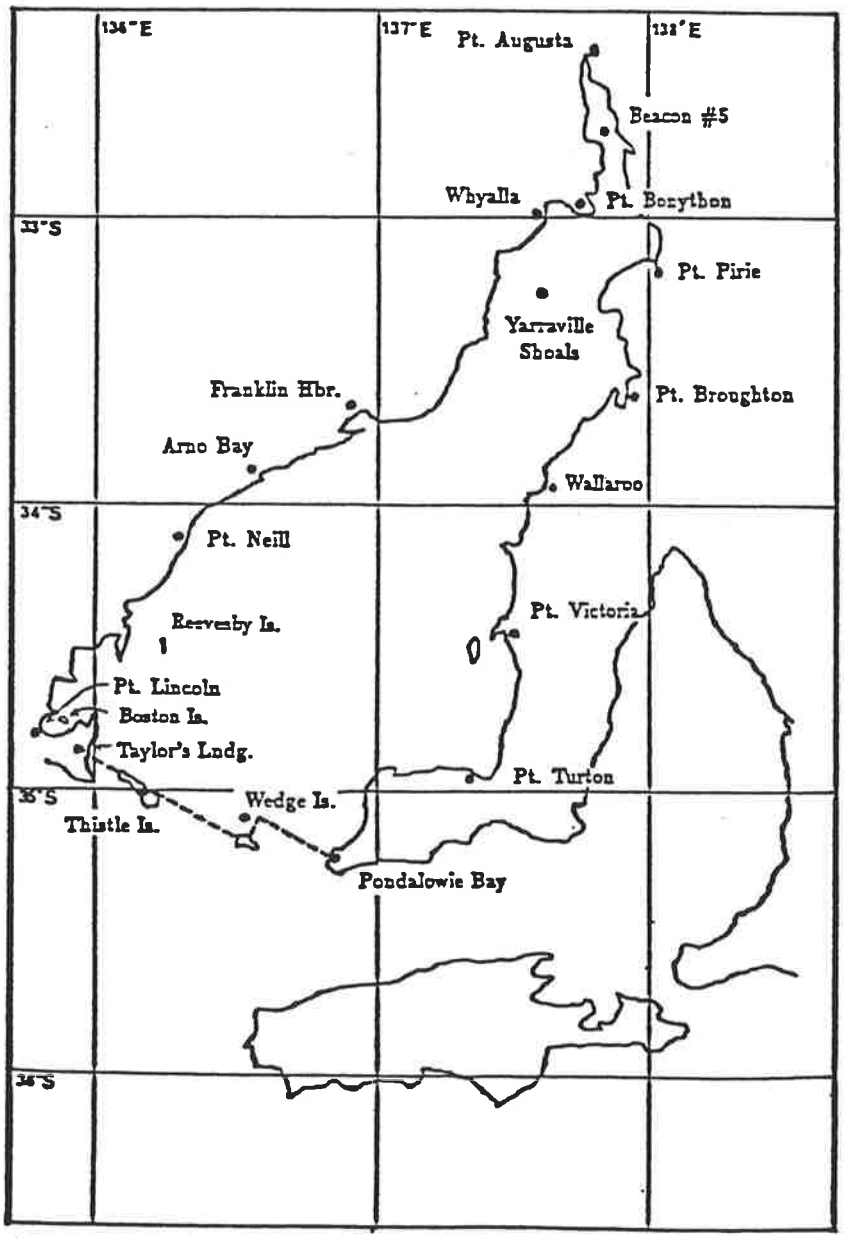


Figure 5.2: *Map showing important features, towns and tidal observation sites within Spencer Gulf. The open boundary line of the model is marked:* - - - -.

author's scholarship disbursing body and in a conference paper by Bills and Noye (1986).

5.2 Review of the literature

Easton (1970) provides a comprehensive survey of the literature on the tides of South Australia, pointing out that the work of Bragg, Inglis, Lyle and Chapman (1892), Chapman and Inglis (1898, 1903) and Chapman (1938) are major contributions to the knowledge of South Australian tides to 1970.

Easton divides the Australian coastline into 13 zones "in which tidal characteristics are so similar that they may be represented by the tide at one port, the 'standard port' of the zone" (Easton, 1970, p.22). The South Australian gulfs constitute a distinct zone in his classification.

To investigate the changes of tidal character that are present within a particular zone, it is necessary to establish a definition of "tidal type". The ratio

$$R = \frac{O_1 + K_1}{M_2 + S_2} \tag{5.1}$$

is used for this purpose, where amplitudes are inferred. Easton finds this to be the most useful ratio for Australian tides. It represents the following tidal types (Easton, 1970, p.27):

- semi-diurnal (SD), if $0 < R < 1/4$,
- semi-diurnal with diurnal inequalities (SI), if $1/4 < R < 3/4$,
- mixed (M), if $3/4 < R < 2$,
- diurnal (D), if $R > 2$.

Easton gives no equalities in these expressions. In Table 5.1 tide-height constants for 18 stations within Spencer Gulf are listed. The constants are supplied by the National Tidal Facility at The Flinders University of South Australia. Kelly (1979) warns that there is a large phase lag in the data for all constituents at Pt. Broughton caused by a long channel at the gauge location, so this data is not used in the model calibration but is presented because it is the best available. Table 5.2 lists the values of R and the associated tidal type for each of the stations and shows that tidal character changes from "mixed" in southern Spencer Gulf to "semi-diurnal with diurnal inequalities" in Northern Spencer Gulf.

A distinctive feature of the tides of Spencer Gulf "is the prominence of S_2 which is either as great as or slightly greater than M_2" (Easton, 1970, p.32) (see also Table 5.1). Chapman and Inglis (1903) outline an explanation for this, based on the "Resonance Theory of the Tides" as described in undated material by Mr. Rollin A. Harris, then Chief of the Tidal Department of the United States Coast and Geodetic Survey. They say: "Just as a succession of properly timed taps may impart a considerable swing to a pendulum, so, if the natural time of oscillation of a large body of water coincides with the periodic action of the tide producing forces, a large oscillation will be the result. Mr. Harris has accordingly attempted to map out the oceans of the world into areas of water each of which would swing in harmony with some of the tidal forces, the natural character and period of oscillation of each area being computed from its dimensions and depth" (ibid., p.13).

Tide-height station	O_1		K_1		M_2		S_2	
	amp	phase	amp	phase	amp	phase	amp	phase
Port Augusta	28.3	52.8	44.0	82.7	64.0	212.2	68.6	272.3
Beacon #5	25.0	48.1	47.0	73.4	57.9	196.0	62.0	255.2
Port Pirie	27.6	49.2	42.5	77.4	48.9	197.2	52.9	258.3
Port Bonython	27.0	42.7	41.6	70.6	45.1	185.3	48.6	245.6
Whyalla	25.7	45.2	40.1	72.8	42.1	184.5	45.4	245.2
Yarraville Sh.	24.4	39.2	37.2	69.8	32.2	175.5	33.9	236.9
Port Broughton	17.4	100.9	27.8	110.4	15.8	214.8	15.2	275.4
Wallaroo	21.8	33.3	32.7	61.9	17.1	132.3	16.8	187.1
Franklin Hbr.	20.0	34.0	30.0	61.0	22.0	114.0	23.0	173.0
Arno Bay	19.9	8.4	29.5	37.4	25.6	66.6	26.8	120.1
Port Victoria	16.9	20.7	24.5	51.5	18.9	61.9	20.3	116.4
Port Neill	20.8	5.3	30.8	36.2	28.6	56.1	31.2	112.1
Port Turton	16.0	22.9	23.4	51.7	18.4	60.6	19.5	115.1
Port Lincoln	16.7	0.9	24.0	27.4	24.1	32.4	26.2	85.5
Taylor's Lndg.	15.3	359.1	21.2	26.7	19.9	17.1	21.0	68.1
Thistle Island	15.7	1.1	22.2	30.2	19.1	21.2	19.7	71.4
Wedge Island	15.1	6.6	21.0	36.3	16.6	24.1	17.1	74.4
Pondalowie Bay	13.1	12.9	16.6	44.3	13.9	26.3	13.8	78.0

Table 5.1: *Tidal constants for the four major tidal constituents at 18 stations within the Spencer Gulf region; amplitude in centimetres, phase in degrees, C.S.T. (−9:30 hr G.M.T.). These constants are supplied by the National Tidal Facility at The Flinders University of South Australia.*

Chapman and Inglis (1903) explain there are three bodies of water — to the south, south-west and west of Australia — which are primarily responsible for South Australian tides. Two of these resonate predominantly at semi-diurnal frequencies, and the other at diurnal frequencies. One of the semi-diurnally oscillating bodies of water is that between the southern Australian coast and the Antarctic continent. It is of such a size and depth that, although both sun and moon are continually acting upon it and the force exerted by the moon is the greater of the two, it naturally tends to "swing" so as to keep time with the sun's efforts to set it moving rather than the moon's. The sun's effect is magnified in consequence. West of this body of water, stretching between the south-eastern shores of Africa and the north of Antarctica, another large body of water naturally responds to the moon's semi-diurnal influence.

The tides along the southern coast of Australia seem to be due mainly to the oscillations in these two areas, the two bodies of water overlapping and the overall effect resulting in solar tides just about equal to lunar tides.

The third important body of water is the Northern Indian Ocean which responds diurnally and produces diurnal tides on the western coast of Australia. These tides propagate southwards, travelling round Australia's southern coasts and giving rise to the diurnal inequality which exists there.

Easton also comments: "The remarkably high value of S_2 ... causes the tides to

Tide-height station	R	Tidal type
Port Augusta	0.545	SI
Beacon #5	0.601	SI
Port Pirie	0.689	SI
Port Bonython	0.732	SI
Whyalla	0.752	M
Yarraville Sh.	0.932	M
Port Broughton	1.455	M
Wallaroo	1.609	M
Franklin Hbr.	1.111	M
Arno Bay	0.942	M
Port Victoria	1.055	M
Port Neill	0.864	M
Port Turton	1.038	M
Port Lincoln	0.810	M
Taylor's Lndg.	0.892	M
Thistle Island	0.974	M
Wedge Island	1.076	M
Pondalowie Bay	1.074	M

Table 5.2: *The value of R and associated "tidal type" for each of the stations listed.*

recur at approximately the same time each day and to cancel at neap tides. When these components [S_2 and M_2] are out of phase, the declinational tides (O_1, K_1, K_2), with ranges of up to 1.7 feet [0.52 m], dominate. Near the equinoxes, these components also vanish, allowing the water level to remain almost constant for a whole day or to vary with the lesser components. Due to the uncertainty of the neap levels, these tides have become known as 'dodging' or 'dodge' tides" (Easton, 1970, p.53). The first explanation of these tides is due to Bragg et al. (1892). Chapman and Inglis (1895) state: "the apparent impossibility of saying when the tide will be at this particular period has presumably gained for it its title of 'The Dodger' " (ibid., p.6).

Easton notes that the semi-diurnal tide, even with the unusually large S_2 constituent, is well represented by the M_2 constituent and the diurnal tide is well represented by the K_1 constituent. His co-amplitude and co-phase charts, with units changed so as to give amplitude in centimetres and phase in local time (Central Standard Time (Australian), −9:30 hr G.M.T.), are presented in Figures 5.3 and 5.4.

Easton says that "because of its deep water, the tide throughout the southern section of Spencer Gulf occurs at approximately the same time" (Easton, 1970, p.53). This statement apparently refers to the suggestion in Figures 5.3(b) and 5.4(b) that, as one moves northwards along the axis of the Gulf, the tides reach the same transverse coastal positions at approximately the same times. However, it will be seen in the numerical studies carried out after Easton's work, including the present one, that while this is true for the semi-diurnals, it is not the case for the diurnals. Moreover, the assumption that the tide travels faster up the axis of the Gulf because it is deeper, as portrayed by the

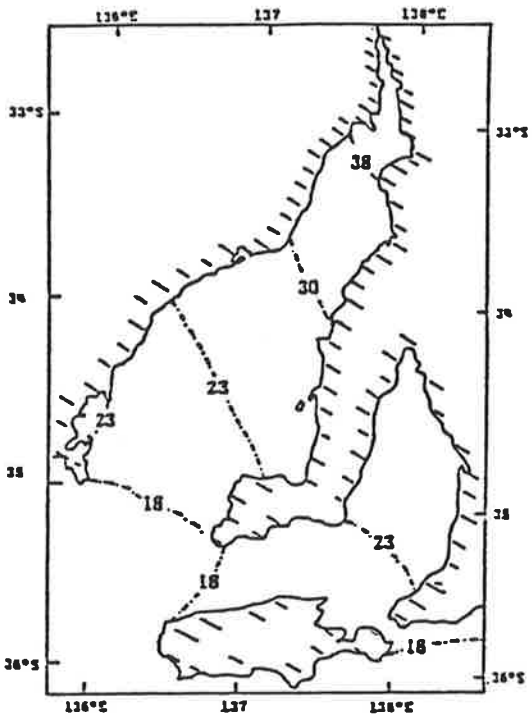


Figure 5.3(a): *Co-amplitude chart for K_1 — amplitude in centimetres (adapted from Easton, 1970).*

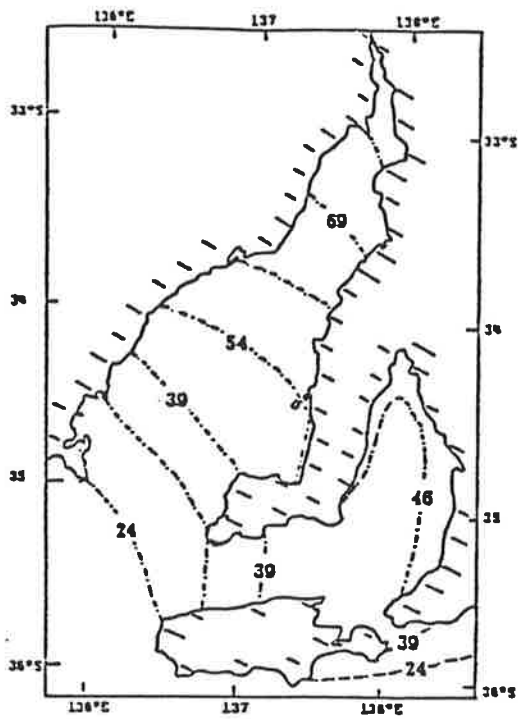


Figure 5.3(b): *Co-phase chart for K_1 — phase in degrees (C.S.T.) (adapted from Easton, 1970).*

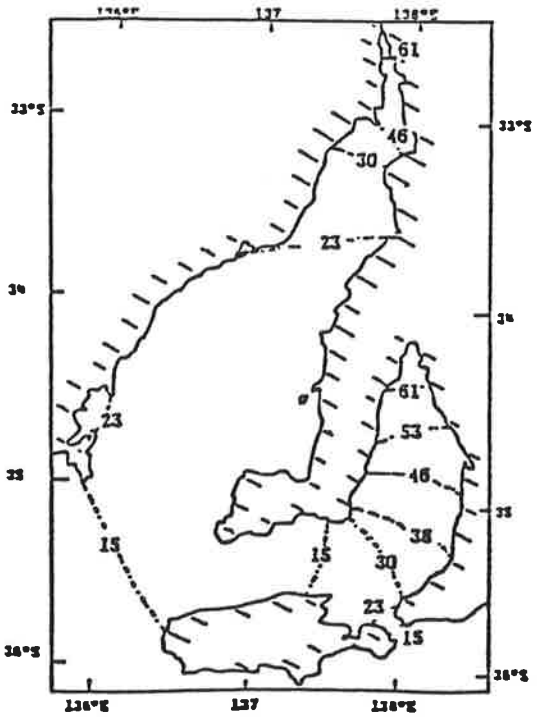


Figure 5.4(a): *Co-amplitude chart for M_2 — amplitude in centimetres (adapted from Easton, 1970).*

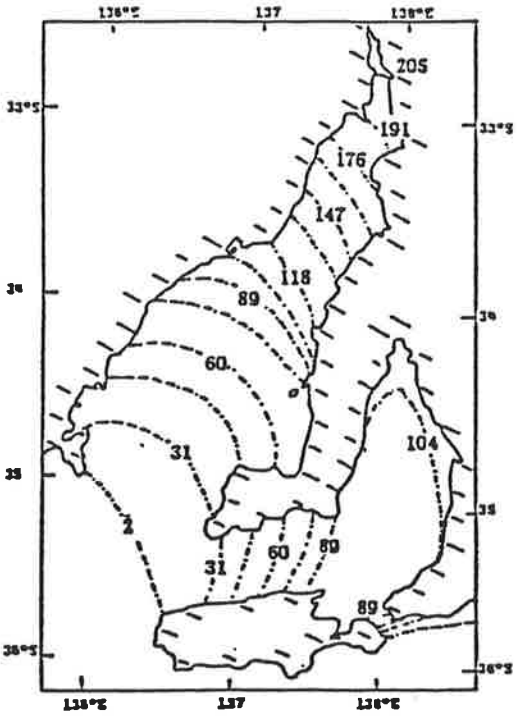


Figure 5.4(b): *Co-phase chart for M_2 — phase in degrees (C.S.T.) (adapted from Easton, 1970).*

northwards bulging lines of Figure 5.4(b), will be seen to be largely erroneous for Spencer Gulf.

Flinders (1814) noted that tidal character differed remarkably over the short distance from Thistle Island to Port Lincoln. Chapman and Inglis (1898) explain: "... at Port Lincoln, the observable tide is really the higher one of the two daily tides. Owing to the direction of the outlet of the harbour the water cannot get out freely, as the harbour catches the ebbing tide from the gulf, with the result that the level of the water falls very slowly; so slowly in fact, that the second lower tide ... does not appreciably raise the level of the water, and so is not apparent as a tide" (ibid., p.3).

The first numerical simulations of Spencer Gulf tides were carried out by Noye and Tronson (1973). Their model was constructed of elements of dimension $(1/12)^\circ$ latitude by $(1/12)^\circ$ longitude and was a depth-averaged model of the combined South Australian gulf system. The model was linear and used $k = 0.0015\,\mathrm{m/sec}$ as the coefficient of bottom friction. Only one tidal constituent was modelled at a time. This is an allowable procedure in the case of linear models so long as the correct background friction, taking into account the other dominant constituents, is defined (see, for example, Bowers et al. (1991)). Model results for M_2 showed general agreement with Easton's charts (Figures 5.4(a),(b)) for Spencer Gulf, but less agreement for St. Vincent's Gulf. Predictions for K_1 were carried out but results were not presented.

Bullock (1973) used a numerical model to determine the non-tidal flows in Spencer Gulf caused by thermohaline and wind forcing. He showed that the thermohaline current is two orders of magnitude smaller than the tidally induced flow.

Tronson (1974) solved the steady-state circulation equations on the combined gulf system and suggested that "as a first approximation the gulf circulation can be described by a linear system of equations and that it is driven by wind stress" (ibid., p.414). Tronson (1975) used numerical models to try to determine the natural resonances of the gulfs, concluding: "As the resonant frequencies of the two gulfs do not coincide with tidal frequencies, the tidal range within the gulf system will be reasonably uniform" (ibid., pp.373–374).

Noye and Tronson (1978) summarize their earlier work acknowledging that their models are too approximate to be used as "precise predicting" tools but may "extend the understanding of the factors governing tidal motion in the area" (ibid., Section 5.2). Therefore, rather than emphasizing the role of particular tidal constituents, they model the combined effects of general diurnal (i.e. 15°/hour) and semi-diurnal (i.e. 30°/hour) forcing. Since the major diurnal and semi-diurnal tidal constituents have approximately the same amplitudes in this region (refer to Table 5.1), they model waves of a representative "double amplitude". Using a linear friction formulation they obtain the results of Figure 5.5. Using a quadratic friction formulation (Figure 5.6) their results compare less favourably with Easton's charts though, as they point out, Easton had very little data with which to construct detailed charts. The present numerical study broadly supports the qualitative picture presented by Noye and Tronson.

Easton (1978) provides an informative analysis of the variation of tidal character along Spencer Gulf, pointing out some errors in Tronson's (1975) conclusions. He suggests, basing his comments on a simple analytical depth-averaged and breadth-dependent model, that (ibid., p.476):

- "... the tide [in Spencer Gulf] is basically a standing wave co-oscillating with the tide in the [Southern] ocean."

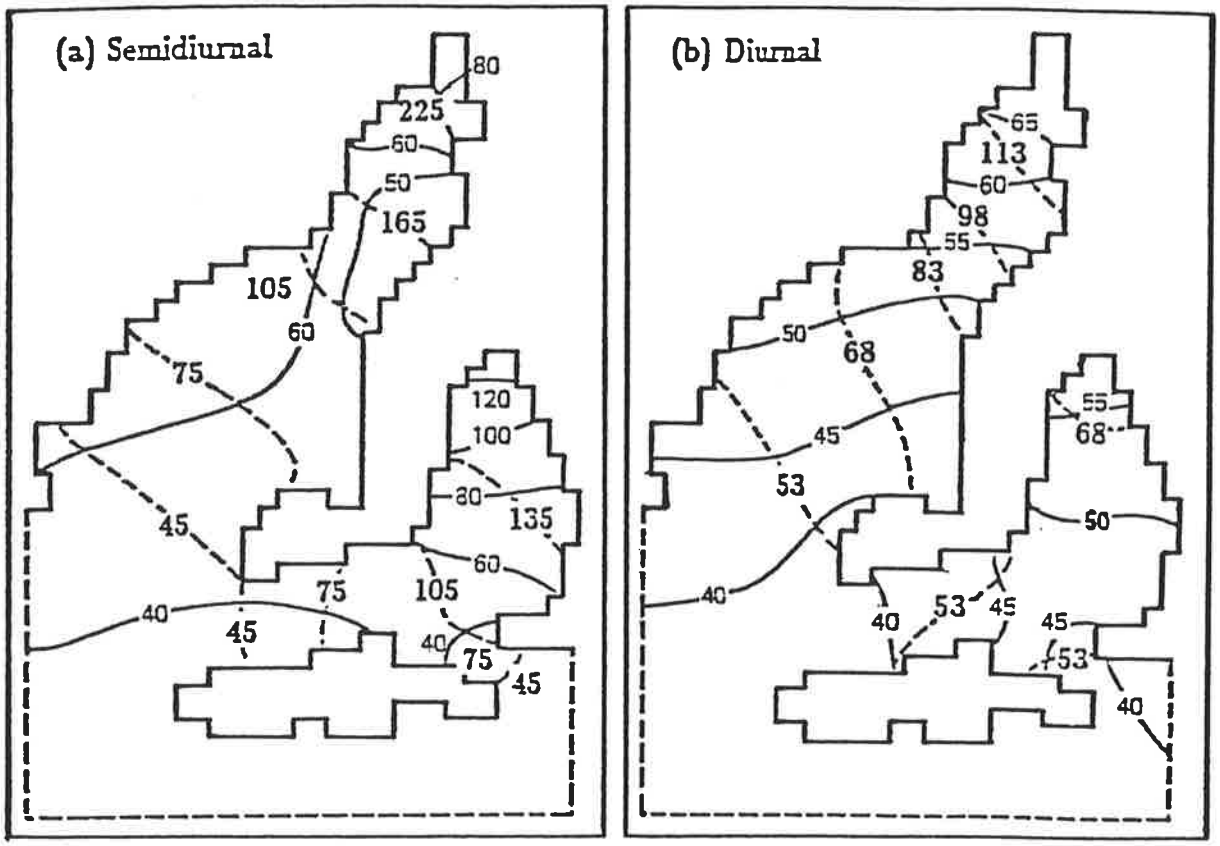


Figure 5.5: *Predicted co-amplitude (——, cm) and co-phase (- - -, degrees, C.S.T.) charts for (a) semi-diurnal and (b) diurnal tidal constituents, using a model with* linear *friction (adapted from Noye and Tronson, 1978).*

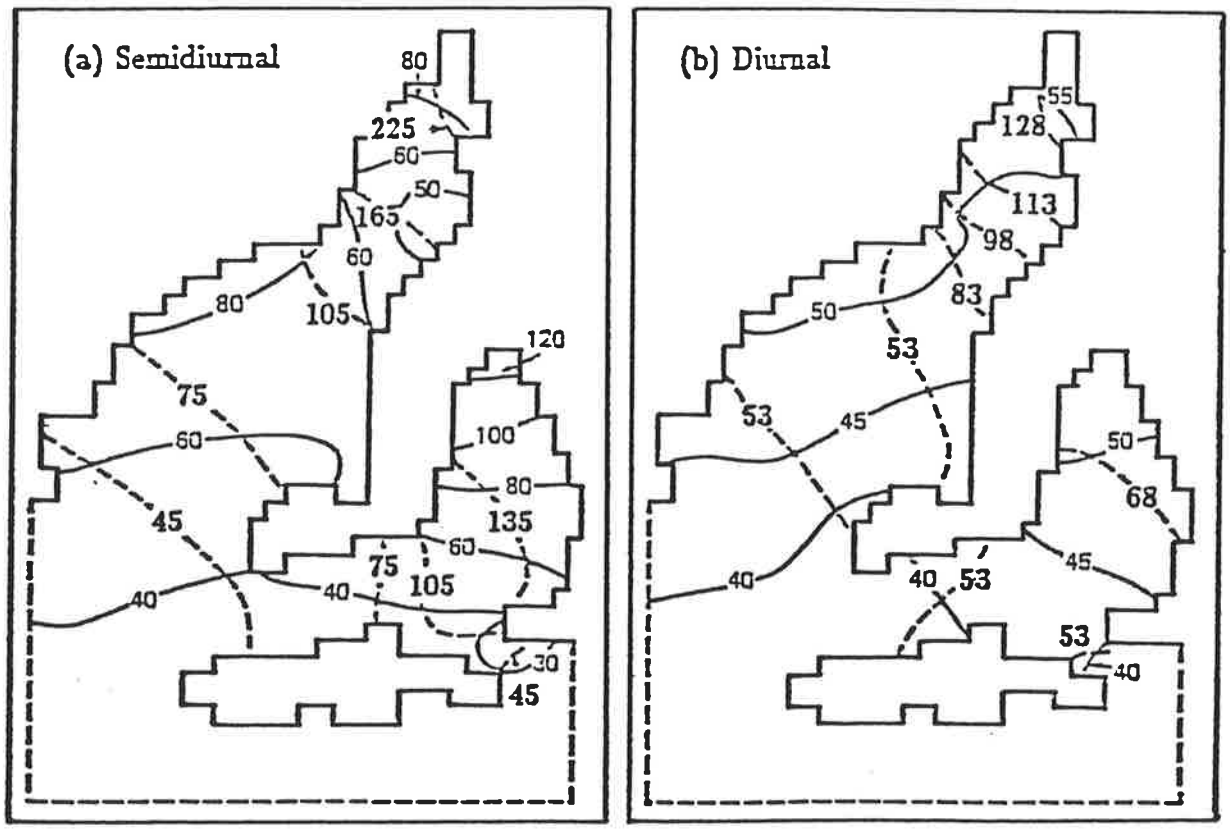


Figure 5.6: *Predicted co-amplitude (——, cm) and co-phase (- - -, degrees, C.S.T.) charts for (a) semi-diurnal and (b) diurnal tidal constituents, using a model with* quadratic *friction (adapted from Noye and Tronson, 1978).*

- "... the semi-diurnal and diurnal tidal constituents have remarkably different characteristics in Spencer Gulf and this is a direct result of their relation to the natural period of oscillation which is determined by the topography of the gulf."
- "For the diurnal constituents the amplitudes increase up the gulf and the phase change is small. The discharge decreases up the gulf but the velocity remains approximately constant."
- "For the semi-diurnal constituents there is a nodal or minimum tidal region south of Wallaroo and the two ends of the gulf are out of phase. The tidal current has a maximum near Wallaroo and a minimum near the mouth."

Easton also suggests that on average tidal currents are by far the major influence on water movement in Spencer Gulf. "Tidal currents near the mouth assume considerable importance for the flushing of the gulf and since the semi-diurnal currents are small, the exchange of water with the ocean is mostly due to the diurnal tidal constituents" (ibid., p.476).

Kelly (1979) carried out simultaneous observations of sea level over an extensive area of Spencer Gulf and obtained results similar to those in Easton's theoretical study.

Noye et al. (1981, 1982) constructed the first three-dimensional numerical model of Spencer Gulf. They used several mathematical transformations to map the Gulf onto a unit cube. A parabolic formulation was used for the vertical eddy viscosity coefficient. Their results are reproduced as Figures 5.7(a),(b) and are similar to those of Noye and Tronson (1978). Input to the model boundary at the entrance to the Gulf was obtained from Easton's charts. Observed values are circled and good agreement between recorded and predicted results is indicated. The 1981 paper is descriptive and highlights their results and the main points of their approach. The 1982 paper details the transformations used, the transformed equations and gives the finite difference approximations.

Provis and Lennon (1983) develop a model of wind-tide interaction which suggests that the strength of the tide is important in the generation of wind-driven currents. For the South Australian gulfs they show that at spring tides, when tidal streams are strongest, there is smaller wind driven circulation than occurs at times such as neaps, when there is less tidal mixing. This indicates that Tronson's (1974) approximation of ignoring the tides in determining the circulation is inadequate.

Steinberg (1983) conducts a simultaneous observation of sea level at four sites spanning the entrance to Spencer Gulf to investigate the tidal characteristics and the tidal currents at the mouth. His co-amplitude and co-phase charts for the K_1 and S_2 constituents in the entrance region are given in Figures 5.8 and 5.9, respectively. This work makes the accurate specification of sea surface height at the open boundary of the present numerical model possible.

Steinberg (1983) says the work of Easton (1978) and Kelly (1979) supports "evidence for the natural period of oscillation for the gulf of 12 hours, suggesting a standing wave oscillation with an antinode at the mouth, and node in the central region. At the antinode it is expected there is little exchange of water between the gulf and ocean due to the semi-diurnal tidal constituents" (Steinberg, 1983, p.1). Steinberg's observations showed that the semi-diurnals exhibit a large variation in wave type, having a more standing wave character on the western side of the mouth, and an increasingly progressive wave character towards the east. The overall effect is such as to exclude the possibility of an

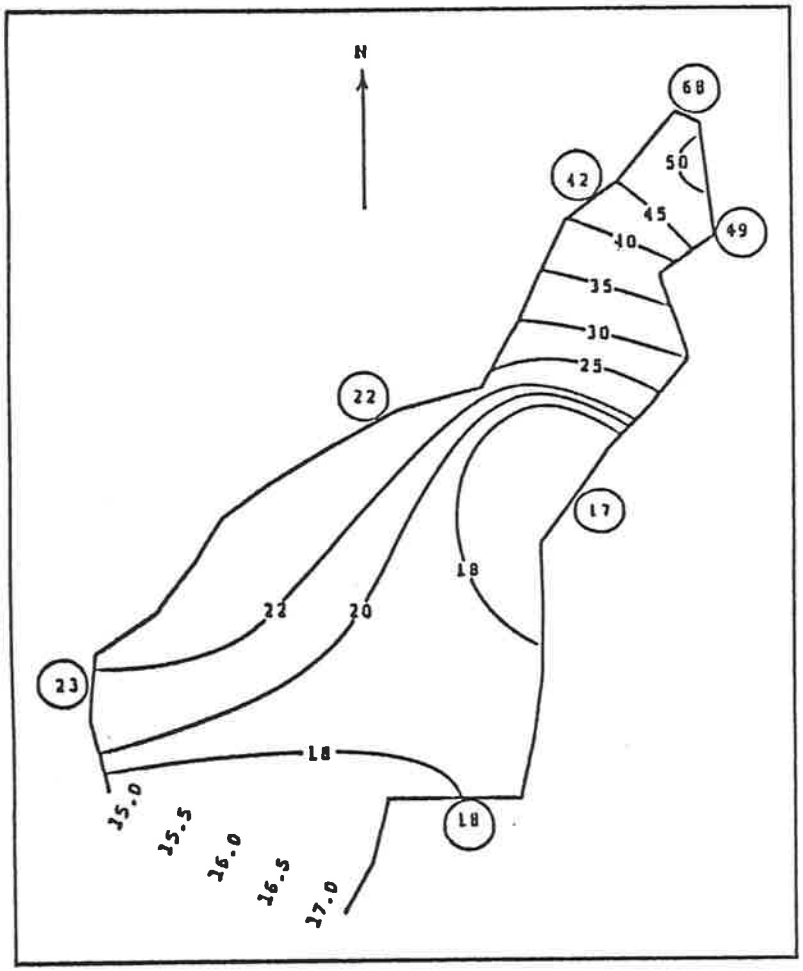


Figure 5.7(a): *Computed* M_2 *co-amplitude lines, in centimetres, using a three-dimensional model. Observed values are circled. Adapted from Noye et al. (1981).*

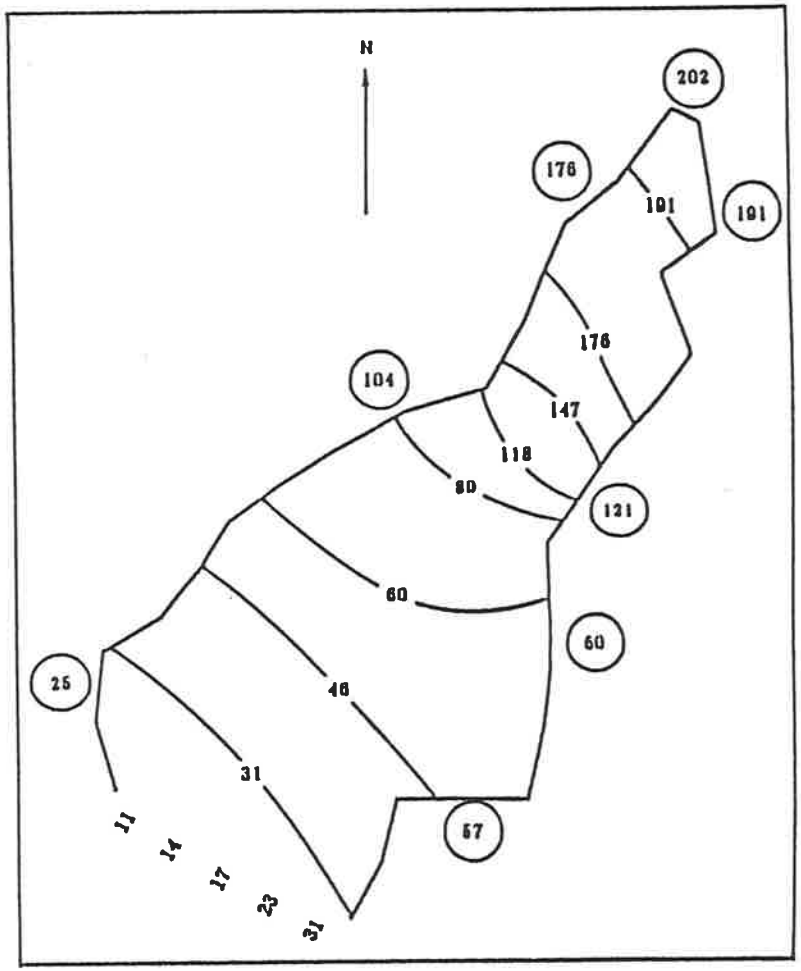


Figure 5.7(b): *Computed* M_2 *co-phase lines, in degrees, C.S.T., using a three-dimensional model. Observed values are circled. Adapted from Noye et al. (1981).*

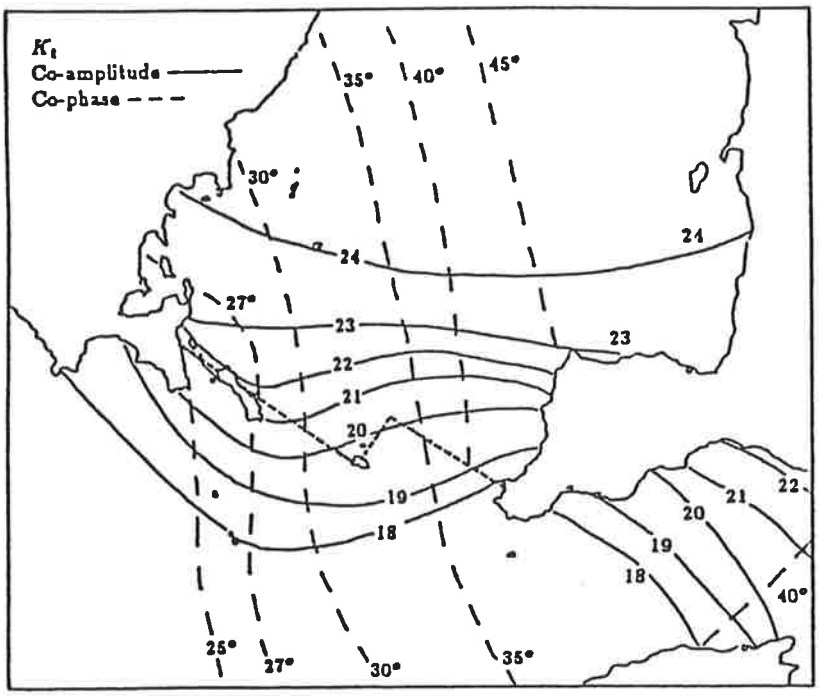


Figure 5.8: *Co-amplitude (cm) and co-phase (degrees, C.S.T.) contours for the* K_1 *constituent of tidal elevation at the entrance of Spencer Gulf (adapted from Steinberg, 1983).*

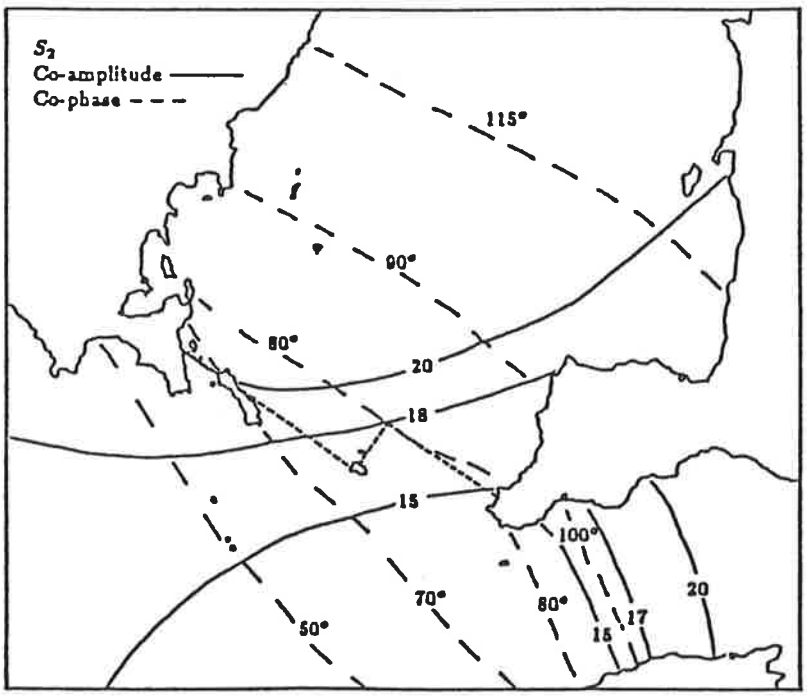


Figure 5.9: *Co-amplitude (cm) and co-phase (degrees, C.S.T.) contours for the* S_2 *constituent of tidal elevation at the entrance of Spencer Gulf (adapted from Steinberg, 1983).*

antinode in the semi-diurnals at the mouth, since the investigation yields a predominantly progressive current at the mouth with appreciable semi-diurnal currents across the whole entrance. The diurnal constituents reveal an even larger variation in wave type across the mouth, again having a more standing wave character on the western side and taking a more progressive wave nature on the eastern side.

Noye (1984c) surveys the present state of knowledge of the physical processes of the Gulf with sections on tidal variation in sea level, storm surges, wind waves and swell, currents produced by tides, winds and variations in temperature and salinity, and pollutants and their dispersal. Some useful data on observations of tide-induced currents is brought together in this paper and he suggests, among other things, the need for a detailed numerical study of flow near Port Bonython in order to identify gyres generated by the ebb current flows.

Green (1984) provides a theoretical explanation for the observed occurrences of residual currents north of Lowly Point (see Figure 5.10 or Figure 1.2) "organized in cells of circulation, driven by the tides but separated by nodes where the rate of exchange of water is minimal" (ibid., p.183). These particular residual currents are not resolvable by the present coarse-grid model which represents this region with only 25 of the 778 grid elements used.

5.3 Depth-averaged model of Spencer Gulf

A cartesian grid — which assumes the Earth is locally flat — is used to model the Gulf. The error incurred by not employing a spherical shell model is estimated as a 0.5% error in the North-South direction.

The model (Figure 5.10) is inclined 33.33° T. This orientation is adopted in order to both accurately represent the coastline near Port Bonython, the region of specific interest, and to align the model with the axial flow in the Gulf. Having stated the model is inclined to north and shown it as such in Figure 5.10, all plots showing model results will be aligned with model axes parallel to the edges of the page so it will be convenient to refer to the direction "up the page" as "north" even though it is more correctly NNE.

It is generally the case that reducing the element size leads to greater accuracy of model predictions. However, limits are imposed on element size by the storage capacity of the computer used as well as the computer time available for running the model. Taking these factors into account the elements of the Spencer Gulf model are chosen to have dimensions $2\Delta x = 2\Delta y = 5715\,\mathrm{m}$.

A time step of $\Delta t = 150\,\mathrm{sec}$ is used. The model runs stably at the value $\Delta t = 180\,\mathrm{sec}$ and initial runs demonstrated that the higher value gave the same error summary (see next section) to three significant figures. But despite these successes it was thought that when values of, for example, the constant quadratic friction coefficient (next section) far from the optimal value were to be used, the larger time step might destabilize the model more readily than the smaller time step. It therefore seemed prudent to use the lower value since many calibration tests were planned and we wished to obtain the most accurate and complete response of the model. So the time step $\Delta t = 150\,\mathrm{sec}$ was used and all the results presented in this chapter use that value. Having done all the tests (next section) and performed some of the runs along the way using $\Delta t = 180\,\mathrm{sec}$, it has been our consistent experience that the larger value gives stable runs with the same corresponding error summaries (to three significant figures), so it seems we could have used it with success all along! (Further

evidence indicating this is that in Chapter 7 the three-dimensional model is run using $\Delta t = 180$ sec because of the sheer length of computing time required. Several calibration tests are conducted with success using that value.)

The model of Spencer Gulf (Figure 5.10) uses 761 Type 1 and 17 Type 2 elements. Each is nine times the area of an element from the fine-grid model used in Chapter 8. Figure 5.11 shows the input array of element types corresponding to the Spencer Gulf model. Computations are carried out only at the gridpoints of the Type 1 elements and forcing for the model is provided using tide heights specified at the Type 2 elements. The Type 4 elements shown serve only to distinguish between water and land elements outside the model boundaries.

Tidal observation station	Map position Lat.(°S)	Long.(°E)	Error in model location (mult. of $2\Delta x$)
Port Augusta	32°30′	137°46′	1.76
Beacon #5	32°43.8′	137°49′	0.13
Port Pirie	33°10′	138°01′	1.16
Port Bonython	33°00′	137°45.8′	0.71
Whyalla	33°01′	137°36′	0.21
Yarraville Shoals	33°17.0′	137°35.6′	0.16
Mike	33°23.7′	137°30.8′	0.50
Port Broughton	33°36.1′	137°55.4′	0.51
Lima	33°45.4′	137°22.0′	0.13
Wallaroo	33°56′	137°37′	0.74
Franklin Harbour	33°42′	136°57′	1.09
Red	33°51.4′	136°47.8′	0.20
Yellow	34°01.2′	137°00.4′	0.24
Blue	34°12.4′	137°17.1′	0.38
White	34°16.6′	137°22.8′	0.21
Arno Bay	33°54.5′	136°35′	0.54
Port Victoria	34°30′	137°27′	0.34
Port Neill	34°07′	136°21′	0.51
Port Turton	34°56′	137°21′	0.33
Port Lincoln	34°43′	135°52′	0.33
Taylor's Landing	34°51.5′	135°57.4′	0.74
Thistle Island	35°00.4′	136°11.0′	0.34
Wedge Island	35°04.3′	136°28.2′	0.46
Pondalowie Bay	35°14.2′	136°49.9′	0.21

Table 5.3: *Map position and error (as a multiple of $2\Delta x$, the element width) in model location of each station at the nearest model elevation gridpoint. Map positions were provided by the National Tidal Facility at The Flinders University of South Australia.*

The open boundary of the model runs across the mouth of the Gulf where tide-height data is available at four sites, each located close to the open boundary line. The four stations are Taylor's Landing, Thistle Island, Wedge Island and Pondalowie Bay. They

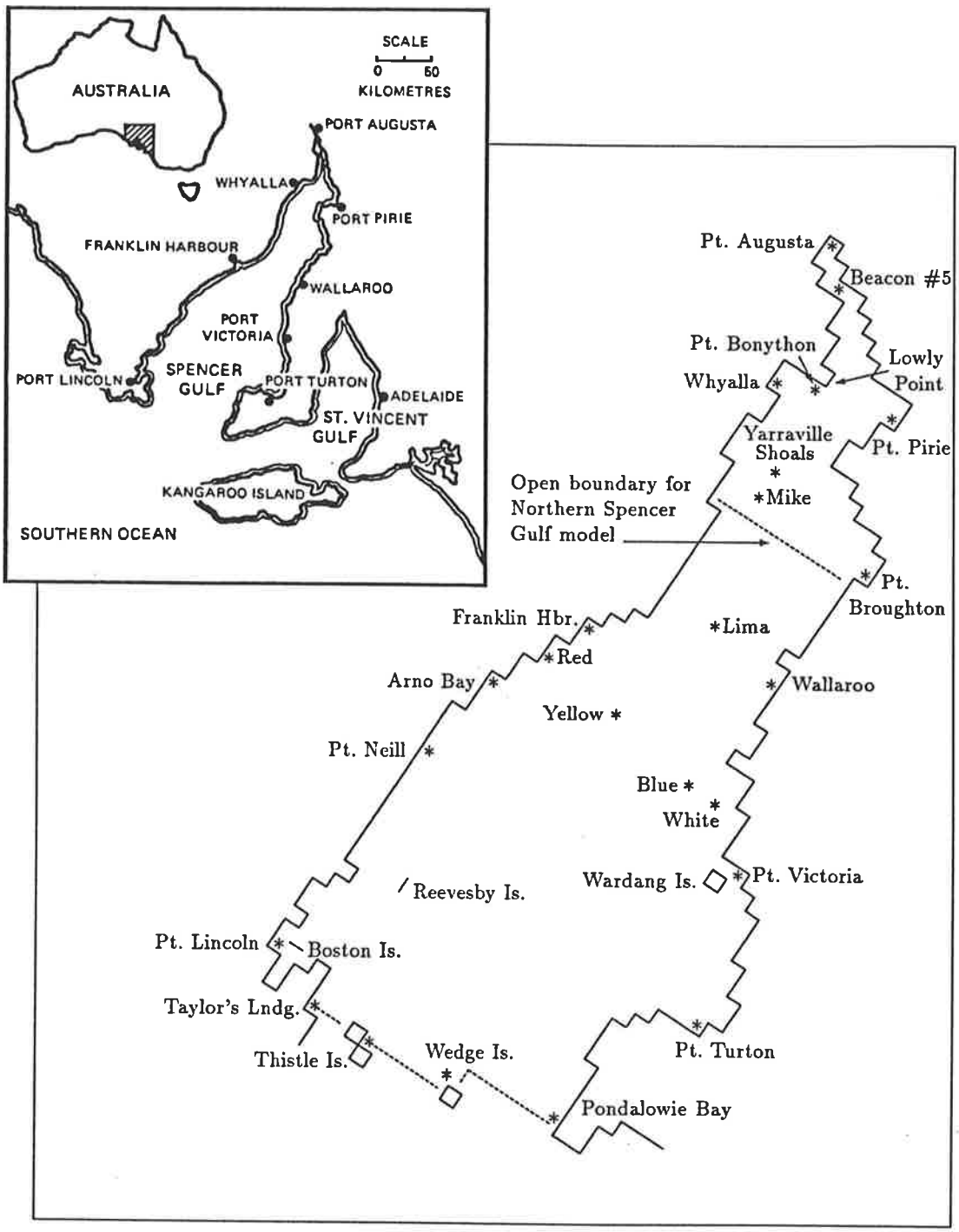


Figure 5.10: *Locality map for the Spencer Gulf model. The model location of each tidal observation station is indicated by *. Boston Is. in Pt. Lincoln harbour is represented as a barrier, as is Reevesby Is. of the Sir Joseph Banks Group. The location of the open boundary for the Northern Spencer Gulf model is marked.*

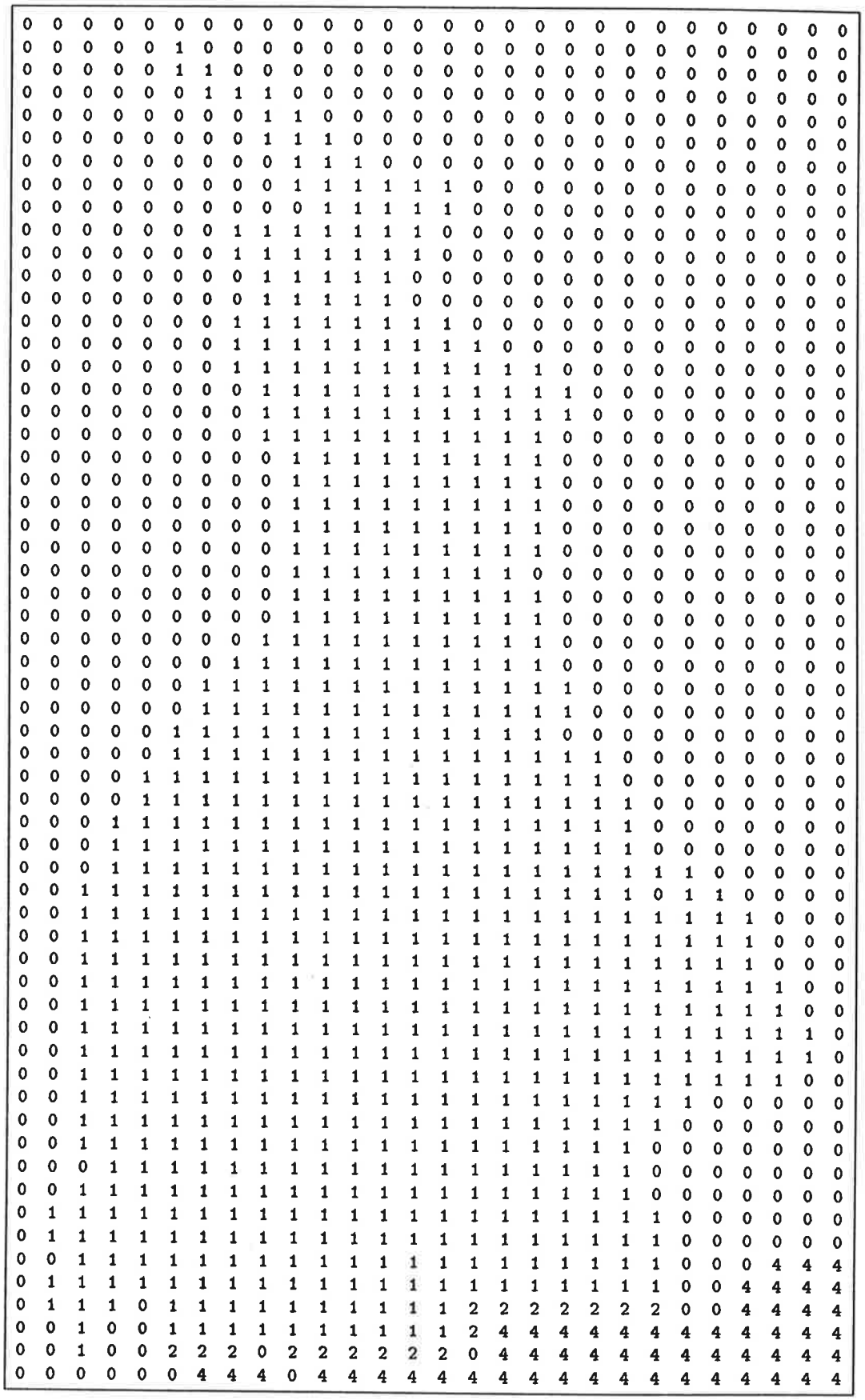


Figure 5.11: *The input array of element types corresponding to the Spencer Gulf model of Figure 5.10.*

Tide-height station	O_1		K_1		M_2		S_2	
	amp	phase	amp	phase	amp	phase	amp	phase
Taylor's Landing	15.3	359.1	21.2	26.7	19.9	17.1	21.0	68.1
Thistle Island	15.7	1.1	22.2	30.2	19.1	21.2	19.7	71.4
Wedge Island	15.1	6.6	21.0	36.3	16.6	24.1	17.1	74.4
Pondalowie Bay	13.1	12.9	16.6	44.3	13.9	26.3	13.8	78.0

Table 5.4: *Amplitude (cm) and phase (degrees, local time) of the four major constituents at four stations sited at the entrance to Spencer Gulf. These constants are supplied by the National Tidal Facility at The Flinders University of South Australia.*

are marked in Figure 5.10 along with other locations at which data has been collected within the Gulf. In Table 5.3 the map position of each station is listed along with the error, as a fraction of grid element width $2\Delta x$, incurred by representing the station at the nearest elevation point of the model. At only seven of the stations, viz. Yarraville Shoals, Mike, Lima, Red, Yellow, Blue and White, observations of tidal current are available. At the remainder of the stations, and at Yarraville Shoals, observations of tide height are available.

The tide-height constants for the four stations at the entrance to the Gulf are given in Table 5.4. The data from these four sites is first linearly extrapolated to the nearest elevation point of the open boundary line, and then data for the remaining points of the line is linearly interpolated from these values in a way consistent with the co-amplitude and co-phase charts drawn for the mouth of Spencer Gulf by Steinberg (1983) (Figures 5.8 and 5.9). The resulting input data set obtained for the 17 elevation points of the open boundary (Figure 5.12) is presented in Table 5.5.

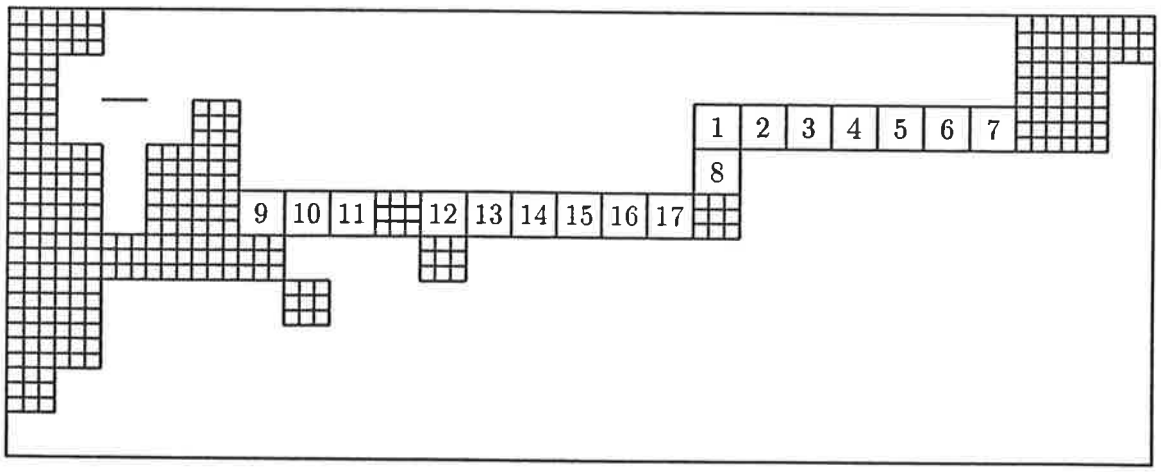


Figure 5.12: *The open boundary region of the Spencer Gulf model showing the element labelling scheme for the 17 boundary elements. The cross-hatched elements represent land.*

Once the model has been calibrated to achieve optimum accuracy with respect to differences between predicted and observed tide-height constants from stations within the

Boundary element	O_1		K_1		M_2		S_2	
	amp	phase	amp	phase	amp	phase	amp	phase
1	15.1	234.9	20.7	251.4	16.3	109.4	16.9	150.0
2	14.7	235.8	20.1	253.1	15.9	109.6	16.4	150.5
3	14.4	236.7	19.4	254.7	15.5	109.9	15.9	151.0
4	14.1	237.6	18.7	256.3	15.1	110.1	15.4	151.4
5	13.8	238.5	18.1	257.9	14.7	110.4	14.9	151.9
6	13.4	239.4	17.4	259.5	14.3	110.6	14.4	152.4
7	13.1	240.3	16.7	261.1	13.9	110.9	13.9	152.9
8	14.8	234.4	20.2	253.7	15.8	108.4	16.3	149.6
9	15.3	226.2	21.2	242.5	20.0	103.0	20.9	143.4
10	15.4	226.8	21.4	243.6	19.8	103.6	20.6	144.1
11	15.5	227.4	21.7	244.7	19.6	104.3	20.4	144.8
12	15.6	228.5	22.1	247.0	19.2	105.6	19.8	146.2
13	15.5	229.4	21.8	248.4	18.5	106.0	19.1	146.7
14	15.3	230.3	21.4	249.9	17.8	106.3	18.4	147.2
15	15.2	231.2	21.1	251.4	17.1	106.6	17.6	147.7
16	15.1	232.0	20.7	252.9	16.3	106.9	16.9	148.3
17	14.9	232.9	20.4	254.4	15.6	107.2	16.2	148.8

Table 5.5: *Amplitude (cm) and phase (degrees, G.M.T.) of the four major constituents at the 17 open boundary elements of Figure 5.12. This is the open boundary data set used for the Spencer Gulf model. The program uses phases in G.M.T. but predicted phases, after tidal analysis, are given in local time (C.S.T.).*

Gulf, boundary forcing for the Northern Spencer Gulf model is obtained (Chapter 8).

5.4 Calibrating the depth-averaged Spencer Gulf model

There are several mechanisms to calibrate the model. Some of these have greater influence than others and all are interdependent — that is, changing one influences the effect of the rest, to varying degrees.

- **Determining the Mean Sea Level depth field.** The bathymetry of the model, once established, is not changed. The datum depth at the elevation point of each Type 1 and Type 2 element is obtained by visually interpolating the data given on Royal Australian Survey Corps hydrographic maps **Aus 776–778**. A more accurate bathymetry can now be obtained following the recent digitising of the available depth information by the South Australian Department of Environment and Planning. At the time of development of the Spencer Gulf model this information was not available.

  Alternatively, a more accurate bathymetry can be specified by visual or digital interpolation to the velocity gridpoints of the model region rather than to the elevation points (Black, 1987). This effectively gives twice the resolution of the "traditional" staggered scheme but doubles the storage requirements for the depth variable. Because of this disadvantage it was not tried, but given that digitised data is now avail-

able this approach will be considered in future research. It may be noted that this alternative would be particularly suited to a model with a rapidly varying bathymetry such as the depth-integrated Gulf of Carpentaria model of Mitchell et al. (1984); in the present case, the bathymetry is relatively smooth.

Depths are required relative to Mean Sea Level (MSL) but chart datum is Indian Spring Low Water (ISLW). Figure 5.13 gives the ISLW depth field obtained for the Spencer Gulf model. Since chart datum is clearly defined it is possible to generate MSL accurately by an iterative process suggested by Mitchell (1985). Rather than hand-estimating MSL by judiciously choosing corrections to add to ISLW from the observed amplitude data for the major constituents at each elevation gridpoint, the model is used to carry out the correction. The ISLW depth field is used as a zeroth estimate for MSL everywhere interior to the model and along the open boundary line. A simulation is then conducted to obtain 29 days of predicted tide heights for each Type 1 elevation point in the model. The predictions are tidally analyzed and a first estimate for MSL is obtained as

$$\mathrm{MSL}^{(1)} = \mathrm{ISLW} + (\mathrm{O}_1 + \mathrm{K}_1 + \mathrm{M}_2 + \mathrm{S}_2)^{(1)}\,, \tag{5.2}$$

where amplitudes are inferred for the bracketed quantities on the right and the superscript "(1)" refers to quantities obtained after the first iteration. Along the open boundary, the added amplitudes are taken from the forcing data so no further adjustment there is required. The program is then run using $\mathrm{MSL}^{(1)}$ as the estimate for the MSL field and from a tidal analysis of a new set of predicted tide heights a second update $\mathrm{MSL}^{(2)}$ is obtained for the interior elements by adding the new set of major constituent amplitudes to ISLW, and so on. Mathematically, the process by which MSL is generated can be summarized as

$$\mathrm{MSL} = \lim_{i\to\infty} \mathrm{MSL}^{(i)} = \mathrm{ISLW} + \lim_{i\to\infty} (\mathrm{O}_1 + \mathrm{K}_1 + \mathrm{M}_2 + \mathrm{S}_2)^{(i)}. \tag{5.3}$$

This expression generates a MSL field to an accuracy at least as good as the ISLW field used. Three iterations are sufficient to obtain a "converged" MSL field, one which is everywhere different from the previous estimate by less than 1 cm. Figure 5.14 gives the MSL depth field for the present model (c.f. Figure 5.13) and shows that while the MSL depths near the open boundary are 0.6–0.8 m greater than the corresponding ISLW depths, the increase at the head of the Gulf is as high as 2.1 m at some elements. Comparing these corrections with the sum of the amplitudes given in Table 5.1 shows that the computed MSL depth field is consistent with a MSL depth field determined by adding the amplitude constants to the ISLW depths at the given stations.

Figure 5.15 shows 5-metre isobaths of the MSL depth field for the region near Wallaroo where, as we shall see, tidal gyres are predicted.

The consequences of using ISLW as the model depth field instead of a better estimate for MSL are significant and are illustrated by the contrast between Figure 5.16(b) where ISLW is used as the estimate for MSL, and Figure 5.17 where the MSL depth field used is the field obtained as the third estimate, viz. $\mathrm{MSL}^{(3)}$. In these figures, programs were run using the values of C_b marked on the horizontal axis; the curves were obtained by interpolation between the resulting error values.

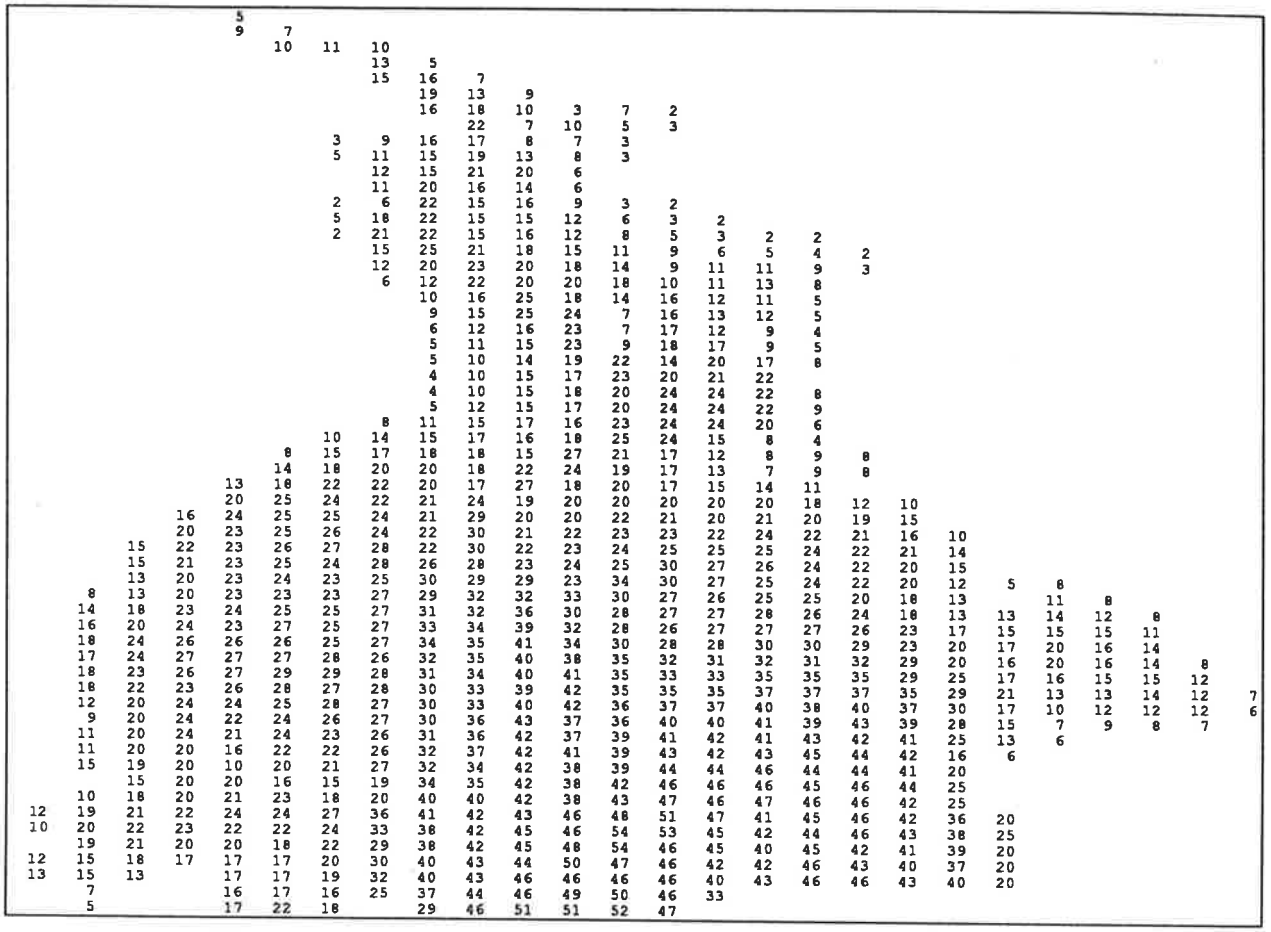


Figure 5.13: *The ISLW depth field (m) for the Spencer Gulf model.*

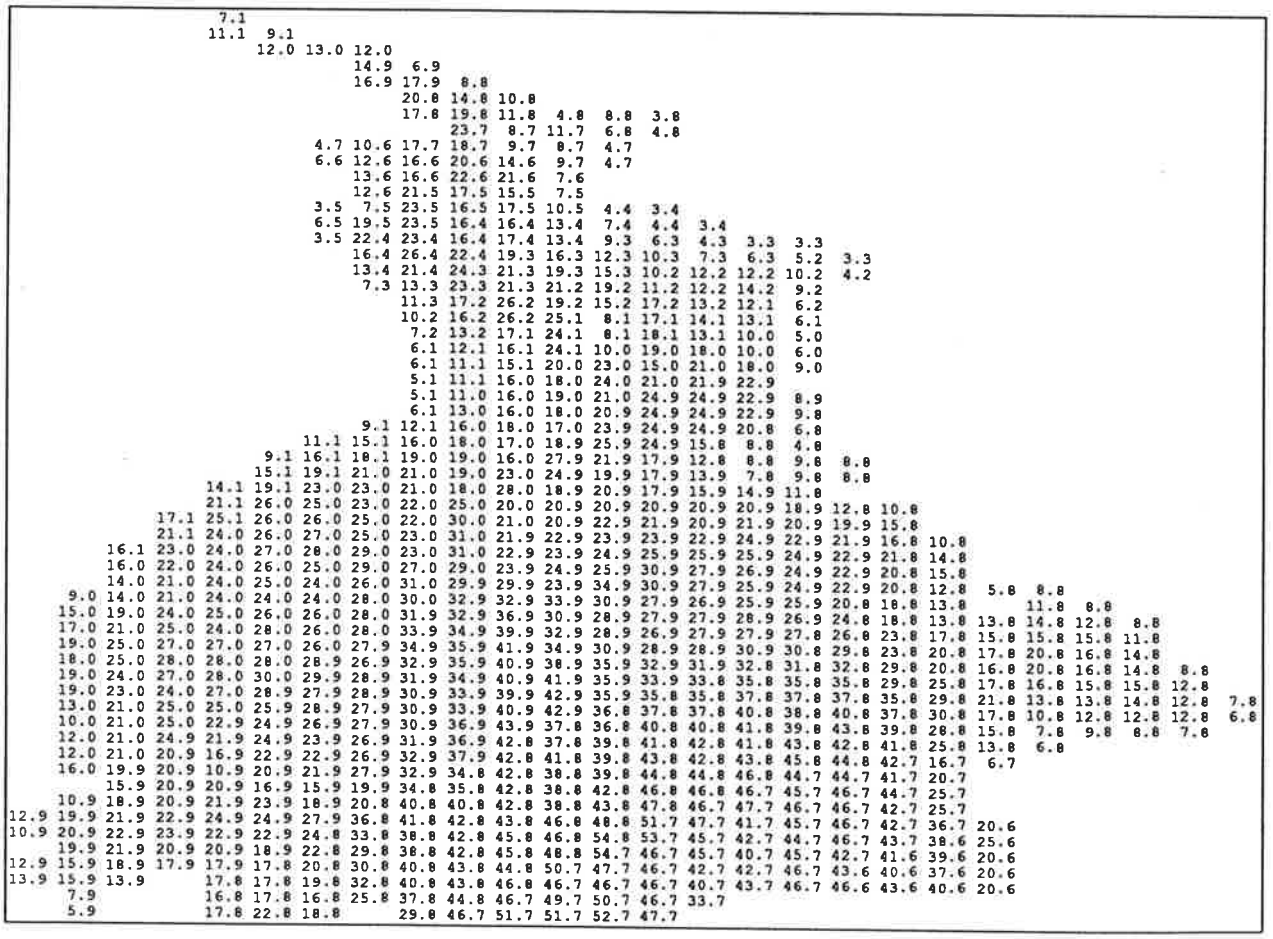


Figure 5.14: *MSL depth field (m) generated from ISLW depths of Figure 5.13 after three iterations.*

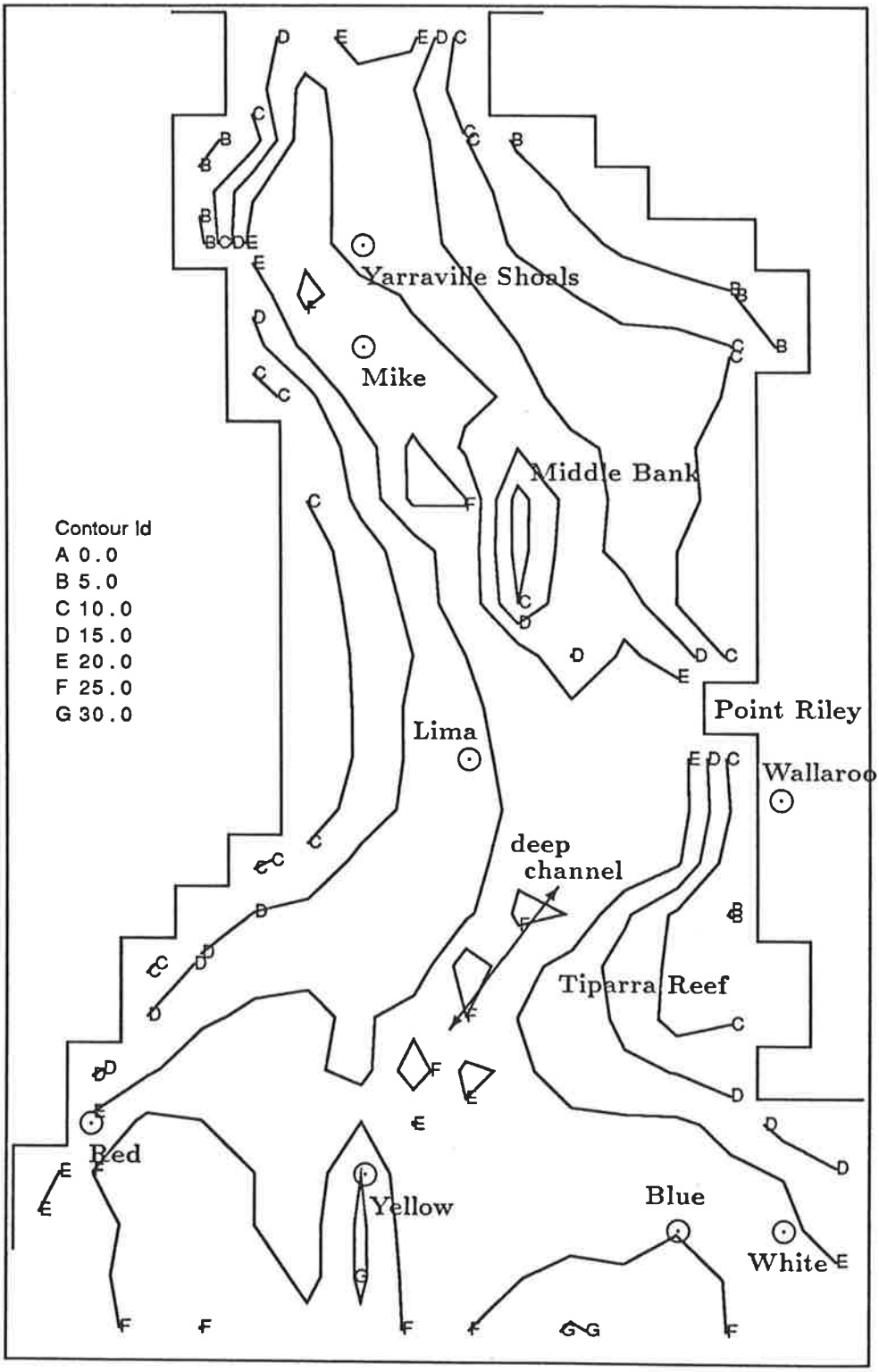


Figure 5.15: *Five-metre isobaths for the narrowing part of Spencer Gulf near Wallaroo. The model positions of all tidal current stations are shown.*

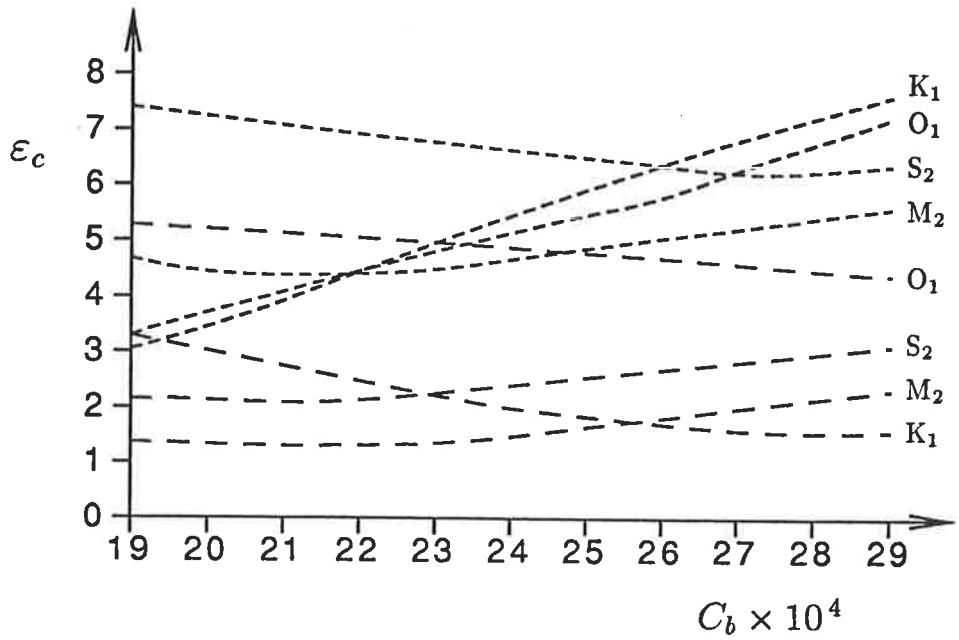


Figure 5.16(a): *Error ε_c in amplitude (– – –, cm) and phase (- - - -, deg) for constituents O_1, K_1, M_2 and S_2 versus constant coefficient of quadratic friction C_b with ISLW taken as the estimate for MSL. The error measure is defined in the text.*

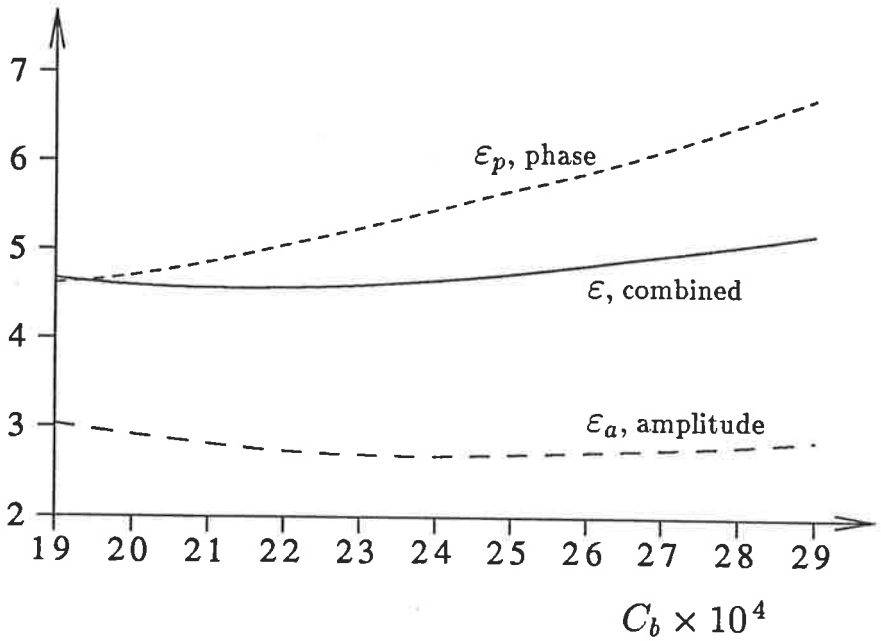


Figure 5.16(b): *Two error summaries of the data of Figure 5.16(a): amplitude error ε_a (– – –, cm) and phase error ε_p (- - - -, deg) are simple averages taken over the four constituents O_1, K_1, M_2 and S_2. While the optimal value of C_b for the ε_a curve is 0.0024, the optimal C_b value for the ε_p curve lies off the graph to the left. Also plotted is error measure ε (———, cm), defined in the text. The optimal value of C_b for the ε curve lies in the range 0.0021–0.0022; the corresponding error value is $\varepsilon = 4.56$ cm.*

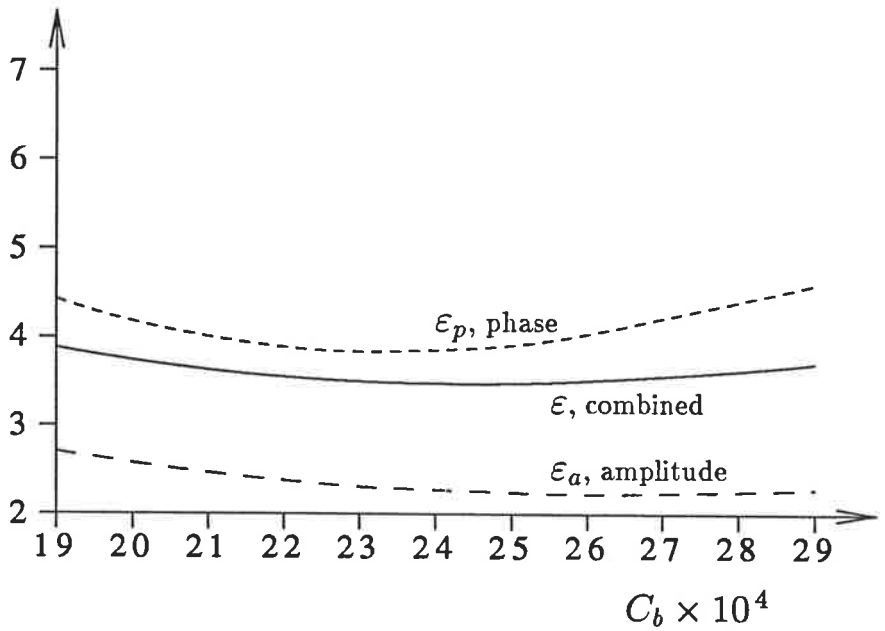


Figure 5.17: *Here the estimate for MSL is taken as the third estimate MSL(3). While the optimal value of C_b for the average phase error (ε_p, - - - -, deg) is 0.0023 and for the average amplitude error (ε_a, — — —, cm) is 0.0027, the optimal value taken from the combined error estimate (ε, ———, cm) is 0.0025 and has associated error value $\varepsilon = 3.49\,cm$.*

The error measures used to enable comparisons to be made between results of different runs are now described. A simple error measure is the absolute difference between observed and predicted amplitude or phase for a particular constituent, averaged over each calibration station in the model. For constituent c, this error measure is

$$\varepsilon_c = \frac{1}{N} \sum_{s=1}^{N} |o_{c,s} - p_{c,s}| \tag{5.4}$$

where

- ε_c is the absolute difference in amplitude (cm) or phase (deg) averaged over all interior calibration stations s for tidal constituent c,
- N is the number of interior calibration stations — those stations whose distance of separation between map position and model position is less than $2\Delta x$, the element dimension,
- $o_{c,s}$ is the observed amplitude (cm) or phase (deg) of constituent c at station s, and
- $p_{c,s}$ is the predicted amplitude (cm) or phase (deg) of constituent c at station s.

Using this error measure, Figure 5.16(a) shows the amplitude and phase errors for the model for each of the four constituents O_1, K_1, M_2 and S_2, plotted for various values of the constant coefficient of quadratic friction C_b with ISLW used as the estimate for MSL. These plots are of limited usefulness in establishing an optimal

C_b value for the model. Furthermore the constituents interact in the non-linear model and so error measures based on their collective performance are sought. In Figure 5.16(b) averages taken of the four amplitude plots and of the four phase plots in Figure 5.16(a) are given. The overall average absolute amplitude error ε_a (cm) is defined as

$$\varepsilon_a = \frac{1}{4}\sum_{c=1}^{4}\varepsilon_c \tag{5.5}$$

where ε_c in this context is the average absolute amplitude error defined for constituent c; an overall average absolute phase error ε_p (deg) is defined in a similar way. However the plots for ε_a and ε_p also do not show a single optimal value for C_b — the minimum in the ε_a curve is at $C_b = 0.0024$ but the minimum in the ε_p curve lies off the graph to the left.

Because the plots for ε_a and ε_p show different minima, Mitchell (1985) proposed expressing the observed and predicted results as complex polar vectors in order to then produce a single error measure. Consider the following measure which is an overall average absolute complex difference between observed and predicted results:

$$\varepsilon = \frac{1}{4N}\sum_{c=1}^{4}\sum_{s=1}^{N}\left|\left[\mu_o e^{i\phi_o}\right]_{c,s} - \left[\mu_p e^{i\phi_p}\right]_{c,s}\right|, \tag{5.6}$$

where

- ε is the absolute complex difference (cm) between observed and predicted results averaged over all interior calibration stations and the four constituents O_1, K_1, M_2 and S_2,
- μ_o, ϕ_o are the observed amplitude (cm) and phase (deg), respectively, of constituent c at station s, and
- μ_p, ϕ_p are the predicted amplitude (cm) and phase (deg), respectively, of constituent c at station s.

This error measure takes the lengths of the differences between the complex vectors given by the observed and predicted results and averages them over all interior calibration stations and the four constituents. It may be alternatively expressed as

$$\varepsilon = \frac{1}{4N}\sum_{c=1}^{4}\sum_{s=1}^{N}\sqrt{\left[\mu_o^2 + \mu_p^2 - 2\mu_o\mu_p\cos(\phi_o - \phi_p)\right]_{c,s}}, \tag{5.7}$$

which has the form of the cosine rule for finding the length of the unknown side of the triangle formed by the observed and predicted vectors. Although different sets of observed and predicted results may give rise to the same value of this error measure, overall it proves to be a useful error measure. In Figure 5.16(b) the combined error measure ε is plotted and shows a minimum of $\varepsilon = 4.56$ cm in the C_b range 0.0021–0.0022.

In formulating the above error measures, no attempt has been made to take into account the amplification effect of tidal constituents as the tide travels northwards along the Gulf, and no attempt has been made to weight the errors in the separate

constituents according to their relative importance at each station; the inaccuracy involved in assuming that the error at a particular station is the same as the error measured at the elevation gridpoint representing that station is not taken into account, although using a large sample of interior "calibration" stations should nullify this effect. Looking ahead at the contour plots for the K_1 and M_2 constituents (Figures 5.23 and 5.24) we see that in the narrowing part of the Gulf near Wallaroo (refer to Figure 5.15 for location) amplitude and phase alter appreciably in the space of a single grid element. Thus the error incurred by taking a station's results from the nearest model elevation point rather than from its actual position can be significant. Dealing with this error is difficult because the separation distance is needed together with the directed gradient of each of the major constituent amplitudes and phases at each station. These sources of inaccuracy in the error measures are noted without attempting to rectify them — to attempt to do so would be complicated. Also, the effects are approximately equal from one run to the next, and so produce only systematic contributions which still enable these error measures to be used accurately as relative measures.

In Figure 5.17 the amplitude error ε_a, phase error ε_p and combined error measure ε are plotted against the constant coefficient of quadratic friction C_b when the third estimate for MSL is used. The optimal values of C_b accompanying these error measures are, respectively, 0.0027, 0.0023–0.0024 and 0.0025, and all are noticeably higher than the corresponding values from Figure 5.16(b); at the same time, the error values are lower at each value of C_b. The optimal value $C_b = 0.0025$ from the combined error measure is a value that is commonly used for models of shallow seas (e.g. Reid and Bodine (1968), Flather and Heaps (1975) and Blumberg (1977)); the associated error value is $\varepsilon = 3.49\,\text{cm}$.

The MSL depth field defined by the third estimate $\text{MSL}^{(3)}$, when the constant coefficient of quadratic friction is $C_b = 0.0025$, is used in all subsequent runs of the depth-averaged Spencer Gulf model. Only the "combined" error measure will be used in the accompanying error graphs.

The MSL field obtained using this technique is only weakly dependent on the value of constant quadratic friction coefficient used to generate it and the quadratic friction parameterization used (see next section). It also depends on the open boundary data set used, but that is assumed fixed for the Spencer Gulf model.

Where model elements are known to periodically wet and dry during the tidal cycle it must be decided whether or not to include them if the program does not incorporate the wetting and drying of tidal flats. Normally these elements will be included but cannot be assigned zero or near zero MSL depth values. A starting value which will allow the program to run without becoming unstable in these regions has to be chosen. A standard value of 2 m is used for such elements; thus all depths given in Figure 5.13 are $\geq 2\,\text{m}$. This choice is somewhat arbitrary and may be unnecessarily large at some elements; the value used for each element must be greater than the sum of the major constituent amplitudes obtained at that element.

These last comments serve to emphasize the need for the program to handle the wetting and drying of tidal flats. The use of such a mechanism may have significant effects on the accurate modelling of a region. The element dimension of the fine reso-

lution Northern Spencer Gulf model enables tidal flats to be adequately represented (see Chapter 8).

- **Changing the coefficient of horizontal diffusion.** In many tidal models of shallow seas the horizontal diffusive terms are omitted (e.g. Flather and Heaps, 1975, Blumberg, 1977). In others, global constants for the coefficients of horizontal diffusion are specified (e.g. Noye et al. 1981, 1982). Greenberg (1983) incorporates expressions for these coefficients taken from Schwiderski (1980), viz.

$$N_x = N_y = (a/2)(2\Delta x)(H_i + H_{i+1})/2 \text{ at } U_i \text{ and} \quad (5.8)$$

$$N_x = N_y = (a/2)(2\Delta y)(H_i + H_{i_2})/2 \text{ at } V_i, \quad (5.9)$$

where a is the reduced eddy coefficient which Greenberg sets to $1.64\times10^{-3}\,\mathrm{sec}^{-1}$ and $2\Delta x$ and $2\Delta y$ are the element dimensions as used in the present work. Greenberg comments that "The addition of this eddy viscosity to the model did not change the tides or qualitatively change the residual circulation" (Greenberg, 1983, p.903). Schwiderski (1980) includes the horizontal diffusive terms in his global models and as a result of numerical experiment finds that the value of the coefficients depends linearly on both the depth and the horizontal mesh size. He comments that while eddy dissipation is significant in deep ocean basins it is negligible in shallow shelf regions (ibid., p.251).

Kullenberg (1982) points out that the coefficients should indeed increase with mesh size since it is a way of reintroducing information ("inhomogeneities") lost by the implied averaging that occurs when mesh size is increased: "The inhomogeneities have a dispersive effect that vanishes insofar as the inhomogeneities disappear. In a *global* way, this can be compensated for by increasing the exchange term by means of augmenting its coefficient" (ibid., p.130). Zimmerman (1978) comments: "the presence of smaller scale turbulent eddies gives rise to a horizontal momentum diffusion, the effect of which is represented by the horizontal eddy viscosity" (ibid., pp.37–38).

Schwiderski states that although the reduced eddy coefficient probably depends in some way on Δt, the time step is generally a fixed quantity for a given model and so a is most easily determined as part of the calibration process. For the Spencer Gulf model, a series of runs with a constant coefficient of quadratic friction $C_b = 0.0025$ is carried out and the resulting error distribution is plotted in Figure 5.18. The optimal value is $a = 0.0055\,\mathrm{sec}^{-1}$ and the associated model error is $\varepsilon = 3.49\,\mathrm{cm}$; this value of a was used in the program runs whose results are summarized in the caption of Figure 5.17. The general flatness of the curve shows that the model is virtually insensitive to this parameter. Even when $a = 0\,\mathrm{sec}^{-1}$ model results are only slightly poorer, the error value being $\varepsilon = 3.54\,\mathrm{cm}$. Nevertheless, the value $a = 0.0055\,\mathrm{sec}^{-1}$ is used in all subsequent program runs and gives values for N_x, N_y that lie in the range 50–$865\,\mathrm{m}^2/\mathrm{sec}$; these values contrast sharply with the value $N_x = N_y = 5\,\mathrm{m}^2/\mathrm{sec}$ used by Noye et al. (1981, 1982) uniformly throughout Spencer Gulf. Greenberg (1983) comments his N_x, N_y lie in the range 14–$3500\,\mathrm{m}^2/\mathrm{sec}$ (ibid., p.903).

Schwiderski points out that the viscosity laws (5.8)–(5.9) explain the huge difference in the horizontal constants of eddy diffusion used by numerical modellers for different models. He further states that extensive computer experiments clearly demonstrate best results for the viscosity laws given by (5.8)–(5.9) rather than $N_x = N_y = 0$ or

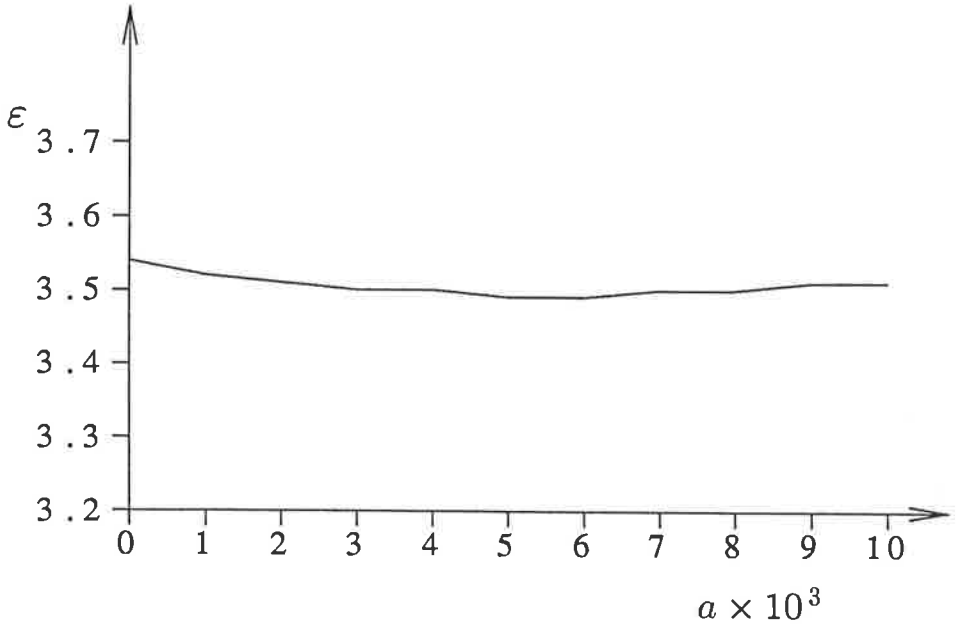


Figure 5.18: *Error measure ε (cm) versus reduced eddy coefficient a (sec^{-1}). The optimal value of a for the Spencer Gulf model is about $5.5 \times 10^{-3}\, sec^{-1}$ and has associated error value $\varepsilon = 3.49$ cm. The near flatness of the plot shows that this model is virtually insensitive to the value of a in the interval [0,0.01]. The non-smoothness of the plot is a consequence of the fineness of the vertical scale and the fact that the ε data values are given to only two decimal places.*

$N_x = N_y = constant > 0$, so it seems important to include the terms in a computer program for general application.

Some authors (e.g. Greenberg (1983), Wolf (1983), Arnold (1986a, 1987)) note that the inclusion of the horizontal diffusive terms smooths or at least partially damps grid-scale oscillations in the depth-averaged velocity components, particularly in deep water near open boundaries. This behaviour is now examined mathematically.

Consider the following expression based on approximation (3.16) for the x-diffusive term:

$$\left\{\frac{\partial^2 U}{\partial x^2}\right\}_i = \frac{1}{(2\Delta x)^2}\left(U_{i+1} - 2U_i + U_{i-1}\right), \tag{5.10}$$

where $(2\Delta x)$ is grid spacing. Let

$$U_i = U_a \exp(\imath \beta x_i), \tag{5.11}$$

real part intended, where U_a is the velocity amplitude, $\imath = \sqrt{-1}$, $\beta = 2\pi/\lambda$ is the wavenumber, λ is the wavelength and $x_i = i(2\Delta x)$, $i \in N$, N is the set of Natural numbers. Substituting this expression into the left hand side of (5.10) gives

$$\left\{\frac{\partial^2 U}{\partial x^2}\right\}_i = -\beta^2 U_i, \tag{5.12}$$

which shows that the diffusive term behaves as a linear friction term. Noye (1986) carries out a similar substitution and shows there is no phase error introduced by differencing of the form (5.10), only a change to the amplitude of the derivative (ibid., p.15) and he suggests that this is a friction-like behaviour.

The linear friction term of the U-momentum equation may take the form $-(k/D)U$ where k is the linear friction coefficient and D is local depth — c.f. equation (5.15). Thus the contribution of the second derivative to the linear friction coefficient k is $\beta^2 D = 4\pi^2 D/\lambda^2$. This contribution is almost negligible for tidal constituents (when λ is large) but is significant for grid-scale oscillations in the velocity components (when λ is small) .

The effect of the Schwiderski formulation for the diffusive coefficient is to increase the friction-like contribution of this term. For Greenberg's (1983) coarse-grid model of the Gulf of Maine which uses a square element of dimension 25 km× 25 km, the Schwiderski diffusive coefficient increases the friction contribution by a factor of 4100 in water of depth 200 m, near the shelf break zone of the model's open boundary.

This is the "true wave" behaviour of the horizontal diffusive term. Consider now the behaviour of the numerical approximation for the term.

Substituting (5.11) into the right hand side of (5.10) gives

$$\frac{1}{(2\Delta x)^2}(U_{i+1} - 2U_i + U_{i-1}) = -\beta^2 U_i \left[\frac{\sin(\beta\Delta x)}{\beta\Delta x}\right]^2 . \tag{5.13}$$

Defining "amplitude response" as the ratio of the output wave to the input wave, the amplitude response of the second derivative approximation is

$$\left[\frac{\sin(\beta\Delta x)}{\beta\Delta x}\right]^2 . \tag{5.14}$$

For a fixed grid spacing, the amplitude response approaches unity for very long waves and reduces monotonically to $(4/\pi^2)$ for the grid-scale wave $\lambda = 4\Delta x$. The wave $\lambda = 4\Delta x$ (twice the grid spacing) is the wave of shortest wavelength that can be resolved on a uniform grid — at least three gridpoints are needed to resolve a numerical wave.

The artificial contribution to the linear friction coefficient from the numerical approximation is therefore slightly less than $\beta^2 D$ for tidal constituents and is $4\beta^2 D/\pi^2 = D/(\Delta x)^2$ for the grid-scale oscillation $\lambda = 4\Delta x$.

For Greenberg's (1983) coarse-grid model near the shelf break, the artificial contribution to a linear friction coefficient introduced by a semi-diurnal constituent using Schwiderski's formulation is about 8.8×10^{-6} m/sec but for the grid-scale wave it is 0.0052 m/sec, about 600 times greater. This seems to explain Greenberg's observations, concerning grid-scale oscillations in the current field, that "An eddy-viscosity formulation based on that of Schwiderski (1980) ... smoothed the results, partially damping out these oscillations. The addition of this term caused no other obvious changes and a recalibration of the model based on the observed tidal data was not necessary" (Greenberg, 1983, pp.889–890). The partial damping is a result of the significant friction effect introduced by the differencing at grid-scale wavelengths,

and the recalibration at tidal frequencies was not needed because the introduced friction effect is only slight in the case of tidal constituents.

In the present model, the inclusion of horizontal diffusion with a Schwiderski formulation introduces an artificial contribution to a linear friction coefficient near the open boundary of about 1.9×10^{-6} m/sec for a semi-diurnal constituent and 0.0058 m/sec for the grid-scale oscillation $\lambda = 4\Delta x$. Shortly, it will be shown that the optimal (calibrated) linear friction coefficient for a linear model of Spencer Gulf is about 0.0009 m/sec which is about one sixth of the value contributed by the diffusive term for the $\lambda = 4\Delta x$ oscillation. Thus the Schwiderski diffusive formulation heavily damps grid-scale oscillations in the velocity components near the open boundary of the present model. This damping effect is useful since grid-scale oscillations in the velocity components are not a physical phenomenon but are produced by the numerical scheme.

The fact that the present model is virtually insensitive to the value of the reduced eddy coefficient a (see Figure 5.18) may suggest that, with the possible exception of the region near the open boundary, there is very little problem with grid-scale oscillations in the velocity components of the Spencer Gulf model. The difference between the model performance using $a = 0\,\mathrm{sec}^{-1}$ when $\varepsilon = 3.54$ cm and using $a = 0.0055\,\mathrm{sec}^{-1}$ when $\varepsilon = 3.49$ cm may be taken as a measure of the extent of the grid-scale problem near the open boundary (and elsewhere).

- **Changing the friction parameterization.** For two-dimensional depth-averaged tidal models, there are two basic types of bottom friction parameterization: linear and quadratic.

Linear parameterization of bottom friction:

The linear parameterization is of the form

$$\underline{\tau}_b = \rho\frac{k}{D}(U,V)\,, \tag{5.15}$$

where $\underline{\tau}_b$ is the bottom stress vector, k is the linear coefficient of bottom friction, D is either MSL depth h or total depth H (Rienecker, 1978), ρ is sea water density and (U,V) are the horizontal components of depth-averaged velocity. The parameter k can be fixed for the whole model region, it can assume fixed values for distinct sub-regions, or it can adopt a unique value for each grid element by being dependent on the mean depth of the element. Greenberg (1975) used three different values for the coefficient of linear friction k in his linear multi-grid model of the Bay of Fundy. He reports that in "the coarse and intermediate grids $k = 0.0025$. In the fine grid $k = 0.0027$, except in the Minas Basin where $k = 0.0064$" (ibid., p.70). Thus Greenberg used larger values of k for shallower regions. Furthermore, he fixed the value of k for three distinct sub-regions of the one model; such an approach introduces discrete jumps in k along the boundaries of the sub-regions which may tend to destabilize a model.

In order to determine the optimal value of the coefficient of linear friction for the Spencer Gulf model, the numerical scheme is linearized. Advective terms are deleted,

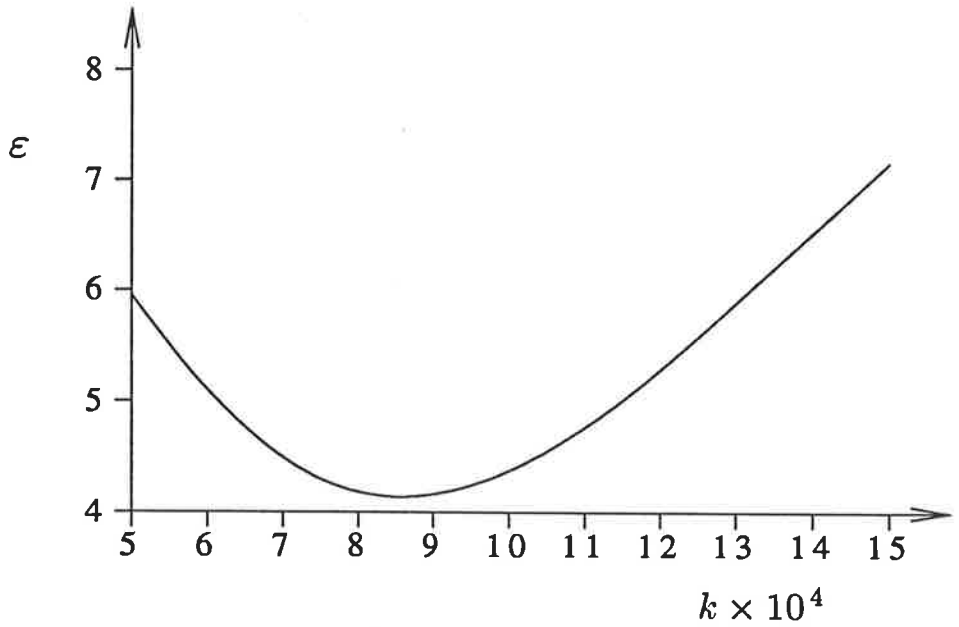


Figure 5.19: *Error measure ε (cm) versus linear friction coefficient k (m/sec). The optimal value of k for the Spencer Gulf model is about 0.0009 m/sec and has corresponding error value ε = 4.16 cm.*

the linear bottom friction parameterization is used and total depth H is not calculated so that only MSL depths h are used. Figure 5.19 shows a plot of error measure ε (cm) versus global linear friction coefficient k; the optimal value of k for the Spencer Gulf model is about 0.0009 m/sec and the corresponding error value is $\varepsilon = 4.16$ cm.

Quadratic parameterization of bottom friction:

The quadratic parameterization is of the form

$$\underline{\tau}_b = \rho \frac{C_b}{H}(U,V)\sqrt{U^2+V^2}, \tag{5.16}$$

where C_b is the dimensionless coefficient of quadratic bottom friction and H is total depth. The coefficient of quadratic friction is either specified as a global constant for the entire model region or it takes a depth-dependent form. In the latter case, as will be seen, a constant such as the "bed roughness height" still remains to be determined unless such a parameter can be satisfactorily established by field observation.

Globally specified constant coefficient of quadratic friction

A common practice is to specify C_b as a global constant for a given model. Typical values lie in the range 0.0010–0.0030 depending on the average depth and overall performance of the model compared to observations within the region. Choosing the optimal value for C_b is a primary means of calibration of the model. Mitchell et al. (1984) found the value 0.0012 to be optimal in their work on the Gulf of Carpentaria.

Reid and Bodine (1968) found the value 0.0025 to be optimal in their early numerical work; Flather and Heaps (1975), Bowden and Hamilton (1975), Pingree and Maddock (1977a), Blumberg (1977) and Flather and Proctor (1983) also use the value

0.0025. Owen (1980) uses 0.0026. Rienecker (1978) reports the use of values in the range

$$0.0024 \leq C_b \leq 0.0030 \tag{5.17}$$

by authors such as Dronkers (1964), Flather (1976) and Nihoul and Ronday (1976). Greenberg (1983) used values of 0.0023 and 0.0024 for his Bay of Fundy-Gulf of Maine model, and 0.0027 for his high resolution Gulf of Maine model. He comments that "Changes in $[C_b]$ larger than 1×10^{-4} did affect the tidal calibration, but did not qualitatively change the residual [current] pattern" (ibid., p.903).

Figure 5.17 shows a plot of error measure ε versus constant quadratic friction coefficient C_b. For values $C_b \leq 0.0018$, the model is unstable. The optimal value for C_b is 0.0025 and is in agreement with values obtained by other authors; the associated error value is $\varepsilon = 3.49\,\text{cm}$. It may be noted that this error value is less than the minimum error obtained in Figure 5.19 using the linear friction formulation. This shows that the non-linear formulation of tidal motions gives more accurate results for a numerical model of Spencer Gulf.

Locally specified coefficient of quadratic friction

In many publications the coefficient of quadratic friction is allowed to vary over the entire model, increasing with decreasing depth of water, and vice versa.

(a) **a logarithmic formula**

Bode and Sobey (1992) give the Colebrook-White formula for a hydraulically rough boundary which may be expressed in the form:

$$C_b = \frac{1}{32} \log_{10}^{-2} \left(\frac{k_b}{14.8H} \right) , \tag{5.18}$$

where k_b is the roughness height, to which Bode and Sobey assign the global value 0.025 m. This formulation was used since it "has a respectable background in turbulent pipe flow and does represent the increased influence of friction in shallow water" (ibid., p.7). In Figure 5.20 an error distribution is presented for a range of global values of k_b for the Spencer Gulf model. The optimal value lies in the range 0.06–0.07 m; the associated error value $\varepsilon = 3.45\,\text{cm}$ is slightly less than that given by the constant quadratic friction coefficient of Figure 5.17. However, computationally the logarithmic formulation is about 12% more expensive than the constant quadratic friction formulation because of the need to evaluate the logarithm.

(b) **the de Chèzy/Manning formula**

Another commonly used formulation, which also incorporates the roughness of the bottom material, is a combination of the de Chèzy and Manning formulae originally developed for the study of channel flows:

$$C_b = \frac{g}{C^2} , \tag{5.19}$$

where (Rienecker, 1978)

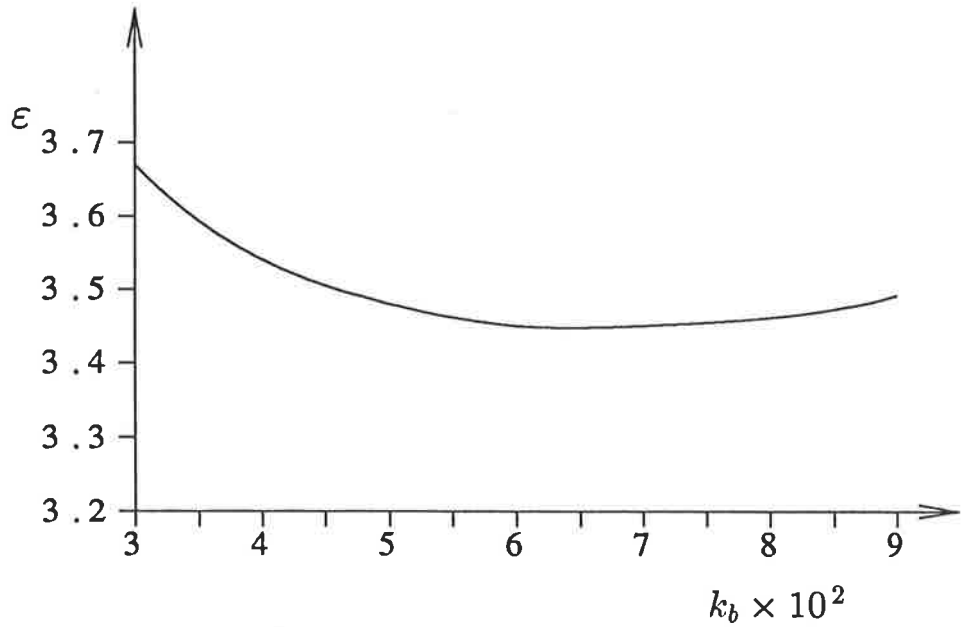


Figure 5.20: *Error measure ε (cm) versus roughness height parameter k_b (m) of the Colebrook-White formulation. The optimal value of k_b for the Spencer Gulf model lies in the range 0.06–0.07 m and has associated error of $\varepsilon = 3.45$ cm.*

C $= (1.003/n)R^{1/6}$ $\mathrm{m}^{1/2}/\mathrm{sec}$,
R is the hydraulic radius (usually taken as H for a shallow sea), and
n is Manning's roughness coefficient which varies with position according to the roughness of the bottom material.

Using $R = H$,

$$C_b = \frac{gn^2}{(1.003)^2 H^{1/3}} \tag{5.20}$$

and since it is not known how n varies over the Gulf, n is treated as a global parameter. Figure 5.21 is a plot of error for a range of values of n. The optimal value of n lies at 0.025 and agrees with values used in the literature; for example, Rienecker cites Teubner (1976) who used $n = 0.030$ and Prandle (1978) who used $n = 0.025$. The value of the error measure associated with the optimal value of n is $\varepsilon = 3.44$ cm and is slightly lower than that obtained using the constant quadratic friction coefficient and is almost the same as that obtained using the Colebrook-White formulation. This approach is computationally more expensive than the use of the constant quadratic friction coefficient because of the need to evaluate the one-third power of H.

5.5 Presentation of results and discussion

In this section model predictions for tidal elevation and depth-averaged tidal current are presented and discussed.

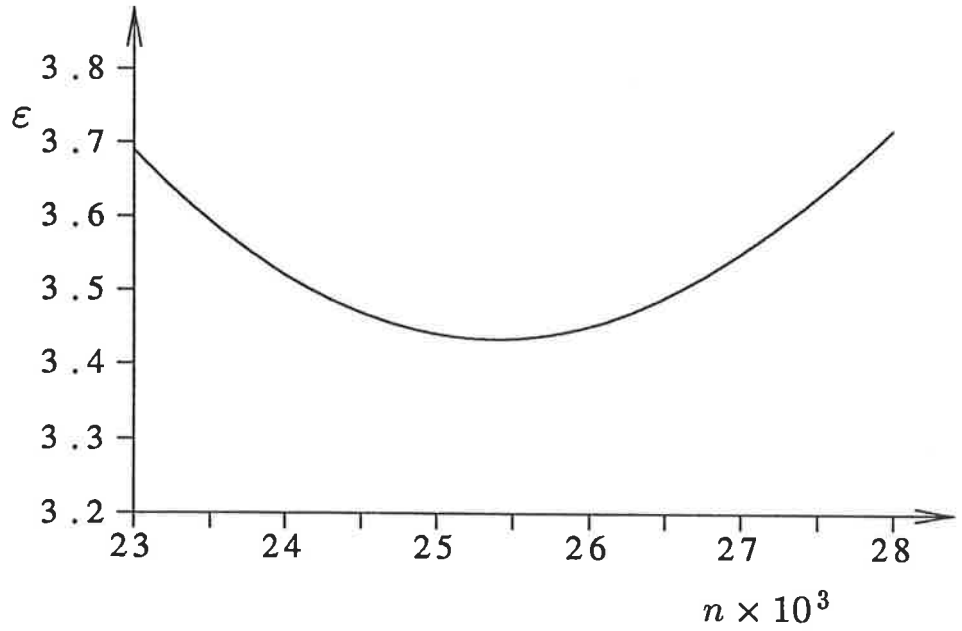


Figure 5.21: *Error measure ε (cm) versus Manning roughness coefficient n. The optimal value of n for the Spencer Gulf model lies at 0.025 and the corresponding error value is ε = 3.44 cm.*

The main interpretations of these results are by means of the **contour charts** of tidal elevation for the diurnal tidal constituents O_1, K_1 and the semi-diurnal constituents M_2, S_2 (Figures 5.22–5.25) and the **ellipse plots** of depth-averaged current for the same four constituents (Figures 5.26–5.29).

The model is run for a simulated time of 32 days. The first 3 days of predictions are assumed contaminated with initial transient waves and are not used. Predictions for the remaining 29 days are saved hourly and are tidally analyzed. It can be shown (e.g., Easton, 1977) that 29 days is the minimum length of hourly records required for accurate analysis of the four major tidal constituents. A further 21 constituents can also be extracted from a tidal series of this duration (ibid., p.16).

Results presented are for a globally specified constant coefficient of quadratic friction with value $C_b = 0.0025$ and are the first numerical predictions obtained from a "non-linear" model of Spencer Gulf driven simultaneously by the four major tidal constituents O_1, K_1, M_2 and S_2.

Calibration table and discussion

The results presented in Table 5.6 include an error summary using both the average absolute difference error measure (expression (5.4)) and the average absolute complex difference error measure (expression (5.6) or (5.7)). The former error measure is included so as to indicate the performance of the model for the amplitude and phase of individual constituents.

Observation station		O_1 amp	O_1 ph	K_1 amp	K_1 ph	M_2 amp	M_2 ph	S_2 amp	S_2 ph
*Port Augusta	Pred.:	37.3	49.3	45.5	80.5	60.0	203.7	62.5	262.9
	Obs.:	28.3	52.8	44.0	82.7	64.0	212.2	68.6	272.3
Beacon #5	Pred.:	36.7	48.7	44.8	79.7	56.5	201.9	58.5	261.2
	Obs.:	25.0	48.1	47.0	73.4	57.9	196.0	62.0	255.2
*Port Pirie	Pred.:	35.1	48.2	43.0	79.0	47.9	199.4	48.8	258.7
	Obs.:	27.6	49.2	42.5	77.4	48.9	197.2	52.9	258.3
Port Bonython	Pred.:	34.0	45.2	41.9	75.7	43.5	191.7	43.7	250.6
	Obs.:	27.0	42.7	41.6	70.6	45.1	185.3	48.6	245.6
Whyalla	Pred.:	33.9	44.7	41.8	75.2	43.0	190.4	43.2	249.2
	Obs.:	25.7	45.2	40.1	72.8	42.1	184.5	45.4	245.2
Yarraville Shoals	Pred.:	31.9	43.5	39.6	73.9	33.9	185.0	33.1	243.4
	Obs.:	24.4	39.2	37.2	69.8	32.2	175.5	33.9	236.9
*Port Broughton	Pred.:	30.6	46.3	38.5	76.8	27.5	189.2	25.9	247.5
	Obs.:	17.4	100.9	27.8	110.4	15.8	214.8	15.2	275.4
Wallaroo	Pred.:	25.3	38.1	33.7	68.2	13.5	143.3	11.6	187.6
	Obs.:	21.8	33.3	32.7	61.9	17.1	132.3	16.8	187.1
*Franklin Harbour	Pred.:	23.2	16.1	32.4	46.2	25.1	86.2	26.4	134.0
	Obs.:	20.0	34.0	30.0	61.0	22.0	114.0	23.0	173.0
Arno Bay	Pred.:	21.5	12.1	30.3	42.2	25.3	69.7	27.3	118.2
	Obs.:	19.9	8.4	29.5	37.4	25.6	66.6	26.8	120.1
Port Victoria	Pred.:	18.7	27.5	26.5	58.0	17.2	63.5	20.3	111.8
	Obs.:	16.9	20.7	24.5	51.5	18.9	61.9	20.3	116.4
Port Neill	Pred.:	20.3	9.0	28.6	38.9	25.0	58.4	27.2	107.6
	Obs.:	20.8	5.3	30.8	36.2	28.6	56.1	31.2	112.1
Port Turton	Pred.:	17.9	28.1	25.2	58.9	17.5	59.9	20.6	110.0
	Obs.:	16.0	22.9	23.4	51.7	18.4	60.6	19.5	115.1
Port Lincoln	Pred.:	17.6	1.4	24.7	30.2	24.1	33.8	25.8	84.0
	Obs.:	16.7	0.9	24.0	27.4	24.1	32.4	26.2	85.5
Wedge Island	Pred.:	15.1	6.6	20.9	36.1	16.2	24.6	16.8	75.6
	Obs.:	15.1	6.6	21.0	36.3	16.6	24.1	17.1	74.4
Ave. absolute differences:		4.05	3.00	1.42	4.54	1.44	4.42	2.07	3.71
Ave. complex differences:		4.41		3.05		3.16		3.36	

Table 5.6: *Comparison of predicted (Pred.) and observed (Obs.) results for amplitude (cm) and phase (deg, C.S.T.) for the four major tidal constituents at 15 stations in Spencer Gulf. Results for the asterisked stations are not used in the calibration process nor in the error summary. The overall average absolute difference, taken over all four constituents and the 11 calibration stations, is $\varepsilon_a = 2.25$ cm in amplitude and $\varepsilon_p = 3.92°$ in phase. The overall average absolute complex difference is $\varepsilon = 3.49$ cm.*

Error Measure	O_1		K_1		M_2		S_2	
	amp	ph	amp	ph	amp	ph	amp	ph
Ave. absolute differences:	4.11	2.82	1.47	4.36	1.23	3.76	1.76	4.03
Ave. complex differences:	4.45		2.98		3.02		3.18	

Table 5.7: *Error summary when results from stations sited more than $0.71(2\Delta x)$ from their representative model elevation point are excluded from the calibration. The differences between these results and those of Table 5.6 are due only to the exclusion of the data for Wallaroo station. The overall average absolute differences are 2.14 cm in amplitude and 3.74° in phase; the overall average absolute complex difference is 3.40 cm.*

Both error expressions exclude data from stations located a distance $2\Delta x$ or more from the nearest interior model elevation point (see Table 5.3) — thus stations Pt. Augusta, Pt. Pirie and Franklin Harbour have not been included in the calibration process. Pt. Broughton is also excluded because of the large phase lag there for all "observed" constituents (see also Table 5.1). The average absolute differences over the four major constituents are 2.25 cm in amplitude and 3.92° in phase; the associated average absolute complex difference is 3.49 cm.

As an addendum to the discussion in the last section about inaccuracies in the error measures, it may be noted that the rule used for including or excluding stations in the calibration process is weighted in favour of including stations along the coastal edge of the model. A station such as Yarraville Shoals within the model is surrounded on all sides by model elements and so the furthest that such a station can be from its representative elevation point is $(2\Delta x)/\sqrt{2}$. If those stations further than $0.71(2\Delta x)$ from their representative model point are excluded from the error measures (i.e., Wallaroo), a "fairer" table of errors is obtained (Table 5.7). The errors so calculated are now slightly smaller. The average absolute differences over the four major constituents are now 2.14 cm in amplitude and 3.74° in phase; the associated average absolute complex difference is 3.40 cm.

Perhaps the best way to accurately determine data for the error measures is to produce fine scale contour plots for the nearby region of each station showing the amplitude and phase of each tidal constituent, and to thereby calculate the predictions for the actual station sites.

However, in the meantime, errors will be presented using the method of Table 5.6 since it is at least a calibration using 11 stations which are located not too far from their representative model elevation point.

Sea surface elevations

The contour charts presented (Figures 5.22–5.25) show lines of constant amplitude (m) and lines of constant phase (deg, C.S.T.). The phase charts show the location of equivalent parts of the constituent wave and since the contour interval is regular (2° contours for the diurnals, 10° contours for the semi-diurnals), the relative positioning of the phase lines also indicates the relative speed of the wave.

Because all observations within the Gulf are made within the same time zone (−9:30 hr

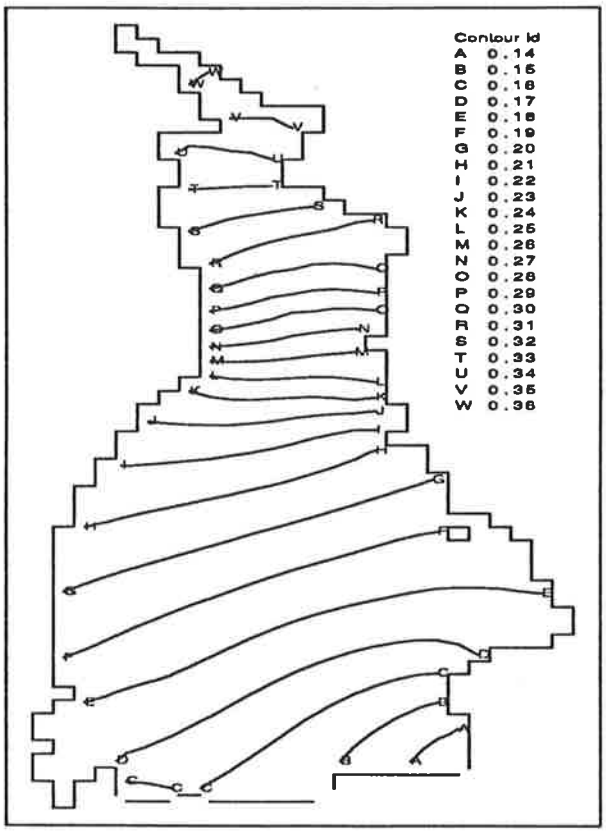


Figure 5.22(a): *Amplitude contours (m) for the O_1 tidal constituent of sea surface elevation.*

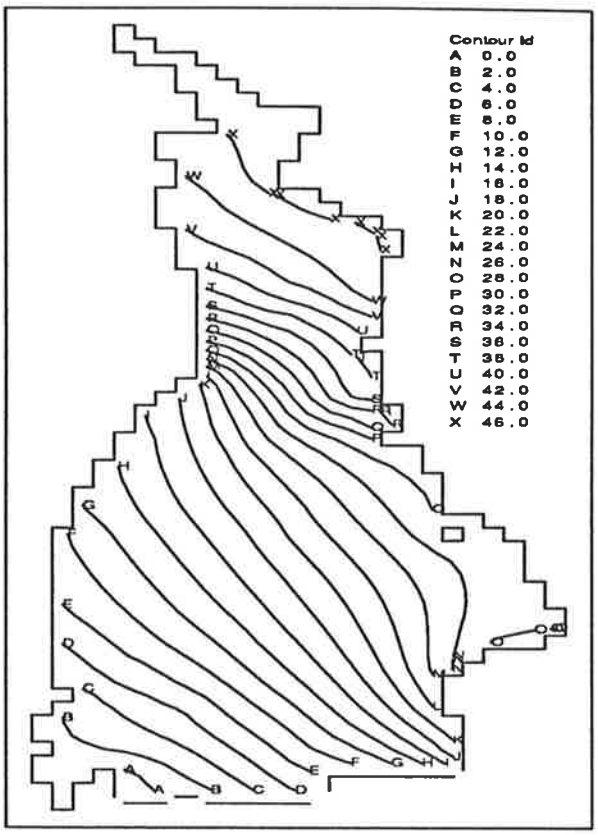


Figure 5.22(b): *Phase contours (deg, C.S.T.) for the O_1 tidal constituent of sea surface elevation.*

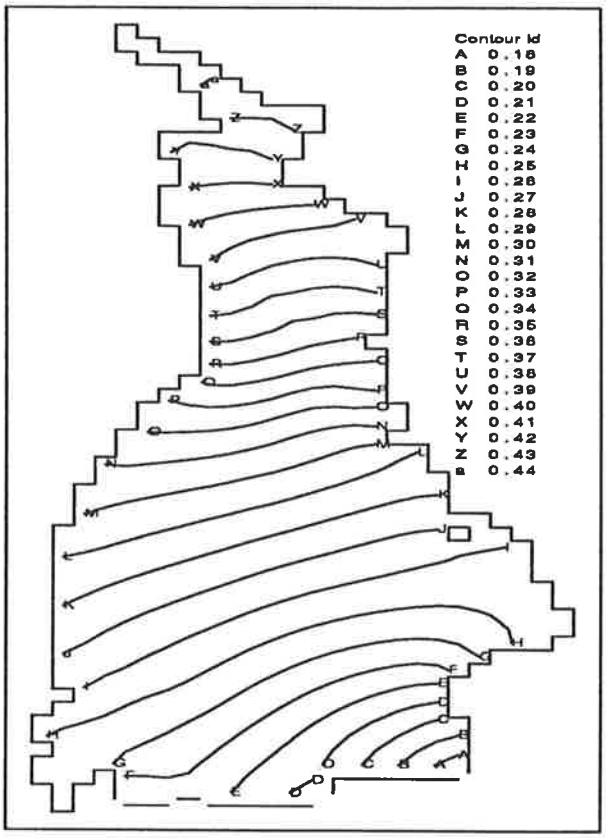


Figure 5.23(a): *Amplitude contours (m) for the K_1 tidal constituent of sea surface elevation.*

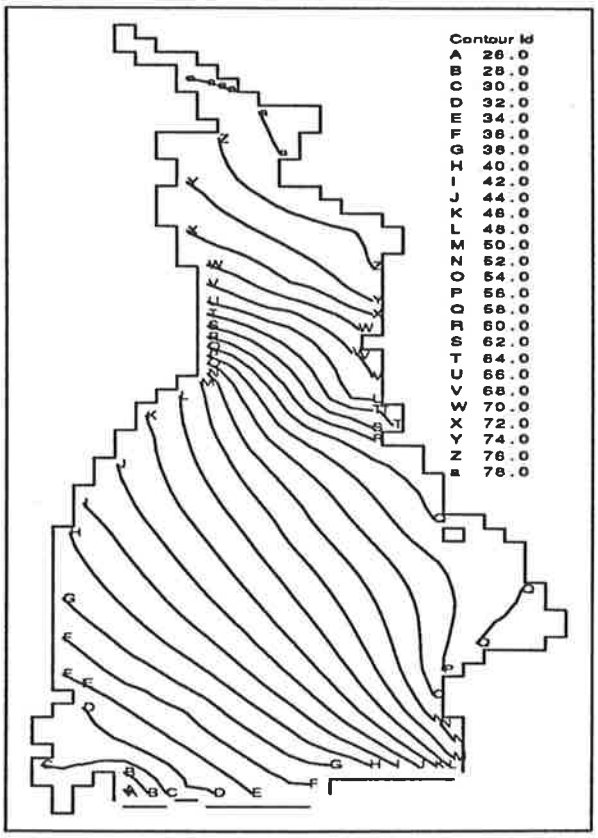


Figure 5.23(b): *Phase contours (deg, C.S.T.) for the K_1 tidal constituent of sea surface elevation.*

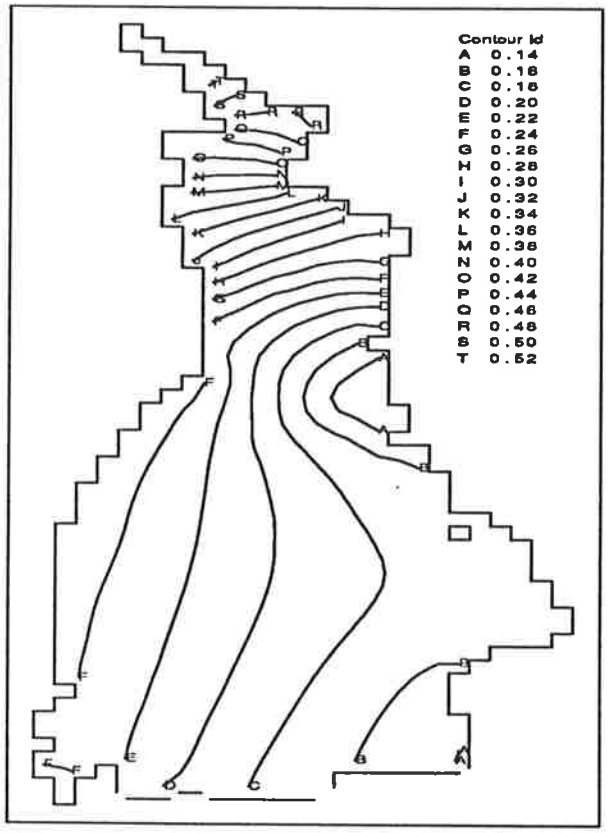


Figure 5.24(a): *Amplitude contours (m) for the M_2 tidal constituent of sea surface elevation.*

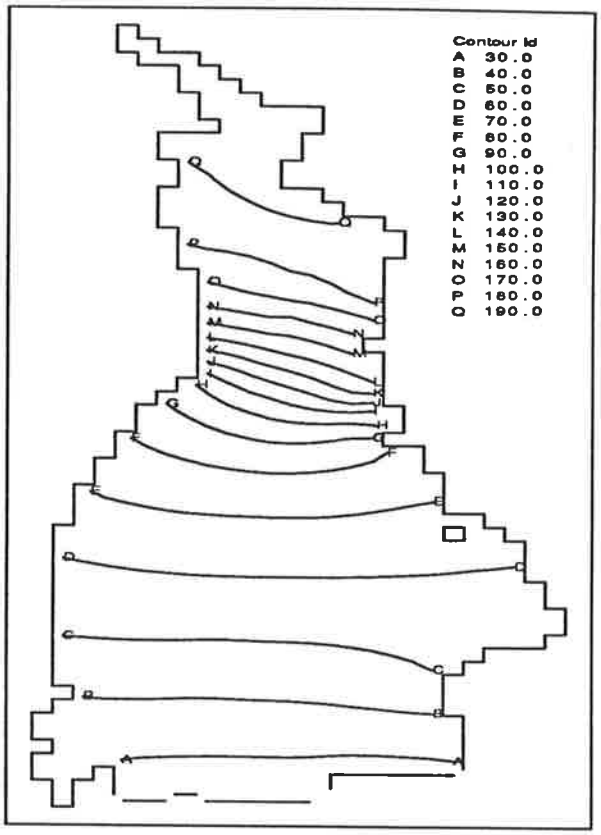


Figure 5.24(b): *Phase contours (deg, C.S.T.) for the M_2 tidal constituent of sea surface elevation.*

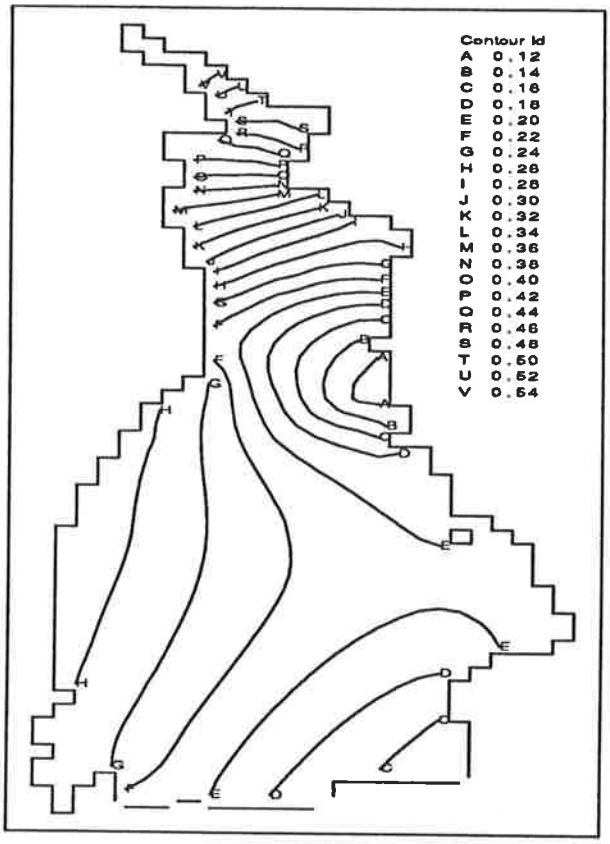


Figure 5.25(a): *Amplitude contours (m) for the S_2 tidal constituent of sea surface elevation.*

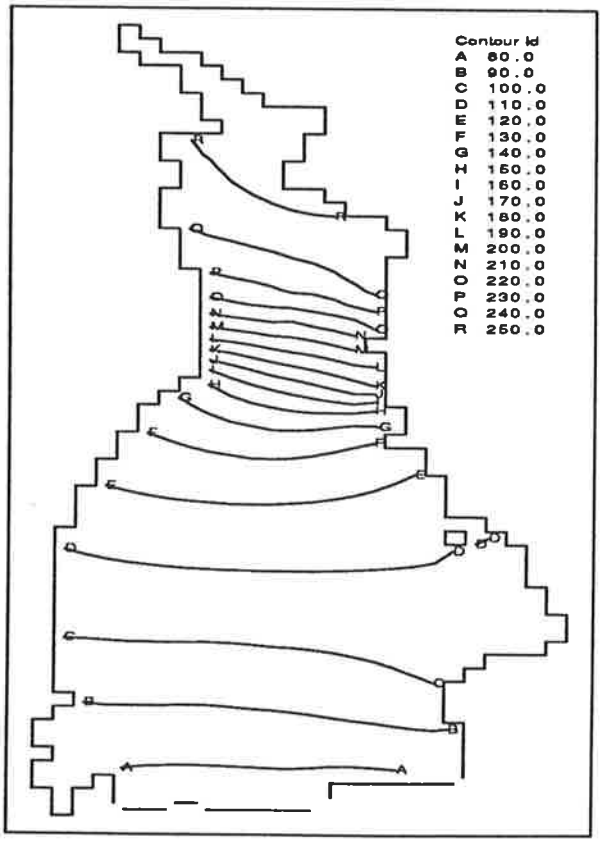


Figure 5.25(b): *Phase contours (deg, C.S.T.) for the S_2 tidal constituent of sea surface elevation.*

G.M.T.) and observations are usually expressed in terms of local time, all phases are also expressed in this way.

The diurnal constituents O_1 and K_1

Comparison of Figures 5.22(a) and 5.23(a) for amplitude, and Figures 5.22(b) and 5.23(b) for phase, shows the similarity in behaviour of the diurnal constituents. Both constituents are more-or-less steadily amplified in their passage northwards along the Gulf. The O_1 signal is the weaker of the two at any given location.

Comparing Easton's Figures 5.3(a),(b) with Figures 5.23(a),(b) for K_1, Easton's amplitude contours are up to 60° in misalignment (note that Easton's charts should be rotated 33.33° clockwise to align them with Figures 5.23) and show some numerical discrepancies. Easton's phase lines are also in misalignment in the southern Gulf region. Noye and Tronson's Figure 5.5(b) shows substantial agreement with the presented results, keeping in mind that they used a representative diurnal wave of double amplitude, but their non-linear model predictions of Figure 5.6(b) are not as good. Noye et al. (1981, 1982) do not present results for a diurnal constituent from their three-dimensional model.

Near the open boundary the model's predictions compare favourably with Steinberg's contours (see Figure 5.8). This is to be anticipated since his data is used to drive the model.

In general then, the model results are in agreement with the published numerical results of other authors, yet supply more detail.

The average absolute differences between observations and predictions at the 11 interior calibration stations (Table 5.6) show errors of 4.05 cm and 3.00° for the O_1 constituent, and 1.42 cm and 4.54° for K_1. Of note is the largeness of the O_1 amplitude error compared to K_1. The errors in phase show that on average the diurnals can be predicted with a timing error of 13 minutes for O_1 and 18 minutes for K_1; in order to interpret these timing errors, note that an error of 15 minutes in the arrival time of a diurnal constituent of frequency 15°/hour is an error of only $15/(24 \times 60) \times 100 \simeq 1\%$.

It can be seen from Table 5.6 that the large error in the amplitude of O_1 is mainly due to increasingly poor predictions north of Arno Bay. Generally, the O_1 amplitude predictions are similar to the observed values as far north as Arno Bay, but further northwards the two sets of values drift increasingly apart. Rerunning the tidal simulation using only O_1 to drive the model again gives larger than expected amplitudes for O_1 north of Arno Bay. Consider also the error values in Table 5.8 for the linear model using a coefficient of linear friction $k = 0.0009$ m/sec. Here the average absolute differences in O_1 and K_1 amplitude are about the same, and inspection of individual station errors shows that predicted O_1 amplitudes tend to maintain their similarity with observed values throughout the length of the Gulf. Thus, perhaps the largeness of the error in O_1 amplitude is due to some non-linear effect. Note in Table 5.8 that K_1 phase error is much higher than in Table 5.6.

The semi-diurnal constituents M_2 and S_2

Comparison of Figures 5.24(a) and 5.25(a), and Figures 5.24(b) and 5.25(b) shows the similarity of the semi-diurnal constituents and illustrates the important role that S_2 plays in the Gulf. The semi-diurnals have approximately equal amplitudes, contrasting with the diurnals (where K_1 has the greater amplitude), and they have very similar phase patterns.

Error Measure	O_1		K_1		M_2		S_2	
	amp	ph	amp	ph	amp	ph	amp	ph
Ave. absolute differences:	1.81	3.52	2.05	7.87	2.52	6.32	3.29	4.60
Ave. complex differences:	2.43		5.23		4.79		4.20	

Table 5.8: *Error summary for the linear model of Spencer Gulf using $k = 0.0009$ m/sec. The overall average absolute differences are $\varepsilon_a = 2.42$ cm in amplitude and $\varepsilon_p = 5.58°$ in phase; the overall average absolute complex difference is $\varepsilon = 4.16$ cm.*

In contrast to the diurnal tide which arrives at points on the western coast noticeably sooner than it arrives on the eastern coast (particularly in the southern Gulf) the semi-diurnal tide travels up the axis of the Gulf reaching equivalent transverse positions at approximately the same time.

Both constituents are amplified in their passage northwards along the Gulf, particularly in the northern Gulf, and each has a region of minimum amplitude near Wallaroo.

In the widening part of the Gulf just after entering from the mouth, the waves decrease speed until half way through the southern part of the Gulf and then accelerate and the phase lines noticeably bulge southwards as they move toward the narrowing part of the Gulf. Maximum wave speed is predicted through the narrowing part of the Gulf near Wallaroo. The narrowing causes amplification of the waves north of the zones of minimum amplitude and this amplification continues further northwards where the Gulf continues to narrow and to become shallower.

Comparing the M_2 amplitude predictions with Easton's (Figure 5.4(a)), detail has been provided for the southern Gulf region. In M_2 phase, whereas Chapman and Inglis (1898) and Easton (Figure 5.4(b)) postulated that the waves would travel faster up the middle of the Gulf — Easton draws the phase lines bulging northwards in the southern Gulf — they bulge first northwards but then southwards in the southern Gulf.

Noye and Tronson's linear model (Figure 5.5(a)) shows general agreement with the presented results and suggests the existence of a zone of minimum amplitude in M_2, but puts it too far north. Their non-linear model puts it even further northwards. However the results of the three-dimensional model of Noye et al. (1981, 1982) (Figures 5.7(a),(b)), show strong agreement. Perhaps with more accurate boundary information their model would have produced even closer agreement.

In the specific region of the open boundary the plots again agree well with Steinberg's hand drawn contours (Figure 5.9), as anticipated.

Thus the model results show strong agreement with the results of Noye et al. (1981, 1982) for M_2, and with Steinberg (1983) for S_2. Table 5.6 shows average absolute differences of 1.44 cm and 4.42° for the M_2 component, and 2.07 cm and 3.71° for S_2. The phase errors represent an accuracy of prediction of the semi-diurnal constituents of 9 minutes for M_2 and of less than 8 minutes for S_2; an error of 8.5 minutes in the arrival time of a semi-diurnal constituent of frequency 30°/hour is an error of $8.5/(12 \times 60) \times 100 \simeq 1\%$.

Tidal currents

The current ellipse plots, Figures 5.26–5.29 show several features of depth-averaged current due to the four major tidal constituents. To understand what these plots convey, consider a single gridpoint and the ellipse of, say, O_1. The ellipse shows the behaviour of the O_1 current constituent over a complete cycle, viz. 25.82 hr, at that gridpoint. At the beginning of the cycle — which corresponds with the start of the epoch (00:00 hr on 1/1/1900, G.M.T.) — a vector (without the arrowhead) is drawn indicating the direction and strength of the current. For example, inspection of the ellipses of Figure 5.30(b), which are enlargements of the ellipses in the row of the grid containing the gridpoint representing station Lima, predicts that at 00:00 hr on 1/1/1900, G.M.T., the tide is on the ebb in the region near the east coast due mainly to the S_2 and K_1 constituents. The M_2 and O_1 constituents contribute very little to the total current at that time, in that region. At every increment of $2\pi/20$ radians after the initial vector is drawn, except for the last two such increments, vectors are calculated but only their endpoints are recorded. The locus of the endpoints generates an elliptical curve. Because the last two increments are not linked, the direction of rotation of the ellipses can be seen. Ellipses are plotted only for alternate grid elements in Figures 5.26–5.29 — this allows the use of a larger scale without too much overlapping of the ellipses.

More formally, suppose from a tidal analysis of model predictions — or field data — of current at a given location, that U_a,U_p are the amplitude (m) and phase (deg), respectively, of the U component and V_a,V_p are the amplitude and phase of the V component of a particular constituent. Here, the U component is in the direction of the positive x-axis and the V component is the component in the direction of the positive y-axis, 90° counterclockwise from the x-axis. It can be shown (e.g. see Foreman, 1978) that the contribution of current due to the constituent of frequency σ cycles/hr can be written in the form

$$\begin{aligned} Q(t) &= Q^+(t) + Q^-(t) \\ &= a^+ \exp\{\imath(\varepsilon^+ + 2\pi\sigma t)\} + a^- \exp\{\imath(\varepsilon^- - 2\pi\sigma t)\} \\ &= \exp\left\{\imath\left(\frac{\varepsilon^+ + \varepsilon^-}{2}\right)\right\}\left[(a^+ + a^-)\cos\left\{\left(\frac{\varepsilon^+ - \varepsilon^-}{2}\right) + 2\pi\sigma t\right\}\right. \\ &\qquad \left. +\imath(a^+ - a^-)\sin\left\{\left(\frac{\varepsilon^+ - \varepsilon^-}{2}\right) + 2\pi\sigma t\right\}\right], \end{aligned} \tag{5.21}$$

where

$$\begin{aligned} a^\pm &= \left[\left(\frac{U_a\cos U_p \pm V_a \sin V_p}{2}\right)^2 + \left(\frac{V_a\cos V_p \mp U_a \sin U_p}{2}\right)^2\right]^{1/2}, \\ \varepsilon^\pm &= \arctan\left(\frac{V_a\cos V_p \mp U_a \sin U_p}{U_a\cos U_p \pm V_a \sin V_p}\right) + \text{Adjust}, \end{aligned} \tag{5.22}$$

and where "Adjust" is the inclination (in degrees) of the x-axis to East. In the present case the x-axis is 33.33° clockwise from East and so Adjust=−33.33°. The contribution consists of two vectors, $Q^+(t)$ and $Q^-(t)$, each rotating at angular speed σ cycles/hr. The former vector rotates counterclockwise, has length a^+ and is at ε^+ degrees counterclockwise from the positive x-axis at time $t = 0$; the latter vector rotates clockwise, has length a^- and

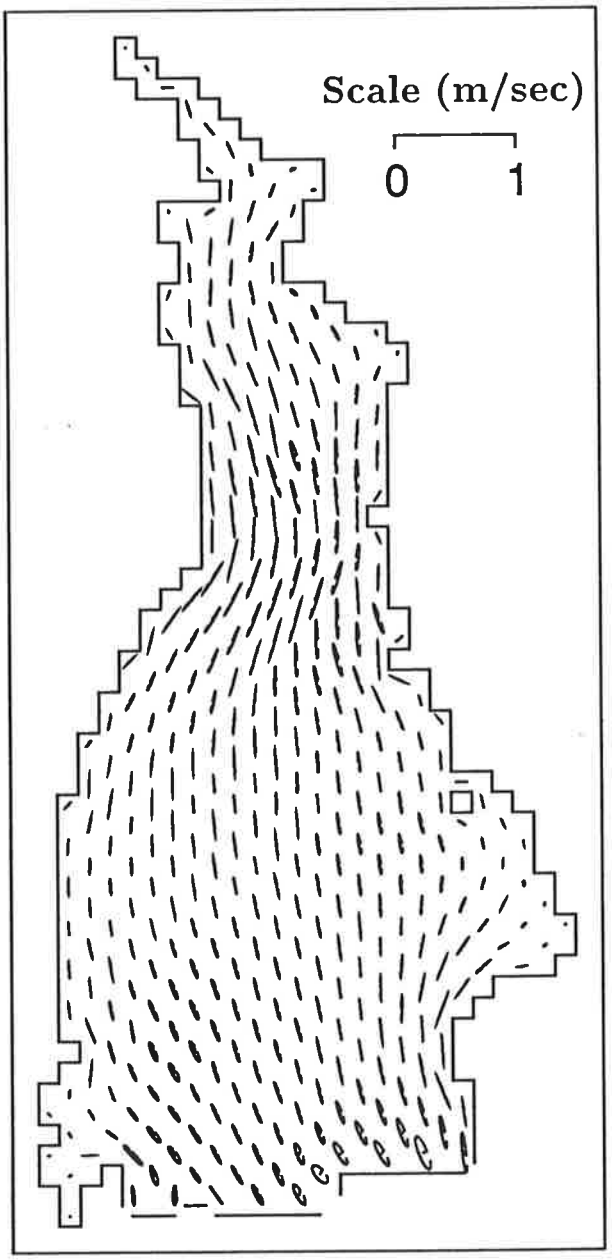


Figure 5.26: *Ellipses for the O_1 tidal constituent of depth-averaged current.*

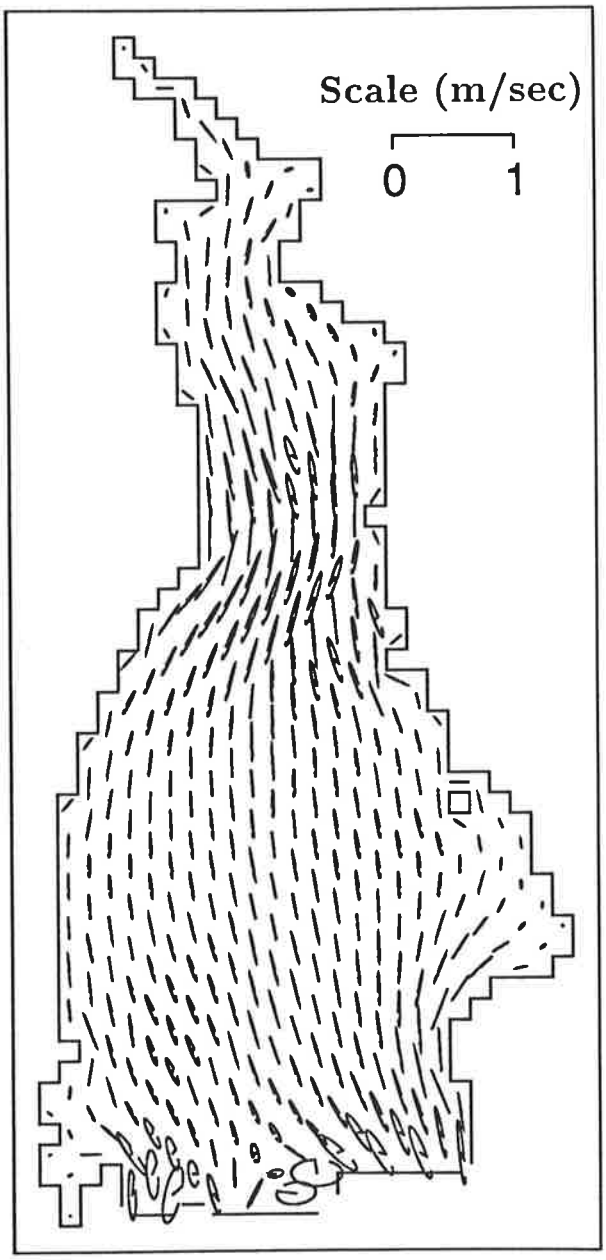


Figure 5.27: *Ellipses for the K_1 tidal constituent of depth-averaged current.*

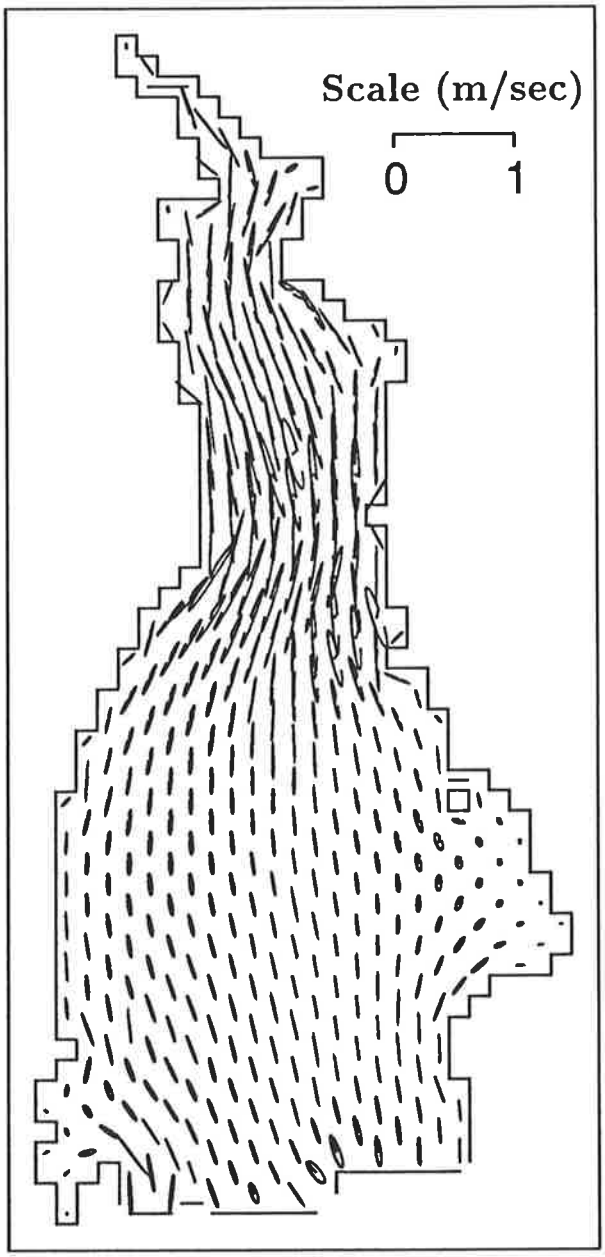


Figure 5.28: *Ellipses for the M_2 tidal constituent of depth-averaged current.*

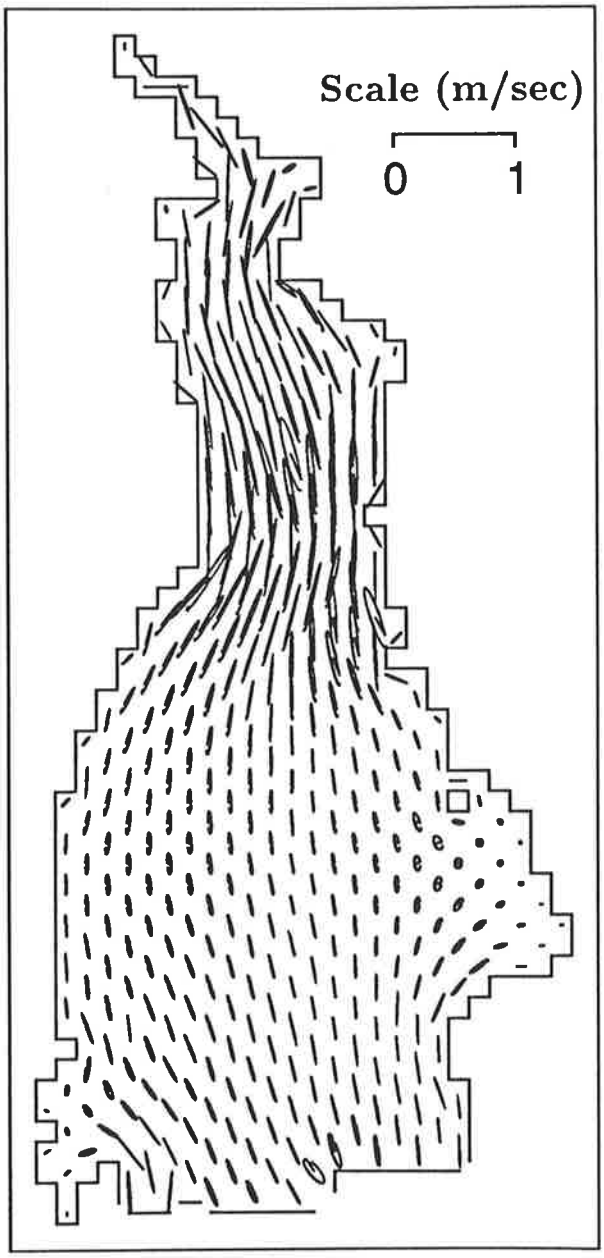


Figure 5.29: *Ellipses for the S_2 tidal constituent of depth-averaged current.*

is at ε^- degrees counterclockwise from the positive x-axis at $t = 0$. "The net rotational effect is that the composite vector $Q(t)$ moves counterclockwise if $a^+ > a^-$, clockwise if $a^+ < a^-$, and linearly if $a^+ = a^-$" (Foreman, 1978, p.11). From expression (5.21), "it is seen that over a time period of $1/\sigma$ hours, the path of the composite vector traces out an ellipse (or a line segment, in the degenerate case when $a^+ = a^-$) whose respective major and minor semi axis lengths are $(a^+ + a^-)$ and $(a^+ - a^-)$, and whose angle of inclination from the positive x axis is $(\varepsilon^+ + \varepsilon^-)/2$ degrees" (ibid., p.11). Furthermore, the phase lag of maximum current is $\{(\varepsilon^- - \varepsilon^+)/2 - \text{Zone} \times \text{Frequency}\}$, where "Zone" is the time difference (hr) of local time relative to G.M.T. — in the present case, Zone=−9.5 hr — and "Frequency" is constituent frequency in deg/hr.

In Figures 5.26–5.29 it is seen that the ellipses for all constituents are generally rectilinear but there are regions where they are more rounded, such as in the narrowing part of the Gulf in the region near Wallaroo and near the open boundary. A group of anticlockwise rotating ellipses to the north-west of Wallaroo and Point Riley correlates with shallow water over Middle Bank (see Figure 5.15), while another anticlockwise rotating group to the south correlates with shallow water over Tiparra Reef (Figure 5.15). There is a third group of clockwise rotating ellipses due west of Wallaroo that correlates with a deep (25 m) channel running along the western boundary of Tiparra Reef; this group extends diagonally across the Gulf to the western coastline.

All four ellipse plots are given to the same scale to facilitate easy comparison of the constituent ellipses at the same gridpoints.

The diurnal ellipses O_1 and K_1

Comparing the O_1 ellipses (Figure 5.26) with the K_1 ellipses (Figure 5.27) it is apparent that K_1 current strength is generally about one and a half times O_1 current strength. Apart from this both constituents show similar behaviour everywhere within the Gulf, according to the model predictions.

The diurnal current is strongest near the open boundary and through the narrowing part of the Gulf near Wallaroo. It is also stronger through the middle of the Gulf and weakens close to the coastal boundaries, where the water is shallower, due to frictional dissipation. It is largely rectilinear in the large southern Spencer Gulf region and is also predominantly rectilinear in the northern region. Near Wallaroo and the open boundary it shows transverse movement as well as axial movement.

A noteworthy feature of both plots is a reversal of rotation of the ellipses near Wallaroo. South of Wallaroo near Tiparra Reef, both diurnal ellipses are anticlockwise rotating. In fact, over the bulk of south-eastern southern Spencer Gulf they are anticlockwise or rectilinear, and clockwise in the north-western corner of southern Spencer Gulf. Diagonally across the Gulf from the western coastline toward Wallaroo are clockwise rotating ellipses. This is clearer in Figure 5.27 than Figure 5.26 and shows that for part of the tidal cycle, the diurnal current flows across the Gulf from the region near Arno Bay toward Wallaroo and vice versa half a cycle later. Directly opposite Wallaroo the ellipses on the western coast rotate anticlockwise while those in the eastern half clearly rotate clockwise. This effect can be seen in Figure 5.30(b). North of Middle Bank this pattern continues — for all constituents there are anticlockwise ellipses on the western side and clockwise ellipses on the eastern side — as shown in the enlarged view of ellipses in Figure 5.30(a), the model row containing station Mike.

Translating these observations concerning the direction of rotation of the constituent ellipses to motions of the constituent currents, it can be deduced that for part of each constituent cycle the diurnal current crosses the Gulf from south-west to north-east (or north-east to south-west) as it passes through the narrowing section near Wallaroo. Accompanying this passage it can be anticipated that an anticlockwise (or clockwise) cell of circulation is set up just north of this flow along the western coast opposite Wallaroo, and that a clockwise (or anticlockwise) cell is set up south of it, along the eastern coast near Wallaroo. More will be said of this in a following section on gyres. These across-Gulf components in the diurnal currents are weak in comparison to the along-Gulf components.

Noye (1984c) summarizes much of the available observations on the tidal currents of Spencer Gulf and reproduces ellipse characteristics due to Lennon (1981). Since model results are depth-averaged and Lennon's are depth-dependent, one expects order-of-magnitude agreement between them, but the currents are generally rectilinear in the region and so strong agreement may be anticipated, depending on the relative depth of the current meters. Results from two stations are given: Mike, close to the western coastline opposite Pt. Broughton (see Figure 5.15) and Lima, slightly westward of centre of the Gulf and opposite Wallaroo. The current meters were placed 10 m from the bottom in 24 m mean depth at Mike and 12 m from the bottom in 18 m mean depth at Lima.

Data 5 m from the bottom at Lima has recently been obtained (Lennon, 1990), along with current data at five new stations namely Yarraville Shoals, Red, Yellow (two levels), Blue (two levels) and White (two levels) — see Figure 5.10 for their location. Map position and error in representation of each of these stations at the nearest model elevation gridpoint have been recorded in Table 5.3.

In Figures 5.30(a),(b) ellipses are plotted for all elements in the rows containing the elevation points representing stations Mike and Lima. In Figure 5.30(a) the Mike ellipses are taken as the third from the left; in Figure 5.30(b) the Lima ellipses are taken as the fourth from the left. Table 5.9 compares predicted values for ellipse characteristics with observations reported by Lennon (1981, 1990) for each of the four major tidal constituents. The model results show general agreement with observations at both Mike and Lima. The differences between predicted and observed ellipse orientation may be due to the way the coastal boundary is approximated in the vicinity of these stations and to the coarseness of the bathymetric representation in the model. It is somewhat meaningless to consider the differences between predicted and observed values in semi-minor axis because the numbers involved are generally very small. In Chapter 7, depth-dependent predictions for ellipse characteristics will be compared with these observations.

Tables 5.10 and 5.11 compare predicted and observed ellipse characteristics at the five new stations which have recently come to light. Apart from Yarraville Shoals, model results show general agreement with observed values. The large differences in semi-major axis values for Yarraville Shoals suggest that observations were taken very near the bed — this is in fact the case. Knowing the relative depths at which the observations were made allows a more quantitative criticism of the model results to be made — see Chapter 7.

Figures 5.26–5.29 suggest K_1 is the strongest of the four major current constituents at the open boundary. Not only does it record the largest semi-major axis values, but it also has the largest semi-minor axis values. These results are in qualitative agreement with observations of along-stream and cross-stream current reported by Steinberg (1983). In particular, Steinberg notes that across the mouth of Spencer Gulf the "major contribution to the cross stream components are from the diurnal constituents" (ibid., p.58).

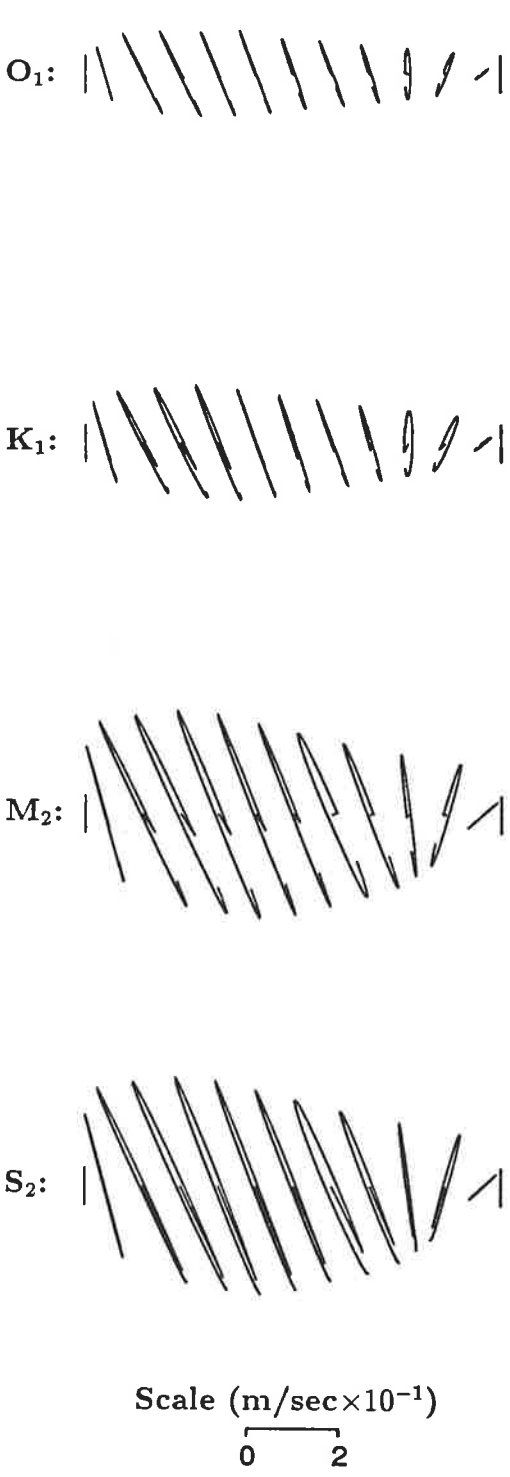


Figure 5.30(a): *Enlarged ellipses for row 17 of Figures 5.26–5.29, for the four major tidal constituents. Ellipses for station Mike are taken as those third from the left.*

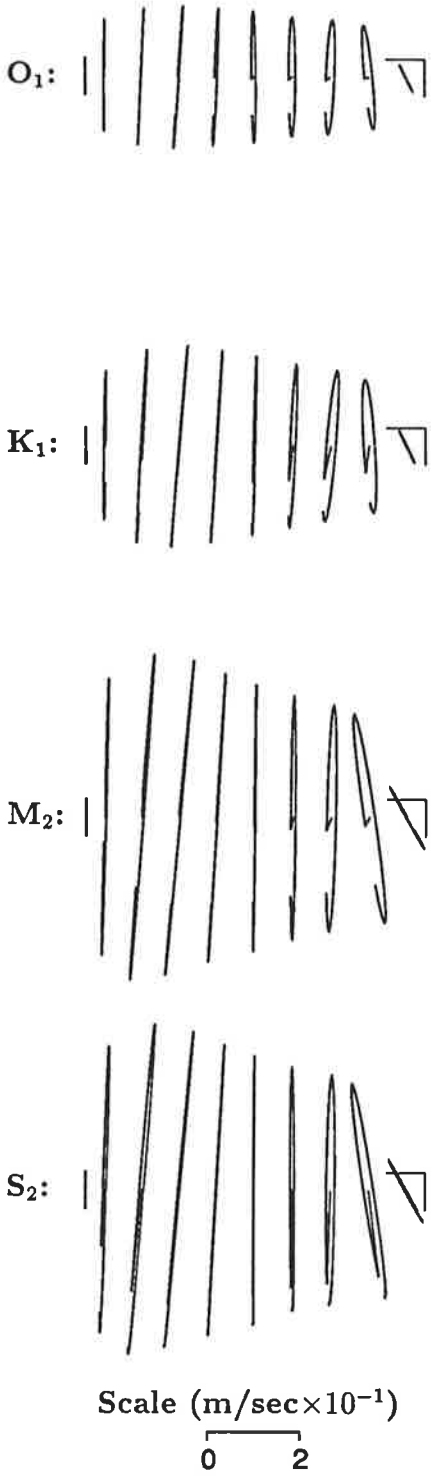


Figure 5.30(b): *Enlarged ellipses for row 25 of Figures 5.26–5.29, for the four major tidal constituents. Ellipses for station Lima are taken as those fourth from the left.*

Tidal constituent		O_1	K_1	M_2	S_2
Mike: meter 10 m from bottom in 24 m mean depth (model: 24.3 m)					
Semi-major axis (cm/sec)	Pred.:	10.1	13.7	24.5	25.4
	Obs.:	10.6	13.9	25.3	27.6
Semi-minor axis (cm/sec)	Pred.:	0.23	0.62	0.81	0.80
	Obs.:	0.33	−0.49	0.20	0.15
Phase lag of maximum (g°)	Pred.:	320	352	108	167
	Obs.:	323	355	106	165
Orientation of major axis (°T)	Pred.:	8.0	8.5	9.1	9.1
	Obs.:	12.4	14.1	14.3	14.1
Direction of rotation	Pred.:	A	A	A	A
	Obs.:	A	C	A	A
Lima: Upper meter 12 m from bottom and Lower meter 5 m from bottom in 18 m mean depth (model: 19.0 m)					
Semi-major axis (cm/sec)	Pred.:	15.2	21.8	32.7	32.7
	Upper:	14.4	19.6	33.5	36.1
	Lower:	11.7	16.9	28.7	31.2
Semi-minor axis (cm/sec)	Pred.:	−0.30	−0.08	−0.09	−0.07
	Upper:	2.02	0.97	0.97	0.51
	Lower:	−0.48	0.67	−0.47	−0.24
Phase lag of maximum (g°)	Pred.:	313	344	97	154
	Upper:	316	336	89	147
	Lower:	306	335	87	145
Orientation of major axis (°T)	Pred.:	35.6	37.0	36.7	36.3
	Upper:	46.0	40.6	42.6	40.2
	Lower:	34.6	41.6	42.5	42.5
Direction of rotation	Pred.:	C	C	C	C
	Upper:	A	A	A	A
	Lower:	C	A	C	C

Table 5.9: *Comparison of predicted (Pred.) and observed (Obs.) ellipse characteristics for the four major tidal current constituents at stations Mike and Lima. Predicted values are from the depth-averaged model, taken at the nearest elevation gridpoints in representation of the actual station location (depths in brackets are corresponding MSL model depths). Observations are from Lennon (1981,1990) except that when an observed rotation for a given constituent is clockwise, the corresponding minor axis value is given a negative sign: this is a convention used in the analysis of the model predictions. Observations from the Upper and Lower meters at Lima are labelled accordingly. Direction of rotation is denoted A = Anticlockwise and C = Clockwise. Phase lag of maximum current is given in local time.*

Tidal constituent		O_1	K_1	M_2	S_2
Yarraville Shoals: meter 1 m from bottom in 9.4 m mean depth (model: 16.4 m mean depth)					
Semi-major axis (cm/sec)	Pred.:	8.9	12.3	23.6	24.7
	Obs.:	3.8	5.4	13.4	13.5
Semi-minor axis (cm/sec)	Pred.:	−0.07	−0.20	−0.06	−0.06
	Obs.:	0.51	0.36	−0.17	−0.17
Phase lag of maximum (g°)	Pred.:	318	348	107	166
	Obs.:	327	325	108	147
Orientation of major axis (°T)	Pred.:	19.2	19.0	18.4	18.5
	Obs.:	10.2	7.8	9.4	8.1
Direction of rotation	Pred.:	C	C	C	C
	Obs.:	A	A	C	C
Red: meter 2.5 m from bottom in 22 m mean depth (model: 21.1 m mean depth)					
Semi-major axis (cm/sec)	Pred.:	5.6	8.3	10.3	9.8
	Obs.:	4.8	7.3	9.7	11.0
Semi-minor axis (cm/sec)	Pred.:	−0.24	−0.40	−0.58	−0.58
	Obs.:	−1.04	−0.61	−1.96	−1.93
Phase lag of maximum (g°)	Pred.:	304	333	66	120
	Obs.:	299	336	54	116
Orientation of major axis (°T)	Pred.:	46.9	46.3	47.0	47.3
	Obs.:	63.9	60.4	52.0	56.6
Direction of rotation	Pred.:	C	C	C	C
	Obs.:	C	C	C	C
Yellow: meters 26 m (Upper) from bottom and 2.5 m (Lower) from bottom in 33 m mean depth (model: 30.0 m mean depth)					
Semi-major axis (cm/sec)	Pred.:	9.5	13.2	14.8	14.1
	Upper:	10.0	13.6	17.2	18.5
	Lower:	6.6	9.2	11.2	12.2
Semi-minor axis (cm/sec)	Pred.:	−0.22	−0.49	−0.86	−0.90
	Upper:	1.33	−0.14	−0.48	1.05
	Lower:	−0.53	−0.88	−2.55	−2.07
Phase lag of maximum (g°)	Pred.:	310	342	80	136
	Upper:	330	355	119	163
	Lower:	334	353	69	128
Orientation of major axis (°T)	Pred.:	42.6	42.7	46.1	47.1
	Upper:	40.8	42.0	56.1	56.6
	Lower:	66.7	65.5	50.7	50.8
Direction of rotation	Pred.:	C	C	C	C
	Upper:	A	C	C	A
	Lower:	C	C	C	C

Table 5.10: *Comparison of predicted and observed ellipse characteristics of the four major tidal current constituents at stations Yarraville Shoals, Red and Yellow. At Yellow, observed values from two meters denoted Yellow "Upper" and Yellow "Lower" are available.*

Tidal constituent		O_1	K_1	M_2	S_2
Blue: meters 17 m (Upper) from bottom and 2.5 m (Lower) from bottom in 23 m mean depth (model: 24.9 m mean depth)					
Semi-major axis (cm/sec)	Pred.:	8.5	11.8	12.4	11.4
	Upper:	12.1	14.7	18.7	20.7
	Lower:	6.4	9.7	10.0	11.7
Semi-minor axis (cm/sec)	Pred.:	−0.14	−0.07	0.59	0.75
	Upper:	2.12	0.37	6.78	6.35
	Lower:	−0.39	2.00	1.77	2.84
Phase lag of maximum (g°)	Pred.:	309	338	82	138
	Upper:	293	326	78	129
	Lower:	287	331	63	123
Orientation of major axis (°T)	Pred.:	20.0	21.2	20.3	19.7
	Upper:	355.4	358.4	8.4	7.0
	Lower:	14.4	18.5	8.6	5.1
Direction of rotation	Pred.:	C	C	A	A
	Upper:	A	A	A	A
	Lower:	C	A	A	A
White: meters 17 m (Upper) from bottom and 2.5 m (Lower) from bottom in 21 m mean depth (model: 21.9 m mean depth)					
Semi-major axis (cm/sec)	Pred.:	6.5	9.2	9.4	8.4
	Upper:	9.2	10.8	13.5	14.8
	Lower:	5.1	8.0	7.8	8.8
Semi-minor axis (cm/sec)	Pred.:	−0.24	−0.31	0.60	0.76
	Upper:	0.51	−1.27	5.43	4.58
	Lower:	−0.76	1.09	0.80	1.91
Phase lag of maximum (g°)	Pred.:	306	334	81	138
	Upper:	283	313	75	129
	Lower:	283	328	58	121
Orientation of major axis (°T)	Pred.:	12.6	13.8	10.1	8.9
	Upper:	358.9	353.1	356.6	358.1
	Lower:	6.1	17.0	359.9	355.2
Direction of rotation	Pred.:	C	C	A	A
	Upper:	A	C	A	A
	Lower:	C	A	A	A

Table 5.11: *Comparison of predicted and observed ellipse characteristics of the four major tidal current constituents at stations Blue and White. There are meters at two levels at both Blue and White.*

The semi-diurnal ellipses M_2 and S_2

Comparing Figures 5.28 and 5.29 for the semi-diurnal currents, they are of approximately equal strength, though S_2 is slightly stronger over the whole Gulf. They also exhibit similar behaviour everywhere in the Gulf.

The semi-diurnal current is strongest in the northern part of the Gulf, particularly through the narrowing section in the vicinity of Wallaroo. It is noticeably weaker around the shallower coastal edges near Pt. Lincoln and in the region between Pt. Turton and Pt. Victoria.

The semi-diurnal current is generally rectilinear along the axis of southern Spencer Gulf, dividing it into two broad regions of oppositely rotating ellipses. On the western side, the ellipses rotate clockwise; on the eastern side they rotate anticlockwise and some of these, those south and south-west of Wardang Island, near Pt. Victoria, are nearly circular. There is a repetition in the semi-diurnal ellipses near Wallaroo of the change in rotation noticed in the diurnal ellipses. The clockwise rotating semi-diurnal ellipses along the western coastline have a transverse component at the narrowing part of the Gulf. Figure 5.30(b) shows that across the Gulf opposite Wallaroo the semi-diurnal current ellipses are either clockwise rotating or rectilinear, and there is almost no transverse component for the ellipses on the central and western side. Several elements north of this region, the ellipses are anticlockwise rotating on the central and western side and Figure 5.30(a) shows this clearly.

Comparisons of predicted and observed data from stations Mike and Lima are presented in Table 5.9 and again suggest substantial agreement at these two sites.

There are large differences in the observed phase lag values for M_2 and S_2 at Yellow, but the predicted values lie between the observed values. We note that the clockwise rotation of the M_2 ellipses at Red and Yellow show plainly in Figure 5.28; similarly the anticlockwise rotation of the M_2 ellipses at Blue and White also show plainly in Figure 5.28. The tendency for the ellipses to rotate clockwise on the western side of the Gulf is also confirmed in Figures 5.28 and 5.29. The fact that predictions for Yarraville Shoals are noticeably different from observations is perhaps because the observations are made low in the water column.

At the open boundary it is clear that there is little across-stream component due to the semi-diurnals; this is also suggested in the observations of Steinberg (1983). The along-stream component is generally stronger than that of O_1, but certainly weaker than that of K_1, again as observed by Steinberg.

Gyres

From the above there is evidence for the existence of circulation zones, eddies or gyres in the region near Wallaroo during the tidal cycle. A general investigation of tidal flows in this region is now made.

In order to establish the timing of the gyral events it is of assistance to first construct a tidal elevation signal representative of the region. Figure 5.31(a) is a plot of the predicted and observed tidal elevation signals at Wallaroo due to the combination of the four major tidal constituents. The predicted signal is reconstituted from the tidal analysis of the numerical results for the elevation point nearest the map location of Wallaroo. Overall agreement is good at the scale used. Figures 5.31(b),(c) show the predicted and observed

signals for days 6–8 corresponding to a neap period, and for days 13.5–15.5 corresponding to a spring period.

Examining the broad nature of the neap flows, Figure 5.32 shows successive 15 min snapshots for predicted depth-averaged tidal current near the 6.5 dy point of the neap flow of Figure 5.31(b). These snapshots are taken direct from the model output, so they are not a presentation of selected constituents. Some "vectors" show as points because they represent tidal magnitudes smaller than the value above which arrowheads are fitted. Also, where tidal magnitude is only just large enough to allow the arrowhead to be fitted, some "vectors" appear as arrowheads with their shaft unable to be discerned because of the blurring effect of the plot reduction process. Inspecting the frames given in Figure 5.32 shows gyres just south of Wallaroo and opposite Wallaroo near the western coastline.

A study of the spring flow near the 14 dy 4 hr point yields similar evidence for gyres (Figure 5.33).

The timing of the gyres seems to correlate with change of tide (i.e. slack water) when current flows are at a relative minimum. These gyres are not sustained from one tidal change to the next, but develop at each change-of-tide event and dissipate before the next.

If these gyres are dominantly tidal they should be detectable in the ellipse plots of the individual constituents given in Figures 5.26–5.29. Rather than plot full ellipses, individual vectors can be plotted at specific times of the constituent tide cycle, where the "time" corresponds to an angle of the oscillating velocity field. The correct rotation of the gyres so obtained will be determined by supplying either an increasing or decreasing sequence of angles (times) and comparing the output vector fields with those given in Figures 5.32 or 5.33.

Figure 5.34 shows a 3.76° progression (corresponding to 15 min intervals) in such vector plots for the K_1 constituent. The particular set of snapshots shown has been chosen to correlate as closely as practicable with the neap events of Figure 5.32 by trying different sequences of angles. During the 120 minutes of the K_1 current flow depicted, at least two gyres are created and dissipated and these correlate with those seen in Figure 5.32. The strongest is the short-lived clockwise gyre near Tiparra Reef (Figure 5.15). It is generated on the waning flood tide, between Wallaroo and Tiparra Reef where the sea bed gradient is steep, and moves south-westward parallel to the bathymetric contours with the general drift of the ebbing tide. It dissipates as the ebb tide strengthens. Similarly, an anticlockwise gyre develops on the western coast opposite Wallaroo, moves toward the centre of the Gulf and dissipates. As well, there seems to be another clockwise gyre that develops along the east coast a few elements north of Point Riley (Figure 5.15), but this is very small. The south-west to north-east flows across the Gulf toward Wallaroo and Point Riley are clearly visible in many of the frames of Figure 5.34 and correlate with the deep channel marked on Figure 5.15.

The scale used in Figure 5.34 is double that of Figure 5.32, so if it is imagined that the neap events are due to predominantly the diurnal constituents, one would expect general agreement between the two figures. While this is true in an overall sense, the greater strength of the vectors in Figure 5.32 and the shorter life span of the gyres, relative to the vectors and gyres in Figure 5.34, suggest a significant semi-diurnal influence in the neap flows of Figure 5.32.

The mechanism of creation of the gyres seems to be topographical and the suggestions of Green (1984) concerning residual eddies can be applied here. Green identifies three

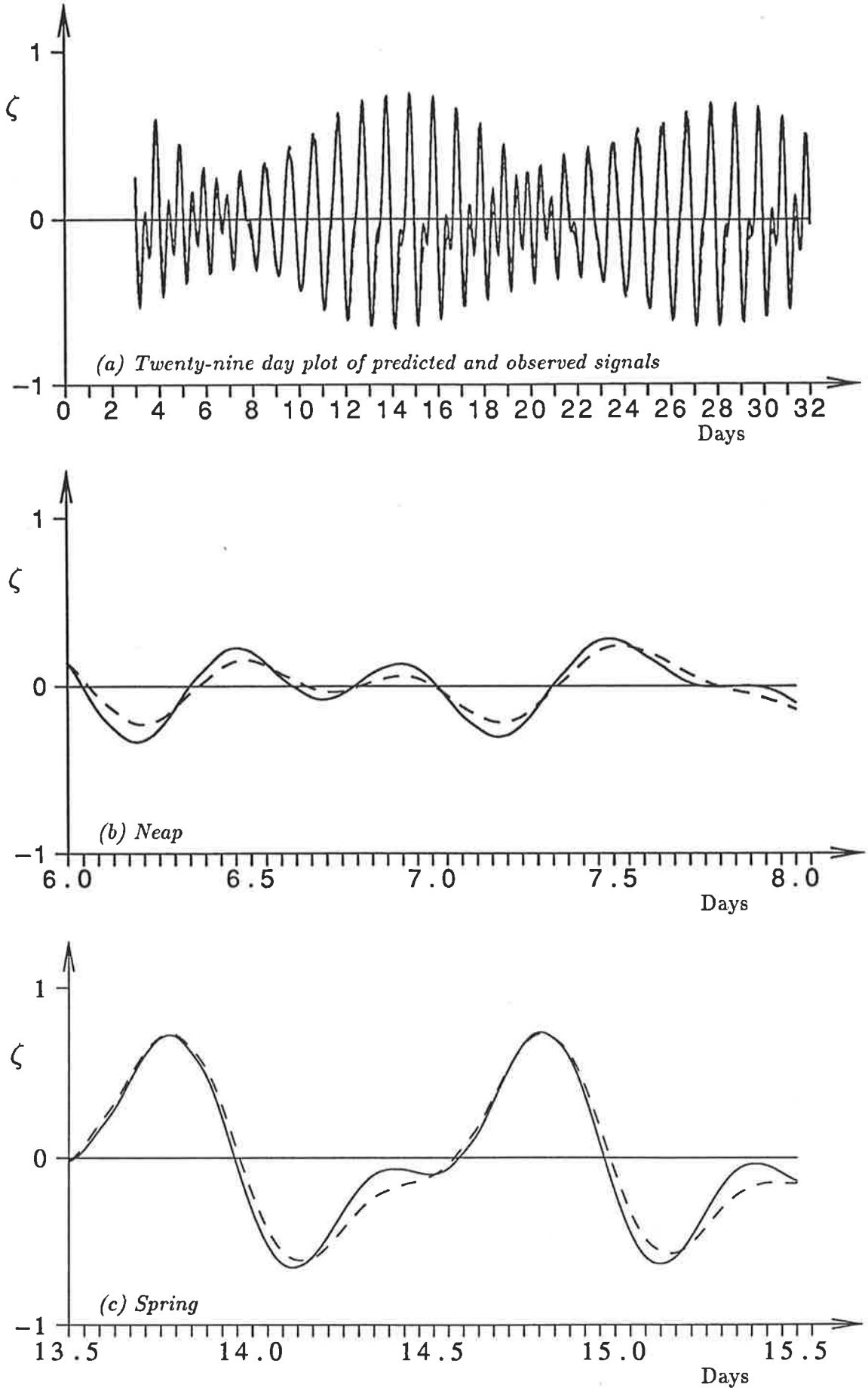


Figure 5.31: *Comparison of predicted (- - - -) and observed (———) tidal elevation ζ (m) for Wallaroo station. Signals are reconstituted using the respective four major constituents. Plot (a) shows a full 29 day period, (b) is a magnification of the neap period at 6–8 days and (c) is a magnification of the spring period at 13.5–15.5 days.*

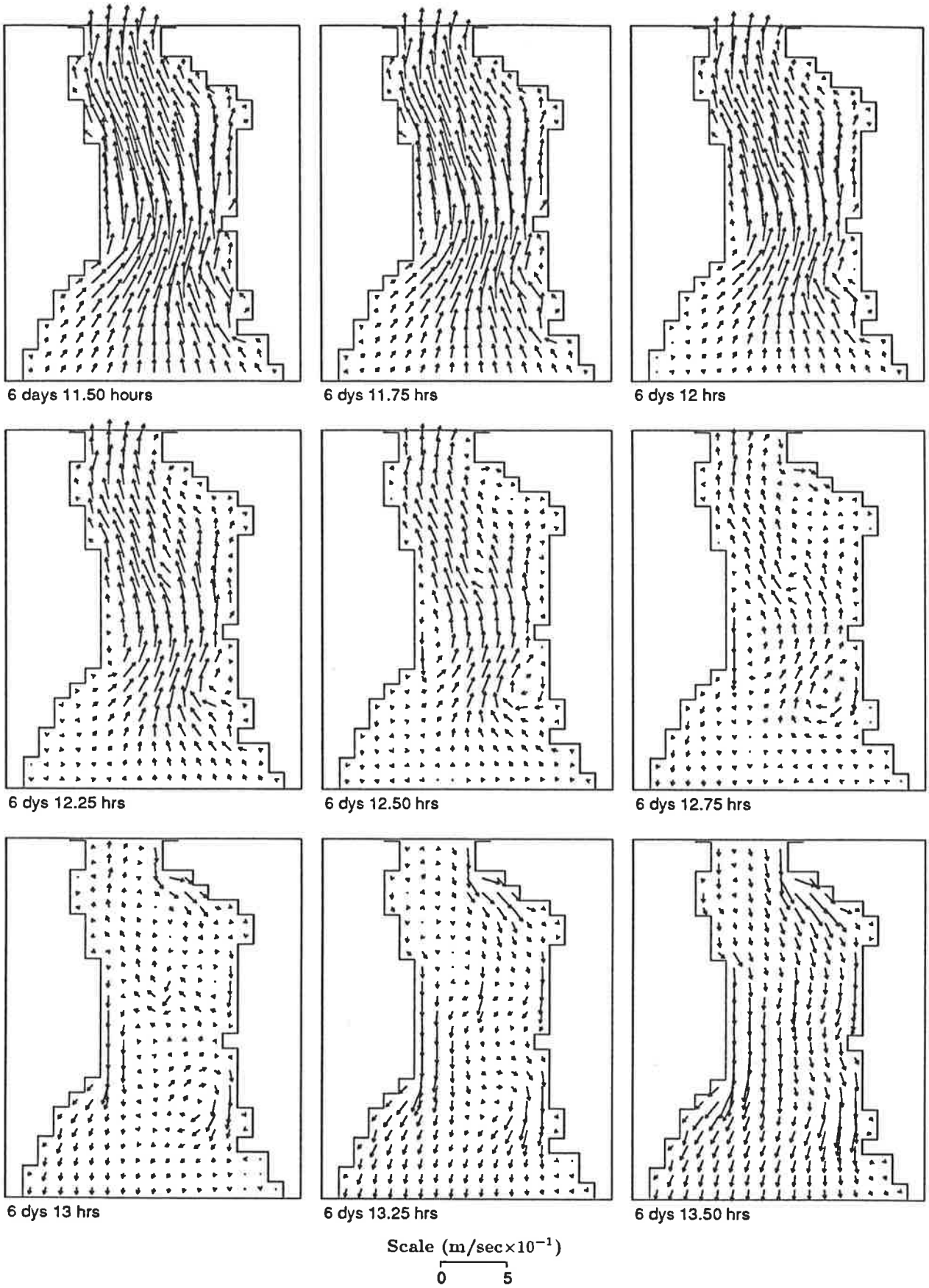


Figure 5.32: *Snapshots of depth-averaged current at 15 min intervals during the neap period at 6–8 days. The sequence shows a change of tide event in the vicinity of Wallaroo. As the flood tide weakens, the ever present gyre formation mechanism suggested by Green (1984) (see text) becomes dominant, and in the Tiparra Reef region a clockwise gyre is created; other weaker gyres are created on the western coastline opposite Wallaroo, and north of Wallaroo on the east coast. All the gyres are swamped by the strengthening ebb flow.*

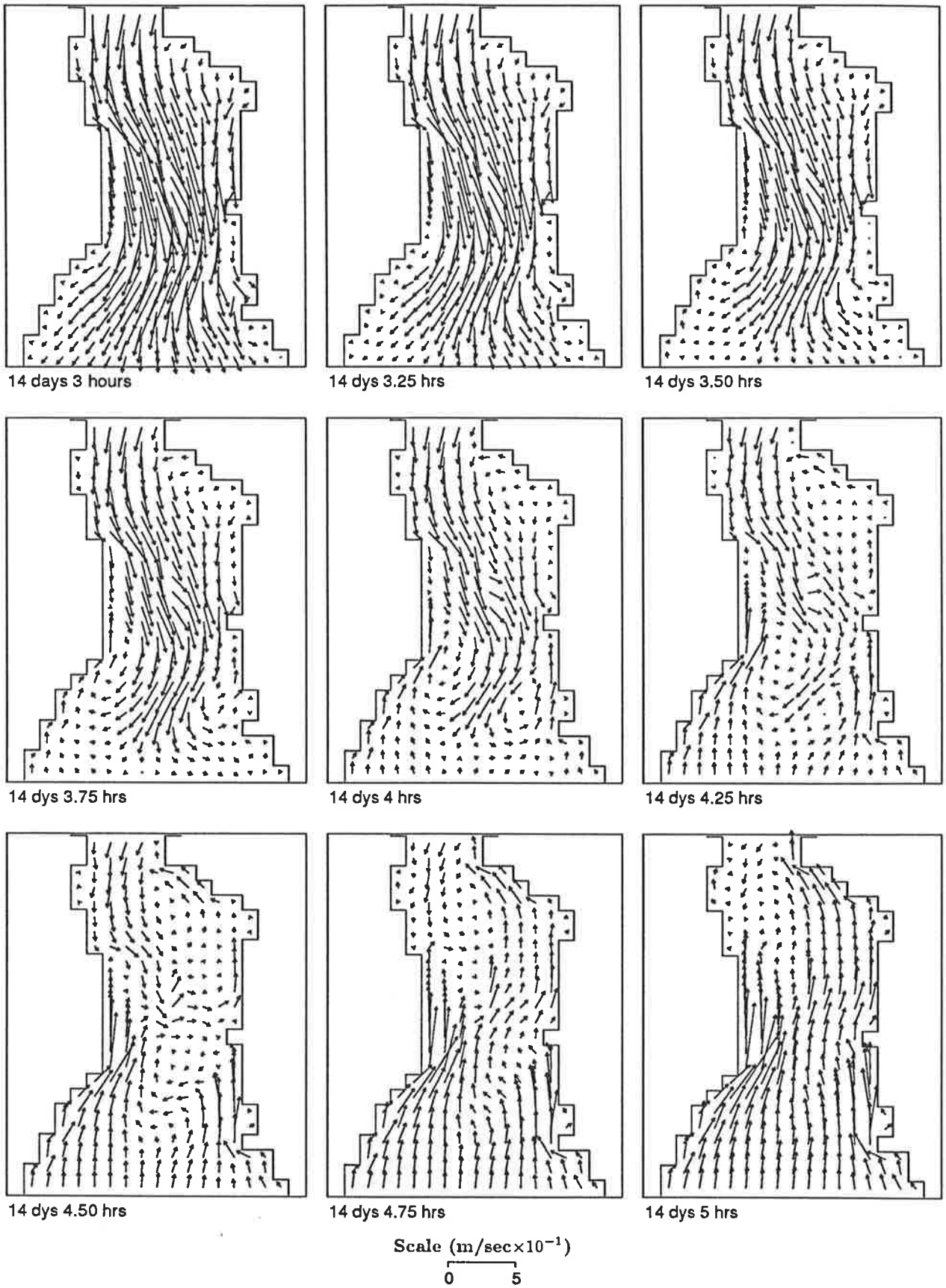


Figure 5.33: *Snapshots of depth-averaged current at 15 min intervals during the spring period at 13.5–15.5 days. The sequence shows a change of tide event in the vicinity of Wallaroo. As the ebb tide weakens, the gyre formation mechanism suggested by Green (1984) (see text) becomes dominant, and in the Tiparra Reef region an anti-clockwise gyre is created; other weaker gyres are created on the western coastline opposite Wallaroo, and north of Wallaroo on the east coast. All the gyres are swamped by the strengthening flood tide.*

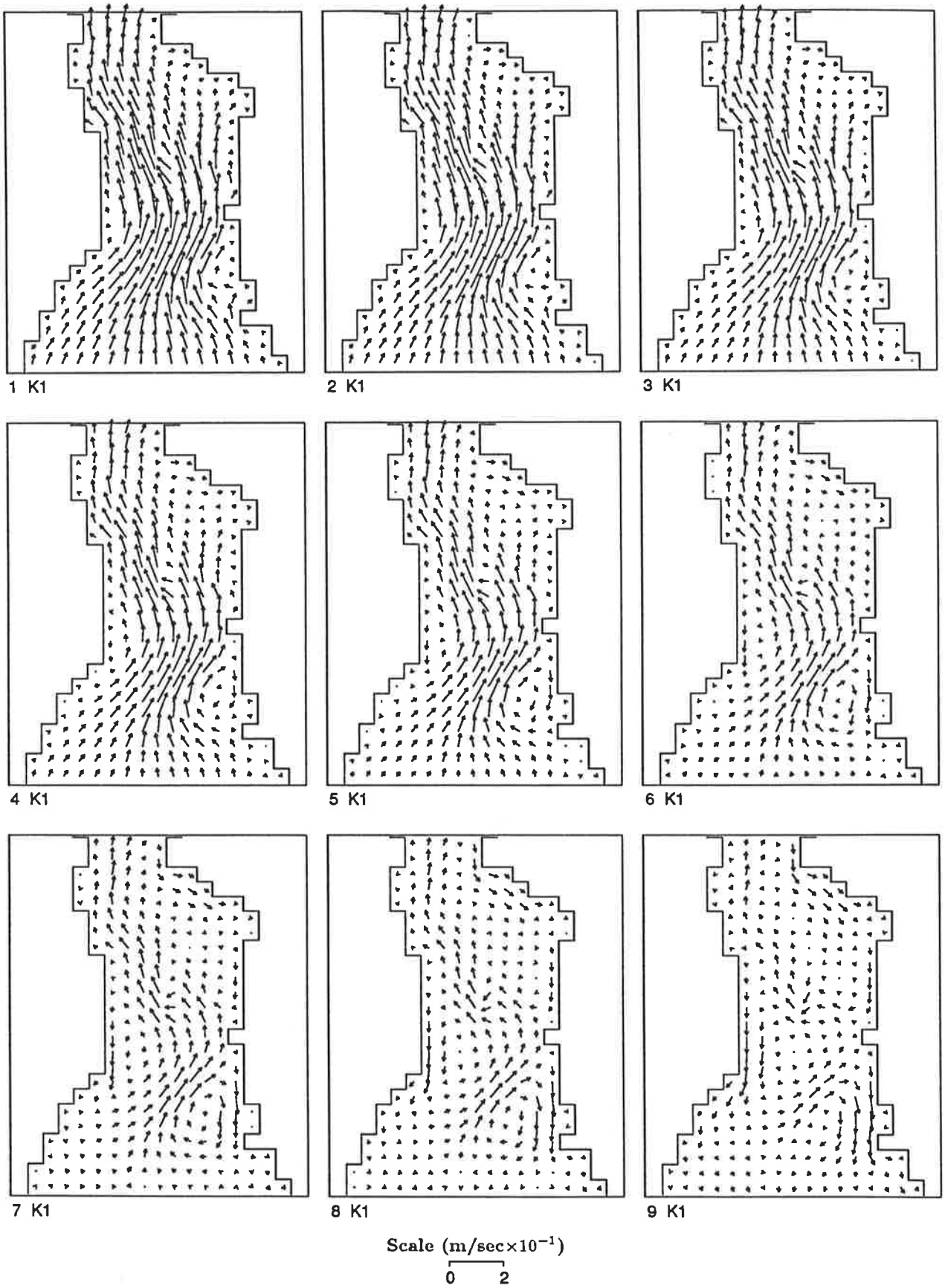


Figure 5.34: *Snapshots of K_1 depth-averaged current taken from the ellipse plots of Figure 5.27. Consecutive frames are separated by 3.76°, which corresponds to 15 min for the K_1 component. The events represented here approximately coincide with the neap event given in Figure 5.32. The scale used here is double that used in Figure 5.32.*

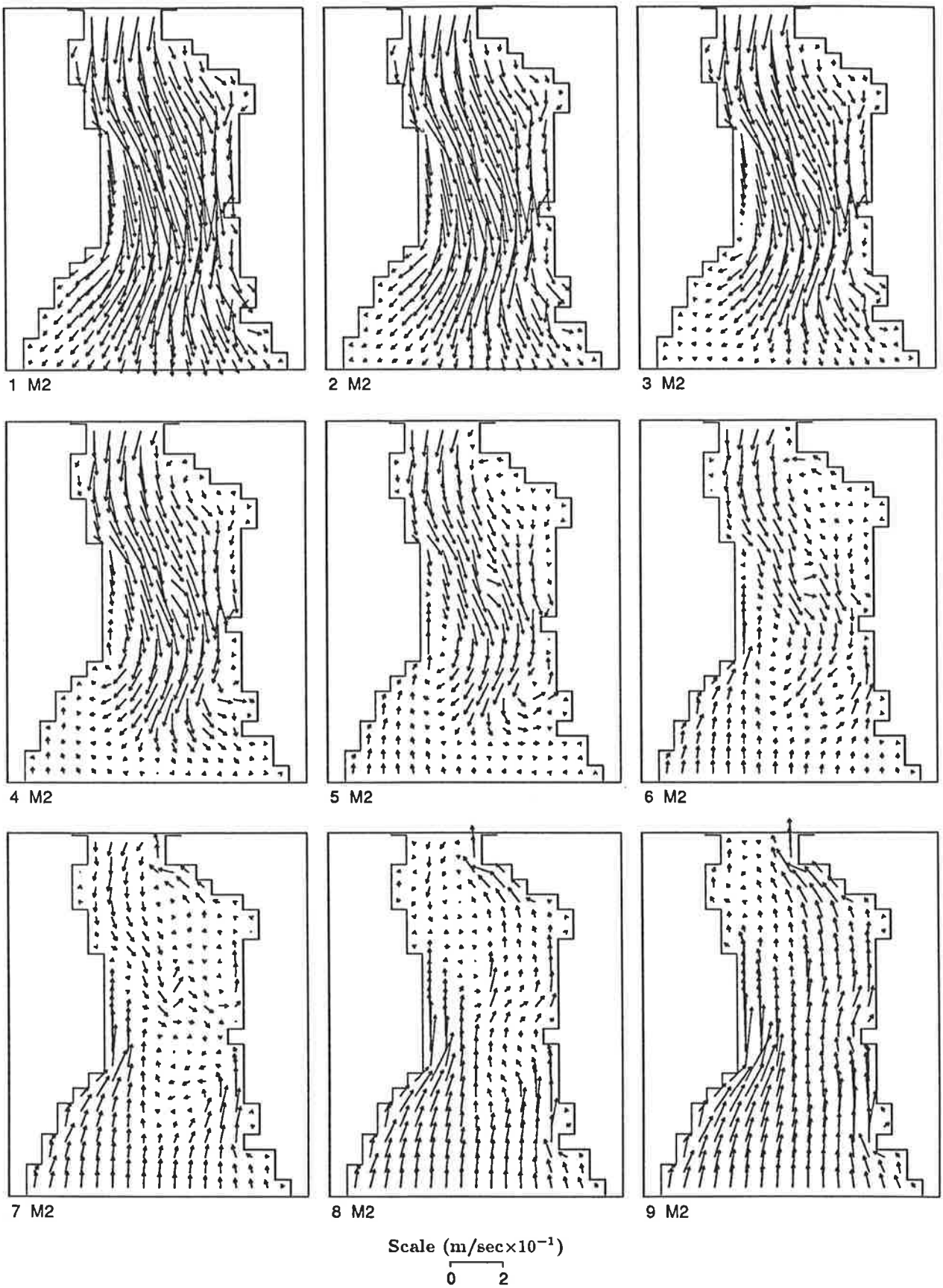


Figure 5.35: *Snapshots of M_2 depth-averaged current at 15 min intervals (corresponding to 7.245°) taken from the ellipse plot of Figure 5.29. The period represented here has been chosen to coincide with the spring event given in Figure 5.33. Note that the scale used here is double that used in Figure 5.33.*

factors which determine the vorticity associated with each constituent of the tidal wave — the sign of their product indicates the direction of rotation of the gyres:

- A depth-dependent factor which can be shown to have a positive average in depth.
- A factor determined by the coastline and the contours of the sea floor which is positive when the depth increases from left to right, from the point of view of an observer moving with the current.
- A factor determined by the rate of convergence or divergence of the streamlines which is negative if there is divergence, from the point of view of an observer moving with the current (ibid., p.189).

If the product of all three factors is positive, the residual currents have an anticlockwise direction; if negative, they have a clockwise direction. Zimmerman (1978) also discusses the topographical generation of gyres. As well, Maddock and Pingree (1978) note in their study of residuals that vorticity is generated by changes in water depth near headlands.

Figure 5.35 shows successive 7.245° (15 min) snapshots of current vector for the M_2 constituent. Current strengths are about twice as strong as K_1 and the evolution of gyres is about twice as fast. Two gyres are created and dissipated in this sequence and correspond with the Tiparra Reef and western coastline gyres of the K_1 constituent. Having developed on the waning ebb tide, these gyres are of opposite rotation to the corresponding gyres of Figure 5.34. Half a cycle later, the same sequence is repeated in the opposite sense.

The snapshots of M_2 current of Figure 5.35 have been chosen to correlate with the spring event of Figure 5.33. Agreement is very good, so since the scale used in Figure 5.35 is double that used in Figure 5.33, it is evident that the events of this spring flow are dominated by the semi-diurnals.

Summarizing, topographically generated tidal gyres are predicted by this model. They occur close to times of either maximum or minimum tidal elevation and correspond to times of minima in current velocity. They develop in the region near Wallaroo, along both eastern and western coastlines and move toward the centre of the Gulf where they dissipate. The diurnal gyres last perhaps one hour, the semi-diurnal gyres half an hour. During their lifetime the tide flows diagonally across the Gulf along a deep channel west of Tiparra Reef. The currents associated with the gyres are weak in comparison to the strong along-Gulf flows at other times in the tidal cycle.

Two gyres seem to be always formed — the strongest near Tiparra Reef and another of opposite rotation directly across from Wallaroo near the west coast. A smaller third gyre, of the same rotation as the strongest gyre, is formed near the east coast opposite Middle Bank. The coarse grid of this model does not permit the resolution of finer scale gyres such as those discussed by Green (1984), off protruding headlands in Northern Spencer Gulf. However, evidence of their existence will be presented in Chapter 8 based on results from a fine-grid model.

Pingree and Maddock (1977a,b) and Maddock and Pingree (1978) present a study of residual gyres in the English Channel focusing on the gyres off a headland called Portland Bill. The gyres discussed in this subsection are dominantly tidal, not residual; they are observed in depth-averaged flows so their actual existence may be subject to question. This was a point made by Proctor (1987). It is also made by Pingree and Maddock (1977a, p.353) and is resolved in their case by using a higher resolution depth-averaged model. In our case we will use the three-dimensional model of Chapter 7 to verify the existence of

the gyres throughout the water column, a method of verification alluded to by Pingree and Maddock (1977a).

Residual plots

The purpose of producing residual plots is to establish the broad regions where model generation of non-linear constituents takes place.

The predicted four major tidal constituents of depth-averaged current are used to reconstitute a time series of tidal current for the 29 day period at each gridpoint. This series is then subtracted from the raw depth-averaged results of the numerical model at the corresponding gridpoints and the difference, for each of the two components of velocity, is averaged by dividing by the number of hourly data points (697) it represents. The result is plotted as a vector and shows the contribution to the mean 29-day circulation due to the non-linearity of the model (see Figures 5.36). By choosing to average over 29 days, the residuals derived are only slightly contaminated by the major constituents. In 29 days there are exactly 58 oscillations of the S_2 constituent and nearly integer multiples of the O_1, K_1 and M_2 periods, viz. 26.96 cycles for O_1, 29.08 cycles for K_1 and 56.04 cycles for M_2.

Since long period constituents are also included by reason of the use of the f and μ corrections to the specified amplitudes and phases along the open boundary of the model (see equation (2.29) of Section 2.2)), the residual circulation obtained is dependent on the period modelled (i.e. the actual dates of the simulation). All simulations reported in this thesis commence at 00:00hr on 1/1/1900 GMT.

As reported in Chapter 3, Section 3.5, a study of velocity residual plots for the Spencer Gulf model lead to a re-evaluation of the differencing used for the advective and diffusive terms of the momentum equations near coastal and open sea boundaries. When subordinate approximations are used, particularly in the advective finite difference forms, the residual plots contain spurious vectors, especially at corners in the boundaries (see Figure 5.36(a)). Note the large vector issuing north-north-westwards from the bottom right hand corner of the plot — careful examination shows a similarly large vector in the same direction issuing from the western side of Thistle Island near the open sea boundary. Note also the zig-zagging vectors that appear along the middle section of the western coastline (between Arno Bay and Franklin Harbour, Figure 5.10) where the coastline is stepped. In an overall sense, there is a general jumbledness in the orientation of the vectors in Northern Spencer Gulf in Figure 5.36(a).

Contrast this with the smoother, and one suspects, more realistic pattern of residuals displayed in Figure 5.36(b). While the interior vectors of both plots are much the same, there are large differences around the boundaries. The large vectors issuing from the open boundary/coastal junctions have disappeared, the vector zig-zagging has settled down into a plausible stepping in the current following the western coastal stepping and again, there is an overall smoothness in the results relative to those of Figure 5.36(a). Evident in both figures is a sizable gyre spanning the Gulf adjacent to Wallaroo (see next subsection).

For Figure 5.36(b), advective and diffusive terms are discarded where they require subordinate approximation. If only diffusive terms are discarded, the resulting velocity residuals are only slightly smoothed, relative to Figure 5.36(a).

In Figure 5.36(a) the residuals are largest where the velocities are largest — viz. through the narrowing part of the Gulf near Wallaroo, and further northwards, and also

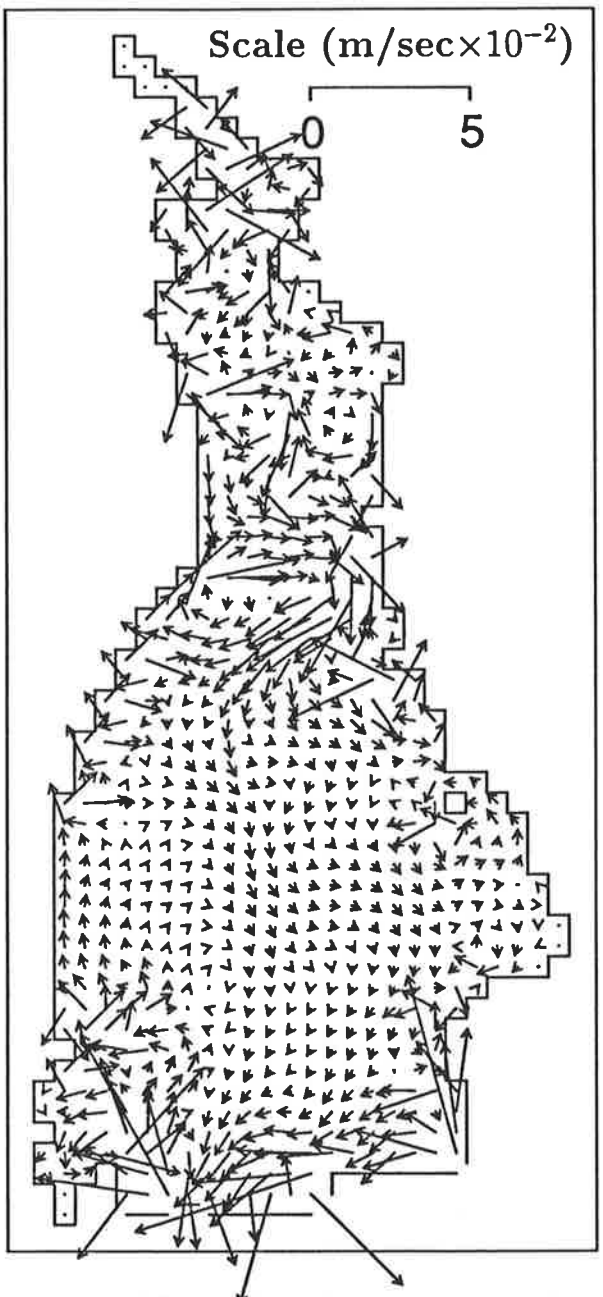


Figure 5.36(a): *Residuals for depth-averaged velocity over a 29 day period with subordinate approximations for advection and diffusion terms included near all boundaries.*

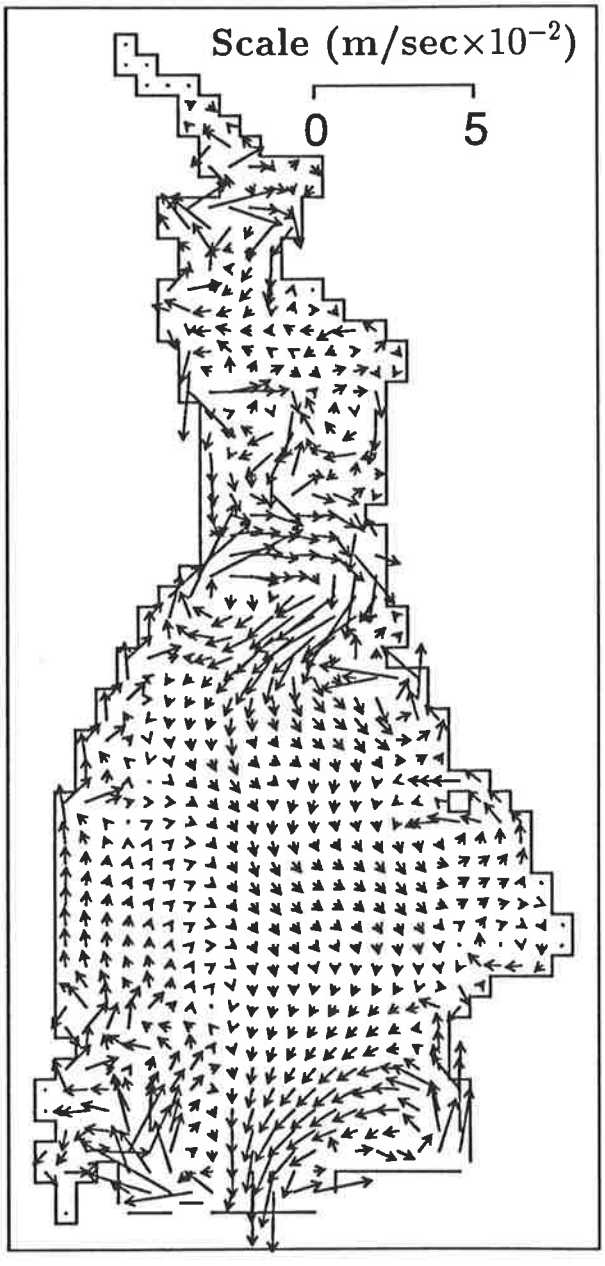


Figure 5.36(b): *Residuals for depth-averaged velocity over the 29 day period with advection and diffusion terms requiring subordinate approximation excluded.*

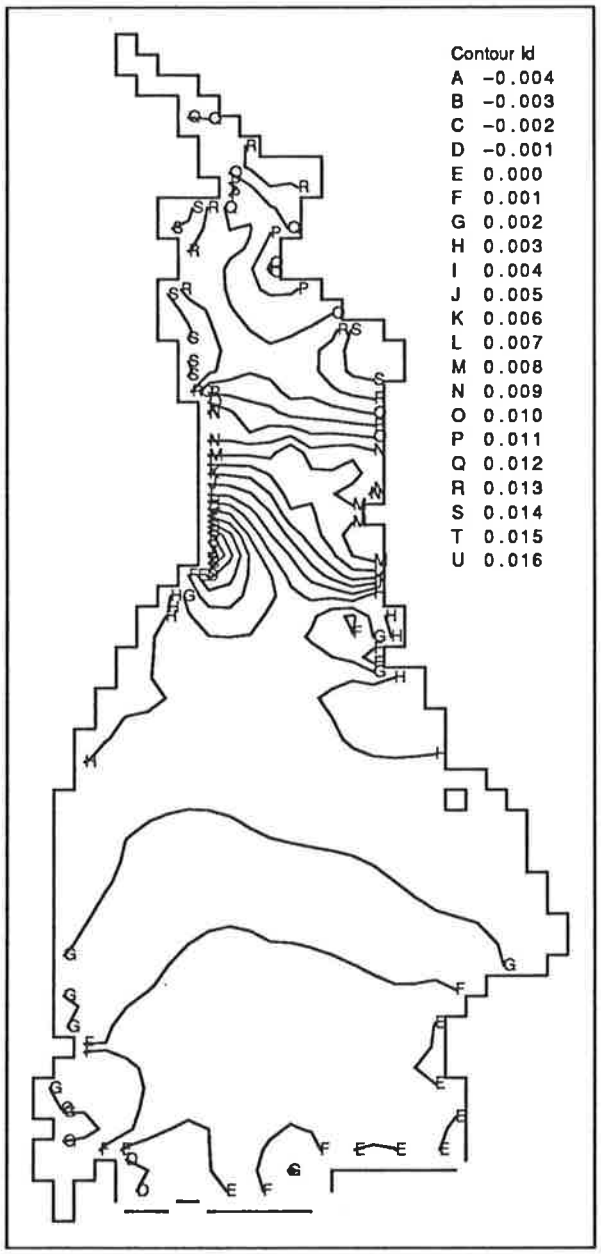


Figure 5.37(a): *Residuals for elevation over a 29 day period. Advection and diffusion terms requiring subordinate approximation are included.*

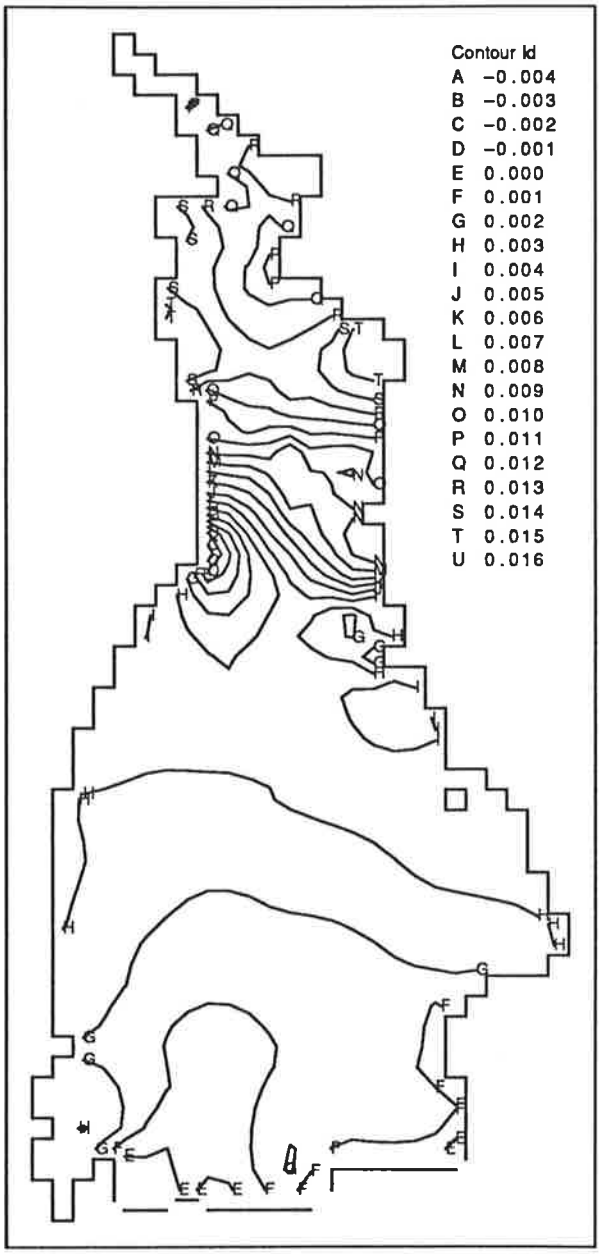


Figure 5.37(b): *Residuals for elevation over the 29 day period with advection and diffusion terms requiring subordinate approximation omitted.*

near the open boundary in the vicinity of Wedge Island — and they are also generally larger in the shallow regions such as near Pt. Lincoln, along the coastlines and in the northern Gulf.

These residuals are a consequence of the non-linearity of the model — a fully linear model would predict zero residual tidal circulation.

The residual contours for elevation, in Figures 5.37(a),(b) show the contribution to sea surface elevation due to the constituents generated by the non-linearity of the model. Immediately opposite Wallaroo on the western coast is a concentric feature in the contours at a corner in the coastal boundary. The contour labels indicate there is a local depression in the sea surface here. This feature correlates with the strong coastal vectors of the large mid-Gulf residual gyre seen in Figure 5.36(b) and referred to as gyre (G) in Figure 5.38. The depressed sea surface is a non-linear effect of residual gyres pointed out by Pingree and Maddock (1977b).

In Figure 5.37(a), subordinate approximation for advective and diffusive terms is included around the boundaries, whilst in Figure 5.37(b) advective and diffusive terms requiring subordinate approximation are omitted. There are slight differences between the plots, Figure 5.37(b) being "smoother" especially near the open boundary. Again, most of the non-linear behaviour occurs in the narrowing and northern parts of the Gulf.

Residual gyres

Figure 5.38 is an enlarged copy of Figure 5.36(b) on which most of the residual gyres of the plot have been schematically marked. The gyres have also been labelled consecutively with a letter starting with "A" at the northern-most marked gyre and moving southwards.

In this text the gyre labels will be bracketed so that they are clearly discernible and less likely to be confused with the written text. The strong clockwise rotating gyre (G) straddling the Gulf opposite Wallaroo has already been mentioned. The southern boundary of this gyre is the "deep channel" marked on Figure 5.15. Just north of it is a small anticlockwise rotating gyre (F) positioned at the southern tip of an submerged sandbar called Middle Bank (Figure 5.15). To the north-east of (F) and against the east coast is another anticlockwise gyre (E). To the west of Mike and Yarraville Shoals are gyres (D) and (C) which are associated with steep bathymetric gradients. Gyres (A) and (B) are sited north and south of Lowly Point, respectively. Gyres (A) and (B) will be studied further in Chapter 8.

South of Tiparra Reef is an anticlockwise rotating gyre (H). Continuing south there is a general anticlockwise rotation through the passage between Wardang Island and Pt. Victoria which has been labelled as gyre (I) in the plot. This gyre is centred south of Wardang Island. Further south still is a weak gyre (J) near Pt. Turton (see Figure 5.10). Gyre (K) is another weak feature. Gyres (L) and (M) seem strongly associated with the headland between them. Gyre (N) seems to be an anticlockwise circulation around Boston Island. Some of these features are very small-scale and a finer grid would be needed to verify their existence.

On the eastern side of the open boundary is a flow which has been suggestively drawn as though it might be part of a rather large gyre. A numerical model with a more southerly open boundary might be able to confirm or refute this speculation. Owen (1980) considers the residual gyres and circulations of the Bristol Channel in a similar manner to the above.

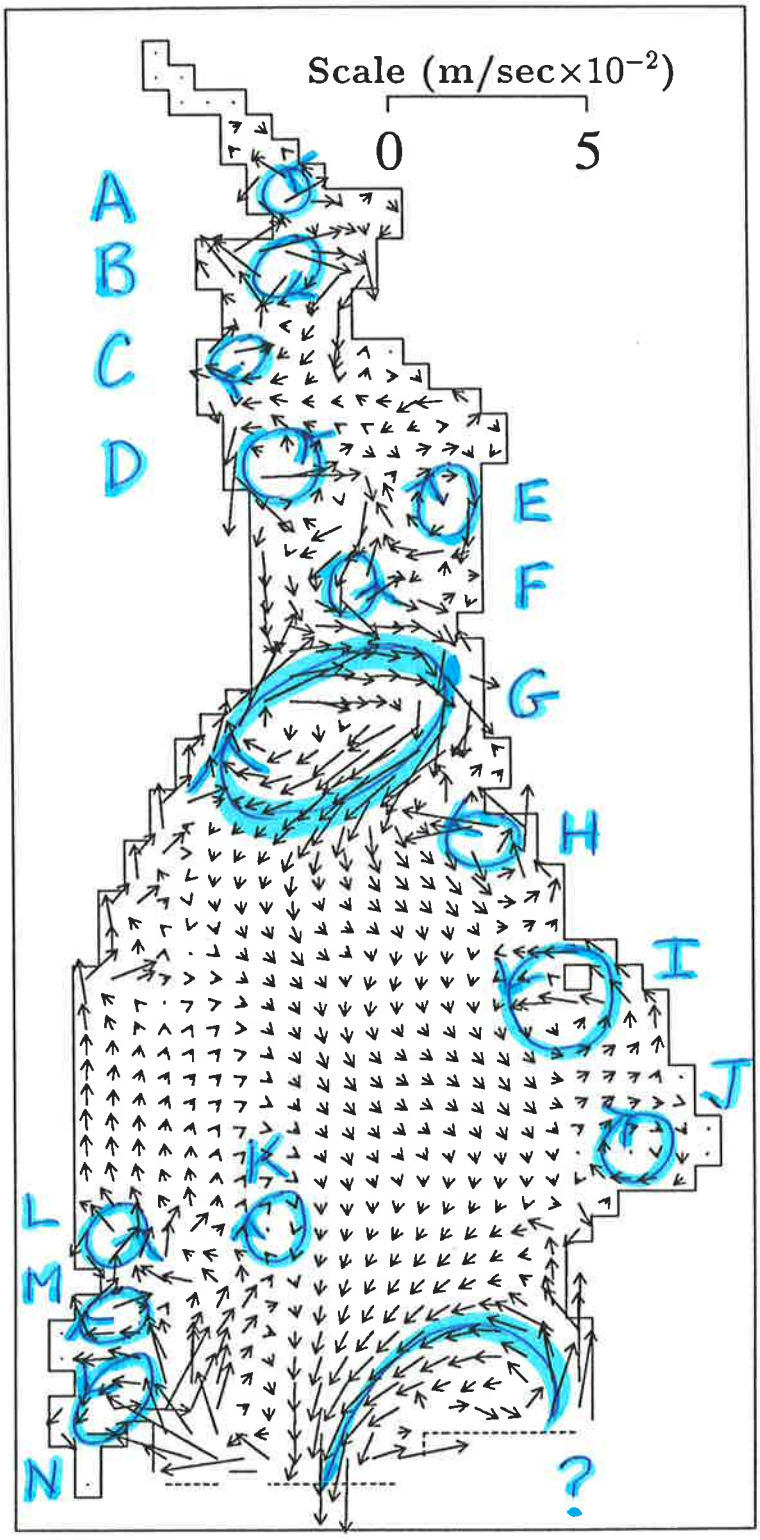


Figure 5.38: *Depth-averaged velocity residuals with residual gyres marked.*

Shallow water constituents

The tidal analysis program used (due to Easton, 1977) is capable of separating out some of the species 3, 4 and higher constituents which, because their amplitudes are much larger than expected especially in shallow water areas, are usually termed "shallow water" constituents. The most important of these have frequencies which are the sum or difference of the frequencies of the major constituents. For 29 days of predictions, the analysis program examines 13 shallow water constituents: MSf, $2SM_2$, MO_3, M_3, MK_3, MN_4, M_4, MS_4, $2MN_6$, M_6, MSN_6, $2MS_6$ and $2SM_6$. However, since N_2 is not included in the open boundary height specification, the analysis produces insignificant results for MN_4, $2MN_6$ and MSN_6.

Table 5.12 lists observed and predicted amplitudes for the seven largest of the 13 separable shallow water constituents. These were selected upon comparing the observed amplitudes of the above 13 constituents. South of Wallaroo most of these constituents have observed amplitudes of less than 1 cm, so the seven were chosen specifically because of their relative strength in the northern Gulf. The average absolute difference between observed and predicted amplitudes taken over the seven constituents for the northernmost six stations is 1.0 cm.

Table 5.12 lists only amplitude values. Zetler (1991) argues in favour of excluding constituents with amplitude "< 0.03 ft" (i.e. less than 0.9 cm) in tidal predictions. He notes the experience of a tidal analyst who "had analysed many continuous individual years of hourly heights at one station and had noticed that, for very small amplitudes, the corresponding phases varied so much that they were essentially random" (ibid., pp.109–110). He argues that "use of these small constituents will deteriorate rather than improve future predictions" (ibid., p.110). In view of Zetler's comments, since about half the observed amplitude values are less than 0.9 cm, the corresponding observed and predicted phase values could be meaningless and so are not given. In Chapter 8, however, phase values will be given for the seven constituents since for the northernmost six stations in Spencer Gulf most of the observed amplitude values are greater than 0.9 cm (see Table 5.12).

Inspecting the values given in the table shows that there is generally order-of-magnitude agreement between predicted and observed amplitudes, with certain qualifications that follow. At Wedge Island station, just inside the open boundary, there is very little generation by the model of minor constituents. None of the shallow water constituents are specified at the open boundary, so this helps explain the discrepancies between the observed and predicted amplitudes at Wedge Island (and elsewhere). The generally large discrepancies at Port Augusta, Beacon #5 and Port Pirie are probably related to the coarseness of the element size used to model the upper Gulf region. The period of MSf is greater than 14.5 days, so a data length of 29 days may not lead to a reliable analysis of this constituent using our package — it is in fact omitted on the lists of observed tide-height constants for stations Port Victoria, Port Neill and Port Turton for which the observational data lengths are no more than 31 days.

By inspection, the largest observed minor constituents are MSf, $2SM_2$ and MS_4. Because of their relative strength, comments about these may be more meaningful than comments about the other four constituents. MSf, $2SM_2$ and MS_4 arise from non-linear interactions involving the two strongest major constituents, M_2 and S_2. Their origin is as follows:

$$M_2 - S_2 \rightarrow MSf$$

Station		MSf	$2SM_2$	MO_3	M_4	MS_4	$2MS_6$	$2SM_6$
Port Augusta	Pred.:	1.7	3.1	4.7	1.7	7.9	2.9	2.9
	Obs.:	1.9	4.9	1.4	0.8	2.4	1.2	1.3
Beacon #5	Pred.:	1.8	2.7	4.0	1.4	6.1	1.4	1.3
	Obs.:	0.1	2.9	1.9	1.0	1.5	1.0	0.9
Port Pirie	Pred.:	1.9	1.7	2.6	0.6	2.2	1.7	1.8
	Obs.:	4.9	2.1	1.3	1.1	2.3	1.1	1.4
Port Bonython	Pred.:	1.8	1.2	1.9	0.5	1.3	1.3	1.2
	Obs.:	5.1	1.9	1.4	0.9	1.9	0.8	1.0
Whyalla	Pred.:	1.9	1.2	1.8	0.5	1.1	1.4	1.3
	Obs.:	1.9	1.9	1.5	0.8	2.0	0.7	0.7
Yarraville Shoals	Pred.:	1.8	0.6	0.7	0.3	0.7	0.7	0.6
	Obs.:	2.5	0.8	1.0	0.3	0.8	0.4	0.5
Wallaroo	Pred.:	1.2	1.6	0.9	0.2	1.0	0.7	0.6
	Obs.:	6.0	1.4	0.3	0.5	1.0	0.4	0.6
Arno Bay	Pred.:	0.4	1.4	1.0	0.3	0.1	0.4	0.2
	Obs.:	0.7	1.0	0.6	0.3	0.4	0.3	0.4
Port Victoria	Pred.:	0.3	1.4	0.9	0.3	0.2	0.3	0.2
	Obs.:	–	0.8	0.1	0.2	0.4	–	0.4
Port Neill	Pred.:	0.3	1.2	0.8	0.4	0.1	0.2	0.1
	Obs.:	–	1.2	0.4	0.3	0.4	–	0.1
Port Turton	Pred.:	0.3	1.2	0.8	0.4	0.2	0.7	0.4
	Obs.:	–	1.1	0.4	0.1	0.4	–	0.3
Port Lincoln	Pred.:	0.2	0.5	0.3	0.2	0.3	0.2	0.3
	Obs.:	5.1	0.5	0.2	0.3	0.6	0.7	1.1
Wedge Island	Pred.:	0.0	0.0	0.0	0.0	0.0	0.0	0.0
	Obs.:	1.0	0.2	0.1	0.3	0.4	0.1	0.1

Table 5.12: *Comparison of predicted (Pred.) and observed (Obs.) amplitudes (cm) for the seven largest shallow water constituents separable by the analysis program. Values are given for 13 stations in Spencer Gulf. Values for Port Broughton are not given because errors exist in the observations recorded there and values for Franklin Harbour are not included because no observations of shallow water constituents are available. Dashes (–) indicate that corresponding observations are not available. The average absolute difference between observed and predicted amplitudes taken over the seven constituents for the northernmost six stations is 1.0 cm.*

$$2S_2 - M_2 \rightarrow 2SM_2$$

and

$$M_2 + S_2 \rightarrow MS_4.$$

While all the predicted amplitudes of MSf are about the same north of Wallaroo, the

observed values exhibit considerable variation and so there may be errors in some of the observed MSf values; the predicted amplitudes of $2SM_2$ are greater than the observed in the southern Gulf and less than the observed north of Wallaroo; for MS_4 the predicted values are smaller than the observed everywhere except in the far north of the Gulf. From Wallaroo northwards, the agreement between predicted and observed values for particularly $2SM_2$ and MS_4 is reasonable, except at Port Augusta (and Beacon #5, in the case of MS_4).

The accuracy of prediction of the minor constituents may be increased by

- decreasing the grid element dimension,
- improving the bathymetric representation,
- improving the basic order of accuracy of the overall numerical scheme,
- incorporating significant minor constituents in the open boundary forcing, and
- including tidal flats.

Since many of these improvement options are incorporated in the fine-grid Northern Spencer Gulf model of Chapter 8, we will take a further look at the prediction of shallow water constituents there (see Section 8.7).

5.6 Summary

A new depth-averaged computer model of tides has been successfully applied to the prediction of the major constituent tidal elevations and depth-averaged currents in Spencer Gulf, South Australia. The model is non-linear, barotropic and includes the effect of Coriolis force. Both linear and quadratic formulations for bottom friction are tried and the non-linear model gives more accurate predictions. It is shown that for this model of Spencer Gulf a global specification of the quadratic friction coefficient is only slightly less accurate than specifications that take into account local depth. These latter formulations also depend on a roughness dimension which is unknown and so to that extent, they have not been fairly tested. On the other hand, they are computationally 12% more expensive. It is also shown that for the Spencer Gulf model it is important to generate MSL since chart datum is given as ISLW. This is done using the model itself.

These are the first results from a non-linear numerical model of Spencer Gulf that has been simultaneously driven by all four major tidal constituents.

For the major constituents, model predictions are in strong agreement with observations made at stations within the Gulf.

Consequently, the model may be regarded as an accurate tool for identifying and predicting the basic tidal characteristics of the Gulf. It has filled certain gaps in knowledge identified by previous authors and has confirmed and extended the results and predictions of recent researchers such as Easton (1978) and Noye et al. (1981, 1982).

Easton (1978) has indicated that at the mouth of the Gulf the semi-diurnal currents are small and that the exchange of water with the Southern Ocean is mostly due to the diurnal constituents. The presented ellipse plots confirm this but also suggest that the role of the semi-diurnal current may be significant in the exchange process. The K_1 current at the mouth is certainly the largest single component of tidal current in that region,

both along-stream and across-stream — it is approximately double the strength of the O_1 current — but the model predicts that the combined effect of the two major semi-diurnal currents has comparable strength to K_1 during spring flows at the mouth, although these flows are rectilinear. A further discussion of exchange at the mouth is given in Chapter 6, Section 6.4.

An interesting prediction of the model is that at regular intervals during the daily tidal cycle there are across-Gulf currents in all major constituents at the entrance to the narrowing part of the Gulf near Wallaroo. This coincides with the topographical generation of gyres in the vicinity of Wallaroo at times of slack tide. The gyres last no longer than one hour: after formation near the coast, they travel towards the centre of the Gulf and are dissipated by the strengthening longitudinal current.

The present model is a reasonably accurate tool for the prediction of the largest of the minor constituents (except possibly MSf) in the northern half of the Gulf (excluding the far northern Gulf where the present grid size is too coarse). Predictions for these constituents may be improved by using a finer grid with its correspondingly more accurate bathymetry, and by including minor constituents in the open boundary forcing. The inclusion of tidal flats may also contribute to more accurate modelling of the minor (and major) constituents. These improvements are incorporated in the Northern Spencer Gulf model of Chapter 8 and the prediction of minor constituents is further considered there. Overall improvement of the accuracy of the finite difference scheme might also improve their prediction. The finite difference formulations of the non-linear terms in particular could be examined to see if these affect the modelling of the minor constituents.

It should be noted, however, that the observed values of the minor constituents are based on observational records of different lengths taken at different times. Because of this, it is likely that different packages will have been used to perform the minor constituent analyses. These factors may have also affected the analyses for the four major constituents. A procedure that might overcome these problems is to firstly reconstitute the tidal signal of each observation station using its observed constants, and then analyse a standard 29-day record using our own package. This is a subject for future research.

The elevation predictions from this coarse-grid study of Spencer Gulf will be used to drive the fine resolution Northern Spencer Gulf model of Chapter 8. This model will facilitate investigation of the circulation flows of Northern Spencer Gulf.

In the next chapter we test the assumption that the height specified open boundary condition is adequate for the Spencer Gulf model: that it is not necessary to use a radiation condition. As we have seen, the non-linear constituents near the open boundary are small; thus we anticipate that height specification will prove to be adequate, especially in the absence of wind forcing.

Chapter 6

An investigation of open boundary conditions for tidal models of shallow seas

6.1 Introduction

The depth-averaged models of Chapter 5 use a height specified open boundary condition (2.29) in which sea surface elevation above mean sea level is specified in terms of the four major tidal constituents. This condition has been successful in the case of shallow sea tidal models (for example, see Heaps (1969), Flather and Heaps (1975), Noye et al. (1981, 1982) and Mitchell et al. (1984)). The depth of water at the open boundary of the Spencer Gulf model is less than 55 m. Mitchell et al. (1984) used the condition with success for a model of the Gulf of Carpentaria with depths of up to 120 m. However Arnold and Noye (1986a) and Arnold (1987) found it to be unsuitable for a tidal model of Bass Strait with depths as great as 3000 m at its eastern open boundary — signs of instability were present even if the maximum depth were set at 500 m. Alternatively, if the data is available the component of current normal to the open boundary can be specified (Heaps (1973), Flather and Heaps (1975), Bennett and McIntosh (1982), Wolf (1983), Bode (1986) and Arnold and Noye (1986a)).

The height/velocity specified condition is perhaps the simplest of a large number of open boundary conditions available for use in tidal and tidal/surge modelling. The question therefore arises as to whether it is the most suitable for a model of Spencer Gulf. A further question concerns the ability of "radiation" open boundary conditions to perform at least as well whilst providing tidal forcing.

If the model basin is perturbed from an initial state of rest, height specification at open boundaries induces transient waves which are physical (*not* numerical) responses of the model basin to the sudden imposition of non-zero forcing (Bennett and McIntosh (1982), Bode and Sobey (1984)). The transients are induced by the "incompatibility between the initial conditions [zero velocity and elevation fields] and the forced response at zero time" (Bode and Sobey, 1984, p.1393). "Their origin is physical, not numerical, although their interaction with a numerical algorithm may excite oscillations with a spatial scale determined by the mesh size" (ibid., p.1371). In shallow water the transients are easily dissipated because the frictional decay time — the time required to reduce the

amplitude of the transients to a small percentage of their initial value — is short, but the decay time rapidly increases as depth increases. Since height specified conditions only allow through the open boundary those waves whose passage is recorded in the height specification, outgoing transients are reflected back into the model at the open boundary and are trapped within the model region. Initial transients in a computer model are a modelled physical phenomenon which cannot be quantified and included in the height specification at the open boundary.

Open boundary conditions incorporating radiation mechanisms are often used instead of height specified conditions in deep water tidal modelling since they permit the unwanted transients to pass through the open boundary and out of the model basin (Bode and Sobey (1984), Arnold and Noye (1986a), Arnold (1987)). While radiation conditions may stabilize predictions, Arnold (1987) shows that for a tidal model it is important to examine the predicted displacements at the open boundary since they may differ significantly in amplitude and/or phase from the specified values. This lead him to develop a modified form of the outgoing radiation condition used by Reid and Bodine (1968). Radiation conditions are also used where meteorological forcing is applied, whether for deep or shallow models; such forcing may continuously generate waves in the interior region which may pass through the open boundary and out of the model if the boundary condition employs a suitable radiation mechanism.

Models including the effect of meteorological forcing are of two general types: *hindcast* models where time series of sea level heights following the passage of a meteorological event are available, and *predictive* models where only an estimate of the effect of a meteorological event can be provided. In principle, the forcing of hindcast models may be carried out through height specification although an open boundary condition with a radiation mechanism may be required when modelling commences so as to deal with initial transients. A radiation mechanism is certainly required for predictive models since this ensures that the height of the sea at the open boundary has adequate freedom of movement and is not "clamped" by the specified information.

The fact that height specified conditions work well in the case of the Spencer Gulf model is seen in Figures 6.1. Figure 6.1(a) compares a **reference signal** with height specified model predictions for elevation at Wedge Island station (see Figure 5.10) for the first 24 hours of simulation. Wedge Island station is located only one grid element inside the open boundary so comparisons made there are a good test of an open boundary condition. The dashed reference curve (which almost coincides with predictions after 24 hr) is a tidal signal synthesized from the observed four major constituents (O_1, K_1, M_2 and S_2). Since the model is driven by only these constituents the reference curve, for practical comparative purposes, is regarded as the "observed" signal. In the graphs the predicted curves start at zero because Wedge Island station is represented at an interior gridpoint and elevation is initially zero at all interior gridpoints. The figure shows that initial transients are not strong and are quickly dissipated. Figure 6.1(b) shows a comparison for the first four days. After 72 hours of model simulation, predictions are very smooth and are stored for later analysis. Provis and Lennon (1983) show that in the case of the South Australian gulfs the wind driven circulation is not independent of the tides — wind and tide effects are related in a non-linear manner. Since it is intended to eventually run the model with meteorological forcing as well as tidal forcing, an open boundary condition will be required which handles starting transients and meteorologically induced oscillations, *and* provides tidal and meteorological forcing from the Southern Ocean.

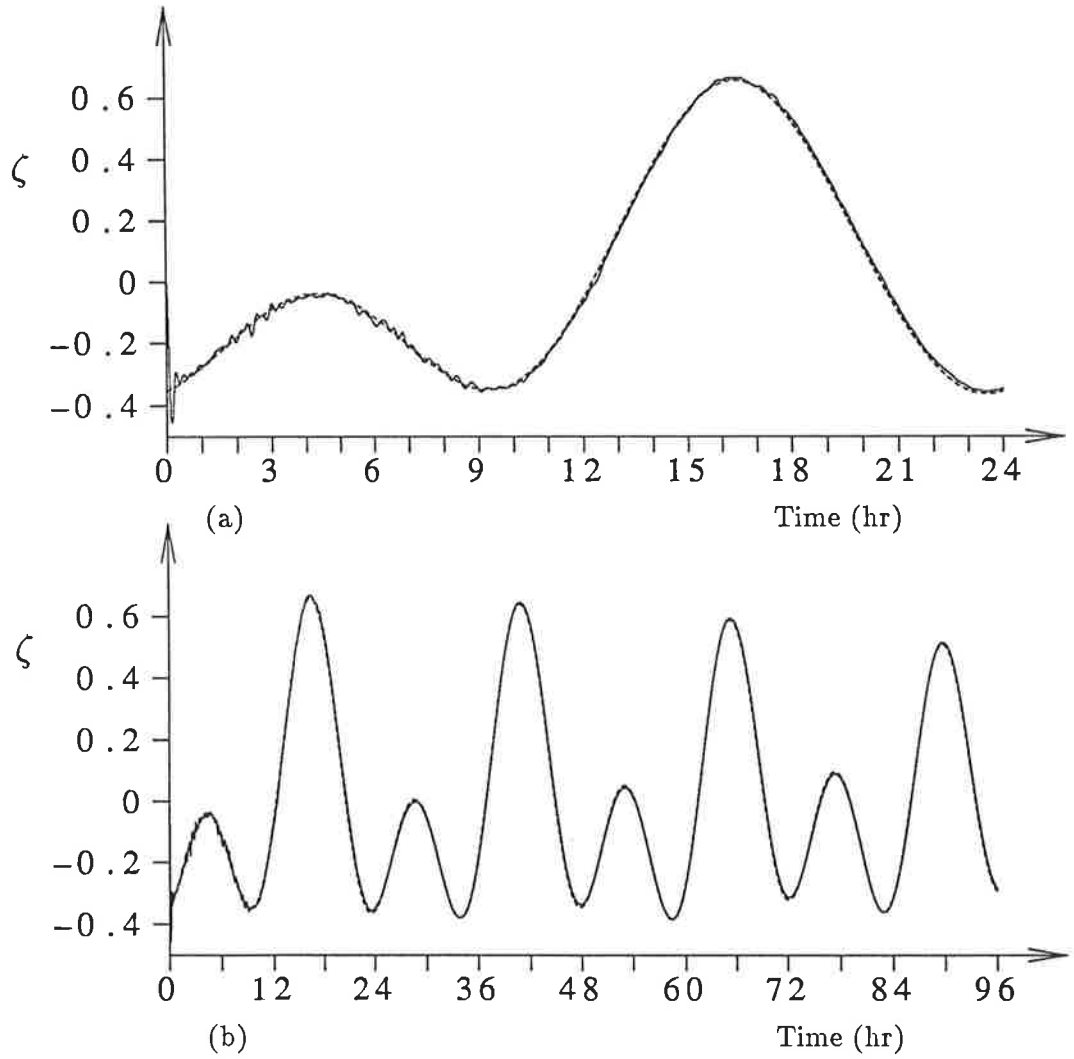


Figure 6.1: *Comparison of the predicted tidal elevation ζ m (solid curve) with the observed signal (dashed curve) at Wedge Island station when the height specified open boundary condition is used. Presented are (a) the first 24 hr of predictions and (b) the first 96 hr of predictions.*

In this chapter, as a first step in the search for such a condition, we seek a stable and accurate discretisation of an open boundary condition employing a radiation mechanism for the depth-averaged *tidal* model of Spencer Gulf. It is assumed that the primary equations representing the open boundary conditions studied are physically sound. The conclusions made should be generally applicable to other shallow sea tidal models.

The discretisation of an open boundary condition is here regarded as "stable" if it is stable in the von Neumann sense (Noye, 1984b). When considered in connection with the schemes used in the interior of the model, the model as a whole is considered "stable" if it runs for the full 32 day simulation without giving rise to exponentially growing grid-scale oscillations. Predicted results are "accurate" if they are close to the set of results from

the height specified model; these are themselves in good agreement with the observed data. The error values obtained in Chapter 5 for the case of a constant quadratic friction coefficient with $C_b = 0.0025$ were $\varepsilon_a = 2.25\,\text{cm}$ in amplitude, $\varepsilon_p = 3.92°$ in phase and the value of the combined error measure was $\varepsilon = 3.49\,\text{cm}$.

Bennett (1976) derives exact outgoing conditions for various types of waves incident at open boundaries of different configurations. However because they all involve weighted space and time averages, "Their numerical implementation would be most complex and would require computer storage approaching that which one is trying to avoid by the introduction of open boundaries" (ibid., p.176). Bennett and McIntosh (1982) examine the construction of exact open boundary conditions for the shallow water equations with rotation, concluding that such conditions are impractical and that there is little justification for using anything more sophisticated than the available *ad hoc*, that is "approximate", open boundary conditions.

Seven of the *ad hoc* conditions are the basis of a comparative study by Chapman (1985) but he does not consider tidal forcing. Chapman encourages modellers to compare the performance of a selection of open boundary conditions before choosing one for their particular model. In a paper published by Hayashi et al. (1986) the performance of several boundary conditions employed in circulation models driven only by wind forcing is examined.

The main findings of this chapter are reported in a workshop paper by Bills and Noye (1987). In that paper advective and horizontal diffusive terms were completely omitted from calculations for elements adjacent to the open boundary line due to programming complexities which have since been overcome. Here, these terms are included in accordance with the findings presented in Chapter 3, Section 3.6. Comparing Figures 6.1 with the corresponding figure in the workshop article (ibid., Figure 1.2), it is seen that the present graphs are significantly smoother. This is due to the greater values of the coefficients of horizontal diffusion used here by reason of the Schwiderski formulation outlined in Chapter 5; in the workshop article the fixed values $N_x = N_y = 5\,\text{m}^2/\text{sec}$ were used, following the choice of Noye et al. (1981, 1982). As well, in the 1987 paper open boundary elements #1, #9 and #12 of Figure 5.12 were made interior elements but here only element #1 is made an interior element. This is discussed in the next section.

6.2 Benchmark solution

The open boundary of the Spencer Gulf model of Chapter 5 consists of 17 elements as shown in Figure 5.12. Tide-height stations are located in elements #7, #9 and #12. Another, Wedge Island station (see Figure 5.10), is located in the interior element immediately adjacent to elements #8 and #17. Data from these four stations provides a very good estimate of the tidal forcing at the mouth of the Gulf.

In order to implement the various *ad hoc* open boundary conditions examined in the following sections, each of which allows the radiation of waves in a uni-directional sense across the boundary, boundary element #1 in Figure 5.12 is here treated as an interior element. This change avoids a complication that arises if the open boundary conditions are applied to a corner element, when one outward normal direction coincides with one part of the boundary line and another coincides with the remaining part. The newly created interior element has a neighbourhood configuration of elements unlike that of the other interior elements since there is no Type 2 element in the (i_2+1)th (i.e. the south-eastern)

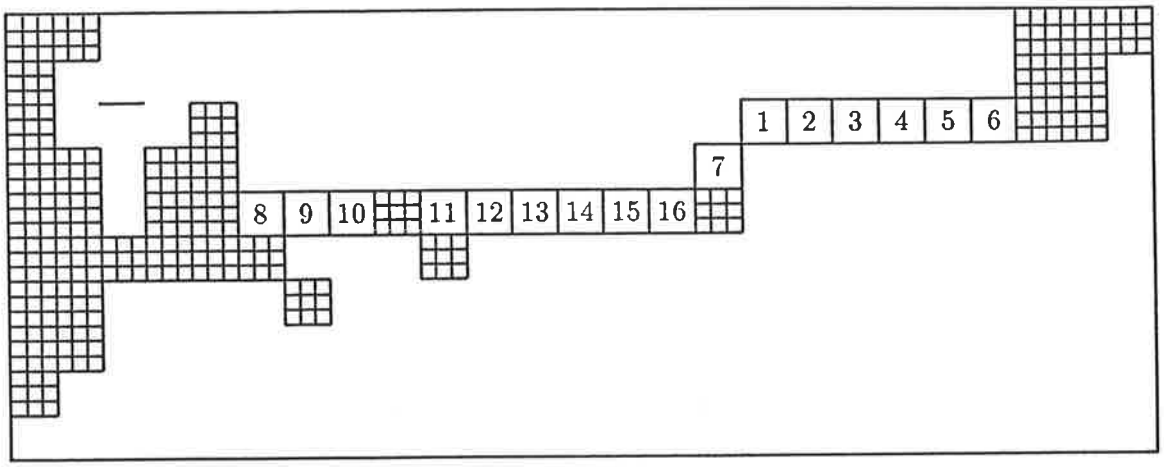


Figure 6.2: *The relabelled open boundary element line of the Spencer Gulf model showing the element labelling scheme used for the program runs of the present chapter; compare with Figure 5.12 of Chapter 5. The cross-hatched areas represent land.*

position; consequently special program code is written for it. This problem cannot be solved by making the south-eastern element a Type 2 element since it would then become a corner element along with the elements to its west and north. The relabelled open boundary element line is given in Figure 6.2. This change reduces the number of open boundary elements supplying information to the model, and may lead to a decrease in the accuracy of results which can be obtained. To test this the height specified model is rerun with the open boundary line as in Figure 6.2 and the errors obtained are indeed found to be slightly larger, viz. $\varepsilon_a = 2.26\,\text{cm}$, $\varepsilon_p = 4.09°$ and $\varepsilon = 3.59\,\text{cm}$. This error set will be used as the benchmark set for the height specified model run with the open boundary line of Figure 6.2.

6.3 Sommerfeld condition

The Sommerfeld condition is tried first. For a wave travelling in the positive x-direction and expressed in terms of elevation, this condition is

$$\frac{\partial \zeta}{\partial t} + c\frac{\partial \zeta}{\partial x} = 0\,, \tag{6.1}$$

where phase velocity $c = \sqrt{gh}$ is locally fixed. Throughout this work, when reference is made to the "Sommerfeld" condition, it is to the use of (6.1) with values of c calculated as stated.

The finite difference approximation used for (6.1) is that due to Orlanski (1976) with height specification introduced through both time and space derivatives, as he suggests. Defining ζ_i^n as the finite difference approximation for $\zeta(i2\Delta x, n\Delta t)$, the difference equation for the first elevation calculation (see Figure 3.4) is

$$\frac{\zeta_i^{n+\frac{1}{2}} - \zeta_s^{n-\frac{1}{2}}}{\Delta t} = -\frac{c}{4\Delta x}\left(\zeta_i^{n+\frac{1}{2}} + \zeta_s^{n-\frac{1}{2}} - 2\zeta_{i-1}^{n}\right), \tag{6.2}$$

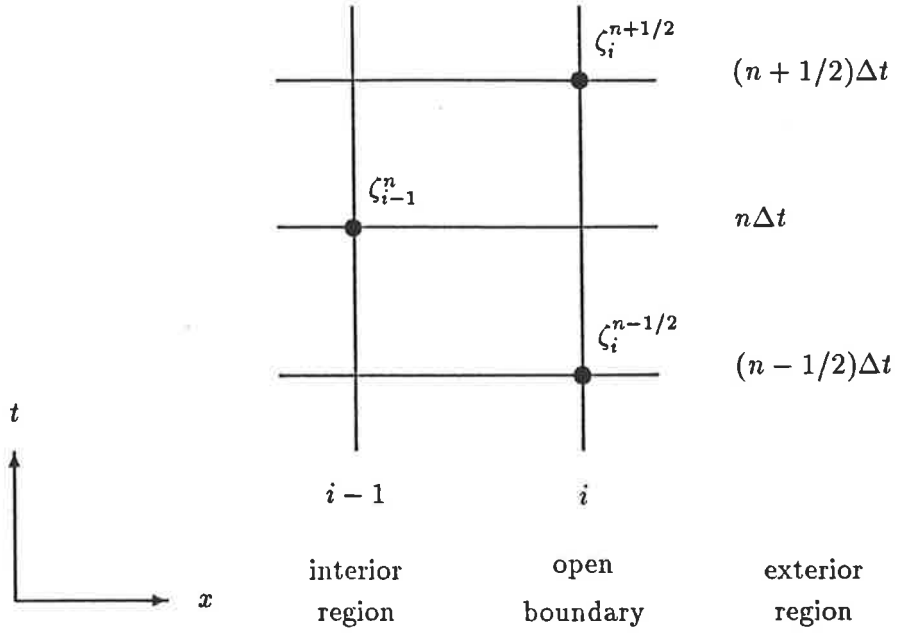


Figure 6.3: *Gridpoints used in the Orlanski differencing of the Sommerfeld equation.*

where $\zeta_i^{n+1/2}$ is the calculated value of ζ on the open boundary at time $(n+1/2)\Delta t$, $\zeta_s^{n-1/2}$ is the specified value at the same position a full time step earlier, and ζ_{i-1}^n is the closest interior value to the boundary at time level n (see Figure 6.3). Similarly, for the second elevation calculation (see Figure 3.4),

$$\frac{\zeta_i^{n+1} - \zeta_s^n}{\Delta t} = -\frac{c}{4\Delta x}\left(\zeta_i^{n+1} + \zeta_s^n - 2\zeta_{i-1}^{n+\frac{1}{2}}\right). \tag{6.3}$$

The differencing used in (6.2) is centred about the ζ_i^n gridpoint. The model's interior difference scheme uses a leap-frog calculation of elevation and Orlanski states that the type of differencing used in (6.2) and (6.3) for the space derivative $\partial\zeta/\partial x$ "is such that it involves only points of the same numerical mode, since it is known that ... schemes such as leap-frog can produce an artificial modal splitting" (Orlanski, 1976, p.252). To obtain the boundary elevation value at time $n\Delta t$, for example, he uses

$$\zeta_i^n = \frac{1}{2}\left(\zeta_i^{n+\frac{1}{2}} + \zeta_i^{n-\frac{1}{2}}\right) + O\left(\Delta t\right)^2, \tag{6.4}$$

and so the space derivative approximation of (6.2) is derived as follows:

$$\begin{aligned}
\left.\frac{\partial\zeta}{\partial x}\right|_i^n &\simeq \frac{1}{4\Delta x}\left(\zeta_{i+1}^n - \zeta_{i-1}^n\right) \\
&\simeq \frac{1}{4\Delta x}\left(\left[2\zeta_i^n - \zeta_{i-1}^n\right] - \zeta_{i-1}^n\right) \\
&\simeq \frac{1}{4\Delta x}\left(\left[\zeta_i^{n+\frac{1}{2}} + \zeta_i^{n-\frac{1}{2}}\right] - 2\zeta_{i-1}^n\right).
\end{aligned} \tag{6.5}$$

A Taylor series expansion of each term in (6.2) or (6.3) about ζ_i^n shows that Orlanski's

discretisation is consistent with

$$\frac{\partial \zeta}{\partial t} + c\frac{\partial \zeta}{\partial x} = O\left((\Delta t)^2, \Delta x\right). \tag{6.6}$$

It is second order accurate in time but only first order accurate in space. In Section 6.11, second order accurate approximations for the space derivative are considered.

We note that a convention of differencing the spatial gradient in the manner

$$\frac{\partial \zeta}{\partial x} \simeq \frac{(\text{exterior value} - \text{interior value})}{\text{spatial separation}} \tag{6.7}$$

automatically sets the correct sign for phase velocity c. In the Spencer Gulf model, there are only two directions that outgoing waves can take: positive x and negative y-directions (see Figure 6.2). These directions will be referred to as "easterly" and "southerly" even though the model is not aligned with its longitudinal axis exactly due North, but in the direction 33.33° T.

The explicit form for $\zeta_i^{n+1/2}$ from (6.2) is

$$\zeta_i^{n+\frac{1}{2}} = \frac{\zeta_s^{n-\frac{1}{2}}(1 - C_x/2) + C_x\zeta_{i-1}^n}{1 + C_x/2}, \tag{6.8}$$

where $C_x = c\Delta t/(2\Delta x)$ is the Courant number in the x-direction; from (6.3), the explicit form for ζ_i^{n+1} is

$$\zeta_i^{n+1} = \frac{\zeta_s^{n}(1 - C_x/2) + C_x\zeta_{i-1}^{n+\frac{1}{2}}}{1 + C_x/2}. \tag{6.9}$$

This differencing reduces to lagged height specification as $C_x \to 0$ because ζ_s^n is one full time step behind ζ_i^{n+1}. In describing the differencing for future schemes only that for the first elevation calculation will be given.

Trapp and Ramshaw (1976) suggest that the stability of the differencing used at the boundary may be tested by using a von Neumann analysis, outlined briefly below (see also Noye, 1984b). Writing (6.8) in the form

$$(1 + C_x/2)\zeta_i^{n+\frac{1}{2}} = C_x\zeta_{i-1}^n + (1 - C_x/2)\zeta_s^{n-\frac{1}{2}}, \tag{6.10}$$

it is assumed that each value ζ consists of the sum of two values, one $\widehat{\zeta}$ which is a true solution of (6.10), the other ξ is an error due to round off. Thus if the expression

$$\zeta = \widehat{\zeta} + \xi \tag{6.11}$$

is substituted into (6.10), the terms in $\widehat{\zeta}$ can be removed since they identically satisfy (6.10) and the resulting error equation is

$$(1 + C_x/2)\xi_i^{n+\frac{1}{2}} = C_x\xi_{i-1}^n. \tag{6.12}$$

It is assumed there is no error associated with the specified value ζ_s. Each error term is now expressed in the complex Fourier form

$$\xi_i^n = \sum_m a_m(G_m)^n \exp\{\imath k_m(i2\Delta x)\}, \tag{6.13}$$

where k_m is the wave number of the mth Fourier mode ($k_m = 2\pi/\lambda_m$), λ_m is the wavelength of the mth mode, $i2\Delta x$ is the x-value of the ith grid position, a_m is the coefficient of the mth term of the linear combination (6.13) and G_m is the corresponding gain, or amplification factor, and carries the time variation of the error term. Since the system is linear, superposition of modes applies and only one mode needs to be investigated. Thus the subscript m may be dropped and the general error term for a single mode can be written as

$$\xi_i^n = (G)^n \exp\{\imath\beta i\}, \tag{6.14}$$

where $\beta = k(2\Delta x) = 4\pi\Delta x/\lambda$. Since a wave requires at least 3 gridpoints for resolution, equivalent to a separation of two element widths ($4\Delta x$), then $2\Delta x$ is at most $\lambda/2$. Therefore, β is constrained to vary in the range

$$0 \leq \beta \leq \pi \ . \tag{6.15}$$

By substituting (6.14) into (6.12) and using 100 equally spaced values, say, for β in the interval $[0, \pi]$, it is possible to numerically establish the stability of (6.2) for a range of values of C_x. If the solution obtained for G has an absolute value greater than unity for any mode (i.e. any value of β), then errors will be amplified without bound and the scheme will be unstable for that particular value of C_x. In the case of equation (6.12), however, it is easy to analytically obtain the stable range of values of C_x, viz. $C_x \in [0, 2]$. Strictly speaking, the von Neumann analysis is valid for constant speeds c, but it can be argued that if $C_x \in [0, 2]$ the analysis may be applied point-by-point along the open boundary line since c can be regarded as being constant locally in space and time.

The model with the Sommerfeld condition is stable and produces reasonably accurate results. The errors obtained are $\varepsilon_a = 2.30\,\text{cm}$ in amplitude and $\varepsilon_p = 6.10°$ in phase; the combined error measure is $\varepsilon = 4.58\,\text{cm}$. Comparing these results with the benchmark set, there is a 1.8% increase in amplitude error and a 49% increase in phase error; the combined error measure ε has increased by 28%.

The Sommerfeld condition is applied to both ingoing and outgoing modes of flow and no distinction is made between these modes. Its use during the inflow mode may be responsible for much of the additional phase error incurred and so an alternative inflow condition proposed by Orlanski (1976) is now investigated.

6.4 Orlanski-Sommerfeld condition

Orlanski (1976) calculates phase velocity using condition (6.1), establishes conditions for inflow and outflow, and applies different boundary conditions for each. This improves the accuracy of model results.

Re-arranging the Sommerfeld condition, Orlanski numerically calculates a value for phase velocity using the relation

$$c = -\frac{\partial\zeta}{\partial t} \Big/ \frac{\partial\zeta}{\partial x} \ . \tag{6.16}$$

The differencing used is that given by Orlanski for the Sommerfeld condition written for the previous half time step and set into the interior of the model by one space step, as explained below. The Courant number C_x is now a function of space and time. In

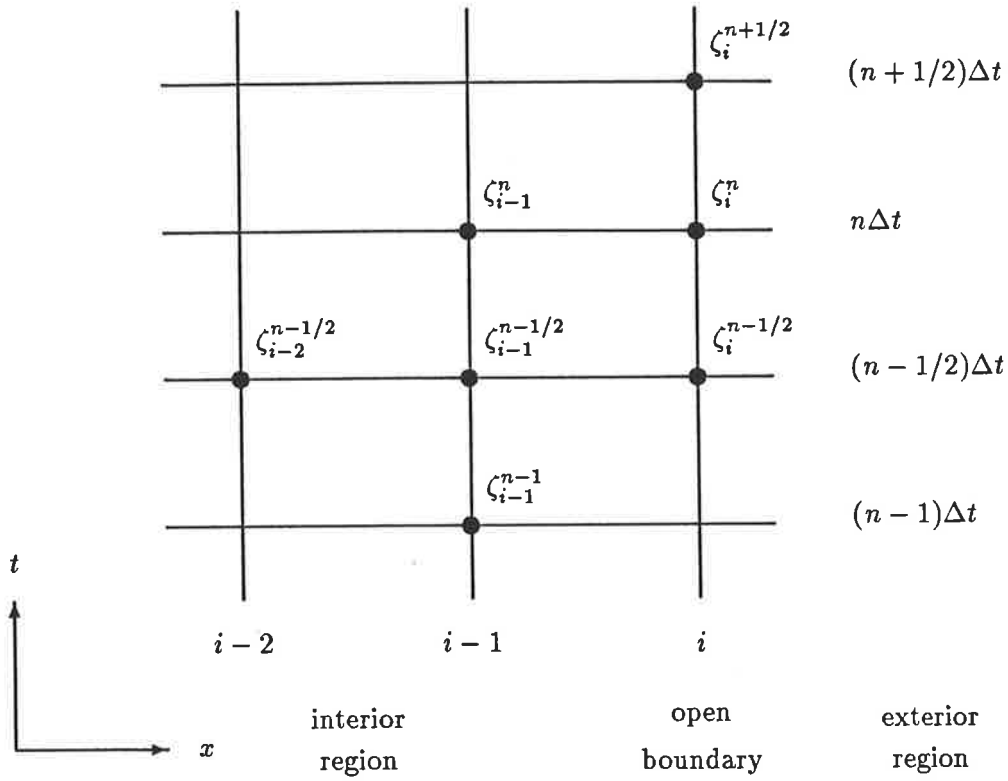


Figure 6.4: *Gridpoints used in the Orlanski-Sommerfeld differencing of the Sommerfeld equation and the equation for the calculation of phase velocity.*

this work, a reference to the Orlanski-Sommerfeld [O-S] condition is a reference to the use of condition (6.1) with calculation of c using equation (6.16). Equation (6.2) can be rearranged to obtain a difference expression for phase velocity in the case of waves travelling in the positive x-direction as follows ... replace $\zeta_s^{n-1/2}$ by $\zeta_i^{n-1/2}$, reduce all time and space indices by one half and by one, respectively, and finally rearrange and obtain:

$$c = -\frac{4\Delta x}{\Delta t}\left(\frac{\zeta_{i-1}^{n} - \zeta_{i-1}^{n-1}}{\zeta_{i-1}^{n} + \zeta_{i-1}^{n-1} - 2\zeta_{i-2}^{n-\frac{1}{2}}}\right). \tag{6.17}$$

Here $\zeta_{i-2}^{n-\frac{1}{2}}$ is the interior elevation value two gridpoints from the boundary. The gridpoints used for (6.17) in combination with (6.2) are illustrated in Figure 6.4. Supposedly more accurate difference forms for c with the above expression (6.17) being used at the corner of a diagonal differencing are suggested by Miller and Thorpe (1981), but are not used here. It is not likely that c will vary significantly over a distance of $2\Delta x$, in the time interval $\Delta t/2$, for the tidal disturbance. In the same manner as before, the differencing of (6.17) can be checked to determine the stable Courant range of operation. The error equation corresponding to (6.17) is

$$(1 + C_x/2)\xi_{i-1}^{n} = C_x\xi_{i-2}^{n-\frac{1}{2}} + (1 - C_x/2)\xi_{i-1}^{n-1}\ . \tag{6.18}$$

The scheme is stable in the range $C_x \in [0, 2]$.

If $c \leq 0$ the flow is defined to be ingoing, if $c > 0$ the flow is outgoing. For ingoing flow, c is set to zero. A restriction is placed on the value of c that may be attained by the outgoing flow. This is necessary because large values may occur when derivatives are very small (Miller and Thorpe, 1981, p.617). The restriction is (Orlanski, 1976, p.254):

$$0 < c \leq 2\Delta x/\Delta t \; . \tag{6.19}$$

Therefore,

- for ingoing flow, c is set to zero;
- for outgoing flow, if $c > 2\Delta x/\Delta t$, c is set to $2\Delta x/\Delta t$ — otherwise it keeps its calculated value.

Expression (6.19) shows that the Courant number is constrained to the interval $[0, 1]$. Thus stability in the interval $C_x \in [0, 1]$ is a sufficient requirement of difference schemes for the combination of equations (6.1) and (6.16).

Initially, all interior values are zero, so the denominator and numerator of (6.17) are zero and c is set to zero. In practice, the numerical value obtained for c remains zero for only the first few time steps along the entire open boundary line. After that it value varies along the boundary with time and position. It is surprising that the numerical calculation of c should indicate outgoing events so soon after initialization but this may be due to several factors: topographical reflection of waves at the irregular sea bed, reflection due to coastal convergence, and the generation of outgoing waves by the initial forcing behaving like a step function, sending waves into the interior and in the opposite direction at the same time. The phenomenon is not due to the forcing at the boundary being ebb tidal information at the commencement of modelling — that possibility can be ruled out by inspecting the reference signal of Figure 6.1 which indicates that initially the tide is on the flood at the boundary.

But the reference signal does provides a clue: initially elevation in the interior of the model is zero while the forcing elevation at the boundary (although on the flood) is about $-0.35\,\mathrm{m}$ (see Figure 6.1). The model basin near the boundary behaves like a dam whose wall is suddenly dropped 0.35 m below the water level. The interior bulk of water moves toward the dam wall and it is largely this movement that is being detected.

Using the O-S condition model results show error values of $\varepsilon_a = 2.27\,\mathrm{cm}$ in amplitude and $\varepsilon_p = 4.70°$ in phase; the combined error measure value is $\varepsilon = 3.87\,\mathrm{cm}$. Comparing these errors with the benchmark set there is now an increase of only 0.44% in amplitude error and 15% in phase error; the increase in the combined error measure ε is 7.8%.

From (6.2), the discretisation for the ingoing O-S condition is the lagged height specified formulation

$$\zeta_i^{n+\frac{1}{2}} = \zeta_s^{n-\frac{1}{2}} \; . \tag{6.20}$$

This may account for most of the improvement in accuracy of the O-S condition over that of the Sommerfeld condition since, as will be shown in Section 6.9, the value $c = 0$ signifying the use of (6.20) is set for 87.3% of the time over the last 29 days of the simulation in the model. This percentage excludes results for open boundary element #7 of Figure 6.2 — they relate to a transverse flow whereas all others relate to longitudinal flows.

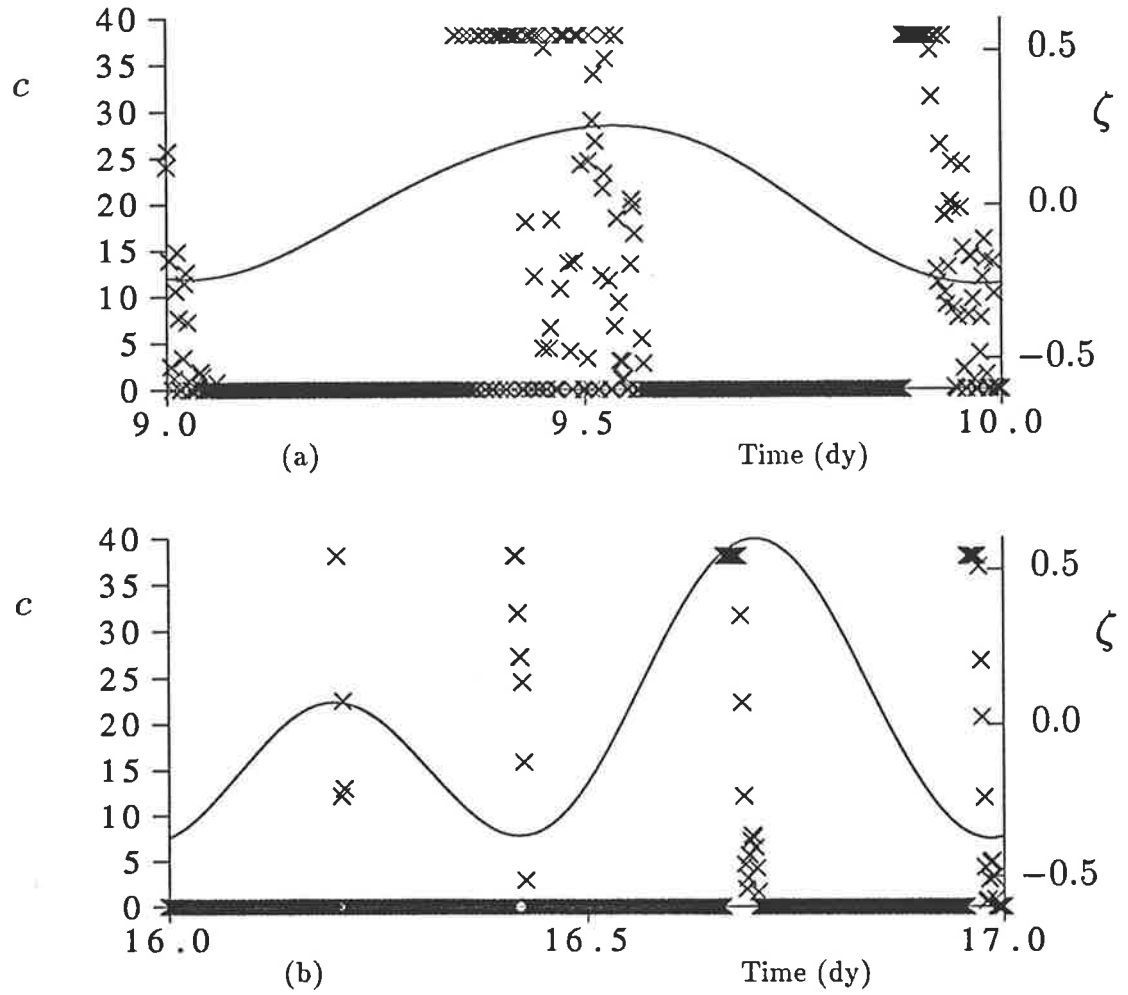


Figure 6.5: *Phase velocity c in m/sec (× 's) calculated using the Orlanski criteria for open boundary element #14 of Figure 6.2. Zero values of c correspond to ingoing flow, non-zero values to outgoing flow. The plots show the values calculated for c for (a) the neap period during days 9–10 after commencement of modelling, and (b) the spring period during days 16–17. Also plotted are the corresponding elevation signals ζ m (solid line) obtained using the tide-height constants for the four major constituents at boundary element #14; the elevation scale is given on the right hand vertical axis.*

Orlanski calculation of c may also contribute to the improved model performance. To test this, the O-S model is rerun with $c = 0$ for the ingoing flow and with $c = \sqrt{gh}$ for the outgoing flow. The results show errors of $\varepsilon_a = 2.26\,\text{cm}$, $\varepsilon_p = 4.70°$ and $\varepsilon = 3.87\,\text{cm}$ suggesting that Orlanski calculation of c for outgoing waves using (6.17) is not a significant improvement in the overall sense compared with using $c = \sqrt{gh}$ for the present tidal model. Consider Figures 6.5 which illustrate the pattern of c values obtained when calculated numerically using the Orlanski criteria. The figures show values of c for every time step $\Delta t = 150\,\text{sec}$ for boundary element #14 (of Figure 6.2) for two 24 hour periods. Figure 6.5(a) shows the values of c for the 9–10 day period after the commencement of the simulation and corresponds to a neap flow; also plotted is the elevation signal for the

same period deduced from the major constituents specified for boundary element #14. Figure 6.5(b) is a plot for the 16–17 day period and corresponds to a spring flow; the elevation signal for the same period is also given and is plotted to the same vertical scale as that in Figure 6.5(a). Both plots show that $c = 0$ for most of the time, i.e. the flow is mostly ingoing. This is to be expected since the dominating and driving influence on the waters at the mouth of Spencer Gulf are the tides which propagate from the Southern Ocean. Non-zero values of c imply outgoing flow. The maximum speed of the outgoing disturbance is the numerical velocity $2\Delta x/\Delta t = 38.1$ m/sec.

Figures 6.5 show that during neaps there is more variability in the computed phase speed values and more occurrences of outflow than during springs. The diurnal inequality is illustrated in the elevation plot of Figure 6.5(a), there being only one high water and one low water during the 24 hour sequence shown. The computed outgoing events lead the elevation signal by one or more hours in the sense that the computed outflow is registered one or more hours before the crest or trough of the tidal wave passes through boundary element #14. During those one or two hours, however, the local flow at boundary element#14 is sometimes registered as being ingoing and this may be the influence of grid-scale oscillations in the computed velocity field during neaps. If this is true, the computed neap flow is not strong enough to over-ride the noise of grid-scale oscillations in the flow near the open boundary. On the other hand, the predicted swapping from outflow to inflow and back to outflow that occurs prior to a crest or trough in the tidal wave may correspond to horizontal mixing. Examining the consecutive values of c during these events, it is found that the events consist of a series of bursts of positive values of c interspersed with groups of zero values. This behaviour seems consistent with the movement of horizontal eddies. Since the tidal streams at neaps are predominantly due to the diurnals, this apparent evidence of mixing at the mouth of the Gulf is consistent with Easton's (1978) finding that the exchange of water with the Southern Ocean is mostly due to the diurnals. Figures 6.5 seem to suggest that mixing mostly takes place during neaps.

Figure 6.5(b) shows a more focused set of outgoing events reflecting the greater strength of the spring flow. The bursts of recorded outflow are brief and only the first of these is contaminated by a lapse into ingoing flow before it is completed. The spring outflow events almost coincide with the crests and troughs of the elevation signal: specifically, the four outflow events occur at times 16.201 dy, 16.413 dy, 16.665 dy and 16.957 dy while the elevation signal correspondingly peaks and troughs at times 16.197 dy, 16.417 dy, 16.698 dy and 16.979 dy. These predictions of outgoing events suggest that at boundary element #14 little exchange of water takes place at springs between Spencer Gulf and the Southern Ocean. Because the spring flows are due mainly to the semi-diurnals, one can infer that exchange at the mouth involving the semi-diurnals is brief and weak compared to the exchange that occurs during neaps due to the diurnals.

All the outgoing sequences depicted, the two neap sequences at times 9.5 dy and 10 dy and the four spring sequences, commence with maximum outgoing velocity $c = 38.1$ m/sec. It is not clear why this should be so. As mentioned above the neap outgoing sequences consist of bursts of positive values with groups of zero values interspersed. Not all of these bursts commence with $c = 38.1$ m/sec. Some start at small values, build to larger values (often 38.1 m/sec) and then gradually reduce to zero. The first half of the outgoing sequence near 9.5 dy is dominated by the occurrence of the maximum value. To study exchange across the mouth of the Gulf more carefully, similar plots at all open boundary elements should be made.

While much variation is shown in the non-zero values of c in Figures 6.5, the average of the non-zero values for the last 29 days of the simulation is 23.2 m/sec and compares well with the value $c = \sqrt{gh} = 22.5$ m/sec for open boundary element #14. This observation is consistent with the similarity of model error observed above when c was first calculated using Orlanski's method and then using $c = \sqrt{gh}$.

The Orlanski approach of separating flows into inflow and outflow regimes, and applying a boundary condition suitable to each, provides improved model performance over the Sommerfeld condition which makes no such distinction. In the present case, the use of a lagged height specified condition (6.20) for the inflow is mostly responsible for the improvement in model results.

6.5 Forcing strategies for the O-S condition

Consider the manner in which forcing is included in the differencing of the Orlanski-Sommerfeld condition. Using Orlanski's numerical expression for phase velocity (6.17), the forcing strategy used in equation (6.2) can be varied by introducing the height specification

(1) only through the time derivative, through one term, or
(2) only through the space derivative, through one term, or
(3) only through the time derivative, through both terms, or
(4) only through the space derivative, through both terms.

Other more trivial combinations are possible but are not considered here.

Using differencing option (1) for calculation of $\zeta_i^{n+1/2}$ gives

$$\frac{\zeta_i^{n+\frac{1}{2}} - \zeta_s^{n-\frac{1}{2}}}{\Delta t} = -\frac{c}{4\Delta x}\left(\zeta_i^{n+\frac{1}{2}} + \zeta_i^{n-\frac{1}{2}} - 2\zeta_{i-1}^{n}\right) \tag{6.21}$$

for an easterly outgoing wave. Here the space derivative is entirely determined from calculated elevation values. Rearranging,

$$\zeta_i^{n+\frac{1}{2}} = \frac{\zeta_s^{n-\frac{1}{2}} - (C_x/2)\,\zeta_i^{n-\frac{1}{2}} + C_x\zeta_{i-1}^{n}}{1 + C_x/2}\,. \tag{6.22}$$

The Spencer Gulf model using this condition is stable and returns errors $\varepsilon_a = 2.26$ cm, $\varepsilon_p = 4.68°$ and $\varepsilon = 3.86$ cm which are marginally smaller errors than using the forcing strategy suggested by Orlanski (equations (6.2),(6.8)). The scheme is stable in the range $C_x \in [0, 1]$ and thus has a narrower range of stable operation than (6.2). However since the boundary scheme need only be stable in the interval $[0, 1]$ the discretisation (6.21) is sufficiently stable.

Using option (2) for the differencing gives

$$\frac{\zeta_i^{n+\frac{1}{2}} - \zeta_i^{n-\frac{1}{2}}}{\Delta t} = -\frac{c}{4\Delta x}\left(\zeta_i^{n+\frac{1}{2}} + \zeta_s^{n-\frac{1}{2}} - 2\zeta_{i-1}^{n}\right). \tag{6.23}$$

Here, the time derivative is determined from calculated values and the condition is driven only through the space derivative. A difficulty with this form is that the ingoing boundary condition is not forced if c is set to zero for inflow. This differencing is also unstable in the von Neumann sense for all $C_x > 0$.

Using option (3) for the differencing gives

$$\frac{\zeta_s^{n+\frac{1}{2}} - \zeta_s^{n-\frac{1}{2}}}{\Delta t} = -\frac{c}{4\Delta x}\left(\zeta_i^{n+\frac{1}{2}} + \zeta_i^{n-\frac{1}{2}} - 2\zeta_{i-1}^{n}\right). \tag{6.24}$$

Here, the time derivative is totally specified. Rearranging gives

$$\zeta_i^{n+\frac{1}{2}} = 2\zeta_{i-1}^{n} - \zeta_i^{n-\frac{1}{2}} - (2/C_x)\left(\zeta_s^{n+\frac{1}{2}} - \zeta_s^{n-\frac{1}{2}}\right). \tag{6.25}$$

Because c is initially zero and is likely to be zero at other times during the modelling, variable phase velocity cannot be used for this option — it could be run using phase velocity calculated from $c = \sqrt{gh}$. However, the differencing is again unstable.

Using option (4) for the differencing gives

$$\frac{\zeta_i^{n+\frac{1}{2}} - \zeta_i^{n-\frac{1}{2}}}{\Delta t} = -\frac{c}{4\Delta x}\left(\zeta_s^{n+\frac{1}{2}} + \zeta_s^{n-\frac{1}{2}} - 2\zeta_{i-1}^{n}\right). \tag{6.26}$$

The time derivative is entirely determined from calculated values and the boundary condition is only driven through the space derivative. The differencing is again unstable and furthermore, when $c = 0$ there is no forcing.

Thus Orlanski's forcing strategy (6.2), where forcing is introduced through both the time and space derivative terms, may not be the best strategy; option (1) differencing gives a slightly improved result and has the necessary stability. Another advantage of option (1) is that the forcing of the discretisation is not directly altered by the value of c — this seems desirable.

6.6 Blumberg and Kantha condition

Blumberg and Kantha [B&K] (1985) have introduced a modified form of the Sommerfeld open boundary condition "which permits the mean subtidal [i.e. meteorological] and tidal forcing to be prescribed and, yet, allows transients generated inside the region to be transmitted outwards" (ibid., p.241). The condition is expressed as

$$\frac{\partial \zeta}{\partial t} + c\frac{\partial \zeta}{\partial x} = -\frac{1}{T_f}(\zeta - \zeta_k)\ , \tag{6.27}$$

where x denotes the outward normal direction, $c = \sqrt{gh}$ is the locally fixed value of phase velocity and ζ_k is an equilibrium solution which is a sum of a mean meteorological value ζ_m and a tidal component ζ_s, both of which must be known *a priori*. B&K comment: "The term on the right represents damping which tends to force the value of ζ at the boundary to some known value ζ_k with a time scale of the order of T_f. $T_f = 0$ corresponds to a clamped boundary in which no disturbances are allowed to pass out through the boundary; and $T_f \to \infty$ represents the pure radiation condition which renders the boundary transparent to waves travelling in the positive x direction with phase speed c" (ibid., p.241).

While the B&K condition was developed for large scale circulation modelling where mean meteorological and tidal forcing is employed, it is of interest to determine the parameters under which the condition operates successfully for the present model which is forced by the tide only.

In the absence of meteorological forcing $\zeta_m = 0$ and so $\zeta_k = \zeta_s$, the time-varying specified elevation at each elevation point of the open boundary. This forcing is applied only through the right hand side.

For the first elevation calculation, the B&K discretisation of (6.27) is

$$\frac{\zeta_i^{n+\frac{1}{2}} - \zeta_i^{n-\frac{1}{2}}}{\Delta t} + \frac{c}{4\Delta x}\left(\zeta_i^{n+\frac{1}{2}} + \zeta_i^{n-\frac{1}{2}} - 2\zeta_{i-1}^{n}\right) = -\frac{1}{T_f}\left(\zeta_i^{n-\frac{1}{2}} - \zeta_k\right). \tag{6.28}$$

The differencing on the left hand side is that due to Orlanski (1976) as before.

As $T_f \to 0$ condition (6.27) becomes a height specified condition which B&K refer to as a "clamped" boundary condition. It is "clamped" in the sense that the height specified condition passes those waves contained in the height specification and no others. To other waves it appears as rigid or fixed and acts as a reflecting barrier.

If ζ_k is differenced as

$$\zeta_k = \zeta_s^{n-\frac{1}{2}}, \tag{6.29}$$

rearrangement of (6.28) yields the following explicit expression for calculation of $\zeta_i^{n+\frac{1}{2}}$:

$$\zeta_i^{n+\frac{1}{2}} = \frac{\zeta_i^{n-\frac{1}{2}}\left(1 - C_x/2 - N_f^{-1}\right) + C_x\zeta_{i-1}^{n} + N_f^{-1}\zeta_s^{n-\frac{1}{2}}}{1 + C_x/2}, \tag{6.30}$$

where $N_f = T_f/\Delta t$. As T_f increases a smaller fraction of the specified information $\zeta_s^{n-1/2}$ is supplied to the model using this formulation. In the limit as $T_f \to \infty$ no forcing is supplied. The error equation associated with (6.30) is

$$(1 + C_x/2)\xi_i^{n+\frac{1}{2}} = C_x\xi_{i-1}^{n} + (1 - C_x/2 - N_f^{-1})\xi_i^{n-\frac{1}{2}}\ . \tag{6.31}$$

It is numerically found that the differencing (6.28),(6.29) is stable for the range of C_x and N_f^{-1} indicated in Figure 6.6(a) where only $T_f \geq \Delta t$ have been considered. The value $N_f^{-1} = 1$ corresponds to $T_f = \Delta t$ sec and larger values of N_f^{-1} correspond to smaller time scales. If instead of using (6.29) ζ_k is differenced as

$$\zeta_k = \zeta_s^{n+\frac{1}{2}} \tag{6.32}$$

and equation (6.27) is correspondingly differenced in the manner

$$\frac{\zeta_i^{n+\frac{1}{2}} - \zeta_i^{n-\frac{1}{2}}}{\Delta t} + \frac{c}{4\Delta x}\left(\zeta_i^{n+\frac{1}{2}} + \zeta_i^{n-\frac{1}{2}} - 2\zeta_{i-1}^{n}\right) = -\frac{1}{T_f}\left(\zeta_i^{n+\frac{1}{2}} - \zeta_s^{n+\frac{1}{2}}\right) \tag{6.33}$$

the exact height specified condition is obtained in the limit as $T_f \to 0$:

$$\zeta_i^{n+\frac{1}{2}} = \zeta_s^{n+\frac{1}{2}}\ . \tag{6.34}$$

The expression for $\zeta_i^{n+1/2}$ is now

$$\zeta_i^{n+\frac{1}{2}} = \frac{\zeta_i^{n-\frac{1}{2}}(1 - C_x/2) + C_x\zeta_{i-1}^{n} + N_f^{-1}\zeta_s^{n+\frac{1}{2}}}{1 + C_x/2 + N_f^{-1}} \tag{6.35}$$

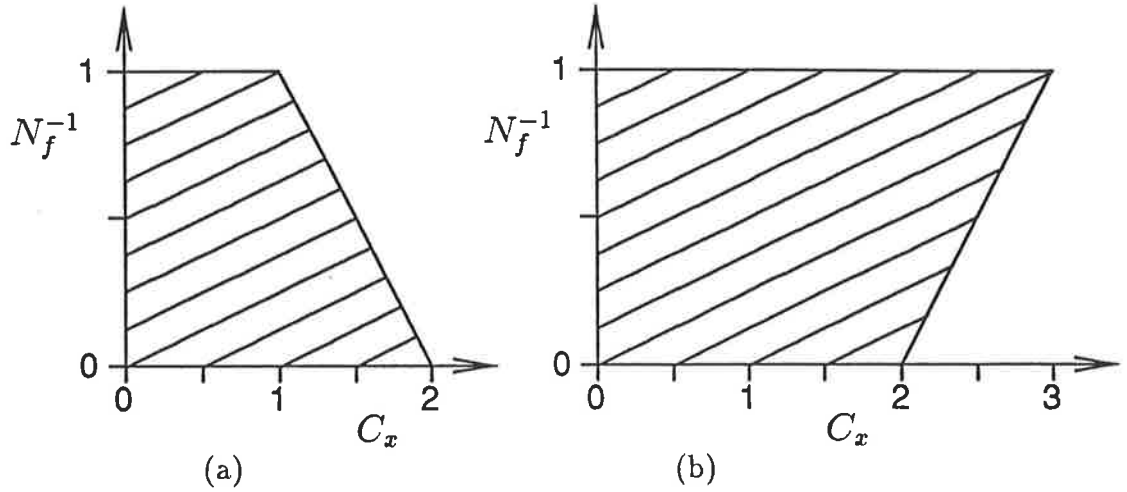


Figure 6.6: *Regions of stable operation (shaded) for the B&K condition discretised as (a) expression (6.30), and (b) expression (6.35). Stability for $N_f^{-1} \in [0,1]$, corresponding to $T_f \geq \Delta t$, is considered.*

or, multiplying the numerator and denominator of the right hand side by T_f,

$$\zeta_i^{n+\frac{1}{2}} = \frac{T_f \zeta_i^{n-\frac{1}{2}} (1 - C_x/2) + T_f C_x \zeta_{i-1}^n + \Delta t \zeta_s^{n+\frac{1}{2}}}{T_f + T_f C_x/2 + \Delta t}. \tag{6.36}$$

Using (6.36) the limiting value $T_f = 0$ may be used to obtain the height specified condition — in fact any value for T_f can be used in this expression. The value $T_f = 0$ cannot be used in expression (6.30).

The stability of expressions (6.35) and (6.36) can also be established using the von Neumann analysis. According to the result presented in Figure 6.6(b), these schemes are stable over a greater range of parameters than the scheme proposed by B&K. It is not clear why they chose to difference the right hand side of (6.27) at the "old" time level — no reason is given. However the average value of Courant number used in their model is very much smaller than unity and one can see from Figures 6.6 that when C_x is small, both schemes are stable.

Expression (6.30) uses forcing at the "old" time level and expressions (6.35) and (6.36) use forcing at the "new" time level. A further expression using forcing at the intermediate time level is unstable for all non-zero values of N_f^{-1}, but stability for the case $N_f^{-1} = 0$ is not useful in the tidal modelling context since no forcing is then supplied. Figures 6.7(a),(b),(c) show, respectively, the performance of the B&K condition (6.30) for $T_f = 150\,\text{sec}$, $T_f = 1\,\text{hr}$ and $T_f = 4\,\text{hr}$. The latter value was considered because B&K use $T_f = 4\,\text{hr}$ in their tide and wind study of the Mid Atlantic Bight. The first two days of simulation for the Spencer Gulf model are presented in each figure. The damping effect of the condition as T_f is increased is clearly demonstrated.

As T_f is increased the model response is increasingly phase shifted as well as damped. When $T_f = \Delta t$ the condition behaves very much like the height specified condition; the amplitude and phase errors for tidal elevation are $\varepsilon_a = 2.28\,\text{cm}$ and $\varepsilon_p = 5.53°$, respectively, while $\varepsilon = 4.28\,\text{cm}$. These errors compare reasonably well with the benchmark error set and are an improvement on the Sommerfeld results. Using $T_f = 3\Delta t\,\text{sec}$ and $T_f = 6\Delta t\,\text{sec}$

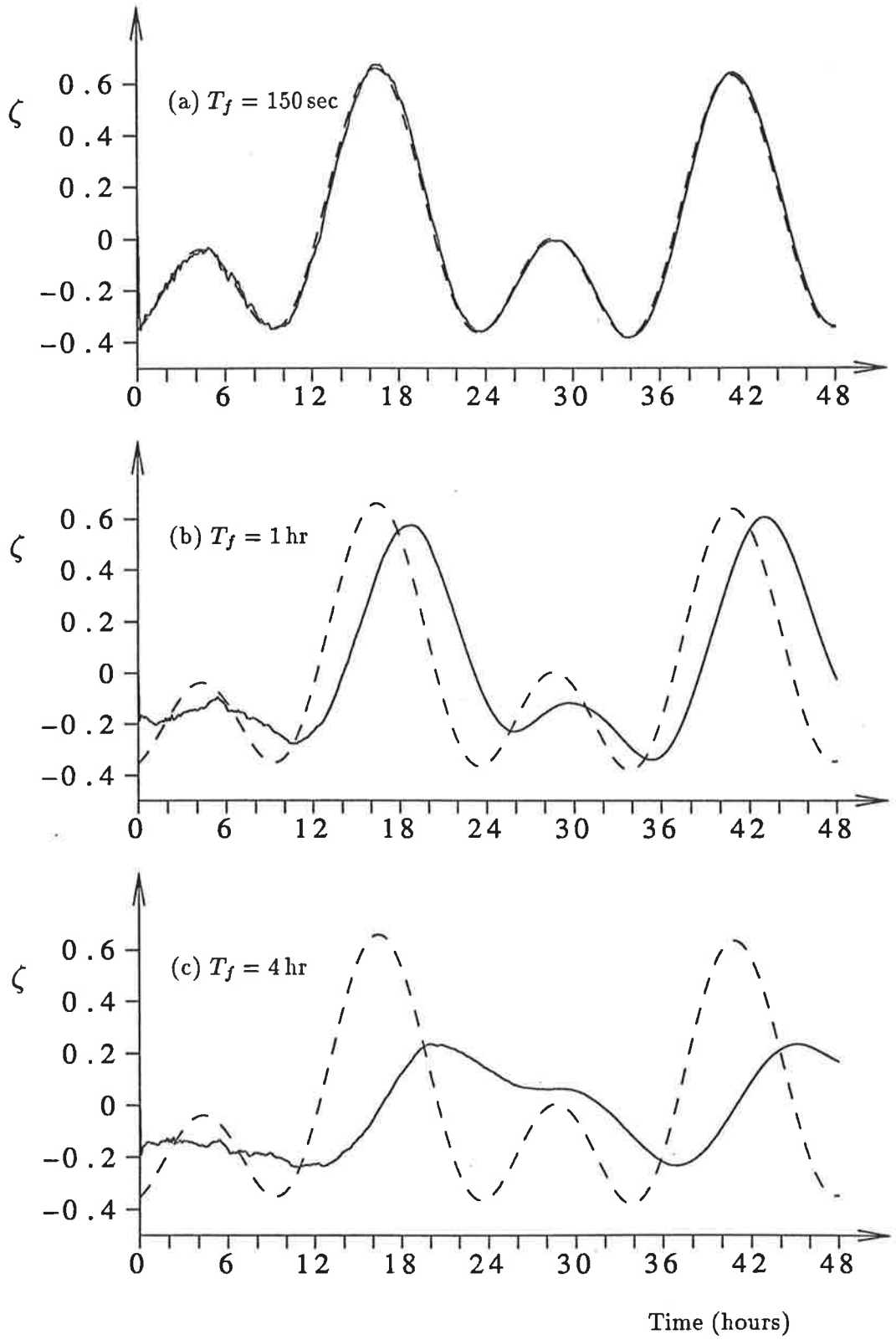


Figure 6.7: *Comparison of the predicted tidal elevation (solid curve) with the observed signal (dashed curve) for the first 48 hr at Wedge Island station when the B&K open boundary condition is used. In (a) $T_f = 150$ sec, in (b) $T_f = 1$ hr and in (c) $T_f = 4$ hr.*

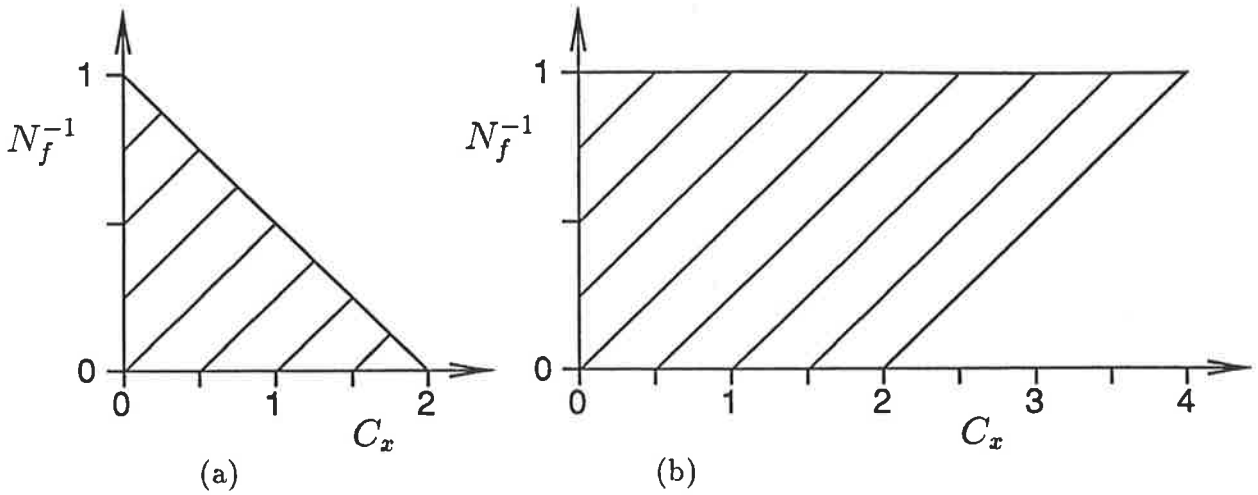


Figure 6.8: *Regions of stable operation (shaded) for the modified B&K condition with the height specified term differenced at (a) the "old" and "intermediate" time levels, and (b) the "new" time level.*

the model is stable for the full 32 day simulation but the errors obtained rapidly increase. It appears that the best performance from the B&K condition for purely tidal forcing for the present model is obtained using small T_f, approximately corresponding to the height specified condition.

6.7 Modified B&K condition

In this section the B&K condition is modified by writing it as a combination of the O-S and height specified conditions. Thus the left hand side of (6.27) is discretised as in (6.2) and c is calculated as in (6.17). It will be shown that model performance is immediately improved at large values of T_f.

There are several choices available for the time level at which to specify forcing in the height specified term on the right hand side of (6.27), the forcing in the O-S term being fixed at time $(n-1/2)\Delta t$ as in (6.2). The forcing can be specified to be at times $(n-1/2)\Delta t$, $n\Delta t$ or $(n+1/2)\Delta t$. Von Neumann analysis of the first two cases gives identical stability regions which are plotted as Figure 6.8(a). The result for forcing at level $(n+1/2)$ is given in Figure 6.8(b). If T_f is of the order of several hours (i.e. $N_f^{-1} \ll 1$) and if C_x is confined to the interval $[0,1]$, the schemes may be regarded as having equivalent stability. To demonstrate the quantitative effect of these choices, two experiments are conducted, one with the forcing in the right hand side of (6.27) specified at $(n-1/2)\Delta t$ and the other at $(n+1/2)\Delta t$.

Thus in the first experiment the differencing of the modified B&K condition is

$$\frac{\zeta_i^{n+\frac{1}{2}} - \zeta_s^{n-\frac{1}{2}}}{\Delta t} + \frac{c}{4\Delta x}\left(\zeta_i^{n+\frac{1}{2}} + \zeta_s^{n-\frac{1}{2}} - 2\zeta_{i-1}^{n}\right) = -\frac{1}{T_f}\left(\zeta_i^{n-\frac{1}{2}} - \zeta_s^{n-\frac{1}{2}}\right) \qquad (6.37)$$

and forcing is uniformly supplied at time $(n-1/2)\Delta t$. The explicit expression for $\zeta_i^{n+1/2}$

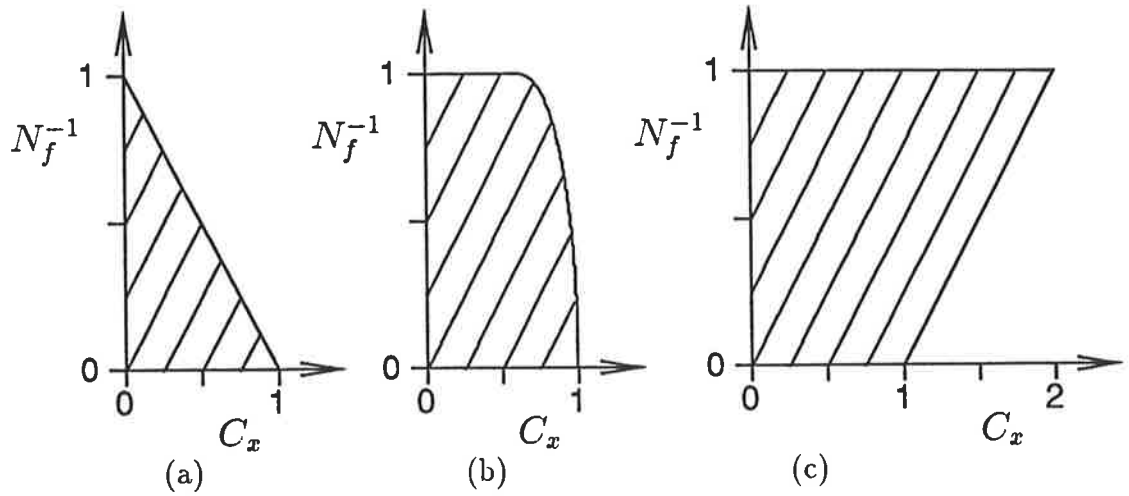


Figure 6.9: *Regions of stable operation (shaded) for the modified B&K condition forcing of only the time derivative approximation and with the height specified term differenced at (a) the "old" time level, (b) the "intermediate" time level, and (c) the "new" time level.*

is

$$\zeta_i^{n+\frac{1}{2}} = \frac{\zeta_s^{n-\frac{1}{2}}\left(1 - C_x/2 + N_f^{-1}\right) + C_x\zeta_{i-1}^n - N_f^{-1}\zeta_i^{n-\frac{1}{2}}}{1 + C_x/2}\,. \tag{6.38}$$

In the second experiment the differencing is

$$\frac{\zeta_i^{n+\frac{1}{2}} - \zeta_s^{n-\frac{1}{2}}}{\Delta t} + \frac{c}{4\Delta x}\left(\zeta_i^{n+\frac{1}{2}} + \zeta_s^{n-\frac{1}{2}} - 2\zeta_{i-1}^n\right) = -\frac{1}{T_f}\left(\zeta_i^{n+\frac{1}{2}} - \zeta_s^{n+\frac{1}{2}}\right) \tag{6.39}$$

and forcing is supplied at different time levels. The explicit expression for $\zeta_i^{n+1/2}$ is

$$\zeta_i^{n+\frac{1}{2}} = \frac{T_f\zeta_s^{n-\frac{1}{2}}(1 - C_x/2) + T_f C_x\zeta_{i-1}^n + \Delta t\zeta_s^{n+\frac{1}{2}}}{T_f + T_f C_x/2 + \Delta t}\,. \tag{6.40}$$

Three values of T_f are used: $T_f = 1, 6, 12$ hr. Schemes (6.38) and (6.40) give almost identical results for each of these values of T_f. For $T_f = 12$ hr the results are nearly the same as those obtained for the O-S model (for scheme (6.38) the errors are $\varepsilon_a = 2.26$ cm, $\varepsilon_p = 4.69°$ and $\varepsilon = 3.87$ cm and for scheme (6.40) the errors are $\varepsilon_a = 2.26$ cm, $\varepsilon_p = 4.70°$ and $\varepsilon = 3.87$ cm). For $T_f = 1$ hr, the results are slightly improved in phase (an error of $4.67°$ is obtained in each case) and ε is 3.86 cm, reflecting the stronger influence of the height specified condition on the right hand side of (6.27). Larger values of T_f correspond to choosing a modified B&K condition with larger proportion of the O-S term. In the limit as $T_f \to \infty$, only the O-S term is significant.

In Section 6.5 it was found that slightly better accuracy is obtained if forcing is omitted from the space derivative of the Sommerfeld term. Stability regions for the three schemes so generated are presented in Figures 6.9(a),(b),(c). The experiments using schemes (6.38) and (6.40) are repeated with the forcing term removed from the spatial gradient of the

boundary condition. The scheme resulting from this modification of (6.38) is

$$\frac{\zeta_i^{n+\frac{1}{2}} - \zeta_s^{n-\frac{1}{2}}}{\Delta t} + \frac{c}{4\Delta x}\left(\zeta_i^{n+\frac{1}{2}} + \zeta_i^{n-\frac{1}{2}} - 2\zeta_{i-1}^{n}\right) = -\frac{1}{T_f}\left(\zeta_i^{n-\frac{1}{2}} - \zeta_s^{n-\frac{1}{2}}\right). \tag{6.41}$$

The explicit expression for $\zeta_i^{n+1/2}$ is

$$\zeta_i^{n+\frac{1}{2}} = \frac{\zeta_s^{n-\frac{1}{2}}\left(1 + N_f^{-1}\right) + C_x\zeta_{i-1}^{n} - \zeta_i^{n-\frac{1}{2}}\left(C_x/2 + N_f^{-1}\right)}{1 + C_x/2}. \tag{6.42}$$

The modified form of scheme (6.40) is

$$\frac{\zeta_i^{n+\frac{1}{2}} - \zeta_s^{n-\frac{1}{2}}}{\Delta t} + \frac{c}{4\Delta x}\left(\zeta_i^{n+\frac{1}{2}} + \zeta_i^{n-\frac{1}{2}} - 2\zeta_{i-1}^{n}\right) = -\frac{1}{T_f}\left(\zeta_i^{n+\frac{1}{2}} - \zeta_s^{n+\frac{1}{2}}\right). \tag{6.43}$$

The explicit expression for $\zeta_i^{n+1/2}$ is

$$\zeta_i^{n+\frac{1}{2}} = \frac{T_f\zeta_s^{n-\frac{1}{2}} - T_f(C_x/2)\zeta_i^{n-\frac{1}{2}} + T_fC_x\zeta_{i-1}^{n} + \Delta t\zeta_s^{n+\frac{1}{2}}}{T_f + T_fC_x/2 + \Delta t}, \tag{6.44}$$

and again employs forcing at different time levels.

Results are improved slightly, as was the experience in Section 6.5. For $T_f = 12\,\text{hr}$ the results are nearly the same as those obtained for the O-S model using option (1) differencing (for scheme (6.42) the errors are $\varepsilon_a = 2.26\,\text{cm}$, $\varepsilon_p = 4.67°$ and $\varepsilon = 3.86\,\text{cm}$ and for scheme (6.44) the errors are $\varepsilon_a = 2.26\,\text{cm}$, $\varepsilon_p = 4.68°$ and $\varepsilon = 3.86\,\text{cm}$). For $T_f = 1\,\text{hr}$, the results are again slightly improved in phase (an error of 4.65° is obtained in each case) and ε is 3.85 cm.

Using the modified B&K scheme is clearly more complicated than using the O-S scheme and there is very little improvement in the results obtained. In the present tidal application, all values for T_f of the order of hours give essentially the same predictions. Having modified the B&K scheme so that it works accurately for the tidal model of Spencer Gulf, results are so similar to those obtained using the O-S scheme that one may choose the latter on the grounds that it is computationally cheaper.

It is possible that if B&K had included forcing in the Sommerfeld condition, calculated phase velocity and separated the flow into ingoing and outgoing modes in the Orlanski manner, they may have had success with that boundary condition for their model of the Mid Atlantic Bight and may not have proposed their "damped" Sommerfeld condition.

6.8 Time varying the influence of the terms of the B&K condition

Consider the following linear combination of the height specified condition and the unforced Sommerfeld condition with a time dependent weight $\gamma(t)$:

$$(1-\gamma)\left(\frac{\partial\zeta}{\partial t} + c\frac{\partial\zeta}{\partial x}\right) + \gamma\left(\frac{\zeta - \zeta_k}{T_{f*}}\right) = 0, \tag{6.45}$$

where $c = \sqrt{gh}$. If it is desired to consider a fixed linear combination of the two conditions, γ is fixed. For a time varying linear combination, γ could be defined as $\gamma = T/T_S$, where T is simulated model time and T_S is a specified time scale relating to the balance of the two conditions. The term T_{f*} is another time scale related, for example, to the time it theoretically takes a wave to traverse the length of the Gulf. Using $T_{f*} = L/c$ the value for T_{f*} in Spencer Gulf is approximately 6 hr (given that $L \simeq 340\,\text{km}$, $c = \sqrt{gh_a}$ and $h_a \simeq 25\,\text{m}$). When $T = 0$, $\gamma = 0$ and expression (6.45) becomes the Sommerfeld condition. When $T = T_S$, $\gamma = 1$ and the condition becomes the height specified condition.

Rearranging (6.45) gives

$$\frac{\partial \zeta}{\partial t} + c\frac{\partial \zeta}{\partial x} = -\frac{\gamma}{1-\gamma}\left(\frac{\zeta - \zeta_k}{T_{f*}}\right) \tag{6.46}$$

or

$$\frac{\partial \zeta}{\partial t} + c\frac{\partial \zeta}{\partial x} = -\frac{T}{T_S - T}\left(\frac{\zeta - \zeta_k}{T_{f*}}\right), \tag{6.47}$$

both of which are identical in form to the B&K condition (6.27). It appears that the B&K condition uses a balance of influences that is present at model time T_B, say, whence

$$T_f = T_{f*}\left(\frac{T_S - T_B}{T_B}\right). \tag{6.48}$$

The B&K condition can therefore be interpreted as a particular linear combination of the Sommerfeld and height specified boundary conditions which is fixed throughout the simulation.

B&K state that in their case "A series of sensitivity studies, in which the wind was abruptly turned off after an equilibrium state was reached, was conducted to determine an appropriate value of T_f" (B&K, 1985, p.243). For a given model, this "sensitivity" study is a test of various values of T_f from which the one that gives best agreement between observed and predicted data is chosen. Choosing an "appropriate value of T_f" implies that a particular choice is made for the fixed balance of Sommerfeld and height specified conditions. In Section 6.6, the experience with the B&K condition in the Spencer Gulf tidal model suggests that the best choice is such that there is no, or very little, Sommerfeld influence.

In the last section, it was seen that if forcing is provided through the Sommerfeld term, along with Orlanski calculation of c, which enables separation of flow into inflow and outflow modes, open boundary conditions can be developed for the present tidal model using a range of values of T_f. However, once again, the value $T_f = 0$ gives the best results and $T_f \neq 0$ gives results little different from the results obtained using the O-S condition. The modified B&K condition also uses fixed linear combinations of the forced Sommerfeld and height specified conditions. Consider time varying combinations of the forced Sommerfeld and height specified conditions. Both the negative exponential and the rectangular hyperbolic functions may be used to provide a smooth proportional variation of conditions with initial dominance of the O-S condition (see Figure 6.10). Thus for the purely tidal problem consider the exponential combination:

$$e^{-T/T_S}\left(\frac{\partial \zeta}{\partial t} + c\frac{\partial \zeta}{\partial x}\right) + \left(1 - e^{-T/T_S}\right)\left(\frac{\zeta - \zeta_k}{T_{f*}}\right) = 0, \tag{6.49}$$

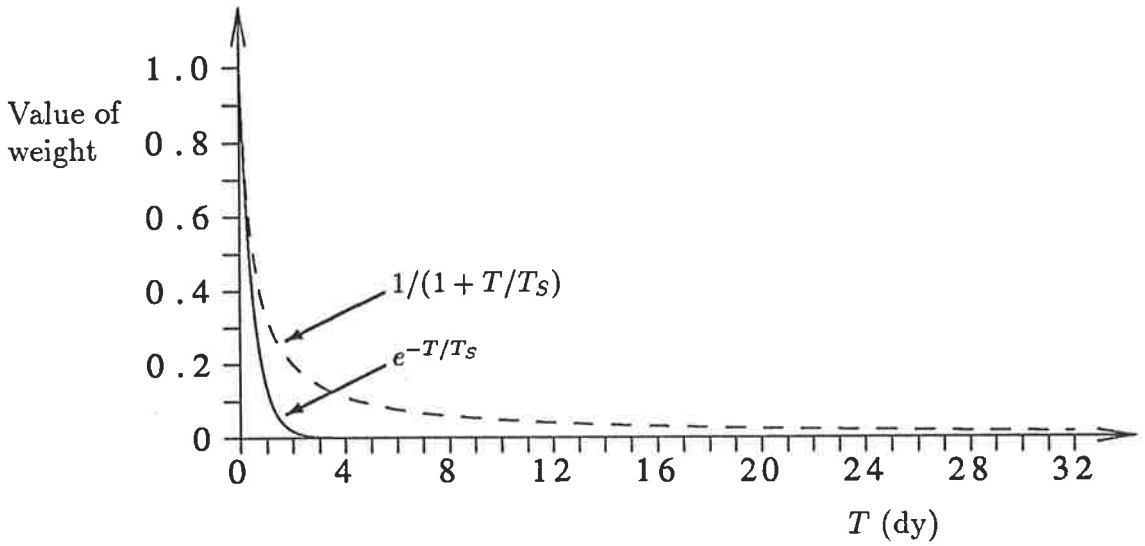


Figure 6.10: *The exponential and hyperbolic weight functions for $T_S = 12\,hr$ over a 32 day simulation period. The exponential function e^{-T/T_S} approaches zero faster than the rectangular hyperbolic function $1/(1+T/T_S)$ as T increases.*

where c is calculated in the Orlanski manner using (6.17). Writing

$$T_{exp} = T_{f*} \Big/ \left(e^{T/T_S} - 1\right) , \tag{6.50}$$

the finite difference expression used for $\zeta_i^{n+\frac{1}{2}}$ is

$$\zeta_i^{n+\frac{1}{2}} = \frac{\zeta_s^{n-\frac{1}{2}} - (C_x/2)\zeta_i^{n-\frac{1}{2}} + C_x\zeta_{i-1}^{n} + (\Delta t/T_{exp})\zeta_s^{n+\frac{1}{2}}}{1 + C_x/2 + \Delta t/T_{exp}} \tag{6.51}$$

for an easterly travelling outgoing wave. Here, forcing is introduced only through the time derivative of the O-S term and the height specified term is differenced at the $(n+1/2)$ time level. For the ingoing wave, this expression simplifies to

$$\zeta_i^{n+\frac{1}{2}} = \frac{\zeta_s^{n-\frac{1}{2}} + (\Delta t/T_{exp})\zeta_s^{n+\frac{1}{2}}}{1 + \Delta t/T_{exp}}. \tag{6.52}$$

Fixing T_{f*} at 6 hr, values of $T_S = 1, 6, 12\,\text{hr}$ and $T_S = 1, 2, 3\,\text{dy}$ are tried. For $T_S = 1\,\text{hr}$ and 6 hr the value of the exponent T/T_S in (6.50) exceeds that allowed as the argument to the Fortran exponential function before the simulation is completed; for the remaining values of T_S, the model is stable with errors increasing as T_S increases. For $T_S = 12\,\text{hr}$, $\varepsilon_a = 2.26\,\text{cm}$, $\varepsilon_p = 4.10°$ and $\varepsilon = 3.59\,\text{cm}$, and these errors are almost as good as the benchmark set; for $T_S = 3\,\text{dy}$, $\varepsilon_a = 2.27\,\text{cm}$, $\varepsilon_p = 4.29°$ and $\varepsilon = 3.69\,\text{cm}$. The smaller the value of T_S, the greater the influence of the height specified condition and the more accurate the results of the model. For $T_S = 12\,\text{hr}$ the influence of the height specified condition increases to 0.998 of the total fraction at simulation time $T = 3\,\text{dy}$, whereafter predictions are stored for tidal analysis; for $T_S = 3\,\text{dy}$, the height specified influence is

only 0.632 of the total fraction at the same time. These results are an improvement on the results for the O-S condition and the modified B&K condition.

If the smooth variation of influences is achieved by using the rectangular hyperbolic function (see Figure 6.10), the following relation is obtained:

$$\frac{1}{1+T/T_S}\left(\frac{\partial\zeta}{\partial t}+c\frac{\partial\zeta}{\partial x}\right)+\frac{T/T_S}{1+T/T_S}\left(\frac{\zeta-\zeta_k}{T_{f*}}\right)=0 \tag{6.53}$$

which simplifies to

$$\frac{\partial\zeta}{\partial t}+c\frac{\partial\zeta}{\partial x}=-\frac{T}{T_S}\left(\frac{\zeta-\zeta_k}{T_{f*}}\right). \tag{6.54}$$

At any given simulation time the proportion of O-S to height specified conditions is $T_S : T$. Writing

$$T_{hyp}=T_{f*}T_S/T, \tag{6.55}$$

the difference forms required are the same as (6.51) and (6.52) with T_{exp} replaced by T_{hyp}.

Using $T_{f*}=6\,\text{hr}$ and $T_S=1,6,12\,\text{hr}$ and $T_S=1,2,3\,\text{dy}$ the model is stable, with errors increasing as T_S increases. With $T_S=1\,\text{hr}$, $\varepsilon_a=2.27\,\text{cm}$, $\varepsilon_p=4.24°$ and $\varepsilon=3.66\,\text{cm}$; with $T_S=12\,\text{hr}$, $\varepsilon_a=2.26\,\text{cm}$, $\varepsilon_p=4.55°$ and $\varepsilon=3.80\,\text{cm}$ and with $T_S=3\,\text{dy}$, $\varepsilon_a=2.26\,\text{cm}$, $\varepsilon_p=4.65°$ and $\varepsilon=3.85\,\text{cm}$. At simulation time $T=3\,\text{dy}$, the proportion of height specified influence is 0.986 if $T_S=1\,\text{hr}$, 0.857 if $T_S=12\,\text{hr}$ and 0.5 if $T_S=3\,\text{dy}$. These results are also an improvement on those of the O-S condition and the modified B&K condition.

Conditions (6.49) and (6.53) certainly provide workable open boundary conditions, given appropriate values of the time scales T_{f*} and T_S. During the transient phase, models employing them allow outward propagation of transient waves and they are more and more accurately driven by height specification for the remaining simulation time. For both conditions, smaller values of T_S correspond to greater influence of the height specified condition.

While these conditions provide a decrease in model error for small values of T_S relative to the O-S and modified B&K conditions, it will be seen in the next section that a reformulation of the O-S condition leads to similar improvement using a much simpler condition.

6.9 Open boundary conditions and forcing

Open boundary conditions in tidal modelling should act as either ingoing or outgoing conditions at any time in a tidal simulation. The ingoing conditions are forced inflow conditions. The outgoing conditions involve both radiation mechanisms and forced outflow conditions. In this section we examine the fact that the forcing role may lead to lagged specification of the forcing term(s), thus contributing to phase error. A simple improvement is proposed.

For an ingoing wave Orlanski sets c to zero in which case the ingoing O-S schemes reduce to (6.20), viz.

$$\zeta_i^{n+\frac{1}{2}}=\zeta_s^{n-\frac{1}{2}}\,. \tag{6.56}$$

This is a lagged height specified condition. A count of the number of times c is set to zero during the operation of the O-S condition in the model of Spencer Gulf was carried out to determine how often the boundary condition behaves as an ingoing condition, and how often as an outgoing condition. The count was conducted over the entire 32 days of simulation and totals were obtained for each consecutive 12 hour period as an average of the results at each boundary element, excluding element #7 of Figure 6.2. Individual element counts were approximately the same except for the easterly count at element #7 which was usually significantly lower and so tends to lower the average. The result for each cycle was then normalized by dividing by the total possible count in a 12 hour period. Normalized results are plotted against 12 hour interval number in Figure 6.11(a) and then each consecutive pair of 12 hourly results is plotted against 24 hour interval number in Figure 6.11(b). Taking the average over the entire simulation shows that the boundary condition behaves as an ingoing condition for 86.9% of the simulation, and for 87.3% of the non-transient modelling time (the last 29 days of simulation). Both figures show that the count value varies with the tidal signal. The semi-diurnal frequency and the spring-neap cycle is clearly evident in Figure 6.11(a). The spring-neap cycle is also clearly evident in Figure 6.11(b).

From (6.56) it is clear that there is a phase lag of Δt for the ingoing aspect of the open boundary condition and this lag operates throughout the tidal simulation. The phase error e so introduced is

$$e \simeq \left(\frac{\Delta t}{43200}\right) 360^\circ \tag{6.57}$$

for a semi-diurnal wave. Using $\Delta t = 150\,\text{sec}$, $e = 1.25^\circ$ for a typical semi-diurnal wave and $e = 0.63^\circ$ for a typical diurnal wave. The average absolute phase error obtained for the O-S model is 4.70° whereas the error from the height specified model is only 4.09° (see Section 6.2). The present model is driven by four major constituents (two diurnal, two semi-diurnal), so a calculation of the error due to the lagging of the forcing terms in the open boundary condition is difficult, but in any case it appears that some of the phase error of the O-S condition can be traced to this lagging error.

Advancing the forcing by one time step the boundary condition can be precisely formulated as an ingoing condition and more correctly formulated as a forced outgoing condition. It is also proposed that only the time derivative approximation of the outgoing condition be forced.

Formally, the suggested ingoing and outgoing combination of conditions is as follows:

- Calculate c in the Orlanski manner:
  1. set $c = 0$ for ingoing waves;
  2. impose inequality (6.19) for outgoing waves.
- Apply the following discretisations:
  1. for ingoing waves, use the height specified condition

$$\zeta_i^{n+\frac{1}{2}} = \zeta_s^{n+\frac{1}{2}}; \tag{6.58}$$

  2. for outgoing waves, use the outgoing condition

$$\zeta_i^{n+\frac{1}{2}} = \frac{\zeta_s^{n+\frac{1}{2}} - (C_x/2)\,\zeta_i^{n-\frac{1}{2}} + C_x\zeta_{i-1}^{n}}{1 + C_x/2}\,. \tag{6.59}$$

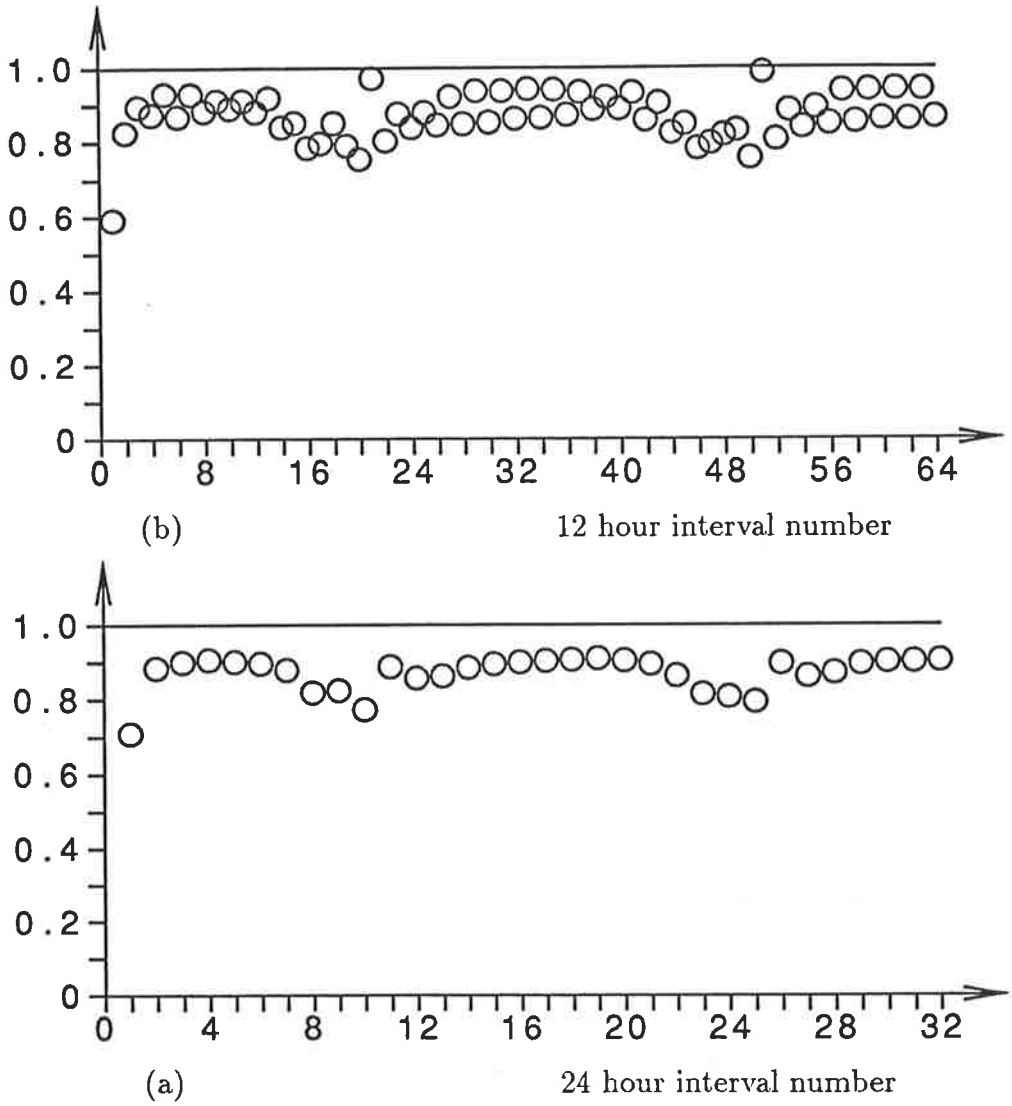


Figure 6.11: *Normalized counts of the occurrence of the zero value for c, calculated in the Orlanski manner, for (a) 12 hr intervals and (b) 24 hr intervals of simulated time. Each circle "○" represents the proportion of times c = 0 in the previous 12 hr or 24 hr period.*

Conditions (6.58) and (6.59) are both expressed by condition (6.59) for programming purposes. The major advantages of (6.59) are that it prescribes the forcing with no time lag and the forcing is contained only in the time derivative approximation and hence is not directly modified by the value of c.

The errors given by the new differencing of the forced O-S condition are $\varepsilon_a = 2.26\,\text{cm}$, $\varepsilon_p = 4.08°$ and $\varepsilon = 3.58\,\text{cm}$. These are slightly better than the benchmark set where $\varepsilon_a = 2.26\,\text{cm}$, $\varepsilon_p = 4.09°$ and $\varepsilon = 3.59\,\text{cm}$. If forcing is included in the space derivative at the new time level the errors are marginally poorer, viz. $\varepsilon_a = 2.27\,\text{cm}$, $\varepsilon_p = 4.09°$ and $\varepsilon = 3.59\,\text{cm}$. If c for outgoing waves is recalculated using $c = \sqrt{gh}$ at each open boundary element there is a further decrease in the error set: $\varepsilon_a = 2.26\,\text{cm}$, $\varepsilon_p = 4.07°$

and $\varepsilon = 3.58\,\text{cm}$.

6.10 Modified B&K conditions, revisited

From the previous section, it is now easy to see why the modified B&K expressions (6.38) and (6.40) perform in such similar fashion to the O-S condition, and why the exponential condition (6.49) and hyperbolic condition (6.53) with small values of T_S and using the differencing of expression (6.51) perform so well.

Taking expression (6.40), the form that applies to ingoing waves is

$$\zeta_i^{n+\frac{1}{2}} = \frac{T_f \zeta_s^{n-\frac{1}{2}} + \Delta t \zeta_s^{n+\frac{1}{2}}}{T_f + \Delta t} \,. \tag{6.60}$$

This differencing is used for approximately 87% of the time in the case of the Spencer Gulf model. For a T_f value of 1 hr, i.e. for $T_f = 24\Delta t$, the numerator and denominator are dominated by the terms in T_f and the expression has the behaviour

$$\zeta_i^{n+\frac{1}{2}} \simeq \zeta_s^{n-\frac{1}{2}}, \tag{6.61}$$

which is approximately the ingoing O-S condition (see condition (6.20)). The corresponding outgoing expression, again for $T_f = 24\Delta t$, behaves as

$$\zeta_i^{n+\frac{1}{2}} \simeq \frac{\zeta_s^{n-\frac{1}{2}}(1 - C_x/2) + C_x \zeta_{i-1}^n}{1 + C_x/2} \,, \tag{6.62}$$

which is approximately the outgoing expression for the O-S condition (6.8). As $T_f \to \infty$ results are increasingly similar to the O-S results. Best results for the modified B&K conditions are obtained for $T_f = 0$ when (6.40) reduces to the height specified condition (6.58) for both ingoing and outgoing waves. Even if T_f is as high as Δt in the case of scheme (6.40), the error set is $\varepsilon_a = 2.26\,\text{cm}$, $\varepsilon_p = 4.37°$ and $\varepsilon = 3.72\,\text{cm}$.

The improvement of schemes (6.42) and (6.44) over schemes (6.38) and (6.40) is only as great as the improvement of (6.22) over (6.8), i.e. slight.

The improvement of the time varying exponential and hyperbolic schemes over (6.38) and (6.40), for small values of T_S, can be deduced from the differencing (6.51) for outgoing waves and (6.52) for ingoing waves. For both outgoing and ingoing flows, when T_S is small, T_{exp} and T_{hyp} are also small and

$$\zeta_i^{n+\frac{1}{2}} \simeq \zeta_s^{n+\frac{1}{2}}. \tag{6.63}$$

This is approximately the correctly timed height specified condition. On the other hand, for larger T_S, T_{exp} and T_{hyp} are larger and the terms $(\Delta t/T_{exp})$ or $(\Delta t/T_{hyp})$ are correspondingly smaller. For $T_{f*} = 6\,\text{hr}$, it can be seen that the ingoing condition, for large T_S, approaches

$$\zeta_i^{n+\frac{1}{2}} \simeq \zeta_s^{n-\frac{1}{2}}, \tag{6.64}$$

the lagged height specified condition. Similarly, for large T_S, the outgoing condition approaches that of the O-S condition. Thus as $T_{f*} \to 0$ errors increase and approach those of the O-S condition.

If the forcing of the O-S term in (6.49) or (6.53) is set at the new time level, one would therefore expect that these time varying conditions would become less sensitive to the value of T_S. This is indeed the case. For the exponentially time varying condition, for $T_S = 12\,\text{hr}$ and for $T_S = 3\,\text{dy}$, the error sets are both as follows: $\varepsilon_a = 2.26\,\text{cm}$, $\varepsilon_p = 4.09°$ and $\varepsilon = 3.58\,\text{cm}$. For the hyperbolic condition, for $T_S = 1\,\text{hr}$, $12\,\text{hr}$ and $3\,\text{dy}$, the three error sets are almost the same. For $T_S = 1\,\text{hr}$, $\varepsilon_a = 2.26\,\text{cm}$, $\varepsilon_p = 4.09°$ and $\varepsilon = 3.58\,\text{cm}$; for $T_S = 12\,\text{hr}$, $\varepsilon_a = 2.26\,\text{cm}$, $\varepsilon_p = 4.08°$ and $\varepsilon = 3.58\,\text{cm}$ and for $T_S = 3\,\text{dy}$, $\varepsilon_a = 2.26\,\text{cm}$, $\varepsilon_p = 4.08°$ and $\varepsilon = 3.58\,\text{cm}$.

All these modified B&K conditions perform no better, in the present case, than the O-S condition with forcing advanced to the new time level and with forcing restricted to just the time derivative approximation, viz. expressions (6.58) and (6.59). Thus since these latter expressions are so much simpler than the various modified B&K expressions they must be preferred on grounds of computational efficiency.

6.11 Second order accurate schemes for the O-S condition

As noted in Section 6.3, the Orlanski discretisation of the forced Sommerfeld equation (6.2) is second order accurate in time but is only first order accurate in space (see equation (6.6)).

To obtain second order accurate space centring, more interior points are used. They enable the definition of an *external* value ζ^n_{i+1} (in the case of the first elevation equation) to third order accuracy. If the *internal* value used in the space derivative approximation is at least third order accurate, then the space derivative differencing will be second order accurate, albeit in only one direction because the open boundary condition itself is uni-directional.

The present numerical scheme is three-level in time. Values are used from each level and ζ^n_{i+1} is expressed as a linear combination of up to six values, the number required to eliminate the zeroth, first and second derivatives in a Taylor expansion. A general approximation is

$$\zeta^n_{i+1} = a\zeta^{n+\frac{1}{2}}_{i-1} + b\zeta^{n+\frac{1}{2}}_{i} + c\zeta^{n}_{i-2} + d\zeta^{n}_{i-1} + e\zeta^{n-\frac{1}{2}}_{i-1} + f\zeta^{n-\frac{1}{2}}_{i} \; . \tag{6.65}$$

Each value on the right hand side is expanded about ζ^n_{i+1} in a Taylor series. To obtain a third order accurate approximation, all coefficients of the zeroth, first and second derivative terms in the expanded form of (6.65) are set to zero. A system of six linear equations in six unknowns is then obtained. When solved, the coefficient of ζ^n_{i-1} is zero, so only five of the points on the right hand side of (6.65) are needed. The solution is

$$\zeta^n_{i+1} = -(3/2)\zeta^{n+\frac{1}{2}}_{i-1} + (3/2)\zeta^{n+\frac{1}{2}}_{i} + \zeta^{n}_{i-2} - (3/2)\zeta^{n-\frac{1}{2}}_{i-1} + (3/2)\zeta^{n-\frac{1}{2}}_{i} \; . \tag{6.66}$$

In a similar way, a third order accurate expansion obtained for ζ^n_{i-1} is

$$\zeta^n_{i-1} = (1/2)\zeta^{n+\frac{1}{2}}_{i-1} - (1/2)\zeta^{n+\frac{1}{2}}_{i} + \zeta^{n}_{i} + (1/2)\zeta^{n-\frac{1}{2}}_{i-1} - (1/2)\zeta^{n-\frac{1}{2}}_{i} \; . \tag{6.67}$$

Equations (6.66) and (6.67) are used to approximate the space derivative to second order accuracy in both space and time and thus produce the following differencing for the

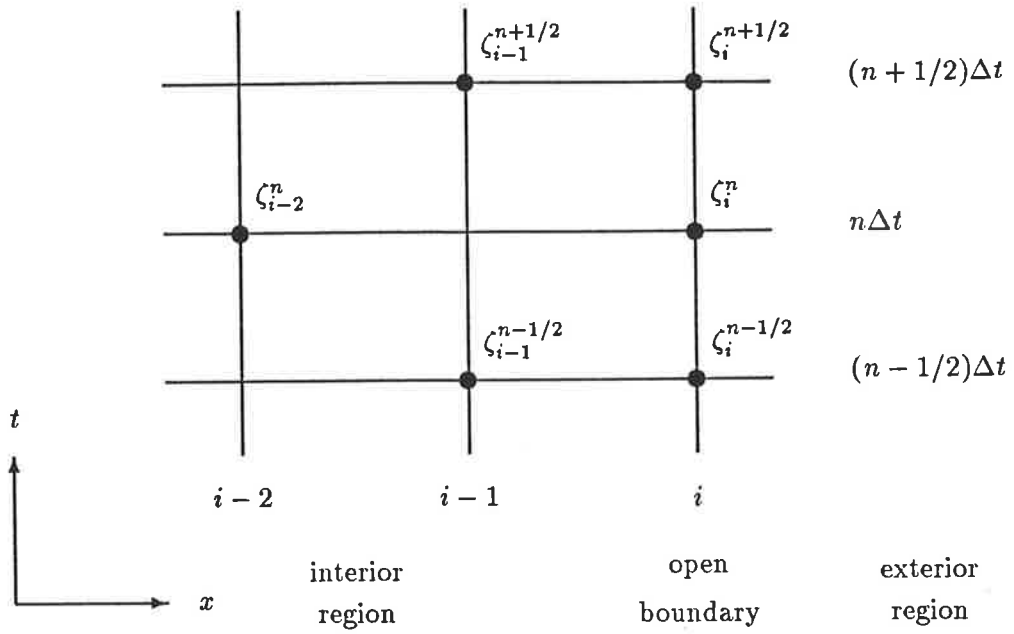


Figure 6.12: *The computational stencil for expression (6.68).*

Sommerfeld equation:

$$\frac{\zeta_i^{n+\frac{1}{2}} - \zeta_i^{n-\frac{1}{2}}}{\Delta t} + \frac{c}{4\Delta x}\left(-2\zeta_{i-1}^{n+\frac{1}{2}} + 2\zeta_i^{n+\frac{1}{2}} + \zeta_{i-2}^n - \zeta_i^n - 2\zeta_{i-1}^{n-\frac{1}{2}} + 2\zeta_i^{n-\frac{1}{2}}\right) = 0\,. \quad (6.68)$$

The computational stencil of this scheme is shown in Figure 6.12. The unforced equation is stable for $C_x \in [0,1]$. If it is assumed that specified values have no error and the equation is forced through the time derivative only through the term $\zeta_i^{n-1/2}$, then (6.68) is stable for $C_x \in [0,0.5]$. If forced through the space derivative at $\zeta_i^{n-1/2}$ as well, it is stable for $C_x \in [0,1]$. Even though greater stability is obtained by providing forcing through the terms $\zeta_i^{n-1/2}$ in both the time and space derivative approximations it is found here, as in Sections 6.5 and 6.7, that when the forcing is provided only through the time derivative better accuracy is achieved.

Thus the forced scheme is chosen to be

$$\zeta_i^{n+\frac{1}{2}} = \frac{\zeta_s^{n-\frac{1}{2}} - \frac{1}{2}C_x\left(-2\zeta_{i-1}^{n+\frac{1}{2}} + \zeta_{i-2}^n - \zeta_i^n - 2\zeta_{i-1}^{n-\frac{1}{2}} + 2\zeta_i^{n-\frac{1}{2}}\right)}{1+C_x}\,. \quad (6.69)$$

Forcing is lagged by Δt, so when $c = 0$ the ingoing condition is the lagged height specified condition. The numerical value of c is calculated from the unforced condition (6.68) using the expression

$$c = -\frac{4\Delta x}{\Delta t}\left(\frac{\zeta_{i-1}^n - \zeta_{i-1}^{n-1}}{-2\zeta_{i-2}^n + 2\zeta_{i-1}^n + \zeta_{i-3}^{n-\frac{1}{2}} - \zeta_{i-1}^{n-\frac{1}{2}} - 2\zeta_{i-2}^{n-1} + 2\zeta_{i-1}^{n-1}}\right). \quad (6.70)$$

The error set obtained using these discretisations is $\varepsilon_a = 2.26\,\text{cm}$, $\varepsilon_p = 4.68°$ and $\varepsilon = 3.86\,\text{cm}$. These results are the same as those obtained using (6.21) which used a first

order accurate space derivative approximation with forcing only in the time derivative approximation. When forcing is included in the space derivative, at $\zeta_i^{n-1/2}$, the error set is $\varepsilon_a = 2.27\,\text{cm}$, $\varepsilon_p = 4.74°$ and $\varepsilon = 3.89\,\text{cm}$. When (6.69) is forced at the new time level, the respective errors improve and are $\varepsilon_a = 2.26\,\text{cm}$, $\varepsilon_p = 4.08°$ and $\varepsilon = 3.59\,\text{cm}$, which is marginally better than the benchmark error set.

The lack of a substantial improvement in performance obtained using a more accurate space derivative discretisation could be due to the possibility that errors in the time discretisation cancel more of the spatial discretisation errors in the lower order method (6.21) (Noye and Hayman, 1986). It may also be partly related to the narrow stability range of scheme (6.69). The local value of Courant number may exceed 0.5 at times in the flow outward across the boundary, due to variations in the value of phase speed c. Such events may be accompanied by short sequences of instability during which inaccurate predictions are generated and included in the overall analysis of results.

In order to check this a count of the number of times the Courant number exceeds 0.5 when using scheme (6.69) with forcing written at the new time level, was performed and is displayed in Figures 6.13. The results are averaged over the number of elements in the boundary line (excluding element #7 of Figure 6.2) and over the total possible count in each 12 hour period in Figure 6.13(a), and in each 24 hour period in Figure 6.13(b). The figures show that the event $C_x > 0.5$ occurs for about 7% of the total model simulation time, so the open boundary scheme does not consistently meet stability requirements.

A search was conducted for schemes satisfying the stability requirement $C_x \in [0, 1]$ for both forced and unforced use, but none was found. The stability of the forced schemes can be increased slightly, but this is accompanied by a reduction in the stability of the unforced schemes as seen in the following example, where instead of using equation (6.67) to replace ζ_{i-1}^n, the value ζ_{i-1}^n itself is used without approximation.

The alternative second order accurate space and time centred differencing for the forced O-S equation is

$$\frac{\zeta_i^{n+\frac{1}{2}} - \zeta_s^{n-\frac{1}{2}}}{\Delta t} + \frac{c}{8\Delta x}\left(-3\zeta_{i-1}^{n+\frac{1}{2}} + 3\zeta_i^{n+\frac{1}{2}} + 2\zeta_{i-2}^n - 2\zeta_{i-1}^n - 3\zeta_{i-1}^{n-\frac{1}{2}} + 3\zeta_i^{n-\frac{1}{2}}\right) = 0. \quad (6.71)$$

This equation is again only forced through the time derivative approximation. When $c = 0$ the ingoing boundary condition is again the lagged height specified condition. The computational stencil for this scheme is shown in Figure 6.14. The scheme is locally stable in the interval $C_x \in [0, 0.503]$. The unforced form of (6.71) is stable for $C_x \in [0, 0.999]$. The explicit expression for $\zeta_i^{n+1/2}$ is

$$\zeta_i^{n+\frac{1}{2}} = \frac{\zeta_s^{n-\frac{1}{2}} - \frac{1}{4}C_x\left(-3\zeta_{i-1}^{n+\frac{1}{2}} + 2\zeta_{i-2}^n - 2\zeta_{i-1}^n - 3\zeta_{i-1}^{n-\frac{1}{2}} + 3\zeta_i^{n-\frac{1}{2}}\right)}{1 + 3C_x/4}. \quad (6.72)$$

The expression for c to be used in (6.72) is taken from the unforced form of (6.71) and is

$$c = -\frac{8\Delta x}{\Delta t}\left(\frac{\zeta_{i-1}^n - \zeta_{i-1}^{n-1}}{-3\zeta_{i-2}^n + 3\zeta_{i-1}^n + 2\zeta_{i-3}^{n-\frac{1}{2}} - 2\zeta_{i-2}^{n-\frac{1}{2}} - 3\zeta_{i-2}^{n-1} + 3\zeta_{i-1}^{n-1}}\right). \quad (6.73)$$

Results using schemes (6.72) and (6.73) show the same errors as schemes (6.69) and (6.70), i.e. $\varepsilon_a = 2.26\,\text{cm}$, $\varepsilon_p = 4.68°$ and $\varepsilon = 3.86\,\text{cm}$. The errors obtained when the schemes

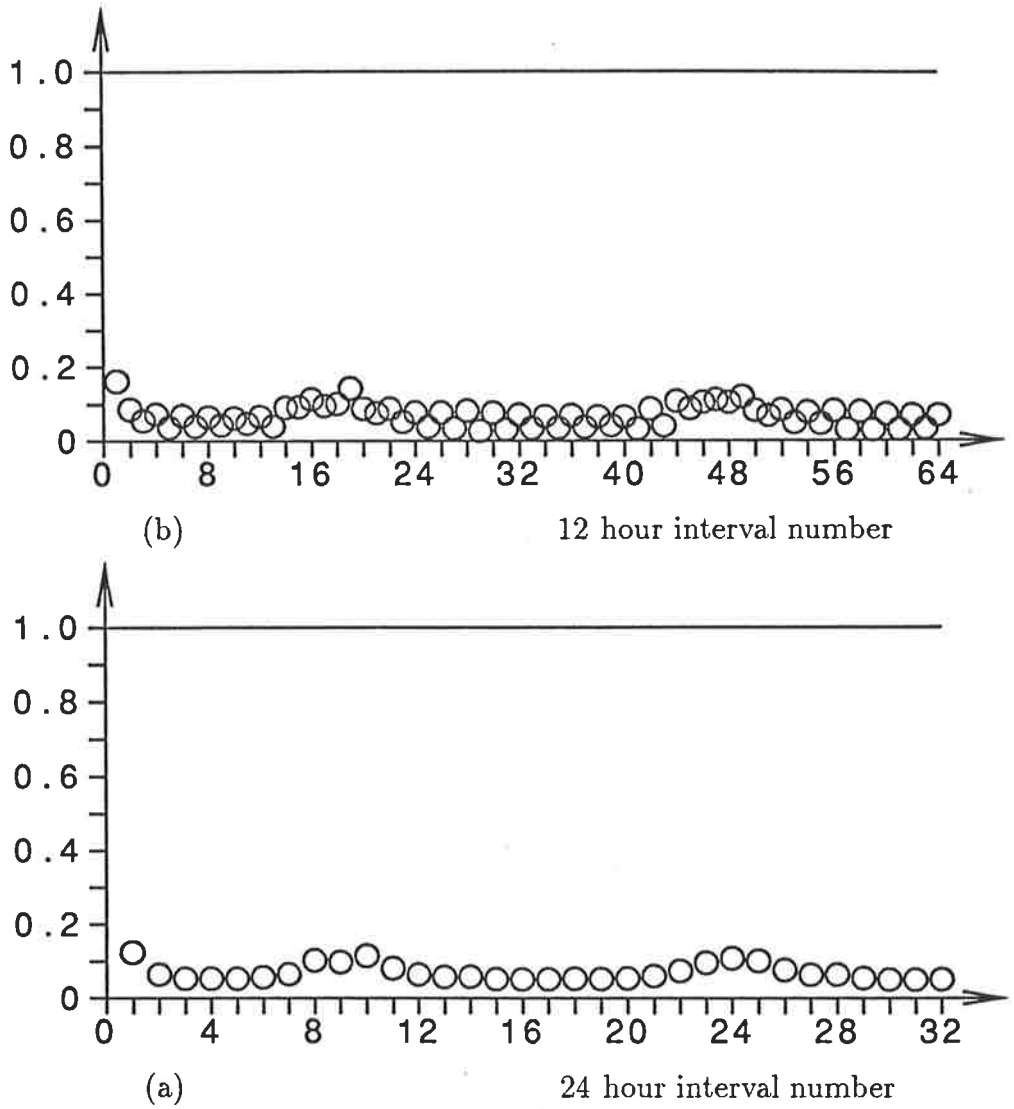


Figure 6.13: *Normalized counts of the occurrence of* $c > 0.5$ *for (a) 12 hr intervals and (b) 24 hr intervals of simulated time, when using scheme (6.69) with forcing written at the new time level. Each circle "O" represents the proportion of times* $c > 0.5$ *for the previous 12 hr or 24 hr period.*

are driven through both derivative approximations are $\varepsilon_a = 2.27\,\text{cm}$, $\varepsilon_p = 4.72°$ and $\varepsilon = 3.88\,\text{cm}$, and the errors obtained when forcing is advanced by Δt in the time derivative, and is removed from the space derivative, are again $\varepsilon_a = 2.26\,\text{cm}$, $\varepsilon_p = 4.08°$ and $\varepsilon = 3.59\,\text{cm}$.

It may be possible to find schemes satisfying the stability requirement $C_x \in [0,1]$ by using more points, or more time levels, or by using an appropriate dynamic weighting of values in schemes like (6.69) as in Noye and Hayman (1986), but the evidence assembled here suggests that the Orlanski first order accurate discretisation of the space derivative is satisfactory.

Vreugdenhil and Booij (1985), in a paper concerning an investigation into the oc-

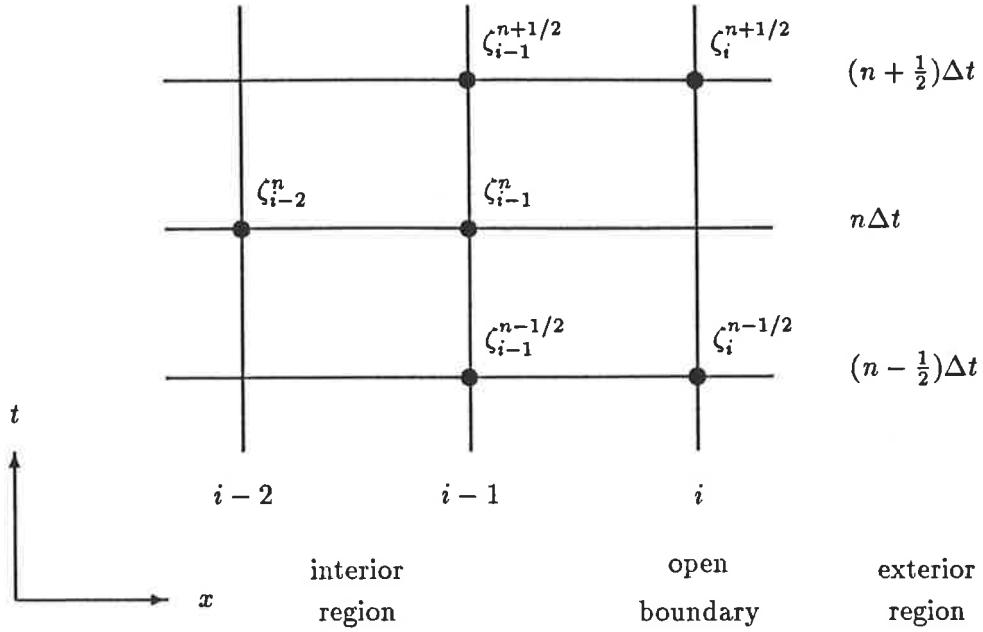


Figure 6.14: *The computational stencil for expression (6.71).*

currence of "wiggles" in the flow pattern near an open boundary, report a result from Gustafsson (1975), viz. that a boundary treatment one order less accurate than internal points will not decrease the overall order of convergence. This seems to be in agreement with the present findings.

Perhaps a more straightforward explanation of the lack of substantial improvement in results using the second order space derivative approximations is found in the fact that in the case of O-S conditions, the differencing used for the space derivative only affects outflow. Improvement in this differencing may reduce reflection of waves at the open boundary, but in any event outflow occurs only 13% of the time during a simulation.

Thus the differencing presented in equations (6.2) and (6.59) is considered adequate.

6.12 Discussion

Open boundary conditions for tidal models must function as forced ingoing or forced outgoing conditions according to the prevailing tidal flow.

Height specified conditions, commonly used in shallow sea tidal models, exhibit both functions and are exact, to the accuracy of the forcing data. They are also unconditionally stable and are not direction-dependent. However for deep water models they may be unsuitable because of their inability to handle the physical modes generated within the model basin in response to the imposed forcing (Arnold, 1987). Such transients are reflected back into the interior basin at the boundary and may grow without bound leading to failure of the model. In shallow sea models these transients are generally quickly damped out.

To overcome this difficulty for deep water models, and for deep and shallow water models with meteorological forcing, various *ad hoc* open boundary conditions employing radiation mechanisms have been developed to allow the transients to move out of the model

basin, and some of the simpler and more popular of these conditions have been examined here. Such conditions are not exact, but by carefully choosing their discretisation, accuracy can be optimised. They may also be discretised so that they are stable for a reasonable range of operational parameters. They are direction-dependent since they only allow the normal component of the outgoing wave to pass through the boundary, but that has not proved to be a liability in the present model, probably because the model axes are aligned with the prevailing flow.

Among these *ad hoc* conditions, the O-S condition performs well. Phase velocity calculation in the Orlanski manner allows the separation of motion into inflow and outflow modes to which appropriate discretisations of the condition are then applied. This separation into inflow and outflow modes mainly accounts for the accuracy of the O-S condition in the present case. Accuracy can be slightly improved by removing forcing from the space derivative approximation. The ingoing form of the O-S condition is the lagged height specified condition. The lagging can be eliminated by specifying the forcing at an appropriate time level. The same can be done for the outgoing form of the condition and doing so does not seem to impair its function as a radiation mechanism.

Chapman (1985), on the other hand, attributes the generally superior performance of the O-S condition in his numerical tests using winds to more accurate calculation of the phase speed for edge waves.

The differencing of the B&K condition, as originally proposed, seems to be inappropriate for use in purely tidal models since it leads to damping of the forcing information to a degree determined by the parameter T_f. The condition combines an unforced Sommerfeld condition with a height specified condition and represents fixed proportions of each. The lack of forcing of the Sommerfeld term results in damping of the specified tidal signal. In this work, the B&K condition was accurate only when the influence of the Sommerfeld term was able to be swamped by the effect of the height specified term — by choosing a very small value for the time scale parameter T_f.

By introducing forcing into the Sommerfeld term, and calculating phase velocity in the Orlanski manner so as to divide motion into inflow/outflow modes, the B&K condition does work for T_f values of the order of several hours. It is now a (fixed) combination of the O-S condition and the height specified condition. Once again, however, best results occur for very small values of T_f and are no better than the results obtained using the O-S condition. The approach of time varying the relative influences of the O-S and height specified conditions works well for the present model. During the transient phase, the O-S condition dominates and helps to remove the initial transients, and during the remainder of the simulation the height specified condition provides accurate forcing without having to deal with starting transients. But again, best results are no better than those obtained using the O-S condition with forcing in only the time derivative, specified at the new time level.

Given the proven usefulness and simplicity of the O-S condition, there seems to be no reason to complicate matters by introducing a modified B&K type scheme. Thus the former scheme is recommended for general use. Meteorological forcing can be just as easily introduced into the O-S scheme, through the forcing terms, as into the B&K schemes.

6.13 Summary

The B&K damped Sommerfeld condition is not an appropriate condition to use in the case of purely tidal forcing. Various modified B&K conditions using Orlanski calculation of phase velocity and including forcing in the Sommerfeld term work for a broad range of values of the time scale parameter T_f but seem unnecessarily complicated in comparison to using the O-S condition.

Thus the O-S condition is recommended for purely tidal modelling in shallow seas if a radiation mechanism is required. Chapman (1985) also recommended it for use as a general outgoing condition in the case of circulation models. In the present case, the success of the O-S condition is attributed mainly to its separation of tidal motions into ingoing and outgoing flows on the basis of which appropriate and accurate discretisations of the condition are applied.

The accuracy of the O-S condition is marginally improved by forcing only the time derivative approximation. Further improvement in accuracy is obtained by deliberately writing the forcing at the "new" time level in both the outgoing and ingoing forms of the condition.

It is possible to construct second order accurate discretisations of the space derivative but model accuracy is not substantially improved.

While the O-S condition with improved discretisations as outlined provides a very slight improvement in model results, compared with the benchmark set, it is evident that the height specified condition is entirely adequate for the present tidal model of Spencer Gulf. This conclusion also follows from the fact that the non-linear constituents in Spencer Gulf, and especially at the open boundary, are relatively weak compared to the four major constituents.

However, it may not be appropriate to use the height specified condition in the more general case of tide and meteorological forcing. For that application, the O-S discretisations developed above will be the subject of further research.

It must be stressed that the results obtained here are for a shallow coastal sea with its open boundary in shallow water. Results may differ for the case of a model of a coastal sea whose open boundary lies in deep water.

In the next chapter, a three-dimensional tidal model of Spencer Gulf will be discussed. Since we are confident in the performance of the height specified condition for Spencer Gulf, the three-dimensional model will be driven using the same height specification as was used to drive the depth-averaged model of Chapter 5.

Chapter 7

A three-dimensional model of Spencer Gulf

7.1 Introduction

The depth-averaged model of Spencer Gulf developed in Chapter 5 is an accurate tool for determining sea level elevations and depth-averaged currents.

In order to determine the vertical current structure, a three-dimensional model of the Gulf based on the finite difference scheme of Chapter 3 is now developed. The same bathymetry and horizontal finite difference grid is used as in the depth-averaged case, and the model is forced along the open boundary using the same set of tide-height constants for the four major constituents.

For the locations of tide-height and tidal current stations and features of Spencer Gulf referred to in this chapter, the reader is directed to Figures 5.10 and 5.15. Unless otherwise indicated, "north" means "up-the-page" and vice versa in the following figures. The positive y-direction of the model is referred to as "north" and this is shorthand for the true orientation of the model, viz. 33° T (or NNE).

7.2 Review of the literature

There is a large body of literature on the subject of the three-dimensional modelling of coastal seas. In this review, only some articles will be reported — these papers consider tide, wind and combined tide and wind forcing on coastal seas.

Noye et al. (1981, 1982) develop a three-dimensional finite difference model for Spencer Gulf. Their model consists of 90 elements in the horizontal and 13 depth levels resulting in 1170 gridpoints for each field of u, v and ω velocity components. The present model uses 761 elements in the horizontal, as for the depth-averaged model of Chapter 5, and 10 depth levels resulting in 7610 gridpoints for each of the u, v and ω components of velocity. Thus a substantial improvement in resolution is achieved in the horizontal by the present model. Along with this, the present model has a more accurate specification of the Gulf's bathymetry and coastline. The three-dimensional model of Noye et al. (1981, 1982) and the present model are the only three-dimensional models of the waters of Spencer Gulf known to the author.

Noye et al. use co-ordinate transformations in all three spatial dimensions, including a

σ-transformation in the vertical, with the result that the Gulf is represented as a unit cube in the transformed domain. The finite difference technique is used to solve the transformed equations on this domain. From Figures 5.7 taken from Noye et al. (1981) it can be seen that the coastline is not well modelled. This is partly because of the small number (15) of transverse sections used and partly because several terms of the transformed equations were omitted in order to achieve a compact set of equations. The omitted terms describe the degree to which each pair of transverse coastal segments is parallel. Unless each pair is nearly parallel the associated terms may not be omitted. Thus the coastal boundary given in Figures 5.7 is stylized and shows broadly parallel transverse segments. If Noye et al. had constructed a model of Spencer Gulf using twice as many transverse sections the resulting need to represent the coastal boundary more accurately may have lead to a violation of the conditions of allowable omission of these terms. Subsequent to this work Stevens and Noye (1984), Noye and Stevens (1987) and Stevens (1990) have outlined a method for including non-parallel coastal segments by means of removing pieces from the computational cube. Using this approach the aforementioned terms may continue to be omitted and the coastal boundary represented accurately.

The explicit finite difference scheme used in the horizontal by Noye et al. (1981, 1982) is forward in time and centred in space — it does not employ the degree of time centredness used in the present scheme. In the vertical a semi-implicit method in the manner of Roberts and Weiss (1966) is used to discretise the vertical eddy viscosity term. If calculations over depth for each spatial position are commenced at the sea bed making use of the bottom boundary condition of zero velocity, the values of velocity at successively higher positions in the water column are found using explicit expressions containing the previously calculated value. It is claimed that the semi-implicit technique "permits the use of relatively large time steps without loss of stability of the finite difference scheme" (Noye et al., 1982, p.425). Results based on simulations of 2–3 days duration are presented for only the M_2 tidal constituent.

Davies and Stephens (1983) solve the three-dimensional non-linear hydrodynamic equations for wind induced flow in a homogeneous sea. In the vertical a σ-transformation is used. The accuracy and computational efficiency (in terms of both computer time and memory requirements) achieved by using given Galerkin and finite difference methods are compared. Davies and Stephens find the Galerkin approach generally "superior" but this conclusion is consequent upon the particular Galerkin and finite difference schemes used and the particular problem solved. Jung et al. (1986) find that two other finite difference methods, one being the present scheme, provide better performance than another Galerkin method chosen.

The variations between the finite difference scheme used by Davies and Stephens (1983) and the present scheme are of interest and noting them will assist in emphasizing the operating details of the present scheme. The scheme used by Davies and Stephens is completely explicit in its calculation of ζ, u, v and w^* (their transformed vertical velocity component); the present scheme is explicit in its calculation of ζ and ω and implicit in its calculation of u and v. Davies and Stephens use forward time approximations throughout whereas the present approach uses time centred approximations as far as possible. In particular, Davies and Stephens do not time centre the vertical eddy viscosity term. Although Davies and Stephens use a variable grid in the vertical and obtain greater accuracy by using finer spacing near both the sea bed and the surface, the variation in thickness of the depth levels is not smooth and the differencing employed at jumps in the

vertical spacing does not seem to take into account the inequality of spacing at the jumps; thus the accuracy of the vertical differencing at the jumps may not be second order in their approach; the present scheme uses a smoothly varying non-uniform vertical spacing of depths levels and the vertical differencing is constructed in such a way as to ensure locally second order accurate calculations.

Wolf (1983) solves the σ-transformed non-linear three-dimensional long-wave equations for tides and wind-driven flow using finite differences in the horizontal and the Galerkin method in the vertical. In order to employ a larger time step than that allowed by using an explicit three-dimensional scheme, the equations are split and the gravity wave terms are treated by an alternating direction implicit (ADI) scheme, while the friction, viscous and advective terms are treated explicitly. The composite "semi-implicit" scheme is compared with a fully explicit scheme in terms of efficiency, accuracy and stability. In tests on rectangular basins with various driving forces the ADI scheme runs stably at higher time steps than the maximum explicit time step but distortions corresponding to grid-scale eddies increasingly appear as the time step is increased.

Wolf applies the scheme to a fine-grid model of the Bristol Channel and allows for wetting and drying banks by incorporating the tidal flats scheme due to Flather and Heaps (1975). The maximum explicit time step is 40 sec. Only the M_2 constituent is modelled and no wind forcing is used. Some problems are encountered with the ADI scheme at closed boundaries and corners and these limit the maximum time step at which the model functions stably. Incorporating tidal flats also tends to destabilise the scheme, limiting the time step to a maximum of 150 sec; removing the flats by artificially increasing MSL by 5 m allows the time step to be increased to 200 sec. A symmetric parabolic vertical eddy viscosity form is used, viz.

$$F(s) = -3.6s^2 + 3.6s + 0.1\,, \tag{7.1}$$

where $s = (z + h)/(\zeta + h)$ is the relative depth and is related to the variable η of the present model by $s = 1 - \eta$. The value of vertical eddy viscosity at level s is calculated from

$$N_s = kH\,F(s)\sqrt{U^2 + V^2}, \tag{7.2}$$

where k is a dimensionless calibration constant. In the formulation for $F(s)$ it can be seen that the surface and bed friction values are 10% of the maximum value, which occurs at mid-depth.

Davies (1985a) σ-transforms the linearized tidal equations and improves the finite difference approach used in Davies and Stephens (1983) by employing vertical grid layers thin enough to accurately resolve high shear near the bed and surface (and across the thermocline). However, once again the thickness of the vertical spacings is set by hand and contains discontinuities (halving/doubling) in the spacing variation at some levels rather than a smooth variation of spacings. The momentum equations are split into two sets, one describing the mean flow (the external mode) and the other describing the deviations from mean flow (the internal mode). Solution for the external mode is achieved economically using an explicit scheme, but semi-implicit differencing (c.f. the semi-implicit approach of Noye et al. (1981, 1982)) is used for the internal mode calculations.

Davies (1985a) suggests that because tidal currents do not fall to zero at the surface as at the sea bed, and remain approximately constant in the upper part of the water

column, the tidally specified eddy viscosity ought not to fall to zero at the sea surface and may remain "fairly constant" above the bottom boundary layer. However it is clear that surface currents fall to zero at predictable times during the tidal cycle. In the present tidal work it will be seen that parabolic eddy viscosity coefficients which fall to small values at the sea surface and sea bed generate physically reasonable velocity profiles. The closer the surface and bed viscosity values approach molecular viscosity the more accurate are the model predictions of tide height compared with tide-height observations for Spencer Gulf. As the surface and bed vertical eddy viscosity values are lowered the resolution of depth levels in the near boundary regions should be correspondingly refined. It will be shown that using molecular viscosity at the surface and bed together with a correspondingly increased vertical resolution of the nearby regions gives rise to optimal results for the three-dimensional Spencer Gulf tidal model.

The present three-dimensional program or its current field predictions have been used by various authors in recent years:

(1) Mitchell and Noye (1983) and Mitchell et al. (1984) have used it to develop a three-dimensional tide and wind-driven model of the Gulf of Carpentaria. These authors use a depth-integrated model over a region incorporating the Arafura Sea, the Gulf of Carpentaria and Torres Strait in order to establish open boundary information for the three-dimensional model of the inner region comprising the Gulf of Carpentaria. There are insufficient tidal records with which to directly establish open boundary information for a model of the Gulf of Carpentaria alone, but there are ample for the larger depth-integrated model. The three-dimensional model is not dynamically nested inside the depth-integrated model. Using the four major tidal constituents O_1, K_1, M_2 and S_2 for both models, excellent agreement is achieved in predicted amplitude and phase of the resulting tide in the region common to both. This agreement is facilitated by the fact that the inner three-dimensional model uses the corresponding gridpoints and bathymetry of the outer model.

(2) Arnold and Noye (1986b) use the present program to develop a three-dimensional tide and wind-driven model of Bass Strait which lies between mainland Australia and Tasmania. It is the first three-dimensional model of that region. (Fandry (1983) presented "depth-dependent" results for the tidal and wind-driven motion of Bass Strait but these were derived from a depth-averaged model.)

(3) Depth-dependent velocity fields obtained from the Spencer Gulf model developed in this chapter have been used by I'Anson (1989) in an inaugural study of prawn post-larvae movement in Northern Spencer Gulf, and

(4) in a succeeding study of the same processes conducted by Wong (1990).

(5) Presently Nixon (1992) is engaged in further extensions of this application of the model and has already modified the numerical scheme in order to achieve vector processing speeds on a Cray supercomputer.

7.3 Calibration of the model

The same set of open boundary data is used to drive the three-dimensional model of Spencer Gulf as is used for the depth-averaged model. The same bathymetric data set

is also used. The values of the coefficients of horizontal eddy viscosity are calculated as for the depth-averaged model of Chapter 5 — using the Schwiderski formulation with the reduced eddy coefficient set at $a = 0.0055\,\mathrm{cm}^2/\mathrm{sec}$. No calibration of the coefficient a is attempted here since, based on the experience of its calibration for the depth-averaged model, its variation is unlikely to be of significant effect.

The value of the time step used is $\Delta t = 180\,\mathrm{sec}$, at which the numerical scheme is stable. This is 20% greater than the value used in the depth-averaged model, and is so chosen to minimize the computer processing time for the three-dimensional model. The program for the three-dimensional model uses approximately 18 hours of processing time to complete a 32 day simulation on a DEC VAX 11/785 — using $\Delta t = 150\,\mathrm{sec}$ would require 21.6 hours.

In the present work, closure in the vertical is achieved by specifying a parabolic vertical eddy viscosity coefficient.

Closure using the so-called "turbulent energy" $(K-\varepsilon)$ method is not investigated here. In that approach, separate equations are written to describe the turbulent kinetic energy and the dissipation of such energy, from which a dynamic estimate for the vertical eddy viscosity coefficient as a property of the flow is sought. This approach promises more accurate modelling of vertical turbulence but does so at the cost of increases in computer processing and memory requirements. Noye and Stevens (1987) claim the time and storage required increases by nearly 30%. These increased costs would be significant in the case of our VAX 11/785. In addition, there is a particular numerical problem associated with the turbulent energy approach, viz. that the additional quantities modelled (turbulent kinetic energy K and the dissipation of turbulent energy ε) must be computed in a positive definite manner. Numerical schemes that produce negative predictions for K or ε at any stage of a simulation cannot be tolerated. This "can occur at times when the values of K and ε are very small" (Noye and Stevens, 1987, p.43). There are also certain parameters that must be specified "a priori" in $K-\varepsilon$ modelling, as well as many simplifying assumptions used in order to make the solution process reasonably tractable, so it is not to be supposed that the need to specify some parameters of the flow is eliminated by using the turbulent energy approach. On the other hand, parameters such as "roughness length" and "mixing length" have physical meaning.

The literature on $K-\varepsilon$ modelling is rapidly growing. Mellor and Yamada (1974) have sought to establish a hierarchy of turbulent models for planetary boundary layer modelling. Johns (1978) has developed a turbulence energy closure scheme to evaluate the flow in an elongated channel approximating the Thames. Mellor and Yamada (1982) have summarised much of their work in $K-\varepsilon$ modelling since 1973 and give a comprehensive list of $K-\varepsilon$ and related papers. Blumberg and Mellor (1983) have imbedded a turbulence closure submodel in their circulation study of the South Atlantic Bight. Arnold and Noye (1984) and Arnold (1985) have successfully used the $K-\varepsilon$ approach in one and two spatial dimensions. Blumberg (1987), Johns and Oguz (1987) and Davies and Jones (1990) have applied the technique to three-dimensional models of coastal seas.

The vertical eddy viscosity coefficient used in the present work takes the form (2.18), viz.

$$N_\eta(x,y,\eta,t) = \alpha + \beta F(\eta) H \sqrt{U^2+V^2}, \tag{7.3}$$

where α and β are constants to be fixed by calibration and $F(\eta)$ is some prescribed vertical variation of the coefficient. From among the many possible choices for this variation, the

parabolic form of Figure 4.21 is chosen, viz.

$$F(\eta) = \gamma_1 \left(1 + 4\eta(1-\eta)\left[N_{\max}/\gamma_1 - 1\right]\right), \quad \gamma_1 \neq 0, \quad \eta \in [0,1], \tag{7.4}$$

for tide only flows. Here, $F(\eta)$ achieves a maximum $N_{\max}$ at mid-depth and has minima γ_1 at both the sea bed and sea surface. This is the form used by Wolf (1983), and is cited by both Johns (1969) and McGregor (1972) as being capable of producing a logarithmic variation of horizontal current for tidal flow. If $\gamma_1 = 0$, the vertical variation is described by

$$F(\eta) = 4N_{\max}\eta(1-\eta). \tag{7.5}$$

Cooper and Pearce (1977) state with respect to the variation of vertical eddy viscosity N_V: "Thus it is concluded that a realistic variation for N_V would be a shape with N_V near zero at the surface and the bottom and a maximum somewhere in between. ... If ... it is assumed that N_V varies parabolically (zero at the surface and the bottom) then the solution for the velocity is a logarithmic profile near the surface and the bottom. Intuitively this ... seems ... correct, since one would expect the velocity to exhibit a logarithmic profile near the surface and the bottom. This intuition is substantiated by laboratory experiments performed by Shemdin (1972)" (ibid., pp.20–21).

Noye and Stevens (1987) state: "Based on a series of numerical experiments using a turbulent kinetic energy ($K - \varepsilon$) closure scheme in typical tidal situations, Noye and Arnold [1987] have shown that a suitable form for N_z is one which depends upon the volume of water transported per unit width and varies quadratically with depth. ... This is a similar result to that used by Cooper and Pearce [1977] and Nihoul [1978] based on the physical structure of tidal currents" (ibid., p.43).

The choice (7.4) differs from that used by Noye et al. (1981, 1982) and Noye and Stevens (1987) in that although they also specify a parabolic variation, maximum eddy viscosity for their formulation occurs at level $\eta = 0.25$. For values of the constants α and β, Noye et al. use $\alpha = 0.0005\,\mathrm{m}^2/\mathrm{sec}$ and $\beta = 0.010$. Mitchell et al. (1984) also use the formulation (7.3) and the same parabolic form as do Noye et al. (1981, 1982). They arrive at values for α and β by numerical experimentation: minimizing the errors between predicted and observed tide-height constants for tide-height stations within the Gulf of Carpentaria they obtain $\alpha = 0.0001\,\mathrm{m}^2/\mathrm{sec}$ and $\beta = 0.0033$.

In the present model, the Kappa method is used to set the spacing of the 10 grid levels in the vertical. In order to accurately extrapolate for the surface velocity values, as well as to accurately resolve the steep gradient of the horizontal velocity components near the sea bed, the vertical grid level spacing follows the fine-coarse-fine pattern described in Chapter 3.

The value of $N_{\max}$ used is immaterial. Following the work of Chapter 4 it is set as

$$N_{\max} = 0.2\,\mathrm{m}^2/\mathrm{sec}. \tag{7.6}$$

Whatever the value of $N_{\max}$ chosen, the optimal value of β is adjusted accordingly. The value of α may be regarded as a "background" level of vertical eddy viscosity so it may not be set to zero.

Initially α is set at $0.0005\,\mathrm{m}^2/\mathrm{sec}$, β at 0.010 and γ_1, from the work of Chapter 4, is set at $0.002\,\mathrm{m}^2/\mathrm{sec}$. The results for the combined error measure (henceforth called the "calibration error") for six integer values of κ, the parameter governing the relative vertical

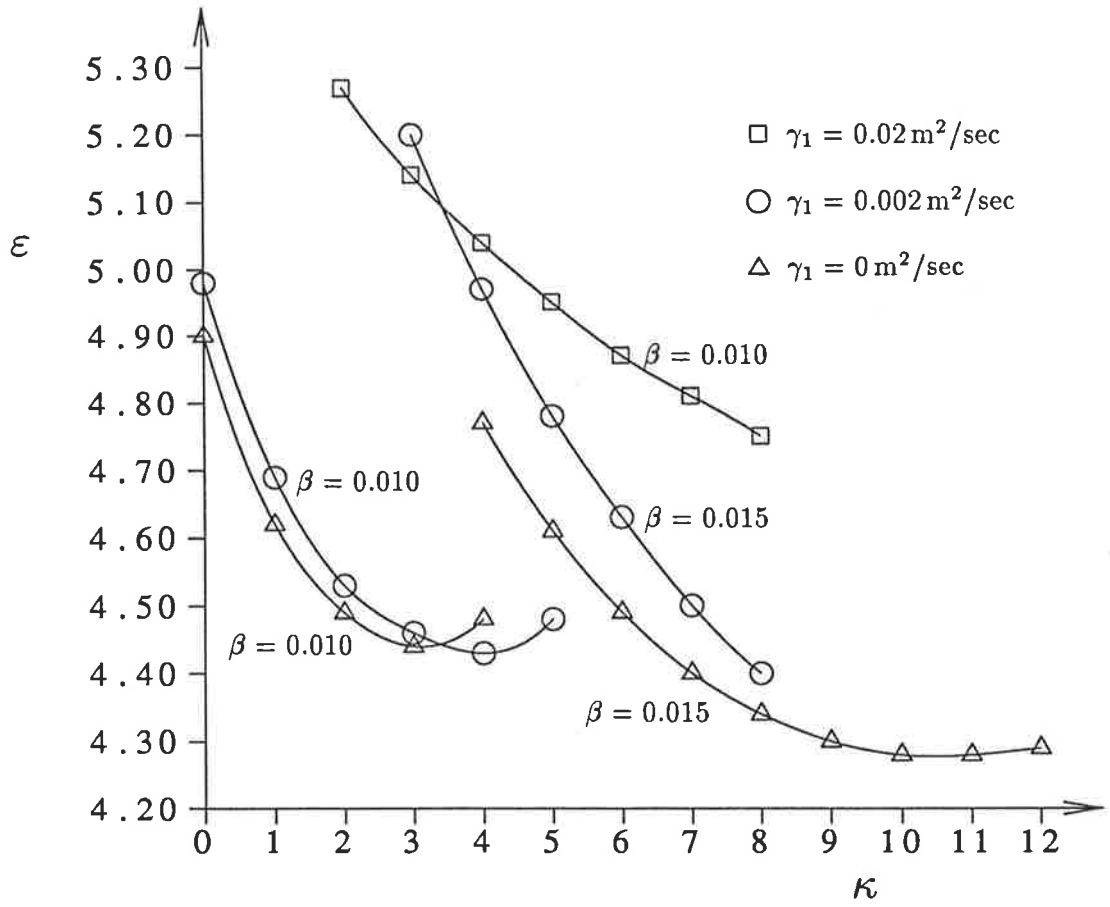
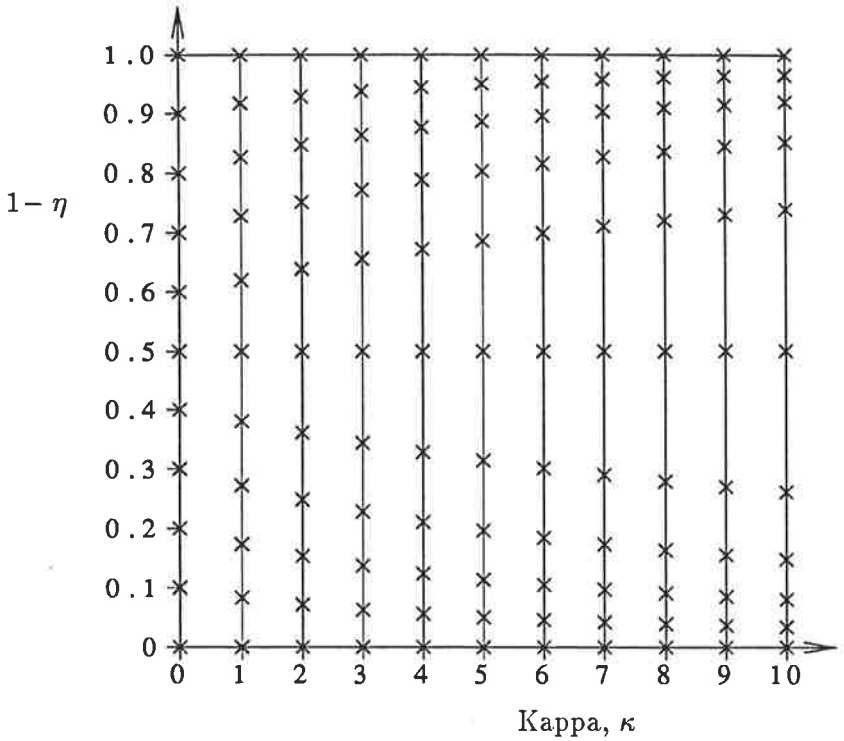


Figure 7.1: *Calibration error ε (cm) plotted against κ. For each of these curves the "background" value of vertical eddy viscosity is $\alpha = 0.0005\,m^2/sec$. Curves marked with squares "□" correspond to program runs with $\gamma_1 = 0.02\,m^2/sec$, curves marked with circles "○" correspond to runs with $\gamma_1 = 0.002\,m^2/sec$ and curves marked with triangles "△" correspond to runs with $\gamma_1 = 0\,m^2/sec$. The values of β used for each set of runs are as marked.*

spacing, are plotted in Figure 7.1 — as the curve on the left with circles "○" marked on it. The circles mark the computed values and the solid curve simply connects these values. The value $\kappa = 4$ returns the least error. The model is unstable for $\kappa = 6$. Keeping α and γ_1 fixed, the value of β is increased to 0.015 and the calibration errors for another range of integer values of κ are plotted and appear as the curve marked with circles "○" to the right. In this case, it is evident that least error (if it exists) will occur for a value of κ greater than eight but we will see that such large values of κ give very little resolution at mid-depths, so no further values of κ are tested.

The procedure used to obtain the calibration error is the same as that used for the depth-averaged model; the calibration is performed by comparing predicted and observed tide-height constants — no velocity data was used because at the time tidal current constants were only available at two stations: Mike and the upper meter at Lima (see Figure 5.10).



Values of η when $\kappa = 5.0$	
k	η
0	0.000000
1	0.050378
2	0.113446
3	0.196401
4	0.313765
5	0.500000
6	0.686235
7	0.803599
8	0.886554
9	0.949622
10	1.000000

Figure 7.2: *Kappa grids: the cross marks "×" on the vertical lines at each integer value of κ mark the relative positions of the depth levels for that κ value. Only 11 depth levels, including the surface and bed levels, are used in the model. The structure of each Kappa grid is fine-coarse-fine symmetrically about mid-depth. On the right is a table of values for relative depth η when $\kappa = 5.0$. The k values number the depth levels from the surface downwards in the direction of increasing η value.*

The influence of κ on the depth level spacings is shown in Figure 7.2 where the positions of the 11 depth levels are plotted for 11 integer values for κ. As κ increases there is a crowding of levels near the bed and the surface and less information is conveyed about the mid-level flow. Perhaps a reasonable spacing of the 11 levels is that obtained at the value $\kappa = 5$.

The calibration errors obtained with the parameters used so far are not less than 4.40 cm (for $\kappa \leq 8$) and are significantly larger than the 3.49 cm error recorded by the optimal depth-averaged model (see Table 5.6).

Increasing the value of γ_1 to $0.02\,\mathrm{m}^2/\mathrm{sec}$ while keeping α at $0.0005\,\mathrm{m}^2/\mathrm{sec}$ and β at 0.010 raises and flattens the calibration error curve, suggesting that γ_1 should be decreased instead. The curve corresponding to these parameters is the top-most curve in Figure 7.1 and has squares "□" marked on it. No values of κ greater than eight were tried for this set of runs.

Reducing γ_1 to zero for $\beta = 0.010$ and $\beta = 0.015$ gives only slight improvement in calibration error over that obtained using $\gamma_1 = 0.002\,\mathrm{m}^2/\mathrm{sec}$. The curves corresponding to these parameters are those with triangles marked on them. In the case of $\beta = 0.010$ the model is unstable for $\kappa = 5$. For $\beta = 0.015$ the model is stable for κ large enough to demonstrate that a minimum is achievable — in this case, at $\kappa = 11$ (see Figure 7.1).

All the plots of Figure 7.1 use $\alpha = 0.0005\,\mathrm{m}^2/\mathrm{sec}$. They demonstrate that smaller calibration errors are achieved for the least possible value of γ_1, viz. $\gamma_1 = 0\,\mathrm{m}^2/\mathrm{sec}$ for a fixed value of β. Increasing β also reduces the calibration error but κ must also be increased.

Let us now experiment with the value of α. Reducing α to $0.0001\,\mathrm{m}^2/\mathrm{sec}$, error curves with significantly reduced minima are obtained for both $\beta = 0.010$ and $\beta = 0.015$. These curves are given in Figure 7.3 as those with circles "O" marked on them. The curve to the left corresponds to $\beta = 0.010$; the model is unstable at $\kappa = 4$ for this set of runs. The curve to the right corresponds to $\beta = 0.015$ and achieves a minimum at $\kappa = 6$.

It seems reasonable to further reduce α to the theoretically smallest value that background vertical eddy viscosity may take, viz. molecular eddy viscosity which is approximately $1.4\times10^{-6}\,\mathrm{m}^2/\mathrm{sec}$. Tee (1979, 1987) uses a bed viscosity value of $1.4\times10^{-6}\,\mathrm{m}^2/\mathrm{sec}$. Taking $\alpha = 1.4\times10^{-6}\,\mathrm{m}^2/\mathrm{sec}$ and $\gamma_1 = 0\,\mathrm{m}^2/\mathrm{sec}$, a series of computer runs using values of β ranging upward from $\beta = 0.010$ to $\beta = 0.025$ are made. For each β value a set of runs using a small range of integer values of κ is used to obtain the corresponding minimum error, except for $\beta = 0.025$ for which $\kappa = 13$ is the highest value of κ used. The resulting calibration error curves, displayed in Figure 7.3 and marked with triangles "$\triangle$" show minima decreasing as β increases.

Because the vertical eddy viscosity coefficient (3.19) is formulated in terms of depth-averaged current, the effect of increasing the value of β is to make the three-dimensional solution more two-dimensional. It is not known whether a global minimum exists for β in the envelope of minimum error values obtained for $\alpha = 1.4 \times 10^{-6}\,\mathrm{m}^2/\mathrm{sec}$ in Figure 7.3. If it does it corresponds to $\kappa \geq 13$. (Increasing κ gives better resolution of flows near the sea bed and hence improves the bottom friction effect.) It seems more likely the envelope approaches a horizontal asymptote representing the optimal response of the model for the number of depth levels used. Using the present number of depth levels (11) it seems unlikely that the three-dimensional model can achieve as small an error value as was obtained for the optimal depth-averaged model of Chapter 5. Increasing the number of depth levels should lead to a smaller error value, probably at a lower value of κ for a given value of β. This has not been done because of the increased computational time implied for individual runs but clearly good resolution of the near-bed layer is vital in the present situation where bed friction is important and a no-slip condition is used. For tide-driven flows, it may be possible that a fine-to-coarse grid spacing, from the sea bed to the surface, will achieve improved accuracy using the present number of grid levels. This has also not been tried. Such a vertical spacing would of course not be appropriate for wind and tide-driven flows where high resolution near the surface is required.

To illustrate what happens as α is increased, the value $\alpha = 0.05\,\mathrm{m}^2/\mathrm{sec}$ was tried with $\gamma_1 = 0\,\mathrm{m}^2/\mathrm{sec}$ and $\beta = 0.015$ for both $\kappa = 5$ and $\kappa = 6$. The calibration errors returned were both in excess of 21 cm and the corresponding tide elevation signals were very strongly damped.

From the curves of Figures 7.1 and 7.3 it seems that the (α, β, γ, κ) selection giving rise to the least calibration error must be associated with very high κ values. A selection of parameters which gives a reasonably low calibration error and good spread of information in the vertical is chosen as:

$$\alpha = 1.4 \times 10^{-6}\,\mathrm{m}^2/\mathrm{sec},\quad \beta = 0.015,\quad \gamma_1 = 0\,\mathrm{m}^2/\mathrm{sec},\quad \kappa = 5. \tag{7.7}$$

The grid value $\kappa = 5$ gives almost the minimum error value when $\beta = 0.015$, $\alpha = 1.4 \times$

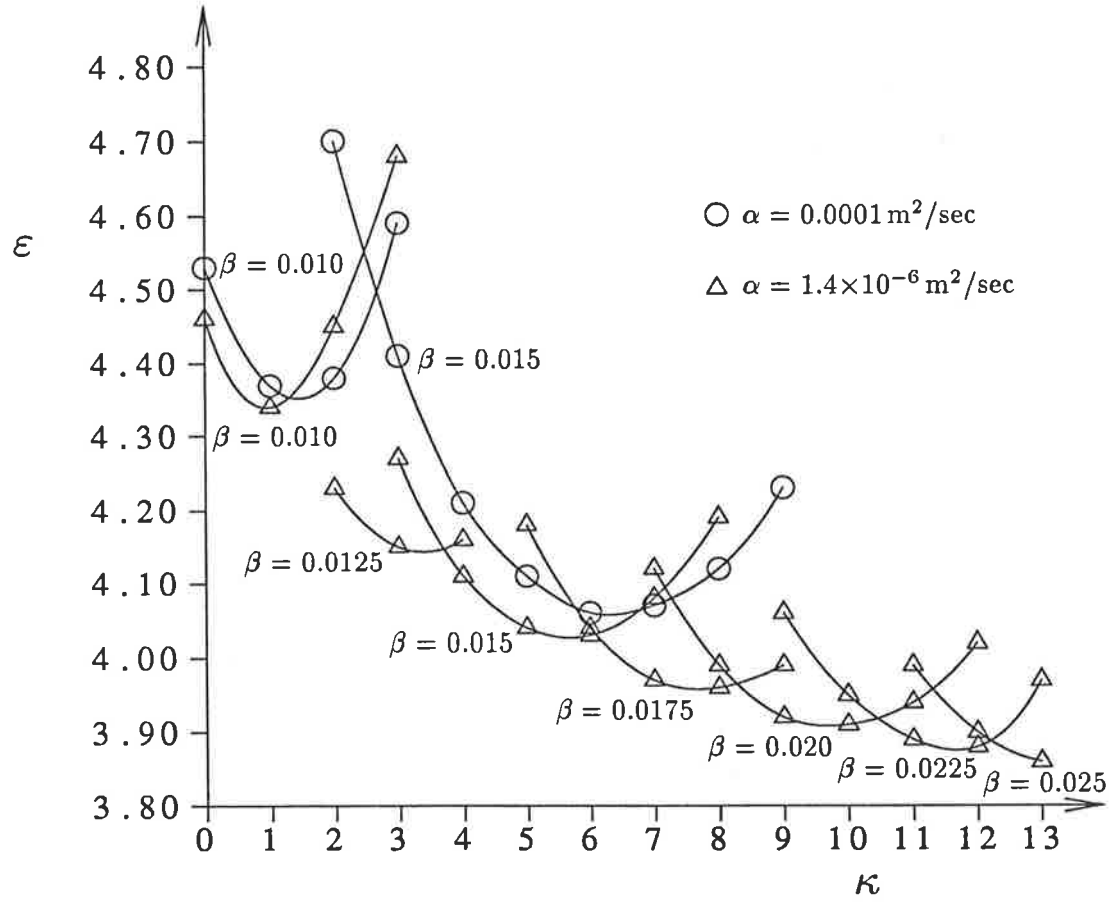


Figure 7.3: *Calibration error ε (cm) plotted against κ. For each of these curves $\gamma_1 = 0\,m^2/sec$. Curves marked with circles "○" correspond to program runs with a background vertical eddy viscosity of $\alpha = 0.0001\,m^2/sec$ and curves marked with triangles "△" correspond to runs with $\alpha = 1.4\times10^{-6}\,m^2/sec$. The values of β used for each set of runs are as marked.*

$10^{-6}\,m^2/sec$ and $\gamma_1 = 0\,m^2/sec$. Results from the three-dimensional model presented in this chapter use these parameter values.

Further experimentation using the parameters α, β and κ with more depth levels and other functional forms of the vertical variation of eddy viscosity is possible but, as already stated, is not carried out here because of the costs in terms of computer processing time. The experiments reported here involve 77 runs of the program and represent more than three months of real time using the VAX 11/785, remembering that the machine is also used for undergraduate teaching and for research by other research students and staff. But similar work in the future need not take so long partly because having done it once we now know how it is likely to proceed. As well, since this work was done computing speeds have increased at least four-fold on machines such as the SUN SPARCstation 1+ available to the "ordinary" research user. The benefits of conducting such calibrations are clear and they ought to be conducted as far as is necessary with each new application of the tidal program.

As mentioned at the start of this section the value $\Delta t = 180\,\text{sec}$ is used for the three-dimensional model runs. For comparison, a model run using the value $\Delta t = 150\,\text{sec}$ together with the parameter values (7.7) was made and, while there were slight differences in the tide-height constants predicted for some of the calibration stations, the overall calibration error was the same to three significant figures, viz. 4.02 cm.

It is evident that the three-dimensional model of Spencer Gulf is no less stable than the depth-averaged model. It also produces accurate answers within the bounds of its stable operation, as does the depth-averaged model.

7.4 Presentation of results and discussion

Using parameter set (7.7) model predictions are obtained for 15 stations in Spencer Gulf. Table 7.1 compares predicted and observed tide-height constants at each of these stations. The predictions may also be compared with those of Table 5.6 for the optimal depth-averaged model. Overall the predictions of the depth-averaged and three-dimensional models are very similar, with results from the latter being slightly poorer.

The contour plots of amplitude and phase for the four major constituents in Figures 7.4–7.7 are also in close agreement with the corresponding Figures 5.22–5.25 of the depth-averaged model. The relatively uniform amplification of the diurnal tide as it travels up the Gulf is predicted by both models (compare Figures 5.22(a) and 7.4(a), and Figures 5.23(a) and 7.5(a)). The major differences between the diurnal and semi-diurnal plots reflect the differences in the error summary "Ave. absolute differences" at the bottom of Tables 5.6 and 7.1. The average absolute amplitude differences in M_2 and S_2 are very small and there is strong agreement between the corresponding amplitude contours, Figures 5.24(a) and 7.6(a) and Figures 5.25(a) and 7.7(a). The location of zones of minimum amplitude in M_2 and S_2 predicted by the depth-averaged model in the vicinity of Wallaroo on the east coast is also predicted by the three-dimensional model, as is the rapid amplification of the semi-diurnals north of Wallaroo. The semi-diurnals are again shown to be approximately 180° out of phase between the mouth and the head of the Gulf (compare Figures 5.24(b) and 7.6(b) and Figures 5.25(b) and 7.7(b)).

Figures 7.8–7.11 are the depth-averaged tidal current ellipses derived from the three-dimensional model for the four major constituents. They show strong agreement with Figures 5.26–5.29 of Chapter 5. The 29-day velocity and elevation residuals of Figures 7.12 and 7.13, respectively, also compare well with Figures 5.36(b) and 5.37(b) of the depth-averaged model. In particular the same residual gyres appear in Figure 7.12 as are found in Figure 5.36(b). The same lowering of the sea surface on the western coast opposite Wallaroo corresponding with the large trans-Gulf residual gyre of Figure 7.12 appears in Figure 7.13 as in Figure 5.37(b). This lowering of sea surface in association with residual eddies is noted by Pingree and Maddock (1977b).

Thus the three-dimensional model reproduces the depth-averaged characteristics of the Gulf faithfully. This is a primary check on the consistency of the program code between the two models. It is also a basic check on the adequacy of the vertical eddy viscosity formulation chosen — if the formulation had been such that the depth-averaged predictions from the three-dimensional model differed markedly from those of the depth-averaged model of Chapter 5, then the choice of formulation would have to be reconsidered. It is possible that other formulations for the vertical eddy viscosity can lead to similar performance of the three-dimensional model in generating depth-averaged results.

Observation station		O_1 amp	O_1 ph	K_1 amp	K_1 ph	M_2 amp	M_2 ph	S_2 amp	S_2 ph
*Port Augusta	Pred.:	38.6	48.4	47.9	79.9	60.9	204.6	64.2	263.3
	Obs.:	28.3	52.8	44.0	82.7	64.0	212.2	68.6	272.3
Beacon #5	Pred.:	37.8	47.9	47.0	79.3	57.3	203.2	59.9	261.9
	Obs.:	25.0	48.1	47.0	73.4	57.9	196.0	62.0	255.2
*Port Pirie	Pred.:	36.1	47.9	45.1	79.1	48.1	201.9	49.5	260.8
	Obs.:	27.6	49.2	42.5	77.4	48.9	197.2	52.9	258.3
Port Bonython	Pred.:	35.0	45.1	43.9	75.8	43.4	194.3	44.0	252.7
	Obs.:	27.0	42.7	41.6	70.6	45.1	185.3	48.6	245.6
Whyalla	Pred.:	34.9	44.5	43.8	75.2	42.9	192.9	43.5	251.2
	Obs.:	25.7	45.2	40.1	72.8	42.1	184.5	45.4	245.2
Yarraville Shoals	Pred.:	32.7	43.4	41.3	74.0	33.5	187.7	32.9	245.6
	Obs.:	24.4	39.2	37.2	69.8	32.2	175.5	33.9	236.9
*Port Broughton	Pred.:	31.3	46.4	40.1	77.2	26.8	192.4	25.3	250.3
	Obs.:	17.4	100.9	27.8	110.4	15.8	214.8	15.2	275.4
Wallaroo	Pred.:	25.7	38.6	34.7	69.0	12.3	144.4	10.5	185.8
	Obs.:	21.8	33.3	32.7	61.9	17.1	132.3	16.8	187.1
*Franklin Harbour	Pred.:	23.5	16.1	33.3	46.3	24.6	86.0	26.3	132.9
	Obs.:	20.0	34.0	30.0	61.0	22.0	114.0	23.0	173.0
Arno Bay	Pred.:	21.7	12.2	31.0	42.4	25.0	69.2	27.4	117.2
	Obs.:	19.9	8.4	29.5	37.4	25.6	66.6	26.8	120.1
Port Victoria	Pred.:	18.8	28.3	26.8	58.9	17.4	61.6	20.8	110.1
	Obs.:	16.9	20.7	24.5	51.5	18.9	61.9	20.3	116.4
Port Neill	Pred.:	20.4	9.0	29.1	38.9	24.9	57.9	27.5	106.7
	Obs.:	20.8	5.3	30.8	36.2	28.6	56.1	31.2	112.1
Port Turton	Pred.:	17.8	29.1	25.3	60.0	17.8	58.5	21.2	108.9
	Obs.:	16.0	22.9	23.4	51.7	18.4	60.6	19.5	115.1
Port Lincoln	Pred.:	17.6	1.1	25.0	29.7	24.2	33.3	26.1	83.3
	Obs.:	16.7	0.9	24.0	27.4	24.1	32.4	26.2	85.5
Wedge Island	Pred.:	15.0	6.5	20.8	35.8	16.2	24.5	16.8	75.2
	Obs.:	15.1	6.6	21.0	36.3	16.6	24.1	17.1	74.4
Ave. absolute differences:		4.45	3.13	1.88	4.71	1.46	5.19	2.06	4.88
Ave. complex differences:		4.85		3.48		3.77		3.98	

Table 7.1: *Comparison of predicted (Pred.) and observed (Obs.) amplitude (cm) and phase (deg, C.S.T.) for the four major tidal constituents at 15 stations in Spencer Gulf. These predictions are generated with the three-dimensional model using* $\alpha = 1.4 \times 10^{-6}\ m^2/sec$, $\beta = 0.015$, $\gamma_1 = 0\ m^2/sec$, $\kappa = 5$ *and the symmetric parabolic vertical eddy viscosity profile, and may be compared with those of the depth-averaged model in Table 5.6. Results for the asterisked stations are not used in the calibration process nor in the error summary. The overall average absolute difference, taken over all four constituents and the 11 calibration stations, is* $\varepsilon_a = 2.46\ cm$ *in amplitude and* $\varepsilon_p = 4.48°$ *in phase. The overall average absolute complex difference is* $\varepsilon = 4.02\ cm$.

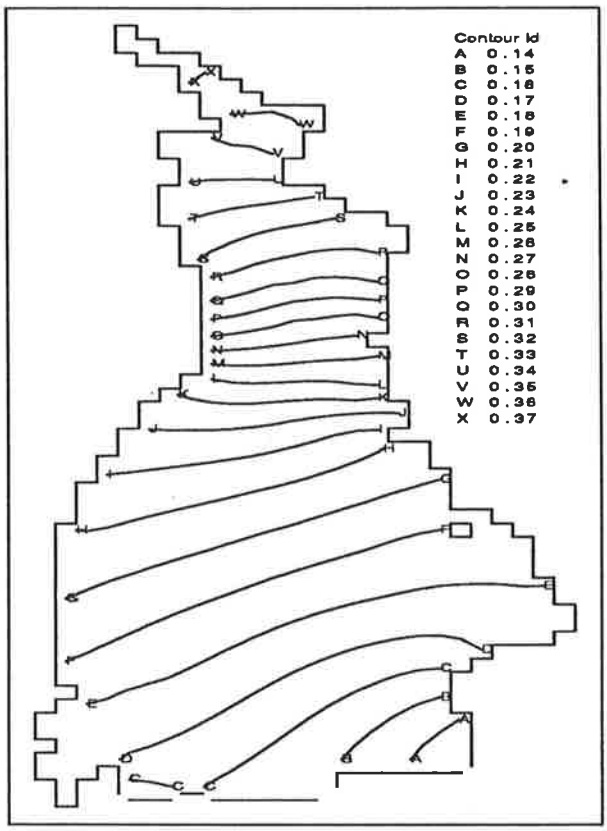


Figure 7.4(a): *Contours for amplitude (m) of the O_1 tidal constituent of sea surface elevation using the three-dimensional model.*

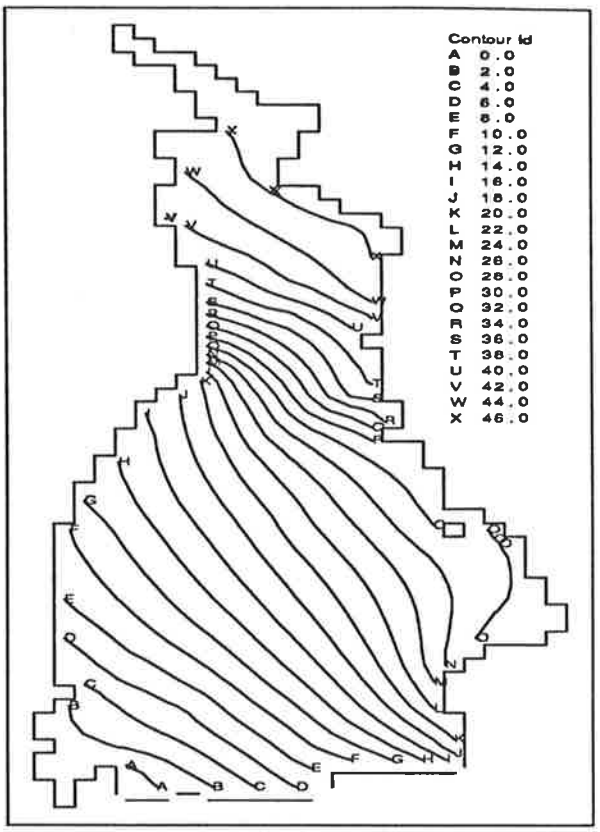


Figure 7.4(b): *Contours for phase (deg, C.S.T.) of the O_1 tidal constituent of sea surface elevation using the three-dimensional model.*

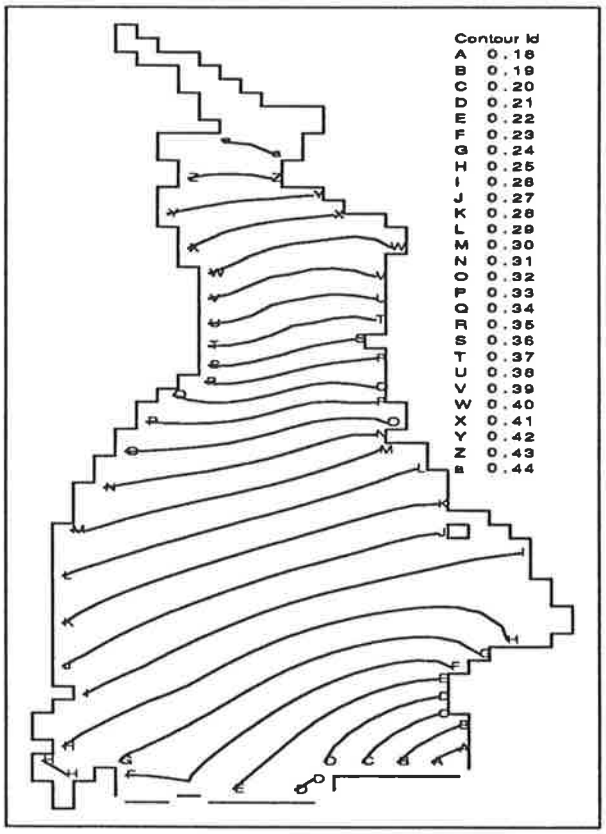


Figure 7.5(a): *Contours for amplitude (m) of the K_1 tidal constituent of sea surface elevation using the three-dimensional model.*

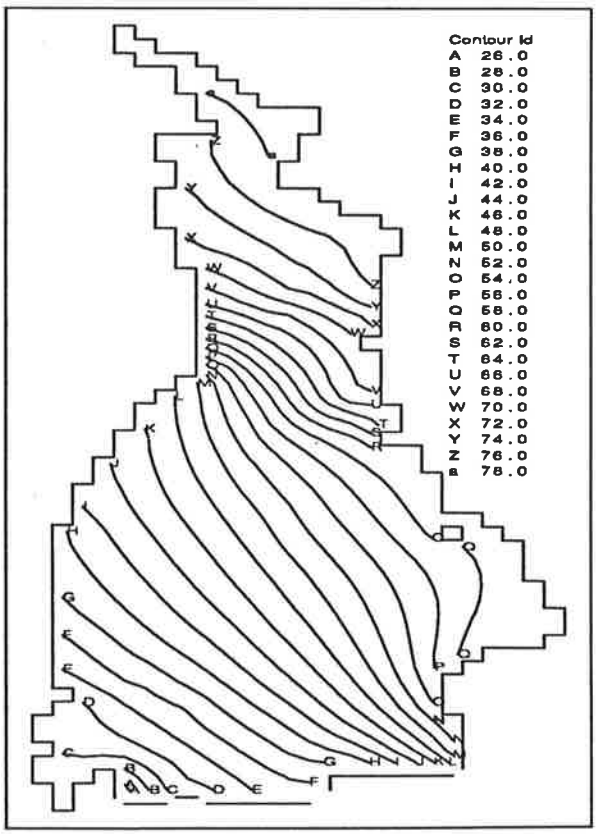


Figure 7.5(b): *Contours for phase (deg, C.S.T.) of the K_1 tidal constituent of sea surface elevation using the three-dimensional model.*

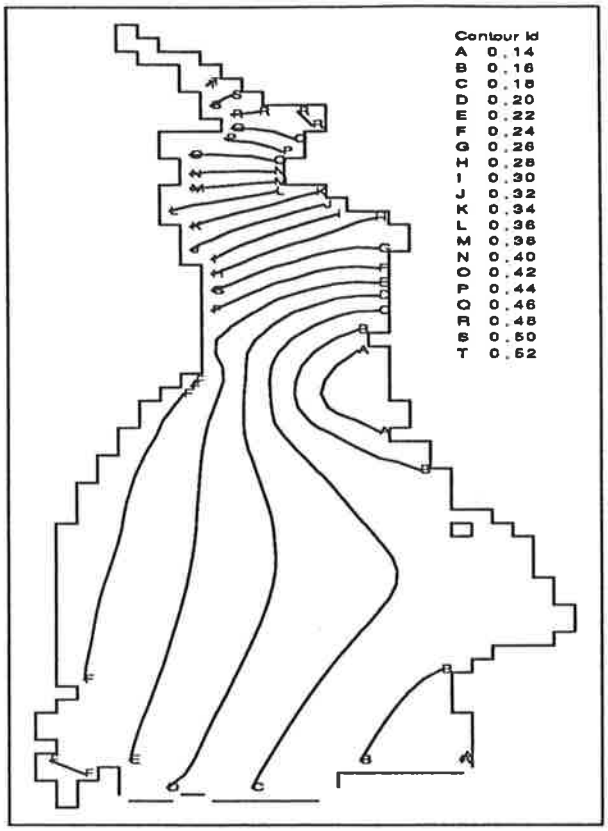


Figure 7.6(a): *Contours for amplitude (m) of the M_2 tidal constituent of sea surface elevation using the three-dimensional model.*

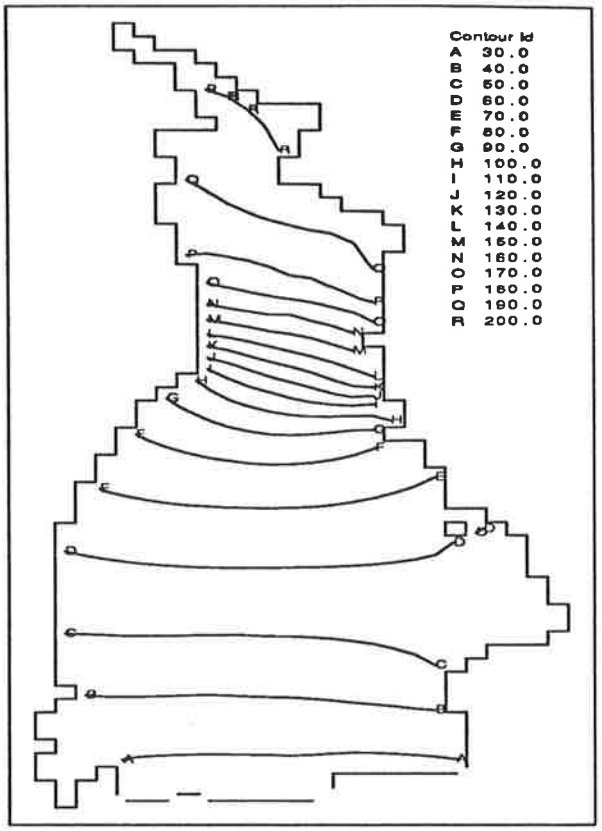


Figure 7.6(b): *Contours for phase (deg, C.S.T.) of the M_2 tidal constituent of sea surface elevation using the three-dimensional model.*

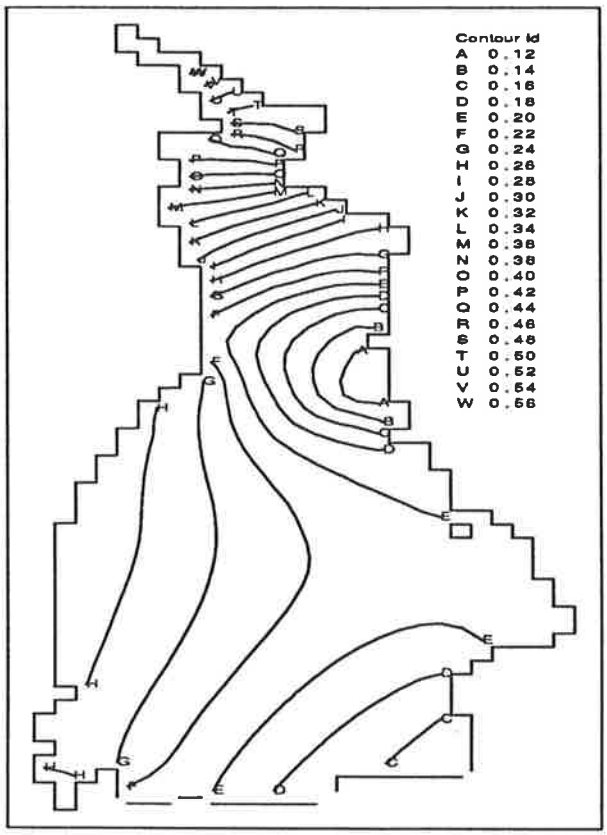


Figure 7.7(a): *Contours for amplitude (m) of the S_2 tidal constituent of sea surface elevation using the three-dimensional model.*

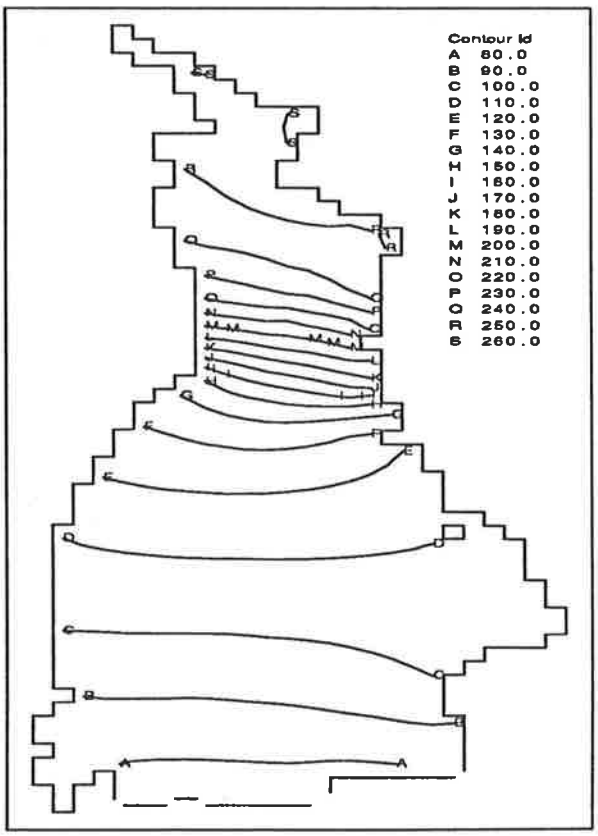


Figure 7.7(b): *Contours for phase (deg, C.S.T.) of the S_2 tidal constituent of sea surface elevation using the three-dimensional model.*

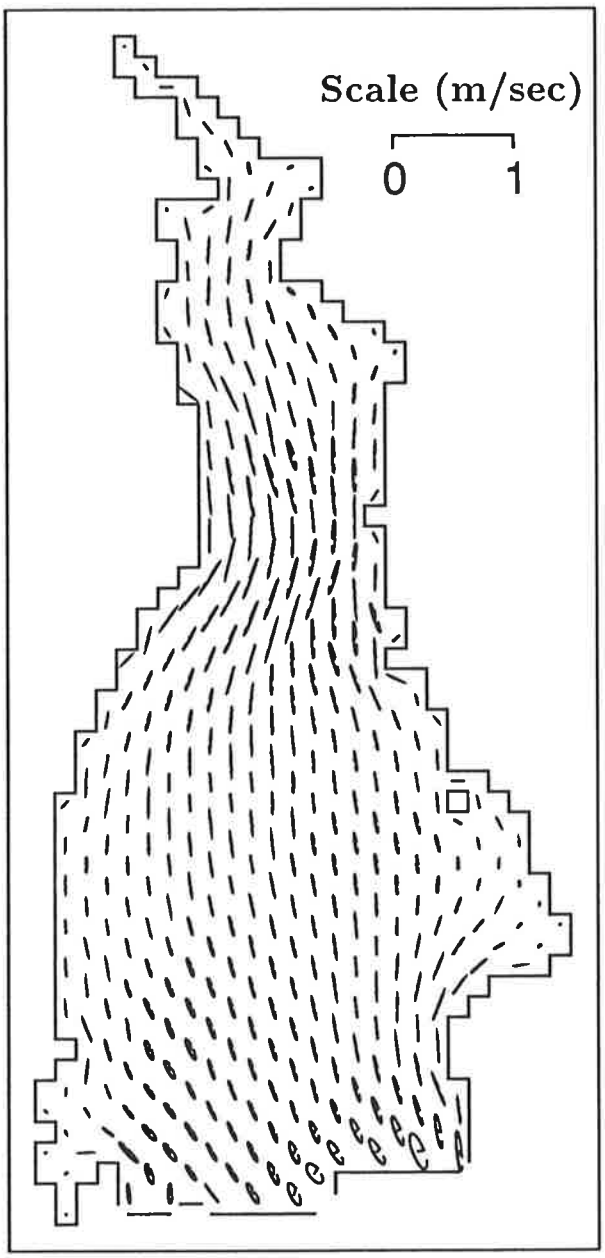


Figure 7.8: *Ellipses for the O_1 tidal constituent of depth-averaged current taken from the three-dimensional model.*

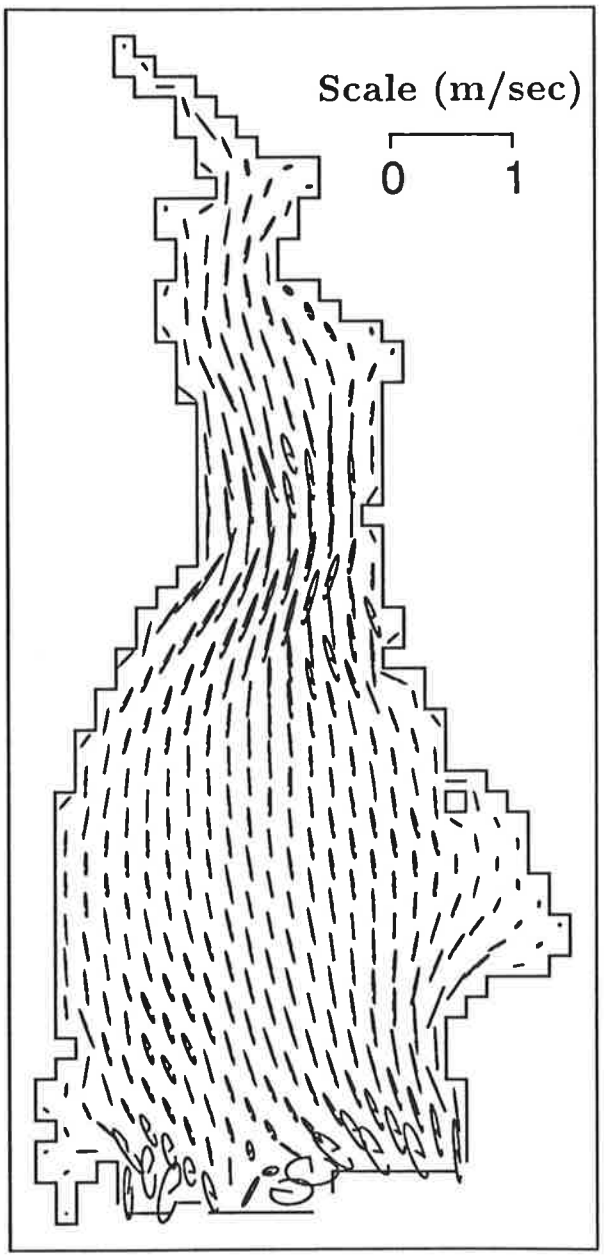


Figure 7.9: *Ellipses for the K_1 tidal constituent of depth-averaged current taken from the three-dimensional model.*

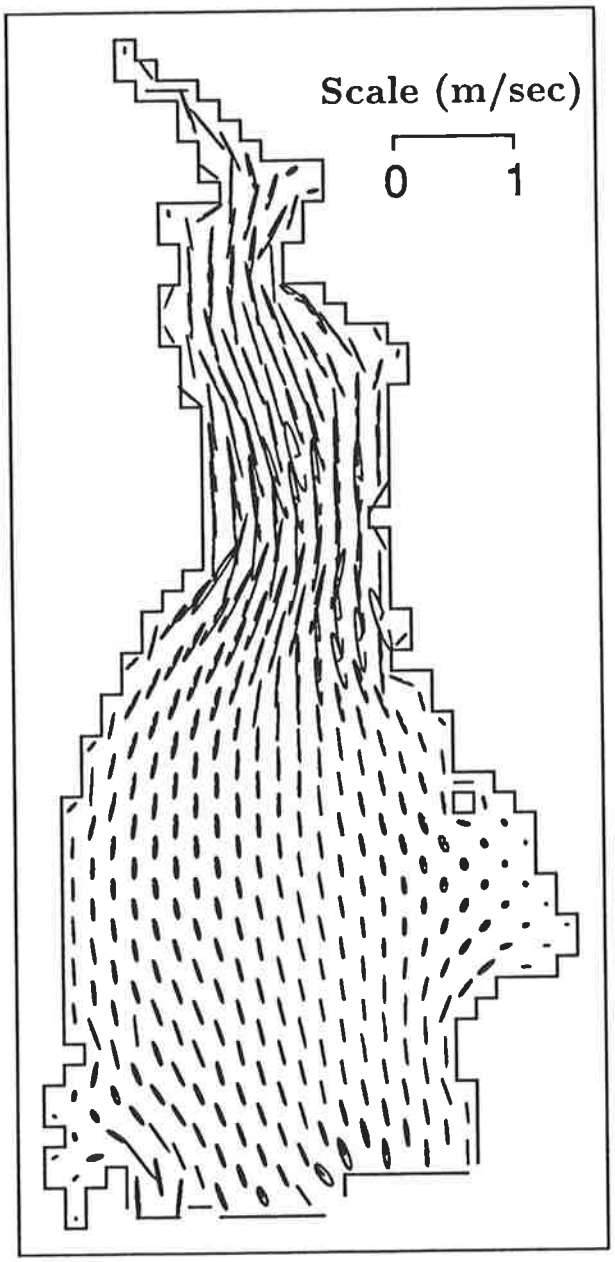


Figure 7.10: *Ellipses for the M_2 tidal constituent of depth-averaged current taken from the three-dimensional model.*

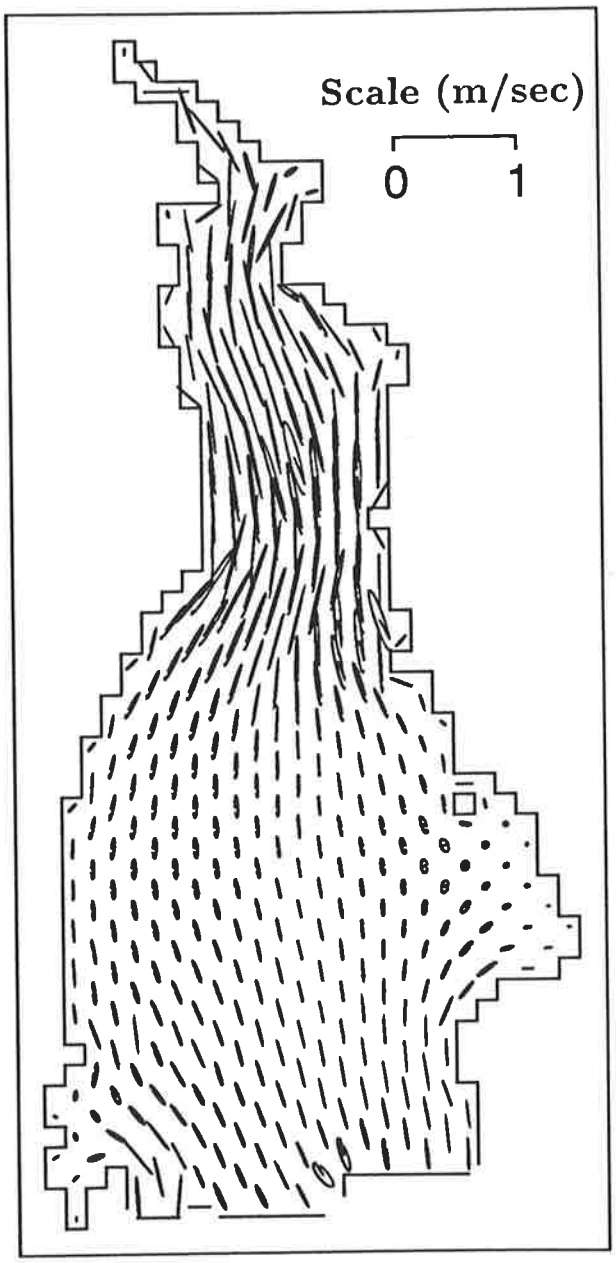


Figure 7.11: *Ellipses for the S_2 tidal constituent of depth-averaged current taken from the three-dimensional model.*

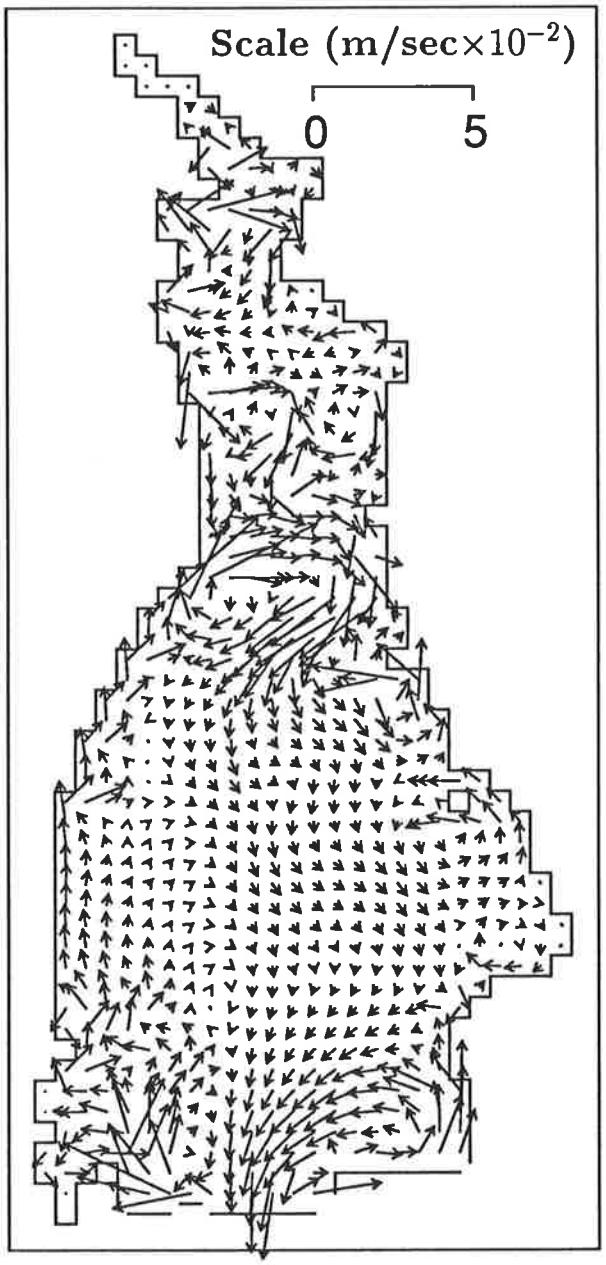


Figure 7.12: *Residuals for depth-averaged velocity (m/sec×10^{-2}) over a 29 day period (with advection and diffusion terms requiring subordinate approximation excluded). Results are taken from the three-dimensional model.*

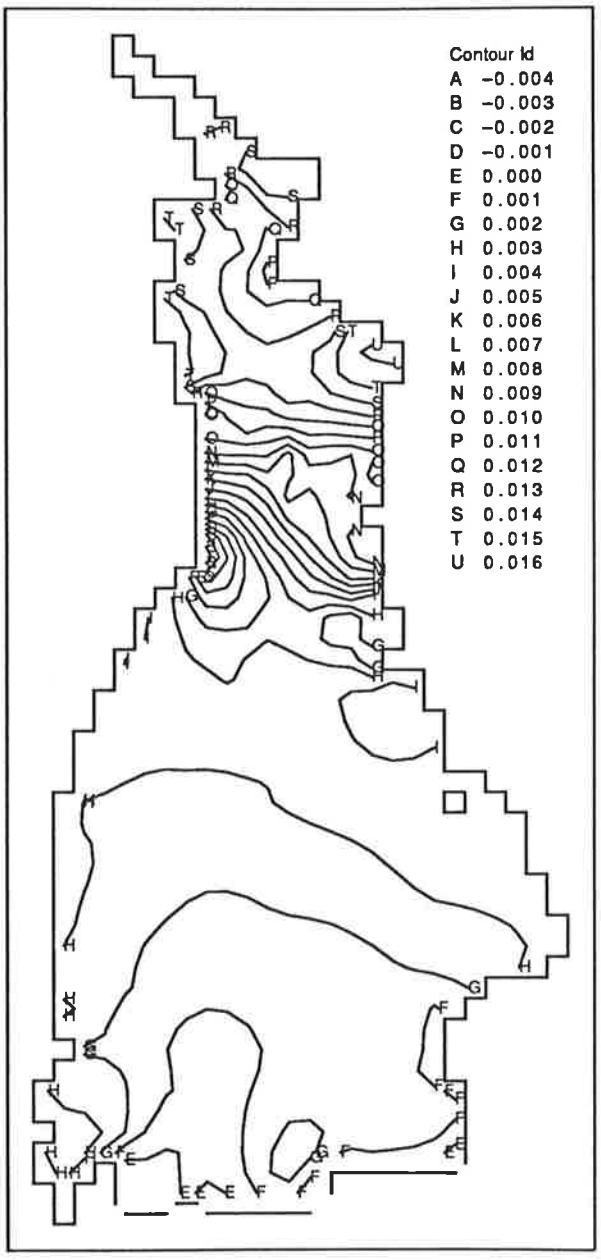


Figure 7.13: *Residuals for elevation (m) over the 29 day period (with advection and diffusion terms requiring subordinate approximation excluded). Results are taken from the three-dimensional model.*

As a further investigation of the depth-averaged flow, amplitude and phase contours for the U and V-components of depth-averaged tidal velocity taken from the three-dimensional model are produced for O_1, K_1, M_2 and S_2 and are presented in Figures 7.14–7.17. For the diurnals the amplitude contours are plotted at 2 cm intervals and for the semi-diurnals they are plotted at 5 cm intervals. Phases are plotted at 30° intervals for the U-component of each constituent and at 10° intervals for each V-component. The V-component is clearly the more dominant for each constituent, although for K_1 the U-component is strong near the open boundary (see Figure 7.15(a)). This observation is consistent with the general rectilinearity and longitudinal alignment of the ellipses seen in Figures 7.8–7.11. The contours for the diurnals (Figures 7.14 and 7.15) demonstrate the similarity of behaviour of O_1 and K_1; the contours for the semi-diurnals (Figures 7.16 and 7.17) demonstrate the similarity of behaviour of M_2 and S_2.

Figures 7.14(a) and 7.15(a) show that high U-component amplitude values occur for the diurnals in the narrowing part of the Gulf near Wallaroo (see Figure 5.15) and near the open boundary. The strongest U-component values (of all the constituents) occur for K_1 near the open boundary (Figure 7.15(a)). Figures 7.14(c) and 7.15(c) show that the peak V-component values also occur mainly in the narrowing part of the Gulf and near the open boundary. Diurnal flows through the narrowing part of the Gulf are dominated by the V-component of each constituent flow. The diurnals gather speed on entry to the narrowing part of the Gulf and then, having passed Point Riley, begin to slow down.

In the diurnal U-component amplitude plots (Figures 7.14(a) and 7.15(a)) north of Wardang Island (see Figure 5.10) there are several oval-shaped zones. The position of these features correlates with the residual gyres of Figure 7.12. Similarly shaped zones in the diurnal V-component amplitude plots of Figures 7.14(c) and 7.15(c) do not correlate with the residual gyres in any obvious way.

The diurnal U-component phase plots of Figures 7.14(b) and 7.15(b) are characterized by closely set bands of contour lines — these occur in the same general locations for both O_1 and K_1. Note that the bands generally consist of six contour lines. Knowing that the U-component phase contour lines are plotted at increments of 30° indicates that from one side to the other the U-component reverses direction. Thus it can be seen that these thick bands of contour lines divide the Gulf into regions of similarly rotating diurnal ellipses. The ellipses in most of the southern Spencer Gulf region are anticlockwise rotating (see Figures 7.8 and 7.9). To the north-west of that region they are clockwise rotating. Stretching across the Gulf from Point Riley (see Figure 5.15) is a band of contour lines which divides the clockwise rotating ellipses just mentioned from a region of anticlockwise rotating ellipses to the north. The direction of rotation of each of the residual gyres of Figure 7.12 is consistent with the direction of rotation of the ellipses within each of the regions of similarly rotating ellipses delineated by the bands of contour lines.

Thus the U-component amplitude and phase plots for both O_1 and K_1 are strongly correlated with the position and direction of rotation of the residual gyres. The U-component phase plots for O_1 and K_1 also delineate the regions where the diurnal ellipses rotate in the same direction.

On the other hand the V-component amplitude and phase plots for O_1 and K_1 are not correlated with the residual gyres in any obvious way.

Consider the semi-diurnal U and V-component amplitude plots of Figures 7.16(a),(c) and 7.17(a),(c). The V-component of semi-diurnal tidal flow clearly dominates the U-component. On the other hand, both components are separately strongest in the narrowing

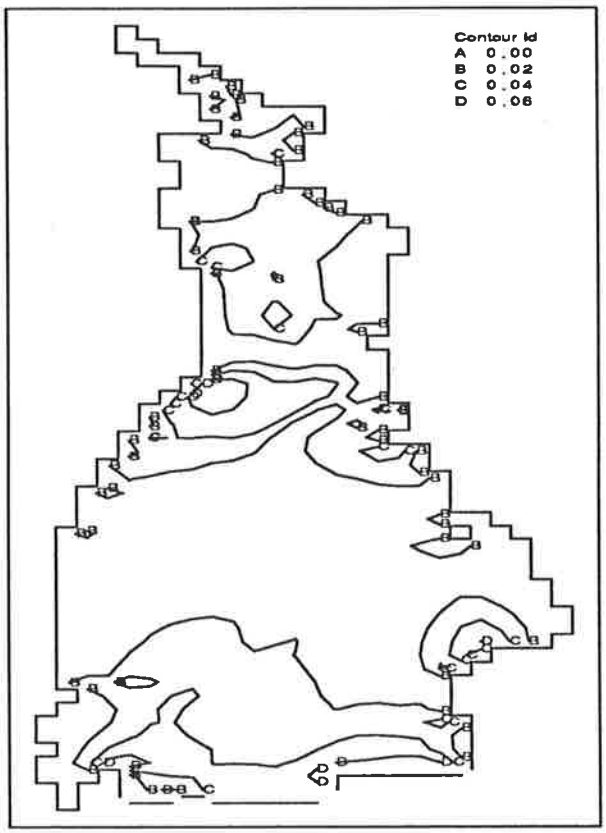


Figure 7.14(a): *Amplitude contours (m) for the U component of the O_1 constituent of depth-averaged tidal current taken from the three-dimensional model.*

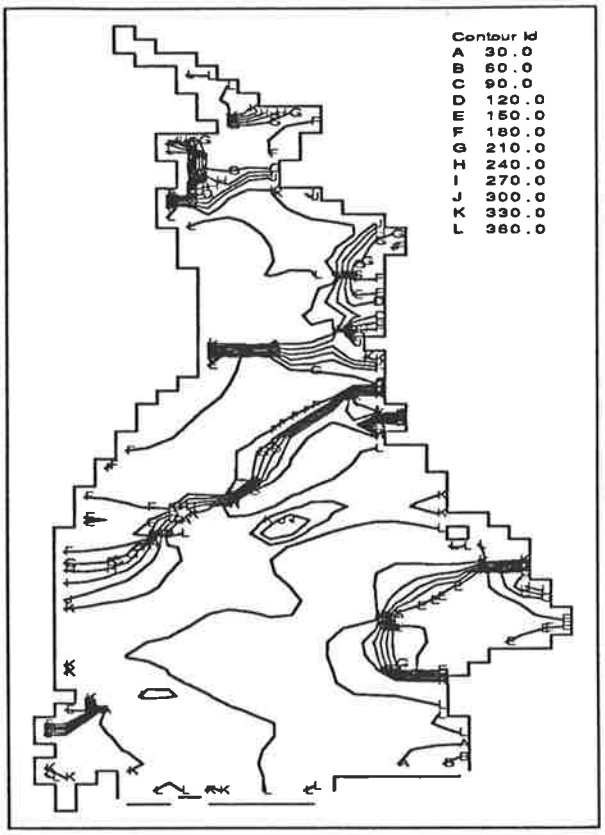


Figure 7.14(b): *Phase contours (deg, C.S.T.) for the U component of the O_1 constituent of depth-averaged tidal current taken from the three-dimensional model.*

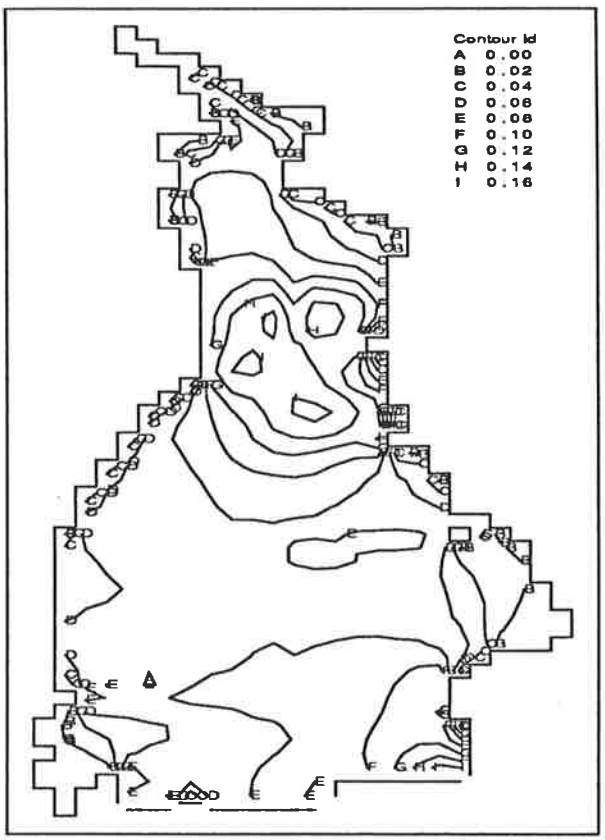


Figure 7.14(c): *Amplitude contours (m) for the V component of the O_1 constituent of depth-averaged tidal current taken from the three-dimensional model.*

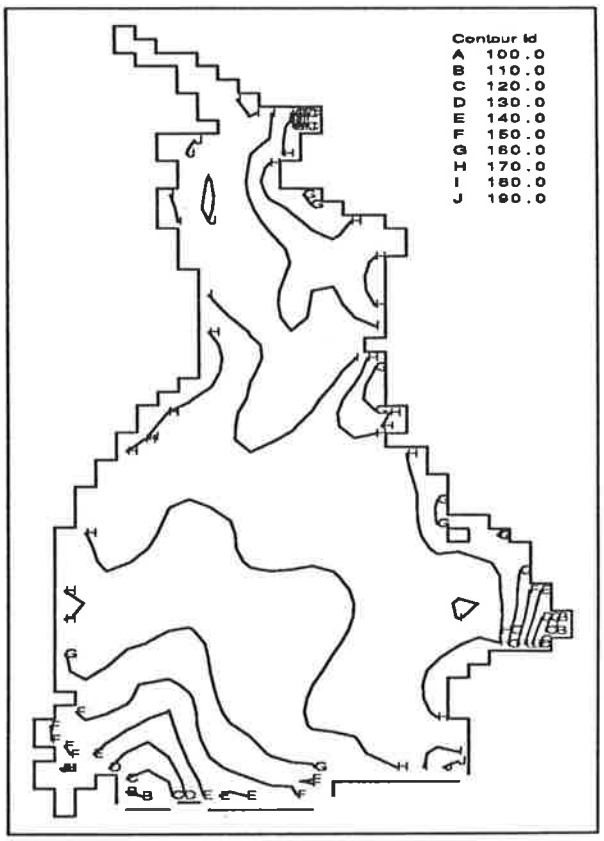


Figure 7.14(d): *Phase contours (deg, C.S.T.) for the V component of the O_1 constituent of depth-averaged tidal current taken from the three-dimensional model.*

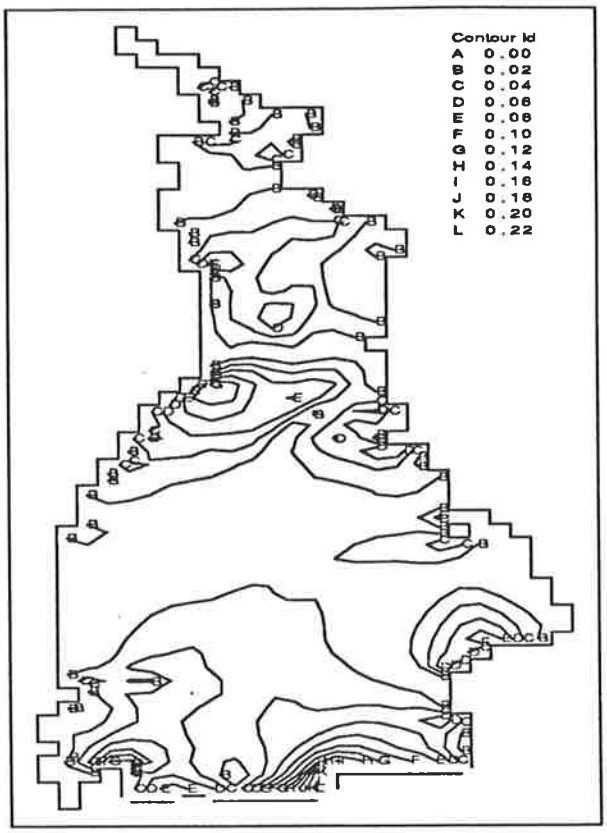


Figure 7.15(a): *Amplitude contours (m) for the U component of the K_1 constituent of depth-averaged tidal current taken from the three-dimensional model.*

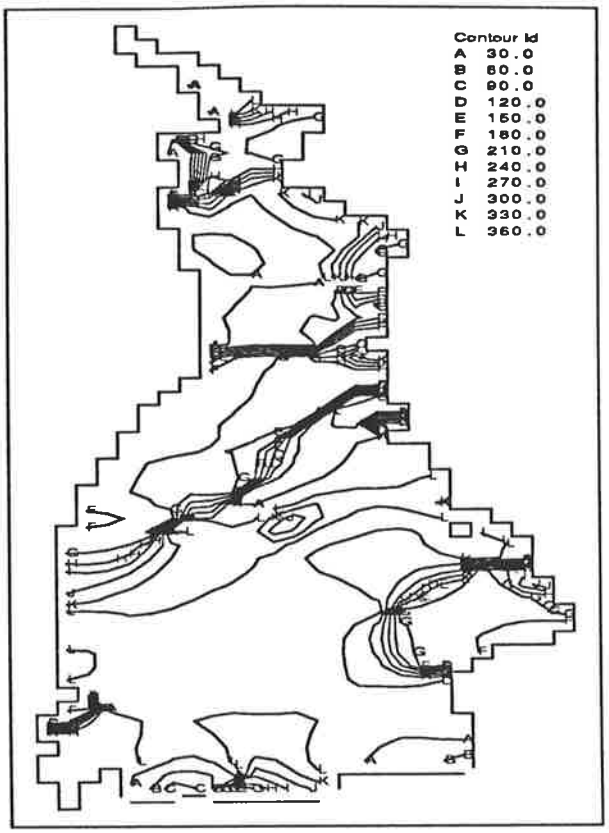


Figure 7.15(b): *Phase contours (deg, C.S.T.) for the U component of the K_1 constituent of depth-averaged tidal current taken from the three-dimensional model.*

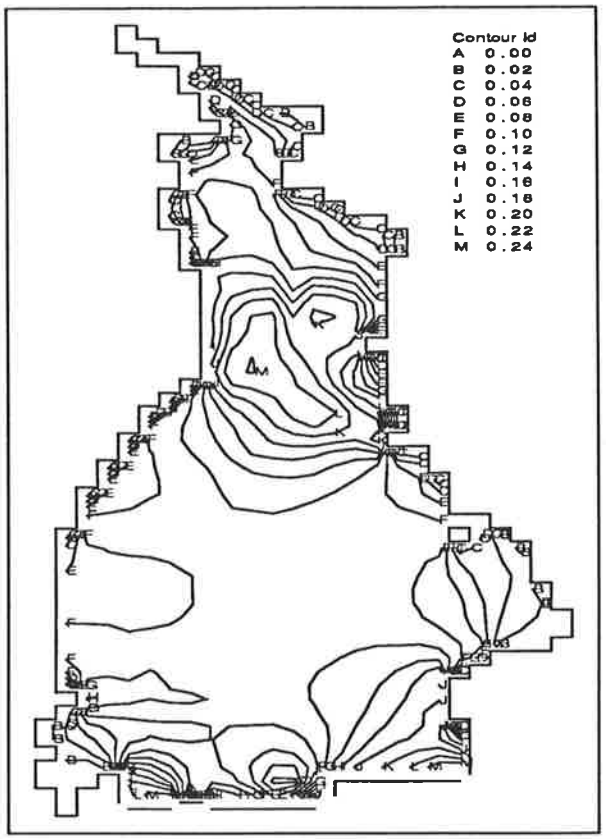


Figure 7.15(c): *Amplitude contours (m) for the V component of the K_1 constituent of depth-averaged tidal current taken from the three-dimensional model.*

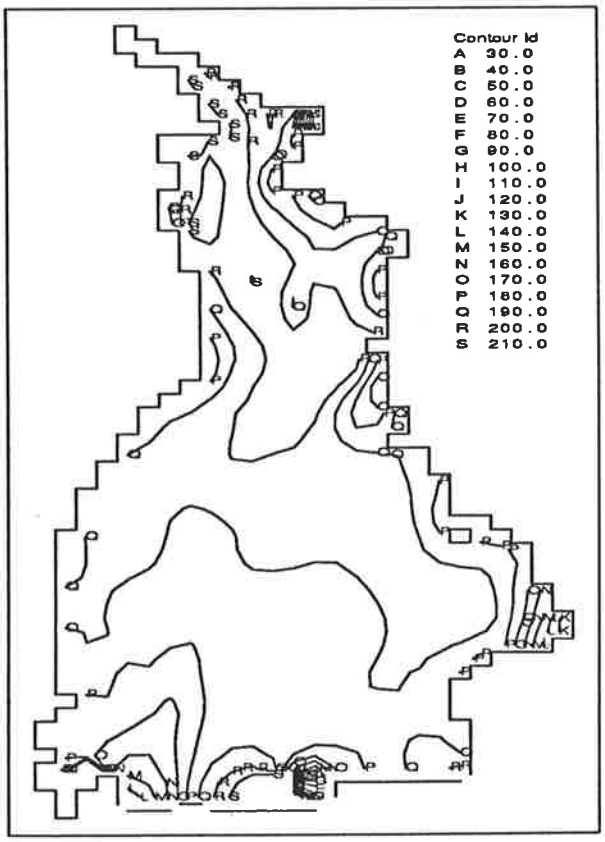


Figure 7.15(d): *Phase contours (deg, C.S.T.) for the V component of the K_1 constituent of depth-averaged tidal current taken from the three-dimensional model.*

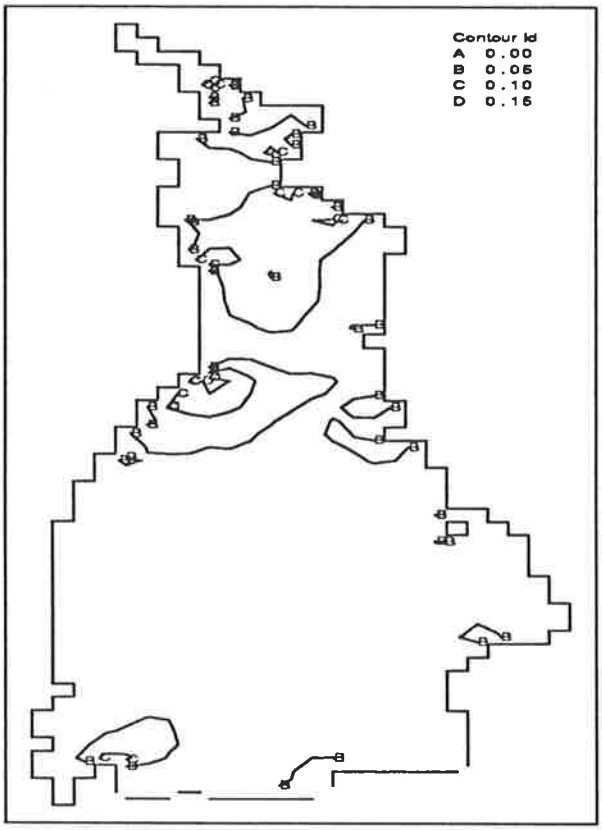


Figure 7.16(a): *Amplitude contours (m) for the U component of the M_2 constituent of depth-averaged tidal current taken from the three-dimensional model.*

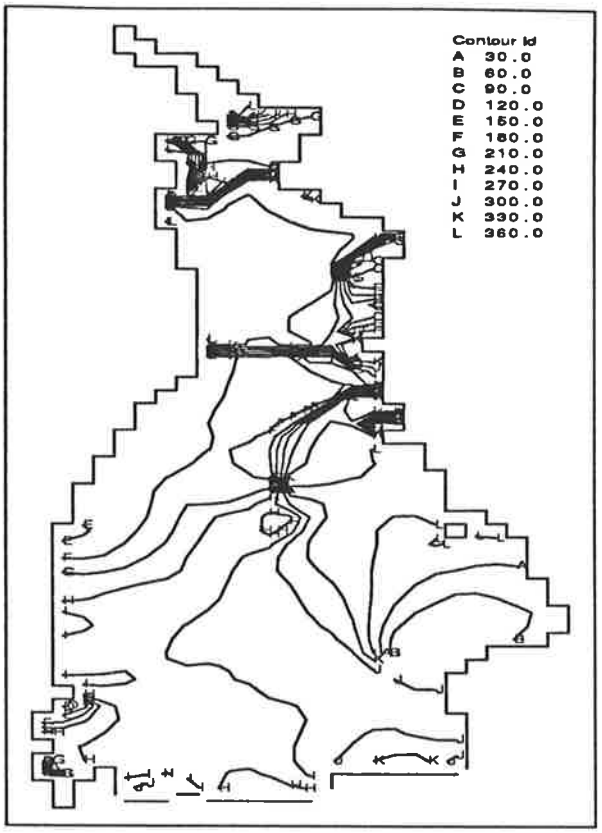


Figure 7.16(b): *Phase contours (deg, C.S.T.) for the U component of the M_2 constituent of depth-averaged tidal current taken from the three-dimensional model.*

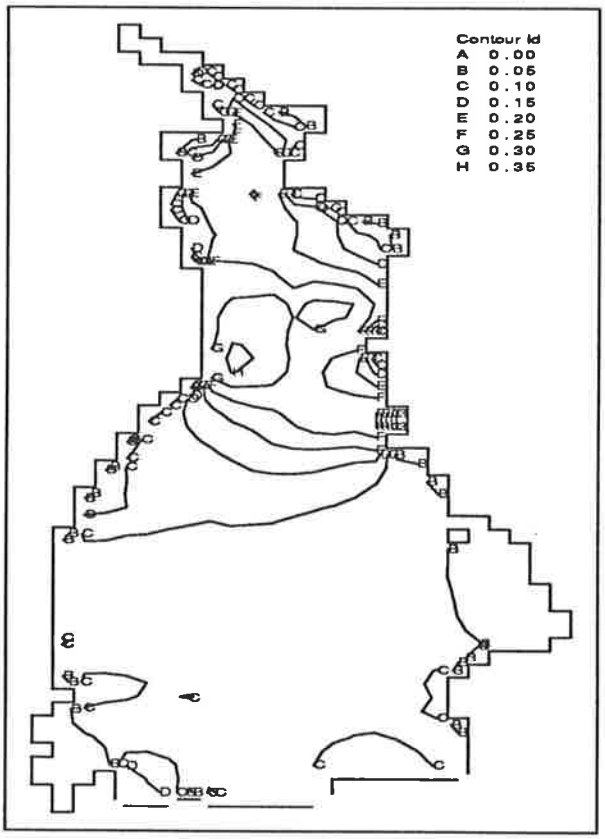


Figure 7.16(c): *Amplitude contours (m) for the V component of the M_2 constituent of depth-averaged tidal current taken from the three-dimensional model.*

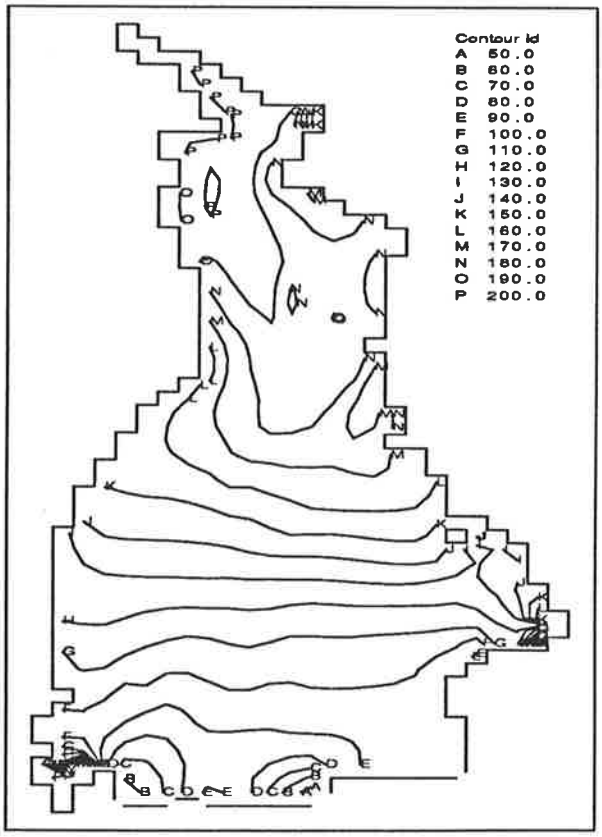


Figure 7.16(d): *Phase contours (deg, C.S.T.) for the V component of the M_2 constituent of depth-averaged tidal current taken from the three-dimensional model.*

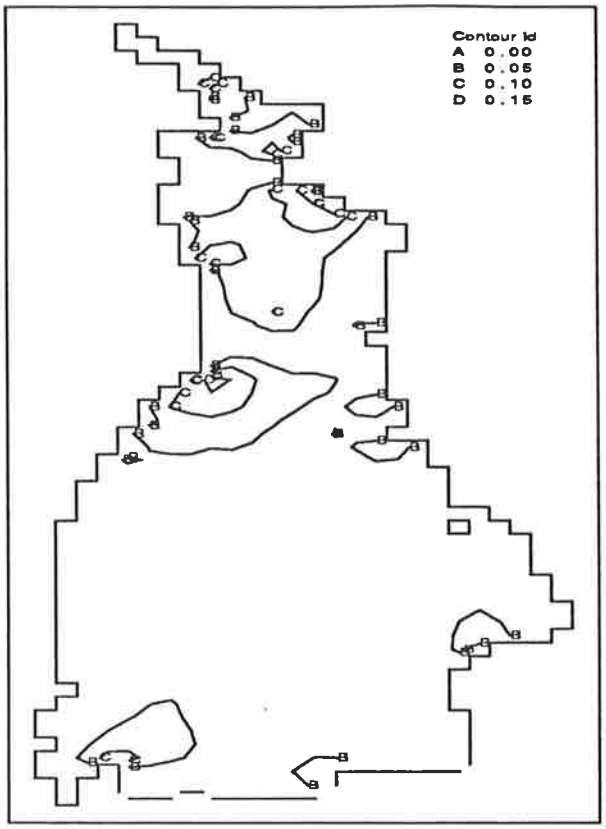


Figure 7.17(a): *Amplitude contours (m) for the U component of the S_2 constituent of depth-averaged tidal current taken from the three-dimensional model.*

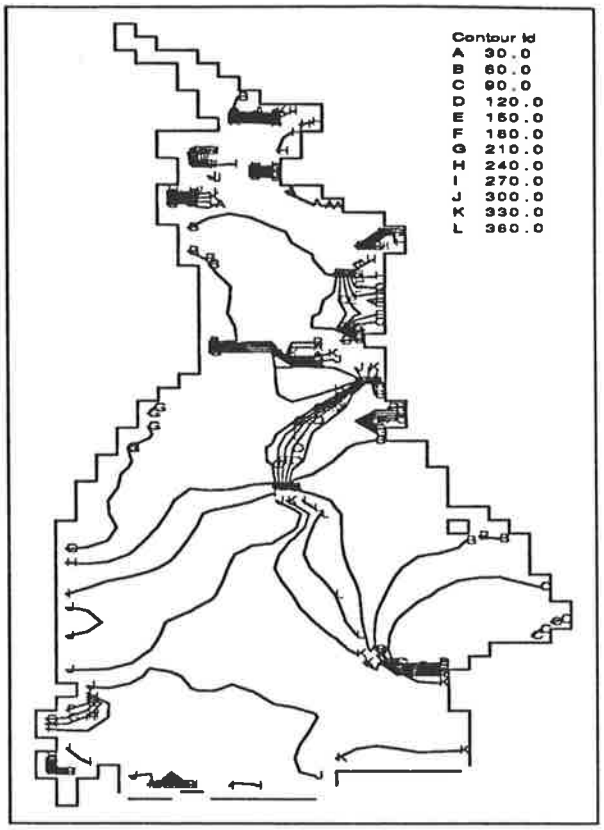


Figure 7.17(b): *Phase contours (deg, C.S.T.) for the U component of the S_2 constituent of depth-averaged tidal current taken from the three-dimensional model.*

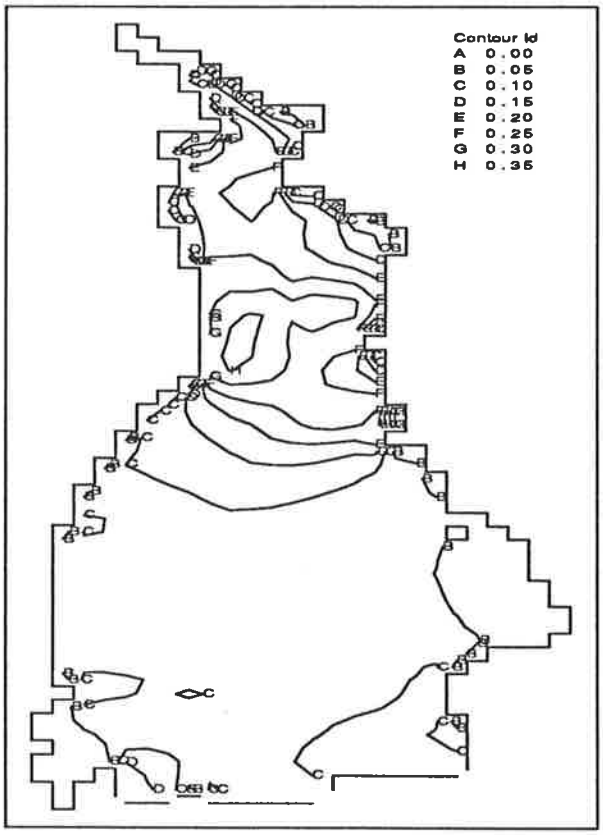


Figure 7.17(c): *Amplitude contours (m) for the V component of the S_2 constituent of depth-averaged tidal current taken from the three-dimensional model.*

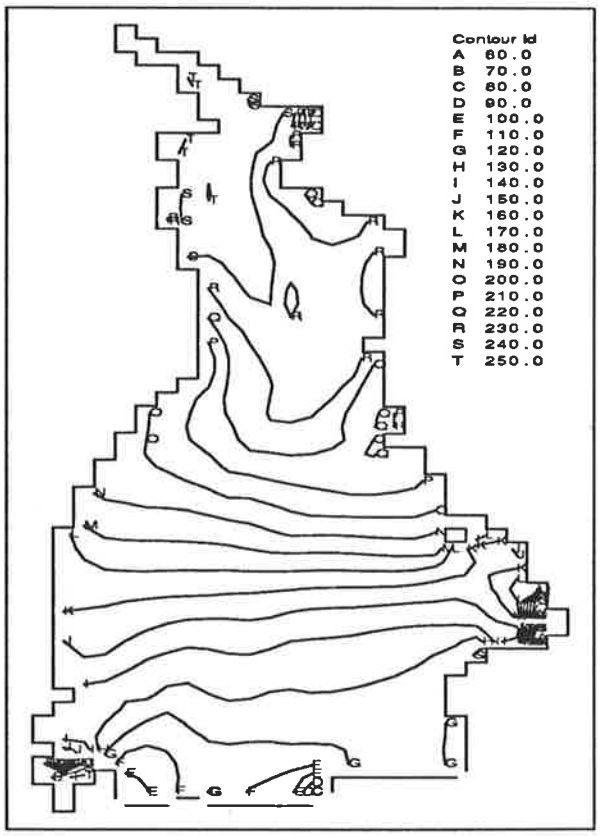


Figure 7.17(d): *Phase contours (deg, C.S.T.) for the V component of the S_2 constituent of depth-averaged tidal current taken from the three-dimensional model.*

part of the Gulf opposite Wallaroo. There is very little variation in amplitude of either the U or V-component of semi-diurnal flow within the southern Spencer Gulf region. This region is conspicuous for the absence of contours of amplitude compared with the situation further northwards in the Gulf. Figures 7.16(c) and 7.17(c) show that the semi-diurnals gather speed on entry to the narrowing part of the Gulf and from about opposite Point Riley they slow down.

The oval-shaped zones of U-component amplitude in the Gulf north of Wardang Island for the semi-diurnals correlate well with the position of the residual gyres of Figure 7.12.

There are several bands of semi-diurnal U-component phase lines in Figures 7.16(b) and 7.17(b) but in general they are not as coherent as in the case of the diurnals. One band cuts directly across the Gulf near Point Riley sharply dividing a region of clockwise rotating semi-diurnal ellipses to the south from a region of anticlockwise rotating ellipses to the north. Another band, for both M_2 and S_2, strikes south-westwards from the position of Wallaroo to a central position in the Gulf from which phase lines radiate towards the west and south. These central positions are amphidromic points in the phase of the U-component of M_2 and S_2 flow. As well, they coincide. It can be seen that there are 12 distinct phase lines emerging from each of these points although five of these enter the amphidromic point bunched together as a band.

The phase lines of semi-diurnal V-component flow in Figures 7.16(d) and 7.17(d) are generally transverse and show quite regular spacing in the southern Gulf. They are generally parallel to the respective elevation phase contours of Figures 7.6(b) and 7.7(b). At the position of Wardang Island these two sets of contours are 90° out of phase showing that here the semi-diurnal tide is dominantly of standing wave character. Everywhere else in the Gulf the semi-diurnal tide adopts a more progressive wave character.

We now consider the depth-dependent predictions of the three-dimensional model. Figures 7.18–7.21 show surface current tidal ellipses for the constituents O_1, K_1, M_2 and S_2. Figures 7.22–7.25 show current ellipses at mid-depth for the same constituents, and Figures 7.26–7.29 show the ellipses for relative depth level $k = 9$ which is just above the bed (about 5% of total depth from the bottom — refer to Figure 7.2). All the ellipses are plotted to the same scale.

As one would expect, the surface current ellipses of Figures 7.18–7.21 show slightly larger semi-major axes than those of the depth-averaged current ellipses of Figures 7.8–7.11. The mid-depth ellipses of Figures 7.22–7.25 are smaller than those at the surface and are approximately the same size as the depth-averaged ellipses of Figures 7.8–7.11. The ellipses of Figures 7.26–7.29 are noticeably smaller than those at the surface and mid-depth levels reflecting the fact that they describe tidal current strength near the sea bed.

There is very little discernible rotation of the semi-major axes in the ellipses at corresponding positions at these three depth levels. However careful inspection reveals a slight rotation in K_1, generally to the right, as one looks downwards from the surface.

Examining the direction of rotation of the ellipses, one notes that at each level depicted the rotation is anticlockwise south of Wallaroo, clockwise opposite Wallaroo and anticlockwise north of Wallaroo. This phenomenon is presumably present at all the intervening levels. Thus one expects to find that the tidal gyral activity reported in Chapter 5, Section 5.5, is present at all levels.

Figures 7.30 and 7.31 are snapshots of the three-dimensional model's predictions for tidal current at separate depth levels during a neap event in the central Gulf region. Fig-

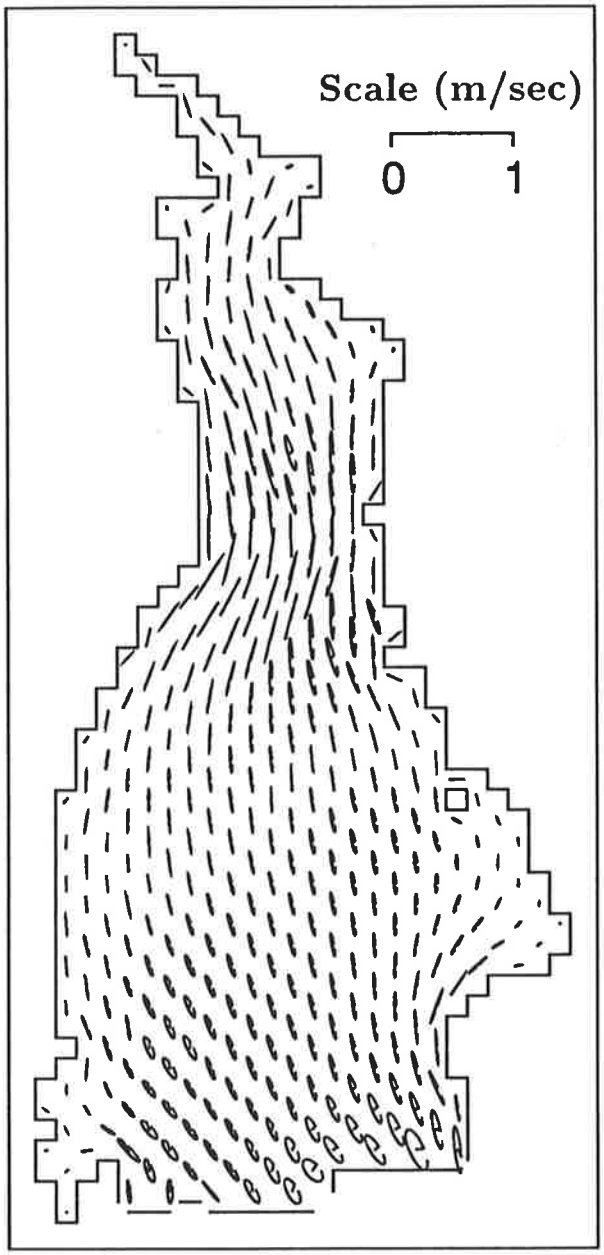


Figure 7.18: *Ellipses for the O_1 constituent of tidal current at $\eta = 0$ (the surface level $k = 0$) taken from the three-dimensional model.*

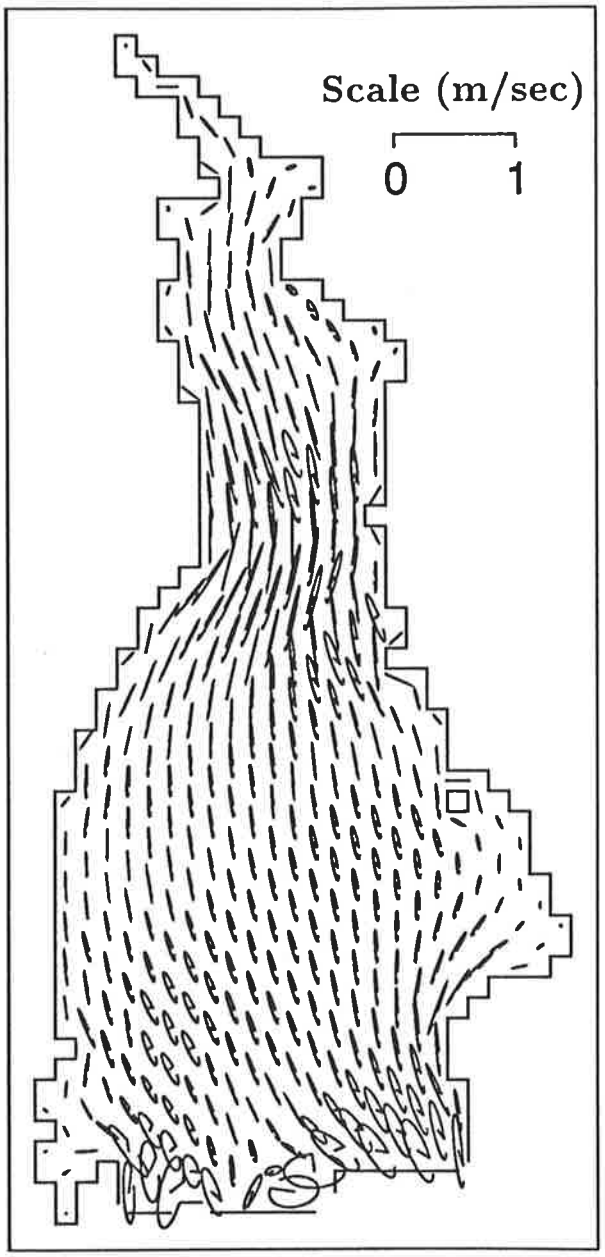


Figure 7.19: *Ellipses for the K_1 constituent of tidal current at $\eta = 0$ (the surface level $k = 0$) taken from the three-dimensional model.*

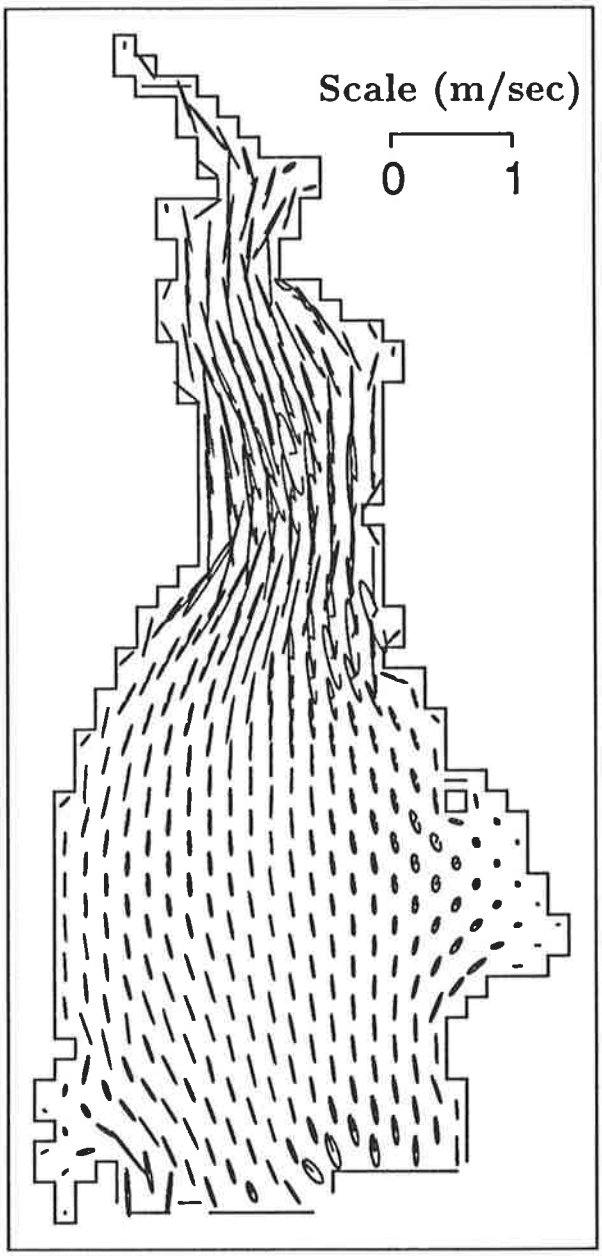


Figure 7.20: *Ellipses for the M_2 constituent of tidal current at $\eta = 0$ (the surface level $k = 0$) taken from the three-dimensional model.*

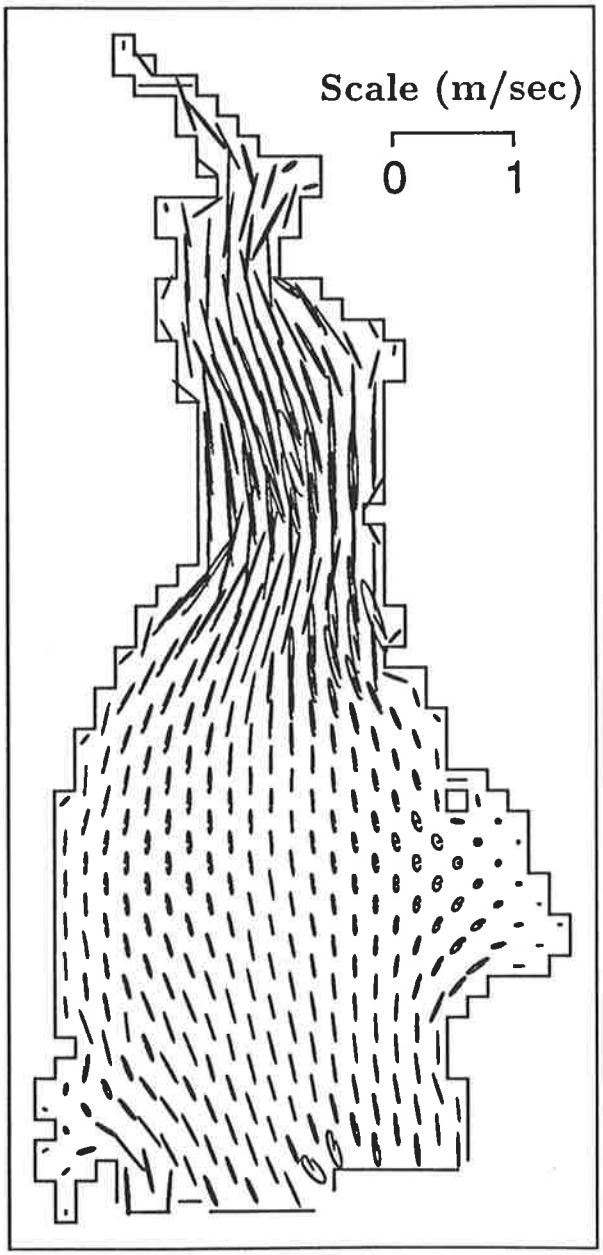


Figure 7.21: *Ellipses for the S_2 constituent of tidal current at $\eta = 0$ (the surface level $k = 0$) taken from the three-dimensional model.*

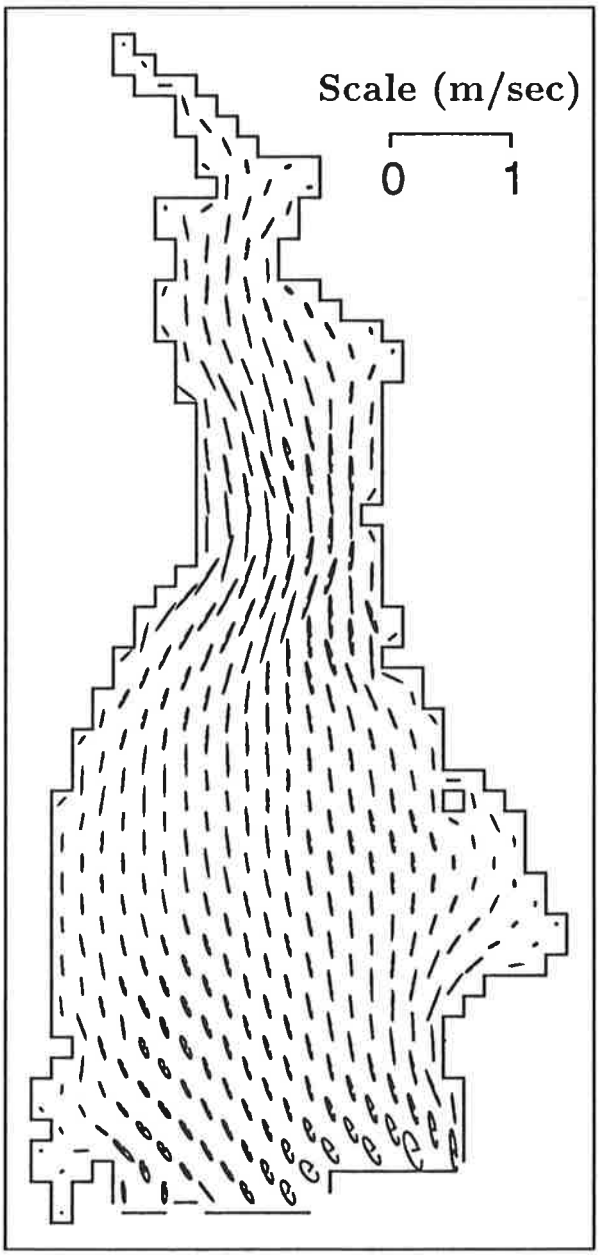


Figure 7.22: *Ellipses for the O_1 constituent of tidal current at $\eta = 0.5$ (the middle level $k = 5$) taken from the three-dimensional model.*

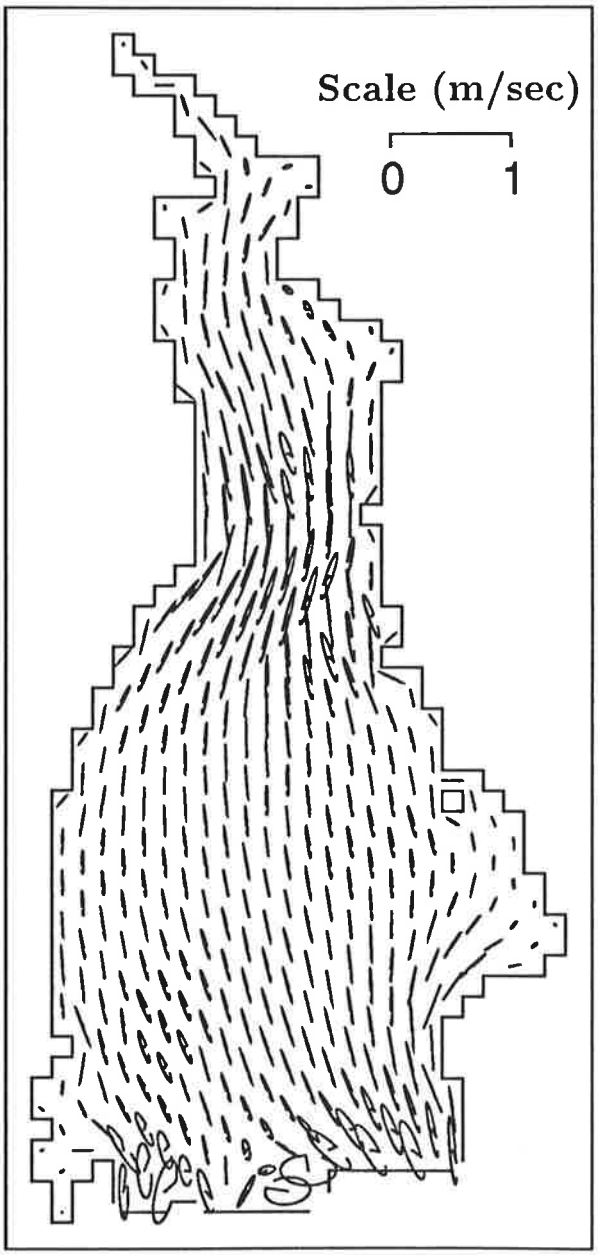


Figure 7.23: *Ellipses for the K_1 constituent of tidal current at $\eta = 0.5$ (the middle level $k = 5$) taken from the three-dimensional model.*

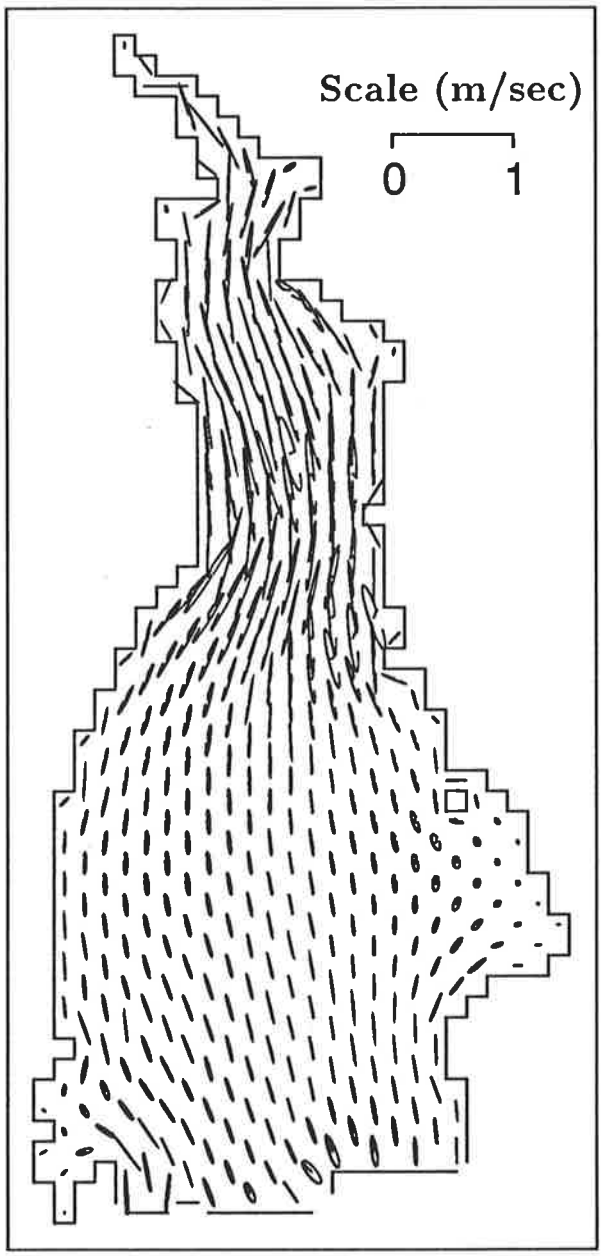


Figure 7.24: *Ellipses for the M_2 constituent of tidal current at $\eta = 0.5$ (the middle level $k = 5$) taken from the three-dimensional model.*

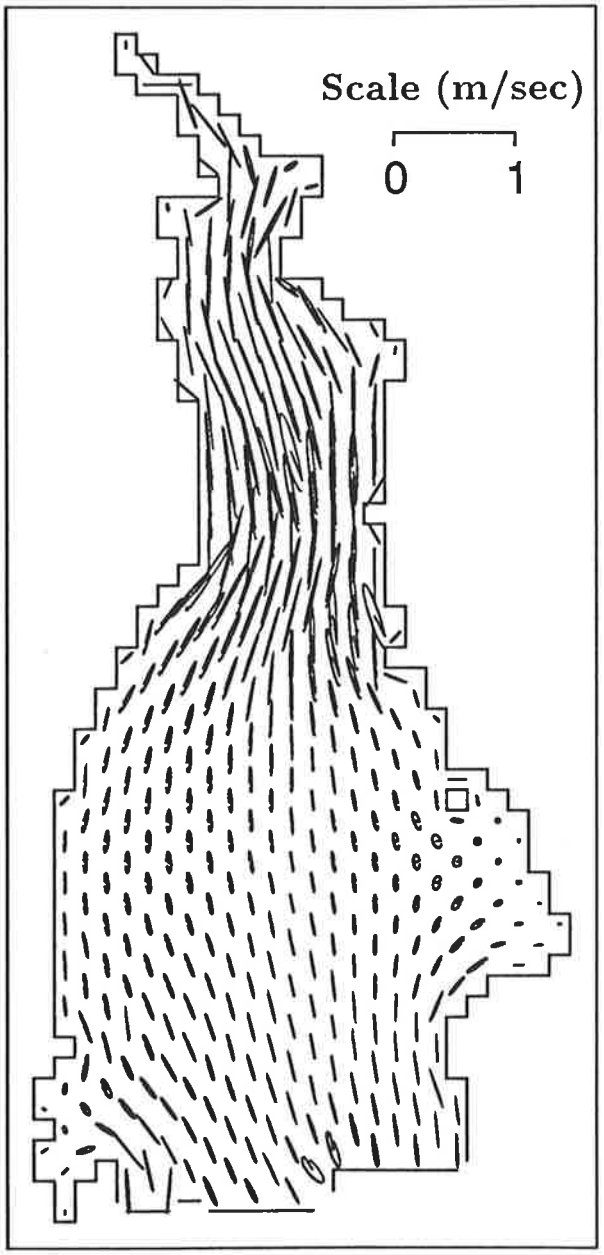


Figure 7.25: *Ellipses for the S_2 constituent of tidal current at $\eta = 0.5$ (the middle level $k = 5$) taken from the three-dimensional model.*

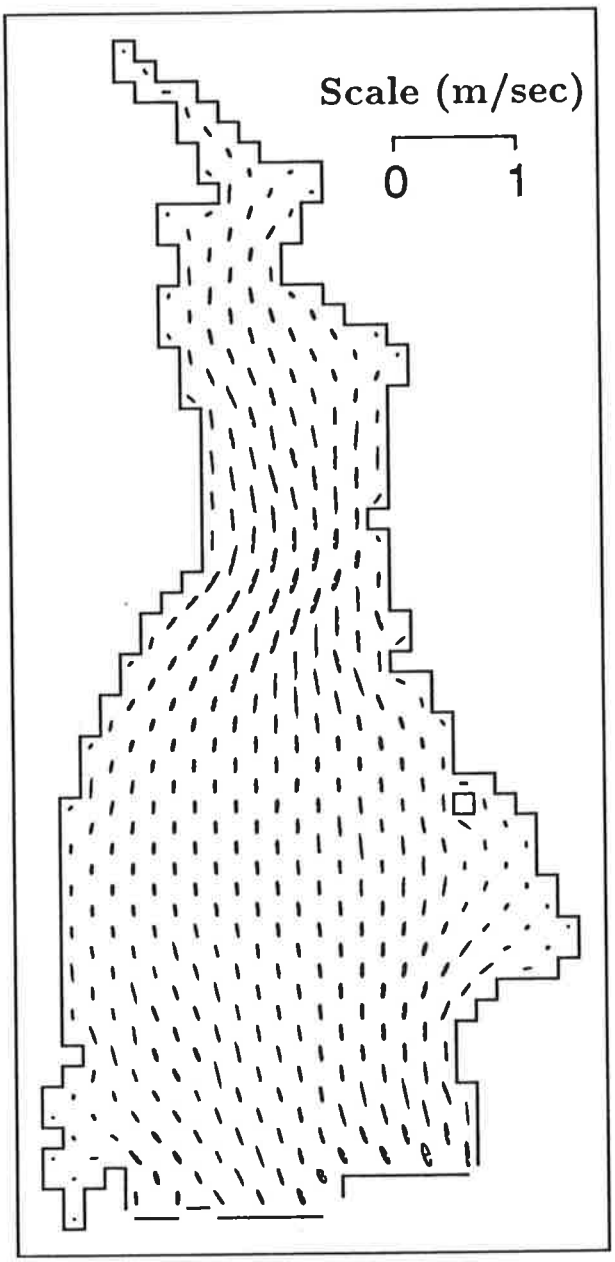


Figure 7.26: *Ellipses for the O_1 constituent of tidal current at $\eta \simeq 0.95$ (level $k = 9$, near the bed) taken from the three-dimensional model.*

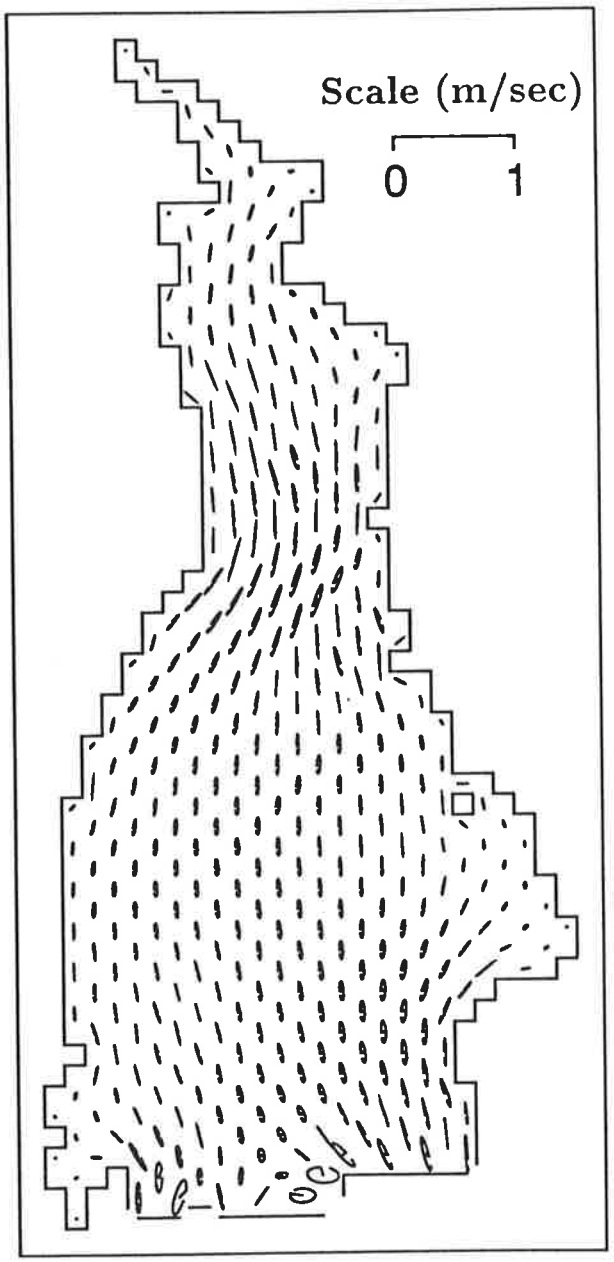


Figure 7.27: *Ellipses for the K_1 constituent of tidal current at $\eta \simeq 0.95$ (level $k = 9$, near the bed) taken from the three-dimensional model.*

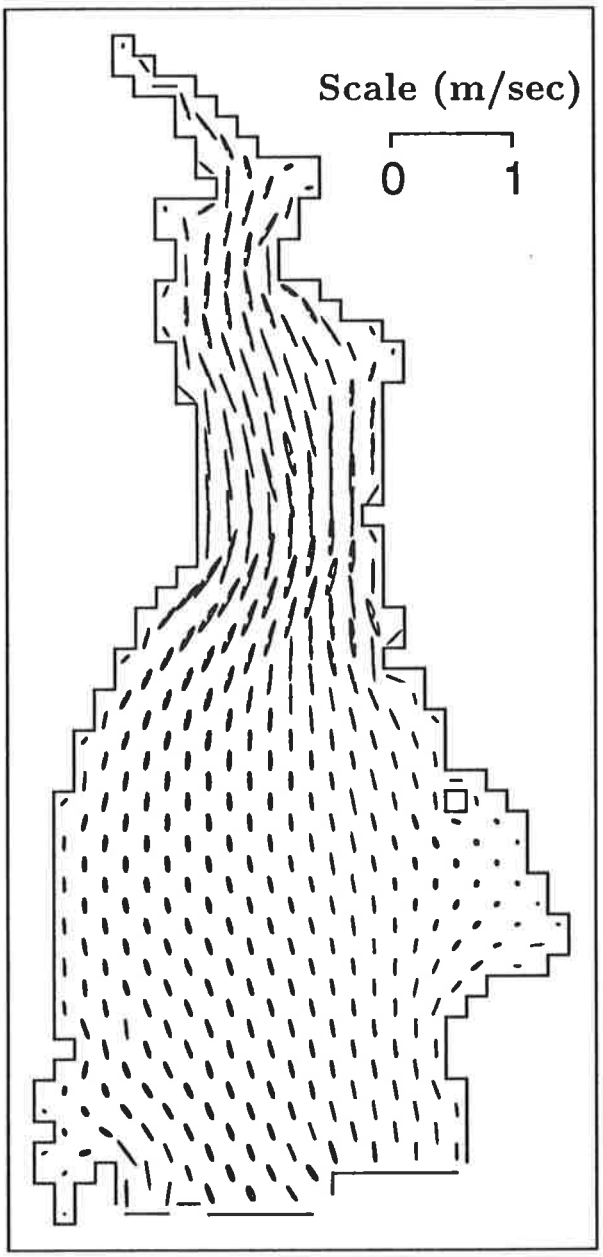


Figure 7.28: *Ellipses for the M_2 constituent of tidal current at $\eta \simeq 0.95$ (level $k = 9$, near the bed) taken from the three-dimensional model.*

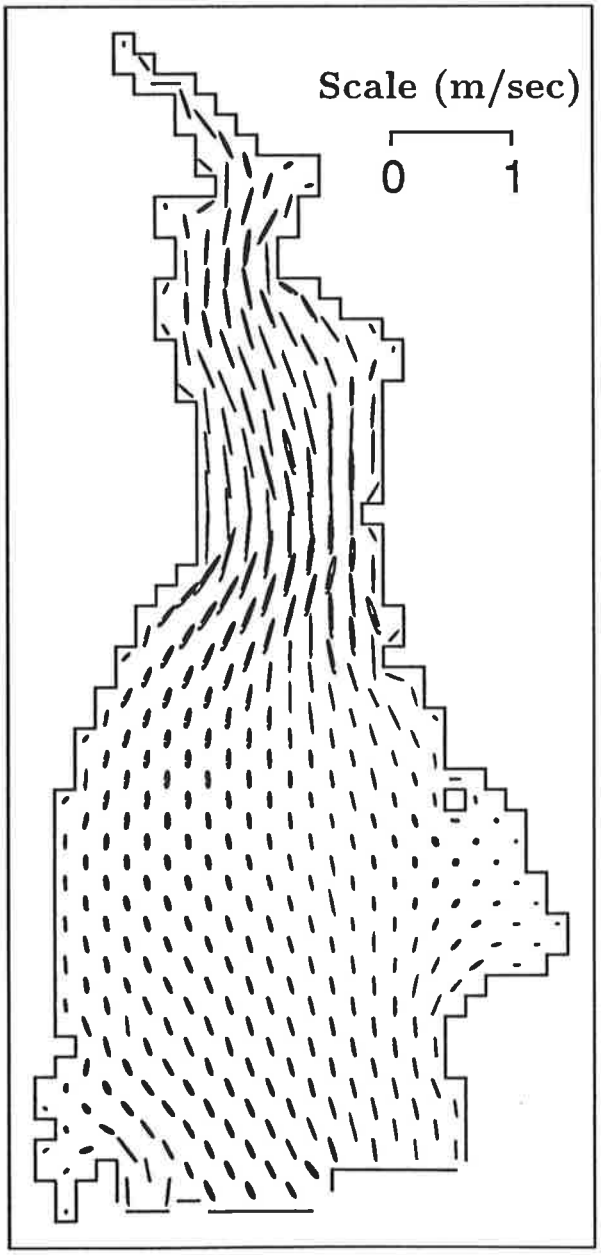


Figure 7.29: *Ellipses for the S_2 constituent of tidal current at $\eta \simeq 0.95$ (level $k = 9$, near the bed) taken from the three-dimensional model.*

ure 7.30 gives surface current predictions and Figure 7.31 gives predictions for mid-depth. The same scale is used for both figures and they show the same gyral movements, suggesting that the gyres created do indeed exist throughout the water column. The flow magnitudes recorded in Figure 7.30 are slightly greater than those of Figure 7.31. These two figures may be directly compared with Figure 5.32 which shows depth-averaged current predictions for the same time sequence. There is strong qualitative and quantitative agreement among the three figures, with Figure 7.31 most closely matching Figure 5.32. This is to be expected since depth-averaging in the case of strongly rectilinear flows generally corresponds with flows near the mid-depth level. Prandle (1982b) develops an analytical theory of the vertical structure of tides which "validates the common engineering assumption that average velocity occurs close to 0.4D [D being MSL depth] above the bed" (ibid, p.195).

Figures 7.32 and 7.33 are snapshots of model predictions at the surface and mid-depth levels, respectively, for the same spring event as is depicted in Figure 5.33. Again, gyral activity in the mid-Gulf region adjacent to Wallaroo is common to each figure.

Returning to the ellipse plots of Figures 7.18–7.29, there are gridpoints at which the direction of rotation of the ellipses reverses over the water column. There is a cluster of these stretching northwards from the south eastern corner of the Gulf, though by no means are they isolated to that region. This phenomenon is not unexpected because of the general rectilinearity of the ellipses in the Gulf — for rectilinear ellipses only a small change in the amplitude and phase of the semi-minor axis is needed to reverse the direction of rotation of the ellipses.

Evidence for the presence of residual gyres is contained in the 29-day velocity residual plots for depth-dependent current given in Figures 7.34–7.36. Each of these plots uses the same scale. The plots correspond respectively to residuals in depth-dependent tidal current at the surface, mid-depth and level $k = 9$ (near the sea floor), and all show a large residual gyre spanning the Gulf opposite Wallaroo. In fact all the residual gyres visible on the depth-averaged velocity residual plot of Figure 7.12 are represented in Figures 7.34–7.36. Thus the residual gyres have a depth-varying structure. The residuals at mid-depth are weaker than at the surface, and the level $k = 9$ residuals are weaker still.

There is a discernible rotation in some of the residual vectors as one looks from Figures 7.34 to 7.35 to 7.36. For example, the velocity residual vectors against the open boundary on the eastern side rotate slightly to the right, from the surface to the bed. The vectors directed out of the interior of the model at the mid-section of the open boundary rotate slightly to the left from the point of view of an observer moving with the outward flow. The vectors along the stepped coastal boundary region between Arno Bay and Franklin Harbour (see Figure 5.10) rotate to the right in the direction of their flow.

In Figures 7.37 and 7.38 the depth-dependent ellipse characteristics for the four major constituents are plotted for stations Mike and Lima, respectively. Recently, observations have been obtained for stations Yarraville Shoals, Red, Yellow, Blue and White. The location of all stations is given in Figure 5.10. The predicted depth-dependent ellipse characteristics at these stations are given in Figures 7.39–7.43. Stations Mike, Lima and Yarraville Shoals lie near the axis of the Gulf north of Wallaroo. Station Yarraville Shoals, as its name suggests, lies in relatively shallow water. Stations Red, Yellow, Blue and White lie on a line which is approximately a transect of the Gulf where it narrows as one looks northwards. Relative depth is plotted on the left of the plots of ellipse characteristics in Figures 7.37–7.43 and model MSL depth is plotted on the right (model MSL depth is an

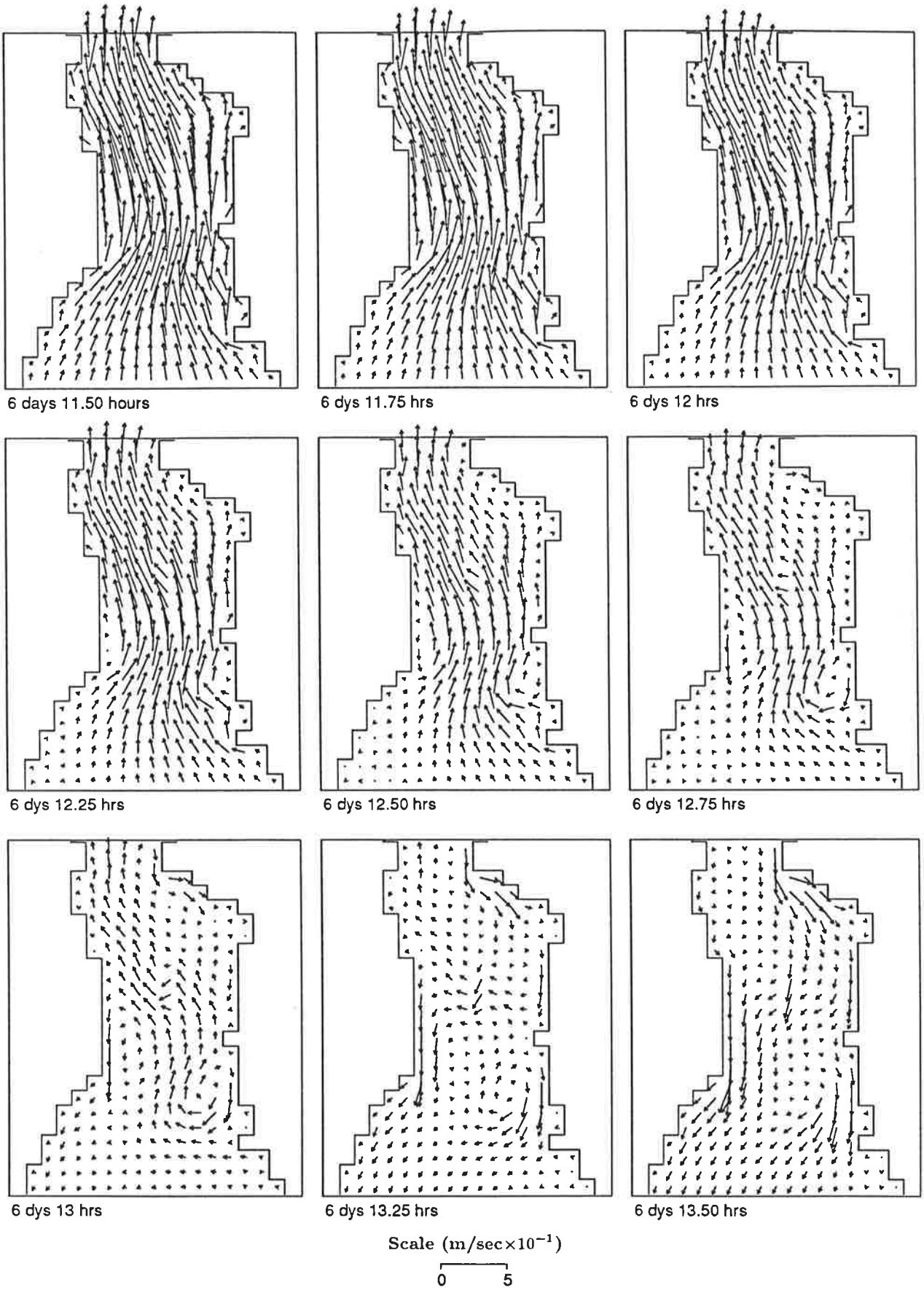


Figure 7.30: *Snapshots of depth-dependent current at the surface level ($k = 0$) at 15 min intervals during the neap event at 6–8 days in the central Gulf region. Compare this sequence with that in Figure 5.32 from the depth-averaged model for the same neap event.*

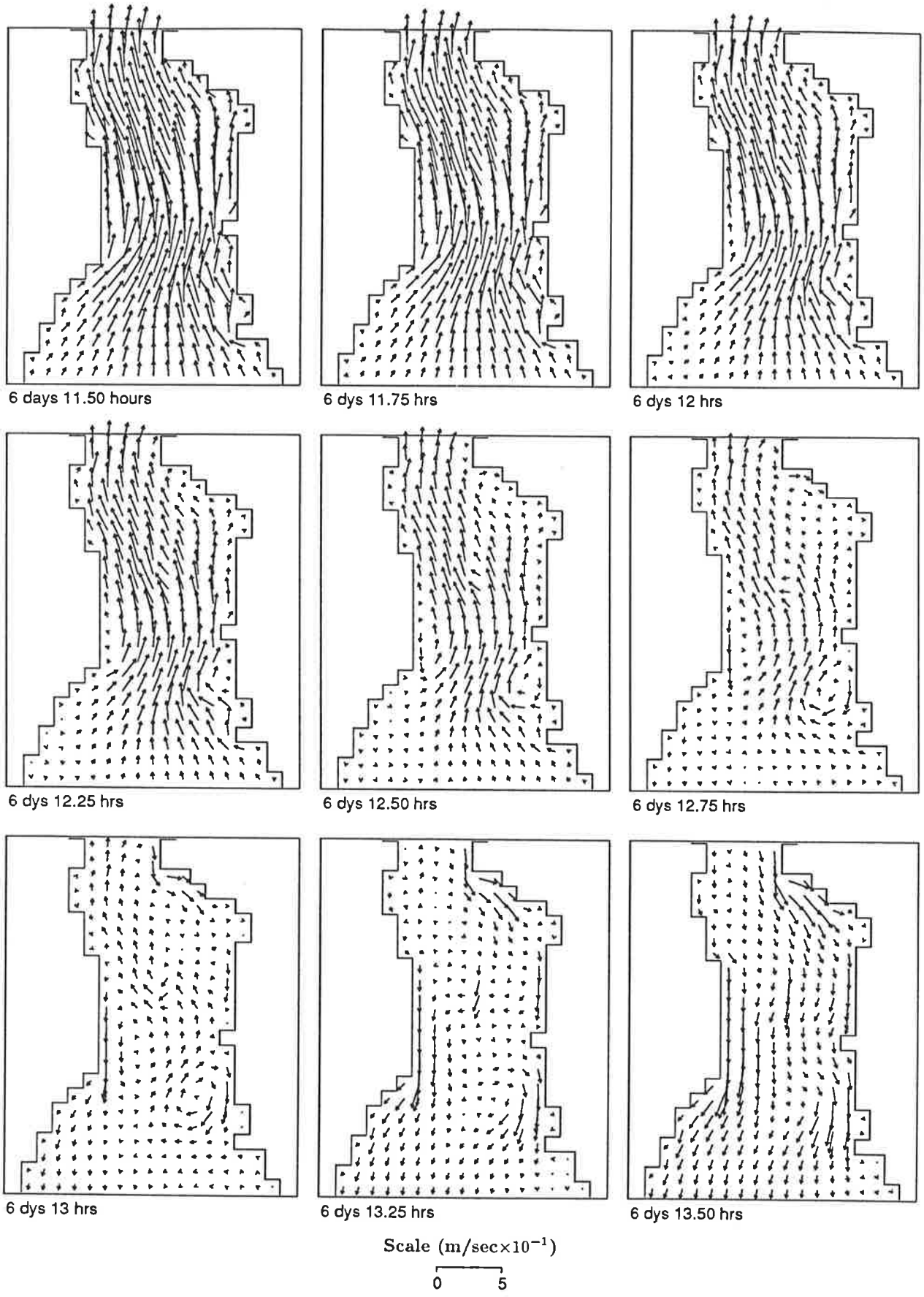


Figure 7.31: *Snapshots of depth-dependent current at mid-depth ($k = 5$) at 15 min intervals during the neap event at 6–8 days. Compare this sequence with that in Figure 5.32 from the depth-averaged model for the same neap event.*

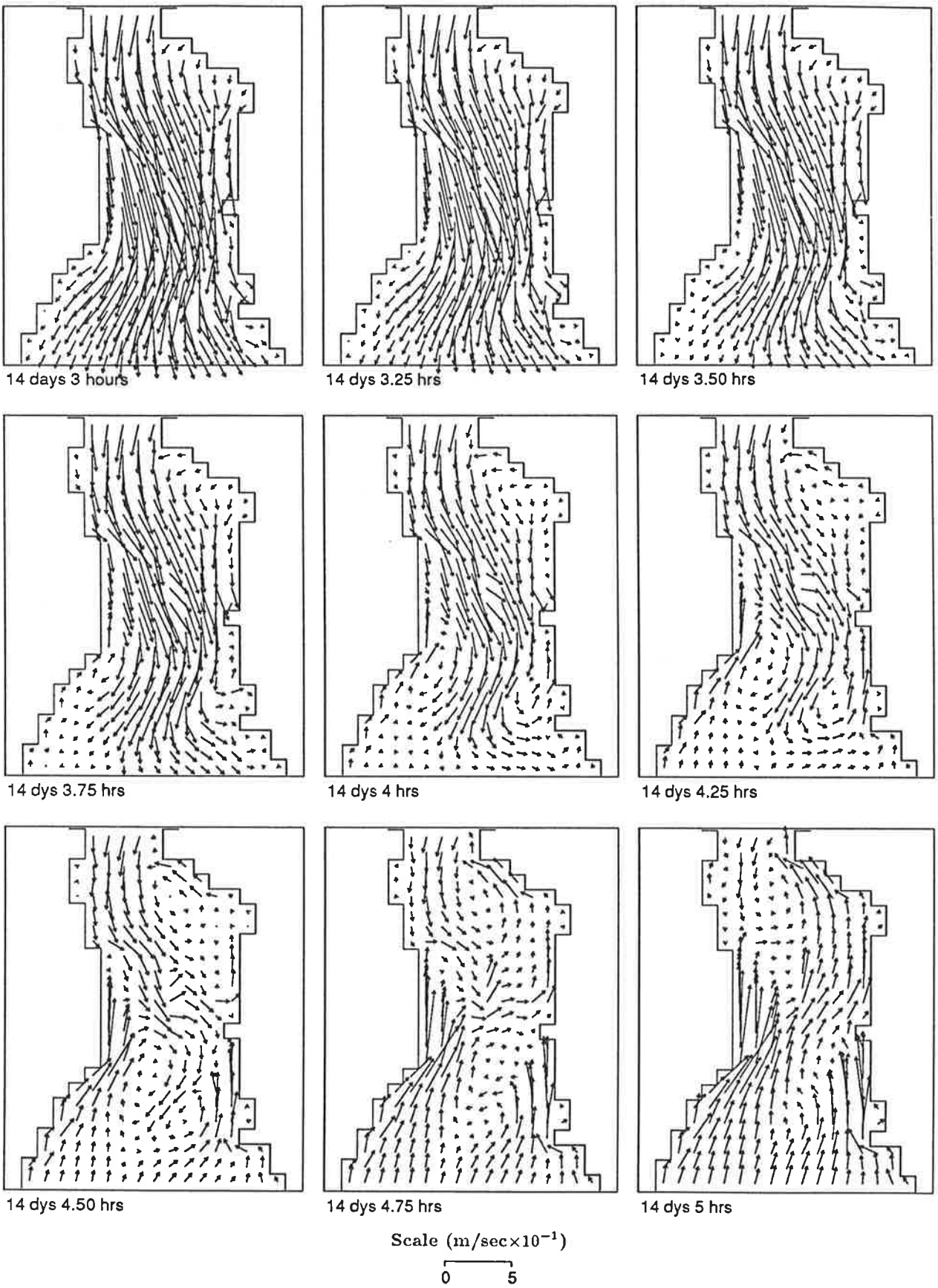


Figure 7.32: *Snapshots of depth-dependent current at the surface level ($k = 0$) at 15 min intervals during the spring event at 13.5–15.5 days in the central Gulf region. Compare this sequence with that in Figure 5.33 from the depth-averaged model for the same spring event.*

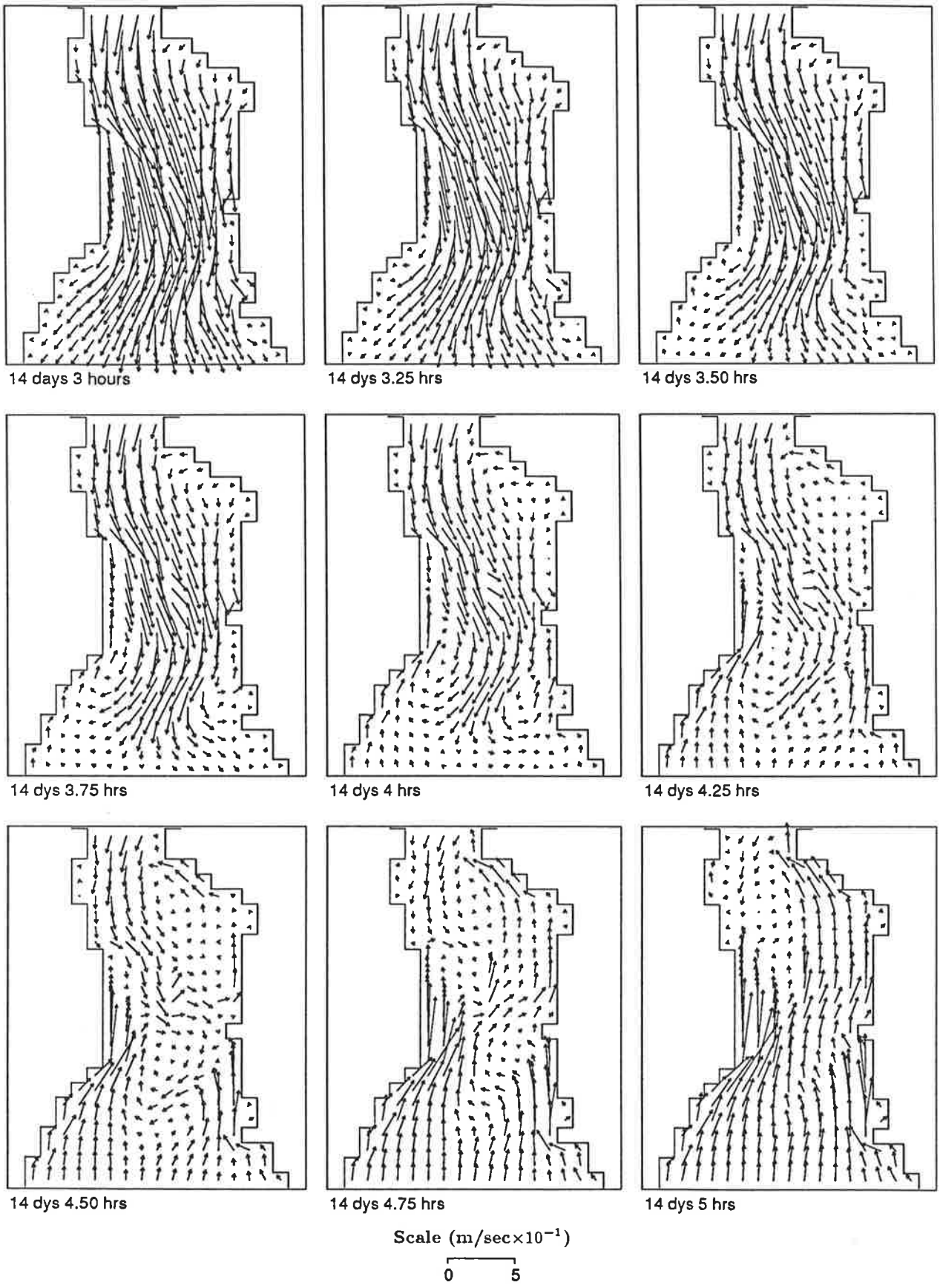


Figure 7.33: *Snapshots of depth-dependent current at mid-depth ($k = 5$) at 15 min intervals during a spring event at 13.5–15.5 days. Compare this sequence with that in Figure 5.33 from the depth-averaged model for the same spring event.*

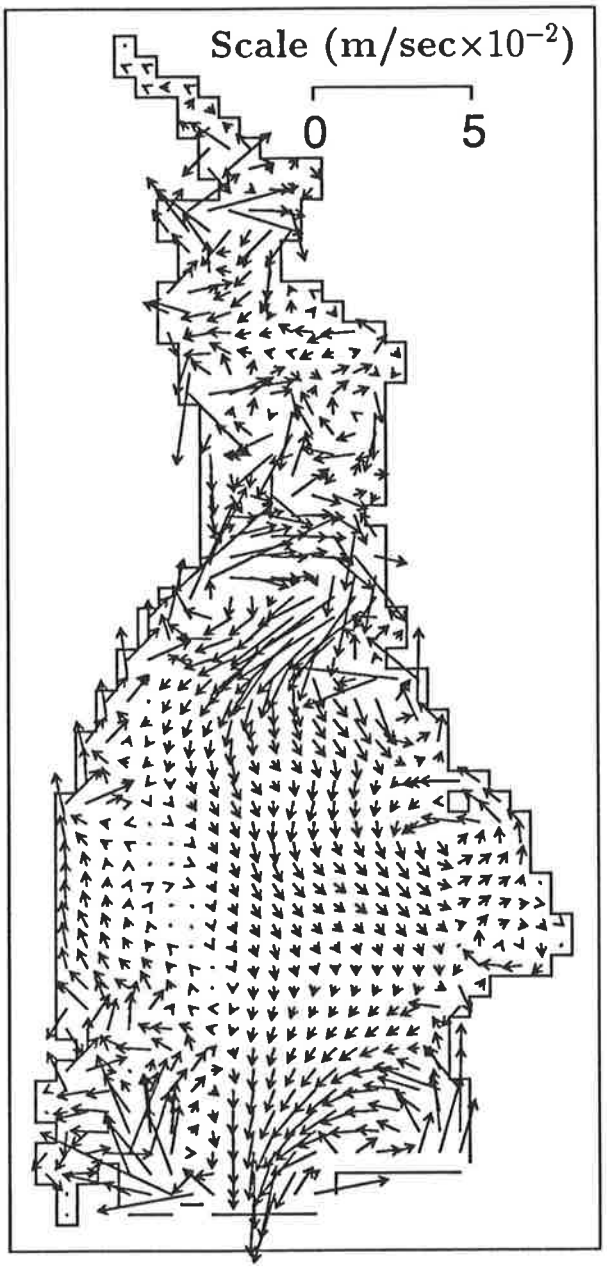


Figure 7.34: *Residuals for depth-dependent velocity ($m/sec \times 10^{-2}$) over a 29 day period (with advection and diffusion terms requiring subordinate approximation excluded). Results are taken from the three-dimensional model at level $k = 0$.*

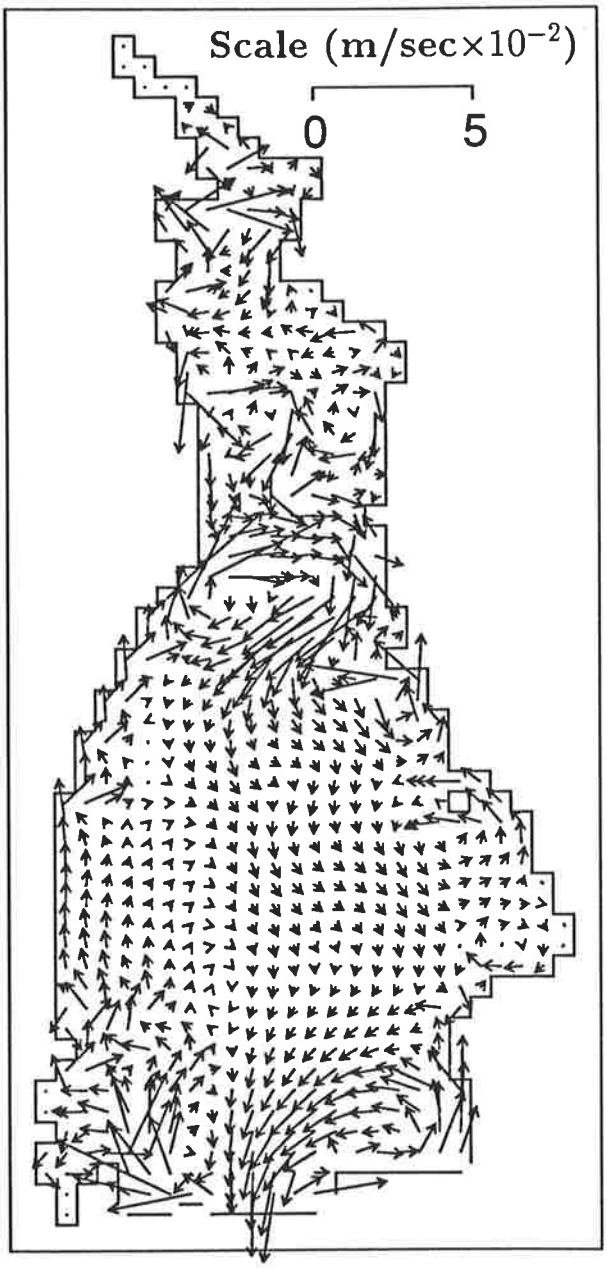


Figure 7.35: *Residuals for depth-dependent velocity ($m/sec \times 10^{-2}$) over a 29 day period (with advection and diffusion terms requiring subordinate approximation excluded). Results are taken from the three-dimensional model at level $k = 5$.*

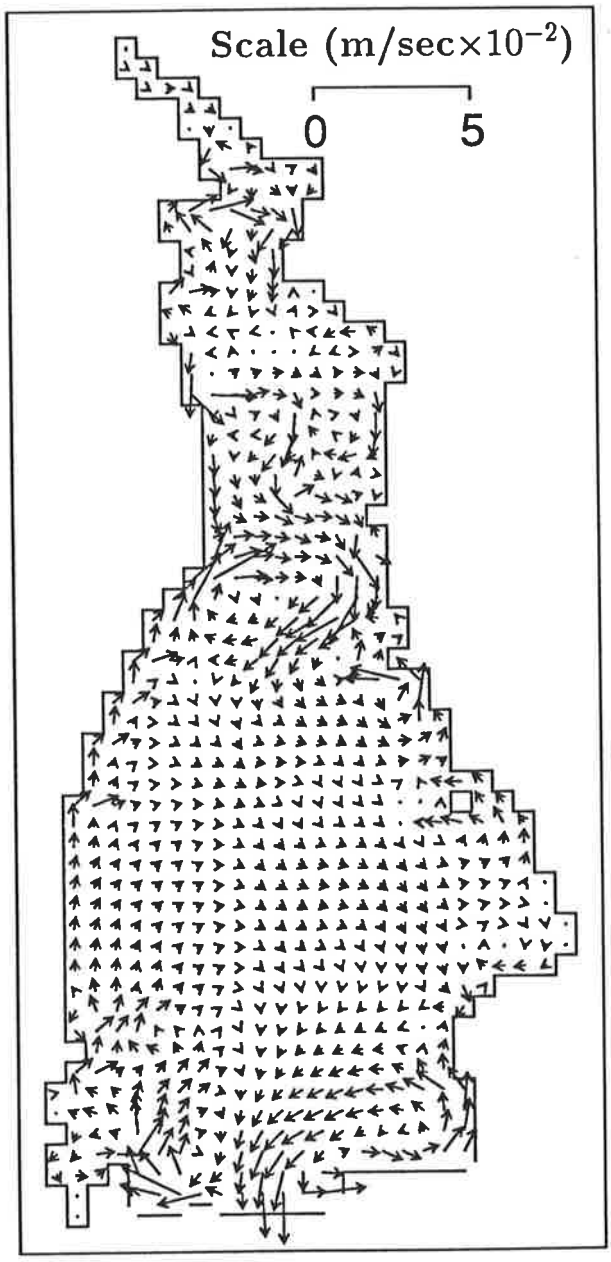


Figure 7.36: *Residuals for depth-dependent velocity ($m/sec \times 10^{-2}$) over a 29 day period (with advection and diffusion terms requiring subordinate approximation excluded). Results are taken from the three-dimensional model at level $k = 9$.*

average depth taken over an entire model element and is different to the spot depth given for the station site).

The fact that the semi-major axes of the ellipses at mid-depth in Figures 7.22–7.25 are only slightly smaller than those at the surface in Figures 7.18–7.21, and that the ellipses for depth level $k = 9$ are very much smaller still, is illustrated in the semi-major axis plots (a) of Figures 7.37–7.43. The high degree of rectilinearity in the ellipses at Mike, Lima and Yarraville Shoals shows in the narrow extent of the semi-minor axis scales (b) of Figures 7.37–7.39 relative to the semi-major axis scales (a) at these three stations.

At Mike, Lima and Yarraville Shoals the semi-major axes of the semi-diurnals M_2 and S_2 have similar strength and are distinct and stronger than the semi-major axes of the diurnals O_1 and K_1; the semi-diurnals have the greater vertical current structure. At Red, Yellow, Blue and White there is no obvious distinction between the semi-diurnals and diurnals. The scale on the horizontal axis for these stations is half that used for the three more northerly stations. Although MSL depth at the seven stations varies by 50%, the vertical profiles of the major axes are similar (in η coordinates), i.e. the shear is similar over depth. This is presumably due to the vertical grid discretisation.

In the semi-minor axis plots (b) of Figures 7.37–7.43 a negative value indicates clockwise ellipse rotation at that level, a zero value indicates a rectilinear ellipse and a positive value indicates anticlockwise rotation. At Mike, Lima and Yarraville Shoals the constituent surface ellipses are predicted to be anticlockwise rotating but proceeding down the water column they all turn clockwise at some level. Along the transect comprising Red, Yellow, Blue and White the surface ellipses are dominantly clockwise rotating on the western side at Red and Yellow, dominantly anticlockwise rotating on the eastern side at Blue and White, but towards the bed all the ellipses become more strongly clockwise rotating. Thus at every station and for each constituent the ellipses become more clockwise rotating over depth towards the bed — the anticlockwise velocity component reduces over depth in relation to the clockwise component. Prandle (1982a,b) has explained the similar, but opposite, effect in the northern hemisphere as friction reducing the clockwise component more than the anticlockwise component over depth. The effect is opposite in the southern hemisphere because Coriolis acts in the opposite rotational direction.

The semi-diurnal phase lags of maximum current have been plotted within a range of values that has the same width for each station (upper plots (c) of Figures 7.37–7.43); similarly for the diurnal phase lags (lower plots (c) of Figures 7.37–7.43). Phase lags for each constituent at each station decrease towards the bed. Thus in every case maximum current occurs at upper levels before it occurs at lower levels. The extent of the decrease in the case of the semi-diurnals is greater for the southern stations. For each constituent the phase lags increase for corresponding depth levels as one proceeds northwards. Although Red lies on the same transect as Yellow, Blue and White, the phase lags recorded for the semi-diurnals at this station are about 15° smaller than those at the other three stations.

The orientation of the semi-major axis is given in degrees measured clockwise from true north. The orientation angle increases for all constituents at each of Mike, Lima and Yarraville Shoals as one looks down the water column. At Red, Yellow, Blue and White, however, the semi-diurnal and diurnal orientations are paired and change in generally opposite directions: while the orientations of the semi-major axes for the semi-diurnals decrease passing down the water column, those for the diurnals increase. At Yellow, Blue and White the rotation direction of the orientation of M_2 is predicted to reverse over depth. Thus the orientation of the semi-major axis is variable in the vertical. Prandle

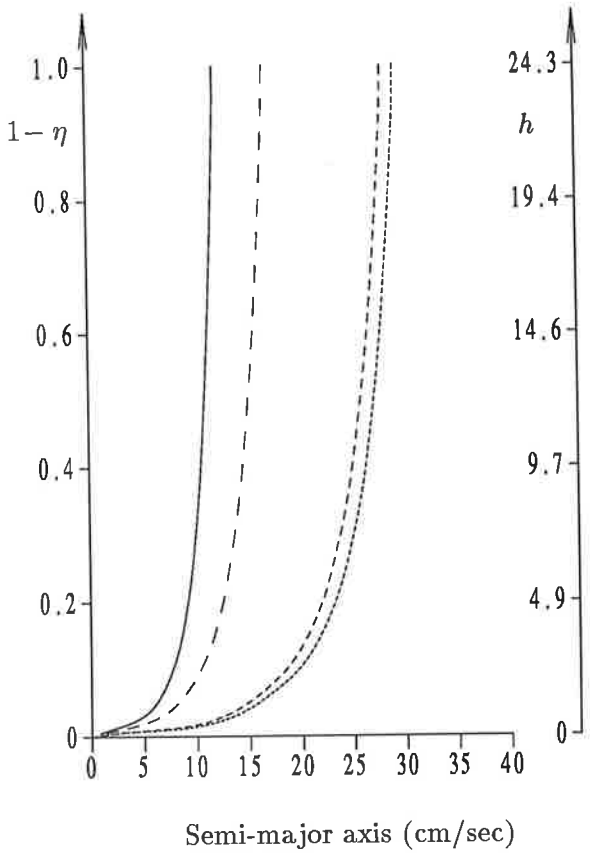


Figure 7.37(a): *Depth-dependent semi-major axis (cm/sec) for the current ellipses of the four major tidal constituents at station Mike.*

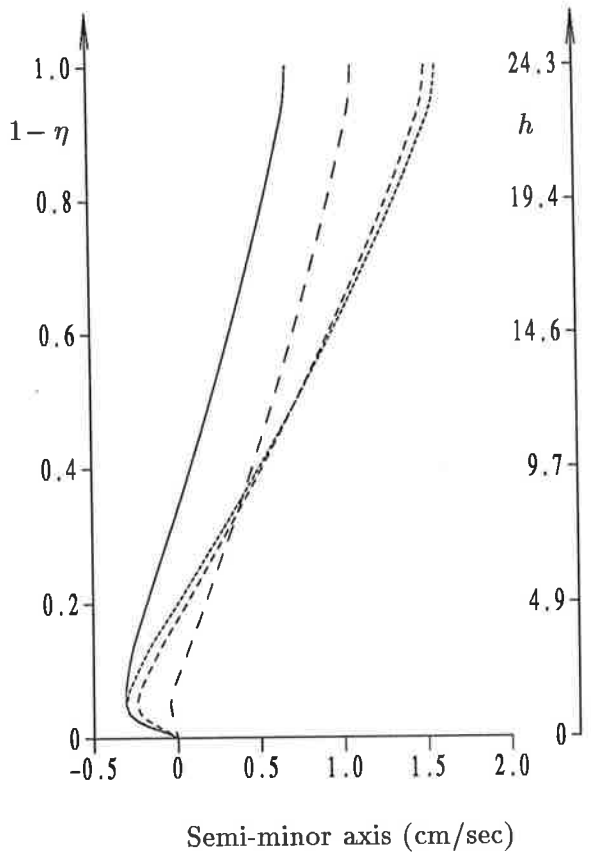


Figure 7.37(b): *Semi-minor axis (cm/sec) (negative value indicates clockwise rotation). MSL depth h (m) is given on right hand axes.*

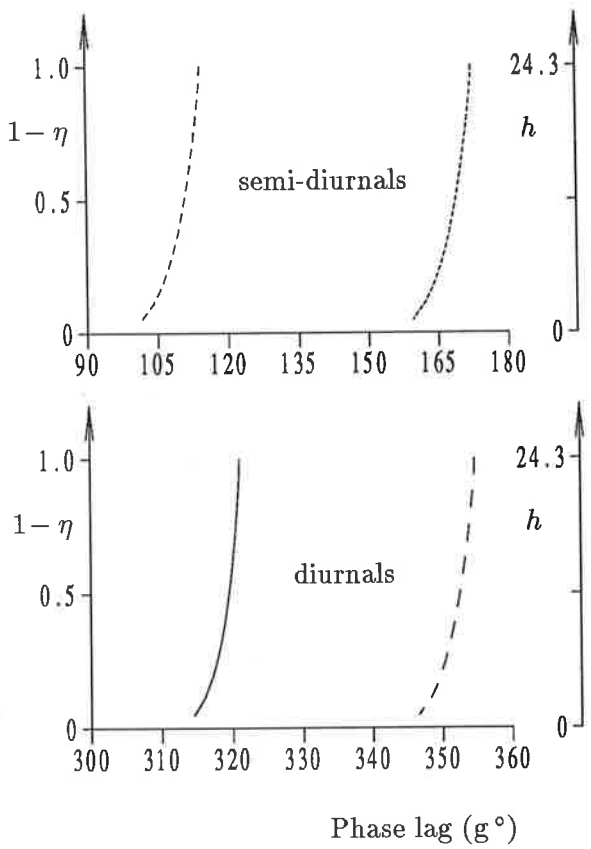


Figure 7.37(c): *Phase lag of maximum (g°) for depth-dependent current ellipses at Mike.*

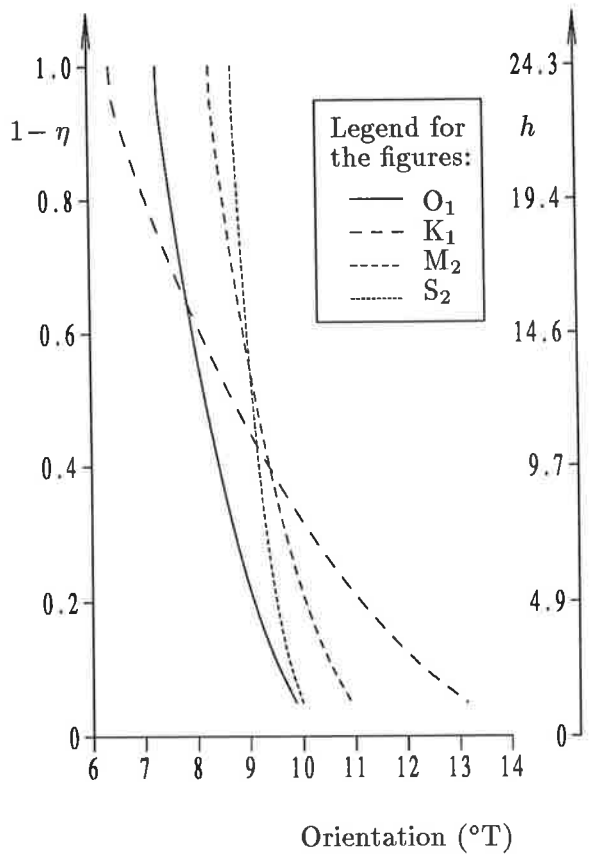


Figure 7.37(d): *Orientation of the semi-major axis (°T).*

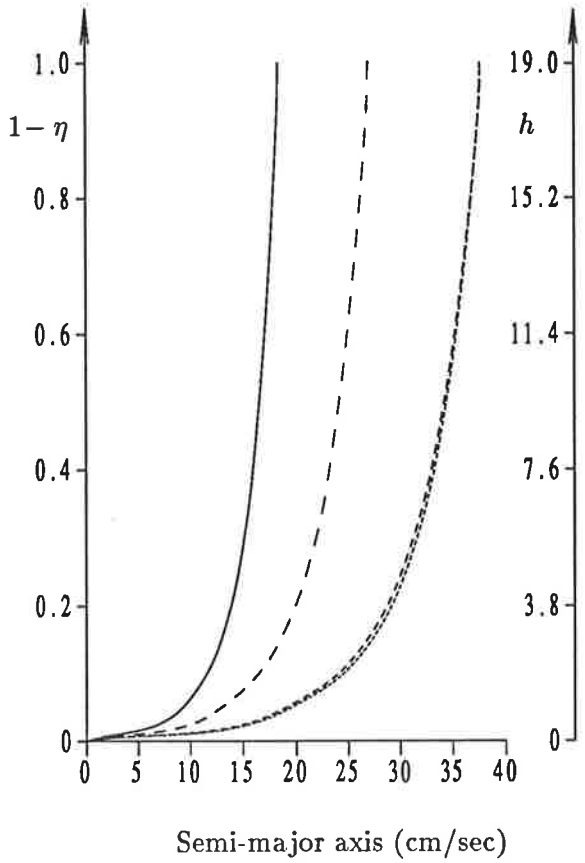


Figure 7.38(a): *Depth-dependent semi-major axis (cm/sec) for the current ellipses of the four major tidal constituents at station Lima.*

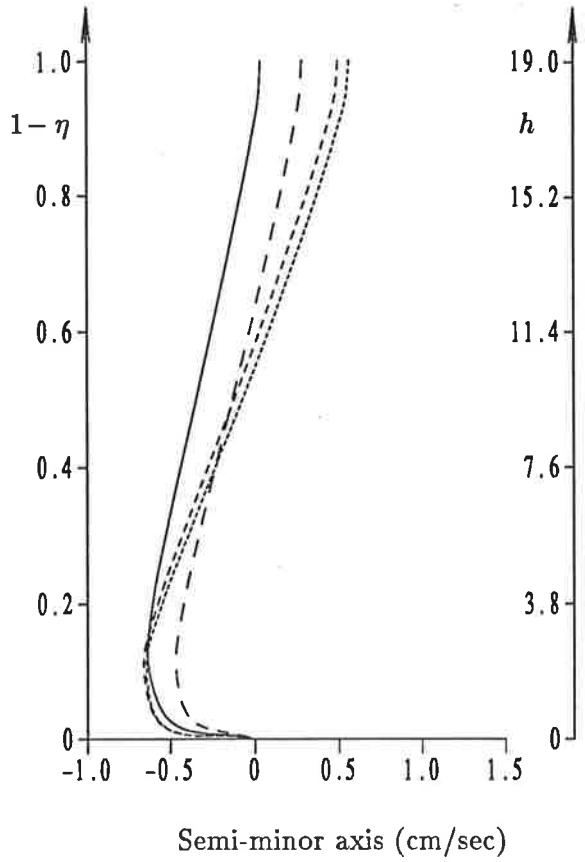


Figure 7.38(b): *Semi-minor axis (cm/sec) (negative value indicates clockwise rotation). MSL depth h (m) is given on right hand axes.*

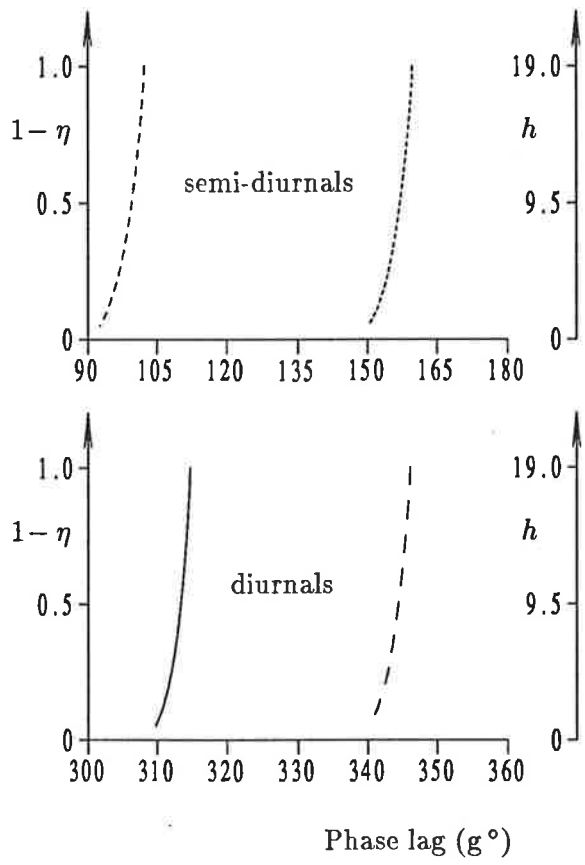


Figure 7.38(c): *Phase lag of maximum (g°) for depth-dependent current ellipses at Lima.*

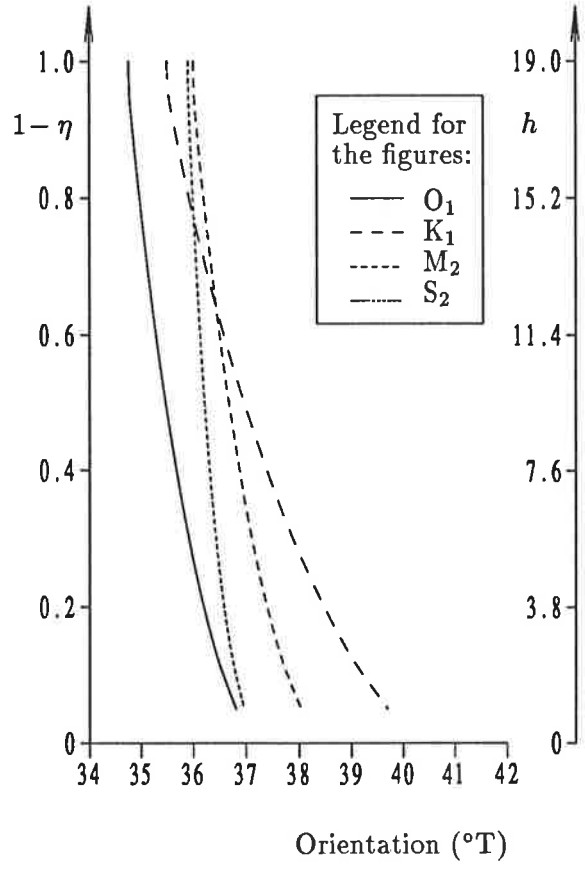


Figure 7.38(d): *Orientation of the semi-major axis (°T).*

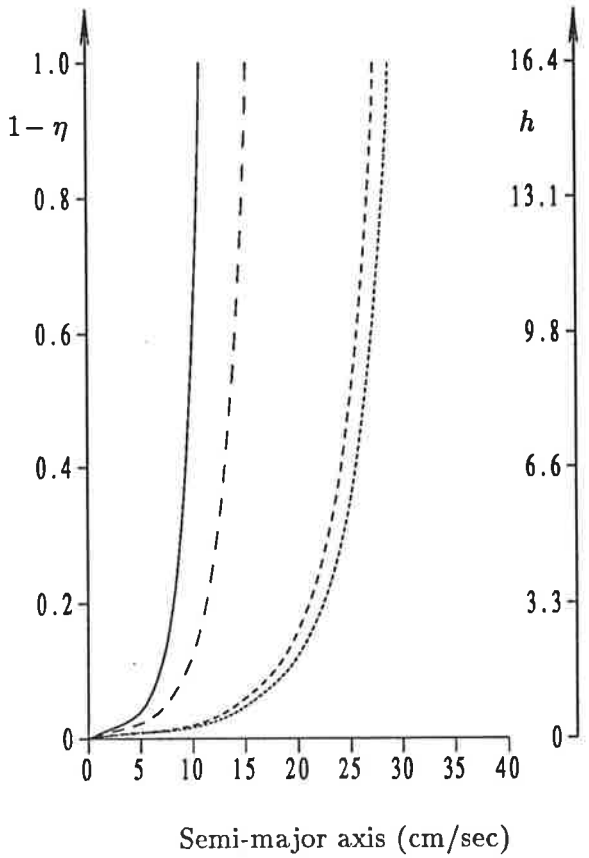


Figure 7.39(a): *Depth-dependent semi-major axis (cm/sec) for the current ellipses of the four major tidal constituents at Yarraville Shoals.*

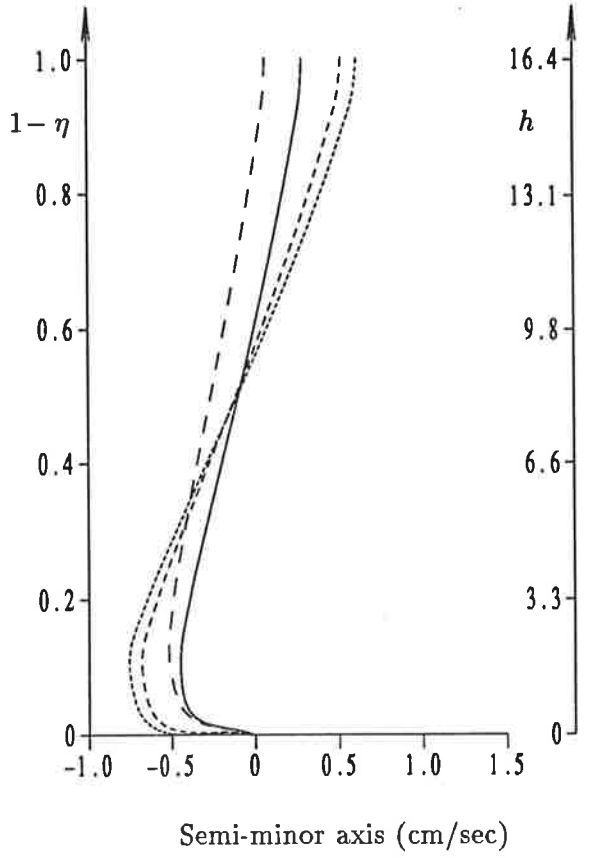


Figure 7.39(b): *Semi-minor axis (cm/sec) (negative value indicates clockwise rotation). MSL depth h (m) is given on right hand axes.*

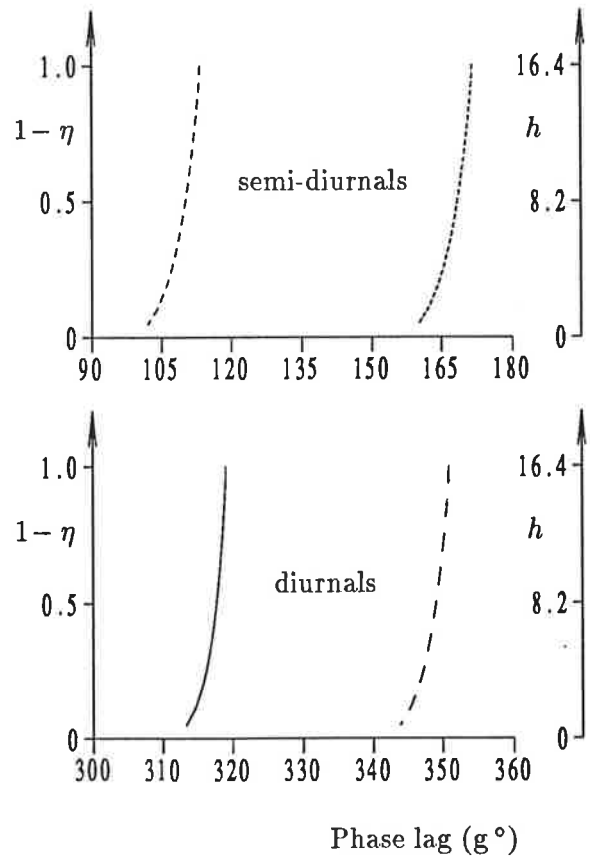


Figure 7.39(c): *Phase lag of maximum (g°) for depth-dependent current ellipses at Yarraville.*

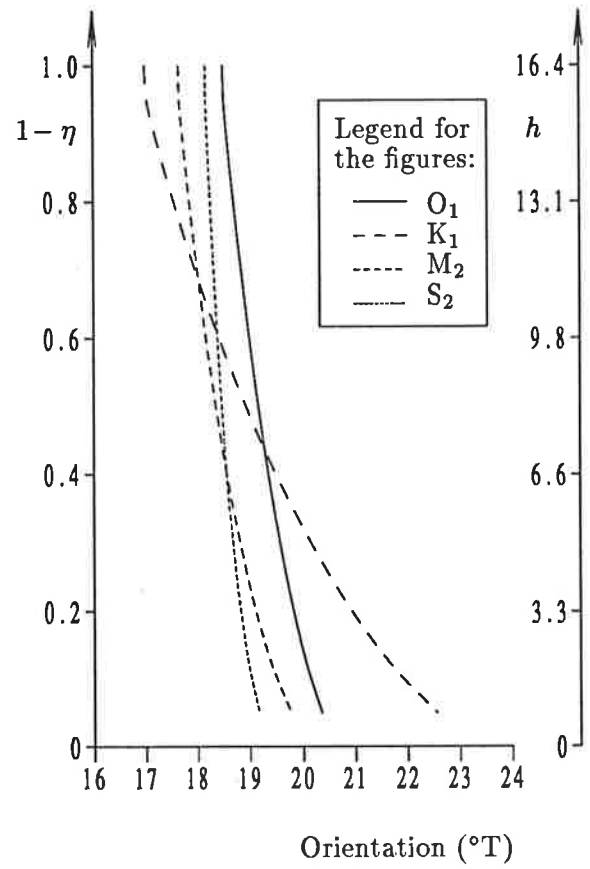


Figure 7.39(d): *Orientation of the semi-major axis (°T).*

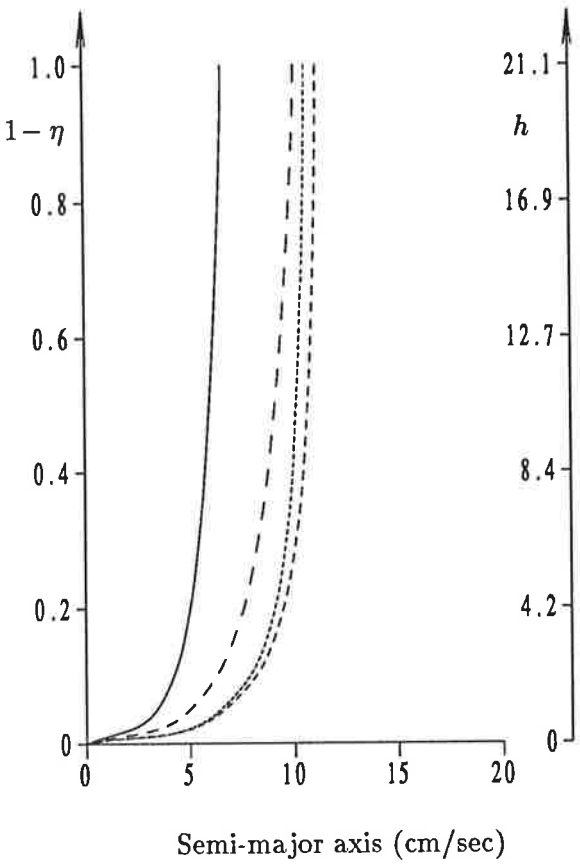


Figure 7.40(a): *Depth-dependent semi-major axis (cm/sec) for the current ellipses of the four major tidal constituents at station Red.*

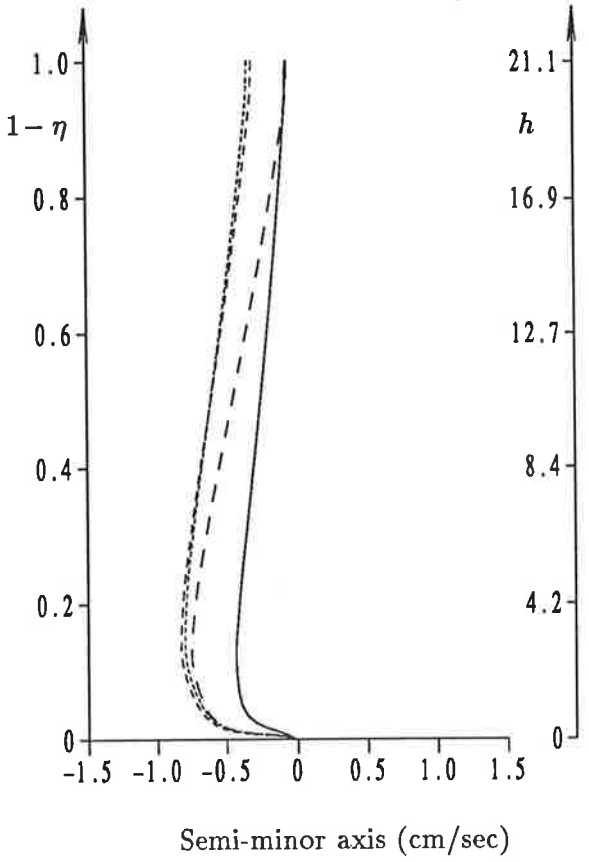


Figure 7.40(b): *Semi-minor axis (cm/sec) (negative value indicates clockwise rotation). MSL depth h (m) is given on right hand axes.*

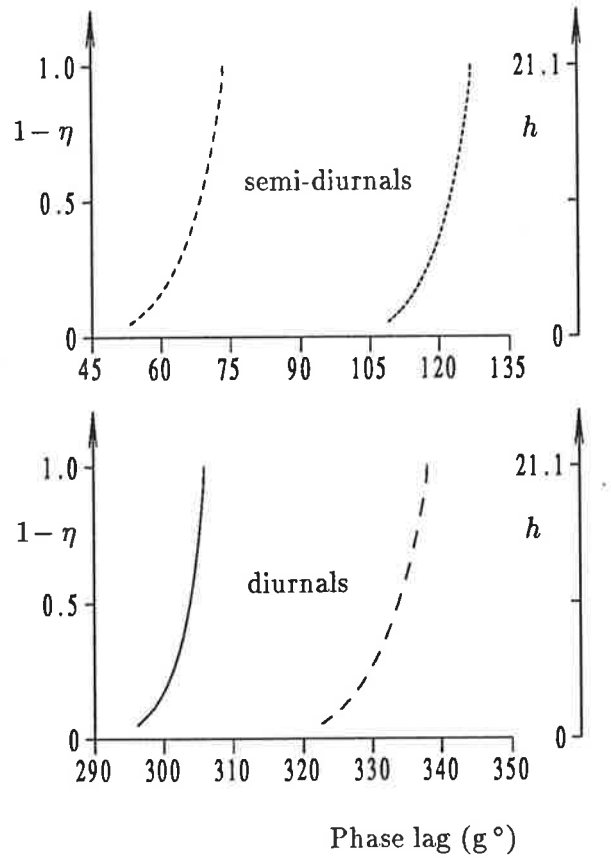


Figure 7.40(c): *Phase lag of maximum (g°) for depth-dependent current ellipses at Red.*

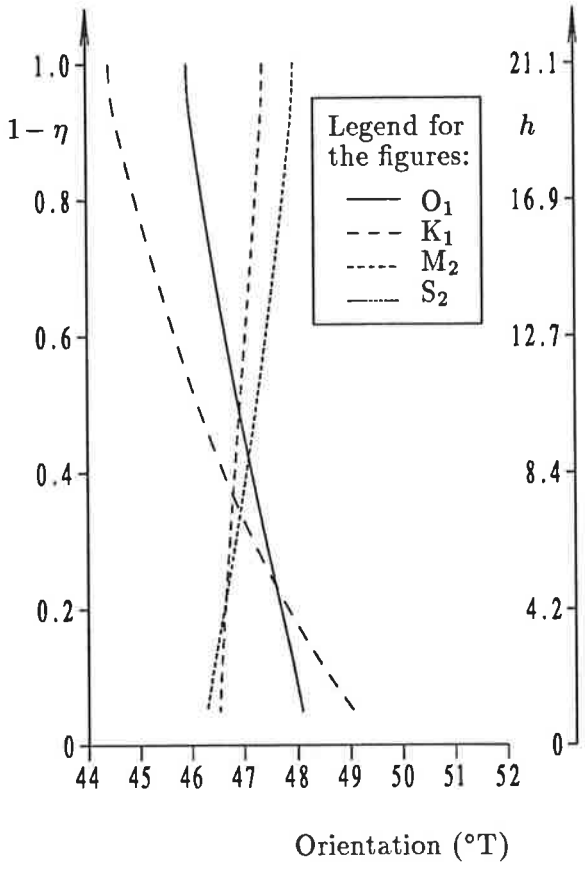


Figure 7.40(d): *Orientation of the semi-major axis (°T).*

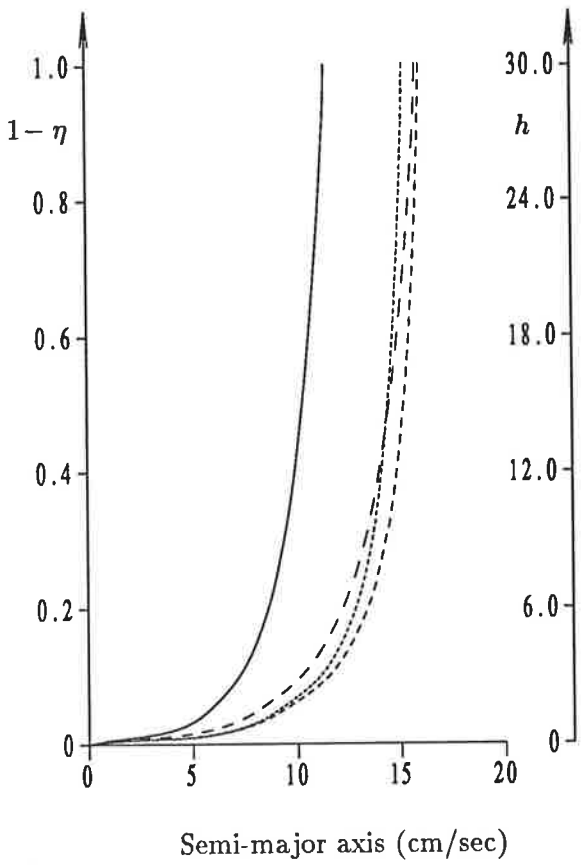


Figure 7.41(a): *Depth-dependent semi-major axis (cm/sec) for the current ellipses of the four major tidal constituents at station Yellow.*

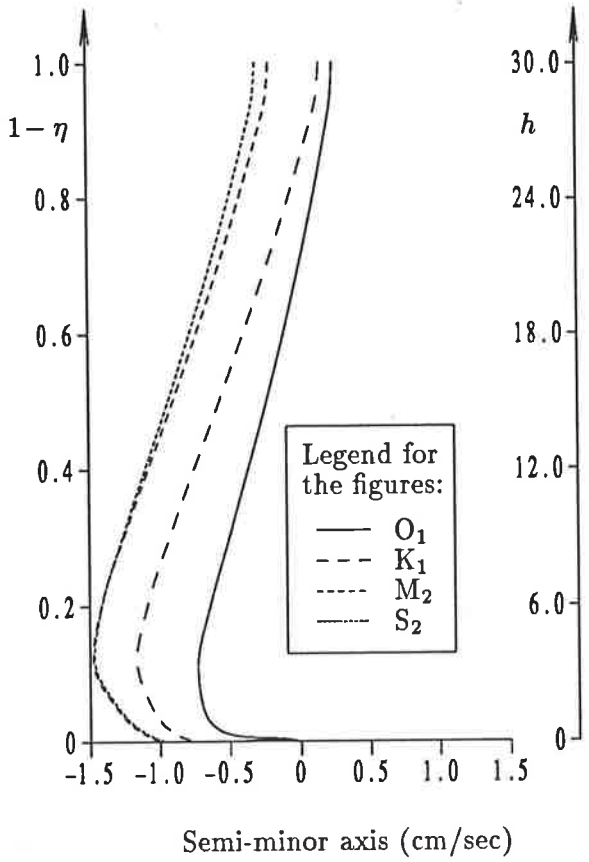


Figure 7.41(b): *Semi-minor axis (cm/sec) (negative value indicates clockwise rotation). MSL depth h (m) is given on right hand axes.*

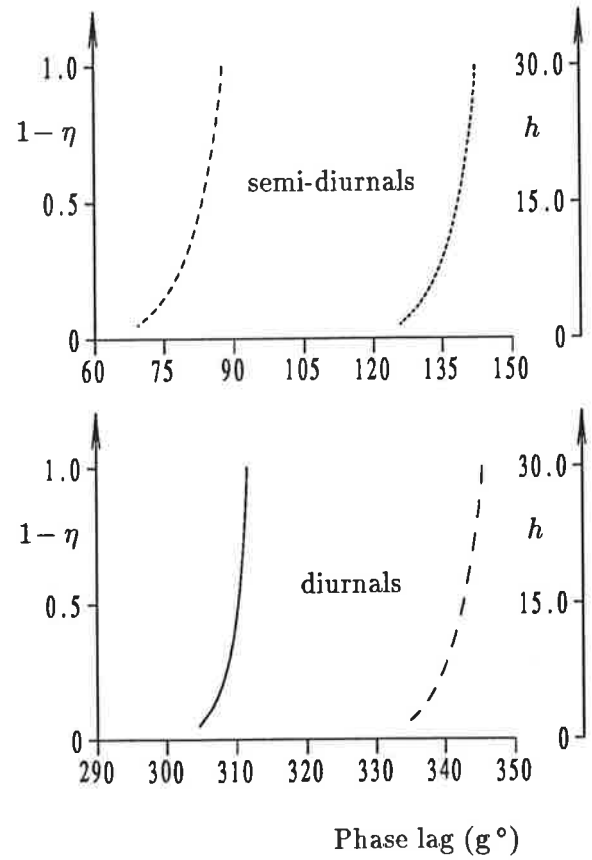


Figure 7.41(c): *Phase lag of maximum (g°) for depth-dependent current ellipses at Yellow.*

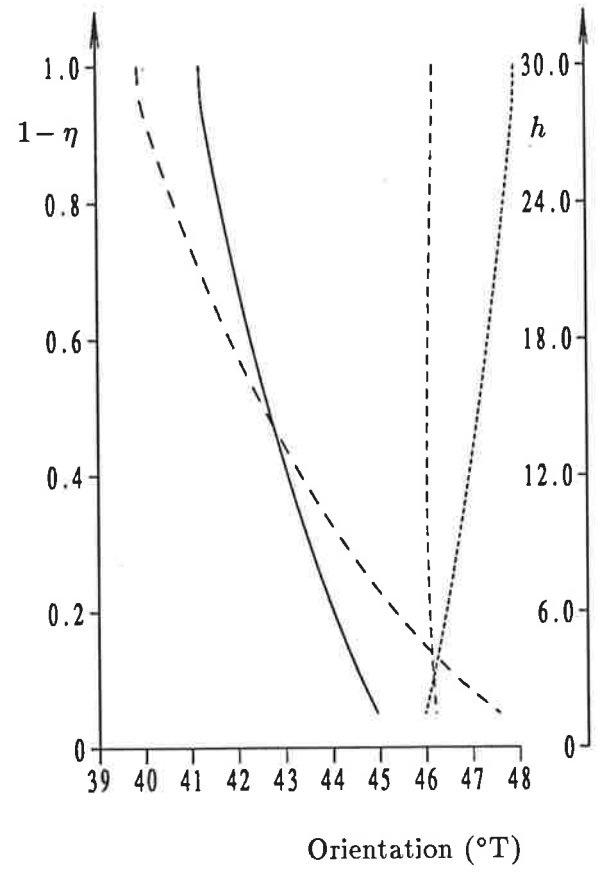


Figure 7.41(d): *Orientation of the semi-major axis (°T).*

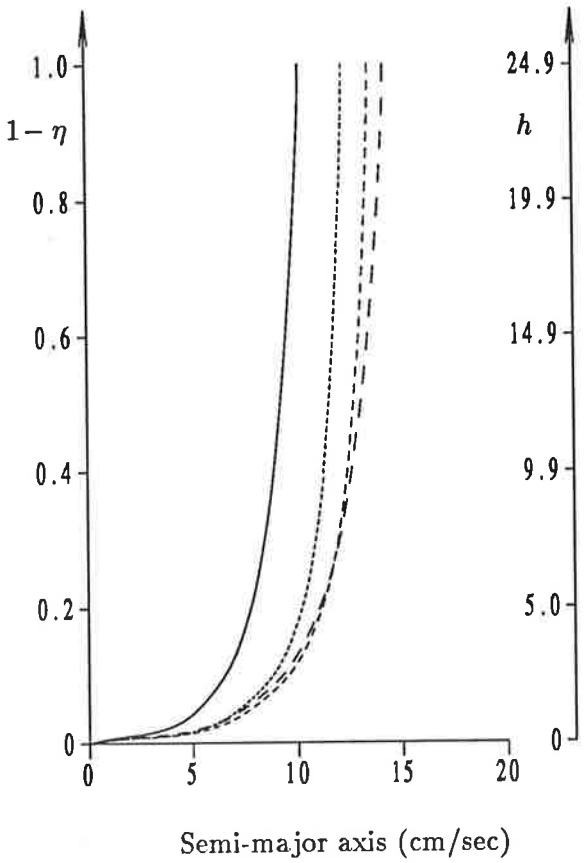


Figure 7.42(a): *Depth-dependent semi-major axis (cm/sec) for the current ellipses of the four major tidal constituents at station Blue.*

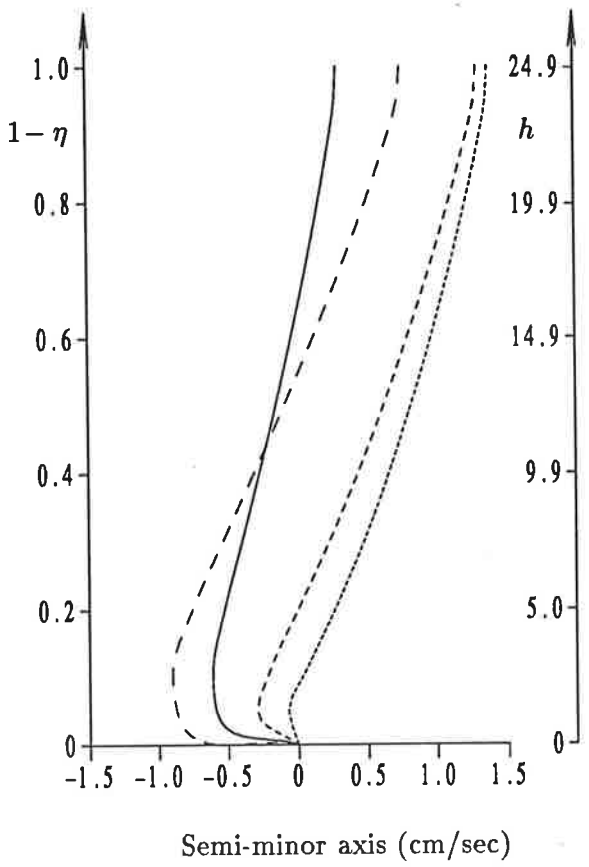


Figure 7.42(b): *Semi-minor axis (cm/sec) (negative value indicates clockwise rotation). MSL depth h (m) is given on right hand axes.*

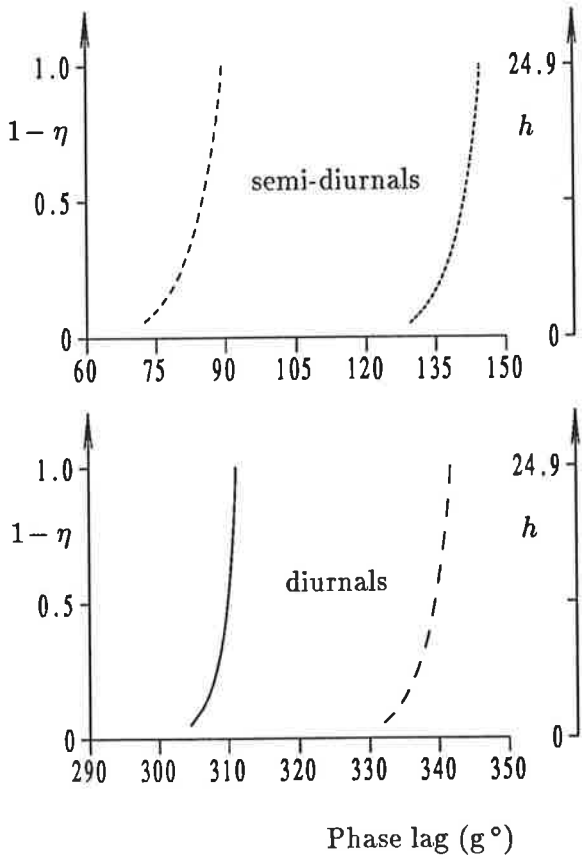


Figure 7.42(c): *Phase lag of maximum (g°) for depth-dependent current ellipses at Blue.*

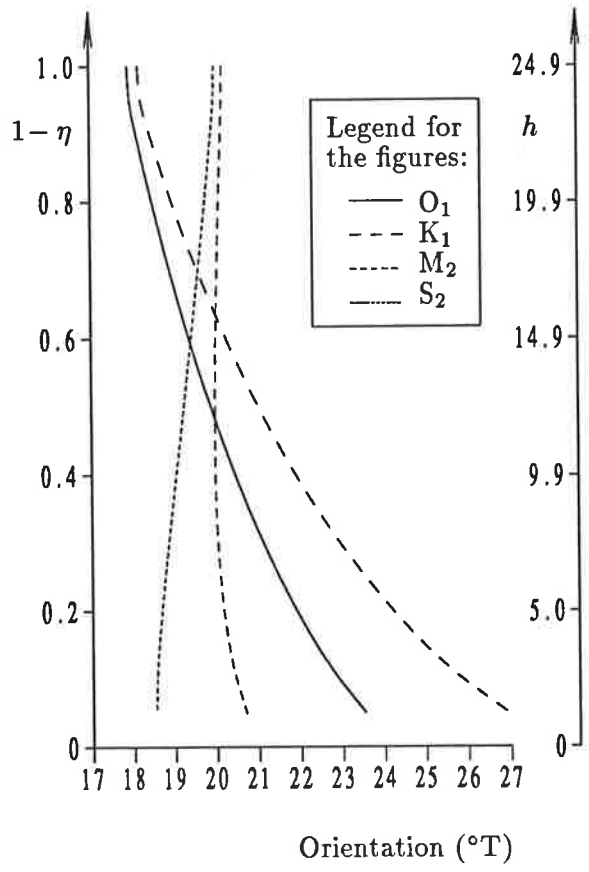


Figure 7.42(d): *Orientation of the semi-major axis (°T).*

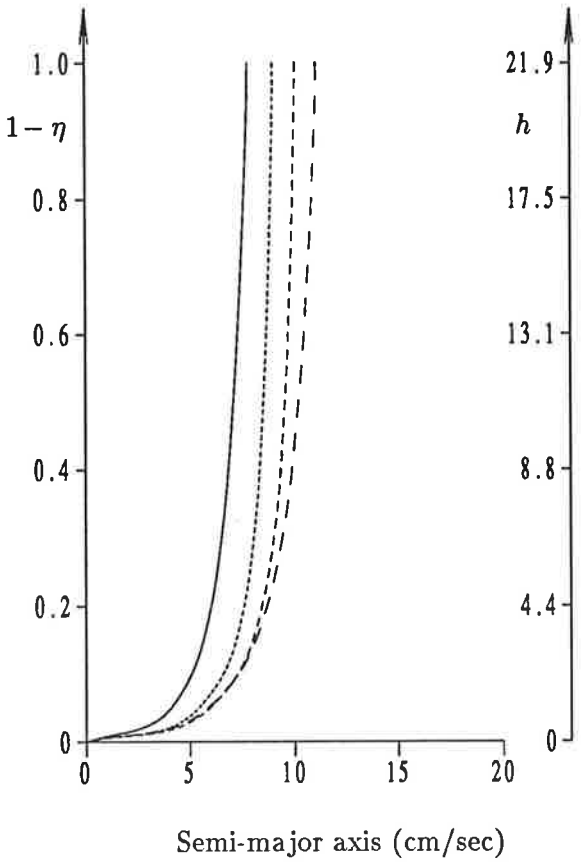


Figure 7.43(a): *Depth-dependent semi-major axis (cm/sec) for the current ellipses of the four major tidal constituents at station White.*

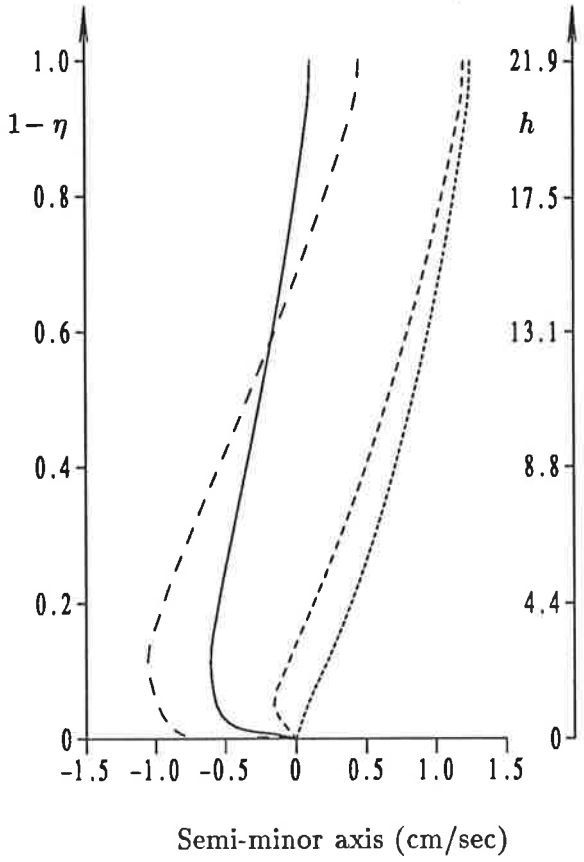


Figure 7.43(b): *Semi-minor axis (cm/sec) (negative value indicates clockwise rotation). MSL depth h (m) is given on right hand axes.*

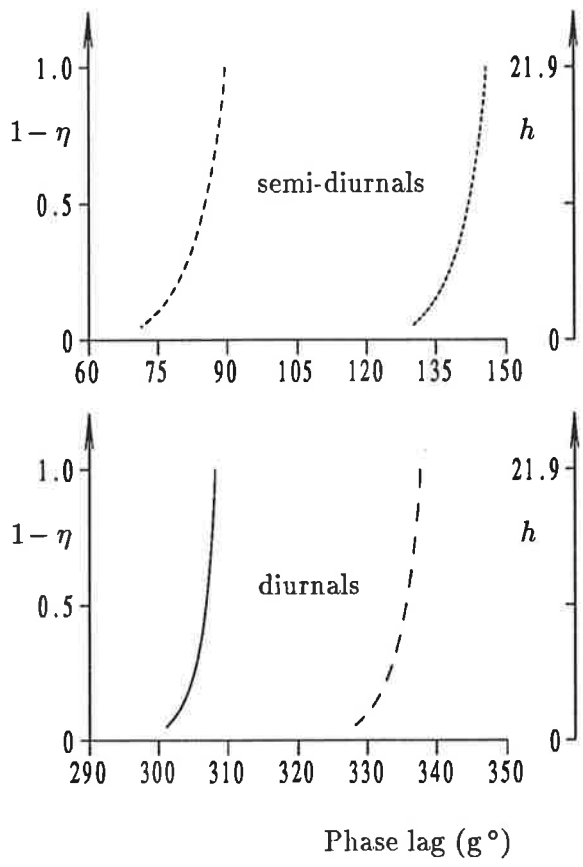


Figure 7.43(c): *Phase lag of maximum (g°) for depth-dependent current ellipses at White.*

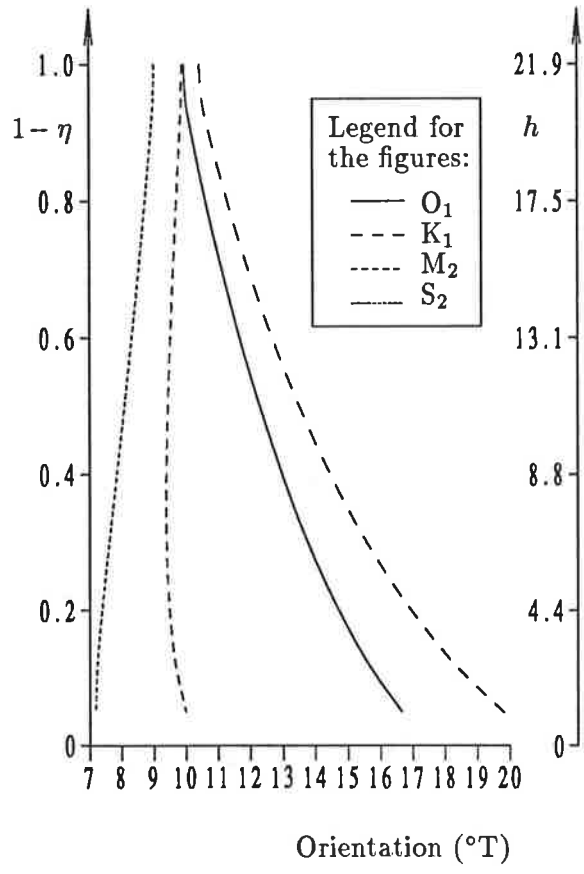


Figure 7.43(d): *Orientation of the semi-major axis (°T).*

(1982a) showed that in the case of an analytical model with constant vertical eddy viscosity, rotation in the direction of the semi-major axis can occur in either sense over depth as vertical eddy viscosity is increased (say).

It is significant that the orientations for the diurnals maintain a steady increase over depth at all stations whilst those for the semi-diurnals do not. This probably reflects the steady progression of the diurnals in both amplitude and phase northwards along the Gulf as seen in the elevation contours of Figures 7.4 and 7.5, whilst the semi-diurnals undergo a major change in character as they pass the transect Red-White and the nearby zone of minimum amplitude on the eastern coast (see Figures 7.6(a) and 7.7(a)).

The reason for the barely discernible rotation over depth of the semi-major axes in the ellipse plots of Figures 7.18–7.29 can be found in plots (d) of Figures 7.37–7.43. For Mike, Lima and Yarraville Shoals the greatest rotation of semi-major axis is shown by K_1 and is of the order of 5°–7° clockwise, looking down the water column. The remaining constituents rotate at most 3° clockwise, according to the model, and this is very difficult to discern in the depth-dependent ellipse plots of Figures 7.18–7.29. For stations Red, Yellow, Blue and White, K_1 again rotates the most, 5° at Red, 8° at Yellow, 9° at Blue and nearly 10° at White. Again Red shows significantly different behaviour to Yellow, Blue and White. Constituent O_1 shows the next greatest rotation but the semi-diurnals rotate by no more than 2° at any of these stations. Having noted that K_1 rotates the most, one can go back to the ellipse plots of Figures 7.18–7.29 and find graphical evidence of that rotation.

The behaviour of the major constituents is noticeably different at Red compared to the other stations of the Red-White transect. A contributing reason for this may be that the semi-diurnals for the four stations are strongest at Red. But by inspecting Figure 5.10 one sees that Red is next to the coastline and this fact, as far as model predictions go, is most likely to be the reason for the compactness of the depth-dependent ellipse characteristics there.

From the three-dimensional model predictions, depth-averaged ellipse characteristics can be derived and compared with those of Tables 5.9–5.11 in Chapter 5. These are presented in Tables 7.2 and 7.3 along with the depth-averaged predictions from Chapter 5 (DA-Chp7 are the depth-averaged results from the three-dimensional model of the present chapter, and DA-Chp5 are the depth-averaged results from Chapter 5). Comparison of these results again confirms the consistency of the two models in their depth-averaged predictions.

Using linear interpolation, ellipse characteristics can be determined from the data of Figures 7.37–7.43 which correspond to the depths levels at which Lennon (1981, 1990) provides observations. This data is collated in Tables 7.4–7.6.

In Table 7.4 predicted and observed ellipse characteristics are given for stations Mike, Yarraville Shoals and Red. Recordings of tidal current are available at only one depth level at these sites. In Table 7.5 characteristics are given for two levels at each of stations Lima and Yellow, and similarly in Table 7.6 characteristics at two levels are given for each of Blue and White.

Accompanying the statement of height above sea bed for the current meter at each station is the mean depth given by Lennon (1981, 1990) for that site and in brackets, the MSL depth used in the model for the gridpoint from which predictions for the corresponding site are made.

At Mike both depth values are similar. At Yarraville Shoals, however, the site depth is

Tidal constituent		O_1	K_1	M_2	S_2
Mike: predicted ellipse characteristics from depth-averaged results					
Semi-major axis (cm/sec)	DA-Chp7:	10.3	14.1	24.2	25.4
	DA-Chp5:	10.1	13.7	24.5	25.4
Semi-minor axis (cm/sec)	DA-Chp7:	0.20	0.57	0.70	0.69
	DA-Chp5:	0.23	0.62	0.81	0.80
Phase lag of maximum (g°)	DA-Chp7:	319	352	111	168
	DA-Chp5:	320	352	108	167
Orientation of major axis (°T)	DA-Chp7:	8.2	8.8	9.2	9.2
	DA-Chp5:	8.0	8.5	9.1	9.1
Direction of rotation	DA-Chp7:	A	A	A	A
	DA-Chp5:	A	A	A	A
Lima: predicted ellipse characteristics from depth-averaged results					
Semi-major axis (cm/sec)	DA-Chp7:	15.6	22.7	32.1	32.3
	DA-Chp5:	15.2	21.8	32.7	32.7
Semi-minor axis (cm/sec)	DA-Chp7:	−0.32	−0.10	−0.09	−0.06
	DA-Chp5:	−0.30	−0.08	−0.09	−0.07
Phase lag of maximum (g°)	DA-Chp7:	313	344	99	157
	DA-Chp5:	313	344	97	154
Orientation of major axis (°T)	DA-Chp7:	35.5	37.0	36.7	36.3
	DA-Chp5:	35.6	37.0	36.7	36.3
Direction of rotation	DA-Chp7:	C	C	C	C
	DA-Chp5:	C	C	C	C
Yarraville Shoals: ellipse characteristics from depth-averaged results					
Semi-major axis (cm/sec)	DA-Chp7:	9.6	12.8	23.4	24.7
	DA-Chp5:	8.9	12.3	23.6	24.7
Semi-minor axis (cm/sec)	DA-Chp7:	−0.09	−0.23	−0.09	−0.09
	DA-Chp5:	−0.07	−0.20	−0.06	−0.06
Phase lag of maximum (g°)	DA-Chp7:	318	349	110	168
	DA-Chp5:	318	348	107	166
Orientation of major axis (°T)	DA-Chp7:	19.2	19.0	18.4	18.6
	DA-Chp5:	19.2	19.0	18.4	18.5
Direction of rotation	DA-Chp7:	C	C	C	C
	DA-Chp5:	C	C	C	C

Table 7.2: *Comparison of predicted ellipse characteristics for the four major tidal current constituents from the depth-averaged results of the three-dimensional (DA-Chp7) and depth-averaged (DA-Chp5) models at stations Mike, Lima and Yarraville Shoals.*

Tidal constituent		O_1	K_1	M_2	S_2
Red: predicted ellipse characteristics from depth-averaged results					
Semi-major axis (cm/sec)	DA-Chp7:	5.6	8.5	10.0	9.5
	DA-Chp5:	5.6	8.3	10.3	9.8
Semi-minor axis (cm/sec)	DA-Chp7:	−0.24	−0.41	−0.57	−0.58
	DA-Chp5:	−0.24	−0.40	−0.58	−0.59
Phase lag of maximum (g°)	DA-Chp7:	303	333	68	122
	DA-Chp5:	304	333	66	120
Orientation of major axis (°T)	DA-Chp7:	46.9	46.3	47.1	47.4
	DA-Chp5:	46.9	46.3	47.0	47.3
Direction of rotation	DA-Chp7:	C	C	C	C
	DA-Chp5:	C	C	C	C
Yellow: predicted ellipse characteristics from depth-averaged results					
Semi-major axis (cm/sec)	DA-Chp7:	9.7	13.6	14.3	13.6
	DA-Chp5:	9.5	13.2	14.8	14.1
Semi-minor axis (cm/sec)	DA-Chp7:	−0.23	−0.51	−0.86	−0.90
	DA-Chp5:	−0.22	−0.49	−0.86	−0.90
Phase lag of maximum (g°)	DA-Chp7:	310	342	83	138
	DA-Chp5:	310	342	80	136
Orientation of major axis (°T)	DA-Chp7:	42.7	42.7	46.3	47.3
	DA-Chp5:	42.6	42.7	46.1	47.1
Direction of rotation	DA-Chp7:	C	C	C	C
	DA-Chp5:	C	C	C	C
Blue: predicted ellipse characteristics from depth-averaged results					
Semi-major axis (cm/sec)	DA-Chp7:	8.7	12.2	12.0	10.9
	DA-Chp5:	8.5	11.8	12.4	11.4
Semi-minor axis (cm/sec)	DA-Chp7:	−0.15	−0.07	0.57	0.74
	DA-Chp5:	−0.14	−0.07	0.59	0.75
Phase lag of maximum (g°)	DA-Chp7:	310	339	85	140
	DA-Chp5:	309	338	82	138
Orientation of major axis (°T)	DA-Chp7:	20.0	21.2	20.3	19.4
	DA-Chp5:	20.0	21.2	20.3	19.7
Direction of rotation	DA-Chp7:	C	C	A	A
	DA-Chp5:	C	C	A	A
White: predicted ellipse characteristics from depth-averaged results					
Semi-major axis (cm/sec)	DA-Chp7:	6.7	9.6	9.0	8.0
	DA-Chp5:	6.5	9.2	9.4	8.4
Semi-minor axis (cm/sec)	DA-Chp7:	−0.24	−0.31	0.60	0.76
	DA-Chp5:	−0.24	−0.31	0.60	0.76
Phase lag of maximum (g°)	DA-Chp7:	306	335	85	141
	DA-Chp5:	306	334	81	138
Orientation of major axis (°T)	DA-Chp7:	12.4	13.8	9.8	8.3
	DA-Chp5:	12.6	13.8	10.1	8.9
Direction of rotation	DA-Chp7:	C	C	A	A
	DA-Chp5:	C	C	A	A

Table 7.3: *Comparison of predicted ellipse characteristics for the four major current constituents from the depth-averaged results of the three-dimensional (DA-Chp7) and depth-averaged (DA-Chp5) models at stations Red, Yellow, Blue and White.*

Tidal constituent		O_1	K_1	M_2	S_2
Mike: meter 10 m from bottom in 24 m mean depth (model: 24.3 m)					
Semi-major axis (cm/sec)	Pred.:	10.6	14.5	25.0	26.2
	Obs.:	10.6	13.9	25.3	27.6
Semi-minor axis (cm/sec)	Pred.:	0.11	0.48	0.55	0.53
	Obs.:	0.33	−0.49	0.20	0.15
Phase lag of maximum (g°)	Pred.:	319	352	110	168
	Obs.:	323	355	106	165
Orientation of major axis (°T)	Pred.:	8.4	9.3	9.4	9.2
	Obs.:	12.4	14.1	14.3	14.1
Direction of rotation	Pred.:	A	A	A	A
	Obs.:	A	C	A	A
Yarraville Shoals: 1 m from bed in 9.4 m mean depth (model: 16.4 m)					
Semi-major axis (cm/sec)	Pred.:	6.9	9.5	17.9	19.1
	Obs.:	3.8	5.4	13.4	13.5
Semi-minor axis (cm/sec)	Pred.:	−0.44	−0.51	−0.68	−0.75
	Obs.:	0.51	0.36	−0.17	−0.17
Phase lag of maximum (g°)	Pred.:	314	345	104	162
	Obs.:	327	325	108	147
Orientation of major axis (°T)	Pred.:	20.1	21.9	19.5	19.0
	Obs.:	10.2	7.8	9.4	8.1
Direction of rotation	Pred.:	C	C	C	C
	Obs.:	A	A	C	C
Red: meter 2.5 m from bottom in 22 m mean depth (model: 21.1 m)					
Semi-major axis (cm/sec)	Pred.:	4.4	6.6	8.4	8.1
	Obs.:	4.8	7.3	9.7	11.0
Semi-minor axis (cm/sec)	Pred.:	−0.43	−0.75	−0.82	−0.79
	Obs.:	−1.04	−0.61	−1.96	−1.93
Phase lag of maximum (g°)	Pred.:	299	326	58	113
	Obs.:	298	336	54	116
Orientation of major axis (°T)	Pred.:	47.9	48.5	46.6	46.4
	Obs.:	63.9	60.4	52.0	56.6
Direction of rotation	Pred.:	C	C	C	C
	Obs.:	C	C	C	C

Table 7.4: *Comparison of predicted (Pred.) and observed (Obs.) ellipse characteristics for the four major tidal current constituents at stations Mike, Yarraville Shoals and Red at the indicated depth levels (depths in brackets are MSL depths for corresponding model elements). Predicted values are obtained by linear interpolation from the results of the three-dimensional model and are for the same relative depth at which observations were made. Observations are from Lennon (1981,1990) but minor-axis values are given a negative sign when the observed rotation is clockwise: this is a convention used in the analysis of the model predictions. Direction of rotation is: A = Anticlockwise, C = Clockwise. Phase lag of maximum current is given in local time.*

Tidal constituent		O_1	K_1	M_2	S_2
Lima: meter 12 m from bottom in 18 m mean depth (model: 19.0 m)					
Semi-major axis (cm/sec)	Pred.:	17.4	25.4	35.8	35.9
	Obs.:	14.4	19.6	33.5	36.1
Semi-minor axis (cm/sec)	Pred.:	−0.19	0.03	0.12	0.18
	Obs.:	2.02	0.97	0.97	0.51
Phase lag of maximum (g°)	Pred.:	314	345	101	158
	Obs.:	316	336	89	147
Orientation of major axis (°T)	Pred.:	35.2	36.4	36.4	36.1
	Obs.:	46.0	40.6	42.6	40.2
Direction of rotation	Pred.:	C	A	A	A
	Obs.:	A	A	A	A
Lima: meter 5 m from bottom in 18 m mean depth (model: 19.0 m)					
Semi-major axis (cm/sec)	Pred.:	14.8	21.4	30.7	31.0
	Obs.:	11.7	16.9	28.7	31.2
Semi-minor axis (cm/sec)	Pred.:	−0.54	−0.35	−0.46	−0.43
	Obs.:	−0.48	0.67	−0.47	−0.24
Phase lag of maximum (g°)	Pred.:	312	343	97	155
	Obs.:	306	335	87	145
Orientation of major axis (°T)	Pred.:	36.0	38.0	37.2	36.5
	Obs.:	34.6	41.6	42.5	42.5
Direction of rotation	Pred.:	C	C	C	C
	Obs.:	C	A	C	C
Yellow: meter 26 m from bottom in 33 m mean depth (model: 30.0 m)					
Semi-major axis (cm/sec)	Pred.:	11.1	15.5	15.8	15.0
	Obs.:	10.0	13.5	17.2	18.5
Semi-minor axis (cm/sec)	Pred.:	0.09	−0.09	−0.43	−0.50
	Obs.:	1.32	−0.13	−0.48	1.05
Phase lag of maximum (g°)	Pred.:	311	345	87	141
	Obs.:	330	355	119	163
Orientation of major axis (°T)	Pred.:	41.7	40.7	46.1	47.7
	Obs.:	40.8	42.0	56.1	56.6
Direction of rotation	Pred.:	A	C	C	C
	Obs.:	A	C	C	A
Yellow: meter 2.5 m from bottom in 33 m mean depth (model: 30.0 m)					
Semi-major axis (cm/sec)	Pred.:	6.5	9.1	10.4	10.1
	Obs.:	6.6	9.2	11.2	12.2
Semi-minor axis (cm/sec)	Pred.:	−0.71	−1.10	−1.38	−1.37
	Obs.:	−0.53	−0.88	−2.55	−2.07
Phase lag of maximum (g°)	Pred.:	305	335	71	127
	Obs.:	334	353	69	128
Orientation of major axis (°T)	Pred.:	44.8	47.1	46.2	46.1
	Obs.:	66.7	65.5	50.7	50.8
Direction of rotation	Pred.:	C	C	C	C
	Obs.:	C	C	C	C

Table 7.5: *Comparison of predicted (Pred.) and observed (Obs.) ellipse characteristics for the four major constituents at stations Lima and Yellow at the indicated depth levels (depths in brackets are MSL depths for corresponding model elements).*

Tidal constituent		O_1	K_1	M_2	S_2
Blue: meter 17 m from bottom in 23 m mean depth (model: 24.9 m)					
Semi-major axis (cm/sec)	Pred.:	9.8	13.8	13.2	12.0
	Obs.:	12.1	14.7	18.7	20.7
Semi-minor axis (cm/sec)	Pred.:	0.10	0.39	1.01	1.14
	Obs.:	2.12	0.37	6.78	6.35
Phase lag of maximum (g°)	Pred.:	311	341	88	143
	Obs.:	293	325	78	129
Orientation of major axis (°T)	Pred.:	18.8	19.3	20.1	19.7
	Obs.:	355	358	8.4	7.0
Direction of rotation	Pred.:	A	A	A	A
	Obs.:	A	A	A	A
Blue: meter 2.5 m from bottom in 23 m mean depth (model: 24.9 m)					
Semi-major axis (cm/sec)	Pred.:	6.7	9.5	9.7	9.0
	Obs.:	6.4	9.7	10.0	11.6
Semi-minor axis (cm/sec)	Pred.:	−0.61	−0.90	−0.20	0.05
	Obs.:	−0.39	2.00	1.77	2.84
Phase lag of maximum (g°)	Pred.:	306	334	76	133
	Obs.:	287	331	63	123
Orientation of major axis (°T)	Pred.:	22.8	25.7	20.4	18.6
	Obs.:	14.4	18.5	8.6	5.1
Direction of rotation	Pred.:	C	C	C	A
	Obs.:	C	A	A	A
White: meter 17 m from bottom in 21 m mean depth (model: 21.9 m)					
Semi-major axis (cm/sec)	Pred.:	7.6	10.9	10.0	8.9
	Obs.:	9.2	10.8	13.5	14.8
Semi-minor axis (cm/sec)	Pred.:	0.01	0.22	1.05	1.14
	Obs.:	0.50	−1.27	5.43	4.58
Phase lag of maximum (g°)	Pred.:	308	337	89	145
	Obs.:	283	313	75	129
Orientation of major axis (°T)	Pred.:	10.6	11.2	9.7	8.8
	Obs.:	359	353	357	358
Direction of rotation	Pred.:	A	A	A	A
	Obs.:	A	C	A	A
White: meter 2.5 m from bottom in 21 m mean depth (model: 21.9 m)					
Semi-major axis (cm/sec)	Pred.:	5.3	7.7	7.6	6.9
	Obs.:	5.1	8.0	7.8	8.8
Semi-minor axis (cm/sec)	Pred.:	−0.60	−1.05	−0.04	0.23
	Obs.:	−0.76	1.09	0.80	1.91
Phase lag of maximum (g°)	Pred.:	303	331	76	134
	Obs.:	283	328	58	121
Orientation of major axis (°T)	Pred.:	15.6	18.3	9.7	7.2
	Obs.:	6.1	17.0	0.0	355
Direction of rotation	Pred.:	C	C	C	A
	Obs.:	C	A	A	A

Table 7.6: *Comparison of predicted (Pred.) and observed (Obs.) ellipse characteristics for the major constituents at stations Blue and White at the indicated depth levels (depths in brackets are MSL depths for corresponding model elements).*

9.4 m whereas the model depth is 16.4 m. The reason for this discrepancy is that Yarraville Shoals as a bathymetric feature is much smaller than the element dimension used in the model. The model value is an estimate of MSL depth for the entire element, but the site value is a "spot" depth. This fact may help explain why model predictions for both tide-height (see Table 7.1) and tidal current (see Table 7.4) at Yarraville Shoals are in such poor agreement with observations. A finer grid would ease the problem and is being developed for the whole Gulf by Nixon (1992) using an element of one third the linear scale of the present grid. The grid of Chapter 8 uses such a fine grid in the Northern Spencer Gulf region and predictions and observations for Yarraville Shoals are further considered there. The predictions for station Yarraville Shoals are given at the same relative depth at which observations are taken. This is done for each of the stations. The station and model depths for Red, Yellow, Blue and White are in general agreement.

Because of the difficulties in matching model depths with actual site depths, linear interpolation of the three-dimensional predictions was considered sufficient in order to deduce the predictions for the same relative level at which observations were made.

Table 7.4 shows that predictions at Mike are very close to observed values. The current meter at Mike is at relative depth $\eta = 14/24 \simeq 0.583$ which puts it at a level where one might expect good agreement with depth-averaged data. Such agreement was seen in Table 5.9. Predictions for Yarraville Shoals are much poorer — the probable reason for this has already been stated. Predictions for Red are in close agreement except for the orientation of the major axis. It is likely that the model position of Red, sited close to a corner in the coastal boundary, is largely responsible for this.

Table 7.5 shows good agreement at both levels for station Lima. Accuracy for the semi-diurnals is better than for the diurnals at Lima. The model correctly predicts changes in rotation direction for both M_2 and S_2 at Lima. Agreement at both levels at Yellow is good except for some large differences in phase lag and orientation of semi-major axis.

Table 7.6 shows reasonable overall agreement for the two meters at Blue. The phase lag and orientation values at Blue are of the order of 20° in error for some constituents at some levels. Agreement in semi-major axis is very good at the lower level at Blue. At White agreement is again reasonable, and again phase lag and orientation values are of the order of 20° in error for some constituents, depending on the level.

The model correctly predicts the direction of rotation of the ellipses at 75% of the sites summarized in Tables 7.4–7.6. This is a good result given the relatively small size of the semi-minor axis values compared to the semi-major axis values, since a shift of only 1 cm is enough to alter the sign of the predicted semi-minor axis and hence the direction of rotation, in most instances.

Consider again the gyral sequences of Figures 7.30 and 7.31 which illustrate the nature of the transition flows of the mid-Gulf region off Wallaroo between times of flood and ebb. A period of only two hours is depicted, so the flood in process at the start of the sequence is not full flood and the ebb in process at the end of the sequence is only just commencing. Similarly, the sequence of plots in Figures 7.32 and 7.33 occur between times of ebb and flood.

We will now consider the vertical profiles of the components of velocity at Mike and Lima during these neap and spring periods. Figure 7.44 shows sequences of velocity component profiles at Mike (left hand plots) and Lima (right hand plots) at the times chosen for the neap gyre plots of Figures 7.30 and 7.31, and Figure 7.45 shows the component profiles at Mike and Lima for the spring current vector plots. The greater vigour of the

spring flow (Figure 7.45) compared to the neap flow (Figure 7.44) is readily seen, especially in the v-component. The flow at Lima is more rectilinear compared to that at Mike, as is indicated by the narrower band of movement shown by the u-component and the broader band of movement shown by the v-component at Lima relative to Mike. Note that the horizontal scale for the u-component for Lima is five times that used for Mike. This was necessary in order to separate the profile curves in u at Lima.

In both the u and v-component plots at Mike and Lima there is reverse-flow at lower depths relative to the surface flow for part of the tidal cycle. Also, it can be seen that the surface flow is not always the strongest! Likewise, though more difficult to imagine, some of the w-component profiles show that while fluid is "rising" at some levels, it can be "falling" at others at the same time. Such is the case in the spring w plots for Mike (bottom left in Figure 7.45) and corresponds to a rise in sea level at Mike during that period — when the surface level is rising w at the surface is increasing but it takes time for this upward velocity to be felt at the bottom layers. At the surface level, negative values of w indicate that the water level is dropping. The magnitude of the w-component flows is about 1/5000 that of the u or v-component flows according to these predictions.

7.5 Summary

A stable and relatively accurate three-dimensional model of Spencer Gulf has been developed. It appears to be as stable as the depth-averaged model developed in Chapter 5. This result is consistent with the fact that the implicit scheme used in the vertical dimension is unconditionally stable, leaving the stability of the overall three-dimensional scheme dependent on its stability in the horizontal dimensions, as for the depth-averaged model.

A vertical eddy viscosity formulation is specified and thorough numerical experimentation is carried out on all the associated parameters. The experiments are conducted for 11 depth levels; experimentation involving more levels is left for future research with faster machines. It is shown that calibration with respect to κ is necessary in order to optimize model performance. This is consistent with the present need to have good resolution in the near-bed region where bed friction is important and a no-slip condition is used. Further improvement in performance may be achieved by calibrating with respect to the vertical eddy viscosity form used.

Using the chosen vertical eddy viscosity coefficient, tide-height predictions are in good agreement with observations taken within the Gulf (see Table 7.1). Very good agreement is achieved in comparing the depth-averaged predictions for ellipse characteristics taken from the three-dimensional model and the depth-averaged model (see Tables 7.2–7.3). Overall good agreement is also obtained when comparing depth-dependent predicted and observed ellipse characteristics (see Tables 7.4–7.6). Agreement at stations Mike and Lima is particularly close. The discrepancies between site depth and model depth at Yarraville Shoals seem to be responsible for the poor agreement obtained there. Such discrepancies and the associated coarseness in bathymetric representation in the present model may be responsible for the poorer agreement at stations Blue and White than was achieved at Mike, Lima, Red and Yellow. A fine-grid model of the same region should improve agreement.

Now that the number of tidal current stations is beginning to match the number of tide-height stations in Spencer Gulf, it will be useful to consider an error measure to more easily gauge the differences between predicted and observed tidal current. An error

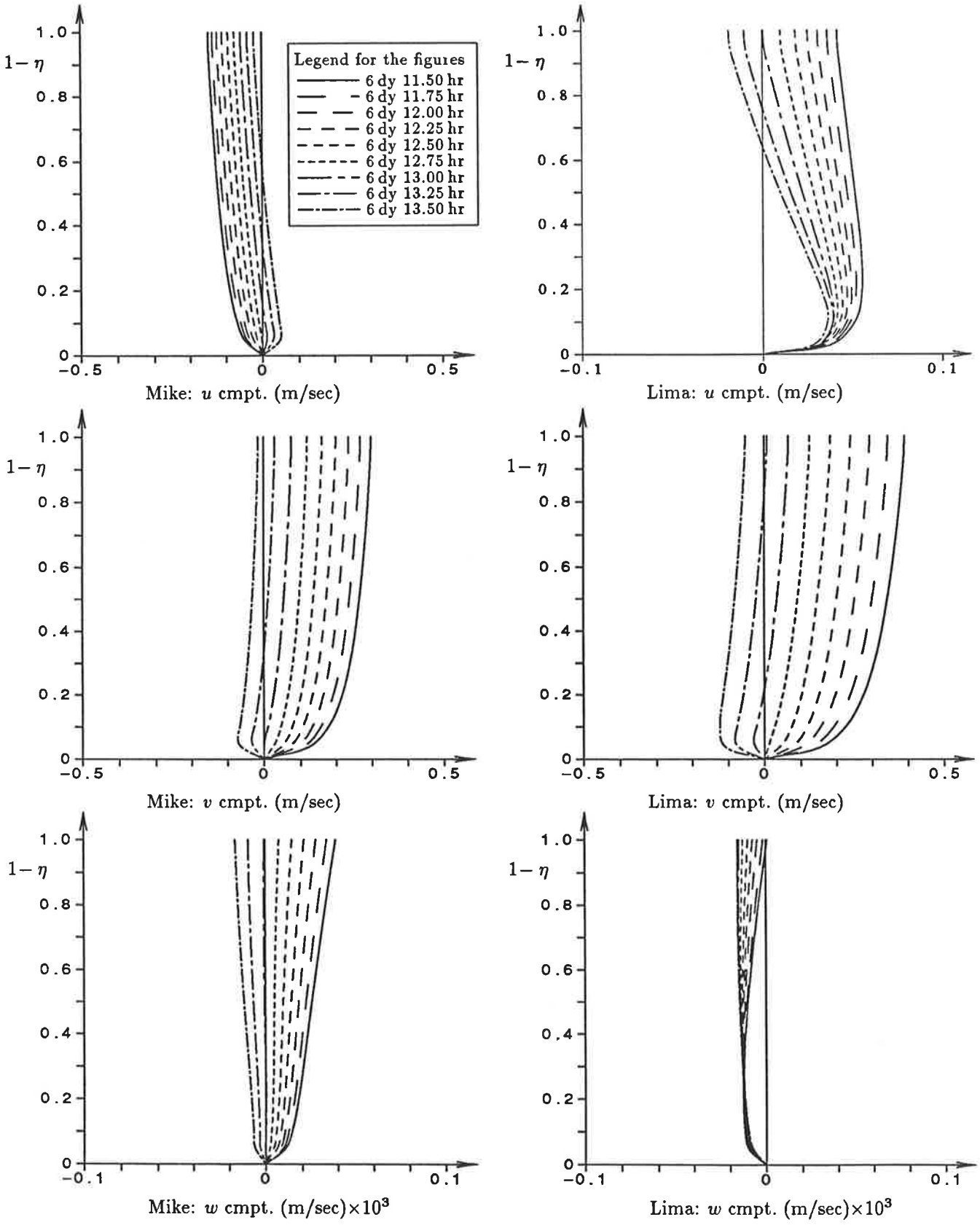


Figure 7.44: *Time sequences of velocity component profiles at Mike (on the left) and Lima (on the right). Time points used are those used for the neap current vector plots of Figures 7.30 and 7.31.*

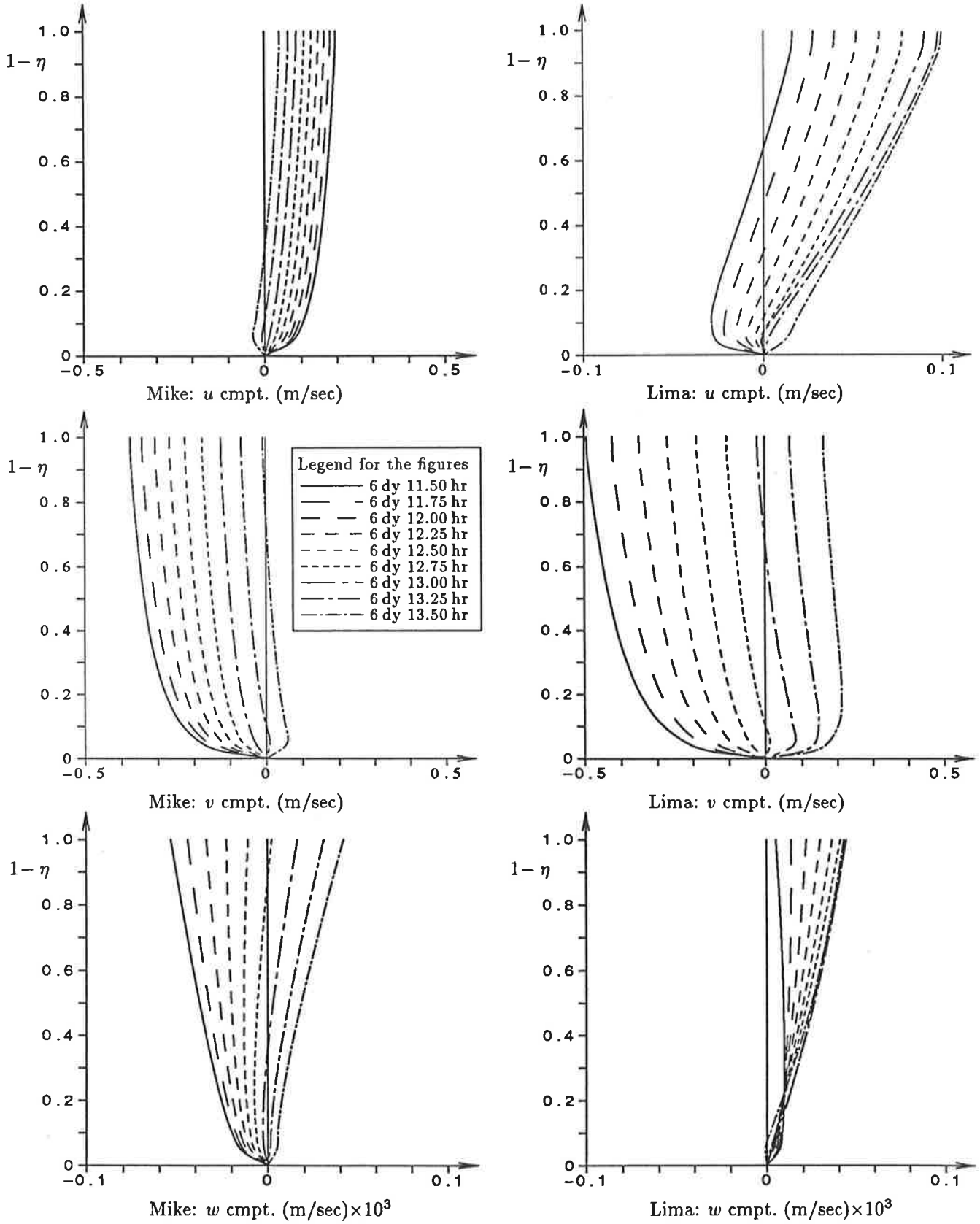


Figure 7.45: *Time sequences of velocity component profiles at Mike (on the left) and Lima (on the right). Time points used are those used for the spring current vector plots of Figures 7.32 and 7.33.*

measure adopting the form of that already used for tide-height can be developed. Since the raw output of the tidal analysis program for the horizontal velocity components is the amplitude and phase for both the u and v-components of the specified constituents, average absolute complex error measures can be written down for both the x and y-directed components of tidal current. Standard error measures could be expressed in terms of East-West and North-South components of tidal velocity if model orientation is not aligned with North.

The three-dimensional model is used to demonstrate that the tidal gyres observed in the neap and spring flows discussed in Chapter 5 are a phenomenon that extends down through the water column. To the best knowledge of the author a three-dimensional study of gyres in this manner has not been carried out before.

The present model increases the three-dimensional predictive resolution for Spencer Gulf by six and a half times compared to the model of Noye et al. (1981, 1982). Whereas they presented results for only one constituent (M_2), predictions for the four major constituents have been presented here.

In the next chapter a fine-grid depth-averaged model of Northern Spencer Gulf, incorporating the wetting and drying of tidal flats, is developed.

Chapter 8

A depth-averaged fine-grid model of Northern Spencer Gulf with tidal flats

8.1 Introduction

A natural extension of a program for modelling the tides of shallow seas is to the covering (wetting) and uncovering (drying) of sand bars and shallow coastal flats.

Such "tidal flats" occur extensively throughout Northern Spencer Gulf. They were not able to be represented properly on the coarse $5.715 \times 5.715\,\mathrm{km}^2$ grid of the Spencer Gulf model of Chapter 5. A finer $1.905 \times 1.905\,\mathrm{km}^2$ grid is used in this chapter to produce a Northern Spencer Gulf (NSG) model in which the tidal flats are represented. The program itself is general and may be applied to any coastal region, with or without tidal flats. The NSG element is linearly one-third that of the coarse-grid element of the Spencer Gulf (SG) model.

Tidal flats in this work are defined as those regions exposed between Indian Spring Low Water and Indian Spring High Water; the permanent coastal boundary is based on the latter. Tidal flats are represented as the shaded elements in the plan view of the model in Figure 8.1. This figure also shows the location of tide-height and tidal current stations, and other geographical features of Northern Spencer Gulf, and may need to be consulted frequently during the reading of this text. Unless otherwise indicated, "north" means "up-the-page" and vice versa, in the figures that follow. The positive y-direction of the model is referred to as "north" and this is shorthand for the true orientation of the model, viz. 33.33° T (or NNE).

Ward Spit and Cockle Spit are two large sand bars depicted in the model. There are many other charted sand bars in this region of Spencer Gulf but these two are exposed at low tide. On an old hydrographic map of the region (Map 403, published at the Admiralty, London, 26th August 1865) it is recorded that Ward Spit "Uncovers at L.W. Springs". At such times it measures 10 km in length and up to several kilometres in width.

The work presented on the depth-averaged NSG tidal flat model in this chapter is summarized in an article by Bills and Noye (1992).

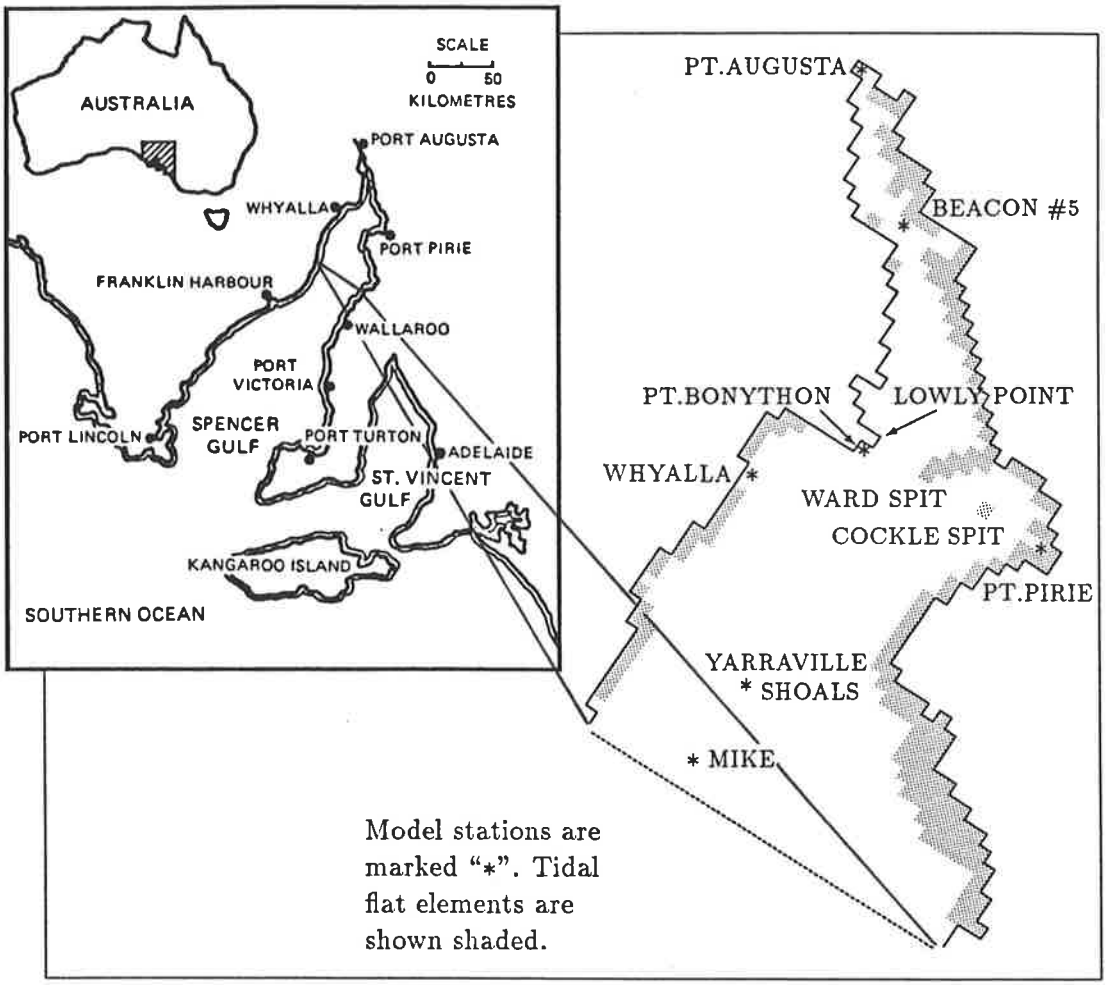


Figure 8.1: *Location map for the Northern Spencer Gulf model.*

8.2 Review of the literature

Over the last two decades, several schemes for modelling the wetting/drying process have been incorporated in depth-averaged tidal programs. Their early development was non-trivial. Leendertse (1970, p.19–20) makes the following comments with respect to his program: "The development of this feature of the model was very difficult for the basic reason that the solutions which can be obtained with the finite-difference model are solutions with variables changing gradually in time and space. If discrete changes are made, local discontinuities are generated which then radiate from the location of change as small waves through the system". He found it necessary to include procedures designed to both decrease the generation of the disturbances and suppress their propagation.

The computational algorithms used to implement wetting/drying can be very complicated. The complexity and length of the schemes may be part of the reason why so few have been published in detail; site dependence and consequent lack of generality of the schemes would also contribute to this state of affairs. Cunge (1977, p.152) notes that "Flather and Heaps (1975) and Leendertse and Gritton (1971) are just about the only

persons to furnish a description of their procedure".

In addition, it may be noted that few of the published schemes have been rigorously verified by comparison with available analytical solutions. The verification provided is usually a generalized qualitative comparison of predictions with observed wetting/drying events.

However, in a paper by Sielecki and Wurtele (1970), and subsequently in work by Chalabi (1979), there is an attempt to compare predictions with analytical solutions, the domain being a paraboloidal bowl and the analytical solution being due to Ball (1964). The work by Chalabi is an adaptation of the method of Flather and Heaps (1975) to the one-dimensional paraboloidal trough considered by Sielecki and Wurtele. Sielecki and Wurtele and Chalabi only allow their simulations to progress a cycle or two, so very little is demonstrated with respect to the stability of their schemes. Graphs of numerical predictions presented by Chalabi suggest that problems were encountered at the coastal edges of the solution domain with grid-scale oscillations. A paper by Runchal (1975), in a format similar to that of Sielecki and Wurtele, examines the performance of a numerical scheme suitable for modelling tidal flats by comparing its performance against analytical solutions for flow in sloping basins and for waves incident on sloping beaches.

The tidal flat scheme of Sielecki and Wurtele is intended to work as a flat extrapolator of sea surface from the interior of the solution domain, where elements are wet, outwards towards the permanent coastal boundary where elements may be dry. The intersection of the extrapolated surface with the sloping sea bed determines the position of the coastline. The method does not seem to have been implemented in a stable manner in a model with complicated coastal boundaries or bathymetry.

Gopalakrishnan (1989) describes a two-dimensional Galerkin finite element approach to tidal flat modelling which has some similarity to that of Sielecki and Wurtele. Finite elements aside, he distinguishes between "moving boundary" models such as his own, and "jumping boundary" models where elements are included or excluded in computations depending on the amount of water in them. A predictor-corrector method, combined with horizontal projection of updated sea surface towards the coast in order to anticipate the new position of the coastline, is used to closely follow the movement of the coastal boundary.

The wetting/drying scheme used in this work is based on that of Flather and Heaps (1975), their's being remarkably simple and easy to implement. However, it is modified in several respects; the changes and the reasons for their implementation are outlined in the following sections. Numerical evidence suggesting that the constant quadratic friction coefficient is incapable of providing stability, at the tidal flat level, together with global model accuracy for the present model is given; the evidence suggests that the coefficient of quadratic friction should depend on local depth. A discussion of grid-scale waves and filtering is also presented.

The qualitative and quantitative results that are presented suggest that the scheme works very well.

The qualitative analysis of predictions includes direct inspection of signals for sea surface elevation at the elements comprising the sand bars Ward Spit and Cockle Spit. Because it is located in the path of the ebbing and flooding tide, the requirement of sensible covering and uncovering of the elements of Ward Spit is a stringent test of the scheme. The simulation is of 32 days duration, predictions for the last 29 being saved for tidal analysis. The length of the simulation by itself is a severe test of the scheme. A

statistic called the "transition" count, a tally of the number of wet-to-dry and dry-to-wet events experienced by each tidal flat element during the 29 days, is used to demonstrate the physical acceptability of the predictions for the simulated time.

The quantitative results presented include a comparison of predicted and observed tidal constants at six tide-height stations in the region, and a comparison of predicted and observed tidal ellipse characteristics at the one available tidal current station called "Mike" (Figure 8.1). In addition, comprehensive contour charts for the four major constituent amplitudes and phases are presented, together with corresponding tidal ellipses.

Wetting/drying sequences at two-hour intervals for both a neap and a spring event are presented as well as velocity residuals showing the net non-linear behaviour of the model. As an example of a possible application of the model, projected wetting/drying sequences for a spring event assuming "Greenhouse" rises or falls in mean sea level are also included.

8.3 The model of Northern Spencer Gulf

Figure 8.2 shows the array of 0's, 1's and 2's used to define the model. There are 921 Type 1 elements and 31 Type 2 elements. The 4's at the bottom of the array indicate that the corresponding elements are water elements outside the model — they are not used in computations. Computations are carried out only on the list of Type 1 elements, with the forcing for the model being provided by tide heights defined at the Type 2 elements.

Because a NSG element is linearly one-third the size of a SG element, all the gridpoints of the SG model within the NSG region coincide with gridpoints of the NSG model. This fact is used in taking the open boundary forcing of the NSG model from the solution field of the SG model. The position of the NSG open boundary in the SG model is marked on Figure 5.10.

Figure 8.3 shows the Indian Spring Low Water (ISLW) depth field (m) used for the NSG model. ISLW is chart datum for the hydrographic map used (map Aus 778). The negative values are estimates for depth above datum of the regions of the map indicated as being dry at low water. Only a few scattered survey values are given for these regions, so the ISLW depths estimated are based on these and on the assumption of having an upward sloping sea bed as one moves toward the permanent coastal boundary.

Figure 8.4 shows the Mean Sea Level depth field used for the model. This field is obtained after the third iteration in the process for determining MSL described in Chapter 5, Section 5.4.

8.4 Mathematical formulation of the tidal flat scheme

The depth-averaged tidal equations of Chapter 2 are used, but take a modified form since we do not study meteorological influences here. Using notation defined in Chapter 2, the continuity equation is

$$\frac{\partial \zeta}{\partial t} = -\frac{\partial (HU)}{\partial x} - \frac{\partial (HV)}{\partial y}. \tag{8.1}$$

Using a quadratic form for bottom friction to parameterize the vertical turbulence, the momentum equations for the depth-averaged horizontal velocity components U,V are,

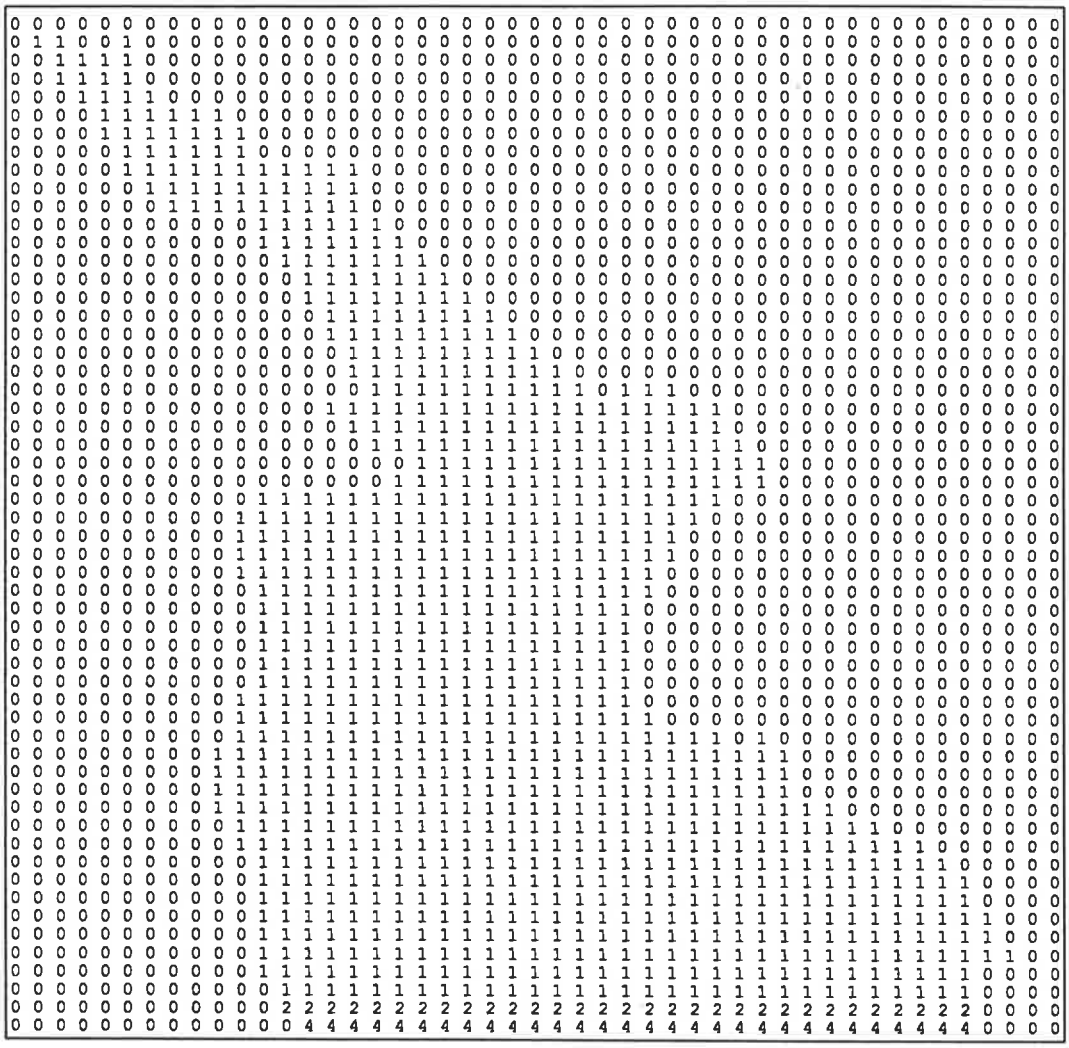


Figure 8.2: *Element code array for the Northern Spencer Gulf model.*

respectively,

$$\frac{\partial U}{\partial t} + U\frac{\partial U}{\partial x} + V\frac{\partial U}{\partial y} - fV = -g\frac{\partial \zeta}{\partial x} + N_x\frac{\partial^2 U}{\partial x^2} + N_y\frac{\partial^2 U}{\partial y^2} - C_b\frac{1}{H}U\sqrt{U^2+V^2}, \qquad (8.2)$$

and

$$\frac{\partial V}{\partial t} + U\frac{\partial V}{\partial x} + V\frac{\partial V}{\partial y} + fU = -g\frac{\partial \zeta}{\partial y} + N_x\frac{\partial^2 V}{\partial x^2} + N_y\frac{\partial^2 V}{\partial y^2} - C_b\frac{1}{H}V\sqrt{U^2+V^2}. \qquad (8.3)$$

In this chapter the symbol C_b will denote the constant quadratic friction coefficient.

The basic procedure of the wetting/drying scheme used is that of Flather and Heaps (1975) upon whose description the following outline is based. The scheme consists of a test carried out before each U and V velocity component calculation in order to determine whether the associated gridpoint is wet or dry. If dry, the component value is set to

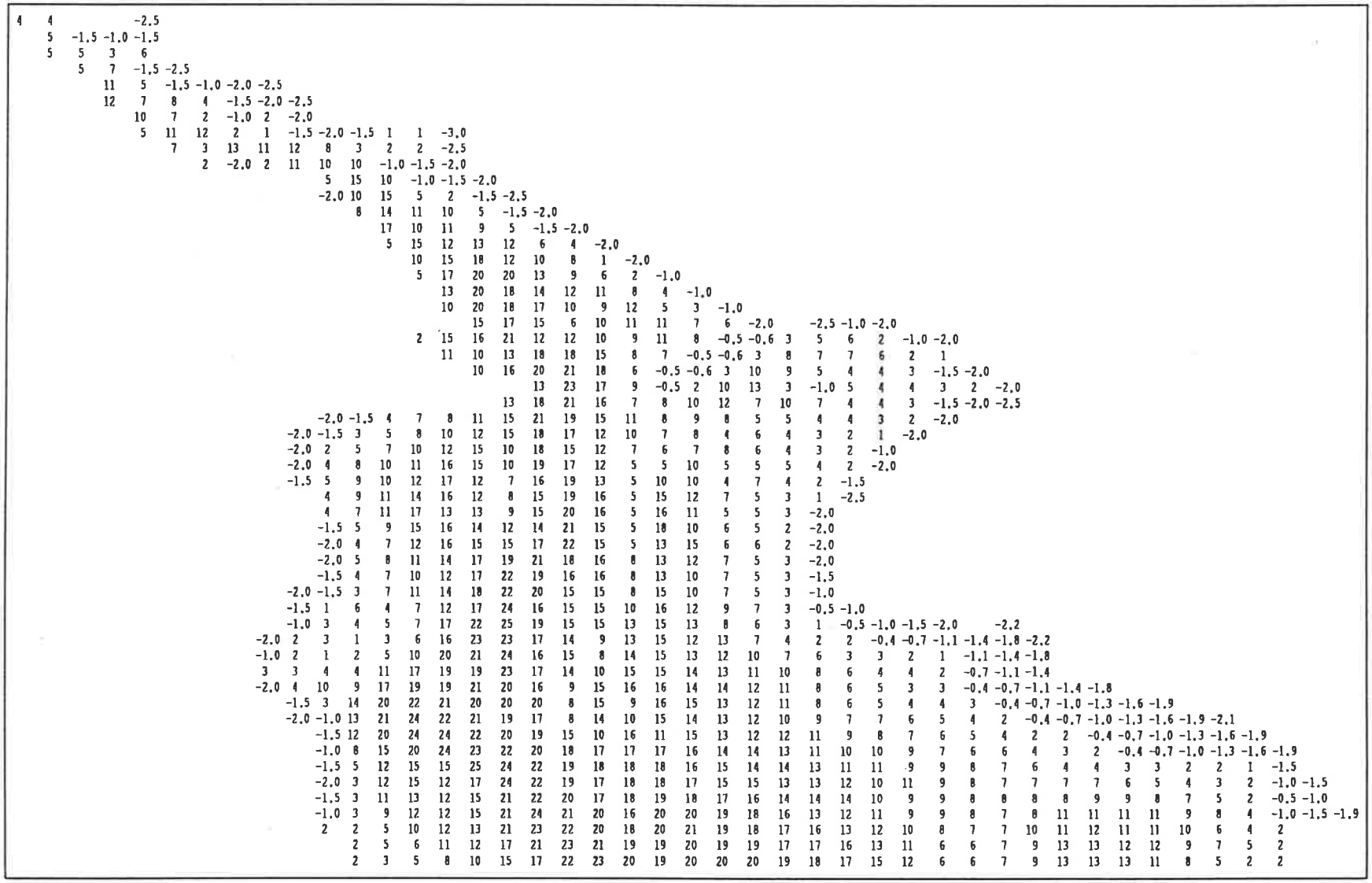


Figure 8.3: *Indian Spring Low Water depth field (m) for the Northern Spencer Gulf model.*



Figure 8.4: *Mean Sea Level depth field (m) for the Northern Spencer Gulf model.*

zero and computations proceed to the next gridpoint; if wet, a new value of U or V is calculated. The test is applied to all elements of the model, not just to those thought to be tidal flat elements. Adapted to the present finite difference scheme, the procedure is as follows:

(1) at the commencement of U^{n+1} calculations, if

(i) $H_i^{n+1/2} > H_{dry}$ and $H_{i+1}^{n+1/2} > H_{dry}$ so that $\frac{1}{2}\left(H_i^{n+1/2} + H_{i+1}^{n+1/2}\right) > H_{dry}$, or

(ii) $H_i^{n+1/2} > H_{dry}$ and $H_{i+1}^{n+1/2} \leq H_{dry}$ and $\frac{1}{2}\left(H_i^{n+1/2} + H_{i+1}^{n+1/2}\right) > H_{dry}$ and $-\left(\zeta_{i+1}^{n+1/2} - \zeta_i^{n+1/2}\right) > \epsilon$, or

(iii) $H_i^{n+1/2} \leq H_{dry}$ and $H_{i+1}^{n+1/2} > H_{dry}$ and $\frac{1}{2}\left(H_i^{n+1/2} + H_{i+1}^{n+1/2}\right) > H_{dry}$ and $\left(\zeta_{i+1}^{n+1/2} - \zeta_i^{n+1/2}\right) > \epsilon$

then proceed to calculate U_i^{n+1} in the usual way, otherwise set $U_i^{n+1} = 0$;

(2) at the commencement of V^{n+1} calculations, if

(i) $H_i^{n+1/2} > H_{dry}$ and $H_{i_2}^{n+1/2} > H_{dry}$ so that $\frac{1}{2}\left(H_i^{n+1/2} + H_{i_2}^{n+1/2}\right) > H_{dry}$, or

(ii) $H_i^{n+1/2} > H_{dry}$ and $H_{i_2}^{n+1/2} \leq H_{dry}$ and $\frac{1}{2}\left(H_i^{n+1/2} + H_{i_2}^{n+1/2}\right) > H_{dry}$ and $\left(\zeta_i^{n+1/2} - \zeta_{i_2}^{n+1/2}\right) > \epsilon$, or

(iii) $H_i^{n+1/2} \leq H_{dry}$ and $H_{i_2}^{n+1/2} > H_{dry}$ and $\frac{1}{2}\left(H_i^{n+1/2} + H_{i_2}^{n+1/2}\right) > H_{dry}$ and $-\left(\zeta_i^{n+1/2} - \zeta_{i_2}^{n+1/2}\right) > \epsilon$

then proceed to calculate V_i^{n+1} in the usual way, otherwise set $V_i^{n+1} = 0$.

The variable ϵ is a free surface slope criterion and H_{dry} is the value of total depth at or below which the associated gridpoint is regarded as dry.

The value of ϵ defines a minimum gradient of the sea surface steeper than which the local water mass is considered to be advancing over the corresponding gridpoint; tests on this parameter are carried out. If the x-direction is eastwards, Flather and Heaps' scheme tests if the tide is advancing towards the east or west coast (see (1) parts (ii) and (iii), respectively), and towards the south or north coast (see (2) parts (ii) and (iii), respectively). If the local water mass is receding over the velocity gridpoint, the corresponding component is set to zero since the associated element is in the process of drying.

Flather and Heaps choose $H_{dry} = 0$ but we carry out tests using various small values of H_{dry} in order to establish an appropriate value for NSG; also, other authors have not used the zero datum. Holsters (1978) recommends using a "marginal thickness ... equivalent to a boundary layer of stagnant water" (ibid., p.173); Ramming and Kowalik (1980) state it "will be sensible to select 0.02m as a coefficient datum" (ibid., p.228). Both these authors introduce a positive datum in an attempt to ensure that overall water mass is properly conserved.

Flather and Heaps also postulate a minimum value of depth H_0 which "terminates the growth of frictional dissipation before it becomes too large and before the depth of fluid becomes so small that boundary layer considerations on which the quadratic law is based are no longer applicable" (ibid., p.495); we also carry out numerical tests on this parameter.

No test for wetness or dryness at elevation gridpoints is carried out before elevation calculations are performed. Elements at which elevation predictions produce total depth values less than H_{dry} are assessed as dry when total depth is updated. Elements for which $H < H_{dry}$ become part of the overall set of tidal flat elements of the model. At drying elements we set $H = H_{dry}$ and $\zeta^{n+\frac{1}{2}} = \zeta^{n+1} = -h$. Since elevation and total depth are calculated at each half time step and total depth is checked both times, we test for wetness/dryness during a time step twice as frequently as did Flather and Heaps (1975).

The modifications that we make to the Flather and Heaps procedure pertain to the calculation of the velocity components and relate in the first instance to the discussion of subordinate approximations of the advective and diffusive terms (see Chapter 3, Section 3.6), and in the second instance to the form of the coefficient of quadratic friction used.

To summarize the work from Section 3.6, recall that at permanent coastal boundaries the zero normal flow condition is discretised in the manner $U_i = 0$ or $V_i = 0$ for all time at each U or V gridpoint on a coastline parallel to the y or x-axis. If the U or V gridpoint does not lie on the permanent coastal boundary, the only terms of the finite difference equations permitted to use the zero boundary value are the quadratic friction and Coriolis terms. Advective and diffusive terms are omitted if their discretisation would otherwise cause them to use such a boundary value, or would involve a value on land or beyond the open boundary. Subordinate approximations in the latter cases give discretisations of only first-order accuracy. The interior finite difference expressions are spatially second-order accurate.

The omitted terms in every case consist of x or y-derivatives of first or second-order normal to the local permanent coastal boundary. Advective and diffusive terms involving derivatives parallel to the local permanent coastal boundary, and whose discretisation does not otherwise violate the conditions of omission by being immediately normal to another segment of the permanent coastal boundary, are retained.

The same pattern of omission of advective and diffusive terms is exercised at velocity gridpoints adjacent to the open sea boundary of the model. Here, if the discretisation requires a value from a velocity point on or beyond the open boundary, subordinate approximation of the unknown value leads to a first-order accurate discretisation, so the corresponding terms are deleted in order to avoid such approximations.

It has been found that first-order accurate approximation of advective terms leads to the appearance of spurious and physically unrealistic velocity vectors in the 29 day residual plots (see Figures 3.23 and 3.24 or Figures 5.36). Furthermore, when a value of the usual space-centred two-point approximation for the derivative factor of an advective term requires a zero boundary value, some unrealistic residual behaviour persists. Such contamination of the overall solution field is prevented by simply omitting the corresponding terms. The effect of the diffusive terms is less obvious because it is at least an order of magnitude smaller. The use of linear interpolation for one of the outer values of the usual three-point discretisation of a diffusive term reduces it to zero anyway. When an outer value requires a zero velocity boundary value, the diffusive term is also omitted because of the similarity of its difference structure with the corresponding advective term. In the interior solution domain no terms in the governing equations are omitted.

As mentioned in Chapter 3, Flather and Heaps (1975, p.499) omit the advective terms within three elements of the open boundary. This seems excessive in the light of our experience of only omitting terms immediately adjacent to the open boundary whose

derivatives are normal to that boundary, but their open boundary configuration is more severe since it includes a corner. We do not omit advective (or diffusive) terms adjacent to the open boundary whose derivatives are parallel to that boundary, except at the edges where these derivatives are normal to the permanent coastal boundary.

At land boundaries Leendertse (1967) seems to adopt a similar convention of omission of advective terms as we do, though only when a value from over the land is called for by the usual discretisation. Flather and Heaps (1975) may have have misinterpreted him on this point. He does not say that he omits **all** advective terms adjacent to the land boundary. Flather and Heaps point out that where the water is likely to be shallow, advective terms should be retained because dimensional analysis shows that they will be important. Therefore one should use accurate discretisations for these terms since inaccurate discretisations feed errors into the solution field. If accurate discretisations are not available it is better to omit the terms. Accurate discretisations involving more gridpoints, inevitably from outside the 9-element block, could be derived for a particular application; but we are interested here in writing automated program code for general coastal regions and this is complicated enough for a 9-element block!

The second major modification of the Flather and Heaps tidal flat scheme relates to the choice of friction coefficient. For the moment we will investigate the constant quadratic friction coefficient C_b used by Flather and Heaps.

8.5 Grid-scale waves

The wetting/drying process superimposes grid-scale oscillations on the solution field of the model because the coastal boundary is caused to move in discrete steps of element size.

If not checked, these grid-scale waves can lead to local and possibly global instability of the model. They are an artifact of the numerical solution process and have no physical existence, so ways of limiting their production and retarding their propagation have been sought by various authors (e.g. Leendertse, 1970 and Flather and Heaps, 1975).

Advective terms are of importance in very shallow waters of tidal flat models. They provide the primary propagative mechanism for grid-scale waves and hence may be associated with any locally unstable behaviour of the tidal flat model.

Flather and Heaps (1975) introduce an explicit grid-scale "filter" in association with the x-advective term of the U-momentum equation and the y-advective term of the V-momentum equation. Its form and use is illustrated by considering the following finite difference approximation (ibid., p.497):

$$\left\{U\frac{\partial U}{\partial x}\right\}_i \simeq \overline{U}_i \left\{\frac{\partial U}{\partial x}\right\}_i, \quad \text{where} \quad \overline{U}_i = \frac{1}{4}(U_{i-1} + 2U_i + U_{i+1}). \tag{8.4}$$

Alpert (1981) describes this filter and compares its properties with generalized implicit filtering in the meteorological context. Alpert is concerned with filtering the solution field of the whole domain — "smoothing" the solution domain. This is not investigated here. We only investigate term-wise filtering such as is carried out by the filter $\overline{U}_i$.

To demonstrate the behaviour of the filter $\overline{U}_i$, suppose

$$U_i = U_a \exp(\imath\alpha x_i), \tag{8.5}$$

real part intended, where U_a is the amplitude of the velocity wave, $\alpha = 2\pi/\lambda$ is the wavenumber, λ is the wavelength, $x_i = i(2\Delta x)$, $i \in N$, where N denotes the set of Natural

numbers. The values U_{i-1} and U_{i+1} are expressed in a similar way and are thereby related to U_i by a translation in space. Expressing wavelength in terms of grid-spacing as

$$\lambda = q(2\Delta x), \quad q \in R, \tag{8.6}$$

where R denotes the set of real numbers, and substituting the resultant forms for U_{i-1}, U_i and U_{i+1} into the expression for the filter $\overline{U}_i$ gives

$$\overline{U}_i = U_i \cos^2(\pi/q). \tag{8.7}$$

Defining "amplitude response" as the ratio of the output wave to the input wave, the amplitude response of the filter is

$$\cos^2(\pi/q). \tag{8.8}$$

The filter returns an attenuated wave, the value of the attenuation being in the interval (0,1). The waves that are "filtered out" are the wave $\lambda = 4\Delta x$ (twice the grid spacing) and its odd harmonics; waves unaffected by the filter are the corresponding even harmonics. The harmonics are only of theoretical interest here because the shortest numerical wave that can be resolved by a uniform grid has wavelength $\lambda = 4\Delta x$ — a numerical wave requires at least three gridpoints for resolution.

For waves of tidal wavelength $\lambda = q(2\Delta x)$ is large; specifically, q is large for tidal waves in the present model where $2\Delta x = 1.905\,\text{km}$. For the NSG model $q \simeq 225$ for a semi-diurnal wave and the amplitude response is 0.9998, so the attenuation is much less than one percent. For a diurnal wave the attenuation is less significant.

The influence of this attenuation on tidal constituents should be considered, however, in case it is accumulatively important over a full 32 day simulation. For the present model $\Delta t = 80\,\text{sec}$ so there are 34560 time steps in a full simulation. With respect to the locally shallow regions where the attenuating effect is strongest, it is unlikely that waves of tidal frequency will be present long enough for the attenuation to be significant. At most of the elements of the model, local water depth is such as to render the effect of the advective terms insignificant. A crude measure of the effect can be gained by examining the calibration error of the model with and without the use of such a filter. This was tried and it was found that using the constant quadratic friction coefficient with a value of 0.0017 there is no difference to three significant figures in the value of the error measure ε. It is probable that the effect of friction in the shallow coastal waters where the tide gauges are located is far greater than the attenuating effect of this filter. In what follows, it is furthermore pointed out that the differencing used for several other terms in the equations, including the important quadratic friction and Coriolis terms, inherently behaves as a grid-scale filter, so the present numerical scheme inherently acts to attenuate waves of tidal frequency regardless of the introduction of this filter. Therefore the effect of the included advective filter is difficult to separately quantify.

For the present model it is possible to arbitrarily restrict the wetting/drying routine to tidal flat elements in order to try to ensure that the attenuating effect of the filter on tidal constituents is strictly localized. But such an approach implies that one knows in advance the elements which are tidal flat elements. Since a future use of the present model is to investigate the effects of wind and of Greenhouse changes in mean sea level, it is clearly preferable to leave it to the program to determine which elements are tidal flat elements in the course of the simulation. We have not chosen to specify which elements these are in

the present model. Thus it is an indication of the accuracy of the wetting/drying facility that the elements the model determines to be tidal flat elements correspond exactly to those elements one expects to be so having defined such elements to be those exposed at the ISLW mark. Again, since it will be seen that other differencing used in the scheme has **built-in** filtering behaviour in any event, there seems no point in isolating the elements to which the filter $\overline{U}_i$ will be applied.

Examining the differencing used for the y-advective term of the U-momentum equation and the x-advective term of the V-momentum equation, it becomes clear that the respective four-point averages inherently behave as grid-scale filters. For example, consider the following differencing based on that of approximation (3.11) for the y-advective term of the U-momentum equation:

$$\left\{V\frac{\partial U}{\partial y}\right\}_{U_i}^{n+\frac{1}{2}} \simeq \frac{1}{4}\left(V_{i_1}^n + V_{i_1+1}^n + V_i^n + V_{i+1}^n\right)\left\{\frac{\partial U}{\partial y}\right\}_{U_i}^n. \tag{8.9}$$

Here, the four-point average of V values is written for time level n. Let us now examine the filtering behaviour of the average

$$\overline{V}_{U_i} = \frac{1}{4}\left(V_{i_1} + V_{i_1+1} + V_i + V_{i+1}\right). \tag{8.10}$$

Put

$$V_{U_i} = V_a \exp(\imath\alpha x_j)\exp(\imath\beta y_k), \tag{8.11}$$

real part intended, where V_a is the velocity amplitude, $\alpha = 2\pi/\lambda_x = \pi/(q\Delta x)$ is the wavenumber in the x-direction and $\beta = 2\pi/\lambda_y = \pi/(k\Delta x)$ is the wavenumber in the y-direction for a square grid with element dimension $(2\Delta x)\times(2\Delta x)$; further, $x_j = j(2\Delta x)$, $j \in N$ is a distance in the x-direction and $y_k = k(2\Delta x)$, $k \in N$ is a distance in the y-direction. Substituting these expressions into V_{U_i} and, in turn, into $\overline{V}_{U_i}$ gives

$$\overline{V}_{U_i} = V_{U_i}\cos^2(\pi/q), \tag{8.12}$$

which has the same form as the filter $\overline{U}_i$ considered earlier.

Therefore, the four-point spatial averaging used in expression (3.11), the Coriolis term (3.13) and the vertical diffusive term (3.19), and its corresponding quadratic friction formulation for depth-averaged flows, intrinsically behaves as a grid-scale filter.

If, further, we consider the effect of time-centring such as in the expression

$$\overline{V}_{U_i}^{n+\frac{1}{2}} = \frac{1}{4}\left(V_{i_1}^{n+1} + V_{i_1+1}^{n+1} + V_i^n + V_{i+1}^n\right), \tag{8.13}$$

taken from (3.11), we find that time-centring filters out waves of period Δt (and the associated even harmonics) that might otherwise propagate in the direction of advancing time. This filtering behaviour is investigated by substituting

$$V_{U_i}^{n+\frac{1}{2}} = V_a \exp(\imath\omega t_{n+\frac{1}{2}})\exp(\imath\alpha x_j)\exp(\imath\beta y_k), \tag{8.14}$$

real part intended, where $\omega = 2\pi/T$ is the angular frequency, $T = r\Delta t$, $r \in R$, is the period and $t_{n+\frac{1}{2}} = (n+\frac{1}{2})\Delta t$, $n \in N$ and the other variables are as before. The substitution leads to

$$\overline{V}_{U_i}^{n+\frac{1}{2}} = V_{U_i}^{n+\frac{1}{2}}\cos(\pi/r + \pi/q)\cos(\pi/q), \tag{8.15}$$

which has the familiar form of a grid-scale filter if $\pi/r = m(2\pi)$, $m \in N$, i.e. if

$$T = \Delta t/(2m),\ m \in N, \tag{8.16}$$

viz. for the wave of period Δt (and its even harmonics). That waves of such short period arise in the present context is due to the scheme being three-level in nature.

In summary, the four-point spatial and temporal averages used in the differencing of the present numerical scheme already act to prevent the advection of the spatial grid-scale wave $\lambda = 4\Delta x$ and the temporal grid-scale wave of period $T = \Delta t$. It only remains to replace the factor U by the filter $\overline{U}_i$ in the x-advective term of the U-momentum equation and the factor V by a similar filter in the y-advective term of the V-momentum equation. This approach removes the non-physical grid-scale waves $\lambda = 4\Delta x$ and $T = \Delta t$, and attenuates grid-scale waves of greater wavelength and longer period. Waves of tidal wavelength and period are only slightly attenuated.

8.6 Calibrating the model of Northern Spencer Gulf

Because the open boundary of the fine-grid Northern Spencer Gulf (NSG) model is relatively distant from tidal observation stations, the driving energy for it is taken from the coarse-grid Spencer Gulf (SG) model of Chapter 5.

At the outset it was decided not to attempt to dynamically couple the SG and NSG models as a way of obtaining the open boundary information for the latter. Although such coupling appears to have been successful in some tidal applications (e.g. Greenberg, 1983), it is simpler to obtain the data by interpolation from the larger model, as do Mitchell et al. (1984) in deriving constants for the open boundary of their three-dimensional model of the Gulf of Carpentaria. Such an approach thereby avoids the inevitable setting-up costs of developing procedures that allow free movement between nested grids without the "jumps" in grid dimension at the grid boundaries giving rise to numerical oscillations that might be de-stabilizing. Flather and Heaps also suggest that "a large-scale encompassing model may offer a most useful source of input data for detailed model studies of coastal seas" (1975, p.516). Pingree and Maddock (1977b, p.870) propose successive applications of this technique in order to achieve finer and finer details of tidal characteristics.

In obtaining the open boundary constants for the NSG model from the SG model there arose the problem of determining which set of tidal constants to use.

At this point in the work, a SUN SPARCstation 1+ became available, so the two-dimensional tidal flat program was ported over from the VAX 11/785 on which most of its development had taken place. The SPARC ran the program in about one quarter the time used by the VAX and was connected to considerably more memory for data storage.

The SG model was recalibrated on the SPARC and differences were noted in the predictions obtained even though the same parameter sets were used. The recalibration suggested that using $C_b = 0.0025$ still produced the least error. Even though SPARC architecture uses a more severe truncation of bits in floating point number representation, surprisingly the optimal error value of $\varepsilon = 3.46$ cm is slightly smaller than the value 3.49 cm obtained using the VAX. The reasons for the difference must extend beyond differences in rounding — they may relate to differences in the accuracy of the run-time libraries used (viz. the trigonometric and square root facilities) and even to the different ways the compilers arrange the order in which arithmetic expressions are evaluated! Certainly, the difference in precision between the machines is not significant.

	Calibration station set				
C_b	(a)	(b)	(c)	(d)	(e)
0.0020	3.76	6.29	5.22	5.49	6.47
0.0021	3.64	6.01	4.97	5.23	6.26
0.0022	3.55	5.78	4.79	5.04	6.10
0.0023	3.49	5.59	4.68	4.91	5.99
0.0024	3.46*	5.45	4.65*	4.85*	5.94*
0.0025	3.46*	5.35	4.70	4.86	5.96
0.0026	3.48	5.30	4.84	4.95	6.02
0.0027	3.52	5.29*	5.03	5.09	6.13
0.0028	3.58	5.30	5.25	5.26	6.27
0.0029	3.65	5.35	5.50	5.46	6.44
0.0030	3.74	5.42	5.77	5.68	6.68

Table 8.1: *Compilation of results corresponding to different expressions for the calibration errors of SG model runs using (a) all calibration stations of the SG model (c.f. Table 5.6), (b) only one NSG station: Yarraville Shoals, (c) three NSG stations: Whyalla, Pt. Bonython, Pt. Pirie, (d) four NSG stations: Yarraville Shoals, Whyalla, Pt. Bonython, Pt. Pirie and (e) all six available NSG stations: Yarraville Shoals, Whyalla, Pt. Bonython, Pt. Pirie, Beacon #5 and Pt. Augusta. The error measure used is the combined error measure ε (cm) defined by expression (5.6). Least error values for each calibration set are asterisked.*

Because calibrations show that error accumulates in a non-uniform manner as one proceeds northwards, it is not immediately clear that the $C_b = 0.0025$ data can be used to drive the NSG tidal flat model. The greater error in the northerly predictions seems mostly due to the amplifying effect of the northern end of the model which corresponds to a similar amplification that occurs in the field (see Table 5.1). In order to obtain open boundary information for the NSG model contaminated as little as possible by the error level of the chosen calibration run of the SG model, the calibration data of the latter is re-examined in several respects and the findings summarized in Table 8.1.

If Yarraville Shoals (see Figure 8.1), the closest station of the NSG model to its open boundary, is used alone for the calibration, the optimal value is $C_b = 0.0027$ (see column (b)). Model agreement with observations at Yarraville Shoals is relatively poor so the next nearest stations, Whyalla, Pt. Bonython and Pt. Pirie, are used and this calibration suggests an optimal value of $C_b = 0.0024$ (see column (c)). Including Yarraville Shoals along with these, the overall optimal C_b remained at $C_b = 0.0024$ and there is very little difference between the performance at $C_b = 0.0024$ and $C_b = 0.0025$ (see column (d)). The addition of Yarraville Shoals increases the value of the least error.

In the SG calibrations of Chapter 5, Pt. Pirie is excluded since it cannot be represented by a reasonably close elevation gridpoint, even though it gives good agreement with ob-

servations (see Table 5.6). The same is true of Pt. Augusta station. Only potentially six calibration stations are available in the Northern Spencer Gulf region, so for that reason and the fact that predictions for stations Pt. Pirie and Pt. Augusta are nonetheless good, they are included in calibration set (e) and will be included in the calibration sets for the NSG model. In the NSG model with its reduced element size the distances between the nearest representative elevation gridpoints and the actual map positions of both Pt. Pirie and Pt. Augusta are much reduced, so using them in the calibration process for the NSG tidal flat model seems a reasonable approach.

If all six available NSG stations are used — Yarraville Shoals, Whyalla, Pt. Bonython, Pt. Pirie, Beacon #5 and Pt. Augusta — the optimal $C_b = 0.0024$ and the associated error is similar to that obtained with $C_b = 0.0025$ (see column (e)).

From the table, the coefficient $C_b = 0.0024$ produces the smallest error values, except for the calibration done with station Yarraville Shoals alone. However, the error obtained using $C_b = 0.0025$ is not significantly different in most of the calibrations. Thus, mainly for reasons of consistency and continuity from the SG to the NSG model, data from the SG run using $C_b = 0.0025$ is used to supply open boundary forcing for the NSG model.

Table 8.2 specifies the tidal constants for the four major constituents at the 31 elevation gridpoints of the open boundary of the NSG model. These are interpolated from constants derived using $C_b = 0.0025$ from the SG model at the 10 elements of the specified transect of that model. The interpolation formulae used for each of the 31 open boundary gridpoints have the same second order discretisation error, i.e. the interpolation is uniformly accurate for the 31 gridpoints of the open boundary.

Returning to Table 8.1 we note that in general the minimum error value increases as progressively more northerly stations are included. This gives evidence, to some degree, of the declining ability of the SG model with its coarse grid element to represent tidal behaviour accurately far from the open boundary of that model. But more significantly, it illustrates the amplifying effect of the northern part of the SG model on errors that are already present in the northerly propagating (numerical) tide — this amplifying effect is noted earlier in this section.

From Table 8.1 the combined (amplitude and phase) error for the SG model using calibration set (e) is 5.96 cm when $C_b = 0.0025$. If all stations of the NSG model are excluded from calibration set (a) the value of the error measure is only 2.20 cm when $C_b = 0.0025$. The ratio of the numbers 5.96 and 2.20 is about 2.7, and this may provide an approximate measure of the amplification effect in the Gulf as one moves northwards. (If only predicted **amplitude** errors are compared, the amplification is 2.6.) Of course, some component of this is due to a decreasing ability of the SG model to accurately resolve the tidal behaviour of the Gulf as one moves northward away from the open boundary — and hence a reason for developing the fine-grid model of this chapter. But the amplification effect of the Gulf (as reproduced by the model) seems to explain the bulk of the error increase, given that the observed amplification in the amplitudes of the constituents is about 1.9 for O_1, 2.1 for K_1, 3.9 for M_2 and 4.1 for S_2, obtained by comparing the tidal constants at Wedge Island and Pt. Augusta (see Table 5.1). The arithmetic mean of these observed amplification values is about 3.0, the geometric mean 2.8 and the harmonic mean 2.7. Since the harmonic mean is often preferred where data values are significantly different, the agreement between the harmonic mean and the value 2.6 calculated above is particularly pleasing.

In the light of this, one may pose the question: if the value $C_b = 0.0025$ gives rise to an

Boundary element	O_1		K_1		M_2		S_2	
	amp	ph	amp	ph	amp	ph	amp	ph
1	31.6	268.4	39.4	288.1	32.5	262.9	31.4	310.9
2	31.4	268.2	39.3	287.8	32.0	262.3	30.9	310.2
3	31.3	268.2	39.2	287.8	31.6	262.1	30.4	309.9
4	31.2	268.1	39.1	287.8	31.2	261.9	29.9	309.7
5	31.1	268.1	39.0	287.7	30.7	261.6	29.5	309.4
6	31.0	268.3	38.9	287.9	30.4	261.8	29.1	309.6
7	30.9	268.4	38.8	288.1	30.0	262.1	28.7	309.9
8	30.8	268.6	38.7	288.3	29.7	262.3	28.3	310.1
9	30.7	268.8	38.6	288.5	29.3	262.6	27.9	310.4
10	30.6	269.0	38.5	288.7	29.0	262.9	27.6	310.7
11	30.6	269.2	38.4	288.9	28.7	263.2	27.2	310.9
12	30.5	269.4	38.4	289.2	28.4	263.7	26.9	311.4
13	30.4	269.7	38.3	289.5	28.1	264.2	26.6	311.9
14	30.4	269.9	38.2	289.7	27.8	264.6	26.3	312.5
15	30.3	270.2	38.1	290.0	27.6	265.1	26.0	313.0
16	30.3	270.4	38.1	290.2	27.4	265.7	25.8	313.5
17	30.3	270.7	38.1	290.5	27.1	266.2	25.5	314.0
18	30.2	270.8	38.0	290.7	26.9	266.5	25.3	314.4
19	30.2	271.0	38.0	290.9	26.7	266.8	25.0	314.8
20	30.1	271.2	37.9	291.1	26.4	267.2	24.7	315.1
21	30.1	271.4	37.9	291.3	26.3	267.7	24.5	315.7
22	30.1	271.6	37.9	291.5	26.1	268.2	24.4	316.2
23	30.1	271.9	37.9	291.8	26.0	268.8	24.2	316.8
24	30.1	272.1	38.0	292.0	26.0	269.4	24.2	317.5
25	30.1	272.4	38.0	292.3	25.9	270.1	24.1	318.1
26	30.1	272.6	38.0	292.5	25.8	270.7	24.0	318.8
27	30.2	272.8	38.0	292.8	25.9	271.3	24.1	319.6
28	30.2	273.1	38.1	293.0	25.9	272.0	24.1	320.3
29	30.2	273.3	38.1	293.2	26.0	272.7	24.2	321.1
30	30.3	273.5	38.2	293.4	26.1	273.4	24.3	321.9
31	30.4	273.7	38.3	293.7	26.3	274.1	24.5	322.6

Table 8.2: *Tidal constants (amplitude in cm, phase in degrees, G.M.T.) for the four major constituents at the 31 open boundary elevation gridpoints of the Northern Spencer Gulf model (c.f. Figures 5.22–5.25 in Chapter 5). This data constitutes one set of forcing information for the NSG model.*

error of 5.96 cm for the six NSG stations from the SG model, can we anticipate a smaller error for the same six stations from the NSG model?

When the NSG model was first run (with $C_b = 0.0025$), the error value obtained was 7.87 cm, much **higher** than the value 5.96 cm!

A possible reason for the discrepancy may be related to the bathymetry proposed for the tidal flat regions. The bathymetry used is an intelligent guess based on a few scattered

heights recorded on the hydrographic map. Without knowing the tidal flat bathymetry as accurately as the interior seabed bathymetry of the model, perhaps one cannot expect to be able to sensibly calibrate the NSG model, nor obtain a lower error value at the finer scale of the NSG model. But a review of the tidal flat bathymetry used lead to no significant change in it, nor to the value of the error measure. Nevertheless, there remains a need to more accurately specify the tidal flat bathymetry.

Meanwhile, an attempt to calibrate the NSG model indicated that significantly reduced errors were attainable by lowering the value of C_b.

Another possible reason for the discrepancy might be that the NSG model is "under-forced" if it is only driven by the four major constituents taken from the SG model — not the full energy from the corresponding transect of the SG model is thereby being input at the open boundary of the NSG model.

Thus a run of the SG model at the time step used for the NSG model was conducted, during which elevation predictions for the gridpoints corresponding to the NSG model were stored. These data files (1.7 MByte each, one file for elevation predictions at half time steps, and one for elevation predictions at full time steps) were then used to provide the boundary forcing for the NSG model, the values being interpolated across the open boundary line to the more closely spaced elevation gridpoints of the NSG model.

The result of this run (using $C_b = 0.0025$) was to reduce the error measure only a little, from 7.87 cm to 7.53 cm. The reason for the relatively slight effect is that although it is true that not all the available tidal energy had been conveyed previously from the SG model using just the four major constituents, at least the energy of those constituents was faithfully conveyed and it is the performance of the NSG model in these constituents that is examined by the error measure used! The reduction nevertheless obtained in the error value must be due to the introduction of the minor constituent energy which may have promoted an appropriate loss of major constituent energy to higher harmonics.

Having considered and dismissed the bathymetry and boundary forcing of the NSG model as being major factors in the surprisingly high initial error value of 7.87 cm, an argument for reducing C_b for the NSG model as being a sensible approach to lowering the error value is now developed. Since it seems reasonable that the friction terms of the depth-averaged momentum equations, viz.

$$\frac{C_b}{H}(U,V)\sqrt{U^2+V^2} \tag{8.17}$$

should have an approximately constant ratio C_b/H for both the SG and NSG models, certainly in the vicinity of the open boundary of the NSG model, and noting that the average depth of the SG model is about 25 m while that of the NSG model is about 10 m, the approximate equivalence

$$\left(\frac{C_b}{H}\right)_{\text{NSG}} \simeq \left(\frac{C_b}{H}\right)_{\text{SG}} \tag{8.18}$$

leading to

$$(C_b)_{\text{NSG}} \simeq 0.0010 \tag{8.19}$$

suggests that a much reduced optimal value for C_b for the NSG model should be expected. Another way to view this is to say that $C_b = 0.0025$ for the SG model corresponds to

$C_b \simeq 0.0010$ for the NSG model! A yet wider interpretation is that the friction coefficient ought to depend on local element depth in some manner.

Running the NSG model with $C_b = 0.0010$ shows that it is a borderline value for a stable NSG model — again, this is reasonable since one would not expect $(C_b)_{\text{NSG}}$ to be as low as the simple correspondence above suggests — but running it with slightly higher values which are somewhat smaller than $C_b = 0.0025$ does produce models with error values less than 5.96 cm which are in a global sense stable, as will be seen shortly.

It is now timely to discuss several parameters used in the tidal flat routine. These are (see Flather and Heaps, 1975, p.495):

- ϵ, a postulated height which, along with grid element dimension, establishes a slope criterion for the coastward advancing wave,
- H_0, a postulated minimum value of depth used to limit frictional dissipation and to prevent there being a singularity in the friction terms as an element dries, and
- H_{dry}, a postulated depth at or below which an element is classified as being "dry" and above which it is "wet".

For their model of Morecambe Bay, Flather and Heaps chose

$$\epsilon = 0.10\,\text{m}, \quad H_0 = 1.0\,\text{m} \quad \text{and} \quad H_{\text{dry}} = 0.0\,\text{m}. \tag{8.20}$$

Their grid elements are square and of dimension 1853 m. In the NSG model the grid elements are square and of dimension 1905 m, and on this basis the value $\epsilon = 0.10$ m is also used here. As well, the values $H_0 = 1.0$ m and $H_{\text{dry}} = 0.0$ m have been used to this point.

In order to investigate the influence of these three parameters in the context of the present model, several numerical experiments are conducted. For the tests, the control set of parameters used is the set (8.20).

Tests with parameter ϵ and C_b

Figure 8.5 shows plots of combined error measure ε versus constant quadratic friction coefficient C_b for three values of ϵ, viz. 0.05 m, 0.10 m and 0.15 m. The solid curve displays error values for the control set (which uses $\epsilon = 0.10$ m) and has minimum value $\varepsilon = 5.62$ cm when $C_b = 0.0013$. The C_b values used are taken from those ticked on the horizontal axis and the solid curve simply connects the corresponding ε values. For $\epsilon = 0.05$ m the minimum error occurs at $C_b = 0.0012$ and for $\epsilon = 0.15$ m the minimum is at $C_b = 0.0013$.

On the basis of the value of the error measure ε, it seems that for runs with $C_b \geq 0.0019$ the model is almost insensitive to ϵ for the values of ϵ used. But it may be misleading to link the ϵ sensitivity of the model directly to the value of ε. After all, the error measure ε is based on predictions at 6 calibration stations none of which are located at tidal flat elements! A measure of performance tied to the tidal flat elements themselves is needed.

For each of the tidal flat elements, a count is kept of the number of times the element wets and dries during the final 29 days of the simulation. Assuming two high waters and two low waters per day, the maximum number of times an element should wet is 58 and the maximum number of times it should dry is also 58 — a total maximum transition count from wet-to-dry and dry-to-wet of 116. Counts greater than 116 will be defined

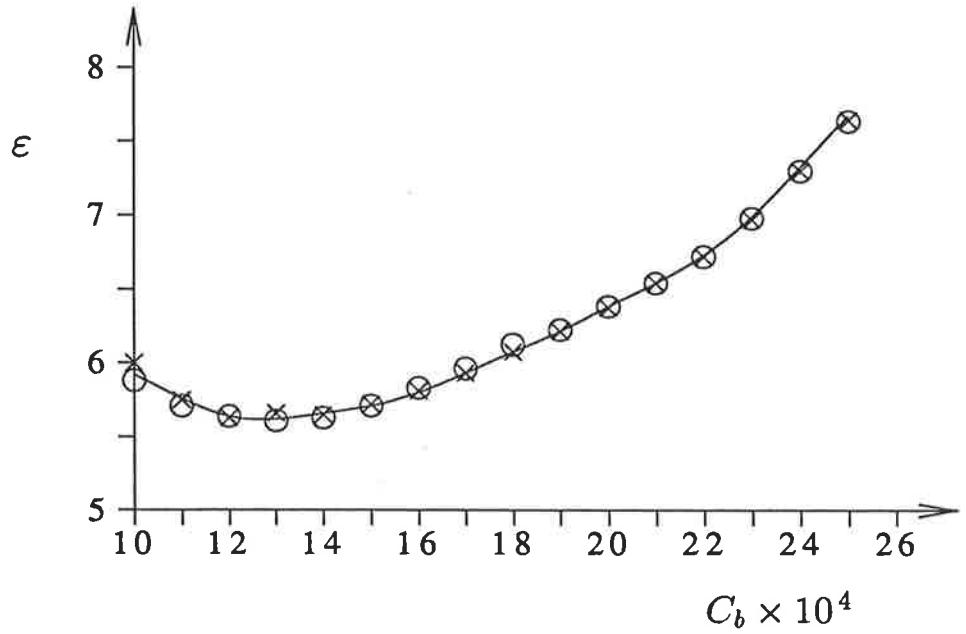


Figure 8.5: *Plots showing the results of numerical tests with parameter ϵ, the slope criterion. For the control set (using $\epsilon = 0.10\,m$) a solid line connects corresponding values of the combined error measure ε (cm). Values for $\epsilon = 0.05\,m$ are marked $\times$ and values for $\epsilon = 0.15\,m$ are marked $\circ$.*

as "unrealistic" counts. In practice, it is found that the 155 tidal flat elements have an average predicted transition count of about 70. The mode (most common) count is in the 90's and is achieved by about 20 elements. The mode interval is the interval 91–100 and is contributed to by 40 elements.

For runs using $\epsilon = 0.05\,m$ unrealistically high counts were predicted for one or more elements for each value of C_b used. For runs using $\epsilon = 0.10\,m$ and $\epsilon = 0.15\,m$, realistic counts were only obtained for $C_b \geq 0.0012$. On this basis, low values for ϵ should not be used as they give rise to too many wetting/drying events.

For the tidal flat elements comprising Ward Spit, the transition counts are about the same when $\epsilon = 0.10\,m$ and $\epsilon = 0.15\,m$ for runs with $C_b \geq 0.0017$. While a further choice between values of ϵ is necessarily difficult in the absence of observational data, the value actually used should lead to transition counts for Ward Spit in accord with the observation that it uncovers only at low springs.

Tests with parameter H_0 and C_b

Figure 8.6 shows plots of error measure ε versus C_b for three values of H_0, viz. 0.5 m, 1.0 m and 2.0 m. The solid curve again corresponds to the control set, for which $H_0 = 1.0\,m$. On the basis of the value of ε, it can be seen that for runs with $C_b \geq 0.0014$ all three values of H_0 return substantially the same result.

On closer examination of these runs it is found that for $H_0 = 0.5\,m$ realistic transition counts are obtained for $0.0010 \leq C_b \leq 0.0021$. Physically realistic counts for $H_0 = 2.0\,m$ were obtained when $C_b \geq 0.0018$. On this basis, low values for H_0 should be used.

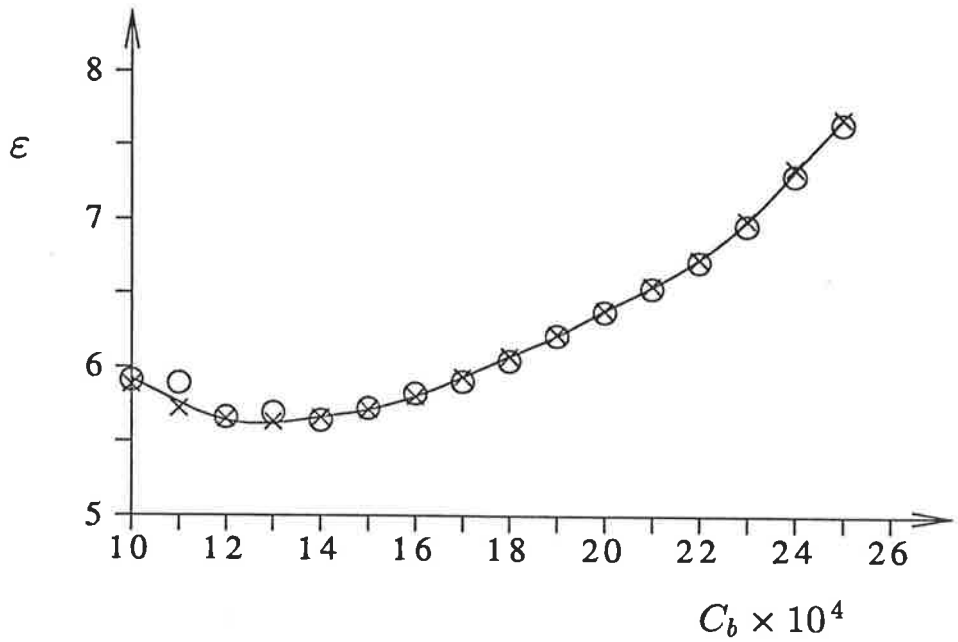


Figure 8.6: *Plots showing the results of numerical tests with parameter H_0, which limits frictional dissipation. For the control set (using $H_0 = 1.0\,m$) a solid line connects corresponding values of the combined error measure ε (cm). Values for $H_0 = 0.5\,m$ are marked $\times$ and values for $H_0 = 2.0\,m$ are marked $\circ$.*

Frictional dissipation may be insufficiently limited if high values are used.

For runs with $C_b \geq 0.0021$ the transition counts for the elements of Ward Spit are in general agreement using $H_0 = 0.5\,\text{m}$ and $H_0 = 1.0\,\text{m}$, and are generally doubled when using $H_0 = 2.0\,\text{m}$.

Tests with parameter H_{dry} and C_b

Figure 8.7 shows plots of error measure ε versus C_b for three values of H_{dry}, viz. 0.0 m, 0.01 m and 0.05 m. The solid curve corresponds to the control set, for which $H_{\text{dry}} = 0.0\,\text{m}$. Positive values of H_{dry} produce much less stable models when $C_b \leq 0.0018$, but return improved values of ε when $C_b > 0.0019$, especially for $H_{\text{dry}} = 0.05\,\text{m}$.

Physically realistic counts are obtained using $H_{\text{dry}} = 0.01\,\text{m}$ for runs using $C_b \geq 0.0015$, and using $H_{\text{dry}} = 0.05\,\text{m}$ for runs using $C_b \geq 0.0019$. However, examining the transition counts shows they are quite variable for the set of C_b values used, for both $H_{\text{dry}} = 0.01\,\text{m}$ and $H_{\text{dry}} = 0.05\,\text{m}$. One expects the counts to settle down at a given element as C_b increases, but this is not the case when $H_{\text{dry}} > 0$. Generally the count values are smaller than the corresponding values for $H_{\text{dry}} = 0.0\,\text{m}$, and they increase as C_b increases, though not reaching as high as the $H_{\text{dry}} = 0.0\,\text{m}$ counts. On this basis positive values for H_{dry} should not be used and $H_{\text{dry}} = 0.0\,\text{m}$ is preferred.

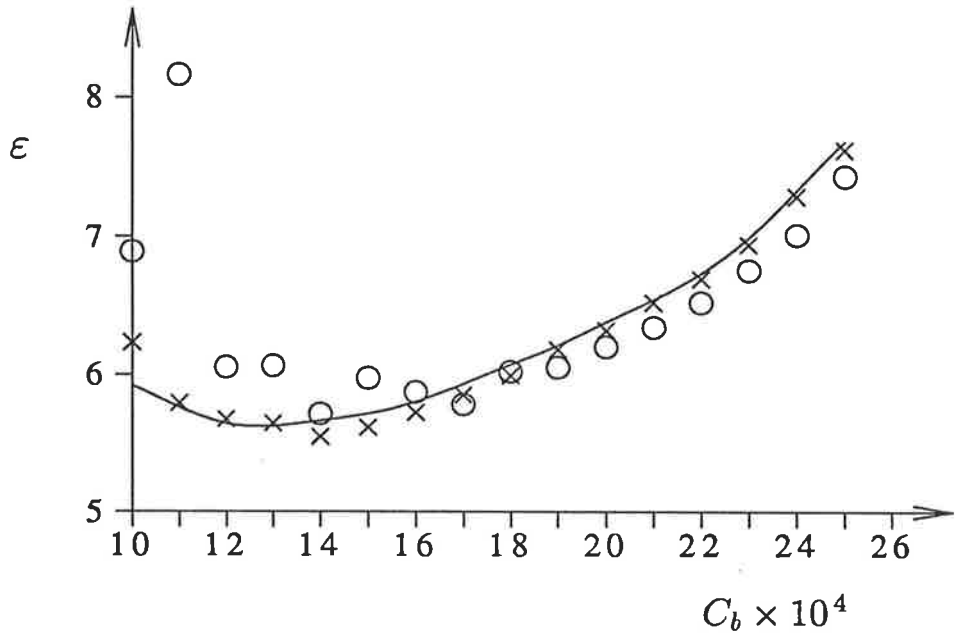


Figure 8.7: *Plots showing the results of numerical tests with parameter H_{dry}, used to determine when an element is "dry". For the control set (using $H_{\text{dry}} = 0.0\,\text{m}$) a solid line connects corresponding values of the combined error measure ε (cm). Values for $H_{\text{dry}} = 0.01\,\text{m}$ are marked $\times$ and values for $H_{\text{dry}} = 0.05\,\text{m}$ are marked $\circ$.*

Summary of tests of ϵ, H_0 and H_{dry} against C_b

The above tests of parameters ϵ, H_0 and H_{dry} against the value of the constant quadratic friction coefficient C_b show that the values used for the control set are a reasonable choice. There is no obvious reason for altering the values that Flather and Heaps chose for these parameters.

Flather and Heaps used $C_b = 0.0025$ for their Morecambe Bay model. They do not report testing other values of C_b. For their model this value may be appropriate since the average depth of their model seems significantly greater than that of the NSG model (see Flather and Heaps (1975), Fig.4, p.500). At the value $C_b = 0.0025$ in the NSG model there is little discernible difference in performance for $\epsilon = 0.10\,\text{m}$ and $\epsilon = 0.15\,\text{m}$, and for $H_0 = 0.5\,\text{m}$ and $H_0 = 1.0\,\text{m}$. From a computational point-of-view it is unwise to use a positive value of H_{dry} because the transition counts obtained are erratic.

It is possible that a finer tuning of the model with respect to the values of these parameters may lead to better performance using the constant quadratic friction coefficient. To investigate this would require further numerical experimentation.

Ward Spit and Cockle Spit

The elements comprising Ward Spit are a local source of instability for the model and for particularly low C_b their transition counts display high sensitivity to the values of ϵ, H_0 and H_{dry}.

Figure 8.8 illustrates the model layout of the spits, their element numbers, ISLW depth

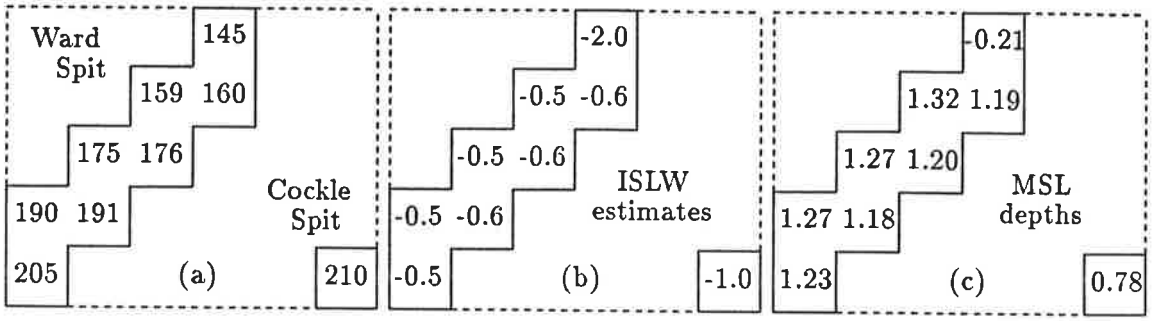


Figure 8.8: *Plan views of Ward Spit and Cockle Spit showing (a) their model element numbers, (b) corresponding estimated ISLW depths and (c) MSL depths (to 3 sig. figs.).*

estimates and MSL depth estimates. Element 145 is not part of Ward Spit but connects it to the permanent coastal boundary. The given ISLW depth estimates are a combination of intelligent guess and numerical experiment — no indication of their datum level is given on the hydrographic charts except in the case of Cockle Spit. If the ISLW levels for the elements of Ward Spit are made too high, say $-1.0\,\mathrm{m}$, the elements wet and dry too frequently, violating the recorded information that they uncover only at low springs. If the datum values for Ward Spit elements are all equal, the western elements (numbers 205,190,175,159) wet/dry two or three times more frequently than the eastern elements, and this seems unrealistic. The stated datum levels lead to wetting/drying events only at low springs for appropriate choices of ϵ, H_0, H_{dry} and C_b.

Figure 8.9 shows a progression of end-of-simulation elevation signals for gradually increasing C_b. Only the last four days of elevation signal are plotted for each C_b value. Although the signals appear smooth above about $C_b = 0.0019$, attention should then be focused on the smoothness of the envelope of high low water levels. These remain unrealistic at Elements 175 and 190, in particular, until about $C_b = 0.0023$. Raising C_b in this way in order to ensure local stability at the elements of Ward Spit extends a damping influence to the rest of the elements and raises the calibration error for the whole model.

The globally constant coefficient of quadratic friction, C_b

It was suggested above that the error measure ε may only be a coarse indicator of performance of the tidal flat model because the observations on which it is based are typically made at permanently wet sites; the error measure ε primarily describes model performance at permanently wet elements.

In general, the transition count discussed above and direct inspection of the predicted elevation signal at individual tidal flat elements offer a more sensitive gauge of the model's performance at tidal flat elements.

The constant quadratic friction coefficient C_b is a rather coarse control in dealing with local instability at tidal flat elements as is demonstrated in Figure 8.9. The minimum value of the error measure did not imply stability locally at Ward Spit elements, and stability there was not achieved until C_b had been raised to about 0.0023.

Because the relationship between friction and depth becomes very important in tidal flat models, a friction coefficient that depends on local depth such as the de Chèzy coefficient n (Chapter 5, Section 5.4) may be a better choice in order to "focus" the influence of

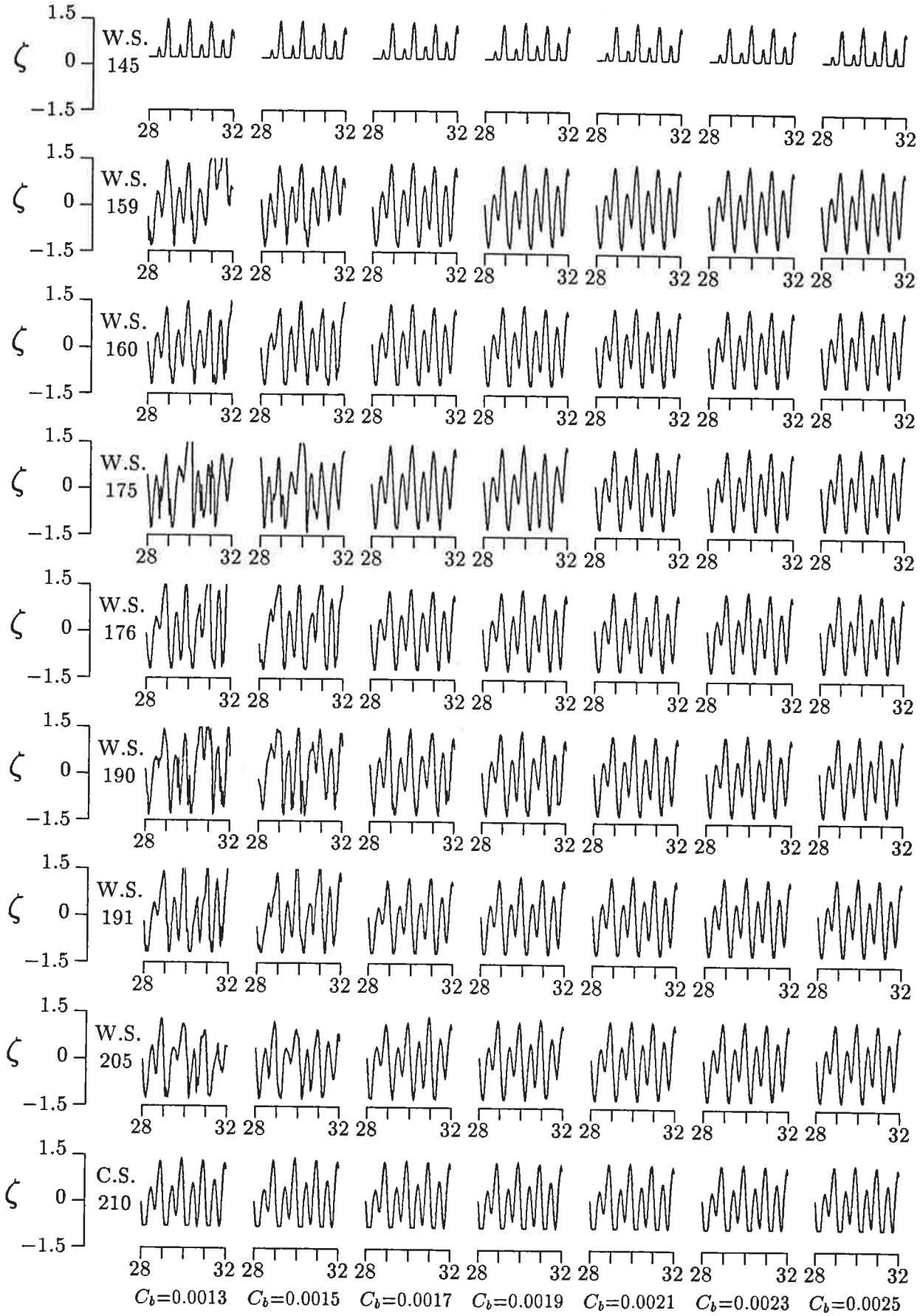


Figure 8.9: *Final four days of predicted elevation signals (ζ in m) at elements corresponding to Ward Spit (W.S.) and Cockle Spit (C.S.), using the values of constant quadratic friction coefficient C_b indicated.*

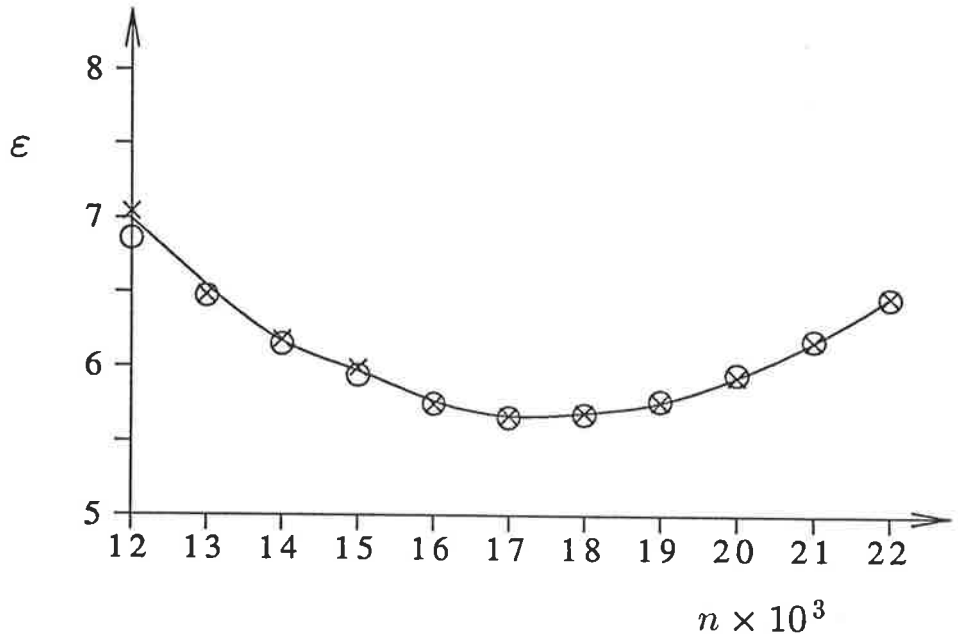


Figure 8.10: *Plots showing the results of numerical tests with parameter ϵ, the slope criterion. For the control set (using $\epsilon = 0.10$ m) a solid line connects corresponding values of the combined error measure ε (cm). Values for $\epsilon = 0.05$ m are marked $\times$ and values for $\epsilon = 0.15$ m are marked $\circ$.*

the friction term. Runchal (1975), Holsters (1978) and Gopalakrishnan (1989) also suggest the use of the de Chèzy coefficient.

Because the influence of the de Chèzy friction coefficient is element dependent, we will see there is less difference between the performance of the model at the optimal value of this coefficient and its performance at the value at which numerical stability is achieved for Ward Spit elements.

But before results using the de Chèzy coefficient are presented, recalibrations for ϵ, H_0 and H_{dry}, as functions of n, are reported.

Tests with parameter ϵ and n

Figure 8.10 shows plots of combined error measure ε versus de Chèzy coefficient n for three values of ϵ, viz. 0.05 m, 0.10 m and 0.15 m. The solid curve connects error values corresponding to the control set, which again we choose to be the set (8.20), and so uses $\epsilon = 0.10$ m. Only the discrete set of values of n indicated on the horizontal axis is used, so the curve simply connects error values at those n. For all three values of ϵ the minimum error occurs at $n = 0.017$. The optimal error for the control set is $\varepsilon = 5.67$ cm.

Based on the value of the error measure ε, it seems that for runs with $n \geq 0.017$ the model is virtually insensitive to ϵ for the set of values of ϵ used.

But for runs using $\epsilon = 0.05$ m unrealistically high transition counts are predicted for one or more elements for each value of n used. For $\epsilon = 0.10$ m realistic counts are obtained for runs using $0.014 \leq n \leq 0.020$, and for $\epsilon = 0.15$ m realistic counts are obtained for runs using n in the same range. Once again low values for ϵ should not be used as they lead

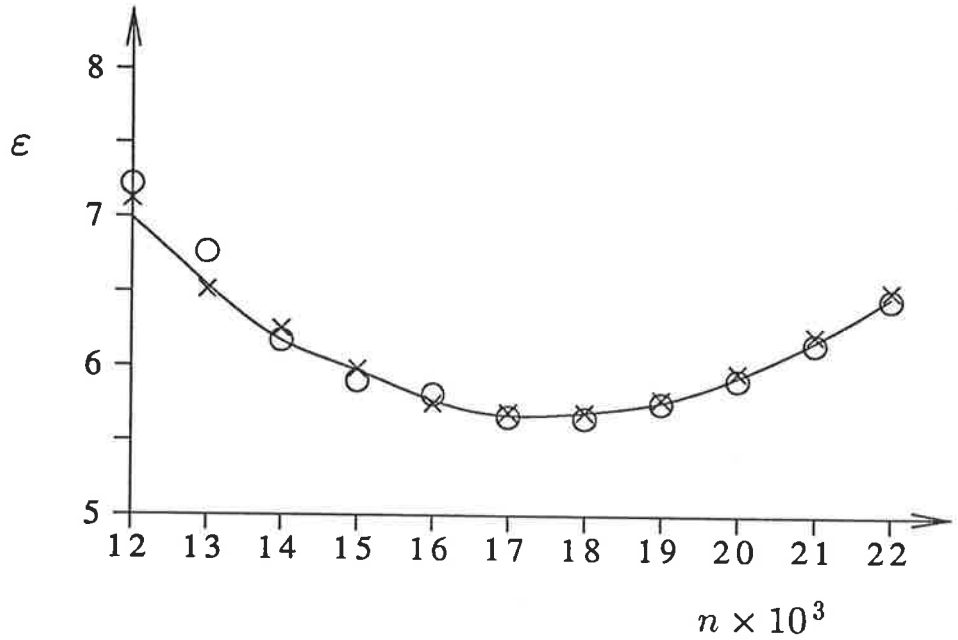


Figure 8.11: *Plots showing the results of numerical tests with parameter H_0, which limits frictional dissipation. For the control set (using $H_0 = 1.0\,m$) a solid line connects corresponding values of the combined error measure ε (cm). Values for $H_0 = 0.5\,m$ are marked $\times$ and values for $H_0 = 2.0\,m$ are marked $\circ$.*

to physically unrealistic wetting/drying events but as well, n should not be too high for $\epsilon = 0.10$ and $\epsilon = 0.15$.

For the tidal flat elements comprising Ward Spit, the transition counts are about the same when $\epsilon = 0.10\,\text{m}$ and $\epsilon = 0.15\,\text{m}$ for runs with $0.016 \leq n \leq 0.020$. A further choice between values of ϵ for optimal performance is necessarily difficult in the absence of observational data.

Tests with parameter H_0 and n

Figure 8.11 shows plots of error measure ε versus de Chèzy quadratic friction coefficient n for three values of H_0, viz. 0.5 m, 1.0 m and 2.0 m. The solid curve corresponds to the control set, for which $H_0 = 1.0\,\text{m}$. Once again, on the basis of the value of ε, it can be seen that for runs with $n \geq 0.017$ all three values of H_0 return substantially the same result and the model seems insensitive to H_0. For runs with $n < 0.017$ the model is sensitive to H_0 and shows unstable behaviour for $H_0 = 2.0\,\text{m}$.

On closer examination of these runs it is found that for $H_0 = 0.5\,\text{m}$ unrealistically high transition counts are obtained for all values of n used. Physically realistic counts for $H_0 = 2.0\,\text{m}$ were obtained when $n \geq 0.017$. On this basis, low values for H_0 should not be used in conjunction with the de Chèzy coefficient.

For runs with $n = 0.019$ and $n = 0.020$ the transition counts for the elements of Ward Spit are in general agreement using $H_0 = 1.0\,\text{m}$ and $H_0 = 2.0\,\text{m}$.

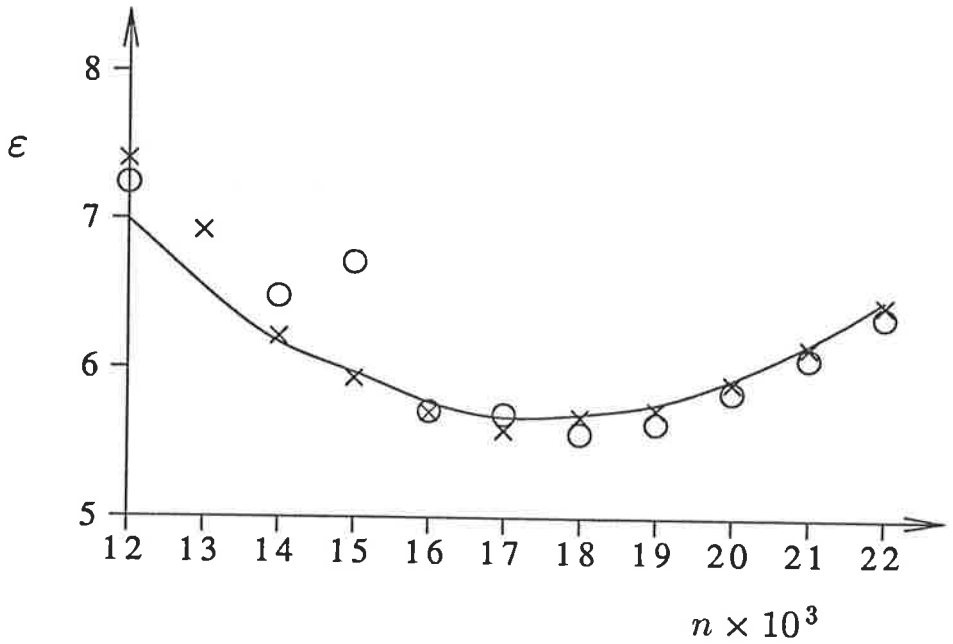


Figure 8.12: *Plots showing the results of numerical tests with parameter H_{dry}, used to determine when an element is "dry". For the control set (using $H_{dry} = 0.0\,m$) a solid line connects corresponding values of the combined error measure ε (cm). Values for $H_{dry} = 0.01\,m$ are marked $\times$ and values for $H_{dry} = 0.05\,m$ are marked $\circ$. The omitted value for $H_{dry} = 0.05\,m$ at $n = 0.013$ is 11.16 cm.*

Tests with parameter H_{dry} and n

Figure 8.12 shows plots of error measure ε versus de Chèzy quadratic friction coefficient n for three values of H_{dry}, viz. 0.0 m, 0.01 m and 0.05 m. The solid curve corresponds to the control set, for which $H_{dry} = 0.0$ m. Positive values of H_{dry} produce much less stable models when $n \leq 0.017$, especially when $H_{dry} = 0.05$ m, but return improved values of ε when $n > 0.017$.

Although the transition counts for runs using $H_{dry} = 0.01$ and $H_{dry} = 0.05$ are reasonable for $n \geq 0.014$ and $n \geq 0.018$, respectively, the counts for a given element as n increases are highly variable for the set of n values used, especially so for $H_{dry} = 0.05$ m. One expects the counts to settle down at a given element as n increases, but this is not the case when $H_{dry} > 0$. On this basis positive values for H_{dry} should not be used and $H_{dry} = 0.0$ m is preferred.

Summary of tests using ϵ, H_0 and H_{dry} against n

From the results of the above experiments with the three parameters and the de Chèzy coefficient it seems that the control set of values is again a reasonable choice and there is no clear reason for changing it. A finer tuning may provide improved model performance but would require substantially more numerical experimentation.

Using the control set of values in the case of both the constant and the de Chèzy quadratic friction coefficients has the advantage of providing a basis for comparison of

performance of the NSG model using these two forms of friction coefficient.

The de Chèzy coefficient of quadratic friction, n

Using the control set of parameters (8.20) and discrete values of the de Chèzy coefficient n ranging from 0.012 to 0.022 in steps of 0.001, the optimal value is $n = 0.017$ ($\varepsilon = 5.67\,\text{cm}$). At this value there is slight instability evident at Element 190 of Ward Spit. Increasing n to 0.018 removes the instability and global model error increases to only $\varepsilon = 5.69\,\text{cm}$. Given that the parameter values of the control set (8.20) are used, this performance of the model using the de Chèzy coefficient contrasts markedly with its performance using the constant quadratic friction coefficient when optimal global error is obtained at $C_b = 0.0013$ ($\varepsilon = 5.62\,\text{cm}$) but stability at Ward Spit is achieved only after raising the coefficient to $C_b = 0.0023$ ($\varepsilon = 6.99\,\text{cm}$).

Consider the value of the coefficient of quadratic friction obtained using the de Chèzy formulation at two elements, one with depth $H = 10\,\text{m}$ (the average depth for the NSG model) and one with depth $H = 1\,\text{m}$ (corresponding to the use of the value $H_0 = 1.0\,\text{m}$). Since the de Chèzy formulation is

$$\text{coefficient of quadratic friction} = \frac{gn^2}{1.003^2 H^{1/3}}, \tag{8.21}$$

the respective values of the coefficient are 0.0013 and 0.0028 when $n = 0.017$. Thus the optimal de Chèzy value $n = 0.017$ gives rise to the optimal constant coefficient value $C_b = 0.0013$ when applied to an element of average model depth. This illustrates the connection between the two forms of quadratic friction coefficient, but also illustrates the difference: while the constant formulation $C_b = 0.0013$ assigns the same value of quadratic friction coefficient to all elements, the de Chèzy parameter $n = 0.017$ produces a coefficient whose value ranges from a value generally of the size 0.0013 to values as high as 0.0028 for tidal flat elements. The de Chèzy coefficient automatically raises the coefficient of friction for shallow elements.

Using $n = 0.018$ the transition counts for Ward Spit and Cockle Spit elements given in Figure 8.13 are obtained. The value $n = 0.018$ is used rather than the globally optimal value $n = 0.017$ because the former gives locally stable results at the elements of Ward Spit while the latter does not. These counts seem realistic — the Ward Spit counts are consistent with the observation that it uncovers only at low springs.

Figure 8.14 displays sets of elevation predictions for all elements given in Figure 8.13. The top eight sets correspond to elements of Ward Spit, the bottom set corresponds to Cockle Spit. The left hand signals, spanning 29 days each, are plotted from hourly data values — each uses 697 hourly data points. The right hand signals, spanning the predictions on Day 16, are plotted from predictions at time step intervals (80 sec) — each of these uses 1081 data points. It can be checked that the lowest elevation level reached by each signal is the negative of the MSL depth for the corresponding element — see Figure 8.8 — and thus corresponds to zero total depth for the element.

The "clipping" of the signals corresponds to drying events. Clipping is hard to see in some of the left hand signals mainly because of the coarseness of interval at which the data is plotted. For this reason the right hand plots were produced and show clipping in each set for Day 16. It can be seen that the drying event depicted is only of one or two hours duration, depending on the element, so is represented in the corresponding left hand signal by only one or two data points.

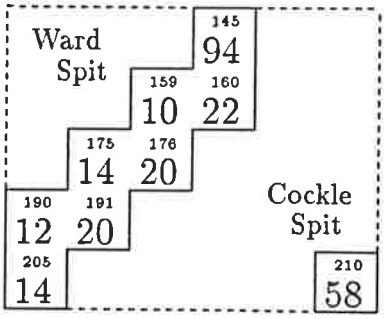


Figure 8.13: *Transition counts (large digits) at the elements (small digits) of Ward Spit and Cockle Spit over a 29 day period using the de Chèzy coefficient with value $n = 0.018$.*

Of further note in the right hand signals are wiggles in the plots immediately following the wetting event. It may be that these wiggles are a continuing manifestation of grid-scale waves — in future work it would be worthwhile investigating whether they could be removed by smoothing the solution field more thoroughly than has so far been achieved using the simple filter and the built-in filter structures associated with many of the difference terms. Again, wetting/drying of the Ward Spit group of elements seems a very difficult test of the tidal flat routine. Flather and Hubbert (1991) offer a plausible explanation for such wiggles: as the value of ϵ is exceeded and flow into a grid box resumes, the "sudden influx causes oscillations, apparent in the time series, which may be interpreted as seiches set up as the water suddenly flows into a newly wet grid box and is reflected" (ibid, p.149). These authors also suggest modifications to Flather and Heaps' (1975) original scheme which appear to reduce the seiching.

Figure 8.15 is a histogram of transition counts for the tidal flat elements of the model simulation over the final 29 days. As already mentioned, during the 29 days, assuming two high waters and two low waters a day, up to a maximum of 116 wetting/drying events might occur at an element. This count is only achieved at one element. The fact that it is not achieved at more elements is a consequence of the fact that for 2–3 days at neaps there is generally either only one high water or only one low water or both (the dodge tide). Of the 952 Type 1 and Type 2 elements in the model, 155 undergo covering/uncovering. These are the elements identified on the hydrographic charts as lying between lowest water and the permanent coastal boundary (highest water) but all elements of the model are treated as potential tidal flat elements and no special treatment of the 155 was used.

From the histogram it can be seen that the mode count is 94, recorded by 17 elements. The average transition count of the 155 tidal flat elements is 69 (nearest integer).

Figure 8.16 shows the tidal flat elements of the south-east coastal region of the Northern Spencer Gulf model, their element numbers and corresponding transition counts for the 29 day period. From the figure, the lowest counts are recorded at those elements which are either furthest seaward, normal to the permanent coastal boundary, or next to the permanent coastal boundary; the highest counts are recorded at elements in between. This is physically reasonable since where there is a grouping of tidal flat elements representing an expansive tidal flat region, elements near the low water mark will spend proportionately most of the time covered, elements near the high water mark will spend most of the time uncovered and elements in between will endure the highest count alternately being covered

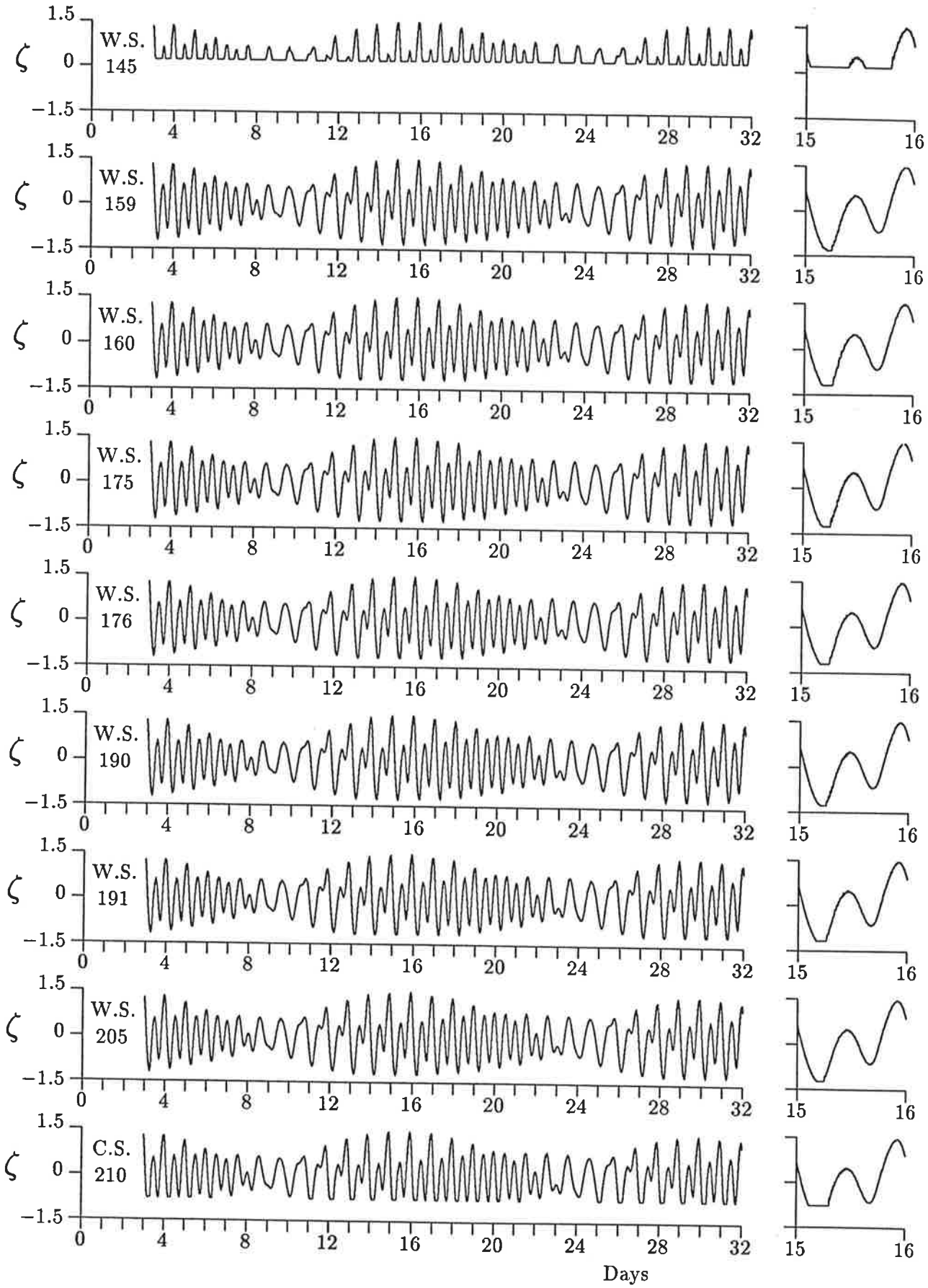


Figure 8.14: *Predicted elevation signals (ζ in m) at elements corresponding to Ward Spit (W.S.) and Cockle Spit (C.S.) generated using the de Chèzy coefficient $n = 0.018$. The signals on the right are plots at time step intervals for Day 16.*

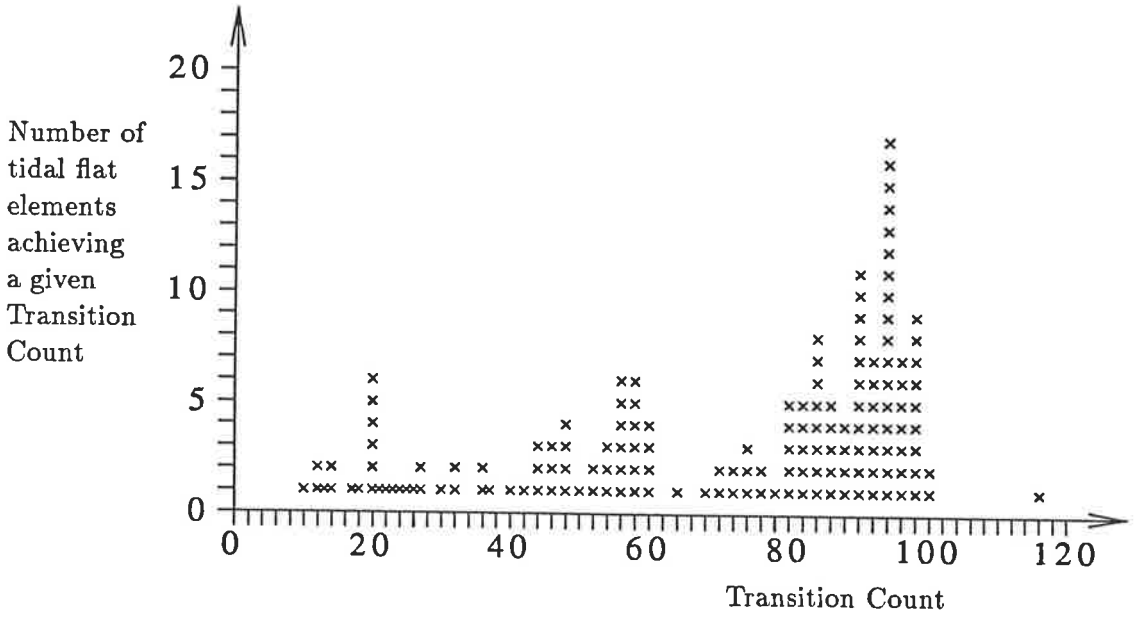


Figure 8.15: *Histogram of transition counts for the 155 tidal flat elements of the Northern Spencer Gulf model over the last 29 days of a 32 day simulation. Parameter values used are* $n = 0.018$, $\epsilon = 0.10\,m$, $H_0 = 1.0\,m$ *and* $H_{\text{dry}} = 0.0\,m$.

and uncovered.

Figure 8.16 shows there are no transition counts at the mode value 94 in the south eastern region of the NSG model. In fact there are none above 90 in this region. One may suspect this is a consequence of the weaker spring-neap cycle in the southern region relative to that in the northern region. If counts are generally lower in the southern region, they must be generally higher further north. This is demonstrated in Figure 8.17. The average transition count for the tidal flat elements in each row of the model is plotted against row number on the horizontal axis. There are 56 rows and some have no tidal flat elements in them, though very few; row one is the northern-most or top row of the model and row 56 is the southern-most. Ward Spit contributes elements to rows 22–25 and a dip in the plot in this region is evident. Generally the averages are above the model average of 69 for the northern rows, and are below the model average for the southern rows, but a clear distinction in this regard does not take place until about row 39, south of which the NSG model broadens and begins to take in the large tidal flat region of the south-east of the model (Figure 8.16).

8.7 Presentation of results and discussion

Here, results following a 32 day simulation using the de Chèzy coefficient of quadratic friction with value $n = 0.018$ are presented and discussed. The time step used is $\Delta t = 80\,\text{sec}$.

As in Chapter 5, these are the first numerical predictions obtained from a non-linear model of the Northern Spencer Gulf region. The model is driven by all the available energy, including that of the generated minor constituents, obtained at gridpoints of the Spencer

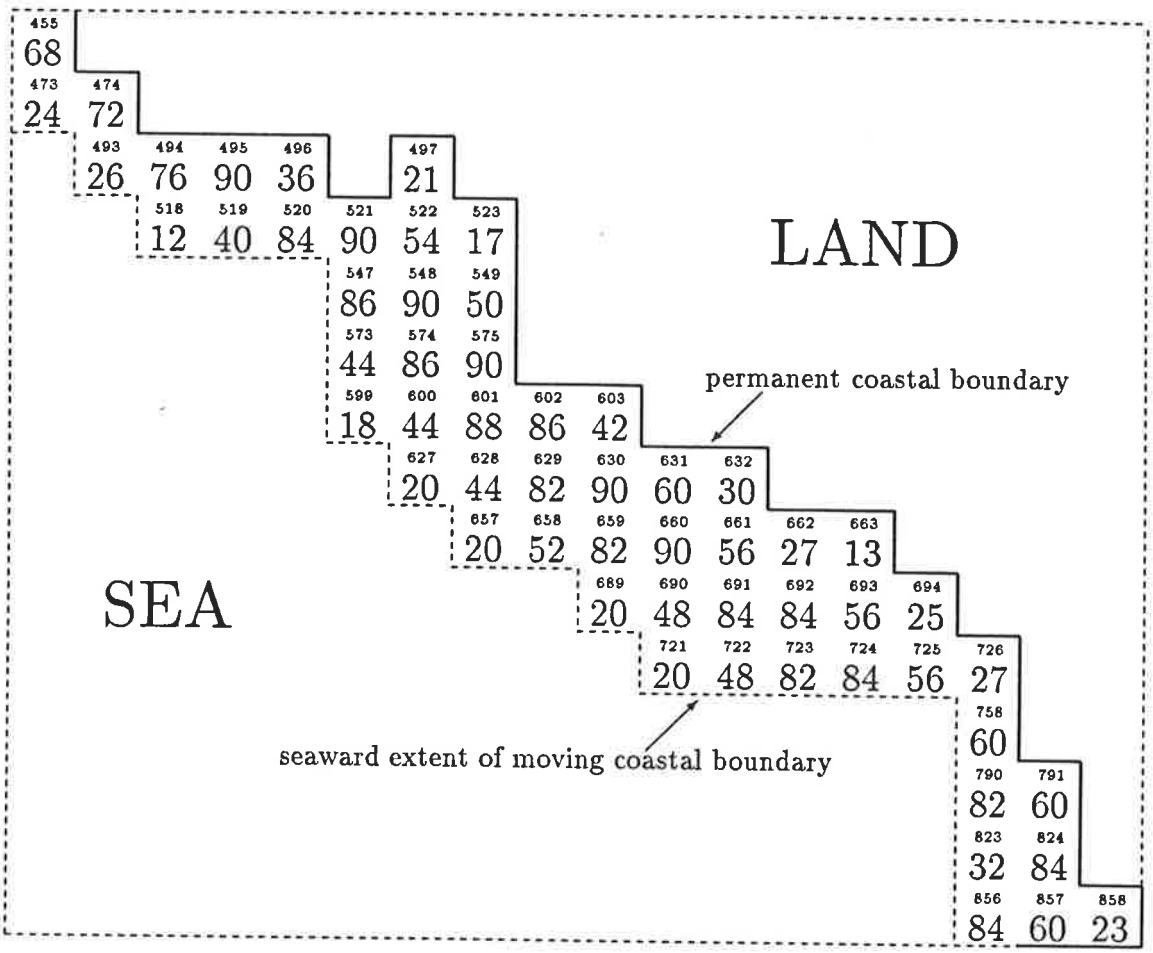


Figure 8.16: *Plan view of the south east coastal region of the Northern Spencer Gulf model showing all tidal flat elements, their element numbers (small digits) and transition counts (large digits).*

Gulf model corresponding to the open boundary line of the NSG model. Furthermore, this model incorporates a tidal flat wetting/drying routine.

Contour charts for tidal amplitude and phase for each of the four major constituents O_1, K_1, M_2 and S_2 are given as well as ellipse plots of depth-averaged current for the same four constituents.

In these plots, shaded elements represent tidal flats, viz. any element which has "wetted" or "dried" during the final 29 days of the simulation. Tidal analyses are carried on tide height and current predictions at elements which are consistently wet during this period; tidal analyses are not attempted at tidal flat elements. Shading the tidal flat elements emphasizes their presence and suggests their role in local tidal dynamics.

Calibration table

Table 8.3 summarizes the differences between predicted and observed tidal constants for the six available tidal stations of the region. Comparing these with corresponding entries

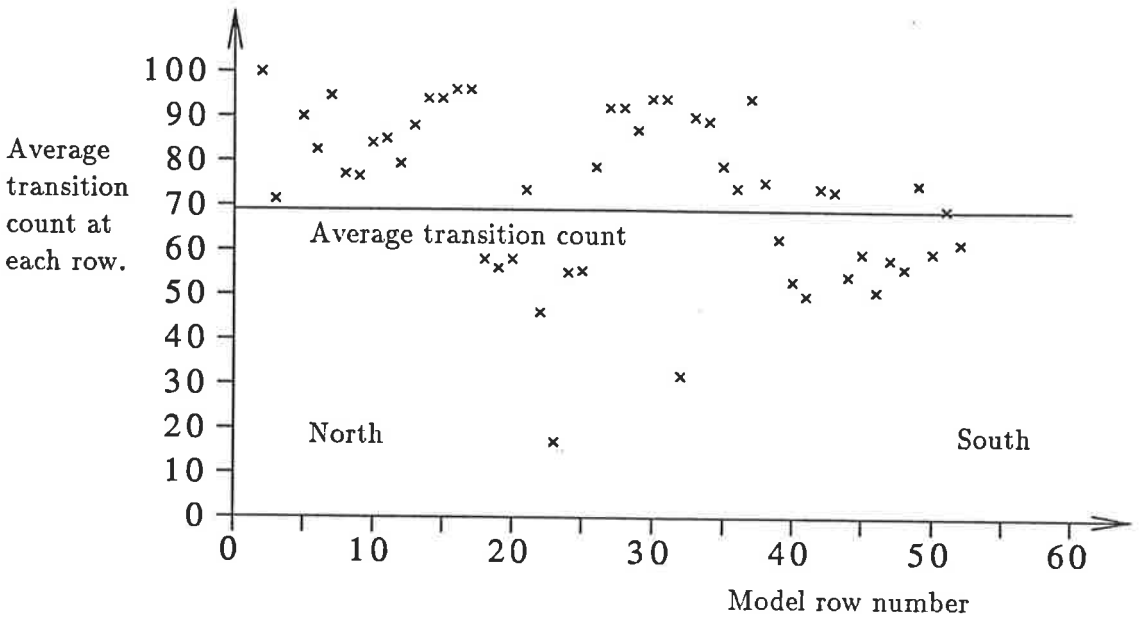


Figure 8.17: *Average transition count for each row of the model. Rows are numbered one to 56, northern-most to southern-most, respectively. Some rows (very few) have no tidal flat elements in them. Ward Spit contributes tidal flat elements to rows 22–25 and a dip in the plot is associated with these rows. The average transition count (69) over the whole model is represented by the horizontal line.*

in Table 5.6, the NSG model performs slightly better overall. This is summarized in the combined error measure value $\varepsilon = 5.69\,\text{cm}$ as compared to $\varepsilon = 5.96\,\text{cm}$ (the equivalent value for the same six stations from the SG model (see Table 8.1, column (e))). However we note that both models give about the same results for the diurnals at these six stations and whereas the SG model over-damps the semi-diurnals, the NSG model under-damps them. The overall improvement of the NSG model seems to come from the slightly improved predictions for S_2.

Note there is still a large difference between predicted and observed amplitude for O_1 — the finer grid has not lead to an improvement in its prediction. It now seems most likely there is either an error in the values we have chosen as the "observed" constants for O_1, or there is an inability in our tidal analysis package to accurately resolve O_1 from the predicted series supplied, or a combination of these, arising from the strength of constituents of similar frequency to O_1. This is something to investigate in the near future!

Contour plots

The contour charts of Figures 8.18–8.21 provide detail missing in Figures 5.22–5.25 for the Northern Spencer Gulf region. The same contour intervals are used for the respective constituent amplitude charts of both models. However, for the phase contours the contour interval is halved in the case of the diurnals, from 2° to 1°, and in the case of the semi-diurnals it is decreased from 10° to 2°. Nevertheless, greater detail is shown in the present phase plots even if the same contour intervals are used, as can be seen by inspection.

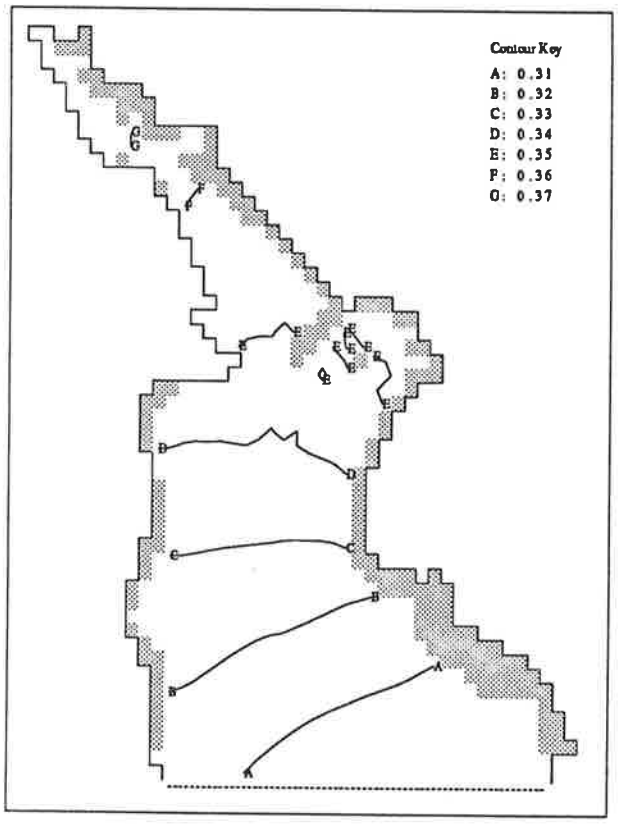


Figure 8.18(a): *Amplitude contours (metres) for the O_1 constituent of sea surface elevation.*

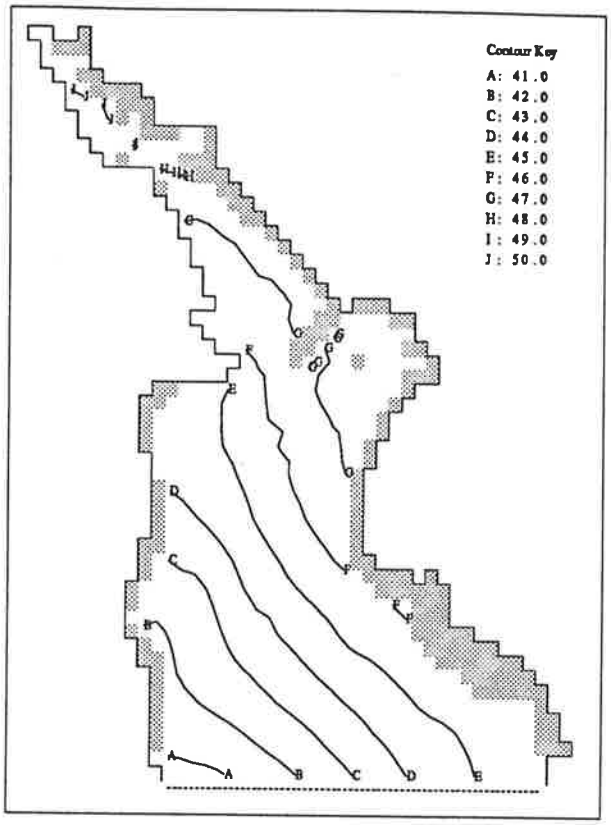


Figure 8.18(b): *Phase contours (degrees, C.S.T.) for the O_1 constituent of sea surface elevation.*

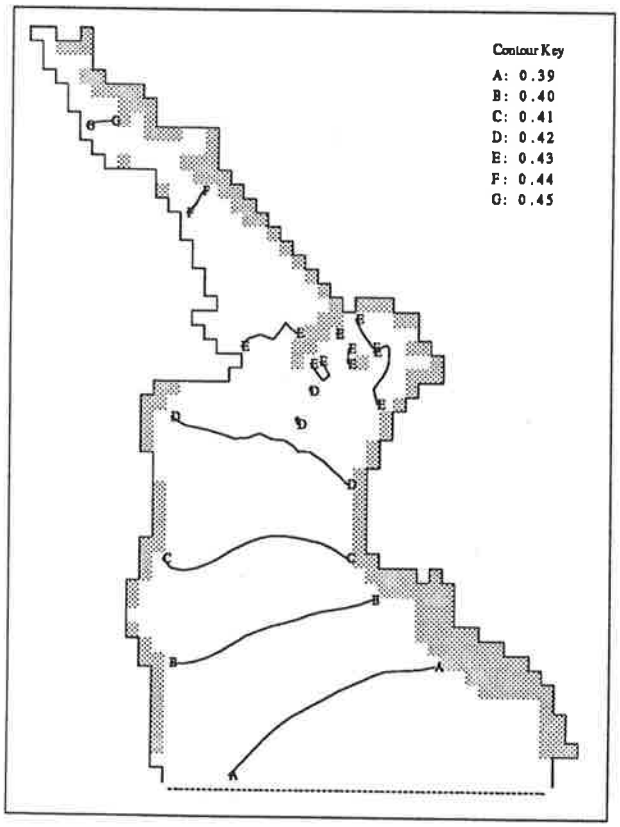


Figure 8.19(a): *Amplitude contours (metres) for the K_1 constituent of sea surface elevation.*

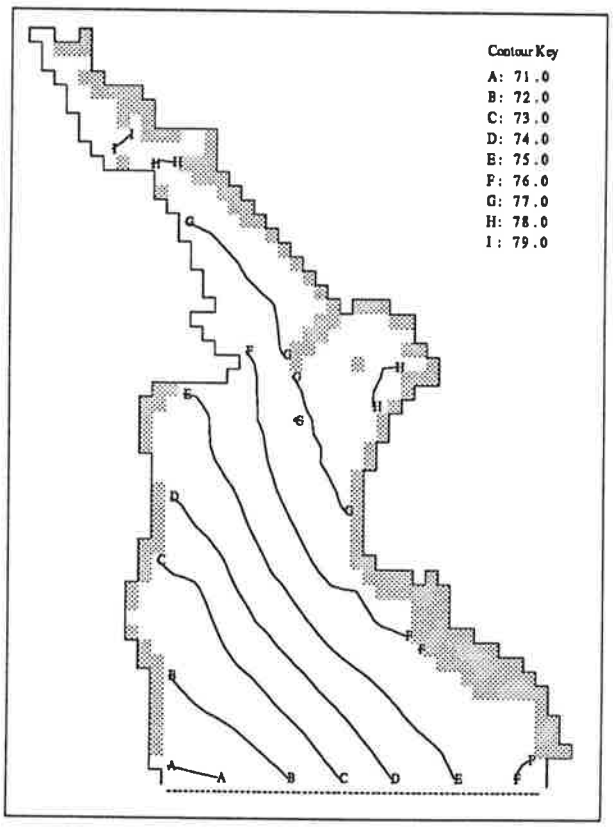


Figure 8.19(b): *Phase contours (degrees, C.S.T.) for the K_1 constituent of sea surface elevation.*

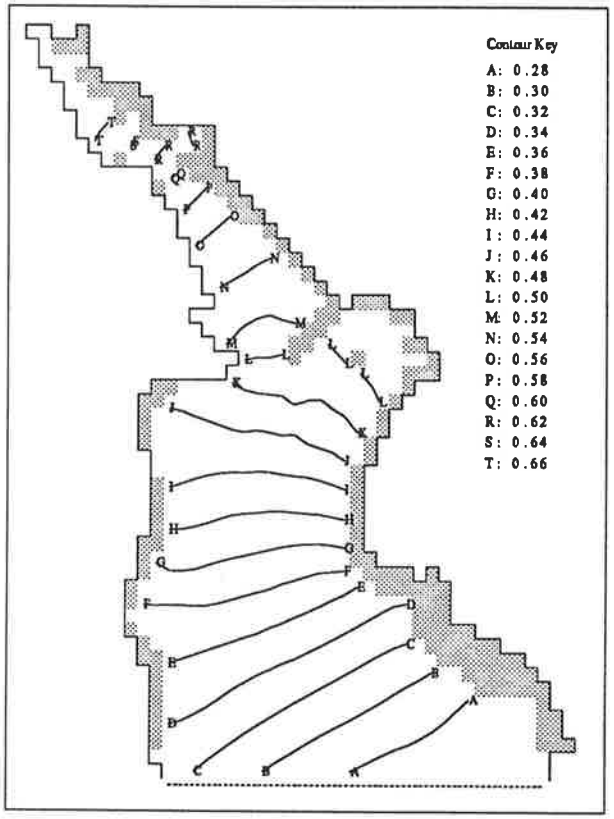


Figure 8.20(a): *Amplitude contours (metres) for the M_2 constituent of sea surface elevation.*

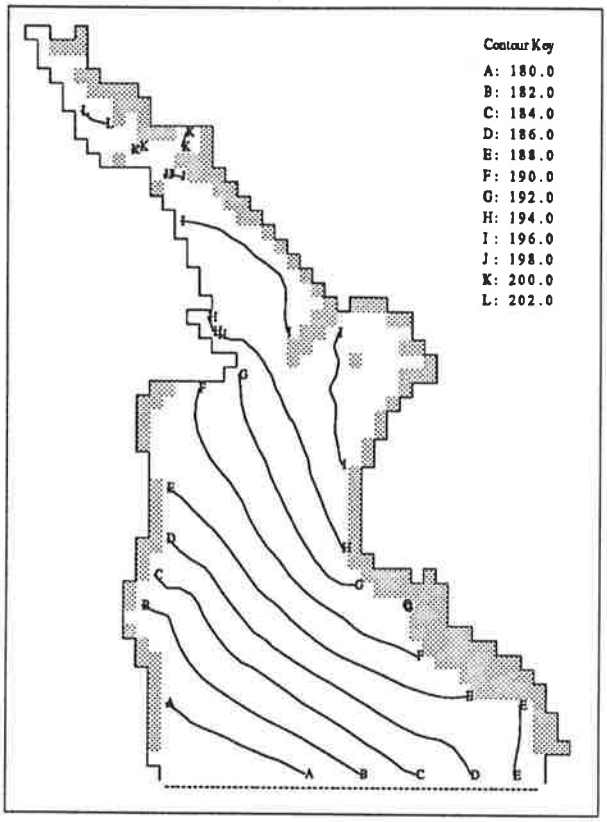


Figure 8.20(b): *Phase contours (degrees, C.S.T.) for the M_2 constituent of sea surface elevation.*

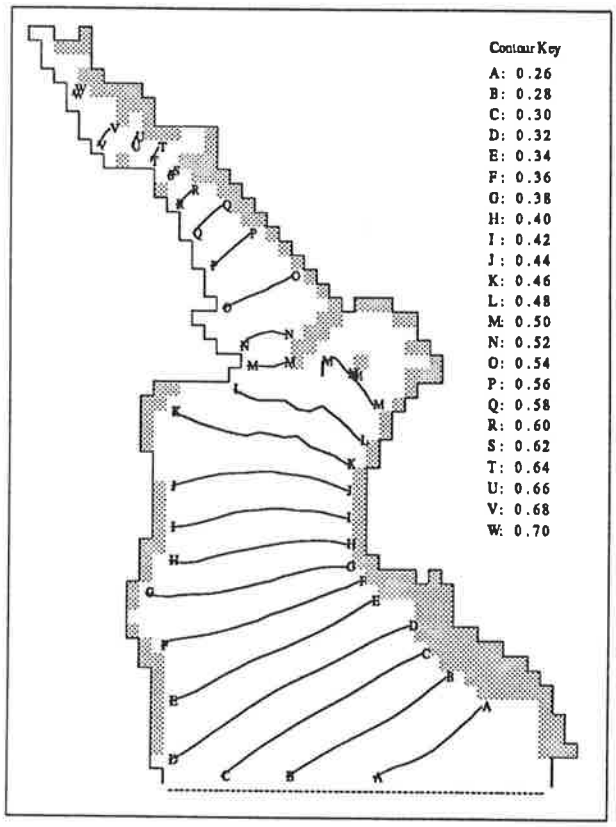


Figure 8.21(a): *Amplitude contours (metres) for the S_2 constituent of sea surface elevation.*

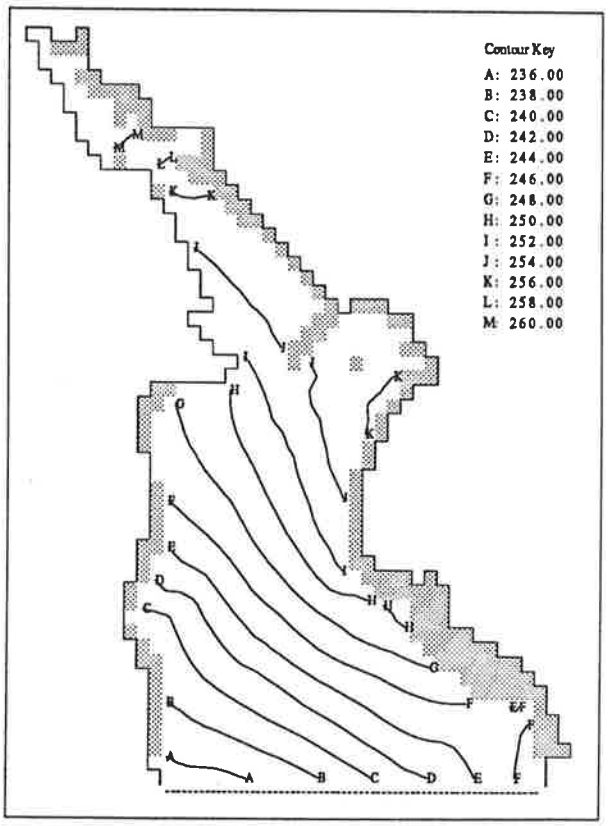


Figure 8.21(b): *Phase contours (degrees, C.S.T.) for the S_2 constituent of sea surface elevation.*

Observation station		O_1 amp	O_1 ph	K_1 amp	K_1 ph	M_2 amp	M_2 ph	S_2 amp	S_2 ph
Port Augusta	Pred.:	37.7	50.2	45.4	79.8	69.3	202.8	71.6	262.0
	Obs.:	28.3	52.8	44.0	82.7	64.0	212.2	68.6	272.3
Beacon #5	Pred.:	36.8	48.8	44.6	78.5	63.0	199.9	64.7	259.0
	Obs.:	25.0	48.1	47.0	73.4	57.9	196.0	62.0	255.2
Port Pirie	Pred.:	35.3	47.5	43.3	77.9	51.3	197.3	51.7	256.0
	Obs.:	27.6	49.2	42.5	77.4	48.9	197.2	52.9	258.3
Port Bonython	Pred.:	34.5	45.0	42.6	75.2	48.5	191.5	48.8	250.2
	Obs.:	27.0	42.7	41.6	70.6	45.1	185.3	48.6	245.6
Whyalla	Pred.:	34.0	44.2	41.9	74.6	45.0	188.7	44.9	247.1
	Obs.:	25.7	45.2	40.1	72.8	42.1	184.5	45.4	245.2
Yarraville Shoals	Pred.:	31.8	43.2	39.7	73.3	34.8	184.4	33.8	242.5
	Obs.:	24.4	39.2	37.2	69.8	32.2	175.5	33.9	236.9
Ave. absolute differences:		8.64	2.07	1.65	3.09	3.61	5.47	1.28	4.75
Ave. complex differences:		8.74		2.91		6.23		4.87	

Table 8.3: *Predicted (Pred.) and observed (Obs.) tide-height constants — amplitude (cm) and phase (degrees, C.S.T.) — for the four major constituents at six stations in Northern Spencer Gulf. Overall average absolute difference, taken over the four constituents and six stations, is 3.80 cm in amplitude and 3.84° in phase. The combined error measure (average absolute complex difference) is $\varepsilon = 5.69$ cm.*

Comparing the corresponding regions of the diurnal plots of Figures 8.18–8.19 and Figures 5.22–5.23 it can be verified that the contour lines approximately coincide. For example, in Figure 8.19(b) the 76° contour starts in the west at the tip of Lowly Point (see Figure 8.1), crosses the Gulf going south-eastwards, "disappears" into the south-eastern tidal flat region and "re-appears" at the south-eastern corner of the model. The same contour in Figure 5.23(b) has the same western starting position, crosses the Gulf, proceeds along the coastline and terminates just below the position of the open boundary of the NSG model.

The model predicts that the diurnal amplitude contours are interrupted by Ward Spit. The effect is quite "noisy" between Ward Spit and Cockle Spit, and may be numerical in origin, probably reflecting the incomplete removal of grid-scale waves. This effect is not as evident in the semi-diurnals, but it must be remembered that they are stronger signals.

Comparison of the corresponding regions of the semi-diurnal contour charts of both models reveals differences of 2–3 cm in amplitude and several degrees in phase at corresponding positions. The fine-grid amplitude charts show significantly more detail: for M_2 the NSG contours run to 66 cm and for S_2 they run to 70 cm, while for the SG model M_2 runs to 52 cm and S_2 to 54 cm. Both NSG amplitude charts show progressive amplification of M_2 and S_2 towards the northern tip of the model. Highest phase values predicted by the NSG model are 10° greater than the highest predicted by the SG model.

Clearly the fine-grid model has enabled more detailed modelling of the far northern region of the Gulf, something that would be expected. This may have been assisted by the inclusion of the modelling of the wetting and drying of tidal flats. There is overall strong agreement between the NSG and SG models in their prediction of the diurnals, and this suggests that the coarse-grid element dimension is adequate for modelling the diurnals (and that the fine-grid dimension is more than adequate). On the other hand there is less agreement in the prediction of the semi-diurnals, suggesting that the coarse-grid element dimension may not be sufficient to model the semi-diurnals well.

Ellipse characteristics

Table 8.4 shows predicted and observed tidal current ellipse characteristics for stations Mike and Yarraville Shoals (Figure 8.1). Results from both the present chapter (Chp8) and Chapter 5 (Chp5) are given to enable easier comparison of these predicted sets.

Because Mike is near the open boundary of the NSG model, we might expect good agreement between predictions for Mike from the NSG and SG models. But while results are much the same for the diurnal major and minor axes, they are worse for the semi-diurnal major and minor axes. The semi-diurnals are under-damped. The model MSL depth value used is 23.4 m which compares well with the station mean depth value of 24 m.

At Yarraville Shoals, results are improved for the diurnal major and minor axes but are also worse for the semi-diurnal major and minor axes. Again the semi-diurnals are under-damped. The model MSL depth value is 10.5 m, similar to the station value of 9.4 m mean depth. This general agreement in depth values contrasts with the relatively poor agreement in depth values in Chapter 5 for Yarraville Shoals, and is a direct consequence of using the finer grid.

The immediate reason for the under-damping of the semi-diurnals, also seen in Table 8.3, must be the present use of an effectively lower value of quadratic friction coefficient compared to the value 0.0025 used in Chapter 5. At Mike the local value of quadratic friction friction is presently 0.0011 (calculated using $n = 0.018$ and the MSL depth 23.4 m from Figure 8.4) and at Yarraville Shoals the local value of quadratic friction coefficient presently used is 0.0014 (calculated using $n = 0.018$ and the MSL depth 10.5 m from Figure 8.4). Both these values are significantly less than 0.0025.

Ellipse plots

A wealth of structure is shown in the ellipse plots of Figures 8.22–8.25. The scale for each plot is deliberately the same to facilitate the comparison of the constituents without losing detail in the weaker diurnal plots.

Inspecting the K_1 ellipse plot of Figure 8.23 shows there are many instances where rotation direction is predicted to change from one region to the next. As we saw in Chapter 5, this is invariably associated with gyral formations in the tidal constituents. These tidal gyres are topographically driven and occur near times of slack tide.

As one would expect in a narrow region of a narrow gulf, the flow is generally rectilinear along the axis of the gulf.

This wealth of detail is conspicuously absent in the ellipses for the NSG region of Figures 5.26–5.29 in Chapter 5, so the present plots contribute much more information about NSG tidal dynamics. Although the ellipses of the NSG region of Chapter 5 are generally rectilinear, it can be seen by inspection that where they show some transverse

Tidal constituent		O_1	K_1	M_2	S_2
Mike: current meter 10 m from bottom in 24 m mean depth					
Semi-major axis (cm/sec)	Chp8:	9.0	13.4	29.9	29.2
	Chp5:	10.1	13.7	24.5	25.4
	Obs.:	10.6	13.9	25.3	27.6
Semi-minor axis (cm/sec)	Chp8:	0.88	1.25	3.37	2.85
	Chp5:	0.23	0.62	0.81	0.80
	Obs.:	0.33	−0.49	0.20	0.15
Phase lag of maximum (g°)	Chp8:	327	340	104	165
	Chp5:	320	352	108	167
	Obs.:	323	355	106	165
Orientation of major axis (°T)	Chp8:	4.1	3.6	8.6	9.3
	Chp5:	8.0	8.5	9.1	9.1
	Obs.:	12.4	14.1	14.3	14.1
Direction of rotation	Chp8:	A	A	A	A
	Chp5:	A	A	A	A
	Obs.:	A	C	A	A
Yarraville Shoals: 1 m from bed in 9.4 m mean depth					
Semi-major axis (cm/sec)	Chp8:	7.9	11.7	29.7	29.4
	Chp5:	8.9	12.3	23.6	24.7
	Obs.:	3.8	5.4	13.4	13.5
Semi-minor axis (cm/sec)	Chp8:	0.70	0.95	2.03	1.67
	Chp5:	−0.07	−0.20	−0.06	−0.06
	Obs.:	0.51	0.36	−0.17	−0.17
Phase lag of maximum (g°)	Chp8:	325	333	99	161
	Chp5:	318	348	107	166
	Obs.:	327	325	108	147
Orientation of major axis (°T)	Chp8:	15.7	13.4	16.6	17.4
	Chp5:	19.2	19.0	18.4	18.5
	Obs.:	10.2	7.8	9.4	8.1
Direction of rotation	Chp8:	A	A	A	A
	Chp5:	C	C	C	C
	Obs.:	A	A	C	C

Table 8.4: *Predicted ("Chp8" are results of the present chapter, and "Chp5" are results from Chapter 5) and observed (Obs.) tidal ellipse characteristics for the four major tidal constituents at stations Mike and Yarraville Shoals. Observations are from Lennon (1981,1990) but observed minor axis values are given a negative sign if the observed rotation is clockwise: this is a convention used in the analysis of the predictions. Direction of rotation is denoted A = Anticlockwise and C = Clockwise. Phase lag of maximum current is given in local time.*

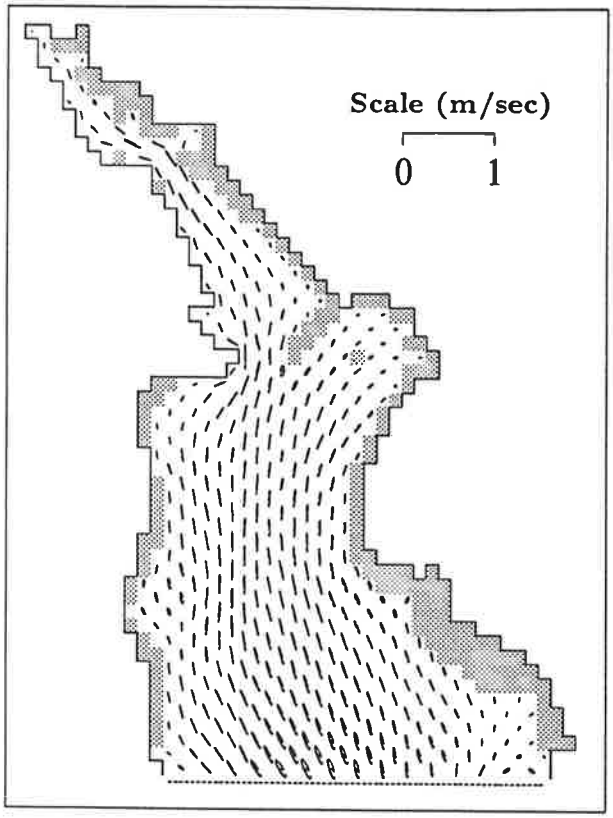


Figure 8.22: *Ellipses for the O_1 constituent of depth-averaged current.*

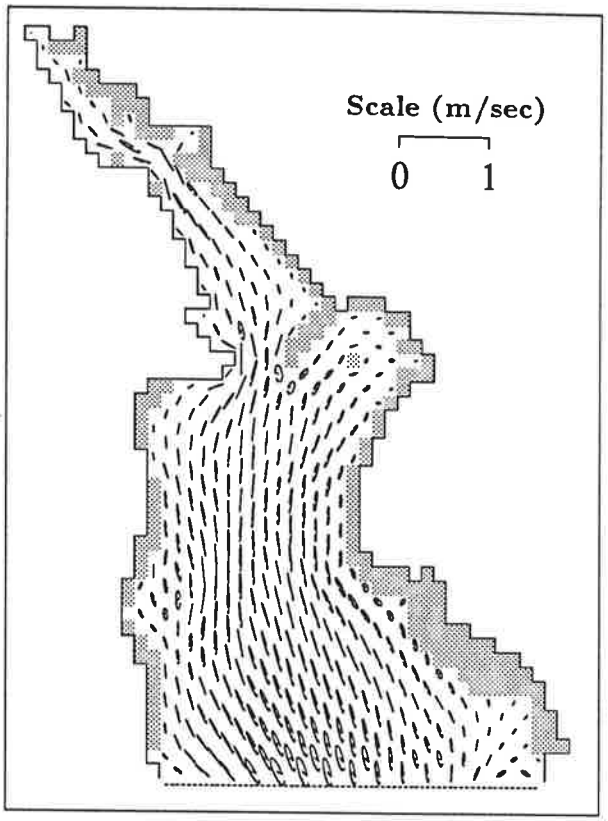


Figure 8.23: *Ellipses for the K_1 constituent of depth-averaged current.*

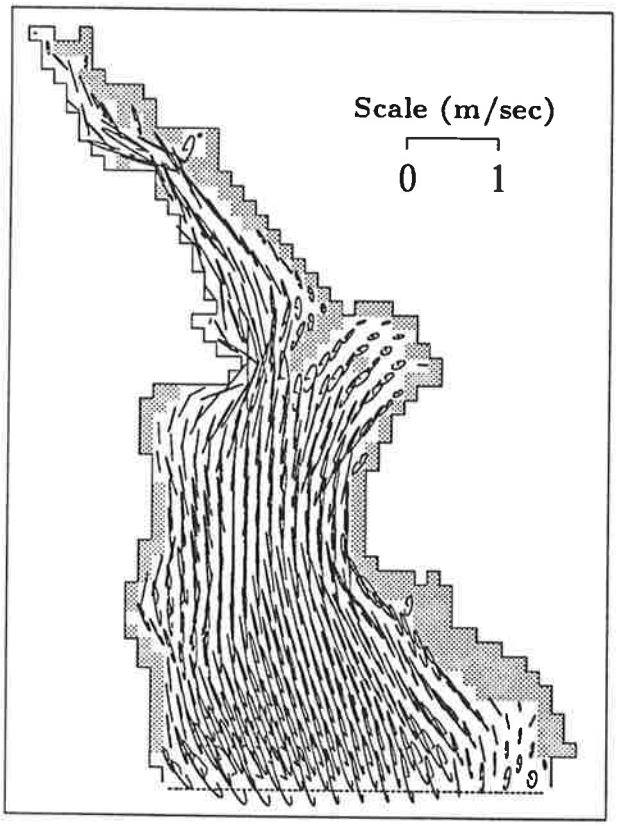


Figure 8.24: *Ellipses for the M_2 constituent of depth-averaged current.*

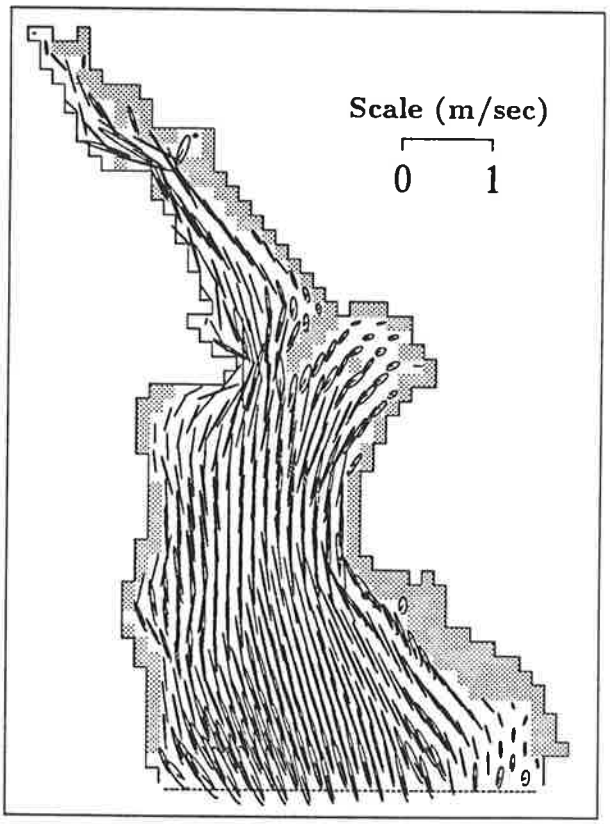


Figure 8.25: *Ellipses for the S_2 constituent of depth-averaged current.*

component they agree in terms of rotation direction with the corresponding NSG ellipses. Note that the ellipses immediately south and east of Lowly Point appear as straight line segments, showing almost no semi-major axis — we will see that this region is characterized by a strong clockwise rotating residual gyre. Just to the north of Lowly Point (Figure 8.1), some of the ellipses have a visibly discernible semi-minor axis — here, a very strong residual gyre is predicted.

Immediately to the east of Lowly Point, the semi-major axis of both the M_2 and S_2 constituents is about 1 m/sec, so together with the semi-major axes of O_1 and K_1 at the same position, a maximum tidal velocity in this position is predicted to be in the vicinity of 2.5 m/sec. Steedman (1983) and Noye (1984c) agree that "In the constricted passage between Point Lowly and Ward Spit, currents may exceed 1.0 m/sec on the western side and decrease to the east" (Steedman, 1983, p.9). On hydrographic map 2389 (of St. Vincent and Spencer Gulfs) tidal velocities of $1\frac{3}{4}$ kn (1.8 m/sec) are recorded at many sites around Spencer Gulf, so velocities as high as 2.5 m/sec in this constricted passage are feasible.

Velocity residuals

The velocity residuals of Figure 8.26(a) also show great detail, this time in the minor constituents. There are many gyres revealed by this plot, perhaps the most obvious being one near the western coast south of Whyalla, and one near the open boundary on the eastern side.

There is a strong residual flow across the open boundary near the western coast, and weaker cross-boundary flows at the mid-point of the open boundary and across much of the eastern quarter. Surprisingly, there is a strong along-boundary flow at the western third of the open boundary. Referring back to Figure 5.36(b), which shows the residuals of the whole SG region, it can be seen that there is a transverse flow at the transect corresponding to the open boundary of the NSG model, so the transverse residuals seen here at the boundary are not anomalous — their cause is probably bathymetric.

Careful inspection of the residuals near Lowly Point suggests there are strong oppositely rotating gyres north and south of Lowly Point. Figure 8.26(c) is a close-up of the Lowly Point region, using the same velocity vector scale, and clearly shows that some of the vectors from the northern gyre have a magnitude of more than 10 cm/sec. The southern gyre is referred to by several authors: for example, quoting Steedman again, "The most spectacular example of non-linear tidal circulation in Northern Spencer Gulf is the gyre formed behind Point Lowly in the ebb flow ... Measurements indicating its existence are described by NSR " [Natural Systems Research Pty Ltd, 1981] (Steedman, 1983, p.9). This gyre received considerable attention at the time that a petrochemical facility was mooted for the Stony Point region; Port Bonython is associated with that facility.

Green (1984) discusses residual velocities in "Upper Spencer Gulf", a part of Spencer Gulf north of Ward Spit (see Figure 1.2) which in turn is a subset of the Northern Spencer Gulf region modelled here. Green comments that "the western shore ... below Blanche Harbour (32° 43′) and the eastern shore above Yatala Harbour (32° 46′) are marked with a series of Points or headlands which constrict the tidal flow and serve to divide the Gulf into a series of cells. ... General hydrodynamical theory predicts the formation of large eddies or vorticities downstream from ... headlands, and hence, in the Gulf, to the north of Points during the incoming tide and to the south of the Points during the outgoing tide.

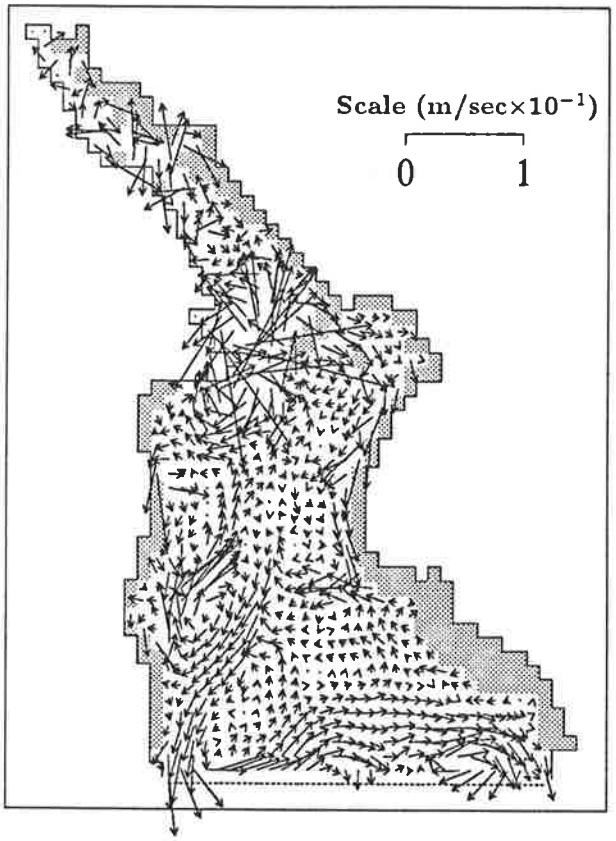


Figure 8.26(a): *Residuals for depth-averaged velocity for the Northern Spencer Gulf model.*

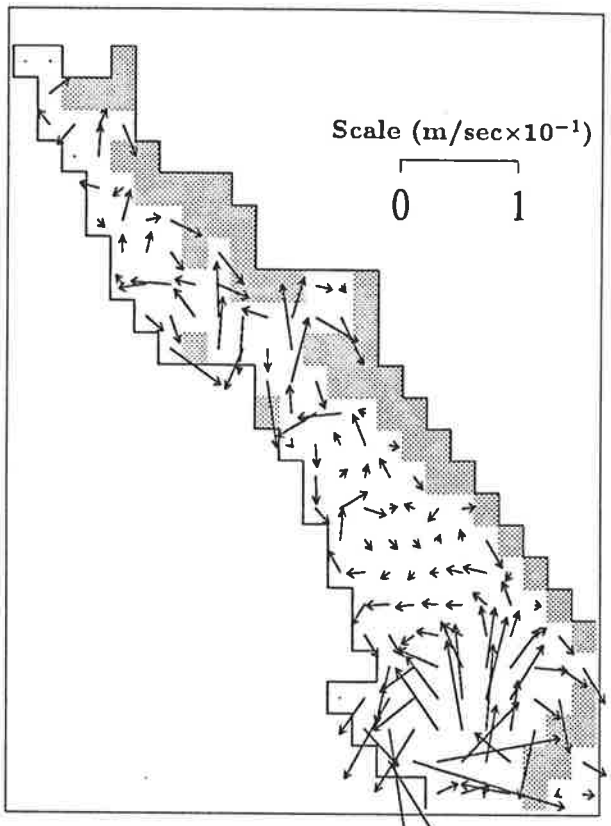


Figure 8.26(b): *Residuals in the far northern region, north of Ward Spit and Point Lowly.*

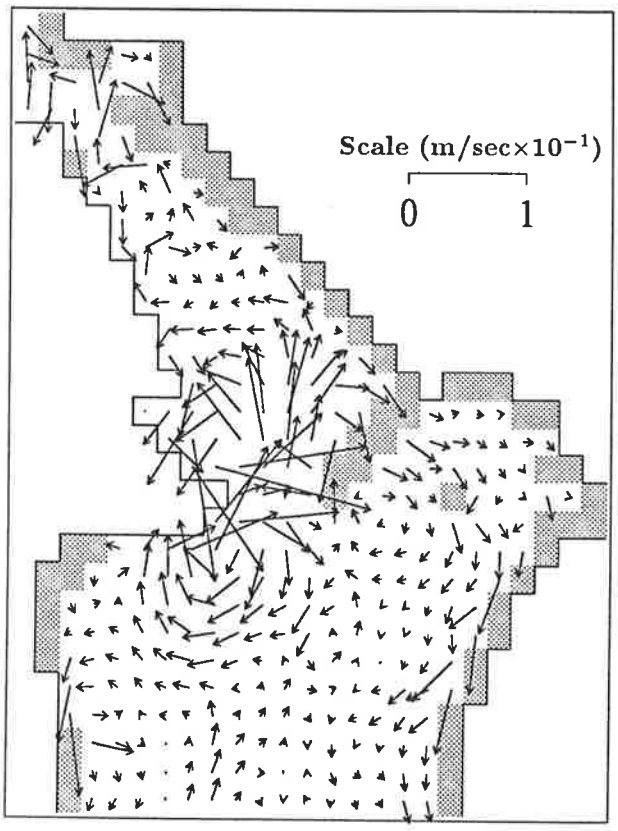


Figure 8.26(c): *Residuals in the Ward Spit and Point Lowly region showing strong oppositely rotating gyres.*

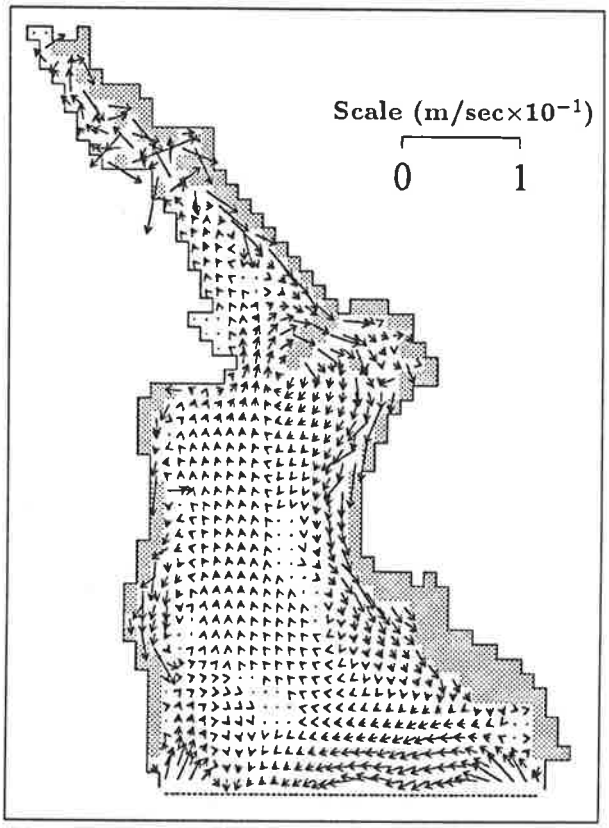


Figure 8.26(d): *Residuals for the Northern Spencer Gulf model obtained with advective terms deleted.*

There is, besides, a theorem about the conservation of vortex motion (see for example Green and Liepnik, 1970, pp.243–244) which ensures that, once formed, such vortices decay only slowly as a result of viscosity" (ibid, p.186). On the basis of this theory, it is not unexpected that there should be gyres north and south of Lowly Point as it is certainly a prominent headland constricting tidal flow.

Examining the residual vectors along a line between Lowly Point and the southern tip of Ward Spit there seems to be no circulation north or south in the deep channel off Lowly Point, although there is some southerly flow across Ward Spit. Green (1984) concluded that "the residual gyres [in Upper Spencer Gulf] are organized in cells of circulation, driven by the tides but separated by nodes where the rate of exchange of water is minimal" (ibid, p.183). It seems that the boundary between the northern and southern gyres at Lowly Point is such a node at the southern extent of Upper Spencer Gulf. Figure 8.26(b) is an enlargement of the Upper Spencer Gulf region, again using the same scale for the velocity vectors. The pattern of the vectors here tends to support Green's analysis for the existence of a series of gyres but a finer element size should be used in order to obtain conclusive numerical support. Green (1984) points to other evidence: "Even more significant are almost discontinuous changes of salinity observed in passing headlands such as Redcliff Point. These abnormally large salinity gradients provide clear indications of the existence of nodes separating distinct cells of circulation to the north and south of major headlands" (ibid, p.187).

The public protest at a proposal to site a Petrochemical plant at Redcliff Point (adjacent to Beacon #5 on the eastern coastline in Figure 8.1; see also Figure 1.2) centred on the limited tidal flushing available in that region in the event of an accidental spill of hydrocarbon or by-product.

Because Ward Spit has been a known feature of Northern Spencer Gulf for well over 100 years, it is evident that the presence of these two strong oppositely rotating gyres with common boundary at Lowly Point does not act to erode it. Rather, the long-term existence of this residual flow across the Gulf from Lowly Point carrying sand sediment seems a likely driving factor behind the creation and maintenance of the Spit. Green (1984) also considers this likely. Pingree and Maddock (1977b) and Pingree (1978) note that eddies may concentrate sediments resulting in the formation of tidal banks. Sediment from both north and south of Lowly Point is likely to be involved. It seems possible that sand sediment cannot have a substantial net migration into the far northern Gulf from south of Lowly Point, and vice versa — in spite of the strong tidal flows at Lowly Point.

Figure 8.26(d) shows the residual circulation when all advective terms are omitted. The scale used is again that of Figure 8.26(a). The residuals in this case are generated by the quadratic friction terms and indirectly via the non-linear formulation of the continuity equation. It must also be remembered that minor constituent energy is fed in at the open boundary by reason of the driving mechanism there. The general residual pattern is substantially quieter than that of Figure 8.26(a), being most active in the shallower northern, eastern and western regions where the friction terms have greater effect. Near the open boundary are some relatively shallow regions which correlate well with the strong residuals shown there. In fact, the stronger residual flows of this figure correlate very well with the shallower regions depicted in Figures 8.3 and 8.4.

Of note in Figure 8.26(d) is that the two gyral formations depicted in Figure 8.26(c) near Lowly Point are absent. Those gyres are therefore residual (advective) in origin. Also, we note there is a south-easterly residual flow across Ward Spit which accounts for

some of the flow across the Spit seen in Figure 8.26(c).

On close inspection, the south-easterly flow across Ward Spit is directed towards Cockle Spit and then mostly takes a path south along the eastern coast, with some of the flow veering northwards through the channel between Lowly Point and Ward Spit. That is, there is a clockwise rotating gyre centred on the southern tip of Ward Spit which may be responsible for the growth and maintenance of Cockle Spit. In that view, Cockle Spit is spawned from Ward Spit. Figure 8.26(c) also shows a significant residual flow towards Cockle Spit from Ward Spit, much of which heads south along the coast with the remainder veering northward and completing a gyral circuit.

It is often reported in the literature that gyral activity is associated with the advective terms (for example, see Pingree and Maddock (1977a, p.346), Zimmerman (1978, p.35)). Leendertse and Langerak (1982) comment: "advection is the primary mechanism to generate tidal residual circulations ... If the advection terms are omitted, the tidal residual circulations are very weak" (ibid., p.298). Comparison of Figures 8.26(a) and 8.26(d) demonstrates this link in the case of the Northern Spencer Gulf model.

Shallow water constituents

Table 8.5 gives observed and predicted amplitudes for the seven shallow water constituents considered in Table 5.12 of Chapter 5. Both fine-grid ("Fine") NSG and coarse-grid ("Coarse") SG model predictions for the constituents are given.

Inspection of the amplitude values given in Table 8.5 shows that there is order-of-magnitude agreement between predicted and observed values in the northern Gulf for these minor constituents. Comparing the fine-grid model's amplitude predictions with those of the coarse-grid model shows that at Pt. Augusta, Beacon #5 and Pt. Pirie they are almost all closer to the observed values in the case of the NSG model — this reflects the fact that the finer grid more accurately models the far northern region. The predictions for MSf and $2SM_2$ are similar for the two models but for MS_4 they are, generally, significantly improved for the fine-grid model. The average absolute difference between predicted and observed amplitudes for the seven constituents at all six stations is 0.7 cm, demonstrating again that the Northern Spencer Gulf model is (slightly) more accurate than the coarse-grid model.

Table 8.6 compares predicted and observed phase values for the fine-grid model. The phase differences for MSf show large variation and again this may be due to inaccuracies in both the observations and the analysis of the predictions for this constituent. For $2SM_2$ the phase values show reasonable agreement, particularly at Beacon #5 and southwards; for MS_4 the phase values show reasonable agreement at Pt. Pirie and southwards; MO_3 is the next strongest constituent and its phase values also show good agreement at Pt. Pirie and southwards. The remaining constituents, M_4, $2MS_6$ and $2SM_6$ are relatively weak and show generally much greater differences between predicted and observed phases. It seems that the comments of Zetler (1991) relating to the variability of phases associated with weak constituents apply here: the weaker the constituent, the more variable the corresponding phase value, both the observed value and the value obtained by analysing the predicted record.

It should be noted that by constrast with the depth-averaged model of Chapter 5, where no minor constituent energy was included in the height specification at the open boundary, here all the energy recorded at the NSG boundary within the depth-averaged

Station		MSf	$2SM_2$	MO_3	M_4	MS_4	$2MS_6$	$2SM_6$
Port Augusta	Fine:	2.3	3.4	0.7	1.7	4.7	1.5	1.4
	Coarse:	1.7	3.1	4.7	1.7	7.9	2.9	2.9
	Obs.:	1.9	4.9	1.4	0.8	2.4	1.2	1.3
Beacon #5	Fine:	2.2	2.5	0.4	0.8	3.2	0.3	0.3
	Coarse:	1.8	2.7	4.0	1.4	6.1	1.4	1.3
	Obs.:	0.1	2.9	1.9	1.0	1.5	1.0	0.9
Port Pirie	Fine:	2.3	1.4	0.5	0.2	1.7	1.3	1.3
	Coarse:	1.9	1.7	2.6	0.6	2.2	1.7	1.8
	Obs.:	4.9	2.1	1.3	1.1	2.3	1.1	1.4
Port Bonython	Fine:	1.9	1.2	0.5	0.1	1.6	0.9	0.7
	Coarse:	1.8	1.2	1.9	0.5	1.3	1.3	1.2
	Obs.:	5.1	1.9	1.4	0.9	1.9	0.8	1.0
Whyalla	Fine:	2.1	1.1	0.5	0.2	1.9	0.8	0.5
	Coarse:	1.9	1.2	1.8	0.5	1.1	1.4	1.3
	Obs.:	1.9	1.9	1.5	0.8	2.0	0.7	0.7
Yarraville Shoals	Fine:	1.8	0.6	0.4	0.2	1.1	0.4	0.4
	Coarse:	1.8	0.6	0.7	0.3	0.7	0.7	0.6
	Obs.:	2.5	0.8	1.0	0.3	0.8	0.4	0.5

Table 8.5: *Comparison of predicted and observed (Obs.) amplitudes (cm) for the seven shallow water constituents considered in Table 5.12 of Chapter 5. Predictions for both the fine-grid (Fine) NSG model of the present chapter and the coarse-grid (Coarse) SG model of Chapter 5 are given. Values from all available stations in Northern Spencer Gulf are presented. The average absolute difference between predicted and observed amplitudes for the seven constituents at the six stations is 0.7 cm for the fine-grid model.*

model is supplied to the present model. However, this does not guarantee improvement in predictions as the open boundary data used for the NSG model carries errors from the larger SG model. No corrections based on nearby stations have been made in order to rectify this. To attempt such corrections would be difficult if at the same time we continued to drive the NSG model using time-step by time-step tide-height predictions taken from the SG model. In order to make such corrections it would be necessary to return to the former method of specifying amplitudes and phases for specific constituents.

Nevertheless, by decreasing the grid box dimensions, improving the bathymetric representation, incorporating minor constituent energy in the open boundary forcing and including tidal flats, we have achieved some improvement in the prediction of the stronger minor constituents.

Neap and Spring wetting/drying sequences

Figure 8.27 is a two-hourly sequence of depth-averaged flow predictions during the neap period illustrated in the left hand elevation signals of Figure 8.14. The flows are generally weak and there is not much wetting/drying activity recorded. Neither Ward Spit nor

Station		Phases						
		MSf	$2SM_2$	MO_3	M_4	MS_4	$2MS_6$	$2SM_6$
Port Augusta	Pred.:	341.7	82.7	98.3	194.5	8.3	228.7	295.3
	Obs.:	73.8	107.8	147.4	315.5	297.1	61.0	137.0
Beacon #5	Pred.:	344.6	84.6	99.4	164.7	14.4	301.9	349.3
	Obs.:	359.1	87.1	139.1	297.4	328.1	12.1	50.1
Port Pirie	Pred.:	355.7	91.2	112.7	97.5	325.0	6.6	107.7
	Obs.:	280.9	108.0	125.3	291.4	328.3	333.8	37.1
Port Bonython	Pred.:	348.0	95.3	101.5	136.9	318.1	348.8	76.8
	Obs.:	260.0	100.7	114.1	281.8	317.6	321.0	14.9
Whyalla	Pred.:	329.2	98.6	102.2	220.4	293.4	329.5	63.6
	Obs.:	128.2	111.6	114.3	259.1	295.8	301.0	2.5
Yarraville Shoals	Pred.:	357.4	135.5	108.1	348.8	258.2	258.2	327.8
	Obs.:	335.8	131.1	100.3	236.5	277.4	234.7	288.0

Table 8.6: *Comparison of predicted (Pred.) and observed (Obs.) phases (degrees, C.S.T.) for the seven shallow water constituents considered in Table 5.12 of Chapter 5.*

Cockle Spit are uncovered at the times depicted.

Figure 8.28 is a two-hourly sequence during the spring period corresponding, in part, to the right hand signals of Figure 8.14. The same scale is used as in Figure 8.27 and one immediately notices the greater vibrancy of spring flows. As well, wetting/drying activity is clearly enhanced. We observe Ward Spit uncovers briefly, and indeed most of the tidal flat elements of the model uncover at that time. Cockle Spit remains uncovered for a more substantial period. Near lower high water at springs, depicted as plot time 15 dy 11 hr, very few elements are uncovered.

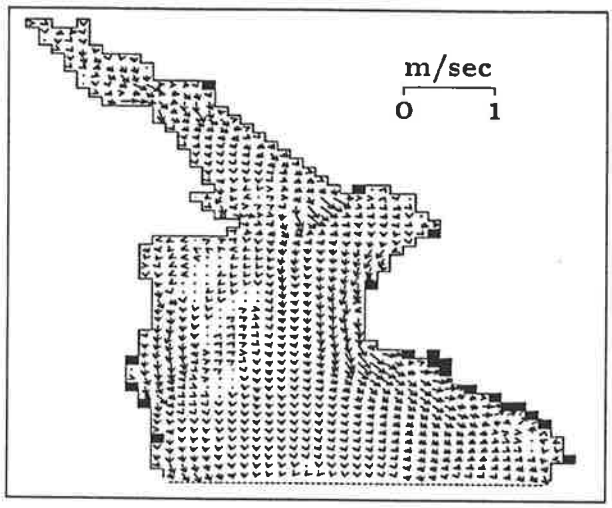
8.8 An application of the tidal flat model

A perhaps topical application of the model is to the prediction of probable changes to coastline due to "Greenhouse" rises in mean sea level. For that matter, changes due to falls in mean sea level can be as easily modelled.

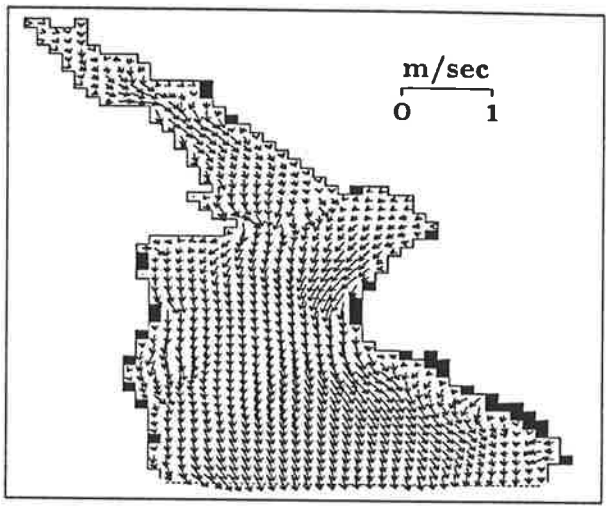
Figures 8.29–8.31 are two-hourly plots of tidal current over the same spring period as considered in Figure 8.28. For the run shown in Figure 8.29, half a metre of water is subtracted from the MSL depth field, for Figure 8.30 half a metre is added, and for Figure 8.31 a full metre is added. The plots in each case seem plausible and demonstrate the obvious: fewer elements behave as tidal flat elements as water is added to the mean sea level depth field, and vice versa.

Several interesting points can be raised, however. For instance, if MSL does rise and if it rises too quickly, the "nursery" role of the coastal tidal flat regions may be jeopardized due to probable die-off in coastal mangroves. Also, regarding the overall tidal dynamics of the Northern Gulf, perhaps a rise in MSL will spell the demise of Ward Spit?

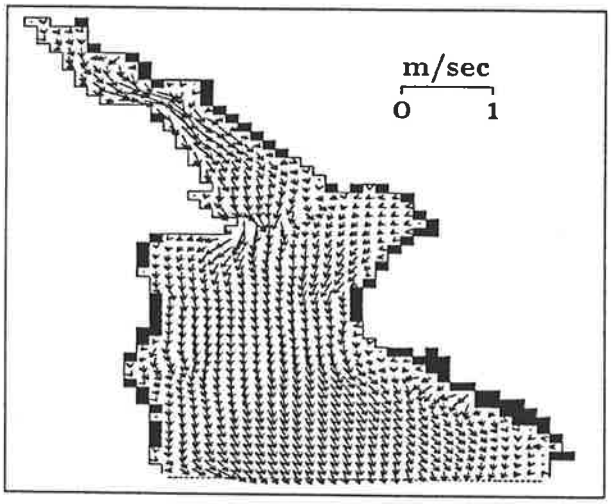
The first point is of importance to the Spencer Gulf fishery, particularly the prawn



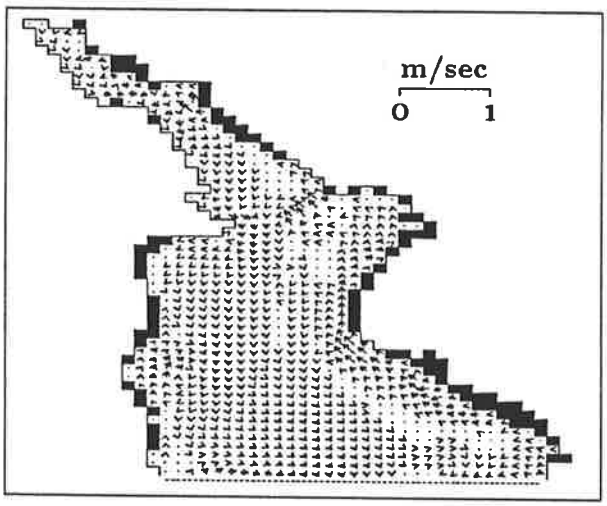
7 dy 14 hr



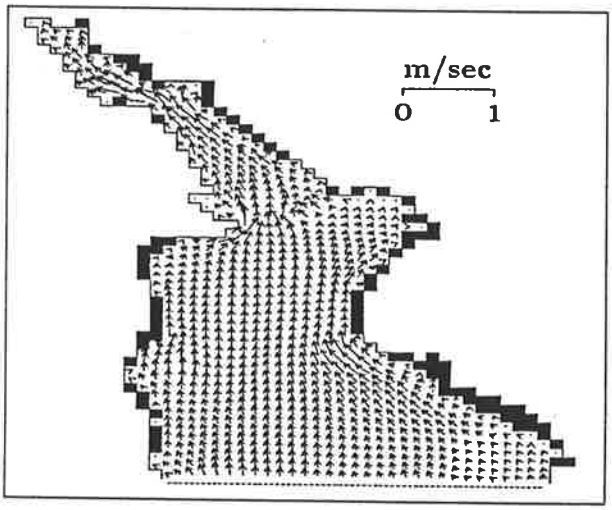
7 dy 16 hr



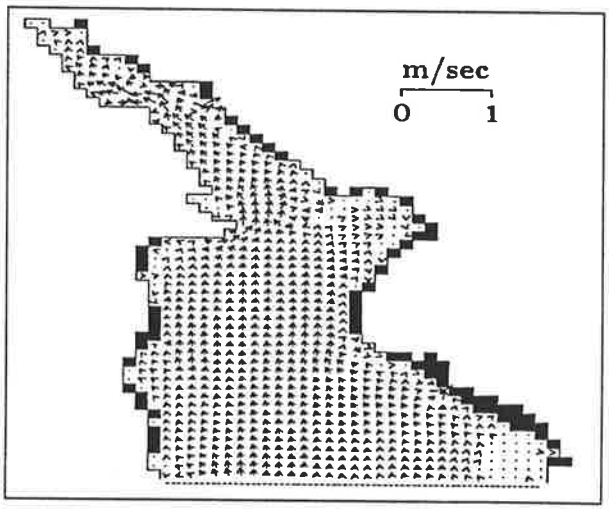
7 dy 18 hr



7 dy 20 hr

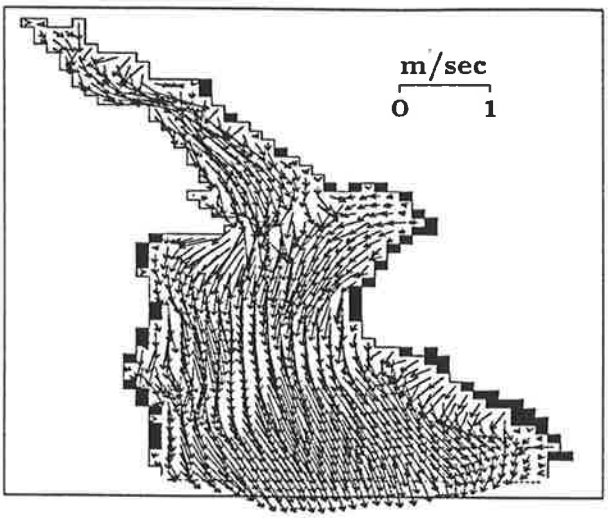


7 dy 22 hr

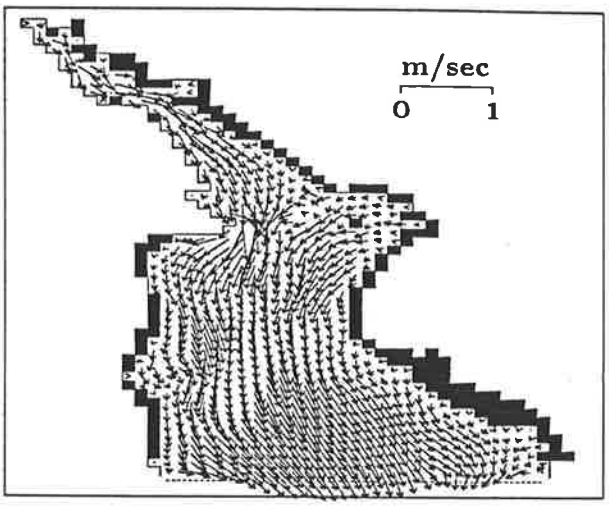


8 dy

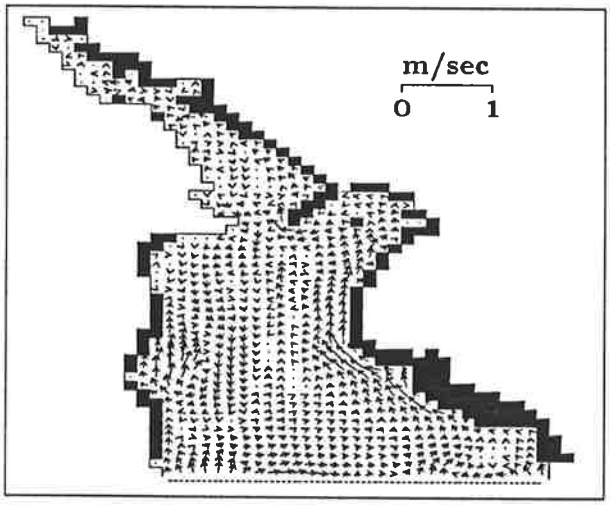
Figure 8.27: *Wetting/drying sequence taken at two hour intervals during a neap event depicted in the left hand signals of Figure 8.14. Model predictions for corresponding depth-averaged velocities are shown. Black elements are "dry", white elements "wet".*



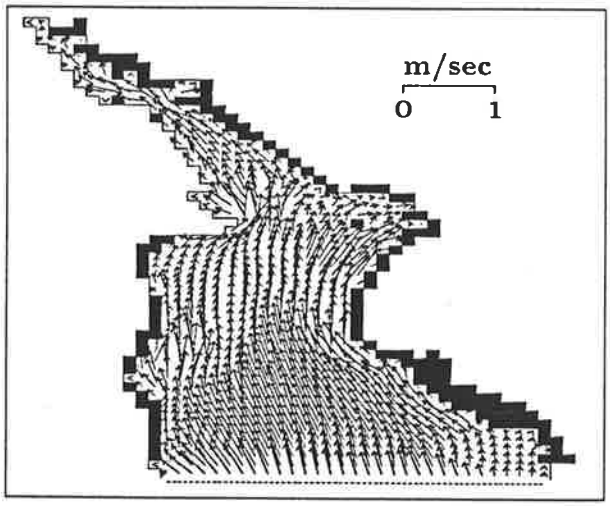
15 dy 1 hr



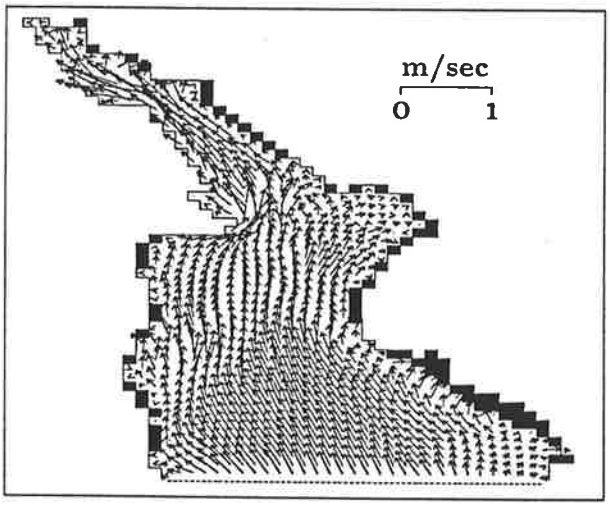
15 dy 3 hr



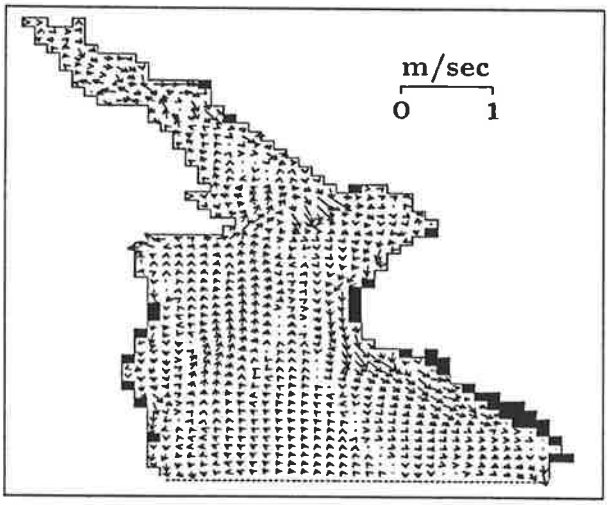
15 dy 5 hr



15 dy 7 hr

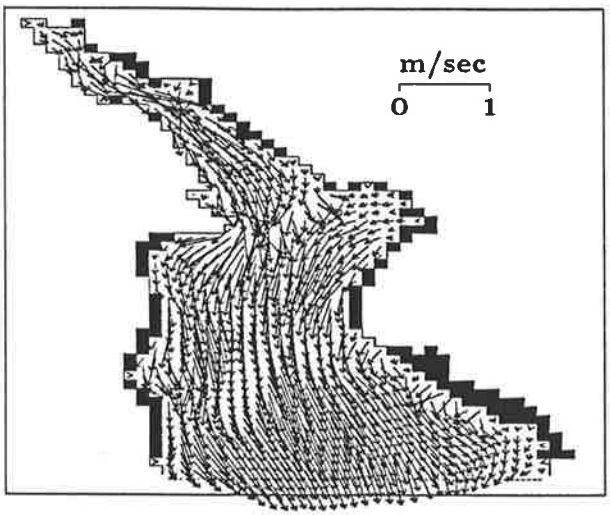


15 dy 9 hr

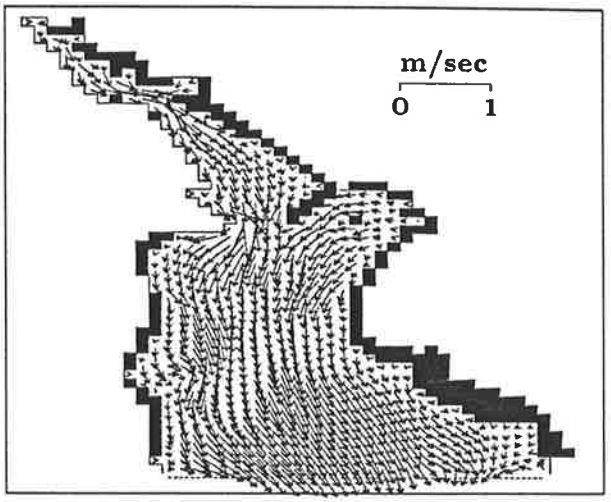


15 dy 11 hr

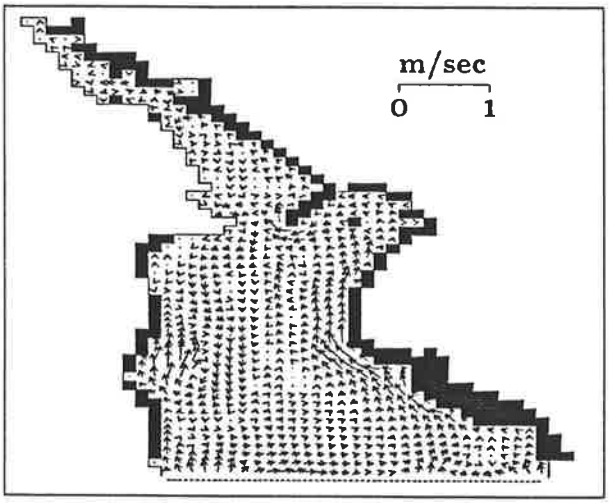
Figure 8.28: *Wetting/drying sequence taken at two hour intervals during the spring event depicted in the right hand signals of Figure 8.14. Model predictions for corresponding depth-averaged velocities are shown. Black elements are "dry", white elements "wet".*



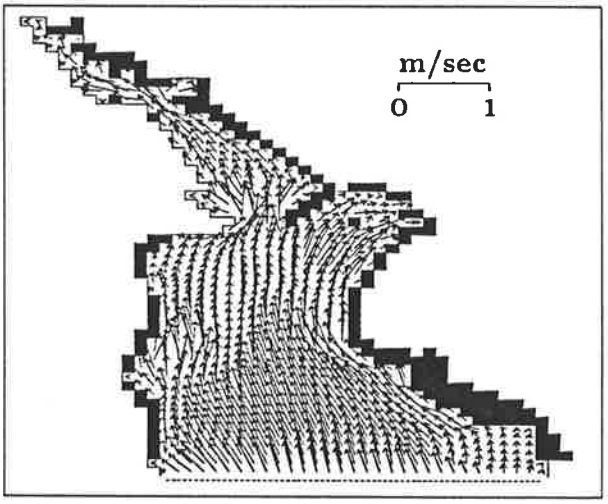
15:01:00 "GH-0.5"



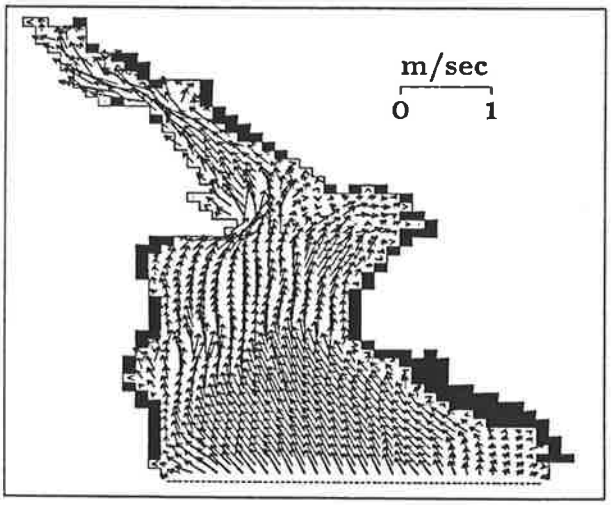
15:03:00 "GH-0.5"



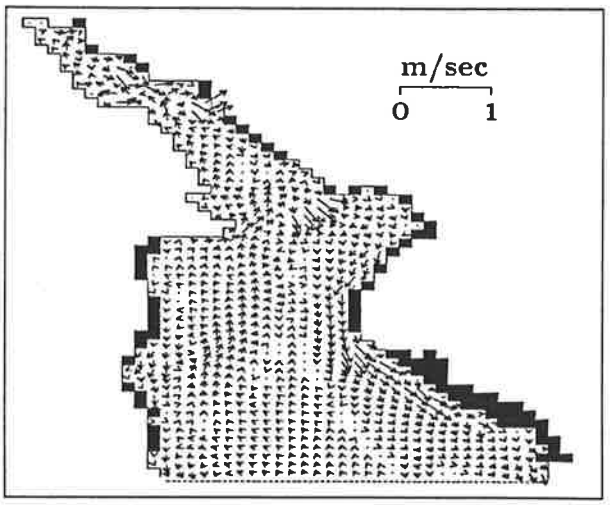
15:05:00 "GH-0.5"



15:07:00 "GH-0.5"

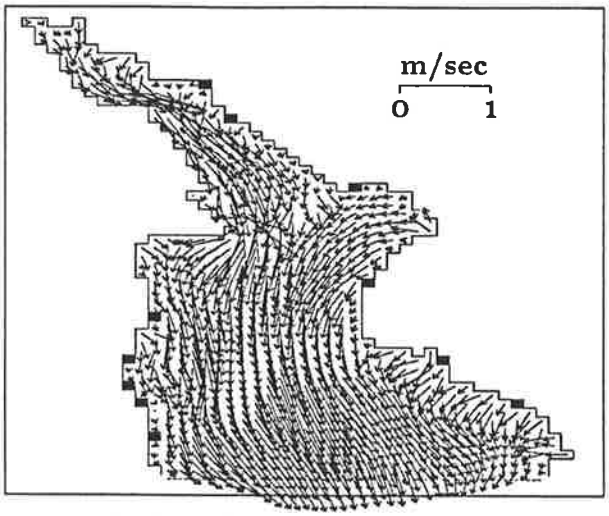


15:09:00 "GH-0.5"

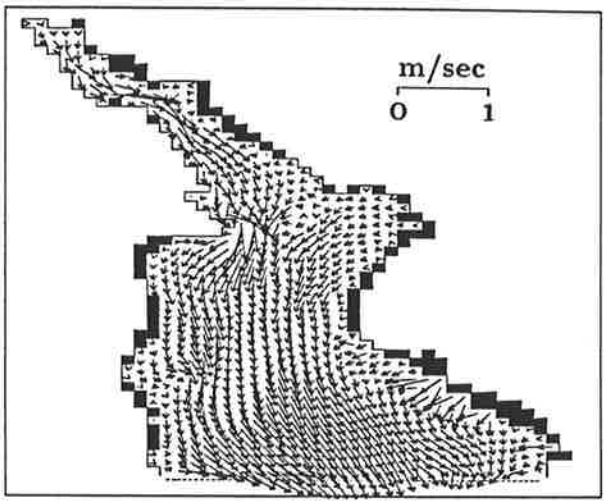


15:11:00 "GH-0.5"

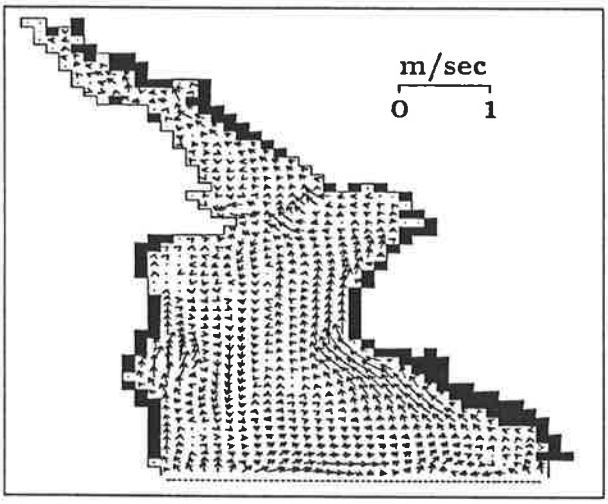
Figure 8.29: *Two-hourly wetting/drying sequence during the spring event corresponding approximately to Figure 8.28 and assuming a fall in MSL of 0.5 m.*



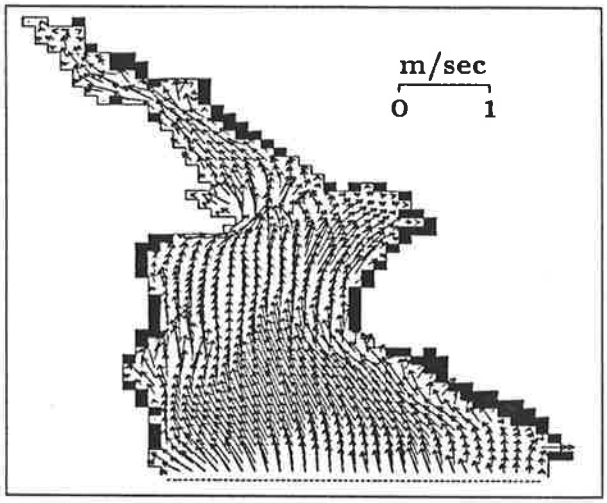
15:01:00 "GH+0.5"



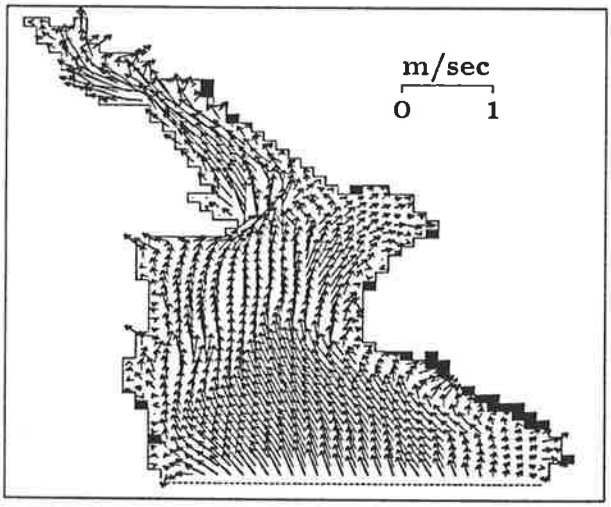
15:03:00 "GH+0.5"



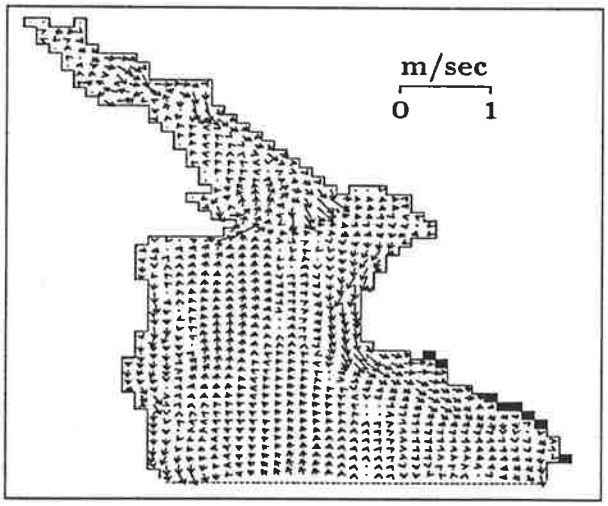
15:05:00 "GH+0.5"



15:07:00 "GH+0.5"

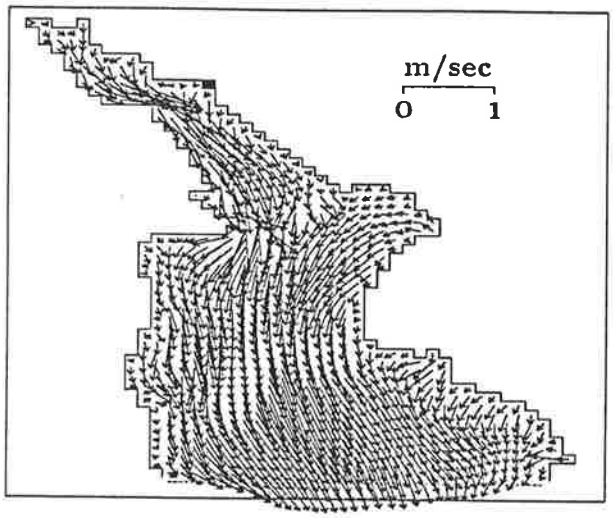


15:09:00 "GH+0.5"

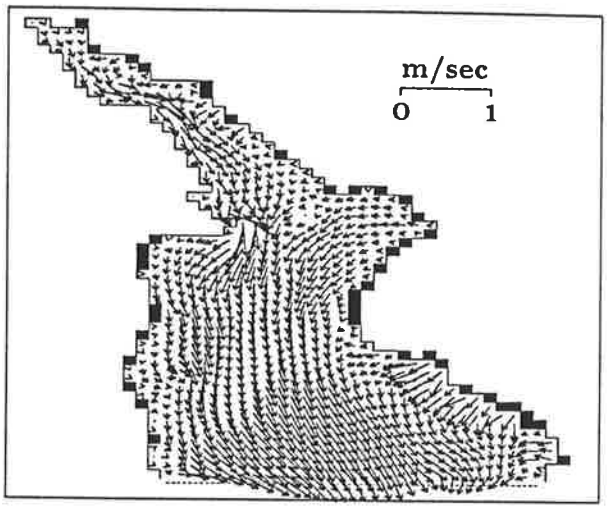


15:11:00 "GH+0.5"

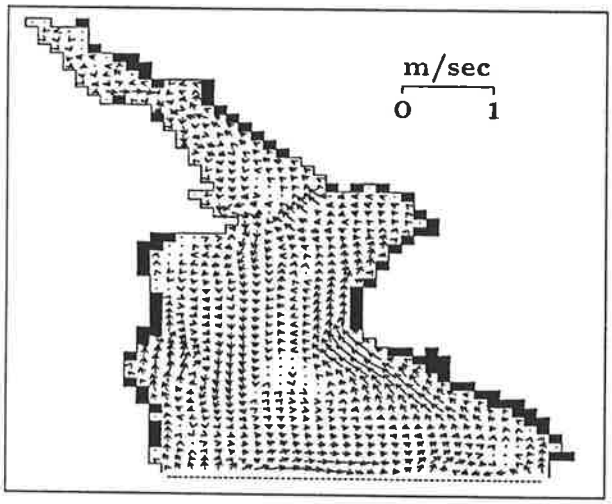
Figure 8.30: *Two-hourly wetting/drying sequence during a spring event corresponding approximately to Figure 8.28 but assuming a "Greenhouse" rise in MSL of 0.5 m.*



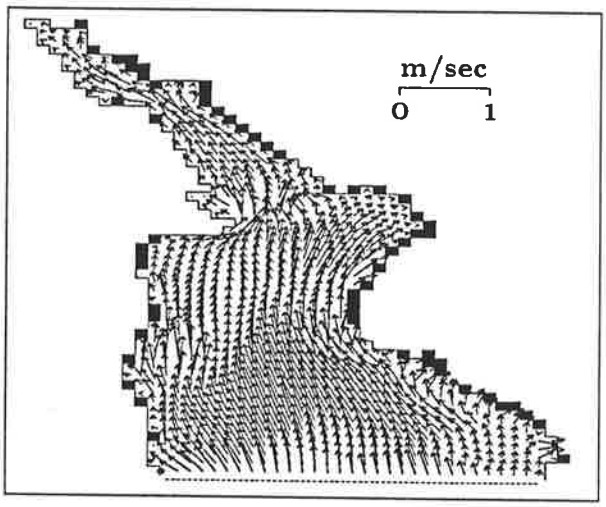
15:01:00 "GH+1.0"



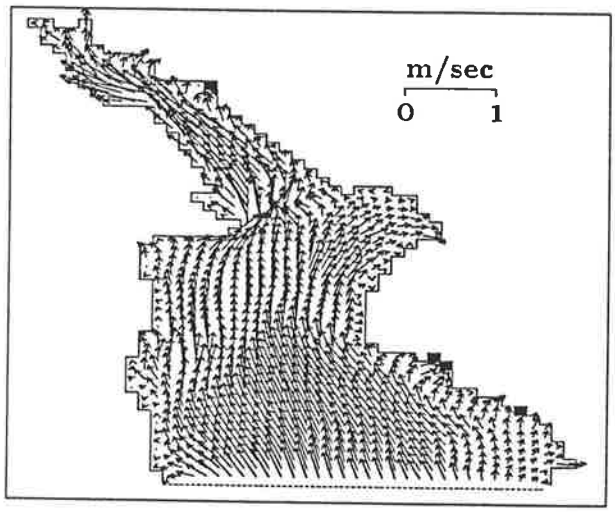
15:03:00 "GH+1.0"



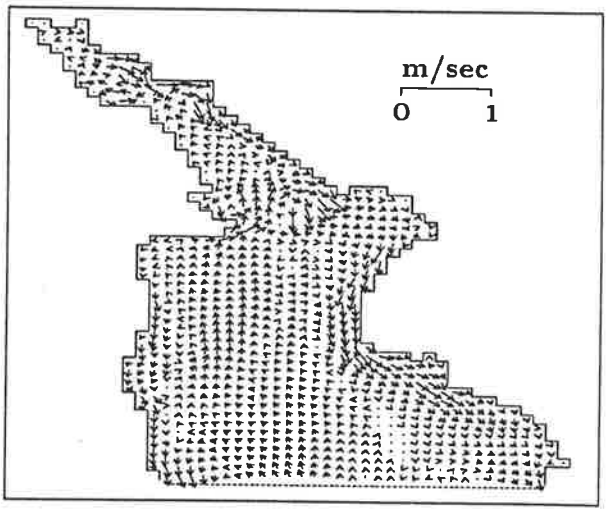
15:05:00 "GH+1.0"



15:07:00 "GH+1.0"



15:09:00 "GH+1.0"



 15:11:00 "GH+1.0"

Figure 8.31: *Two-hourly wetting/drying sequence during a spring event corresponding approximately to Figure 8.28 but assuming a "Greenhouse" rise in MSL of 1.0 m.*

Adjustment to MSL depth field	Average absolute error measure		
	Ampl ε_a cm	Phase ε_p deg	Combined ε cm
−0.5 m	3.67	3.87	5.61
No change	3.80	3.84	5.69
+0.5 m	3.71	3.82	5.63
+1.0 m	3.56	3.83	5.58
+2.0 m	3.33	4.20	5.67
+5.0 m	5.73	6.43	8.41

Table 8.7: *Error values corresponding to various adjustments to the MSL depth field. The entries in this table summarize comparisons between predicted and observed tide-height constants at the six available stations in the NSG region. The entries in the case of "No change" to MSL are taken from the caption of Table 8.3.*

fishery which is worth $20 million annually to the South Australian economy — the total fishery in Spencer Gulf generates about $40 million per annum. The second point can be answered with some authority by considering the depth-averaged residual plots for the Ward Spit area generated from these runs. These are given in Figures 8.32. Careful inspection of these residuals in the Ward Spit region shows that there is little change in the character and strength of the net circulation across Ward Spit, even in Figure 8.31 where the Spit no longer uncovers during the 29-day period simulated. So if MSL were to rise, some erosion of Ward Spit may occur, but a strong mechanism for its removal is not evident in these plots. It seems more likely that the Spit would remain, albeit perhaps as a submerged sand bar along with the many other such sand bars in the general region.

A further interest in conducting these experiments is to observe any changes in the values of the error measures used. Bearing in mind that each run uses the same open boundary forcing set, same de Chèzy friction parameter n and same ϵ, H_0 and H_{dry} values, consider the errors displayed in Table 8.7. Artificial adjustment in mean sea level leads to changes in the error measures — for small rises (or falls) in MSL, the overall error values tend to decrease, but for very large rises they increase.

This effect is also seen by Wolf (1983) who, in adding 5 m to the MSL of her three-dimensional fine-grid model of the Bristol Channel in an attempt to raise its stable time step, recalibrates and increases the value of the coefficient of vertical eddy viscosity four-fold.

Finally, some limitations in conducting these experiments are listed:

- If, for example, half a metre of water were added to MSL, the open boundary information for the NSG model would change. A first approximation for the corrected open boundary input could be obtained by running the Spencer Gulf model with an additional half metre of water, performing a recalibration and taking the boundary information from it for the NSG model. A better approximation would result if the driving constants for the Spencer Gulf model for the new value of MSL were obtained from a global ocean model. The impact of changing MSL will likely have stronger local effects than global ones. Increased depths may take coastal systems closer to or further from resonant tidal response.

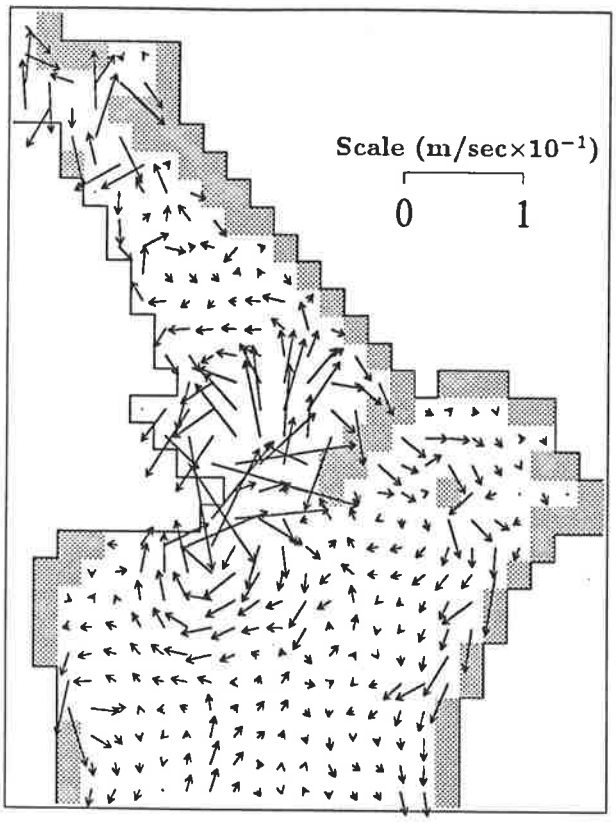


Figure 8.32(a): *Residuals for depth-averaged velocity given a fall of 0.5 m in the mean sea level (MSL) field.*

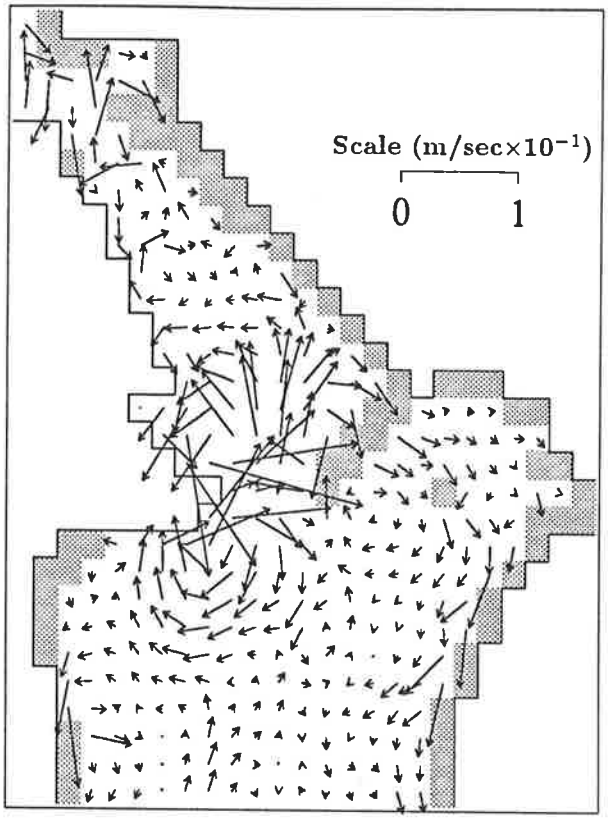


Figure 8.32(b): *Residuals for depth-averaged velocity as given in Figure 8.26(c) — present-day MSL field used.*

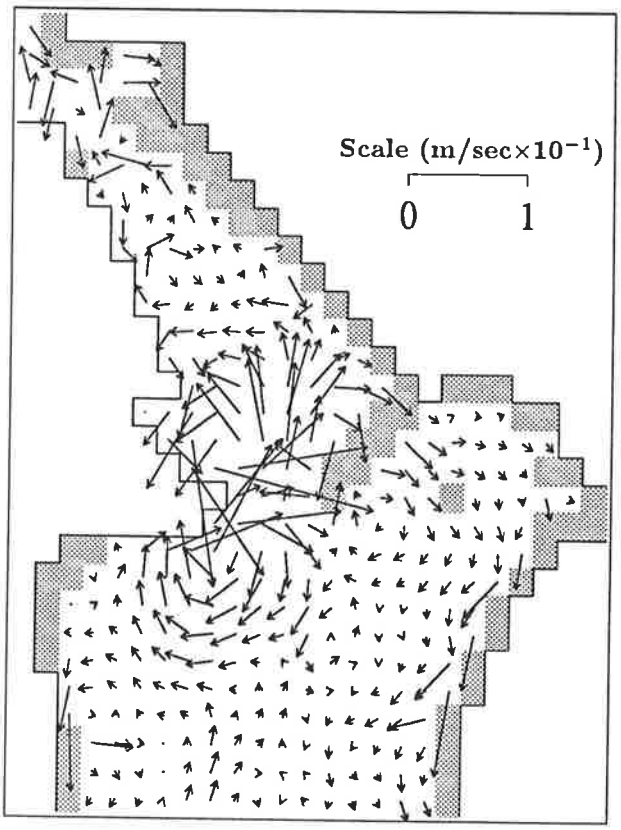


Figure 8.32(c): *Residuals for depth-averaged velocity given a rise of 0.5 m in MSL. As MSL rises, the number of tidal flat elements declines.*

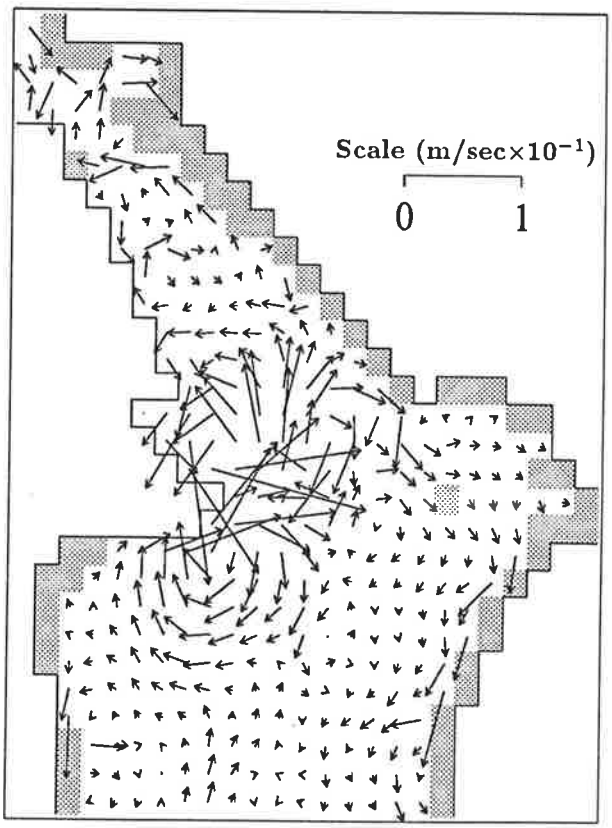


Figure 8.32(d): *Residuals for depth-averaged velocity given a rise of 1.0 m in MSL. Ward Spit no longer uncovers.*

- The error measure values of Table 8.7 are comparisons of predicted and observed constants at gridpoints representative of certain tidal stations. Account is not taken of the likelihood that if MSL changes, the observed constants will also change.

- The sequences shown in Figures 8.29–8.31 show the same times, but won't generally correspond to the same events. One of the effects of adding, say, 0.5 m to MSL will be to shift the timing of the spring event depicted.

- A more thorough modelling of the effect of adding, for example, 0.5 m to MSL will involve expanding the "permanent" coastal boundary to include elements out to the present 1 m, 2 m or perhaps 5 m land contours. It is necessary to include land elements far above the chosen MSL adjustment in order to take into account possible wind-induced flooding at high spring tides, though it is not necessarily the case that the wind effect will increase the risk of coastal flooding: firstly, the effect of increased depth may actually reduce tide height and secondly, because the wind effect is proportional to the ratio of wind speed to water depth (see Chapter 2), an increase in depth at a given location will cause a decrease in wind effect for a given wind stress. These various possibilities emphasize the need for a model that can provide clear predictions of the effects of rises in MSL.

8.9 Summary

A depth-averaged tidal flat model which predicts the covering and uncovering of tidal flats in Northern Spencer Gulf in a qualitatively reasonable manner has been produced.

Quantitatively, the NSG model gives a slightly smaller calibration error than the SG model when compared with observed tide-height constants at the six northern-most stations of the Gulf. While both models predict similar diurnal tide-height constants, the SG model over-damps the semi-diurnals while the NSG model under-damps them. Comparing the predicted and observed tidal ellipse characteristics, both models again give similar diurnal characteristics and again the SG model over-damps the semi-diurnals and the NSG model under-damps them.

Based on the semi-major and semi-minor ellipse values, results at Mike are worse for the NSG model and the immediate reason for this (and the under-damping of the semi-diurnals) must be the lower value of friction coefficient presently used in the local vicinity of Mike.

The built-in filtering behaviour of the common four-point differencing used to approximate V_i (or U_i) in the Coriolis, quadratic friction and one of the advective terms of the U (or V) momentum equation, has been demonstrated. The additional use of a filter combined with the remaining advective term, whilst using a constant quadratic friction coefficient, has been shown to be globally inaccurate in achieving local stability at the Ward Spit elements of the Northern Spencer Gulf model relative to using the de Chèzy friction formulation, which focuses the influence of bottom friction in shallow elements by reason of its dependence on depth.

The fact that the value of the constant coefficient of quadratic friction had to be significantly decreased when going from the coarse-grid Spencer Gulf model to the fine-grid Northern Spencer Gulf model is consistent with this, and indeed suggests that one should use a depth-dependent quadratic friction coefficient for tidal flat models and very

shallow models in general. The constant quadratic friction formulation is too coarse a formulation for such models.

It may be possible that more careful adjustment of the parameters ϵ and H_0 will lead to smoother wetting and drying activity, so this should be further investigated.

The fine-grid model proves to be slightly more accurate than the coarse-grid model in its prediction of the largest of the minor constituents. The improvement of predictions, particularly for the northern-most stations, is most likely due to the finer grid size used and its correspondingly improved bathymetry.

A greater understanding of the tidal dynamics of Northern Spencer Gulf has been achieved by the use of the present model. In particular, the hitherto theoretical prediction that the circulation in the far north of the Gulf is largely isolated from that of the remainder of the Gulf has been given strong numerical support using this model. In the process, plausible explanations concerning the creation and maintenance of both Ward Spit and Cockle Spit have been stated. The existence of a strong residual gyre south of Lowly Point has been numerically confirmed, and an even stronger residual gyre north of Lowly Point has been predicted. A still finer model of the Lowly Point region would help to resolve some of these issues.

A possible use of the model in predicting the effects of rises and falls in mean sea level has been outlined and demonstrated in a limited way. Wind effects are likely to be important in such models. Present day application to shallow coastal regions where storm damage might be expected to be high is another potential use of the model.

Further work in benignly removing numerically generated grid-scale oscillations is required. While under control in the present model, the wiggles in the elevation signals on the right of Figure 8.14 indicate that they have not been removed. It is likely that grid-scale waves of wavelength longer than twice the grid spacing are present. By considering the application of filters to the whole solution field, rather than term-wise as at present, it may be possible to devise or make use of schemes that will more thoroughly purge the predictions of grid-scale waves as a general species and leave the tidal constituents intact. Such smoothing would be applied either at every time step or at a group of time steps. Perhaps the net result of these efforts will be to allow the overall friction coefficient to be increased and the semi-diurnals to be more accurately modelled, while maintaining an overall low model error.

In this model the same value of reduced eddy coefficient a was used as was obtained by calibration for the SG model of Chapter 5 (Section 5.4). It was not thought necessary to change it here: surely the diffusive terms would be even less influential in the NSG model than in the SG model!? The work of Section 5.4, showing that diffusive terms remove or damp grid-scale oscillations near the open boundary, has been only recently completed. The SG model proved to be relatively insensitive to the value of a and relatively free of grid-scale oscillations. But by the nature of the tidal flat scheme, grid-scale oscillations are superimposed on the solution field in the shallow coastal waters. Performing a calibration on a using the de Chèzy coefficient with value $n = 0.018$ shows that the optimal value is $a = 0.045\,\mathrm{sec}^{-1}$ for the present model (with corresponding combined error measure $\varepsilon = 5.26\,\mathrm{cm}$). But until further calibrations using other values of n are carried out, this is only an estimate of a more accurate value of a for the NSG model, though it does suggest that a value about eight times that used in Chapter 5 should be used and that increasing a will lead to a decrease in the global error measure for the model. This is evidence for our suspicion that there is still significant grid-scale energy present in the solution field in

spite of the use of filters. Adjustment of a in order to reduce this is a promising area of further research.

Because Wolf (1983) uses a Galerkin method in the vertical, her application of Flather and Heaps' (1975) tidal flat scheme is essentially two-dimensional and not three-dimensional. However, an extension of the tidal flat scheme into three dimensions does seem feasible. In the same way that a minimum depth is postulated in the present model (following Flather and Heaps), the same (or similar) could be postulated for the solution of the tidal equations in the vertical for all three components of tidal velocity. Vertical turbulence in the case of the three-dimensional model is already formulated in terms of element depth, so the need to focus the influence of this process in very shallow water is built-in. This work is not developed in the present thesis but is another subject of further research.

The modelling of the movement of prawn larvae from spawning grounds to coastal nurseries seems an ideal application of a three-dimensional tidal flat model. The larvae have little ability to move in the horizontal but have a buoyancy-related ability to move in the vertical so as to spend nights near the surface and days near the bed, thus avoiding the extremes of summer sunlight as well as daylight surface predators. A knowledge of the vertical current profile is therefore essential in order to correctly model their movement into shallow coastal nursery grounds. This application is further discussed in Chapter 9.

Chapter 9

Conclusions

In this thesis, three programs for computing tides in the shallow seas of Spencer Gulf have been described. One of these solves the σ-transformed three-dimensional barotropic non-linear long-wave equations using the method of finite differences. It uses a non-uniform spacing of depth-levels in the vertical calculated using the Kappa method (Noye, 1984a), which gives locally second-order accuracy at each depth level. The finite difference scheme is explicit in the horizontal dimensions and centred-time implicit in the vertical. Another program is the depth-averaged analogue of the first, and the associated finite difference scheme is explicit. These first two programs have equivalent stability, the implicit scheme of the three-dimensional program being unconditionally stable so that its stability is determined by that of the horizontal scheme. The third program is an extension of the depth-averaged program to take account of the wetting and drying of tidal flats.

Four grid element types are defined on the basis of the location of the elevation grid-point of each element. Only three of these element types are used in computations, the fourth being used for aesthetic reasons only: to distinguish water elements outside the model from those inside. The subroutines for the calculation of elevation and the velocity components are automated so as to solve precisely the form of the finite difference equations that apply for each given configuration of model elements. The automation is achieved by the use of integer arithmetic switches which use the element type numbers to select the appropriate parts of generalized finite difference expressions written for each differential equation. The flexibility of the automated program code has been demonstrated by Mitchell et al. (1984) and Arnold and Noye (1986b) who have applied the three-dimensional program to the modelling of tide and wind-driven flow in the Gulf of Carpentaria and Bass Strait, respectively.

Computations are carried out only on interior model elements. The program variables are declared as lists rather than arrays. This not only maximizes computational efficiency for the types of scalar computers available for present use but also produces a program code which is already prepared for vectorization. Nixon (1992) has vectorized the three-dimensional program code for efficient running on a Cray Y-MP 2D 2-16.

Because the automated program code is complicated, thorough testing is required. The programming of the differencing used for all major terms of the differential equations is checked by numerical experiment using bays of simple geometry for which analytical solutions are available. The performance of the schemes in propagating waves of the major tidal species is tested. In linear cases, the performance of the schemes is gauged using wave propagation analyses. These do not take into account boundary conditions. The

special forms of the finite difference schemes used near boundaries are separately analysed after the manner of Trapp and Ramshaw (1976). The finite difference expressions perform accurately using model values of grid spacings per wavelength applying to the propagation of these waves.

The depth-averaged program is applied to a model of Spencer Gulf (SG). It is driven at the mouth of the Gulf by a height specified condition employing tide-height constants extrapolated from observations at four nearby stations. A method of determining mean sea level (MSL) from the Indian Spring Low Water (ISLW) chart datum is demonstrated. It uses the program in an iterative process and takes only three iterations to produce a MSL field which differs everywhere from the previous iteration by less than 1 cm. It generates a MSL field to an accuracy at least as good as the ISLW field used.

Expressing the tide-height amplitude and phase of a given constituent at a given station as a complex polar vector, an error measure (denoted ε, in cm) is defined that combines the absolute differences of these predicted and observed complex vectors for the four major constituents at selected interior tide-height stations. It's chief value is as a comparative error measure in calibration experiments for the optimal values of the reduced eddy coefficient a, the linear friction coefficient k and three forms of quadratic friction coefficient (see Section 5.4).

The reduced eddy coefficient is a parameter used in the Schwiderski (1980) formulation for the horizontal eddy diffusive coefficients. For the SG model the optimal value of a using a constant quadratic friction coefficient of value $C_b = 0.0025$ is $a = 0.0055\,\mathrm{sec}^{-1}$, but the model is virtually insensitive to this parameter. It is demonstrated analytically that the second order derivatives that comprise the horizontal diffusive terms behave like linear friction terms, the value of the damping so introduced depending on the square of constituent wavenumber. For a tidal constituent the contribution to a linear friction coefficient made by these terms is almost negligible for the SG model, even at the open boundary where maximum depth is close to 55 m. For a grid-scale wave near the open boundary, however, the contribution is two to three orders of magnitude greater. Examining the behaviour of the differencing used for the second derivative approximation, and comparing this with the theoretical response of the derivative term, shows that the selective grid-scale damping effect is enhanced and there is still very little effect on a tidal constituent. The effect of the Schwiderski formulation is to multiply the respective damping effects by a factor which depends on local depth. Thus at the open boundary where the model is deepest the damping effect on the grid-scale wave is greatest. Since one expects to find grid-scale waves generated at the open boundaries of a tidal model, such an effect is fortuitous to say the least and must be a powerful argument for the inclusion of the horizontal diffusive terms, remembering that the effect on tidal constituents is almost negligible. The fact that the SG model is virtually insensitive to the reduced eddy coefficient a therefore indicates that it is relatively free of grid-scale oscillations.

A calibration to determine the optimal value of the linear friction coefficient for the SG model shows that it is $k = 0.0009\,\mathrm{m/sec}$ with a corresponding value of the combined error measure of $\varepsilon = 4.16\,\mathrm{cm}$.

A calibration for the optimal value of the constant quadratic friction coefficient gives the value $C_b = 0.0025$ with a corresponding combined error of $\varepsilon = 3.49\,\mathrm{cm}$. Therefore the tidal dynamics of Spencer Gulf are best modelled using the non-linear formulation.

Calibrations for the Colebrook-White logarithmic quadratic friction coefficient and the de Chèzy coefficient show that the optimal value of the roughness coefficient k_b for the

former lies in the range 0.06–0.07 m ($\varepsilon = 3.45$ cm) and the optimal value of the Manning coefficient is $n = 0.025$ ($\varepsilon = 3.44$ cm).

Since the errors associated with these three quadratic friction coefficients are very similar, it was decided to obtain results from the SG model using the optimal value of the constant quadratic friction coefficient on the basis that runs using the other coefficients are at least 12% more computationally expensive.

Amplitude and phase contours (Figures 5.22–5.25) and ellipse plots (Figures 5.26–5.29) are presented for the four major tidal constituents. These are the first results presented from a tidal model of Spencer Gulf driven by the four major constituents. They are derived from a simulation of 32 days duration, of which the last 29 days of predictions are tidally analysed. The length of the simulation indicates that the program is stable, and the length of the data set analysed gives a greater assurance of accurate resolution of the diurnal and semi-diurnal pairs by the tidal analysis program. However, the amplitude predictions of the O_1 constituent are unduly amplified. The reason for this is not clear. In contrast, the K_1 constituent is modelled well.

The contour charts presented show that the model replicates the known features of the tides of Spencer Gulf. The ellipse plots suggest that tidal (not residual) gyres or eddies are created at times near slack tide and are dissipated by the strengthening ebb or flood movement, only to be created and subsequently dissipated at the next slack tide. Sightings of these events have not been made. This gyral activity is predicted for the region off Wallaroo (see Figure 5.15) where two relatively large oppositely rotating gyres are created during neaps and springs. These gyres may be a means by which prawn larvae are transported from the Wallaroo spawning ground to the fertile nursery grounds within Franklin Harbour (Figure 1.1) (see subsection "Modelling prawn larvae movement in Spencer Gulf" at the end of this chapter). The gyres last for up to an hour. Sequences of velocity vectors are presented from the depth-averaged model predictions to indicate that the tidal gyres exist within the context of overall depth-averaged flows (Figures 5.32 and 5.33). The fact that the gyres originate from the major constituents is shown by plotting the constituent ellipse plots as snapshots at different stages of each constituent tidal cycle (Figures 5.34 and 5.35). On this basis it is predicted that the diurnal gyres last perhaps one hour and the semi-diurnal gyres half an hour.

Since the gyres are caused by the inherent vorticity of the tidal current field, it may be a useful future project to perform vorticity calculations for the purposes of direct comparison.

There is good agreement between predicted and observed tidal current ellipse characteristics at station Mike (see Figure 5.15 for location, Table 5.9 for characteristics), and reasonably good agreement at all other tidal current stations except Yarraville Shoals (Figure 5.15, Tables 5.9–5.11). Model depth is relatively close to observed depth at all stations except Yarraville Shoals which is in a region of shallow water occupying only a small fraction of a horizontal grid element.

Residuals calculated from the 29-day data sets are produced for both the tidal current (Figure 5.36(b)) and tidal elevation (Figure 5.37(b)). The tidal gyres of Figures 5.32 and 5.33 (or Figures 5.34 and 5.35) do not clearly correspond with the residual gyres of Figure 5.36(b), although they do seem to share a common flow corresponding to the position of the deep channel marked on Figure 5.15. Since the gyres of Figures 5.32–5.35 are generated by the major constituents one would not expect them to leave a signature in the velocity residuals.

Many residual gyres populate Figure 5.36(b). The most prominent is a clockwise rotating gyre which straddles the mid-section of the Gulf. The deep channel referred to above marks its southern extent. Two other gyres, although difficult to detect in the plot, are found north and south of Lowly Point (Figure 5.10). These are more clearly seen in the residuals from the fine-grid model of Northern Spencer Gulf in Chapter 8 (Figures 8.26).

The elevation residuals show that the sea surface is depressed on the west coast where the large central residual gyre has relatively strong vectors. This is a non-linear effect of residual gyres pointed out by Pingree and Maddock (1977b).

The appearance of spurious and physically unrealistic velocity residuals along the coastline and open sea boundary when first order accurate subordinate approximations for the advective terms are used has lead to the omission of these terms in those instances (contrast Figures 5.36(a) and 5.36(b)). First order approximations used as subordinate approximations for the diffusive terms give them zero value. Advective and diffusive terms requiring a zero boundary value on a coastline are also omitted because spurious and unrealistic behaviour in the velocity residuals persists. When all these terms are omitted under the stated conditions the velocity residuals are much smoother and show no signs of unrealistic behaviour. Figures demonstrating these effects are given in Chapter 3 as Figures 3.23(a),(b),(c). It is preferable to omit these terms and the corresponding subordinate approximations than to include them and have the solution contaminated by spurious effects. The omission only involves approximations to spatial derivatives of velocity normal to a coastal or open sea boundary, a grid value of which either lies beyond the coastal boundary on land or beyond the open sea boundary, or lies on the coastal boundary or on the open boundary. Spatial derivatives of velocity parallel to coastal or open sea boundaries are not omitted unless they satisfy the aforementioned terms of omission by being near a corner in the boundaries so that they are also normal to a coastal or open sea boundary.

Considering the zones of minimum amplitude in both the M_2 and S_2 constituents (Figures 5.24(a) and 5.25(a)) it is noted that their position coincides with the shallow coastal areas of Wallaroo and Tiparra Reef (see Figure 5.15). These areas are bordered by steep bathymetric gradients (see Figures 5.13–5.15). Pingree and Maddock (1977b) note that converging and curving streamlines lead to a depression of the sea surface, so it may be possible that these minima in the semi-diurnals are indirectly a result of such behaviour of the tidal streams which surely do veer and converge from both north and south directions on the ebb and flood tides in this region. The semi-diurnals alone seem to be affected, so perhaps these bathymetric features are not "seen" by the diurnals. This is a subject of further investigation.

The depth-averaged model is a reasonably accurate tool for the prediction of two of the largest minor constituents, $2SM_2$ and MS_4, except immediately adjacent to the open boundary (where the minor constituents are not part of the height specification) and in the far north of the Gulf (which is poorly represented by the coarse element dimension of the model). Agreement between observation and prediction for MSf, the largest of the sampled minor constituents, is more variable and this could be due both to the short length of the predicted record (29 days) and possible errors in the observed values. The observed amplitudes given in Table 5.12 show that the non-linear constituents in the Gulf are generally small. Improved modelling of the minor constituents would at least require a finer grid and better bathymetric representation. These improvements are included in the Northern Spencer Gulf of Chapter 8 and so the minor constituents are re-examined

there.

We then investigated whether height specification is the most suitable open boundary condition for the model and whether a radiation condition could provide tidal forcing and produce a model of equivalent or better accuracy than the optimal model of Chapter 5. In order to apply radiation boundary conditions to the model, the open bounadry had to be modified by re-classifying boundary element #1 of Figure 5.12 as a Type 1 element. The combined error of the model using the height specified open boundary condition is then $\varepsilon = 3.59\,\text{cm}$. The Sommerfeld condition produces a stable model but gives a result which is significantly less accurate ($\varepsilon = 4.58\,\text{cm}$). The Orlanski-Sommerfeld condition gives improved performance ($\varepsilon = 3.87\,\text{cm}$). The reasons for this are the Orlanski separation of flows at the open boundary into ingoing and outgoing modes and the application of height specification in the case of ingoing flows. It is found that the flow is ingoing for 87.3% of the simulation so the Orlanski-Sommerfeld condition supplies correct forcing information for that proportion of the time. Orlanski also numerically calculates the outgoing phase velocity, but when the phase velocity is calculated in the Sommerfeld manner using $c = \sqrt{gh}$, where h is local MSL depth, the same error value results (viz. $\varepsilon = 3.87\,\text{cm}$).

An examination of the numerically calculated values of phase velocity c shows that outgoing events occur just prior to peaks or troughs in the elevation at the open boundary, and are most intense during neaps. This suggests that exchange with the Southern Ocean, known to be dominated by the diurnals, occurs predominantly during neaps.

A very slight improvement in model performance is achieved by forcing the Orlanski-Sommerfeld condition only through the time derivative ($\varepsilon = 3.86\,\text{cm}$). Advancing the timing of the height specification in the modified Orlanski-Sommerfeld condition during ingoing flows by one time step reduces the error to $\varepsilon = 3.58\,\text{cm}$ which is almost identical to the error for pure height specification. The Blumberg and Kantha (1985) condition is also examined and found to be unsuitable unless modified so that the height specified aspect of the condition dominates. Their condition is essentially a fixed linear combination of the height specified and Sommerfeld conditions, so if it is to perform well for the tide-driven SG model one has to emphasize the former behaviour at the expense of the latter. Having modified the Blumberg and Kantha condition so that it gives better model performance in the present case, it is no better than the simpler Orlanski-Sommerfeld condition and so the Blumberg and Kantha condition is not recommended for tide-driven flows. Spatially second order accurate Orlanski-Sommerfeld conditions can be derived and after they are improved in the same way that the spatially first-order accurate Orlanski-Sommerfeld condition was, they give errors no smaller than the first-order accurate scheme. This finding is consistent with a theoretical result due to Gustafsson (1975) which says that a boundary treatment one order less accurate than the internal points will not decrease the overall order of convergence of the finite difference scheme.

Thus the height specified open boundary condition is entirely adequate for the depth-averaged SG model. It should be noted that this finding is consistent with the fact that the minor constituents are small in Spencer Gulf.

The performance of a three-dimensional model of the Gulf is then described. It uses the same horizontal grid, bathymetry and height specified boundary condition as the depth-averaged SG model. A parabolic symmetric vertical eddy viscosity coefficient is used to parameterise the effect of vertical turbulence. The maximum value of this coefficient occurs at mid-depth and the minimum values γ_1 occur at the sea surface and sea bed. Numerical

experiments are carried out to seek the optimal values of the parameters governing this coefficient. It is found that setting $\gamma_1 = 0\,\mathrm{m}^2/\mathrm{sec}$ and specifying the background vertical eddy viscosity α to be equal to molecular viscosity leads to a model that produces minimal error if the values of a coefficient β (see expression (7.3)) and the vertical depth spacing parameter κ are chosen appropriately. The three-dimensional model responds readily to changes in the value of κ but it is evident that the model is not able to give an error value as low as the optimal depth-averaged model by using only 11 depth levels. Thus for the Spencer Gulf model, 11 depth levels do not provide a resolution of the bottom boundary layer sufficient to model the shear stresses as accurately as the depth-averaged model parameterises the log layer using a quadratic friction coefficient. More depth levels should be used, but in view of the length of the present simulations on the VAX 11/785, such runs are left for future research on faster machines. A selection for the various parameters is made and the corresponding predictions of the three-dimensional model are presented.

The depth-averaged results obtained from the three-dimensional model of Chapter 7 such as the depth-averaged velocity ellipses (Figures 7.8–7.11) and depth-averaged velocity residuals (Figure 7.12) show excellent agreement with the corresponding results of the optimal depth-averaged model of Chapter 5. Therefore one concludes that the vertical eddy viscosity form chosen for the three-dimensional model is appropriate, at least as far as being able to reproduce the depth-averaged model results. The amplitude and phase contours (Figures 7.4–7.7) and elevation residuals (Figure 7.13) predicted by the three-dimensional model also show strong agreement with those of the depth-averaged model.

Plots of velocity vectors during neaps (Figures 7.30 and 7.31) and springs (Figures 7.32 and 7.33) at both the surface and mid-depth levels confirm the existence of the tidal gyres predicted by the depth-averaged model of Chapter 5. These gyres therefore have three-dimensional structure. Plots of residual vectors at surface, mid-depth and near-bed levels (Figures 7.34–7.36) show that the velocity residuals also have depth-varying structure.

Comparison of model predictions for tide-height constants with observed values (Figure 7.1) shows that the three-dimensional model gives only slightly poorer results ($\varepsilon = 4.02\,\mathrm{cm}$) than the depth-averaged model.

Comparison of model predictions for depth-dependent current ellipse characteristics with characteristics derived from observations show good overall agreement (Figures 7.37–7.43, Tables 7.2–7.6). Agreement at stations Mike and Lima is particularly close. The model successfully predicts a change in rotation direction of the semi-diurnals at Lima, looking down the water column. Discrepancies between model depth and station depth at Yarraville Shoals seem to be responsible for poor agreement obtained there. Depth discrepancies and the associated coarseness in bathymetric representation in the model may be responsible for the poorer agreement at stations Blue and White than was achieved at stations Mike, Lima, Red and Yellow.

As the number of tidal current stations increases and matches the number of available tide-height stations, it will be useful to consider an error measure similar to that used for the comparison of tide-height constants, in order to more quantitatively gauge the difference between predicted and observed tidal current constants. Since the tidal analysis program produces amplitude and phase for both components of tidal current, average absolute complex error measures for the u and v-components can be developed.

Snapshots of the vertical profiles of the velocity components show that reverse horizontal flows may occur near the sea bed and that these lead the surface flows that occupy the same horizontal position (see the u and v-component neap and spring profiles for stations

Mike and Lima in Figures 7.44 and 7.45).

In Chapter 8 a fine-grid depth-averaged Northern Spencer Gulf (NSG) model is developed. It models the wetting and drying of tidal flats. The open boundary information used to drive the model is obtained from the optimal depth-averaged SG model at a transect of that model. Rather than use only the major constituent amplitudes and phases at that transect, the entire spectrum of energy, including the minor constituents generated by the SG model and detected at the transect, is used.

The tidal flat scheme used is based on that of Flather and Heaps (1975), modified according to the discovery that advective and diffusive terms ought to be omitted in certain circumstances, as briefly discussed above (and at length in Chapter 3, Section 3.6, or as summarized in Chapter 8, Section 8.4).

The modelling of the wetting and drying process superimposes grid-scale oscillations on the solution field of the model because the coastal boundary is caused to move in discrete steps of element size. Following Flather and Heaps (1975) a three-point filter on the u factor of the x-advective term and on the v factor of the y-advective term is introduced. It is shown analytically that a filter of this form removes the grid-scale oscillation of wavelength equal to twice the grid spacing and that it attenuates the amplitude of all other waves, although its effect on the tidal constituents is very small.

The common four-point spatial averaging employed for the Coriolis velocity term, the remaining horizontal advective terms and in the quadratic friction terms is shown to have the same characteristics as the introduced filter. That is, the use of these four-point spatial averages is a built-in filtering feature of the difference scheme. It is further shown that time-centring the four-point spatial averages filters out temporal grid-scale waves of period equal to the time step.

Applying the scheme to the NSG model and using the constant quadratic friction coefficient used in the optimal depth-averaged model of Chapter 5 ($C_b = 0.0025$), the model gives results of poor accuracy. A calibration against constant quadratic friction coefficient gives an optimal global value of $C_b = 0.0013$ for the NSG model. This value is decreased in approximately the same proportion as the average depth of the model is reduced.

Using the value $C_b = 0.0013$ the elevation signals for Ward Spit reveal local instability towards the end of the 32-day simulation, the duration of which is admittedly a severe test of the scheme. Therefore filtering alone is not an adequate protection of the NSG model from the influence of the grid-scale oscillations generated by the tidal flat scheme. Locally stable behaviour is restored to the elements of Ward Spit only when the constant quadratic friction coefficient is increased to $C_b \simeq 0.0023$ (Figure 8.9) at which value global model accuracy has returned to "poor" status. The problem of poor global accuracy resides, in the immediate sense, in the uniformity of the constant quadratic friction coefficient. As we increase it, local instabilities at Ward Spit are gradually brought under control but tidal flows throughout the rest of the model are damped as a by-product.

Thus we seek a quadratic friction coefficient which is more able to focus the effect of friction in very shallow water where it is needed. The de Chèzy coefficient depends on a parameter n and the inverse cube-root of depth and has the ability to locally increase frictional dissipation in very shallow water. A calibration performed against the de Chèzy parameter gave an optimal value of $n = 0.017$ and a corresponding global accuracy slightly worse than that achieved by using $C_b = 0.0013$. The optimal value of n does not completely suppress the local instabilities at Ward Spit at the end of the simulation.

However, increasing the parameter to $n = 0.018$ is sufficient to control these instabilities and the corresponding decrease in global accuracy is small. That is, using $n = 0.018$ gives a significantly better global accuracy than using $C_b = 0.0023$.

Amplitude and phase contours (Figures 8.18–8.21), and ellipse plots (Figures 8.22–8.25) are presented for the four major constituents for the NSG model and these are the most detailed and accurate available to date. The tidal flat scheme correctly predicts that Ward Spit is uncovered only at Low Springs.

Comparison of predicted and observed tide-height constants (Table 8.3) for the six available stations in Northern Spencer Gulf gives a slightly improved combined error value for the NSG model compared to the error derived from an equivalent comparison of constants from the optimal depth-averaged model of Chapter 5 (Table 8.1). Both models predict similar constants for the diurnals, but whereas the SG model over-damps the semi-diurnals, the NSG model under-damps them.

The NSG model also provides slightly more accurate results for two of the largest minor constituents, $2SM_2$ and MS_4, which it predicts with reasonable accuracy.

The finer grid of the NSG model does not lead to an improvement in the prediction of the O_1 constituent — its amplitude is still more than 9 cm too high at Pt. Augusta. Both Tronson (1975) and Easton (1978) agree that none of the resonant frequencies of the Gulf coincide with the frequencies of the major tidal constituents, so the problem with O_1 is unlikely to be a resonant amplification of O_1 in the model. (However it is a project for future research to determine the resonant frequencies of the model itself.)

We come back to the fact that the NSG model is driven by data taken from the SG model and note that the SG data already has a significant O_1 error in it. The problem must have its root in the SG model. It may be that the open boundary specification of O_1 in the SG model is in error. This matter will be further researched.

The velocity residuals plot for the NSG model (Figure 8.26(a)) reveals a wealth of residual gyres in the region. The most prominent of these are two gyres off Lowly Point. One is anticlockwise rotating and is north of Lowly Point; the other is clockwise rotating and is south of Lowly Point (Figure 8.26(c)). These gyres most likely sustain Ward Spit, a suggestion also made by Green (1984). They are purely residual gyres because they are not present in the residuals if the advective terms are deleted (Figure 8.26(d)).

The common boundary of the two gyres is a line stretching from Lowly point to Ward Spit (Figure 8.26(c)). This line seems to mark a boundary of tidal circulation between the Gulf north and south of it. North of the line there seem to be small residual gyres between headlands, as Green (1984) has predicted (Figure 8.26(b)). A still finer grid from the Lowly Point region northwards may provide conclusive support for this, and help clarify uncertainties regarding upper Gulf flushing and the formation of Ward Spit.

Despite the high global accuracy achieved using the de Chèzy coefficient, there are indications that grid-scale oscillations persist in the model. As well, the NSG model under-damps the semi-diurnals and gives worse agreement with observed tidal current ellipse characteristics at stations Mike and Yarraville Shoals (see Figure 8.1 for location, Table 8.4 for characteristics) than does the SG model.

Recent work suggests that a recalibration of the value of reduced eddy coefficient a should be done for the NSG model. A value eight times greater than that used in the SG model may have to be used, and this in itself points to a much greater problem with grid-scale oscillations than was experienced with the SG model. It seems possible that using an appropriately large value of a will significantly reduce the grid-scale problem and may

even improve the prediction of the semi-diurnals so that they are no longer under-damped. It is not likely that adjusting a will significantly affect the diurnals. This is speculative and is the subject of further research.

A possible application of the NSG model is demonstrated. In order to model the effects of Greenhouse rises or falls in mean sea level, one can artificially add a layer of water of arbitrary thickness to the MSL of the model. Provided open boundary data can then be suitably prescribed and land contours are inserted to allow the coastal boundary to move inland where necessary, predictions of the inland movement can be obtained. The effect of wind in such scenarios will be particularly important.

The effect of wind in the case of the present NSG model is a subject for further research. Under the action of a strong wind one would expect wetting and drying activity to be strongly influenced.

Another further research project is the development of a three-dimensional tidal flat model of Northern Spencer Gulf. The extension into three dimensions seems straightforward, but it has been essential to fully explore the model's performance in the depth-averaged case before attempting it.

Another interesting area for future research is a suggestion by Black (1987) to specify depth at the velocity gridpoints. This practice would double the resolution of the present SG or NSG models without changing the grid size. The finite difference scheme would be simplified by no longer having to calculate the depths at velocity gridpoints by averaging depths at adjacent elevation gridpoints. In the case of Spencer Gulf the bathymetric data has been digitised and is now on a database, so obtaining the new set of depths ought to be straightforward and not necessarily a time-consuming exercise.

Recent developments in tidal modelling

A number of developments in the tidal modelling field have occurred in recent years which have not so far been acknowledged. It will be useful to view the present work alongside some of this recent work of other researchers.

Hearn and Hunter (1988) consider afresh the parameterization of bottom stress in depth-averaged models. The conventional parameterization, in terms of the depth-averaged current, is valid provided the vertical current profile is fairly uniform. Such is the case for flows driven by a pressure gradient: barotropic pressure-induced flows distribute the momentum input throughout the water column and flows of this nature have been considered in this thesis. However, for wind-driven motion the current may change markedly in the vertical and the conventional form of bottom stress parameterization may then be invalid. Consider a wind stress acting on a closed flat-bottomed basin. In the non-rotating case, the depth-averaged current and hence the conventional friction parameterization are both zero, but clearly there is non-zero bottom stress by reason of the return currents near the bed.

Davies (1988) also considers the deficiencies of the bed stress parameterization in terms of the depth mean current. The conventional approach requires that the bed stress formulation be in the same direction and be in phase with the depth mean current, and have a magnitude tied to that of the mean current. A more realistic parameterization would be to compute the bed stress from the near-bed current. In near-coastal wind-driven circulations the bottom current and depth mean current may be significantly different in both magnitude and direction to each other. Further, the influence of surface waves upon

the bed stress will be important in the shallow coastal regions and should be included in bed stress formulations, particularly in sediment transport models.

Hearn and Hunter (1988) describe a method of solving the depth-averaged equations in which bottom friction is expressed as a convolution integral derived from the three-dimensional equations. The convolution expresses the relationship between the bottom stress and the past histories of the sea surface stress and sea surface slope. Once the time history of bottom stress is derived the vertical profile of velocity at any horizontal gridpoint may be obtained by time integration of the horizontal dynamical equation. The method is designed to exactly reproduce the steady state velocities that arise in shallow waters as a result of a steady applied wind stress.

At this point it should be acknowledged that it is not unusual for authors of depth-averaged or vertically-integrated models to use a parameterization of bottom stress which includes a component directly related to the surface stress by means of a "wind correction factor". Arnold (1985, p.6) mentions several such authors, as do Jamart and Ozer (1987, p.405). Davies (1988, p.1258) also considers this approach and carries out numerical experiments to determine the value of the wind correction factor needed under different conditions of ratio of Ekman depth to water depth, eddy viscosity profile and friction coefficient. Davies (1988) concludes that the assignment of a single value to the wind correction factor is probably not physically justifiable. He finds that an optimized value of wind correction factor cannot take into account the various phase differences between depth mean current and bed stress that can be incorporated in his convolution model.

Hunter and Hearn (1989) demonstrate that the convolution technique gives steady-state results differing by less than 0.3% from benchmark solutions in one-dimensional and two-dimensional depth-averaged tests involving idealized geometries. However, there are several problems with the method. A fundamental problem is the inability of the method to remove unwanted inertial oscillations. Hunter and Hearn (1988) have investigated these and comment that they "reflect a basic sensitivity of the exact two-dimensional equations to numerical error at the inertial frequency" (ibid, p.1754). A further point is that, unlike the conventional method, their "single relaxation" approximation yields a final steady-state solution that is dependent on the initial conditions and is only physically correct when the initial velocity field is zero valued.

Apart from these difficulties, the problems reported as being solved by the method are completely linear and do not include the advective terms in the situation where they are most likely to be significant, viz. shallow waters. Also, in these days, concerns about the storage costs of three-dimensional models, which in part enliven the discussion of the convolution approximation, are increasingly less valid for the simple reason that storage is now cheaper to provide. Also, the objection that 2D models are fundamentally flawed in certain circumstances is irrelevant when one turns to 3D modelling, although other problems arise which must then be addressed.

Hearn and Hunter (1990) show that certain two and three-dimensional linear barotropic models of wind-driven flow in shallow seas are equivalent in that the predicted steady-state currents and the predicted surface slopes differ by only constant scaling factors. In the way that we considered, in Section 5.5, that the topographic gyres predicted by the depth-averaged model may possibly be an artifact of the depth-averaging process and not a real phenomenon, Hearn and Hunter (1990) ask whether one can assume that features of depth-averaged wind-driven flows will also be produced by three-dimensional models. Under restricted conditions they prove that features such as gyres are not suppressed in

the 3D model by the combination of vertical shear and a proper description of bottom stress. They also show it is possible to choose a value of bottom friction that allows a depth-averaged model to produce a current field identical to that derived from a three-dimensional model. This provides support for the common practice of calibrating linear depth-averaged models by adjusting the bottom friction factor to give agreement with observed current fields. Perhaps implicit in this result is another which would support our calibration of the linear depth-averaged model of Chapter 5 by adjusting the friction factor so as to minimize the difference between predicted and observed tide-height constants.

Hunter and Hearn (1991) investigate the steady-state limit of the convolution method. They establish criteria for ensuring that depth-averaged models, using the convolution parameterization of bottom friction, converge to a steady-state that is compatible with the (linearized) three-dimensional solution.

Lardner and Cekirge (1988) describe a "vertical/horizontal splitting (VHS) algorithm" for tidal and storm surge computations. This work is the basis of a series of articles they have published, many written with other researchers in connection with modelling studies of the Arabian Gulf.

At each time step, first the elevation and depth-averaged velocity components are computed by solving the non-linear depth-averaged equations. The ζ, U and V fields so generated are then used to compute the vertical velocity profiles by solving the linearized three-dimensional momentum equations.

The depth-averaged equations are solved by the method of characteristics. Details of the method are given by Lardner et al. (1986) and an application is given in a paper by Cekirge et al. (1986). (In an earlier paper by Lardner et al. (1982) the depth-averaged equations were solved by finite differences.) The three-dimensional equations are differenced using a weighted Crank-Nicolson scheme and are solved on a uniform grid with 11 depth levels. The stability of the Crank-Nicolson scheme is analytically verified by Lardner (1990). The vertical integration, which employs a bottom slip condition, is unconditionally stable. (The present scheme, using a no-slip condition, is also unconditionally stable — see Section 7.6.) Thus the stability of their overall scheme is determined by the stability of the scheme for solving the depth-averaged equations. It is possible they would obtain greater accuracy in the vertical for the same number of levels by using a non-uniform grid such as the κ-grid of Section 3.2. More recent work on the VHS scheme includes the use of sigma coordinates (see below), so further implementing a non-uniform grid may be straight-forward. Alternatively, greater accuracy in the vertical is obtained simply by using more grid levels (also implemented in more recent work — see below) but this will increase computational costs. Accuracy should also be improved by the inclusion of the advective terms in the three-dimensional equations. All non-linearity is relegated to the depth-averaged equations and here the computationally expensive advective terms are evaluated only once per time step at a given gridpoint in the horizontal plane — if included in the three-dimensional equations they would have to be evaluated at each depth level as well.

An advantage of solving both the depth-averaged and three-dimensional equations at the same time step in the VHS scheme is that the velocity profiles from the latter equations can be fed into the depth-averaged computations enabling their more accurate solution at the next time step. Specifically, the approximations

$$\frac{1}{H}\int_{-h}^{\zeta} u^2\,dz \simeq U^2,\quad \frac{1}{H}\int_{-h}^{\zeta} uv\,dz \simeq UV \quad\text{and}\quad \frac{1}{H}\int_{-h}^{\zeta} v^2\,dz \simeq V^2 \tag{9.1}$$

(c.f. equations (2.36)), conventionally used to simplify the depth-averaged expressions for the advective terms, do not need to be made since the integrals on the left hand sides of these expressions can now be evaluated directly. Further, since a slip bottom boundary condition is used in the three-dimensional equations, the computed value of bottom velocity can be used in the bottom friction term of the depth-averaged equations rather than the value of depth-averaged velocity. This presumably requires recalibration of the coefficient of quadratic friction.

Lardner and Cekirge (1988) test their scheme on the same model problem used by Davies and Owen (1979), viz. a constant wind blowing over a rectangular lake with dimensions similar to those of the North Sea. They find that the improved evaluation of the depth-averaged advective terms leads to little improvement in overall model accuracy for the test problem. This is not surprising given the lake has depth 65 m. However, the authors do suggest that in cases involving rapid flow in shallow regions it may be preferable to evaluate the integrals rather than make the approximations (9.1). In the case of the three-dimensional model of Spencer Gulf in Chapter 7 it will be interesting to test the validity of approximations (9.1) as a topic of future research.

Lardner and Cekirge (1988) claim that "an N-level finite difference algorithm with 11 vertical levels would be about 10 times slower than a 2D algorithm. In addition, the storage requirements of the present algorithm are about half those of the standard N-level algorithms since only two three dimensional arrays (for u and v) are required rather than four (for the current and new u and v)" (ibid, p.479). These comments may be generally true but in our case the **fully non-linear** three-dimensional 11-level model of Chapter 7 is only seven times slower than the depth-averaged model of Chapter 5. Their improved computational efficiency is obtained at the expense of a loss of accuracy which accompanies the linearization of the three-dimensional equations. In addition, as pointed out at the end of Section 3.3, the three-dimensional model developed here only uses two arrays (actually lists) for the u and v fields.

We also note that in their work on the Arabian Gulf Lardner et al. (1986) use a constant correction to the depth field obtained from hydrographic maps in order to produce a mean sea level field. The value of the correction is obtained in the course of tuning the model. We produced a correction for mean sea level **at every gridpoint** for our depth-averaged model of Spencer Gulf in Chapter 5.

Lardner et al. (1989) discuss certain implementation details of their model. In particular, they consider appropriate values for the model's hydrodynamic parameters and an interpolation scheme for calculating current velocities at non-gridpoint positions.

Al-Rabeh et al. (1990) extend the VHS model of Lardner and Cekirge (1988). They construct hydrodynamic models of the Arabian Gulf for wind-driven and tidal circulation. Instead of solving the depth-averaged equations by the method of characteristics, as did Lardner and Cekirge (1988), they use a finite difference scheme based on that of Leendertse (1967). (This signifies a return to the earlier use of finite differences for the solution of the depth-averaged equations by members of this modelling group — Lardner et al. (1982) also used finite differences based upon Leendertse's (1967) scheme for the depth-averaged equations.) Whereas bottom stress is generally expressed in terms of the depth-averaged current in most depth-averaged tidal models, Al-Rabeh et al. (1990) use the bottom current computed by the three-dimensional part of the VHS scheme, arguing that bottom stress is physically determined by bottom current. Thus they employ a slip condition at the bottom in both their depth-averaged and three-dimensional schemes.

In the vertical Al-Rabeh et al. (1990) depart from using the fixed finite difference grid of Lardner and Cekirge (1988) and introduce sigma coordinates. They do not use a non-uniform grid in the vertical but instead use 50 equally spaced levels. They use a piece-wise linear vertical eddy viscosity similar to that used by Davies (1980), Heaps and Jones (1981), Davies and Stephens (1983) and Davies and Furnes (1986).

Two implementations of their work are presented: (1) a model for computing tides and wind-driven circulation over the entire Arabian Gulf — employing a two-block variable grid system with a finer grid on the western coast along Saudi Arabia — and (2), a model for computing the tidal and wind-driven circulation for any user-defined area and enabling the user to examine the hydrodynamics of a particular region of interest in detail. Both implementations carry out three-dimensional computations when the conventional two-dimensional hypotheses are locally inadequate or when directed by the user. Otherwise, only the depth-averaged computation is carried out.

For the Strait of Hormuz, across which the open boundary of their Arabian Gulf model runs, they specify the amplitudes and phases of the nine most significant tidal constituents. Al-Rabeh et al. (1990) state that the models run for "74 hours of real [i.e. simulated] time to reach conditions that are reproduced from one tidal period to another indepedent of initial conditions" (ibid, p.414). This suggests that model starting transients are not dissipated until that time, after which they store predictions for tidal analysis. This is very similar to our experience with the Spencer Gulf models where starting transients seemed largely to have dissipated by 72 hours simulated time. Al-Rabeh et al. (1990) do not state how long their overall simulation lasts, but it is presumably long enough to enable the four major constituents (O_1, K_1, M_2 and S_2) to be separated out. Results for these show reasonable agreement with observed values. We infer they forced the model at the open boundary using all nine constituents simultaneously. Open boundary elevations for the finer grid model are supplied from the Arabian Gulf model.

Lardner and Smoczynski (1990) present a number of further extensions of the VHS algorithm. An alternative approach to the vertical part of the algorithm, based on finite elements, is given and has the advantage of being unconditionally stable. The only restriction on the time step comes from the CFL (Courant-Friedrichs-Lewy) requirement imposed by the horizontal part of the scheme. The advective terms of the three-dimensional momentum equations are now included and so are sigma coordinates in the vertical. The authors explain that for deep water flows these latter inclusions have little effect, but for rapid flows in shallow waters, or sharply varying bathymetries, it is probably essential to include them. They also report that the depth-averaged equations are solved using an explicit finite-difference leap-frog algorithm which appears to be more accurate than their earlier algorithm using the method of characteristics. Their finite difference grid is staggered in both space and time, producing second order accuracy in all the dominant terms whilst being fully explicit and therefore fast. They do not include the horizontal diffusion of momentum. They use a bottom stress condition formulated as a combination of linear and quadratic friction, and expressed in terms of the bottom velocity components rather than the depth-averaged components. Coastal boundary volume flux components are treated by either setting them to zero at each such point according to the direction of the coastal line segment at that point, or by using the actual orientation of the coastline. The authors find that their algorithm is, depending on whether the time-consumptive non-linear advective terms are included, four to seven times slower than a standard depth-averaged model. This means their scheme is approximately as computationally efficient

as our own three-dimensional scheme.

Lardner et al. (1988b) develop a pollutant transport model for the Arabian Gulf. Their main interest is to simulate oil spills since oil is the most widespread pollutant in the Gulf region, with estimates as high as 1.5 million tons spilled annually. Furthermore, it is a complex pollutant. Not only does it form a subsurface plume as well as a surface slick, both of which are subject to advective and diffusive motions, but it is a multicomponent hydrocarbon on a distinctly different fluid (sea water) subject to weathering effects and other phenomena. Not surprisingly, then, small experimental spills have been conducted in order to gather empirical data from which to formulate spreading formulae and the like (Lehr et al., 1984a,b). Since Lardner et al. (1988b) believe the residual currents adjacent to the coast of Saudi Arabia are dominated by wind-forcing, they compute the mean wind-driven currents for each month. In earlier papers, Lardner et al. (1987, 1988a) estimate the density-driven and wind-driven currents in the Gulf and compare their estimates with empirical data. Here, Lardner et al. (1988b) simulate a 5000-barrel surface oil spill and present results which emphasize the importance of the subsurface plume. Estimates for the percentage of oil that evaporates and that reaches landfall are also presented.

Cekirge et al. (1989) develop an algorithm for determining surface currents under given wind conditions for the prediction of surface oil spill trajectories in the Arabian Gulf. The algorithm interpolates from sets of surface current velocities already obtained from a three-dimensional VHS hydrodynamic model of the Arabian Gulf. Runs of that model have been conducted using prespecified wind velocities that are combinations of the eight cardinal wind directions and seven wind speeds, and a database of surface current velocities for the selected wind conditions has been created. The proposed algorithm uses the database to compute surface currents for various wind conditions. The intention is that estimates of spill trajectories be able to be conducted by users who do not have access to a computer on which could be run the VHS model.

Lardner and Das (1991) compute the flow driven by density gradients in the Arabian Gulf using a different method to that used by Lardner et al. (1987). Their results, however, are very similar and they also conclude that the density driven flows are much less significant than wind-driven flows.

Davies (1990) considers the extension of the spectral/modal approach in the vertical to include the no-slip bottom condition and a time-varying vertical eddy viscosity coefficient. Both of these extensions are features of the three-dimensional finite difference model developed in Chapter 7. Davies (1990) suggests that it is important to include a time-varying vertical eddy viscosity coefficient to facilitate the accurate generation of higher harmonics. A study of this phenomenon should be carried out in the case of the three-dimensinal model of Chapter 7. He also states that his studies show it is necessary to include of the order of 45 depth levels in a vertical finite difference scheme on a logarithmically transformed grid.

Davies and Proctor (1990) discuss an algorithm for solving the three-dimensional linearized tidal equations and the vectorization of the corresponding computer code for running on a CRAY X-MP. A decomposition into equations describing changes in the sea surface elevation and equations describing vertical current structure is carried out. The resulting algorithm uses an explicit finite difference scheme in the horizontal and an implicit spectral approach in the vertical, both of which are vectorizable. In one approach to vectorizing in the horizontal, computations are carried out at all elements of the rectangular grid which encompasses the model region, regardless of whether they concern land

or active sea elements. Thus the vectors used are as long as the number of elements in the rectangular grid. A mask (either a bit mask or an integer mask of 0 and 1) is used to mask out unwanted calculations.

Davies and Proctor (1990) point out that vector performance on the CRAY is optimized when the vector registers (of 64 words each) are full. They discuss two approaches to vectorizing in the vertical. In the first they compute horizontally row-wise, only over water elements, vectorizing in the vertical. This approach may be computationally more efficient when a major part of the model region does not contain water elements and an expansion in terms of many modes (or register-multiples of modes) is sought. In the second they compute by vertical mode, over all elements, vectorizing in the horizontal. This approach uses a mask and may be more efficient when most elements are active and an expansion in terms of much fewer than 64 modes is required. This second approach is essentially how Nixon (1992) has vectorized the three-dimensional finite difference program discussed in Chapter 7 and makes the finite difference vertical solution as amenable to vectorization as Davies (1991) finds the modal approach is vectorizable.

It is certainly true, as Davies and Proctor (1990) state, that the advent of vector (and parallel) machines has required programmers to re-examine their algorithms and either reapply them to suit the design of the machine or develop new approaches. Efficient programming methods on scalar machines do not necessarily transfer to the new machines as efficient methods.

Because the gathering of tidal data is so crucial to the proper forcing of models and to their accurate calibration, some recent developments in data collection will now be reviewed.

In the last ten years, new techniques have been developed for gathering information about tidal currents. To this point, data has been collected by current meters at usually widely separated locations and at a small number of depth levels in the water column. The new technologies, however, show a promise of gathering continuous (depth-dependent) data over substantial time periods and over large areas.

Land-based HF radar (specifically, a unit called OSCR, "Ocean Surface Current Radar") has been used by Prandle and Ryder (1989) to map tidal ellipse distributions. The OSCR unit measures radial components of tidal velocity at intervals of 1.2 km along each of up to 16 beams to an offshore range of 50 km. "By deploying two units with overlapping beams, surface current vectors can be resolved at approximately 1.8 km intervals over a region 18 km square" (ibid, p.942). Amplitudes, phases and directions of M_2 and M_4 tidal ellipses are shown to be in reasonable agreement with predictions from a numerical model using square elements of dimension 1 km×1 km.

Simpson et al. (1990) have used a ship mounted acoustic Doppler current profiler (ADCP) to determine the velocity profile of water in a channel. The volume backscattering of sound is used to determine the vertical profile from the Doppler shift in the frequency of a returned signal. This can be done as the ship is moving, but the relatively slow speed of the ship forces a compromise between the spatial/temporal coverage of flow events and the vertical gathering of data in the water column, preventing direct observation of velocity shear in the near-surface and near-bottom zones. However, the ADCP-determined flow structure is found to be consistent with the M_2 predictions of a numerical model.

Modelling prawn larvae movement in Spencer Gulf

Spencer Gulf supports a substantial prawn fishing fleet (39 boats in 1988) whose annual catch is valued at approximately $20 million (Australian). The fleet operates predominantly in the vicinity of Wallaroo. Following the first depth-averaged model predictions of tidal gyres and cross-Gulf currents made by the author in 1985 (see Bills and Noye, 1986) it seemed possible that the gyres may influence the distribution of prawns and prawn larvae in the region.

Contact with Mr. Neil Carrick of the South Australian Department of Fisheries has provided some weight to this possibility and has lead to the instigation of collaborative investigations of prawn larvae movement in the Gulf. On the basis of frequent sampling and tagging operations, the Dept. of Fisheries stringently controls both the areas where fishing may take place and the size of the subsequent catch in order to prevent over-fishing of the prawns. Depletion of the resource could easily occur because of the size of the fleet and the "high-tech" fishing methods employed.

The field sampling programs have shown that by some means the larvae move from spawning grounds between Wallaroo and Lima (see Figure 5.15) to nursery grounds on the coast west of Lima, crossing the deep channel between. This has been a surprising outcome of field investigations since the presumed rectilinear tidal flows in the central Gulf combined with the assumption that the larvae can move only in the vertical under their own propulsion and are otherwise swept along by the prevailing longitudinal flows, suggest there is no means for the larvae to make the crossing. However, a mechanism for their transport may involve the cross-Gulf flows predicted by both the depth-averaged model of Chapter 5 (see Figures 5.32–5.35) and the three-dimensional model of Chapter 7 (see Figures 7.30–7.33).

As part of research presently being undertaken by Nixon (1992) it is proposed to first model the movement of the larvae throughout the whole Gulf and then to run detailed simulations focusing on the region north of the Franklin Harbour transect. At present SADOF is conducting an intensive field study of the daily life cycle of the prawns in their development from larvae to adults. In a 24 hour period it is believed the larvae spend different lengths of time at different levels in the water column and that these diurnal characteristics alter as the larvae develop into adulthood. Rothlisberg et al. (1983) have proposed nine separate models of diurnal activity for prawns of the Gulf of Carpentaria region, but it is thought that different prawn species have different characteristic diurnal patterns. The South Australian prawn has only recently become the subject of close investigation.

Given models of the diurnal behaviour of the larvae it is straightforward to use the three-dimensional program to determine the prevailing tidal and wind-driven spatial amd temporal velocity fields and so find the dominant pattern of movement of the larvae. The velocity fields are in fact used as input to an advection-diffusion model of larval movement (see Noye et al., 1992) for which appropriate boundary conditions need to be established and appropriate capture criteria at coastal nursery areas need to be developed. Comparing model results with the results of field studies will assist in determining which of the proposed diurnal models of larval activity is most accurate, and this in turn should lead to more accurate models. The three-dimensional current structure given by the tidal model is required because the larvae are located at different levels at different times and are subjected to different lateral forces at each level. The vertical velocity of the water

is not significant in this because of the control the larvae seem to have over their own vertical position.

It is preferable to generate the three-dimensional current predictions first and then apply each proposed diurnal larval model to the resultant velocity fields than to consecutively incorporate each diurnal model into three-dimensional simulations. This is because the generation of tidal current fields over such a vast region at the fine scale proposed is prohibitively expensive, whereas runs of the advection-diffusion model are relatively cheap. The former approach also allows the researcher to investigate the dispersion of larvae from different spawning grounds with ease. It is because of the lengthy processing time required for the tidal computations that the use of a supercomputer has been sought. Any meaningful study will involve simulations spanning both seasonal spawnings of the prawns (mid-December and mid-February each season) and so requires tidal simulations of six months duration. Realistic wind fields will be used in the simulations.

The work on this to date is summarized in Noye et al. (1992). Vectorization of the Fortran code of the three-dimensional program so that the tidal simulations can run efficiently on a Cray is described in Nixon (1992). Some modifications to the overall numerical scheme have been implemented by Nixon with the result that the vectorized program uses only 4 min of Cray processor time to perform a 32-day tidal simulation on the coarse-grid three-dimensional model of Spencer Gulf.

Bibliography

Alpert, P. (1981), "Implicit filtering in conjunction with explicit filtering", Journal of Computational Physics, **44**, pp. 212–219.

Al-Rabeh, A. H., Gunay, N. and Cekirge, H. M. (1990), "A hydrodynamic model for wind-driven and tidal circulation in the Arabian Gulf", Applied Mathematical Modelling, **14**, pp. 410–419.

Arakawa, A. and Lamb, V. R. (1977), "Computational design of the basic dynamical processes of the UCLA general circulation model", Methods in Computational Physics, **17**, pp. 173–265.

Arnold, R. J. (1985), "Mathematical modelling of wind effects on closed lakes", Ph. D. thesis, University of Adelaide, South Australia, 240 pp.

Arnold, R. J. (1987), "An improved open boundary condition for a tidal model of Bass Strait", in "Numerical Modelling: Applications to Marine Systems", ed. J. Noye, Elsevier Science Publishers B. V. (North-Holland), pp. 145–158.

Arnold, R. J. and Noye, B. J. (1984), "On the performance of turbulent energy closure schemes for wind driven flows in shallow seas", in "Computational Techniques and Applications: CTAC-83", eds. J. Noye and C. Fletcher, Elsevier Science Publishers B. V. (North-Holland), pp. 425–437.

Arnold, R. J. and Noye, B. J. (1986a), "Open boundary conditions for a tidal and storm surge model of Bass Strait", in "Computational Techniques and Applications: CTAC-85", eds. J. Noye and R. May, Elsevier Science Publishers B. V. (North-Holland), pp. 503–517.

Arnold, R. J. and Noye, B. J. (1986b), "A three-dimensional tidal and storm surge model of Bass Strait", Appendix 4 in "Numerical tidal and storm surge models of Bass Strait", Report to Marine Sciences and Technologies Scheme (Grant 82/1033), The University of Adelaide, South Australia. Also submitted to "Progress in Oceanography".

Backhaus, J. O., Crean, P. B. and Lee, D. K. (1987), "On the application of a three-dimensional numerical model to the waters between Vancouver Island and the mainland coast of British Columbia and Washington State", in "Three-Dimensional Coastal Ocean Models", Coastal and Estuarine Sciences **4**, ed. N. S. Heaps, American Geophysical Union, Washington, D. C., pp. 149–175.

Ball, F. K. (1964), "An exact theory of simple finite shallow water oscillations on a rotating earth", in Proceedings First Australian Conference on Hydraulics and Fluid Mechanics, University of Western Australia, December 1962, Pergamon Press, pp. 293–305.

Batten, M. L. and Han, Y.-J. (1981), "On the computational noise of finite-difference

schemes used in ocean models", Tellus, **33**, pp. 387–396.

Bennett, A. F. (1976), "Open boundary conditions for dispersive waves", Journal of the Atmospheric Sciences, **33**, pp. 176–182.

Bennett, A. F. and McIntosh, P. C. (1982), "Open ocean modelling as an inverse problem: tidal theory", Journal of Physical Oceanography, **12**, No. 10, pp. 1004–1018.

Bills, P. J. (1981), "Sea transport study of Spencer Gulf, South Australia", research progress report to the South Australian Department of Transport, November 1981, 49 pp.

Bills, P. J. (1982), "Sea transport study of Spencer Gulf, South Australia", research progress report to the South Australian Department of Transport, December 1982, 90 pp.

Bills, P. J. (1985), "Sea transport study of Spencer Gulf, South Australia", research progress report to the South Australian Department of Transport, July 1985, 97 pp.

Bills, P. J. and Noye, B. J. (1984), "Verification of a three-dimensional tidal model for coastal seas", in "Computational Techniques and Applications: CTAC-83", eds. J. Noye and C. Fletcher, Elsevier Science Publishers B. V. (North-Holland), pp. 394–410.

Bills, P. J. and Noye, B. J. (1986), "Tides of Spencer Gulf, South Australia", in "Computational Techniques and Applications: CTAC-85", eds. J. Noye and R. May, Elsevier Science Publishers B. V. (North-Holland), pp. 519–531.

Bills, P. J. and Noye, B. J. (1987), "An investigation of open boundary conditions for tidal models of shallow seas", in "Numerical modelling: Applications to Marine Systems", ed. J. Noye, Elsevier Science Publishers B. V. (North-Holland), pp. 159–194.

Bills, P. J. and Noye, B. J. (1992), "Numerical model of a coastal sea with tidal flats", to be published in "Computational Techniques and Applications: CTAC-91", eds. J. Noye, B. Benjamin and L. Colgan.

Black, K. P. (1987), "The hydrodynamic model, 2DD", personal communication.

Blumberg, A. F. (1977), "Numerical tidal model of Chesapeake Bay", Journal. Hydraulics Division, American Society of Civil Engineers, **103**, No. HY1, pp. 1–10.

Blumberg, A. F. (1987), "A description of a three-dimensional coastal ocean model", in "Three-Dimensional Coastal Ocean Models", Coastal and Estuarine Sciences 4, ed. N. S. Heaps, American Geophysical Union, Washington, D. C., pp. 1–16.

Blumberg, A. F. and Kantha, L. H. (1985), "Open boundary condition for circulation models", Journal of Hydraulic Engineering, American Society of Civil Engineers, **111**, No. 2, pp. 237–255.

Blumberg, A. F. and Mellor, G. L. (1983), "Diagnostic and prognostic numerical circulation studies of the South Atlantic Bight", Journal of Geophysical Research, **88**, No. C8, pp. 4579–4592.

Bode, L. (1986), Discussion to "Modelling tidal circulation in an island's wake", by R. A. Falconer, E. Wolanski and L. Mardapitta-Hadjipandeli, Journal. Waterway, Port, Coastal, and Ocean Engineering, American Society of Civil Engineers, **112**, No. 2, pp. 234–254, March 1986.

Bode, L. and Sobey, R. J. (1984), "Initial transients in long wave computations", Journal of Hydraulic Engineering, American Society of Civil Engineers, **110**, No. 10, pp. 1371–1397.

Bode, L. and Sobey, R. J. (1992), "Hurricane storm surge", to be published in "Tides and Surges", ed. J. Noye, Monograph of the American Geophysical Union.

Bowden, K. F. (1978), "Physical problems of the benthic boundary layer", Geophysical Surveys, **3**, pp. 255–296.

Bowden, K. F., Fairbairn, L. A. and Hughes, P. (1959), "The distribution of shearing stresses in a tidal current", Geophysical Journal. Royal Astronomical Society, **2**, pp. 288–305.

Bowden, K. F. and Hamilton, Peter (1975), "Some experiments with a numerical model of circulation and mixing in a tidal estuary", Estuarine and Coastal Marine Science, **3**, pp. 281–301.

Bowers, D. G., Rippeth, T. P. and Simpson, J. H. (1991), "Tidal friction in a sea with two equal semidiurnal tidal constituents", Continental Shelf Research, **11**, No. 2, pp. 203–209.

Bragg, W. H., Inglis, A., Lyle, T. R. and Chapman, R. W. (1892), "The tides of the coast of South Australia", Report of Committee No. 2, Australasian Association for the Advancement of Science, Hobart, Tasmania.

Bullock, D. A. (1973), "The general circulation of St. Vincent's Gulf and Spencer Gulf", in "Physical Oceanography", Proceedings Second South Australian Regional Conference, Department of Applied Mathematics, University of Adelaide, B. J. Noye Convenor, pp. 19–50.

Cekirge, H. M., Al-Rabeh, A. H. and Gunay, N. (1989), "Determining the wind-driven surface currents for prediction of movements of oil slicks in the Arabian Gulf", Computers and Mathematics with Applications, **17**, No. 11, pp. 1449–1453.

Cekirge, H. M., Lardner, R. W. and Fraga, R. J. (1986), "Adaption of the solution of the two-dimensional tidal equations using the method of characteristics to wind-induced currents and storm surges", Computers and Mathematics with Applications, **12A**, No. 10, pp. 1081–1090.

Charnock, H. (1959), "Tidal friction from currents near the seabed", Geophysical Journal. Royal Astronomical Society, **2**, No. 2, pp. 215–221.

Chalabi, A. (1979), "Resolution numerique des equations de Saint-Venant dans un domaine a frontiere variable". (Marked as paper No. 314, pp. 15. Source unknown.)

Chapman, D. C. (1985), "Numerical treatment of cross-shelf open boundaries in a barotropic coastal ocean model", Journal of Physical Oceanography, **15**, No. 8, pp. 1060–1075.

Chapman, R. W. (1938), "The tides of Australia", The Official Year Book of the Commonwealth of Australia, **31**, pp. 972–984.

Chapman, R. W. and Inglis, A. (1898), "The tides of South Australia", Australasian Association for the Advancement of Science, Sydney, Australia.

Chapman, R. W. and Captain Inglis (1895), "The tides of South Australia", Royal Geographical Society of Australasia, South Australian Branch.

Chapman, R. W. and Inglis, A. (1903), "Australian tides", Geographical Society of South Australia, 18 pp.

Cooper, C. K. and Pearce, B. R. (1977), "A three-dimensional numerical model to calculate currents in coastal waters utilizing a depth varying vertical eddy viscosity", Ralph M. Parsons Laboratory for Water Resources and Hydrodynamics, Report No. 226, MIT, Dept. Civil Engineering, Cambridge, Mass., 147 pp.

Cunge, J. A. (1977), "Difficulties of open channel hydraulic mathematical modelling as

applied to real life situations", in Applied Mathematical Modelling, ed. C. A. Brebbia, Pentech Press, London.

Davies, A. M. (1980), "On formulating a three-dimensional hydro-dynamic sea model with an arbitrary variation of vertical eddy-viscosity", Computer Methods in Applied Mechanics and Engineering, **22**, pp. 187–211.

Davies, A. M. (1985a), "Application of a sigma coordinate sea model to the calculation of wind induced currents", Continental Shelf Research, **4**(4), pp. 389–423.

Davies, A. M. (1985b), "Application of the DuFort-Frankel and Saul'Ev methods with time splitting to the formulation of a three dimensional hydrodynamic sea model", International Journal of Numerical Methods in Fluids, **5**, pp. 405–425.

Davies, A. M. (1985c), "A three dimensional model of wind induced flow in a sea region", Progress in Oceanography, **15**, pp. 71–128.

Davies, A. M. (1988), "On formulating two-dimensional vertically integrated hydrodynamic numerical models with an enhanced representation of bed stress", Journal of Geophysical Research, **93**, No. C2, pp. 1241–1263.

Davies, A. M. (1990), "On the importance of time varying eddy viscosity in generating higher tidal harmonics", Journal of Geophysical Research, **95**, No. C11, pp. 20287–20312.

Davies, A. M. (1991), On the accuracy of finite difference and modal methods for computing tidal and wind wave current profiles", International Journal for Numerical Methods in Fluids, **12**, No. 2, pp. 101–124.

Davies, A. M. and Furnes, G. K. (1986), "On determination of vertical structure functions for time dependent flow problems", Tellus, **38A**, pp. 462–477.

Davies, A. M. and Jones, J. E. (1990), "Application of a three-dimensional turbulence energy model to the determination of tidal currents on the northwest European shelf", Journal of Geophysical Research, **95**, No. C10, pp. 18143–18162.

Davies, A. M. and Owen, A. (1979), "Three dimensional numerical sea model using the Galerkin method with a polynomial basis set", Applied Mathematical Modelling, **3**, pp. 421–428.

Davies, A. M. and Proctor, R. (1990), "Developing and optimizing a 3-D-spectral/finite difference hydrodynamic model for the CRAY X-MP", Computers and Fluids, **18**, No. 3, pp. 259–270.

Davies, A. M. and Stephens, C. V. (1983), "Comparison of the finite difference and Galerkin methods as applied to the solution of the hydrodynamic equations", Applied Mathematical Modelling, **7**, pp. 226–240.

Dronkers, J. J. (1964), "Tidal computations in rivers and coastal waters", published by North-Holland, 518 pp.

Dube, S. K., Sinha, P. C. and Roy, G. D. (1986), "The effect of a continuously deforming coastline on the numerical simulation of storm surges in Bangladesh", Mathematics and Computers in Simulation, **28**, pp. 41–56.

Easton, A. K. (1970), "The Tides of the Continent of Australia", Research paper No. 37, Horace Lamb Centre for Oceanographical Research, Flinders University of South Australia, South Australia, 326 pp.

Easton, A. K. (1977), "Selected programs for tidal analysis and prediction", Computing Report No. 9, Flinders Institute for Atmospheric and Marine Sciences, Flinders University of South Australia.

Easton, A. K. (1978), "A reappraisal of the tides in Spencer Gulf, South Australia",

Australian Journal of Marine and Freshwater Research, 1978, **29**, pp. 467–477.

Fandry, C. B. (1983), "Model for the three-dimensional structure of wind-driven and tidal circulation in Bass Strait", Australian Journal of Marine and Freshwater Research, **34**, pp. 121–141.

Flather, R. A. (1972), "Analytical and numerical studies in the theory of tides and storm surges", Ph. D. Thesis, University of Liverpool, 214 pp.

Flather, R. A. (1976), "A tidal model of the North-West European Continental Shelf", Memoires. Societe Royale des Sciences de Liege, 6^{e} série, tome X, pp. 141–164.

Flather, R. A. and Heaps, N. S. (1975), "Tidal computations for Morecambe Bay", Geophysical Journal. Royal Astronomical Society, **42**, pp. 489–517.

Flather, R. A. and Hubbert, K. P. (1990), "Tide and surge models for shallow water — Morecambe Bay revisited", in "Modeling Marine Systems", Volume 1, ed. A. M. Davies, CRC Press, Boca Raton, Florida, pp. 135–166.

Flather, R. A. and Proctor, R. (1983), "Prediction of North Sea storm surges using numerical models: recent developments in U.K.", in "North Sea Dynamics", ed. by Sündermann/Lenz, Springer-Verlag Berlin Heidelberg, pp. 299–317.

Flinders, M. (1814), "A voyage to Terra Australis". G. & W. Nicol, London, Vol. 1, p. 150.

Foreman, M. G. G. (1978), "Manual for tidal current analysis and prediction", Pacific Marine Science Report 78–6, Institute of Ocean Sciences, Patricia Bay, Sidney, B. C., Canada.

Freeman, N. G. S. (1970), "The application of sigma coordinates to the numerical modelling of Great Lakes' hydrodynamics", M. App. Sc. thesis, University of Waterloo.

Freeman, N. G., Hale, A. M. and Danard, M. B. (1972), "A modified sigma equations' approach to the numerical modelling of Great Lakes hydrodynamics", Journal of Geophysical Research, **77**, No. 6, pp. 1050–1060.

Gopalakrishnan, T. C. (1989), "A moving boundary circulation model for regions with large tidal flats", International Journal for Numerical Methods in Engineering, **28**, pp. 245–260.

Green, H. S. (1984), "Fluid transport processes in Upper Spencer Gulf", Marine Geology, **61**, pp. 181–195.

Green, H. S. and Liepnik, R. B. (1970), "Sources of Plasma Physics", published by Wolters-Noordhoff, Groningen, 630 pp.

Greenberg, D. A. (1975), "Mathematical studies of tidal behaviour in the Bay of Fundy", Ph. D. thesis, University of Liverpool, England.

Greenberg, D. A. (1983), "Modeling the mean barotropic circulation in the Bay of Fundy and Gulf of Maine", Journal of Physical Oceanography, **13**, pp. 886–904.

Gustafsson, B. (1975), "The convergence rate for difference approximations to mixed initial boundary value problems", Mathematics of Computation, **29**, No. 130, pp. 396–406.

Hansen, W. (1962), "Hydrodynamical methods applied to oceanographic problems", in Proc. Symp. Math. Hydro. Methods of Phys. Oceanography, Sept. 1961, Mitt. Inst. Meeresk. Univ. Hamburg, No. 1, pp. 25–34.

Hayashi, T., Greenberg, D. A. and Garrett, C. J. R. (1986), "Open boundary conditions for numerical models of shelf sea circulation", Continental Shelf Research, **5**, No. 4, pp. 487–497.

Heaps, N. S. (1969), "A two-dimensional numerical sea model", Philosophical Transactions. Royal Society of London. Series A. Mathematical and Physical Sciences,

265, pp. 93–137.

Heaps, N. S. (1973), "Three-dimensional numerical model of the Irish Sea", Geophysical Journal. Royal Astronomical Society, **35**, pp. 99–120.

Heaps, N. S. and Jones, J. (1981), "Three-dimensional model for tides and surges with vertical eddy viscosity prescribed in two layers – II. Irish Sea with bed friction layer", Geophysical Journal. Royal Astronomical Society, **64**, pp. 303–320.

Hearn, C. J. and Hunter, J. R. (1988), "A new method of describing bottom stress in two-dimensional hydrodynamical models of shallow homogeneous seas, estuaries and lakes", Applied Mathematical Modelling, **12**, pp. 573–580.

Hearn, C. J. and Hunter, J. R. (1990), "A note on the equivalence of some two- and three-dimensional models of wind-driven barotropic flow in shallow seas", Applied Mathematical Modelling, **14**, pp. 553–556.

Henry, R. F. (1982a), "Automated programming of explicit shallow-water models. Part I. Linearized models with linear or quadratic friction", Canadian Technical Report of Hydrography and Ocean Sciences No. 3: iv + 70 p.

Henry, R. F. (1982b), "Automated digital simulation of tides and long waves", Paper No. 58, Abstracts, 18th International Conference on Coastal Engineering, Capetown, November 1982, pp. 114–116.

Holsters, H. (1978), "Mathematical modelling of tidal flats: a few remarks", in "Lecture Notes on Coastal and Estuarine Studies. Volume 1. Mathematical Modelling of Estuarine Physics", Proceedings of an International Symposium held at the German Hydrographic Institute, Hamburg, August 24–26, 1978, pp. 172–177.

Hunter, J. R. and Hearn, C. J. (1988), "On the convolution method of describing bottom friction in depth-averaged models", Journal of Physical Oceanography, **18**, pp. 1752–1754.

Hunter, J. R. and Hearn, C. J. (1989), "The single relaxation approximation for bottom stress in two-dimensional hydrodynamic models of shallow seas", Continental Shelf Research, **9**, No. 5, pp. 465–478.

Hunter, J. R. and Hearn, C. J. (1991), "On obtaining the steady-state solutions of the linearized three-dimensional hydrodynamic equations", Applied Mathematical Modelling, **15**, pp. 200–208.

I'Anson, K. (1989), "A numerical model of the movement of prawn larvae in Spencer Gulf", Honours thesis, The University of Adelaide, 164 pp.

Jamart, B. M. and Ozer, J. (1987), "Comparison of 2-D and 3-D models of the steady wind-driven circulation in shallow waters", Coastal Engineering, **11**, pp. 393–413.

Johns, B. (1966), "On the vertical structure of tidal flow in river estuaries", Geophysical Journal. Royal Astronomical Society, **12**, pp. 103–110.

Johns, B. (1969), "On the representation of the Reynolds stresses in a tidal estuary", Geophysical Journal. Royal Astronomical Society, **17**, pp. 39–44.

Johns, B. (1978), "The modeling of tidal flow in a channel using a turbulence energy closure scheme", Journal of Physical Oceanography, **8**, pp. 1042–1049.

Johns, B. and Oguz, T. (1987), "Turbulent energy closure schemes", in "Three-Dimensional Coastal Ocean Models", Coastal and Estuarine Sciences **4**, ed. N. S. Heaps, American Geophysical Union, Washington, D. C., pp. 17–39.

Jung, K., Bills, P. J. and Noye, J. (1986), "A comparison of the finite difference and Galerkin methods in modelling depth-dependent channel flow", in "Computational Techniques and Applications: CTAC-85", eds. J. Noye and R. May, Elsevier Sci-

ence Publishers B. V. (North-Holland), pp. 533–553.
Jung, K., Bills, P., Stevens, M. and Noye, J. (1987), "Comparison of finite difference and Galerkin methods in modelling depth-dependent tidal flow in channels", in "Numerical modelling: Applications to Marine Systems", ed. J. Noye, Elsevier Science Publishers B. V. (North-Holland), pp. 123–143.
Kelly, L. R. (1979), "Tidal characteristics of the Spencer Gulf, South Australia", Honours thesis (unpublished), Flinders University of South Australia, 62 pp.
Knight, D. W. (1973), "Long wave propagation in idealized estuary", Journal of the Hydraulics Division, American Society of Civil Engineers, **99**, No. HY7, pp. 993–1007.
Kullenberg, G. (1982), "Pollutant Transfer and Transport in the Sea", Vol. 1, ed. G. Kullenberg, CRC Press, Inc., Boca Raton, Florida, 227 pp.
Landau, L. D. and Lifshitz, E. M. (1989), "Fluid Mechanics", second edition, Maxwell MacMillan International, pp. 539.
Lardner, R. W. (1990), "Stability of the numerical solution of a parabolic system with integral subsidiary conditions", Computers and Mathematics with Applications, **19**, No. 12, pp. 41–46.
Lardner, R. W., Al-Rabeh, A. H., Gunay, N. and Cekirge, H. M. (1989), "Implementation of the three-dimensional hydrodynamic model for the Arabian Gulf", Advances in Water Resources, **12**, pp. 2–8.
Lardner, R. W., Belen, M. S. and Cekirge, H. M. (1982), "Finite difference model for tidal flows in the Arabian Gulf", Computers and Mathematics with Applications, **8**, No. 6, pp. 425–444.
Lardner, R. W. and Cekirge, H. M. (1988), "A new algorithm for three-dimensional tidal and storm surge computations", Applied Mathematical Modelling, **12**, pp. 471–481.
Lardner, R. W., Cekirge, H. M. and Gunay, N. (1986), "Numerical solution of the two-dimensional tidal equations using the method of characteristics", Computers and Mathematics with Applications, **12A**, No. 10, pp. 1065–1080.
Lardner, R. W. and Das, S. K. (1991), "On the computation of flows driven by density gradient: residual currents in the Arabian Gulf", Applied Mathematical Modelling, **15**, pp. 282–294.
Lardner, R. W., Fraga, R. J., Lehr, W. J. and Sarhan, M. A. (1988a), "Residual circulation in the Arabian Gulf II: wind-driven flow", The Arabian Journal for Science and Engineering, **13**, No. 3, pp. 411–423.
Lardner, R. W., Lehr, W. J., Fraga, R. J. and Sarhan, M. A. (1988b), "A model of residual currents and pollutant transport in the Arabian Gulf", Applied Mathematical Modelling, **12**, pp. 379–390.
Lardner, R. W., Lehr, W. J., Fraga, R. J. and Sarhan, M. A. (1987), "Residual circulation in the Arabian Gulf. I: Density-driven flow", The Arabian Journal for Science and Engineering, **12**, No. 3, pp. 341–354.
Lardner, R. W. and Smoczynski, P. (1990), "A vertical/horizontal splitting algorithm for three-dimensional tidal and storm surge computations", Proceedings. Royal Society of London. Series A. Mathematical and Physical Sciences, **430**, No. 1879, pp. 263–283.
Leendertse, J. J. (1967), "Aspects of a computational model for long-period water-wave propagation", The Rand Corporation, Rpt. RM–5294–PR, 165 pp.
Leendertse, J. J. (1970), "A water-quality simulation model for well-mixed estuaries and

coastal seas: Volume I, Principles of Computation", The Rand Corporation, RM-6230-RC.

Leendertse, J. J., Alexander, R. C. and Liu, S-K. (1973), "A three-dimensional model for estuaries and coastal seas: Volume I, Principles of Computation", The Rand Corporation, R-1417-OWRR.

Leendertse, J. J. and Gritton, E. C. (1971), "A water-quality simulation model for well-mixed estuaries and coastal seas: Volume II, Computational Procedures", The Rand Corporation, R-708-NYC.

Leendertse, J. J. and Langerak, A. (1982), "Sensitivity of parameters and approximations in models of tidal propagation and circulation", Paper No. 151, Abstracts, 18th International Conference on Coastal Engineering, Capetown, 14–19 November 1982, pp. 297–298.

Lehr, W.J., Fraga, R. J., Belen, M. S. and Cekirge, H. M. (1984a), "A new technique to estimate initial spill size using a modified Fay-type spreading formula", Marine Pollution Bulletin, **15**, No. 9, pp. 326–329.

Lehr, W.J., Cekirge, H. M., Fraga, R. J. and Belen, M. S. (1984b), "Empirical studies of the spreading of oil spills", Oil & Petrochemical Pollution, **2**, No. 1, pp. 7–11.

Lennon, G. W. (1981), "Physical Oceanography", Paper 15 in "Draft Environmental Impact Statement for Port and Terminal Facilities at Stony Point, South Australia — Background Papers", SANTOS Limited, pp. 208–234.

Lennon, G. W. (1990), personal communication.

Lynch, D. R. and Gray, W. G. (1978), "Analytic solutions for computer flow model testing", Journal of the Hydraulics Division, American Society of Civil Engineers, **104**, No. HY10, pp. 1409-1428.

MACSYMA (REX) (1982), Release 309.5, M.I.T.

Maddock, L. and Pingree, R. D. (1978), "Numerical simulation of the Portland tidal eddies", Estuarine and Coastal Marine Science, **6**, pp. 353–363.

McCowan, A. D. and Blackman, D. R. (1988), "The equations for long waves and their application", in "Computational Techniques and Applications: CTAC-87", eds. J. Noye and C. Fletcher, Elsevier Science Publishers B. V. (North-Holland), pp. 475–486.

McGregor, R. C. (1972), "The influence of eddy viscosity on the vertical distribution of velocity in the tidal estuary", Geophysical Journal. Royal Astronomical Society, **29**, pp. 103–108.

McIntosh, P. (1985), personal communication.

Mellor, G. L. and Yamada, T. (1974), "A hierarchy of turbulence closure models for planetary boundary layers", Journal of the Atmospheric Sciences, **31**, pp. 1791–1806. (See also "Corrigenda", Journal of the Atmospheric Sciences (1977), **34**, p. 1482.)

Mellor, G. L. and Yamada, T. (1982), "Development of a turbulence closure model for geophysical fluid problems", Reviews of Geophysics and Space Physics, **20**, No. 4, pp. 851–875.

Miller, M. J. and Thorpe, A. J. (1981), "Radiation conditions for the lateral boundaries of limited-area numerical models", Quarterly Journal. Royal Meteorological Society, **107**, pp. 615–628.

Mitchell, W. M. (1985), personal communication.

Mitchell, W. L. and Noye, B. J. (1983), "Numerical predictions of tides and currents in

the Gulf of Carpentaria", Report to Marine Sciences and Technologies Scheme, Project 80-2027R, The University of Adelaide, South Australia.

Mitchell, W. L., Beard, D. A., Bills, P. J. and Noye, B. J. (1984), "An application of a three-dimensional tidal model to the Gulf of Carpentaria", in "Computational Techniques and Applications: CTAC-83", eds. J. Noye and C. Fletcher, Elsevier Science Publishers B. V. (North-Holland), pp. 411–424.

Natural Systems Research (1981), "Report on the Stony Point summer investigation: oil spill trajectory study — Cooper Basin liquids project", Published in Draft Environmental Impact Statement for port and terminal facilities at Stony Point, South Australia — Background Papers, Vol. 2, SANTOS Ltd., 26 pp.

Nihoul, J. C. J. (1975), "Marine systems analysis", in "Modelling of Marine Systems", ed. J. C. J. Nihoul, Elsevier Oceanography Series, **10**, Elsevier Scientific Publ. Co., pp. 3–39.

Nihoul, J. C. J. (1978), "Three-dimensional modelling of marine circulation", in "Applied Numerical Modelling", ed. C. A. Brebbia, Pentech Press, Southhampton, England, pp. 73–81.

Nihoul, J. C. J. and Ronday, F. C. (1976), "Hydrodynamic models of the North Sea: a comparative assessment", Memoires. Societe Royale des Sciences de Liege, 6^e série, tome X, pp. 61–96.

Nixon, J. (1992), "From minicomputer to supercomputer: optimization of a three-dimensional tidal model", to be published in "Computational Techniques and Applications: CTAC-91", eds. J. Noye, B. Benjamin and L. Colgan.

Noye, B. J. (1984a), "Finite difference techniques for partial differential equations", in "Computational Techniques for Differential Equations", ed. J. Noye, North-Holland Mathematics Studies No. 83, pp. 95–354.

Noye, B. J. (1984b), "Wave propagation characteristics of a numerical model of tidal motion", in "Computational Techniques and Applications: CTAC-83", eds. J. Noye and C. Fletcher, Elsevier Science Publishers B. V. (North-Holland), pp. 360–374.

Noye, B. J. (1984c), "Physical processes and pollution in the water of Spencer Gulf", Marine Geology, **61**, pp. 197–220.

Noye, B. J. (1986), "Finite difference methods for partial differential equations", Lecture notes, First Regional Workshop on Computational Mathematics, Centre for Quantitative Studies, National University of Malaysia, 24–28 November 1988, pp. 328+ references.

Noye, B. J. (1986), "Three-point two-level finite difference methods for the one-dimensional advection equation", in "Computational Techniques and Applications: CTAC-85", eds. J. Noye and R. May, Elsevier Science Publishers B. V. (North-Holland), pp. 159–192.

Noye, B. J. and Bills, P. J. (1990), "A three-dimensional tidal model for coastal seas", in "Proceedings of the Third Australian Supercomputer Conference", The University of Melbourne, Australia, December 3–6, 1990.

Noye, B. J. and Bills, P. J. (1992), "A three-dimensional tidal model for coastal seas", to be published in "Computational Techniques and Applications: CTAC-91", eds. J. Noye, B. Benjamin and L. Colgan.

Noye, B. J., Bills, P. J., I'Anson, K. and Wong, C.C. (1992), "Prediction of prawn larvae movement in a coastal sea", to be published in "Computational Techniques and Applications: CTAC-91", eds. J. Noye, B. Benjamin and L. Colgan.

Noye, B. J. and Hayman, K. J. (1986), "An accurate five-point explicit finite difference method for solving the one-dimensional linear diffusion equation", in "Computational Techniques and Applications: CTAC-85", eds. J. Noye and R. May, Elsevier Science Publishers B. V. (North-Holland), pp. 205–216.

Noye, B. J., May, R. L. and Teubner, M. D. (1981), "Three-dimensional numerical model of tides in Spencer Gulf", Ocean Management, **6**, pp. 137–147.

Noye, B. J., May, R. L. and Teubner, M. D. (1982), "A three-dimensional tidal model for a shallow gulf", in "Numerical Solutions of Partial Differential Equations", ed. J. Noye (North-Holland), pp. 417–436.

Noye, J. and Stevens, M. (1987), "A three-dimensional model of tidal propagation using transformations and variable grids", in "Three-Dimensional Coastal Ocean Models", Coastal and Estuarine Sciences **4**, ed. N. S. Heaps, American Geophysical Union, Washington, D. C., pp. 41–69.

Noye, B. J. and Tronson, K. C. S. (1973), "Numerical simulation of tides in the South Australian gulfs", in "Physical Oceanography", Proceedings Second South Australian Regional Conference, Department of Applied Mathematics, University of Adelaide, B. J. Noye Convenor, pp. 2–17.

Noye, B. J. and Tronson, K. C. S. (1978), "Finite difference techniques applied to the simulation of tides and currents in gulfs", in "Numerical Simulation of Fluid Motion", ed. J. Noye (North-Holland), pp. 285–356.

Orlanski, I. (1976), "A simple boundary condition for unbounded hyperbolic flows", Journal of Computational Physics, **21**, pp. 251–269.

Owen, A. (1980), "The tidal regime of the Bristol Channel: a numerical modelling approach", Geophysical Journal. Royal Astronomical Society, **62**, pp. 59–75.

Phillips, N. A. (1957), "A coordinate system having some special advantages for numerical forecasting", Journal of Meteorology, **14**, pp. 184–185.

Pingree, R. D. (1978), "The formation of the Shambles and other banks by tidal stirring of the seas", Journal of the Marine Biological Association of the United Kingdom, **58**, pp. 211–226.

Pingree, R. D. and Maddock, L. (1977a), "Tidal residuals in the English Channel", Journal of the Marine Biological Association of the United Kingdom, **57**, pp. 339–354.

Pingree, R. D. and Maddock, L. (1977b), "Tidal eddies and coastal discharge", Journal of the Marine Biological Association of the United Kingdom, **57**, pp. 869–875.

Platzmann, G. W. (1958), "A numerical computation of the surge of 26 June 1954 on Lake Michigan", Geophysica, **6**, pp. 407–438.

Prandle, D. (1978), "Residual flows and elevations in the southern North Sea", Proceedings. Royal Society of London. Series A. Mathematical and Physical Sciences, **359**, pp. 189–228.

Prandle, D. (1982a), "The vertical structure of tidal currents", Geophysical and Astrophysical Fluid Dynamics, **22**, pp. 29–49.

Prandle, D. (1982b), "The vertical structure of tidal currents and other oscillatory flows", Continental Shelf Research, **1**, No. 2, pp. 191–207.

Prandle, D. and Ryder, D. K. (1989), "Comparison of observed (HF radar) and modelled nearshore velocities", Continental Shelf Research, **9**, No. 11, pp. 941–963.

Proctor, R. (1987), personal communication.

Proudman, J. (1957), "Oscillations of tide and surge in an estuary of finite length", Journal of Fluid Mechanics, **2**, pp. 371–382.

Provis, D. G. and Lennon, G. W. (1983), "Eddy viscosity and tidal cycles in a shallow sea", Estuarine, Coastal and Shelf Science, **16**, pp. 351–361.

Ramming, H-G. and Kowalik, Z. (1980), "Numerical modelling of marine hydrodynamics: applications to dynamic physical processes", Elsevier Oceanography Series, **26**, 368 pp.

REDUCE, Release 3.3, 15-Jan-88.

Reid, R. O. and Bodine, B. R. (1968), "Numerical model for storm surges in Galveston Bay", Journal. Waterways and Harbors Division, American Society of Civil Engineers, **94**, No. WW1, pp. 34–57.

Rienecker, M. M. (1978), "Tidal Propagation in the Gulf of Carpentaria", Ph. D. thesis, The University of Adelaide, South Australia, 143 pp.

Rienecker, M. M. and Teubner, M. D. (1980), "A note on frictional effects in Taylor's problem", Journal of Marine Research, **38**, No. 2, pp. 183–191.

Roberts, K. V. and Weiss, N. O. (1966), "Convective Difference Schemes", Mathematics of Computation, **20**, pp. 272–299.

Rothlisberg, P. C., Church, J. A. and Forbes, A. M. G. (1983), "Modelling the advection of vertically migrating shrimp larvae", Journal of Marine Research, **41**, pp. 511–538.

Runchal, A. K. (1975), "Numerical model for storm surge and tidal run-up studies", in "Symposium on Modeling Techniques", Volume II, 2nd Annual Symposium of the Waterways, Harbors and Coastal Engineering Division of American Society of Civil Engineers, Sept. 3–5, 1975, pp. 1516–1534.

SANTOS Limited (1981), "Draft Environmental Impact Statement for Port and Terminal Facilities at Stony Point, South Australia", 295+ pp.

Schwiderski, E. W. (1980), "On charting global ocean tides", Reviews of Geophysics and Space Physics, **18**, No. 1, pp. 243–268.

Shemdin, O. H. (1972), "Wind-generated current and phase speed of wind waves", Journal of Physical Oceanography, **2**, pp. 411–419.

Sielecki, A. and Wurtele, M. G. (1970), "The numerical integration of the nonlinear shallow-water equations with sloping boundaries", Journal Computational Physics, **6**, pp. 219–236.

Simpson, J. H., Mitchelson-Jacob, E. G. and Hill, A. E. (1990), "Flow structure in a channel from an acoustic current Doppler profiler", Continental Shelf Research, **10**, No. 6, pp. 589–603.

Spaulding, M. L. (1974), "Laterally-integrated numerical water quality model", Paper 20 in "Numerical Methods in Fluid Dynamics", eds. C. A. Brebbia and J. J. Conner, Pentech Press, London.

Steedman, R. K. and Associates (1983), "Review of Northern Spencer Gulf water circulation and dispersion", prepared for the Department of Environment and Planning, South Australian Government, 89 pp.

Steinberg, C. R. (1983), "Tidal exchanges at the mouth of Spencer Gulf, South Australia", Honours thesis, Flinders University of South Australia, 79 pp.

Stevens, M. (1988), personal communication.

Stevens, M. W. (1990), "A Three-Dimensional Tidal Model for Shallow Waters using Transformations and Variably Spaced Grids", Ph.D thesis, The University of Adelaide, 247 pp.

Stevens, M. and Noye, J. (1984), "An improved three-dimensional tidal model for a shallow gulf", in "Computational Techniques and Applications: CTAC-83", eds. J. Noye

and C. Fletcher, Elsevier Science Publishers B. V. (North-Holland), pp. 375–393.
Sundqvist, H. and Veronis, G. (1970), "A simple finite-difference grid with non-constant intervals", Tellus XXII, **1**, pp. 26–31.
Tee, K-T. (1979), "The structure of three-dimensional tide-generating currents, Part I: Oscillating currents", Journal of Physical Oceanography, **9**, pp. 930–944.
Tee, K-T. (1987), "Simple models to simulate three-dimensional tidal and residual currents", in "Three-Dimensional Coastal Ocean Models", Coastal and Estuarine Sciences **4**, ed. N. S. Heaps, American Geophysical Union, Washington, D. C., pp. 125–147.
Teubner, M. D. (1976), "Tidal and thermal propagation in the Port River estuary", Ph. D. thesis, University of Adelaide, South Australia, 167 pp.
Thomas, L. H. (1949), "Elliptic problems in linear difference equations over a network", Watson Scientific Computing Laboratory, Columbia University, New York.
Trapp, J. A. and Ramshaw, J. D. (1976), "A simple heuristic method for analyzing the effect of boundary conditions on numerical stability", Journal of Computational Physics, **20**, pp. 238–242.
Tronson, K. (1974), "The hydraulics of the South Australian gulf system. I. Circulation", Australian Journal of Marine and Freshwater Research, **25**, pp. 413–26.
Tronson, K. (1975), "The hydraulics of the South Australian gulf system. II. Resonances", Australian Journal of Marine and Freshwater Research, **26**, pp. 363–74.
Vreugdenhil, C. B. and Booij, N. (1985), "Numerical outflow boundary conditions for the shallow-water equations", International Journal for Numerical Methods in Fluids, **5**, pp. 393–397.
Webber, B. (1980), "An analysis of naturally-induced water motion within both open and closed basins", M. Sc. thesis, University of Adelaide, South Australia, 190 pp.
Wolf, J. (1983), "A comparison of a semi-implicit with an explicit scheme in a three-dimensional hydrodynamic model", Continental Shelf Research, **2**, No. 4, pp. 215–229.
Wong, C. C. (1990), "Numerical simulation of prawn larvae dispersal in Spencer Gulf", Honours thesis, The University of Adelaide, pp. 125+
Wu, J. (1982), "Wind stress coefficients over sea surface from breeze to hurricane", Journal of Geophysical Research, **87**, pp. 9704–9706.
Zetler, Bernard D. (1991), "A necessary constraint on the use of extended harmonic analysis for tide predictions", International Hydrographic Review, Monaco, LXVIII(2), pp. 109–111.
Zimmerman, J. T. F. (1978), "Topographic generation of residual circulation by oscillatory (tidal) currents", Geophysical and Astrophysical Fluid Dynamics, **11**, pp. 35–47.